

**A Study on Natural Clay Decorated Self-Poled Polymeric
Membranes for Piezocatalytic Wastewater Remediation
and Piezoelectric Energy Harvesting**

Thesis submitted to

Jadavpur University



By

Dhananjoy Mondal

In partial fulfilment of the requirements for the degree of

Doctor of Philosophy (Ph.D.) in Science

Department of Physics

Jadavpur University

Jadavpur, Kolkata-700032

West Bengal, India

2024

যাদবপুর বিশ্ববিদ্যালয়
কলকাতা-৭০০০৩২, ভারত

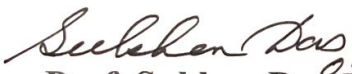


JADAVPUR UNIVERSITY
KOLKATA-700032, INDIA

FACULTY OF SCIENCE : DEPARTMENT OF PHYSICS


Certificate from the Supervisors

This is to certify that the thesis entitled "*A Study on Natural Clay Decorated Self-Poled Polymeric Membranes for Piezocatalytic Wastewater Remediation and Piezoelectric Energy Harvesting*" Submitted by Mr. Dhananjoy Mondal who got his name registered on 08/03/2022 (Index no.: **89/22/Phys./27** & Registration Number: **SOPHY1208922**) for the award of Ph.D. (Science) Degree of Jadavpur University, is absolutely based upon his own work under the supervision of Prof. Sukhen Das and Dr. Soumyaditya Sutradhar and that neither this thesis nor any part of it has been submitted for either any degree/diploma or any other academic award anywhere before.


Prof. Sukhen Das 05/04/2024
Professor
Department of Physics
Jadavpur University



Prof. Sukhen Das
Department of Physics,
Jadavpur University
Kolkata - 700 032


Dr. Soumyaditya Sutradhar 05/04/2024
Assistant Professor
Department of Physics
Jadavpur University



Dr. Soumyaditya Sutradhar
Assistant Professor
Department of Physics
Jadavpur University
Kolkata-700032

* Established on and from 24th December, 1955 vide Notification No.10986-Edn/IU-42/55 dated 6th December, 1955 under Jadavpur University Act, 1955 (West Bengal Act XXXIII of 1955) followed by Jadavpur University Act, 1981 (West Bengal Act XXIV of 1981)

ফোন : +৯১-৩৩-২৪১৩-৮৯১৭
ফ্যাক্স : +৯১-৩৩-২৪১৩-৮৯১৭

Website : www.jadavpur.edu

Phone : + 91-33-2413-8917
Fax : + 91-33-2413-8917



Certificate of Similarity Check

This is to certify that the plagiarism checking for this thesis entitled "A Study on Natural Clay Decorated Self-Poled Polymeric Membranes for Piezocatalytic Wastewater Remediation and Piezoelectric Energy Harvesting" authored by Mr. Dhananjay Mondal has been performed using professional plagiarism prevention software iThenticate. According to the report generated after plagiarism checking there is 03 % similarity in this thesis, which is in the category "Level 0" (minor similarities) as per the "Promotion of Academic Integrity and Prevention of Plagiarism in Higher Education Institutions Regulations, 2018" of the University Grand Commission (UGC) of India. The common knowledge or coincidental terms up to 10 (ten) consecutive words [as prescribed in UGC Regulation up to 14 (fourteen) terms can be excluded] and own works of the candidate published in various peer-reviewed journals (those are attached in the thesis) are excluded from the similarity checking. It is certified that the present thesis submitted by Mr. Dhananjay Mondal is plagiarism-free and has followed standard norms of academic integrity and scientific ethics.


Prof. Sukhen Das 05/04/2024

Professor
Department of Physics
Jadavpur University



Prof. Sukhen Das
Department of Physics,
Jadavpur University
Kolkata - 700 032


Dr. Soumyaditya Sutradhar 05/04/2024

Assistant Professor
Department of Physics
Jadavpur University



Dr. Soumyaditya Sutradhar
Assistant Professor
Department of Physics
Jadavpur University
Kolkata-700032

*To my
“Family” & “Supervisors”*

Abstract

A Study on Natural Clay Decorated Self-Poled Polymeric Membranes for Piezocatalytic Wastewater Remediation and Piezoelectric Energy Harvesting

Dhananjoy Mondal

Index No.: 89/22/Phys./27

Registration No.: SOPHY1208922

Abstract: In recent years, increasing population, urbanization, and industrialization have caused an energy crisis and fatal water pollution levels, which have harmed the ecological balance. Organic pollutants like carcinogenic dyes and pharmaceuticals are discharged from various industries creating a deficiency of potable water and harming the waterbodies. Researchers are putting efforts into different technologies for combating such issues. Different nanomaterials are gaining interest owing to their functionality in the nano regime. Conventional piezo-responsive nanomaterials have come in the front row in the last few decades for their capability in energy generation and wastewater remediation under mechanical stress. However, these types of chemically derived nanomaterials are suffering from biocompatibility, toxicity, and extraction from the medium. In order to fix these issues scientists and technologists are trying to develop various types of membrane-based piezocatalyst exploiting the conventional piezo-materials. However, a minimal amount of interest has been paid so far on natural material-based piezocatalysts. Keeping this in mind the present work focuses on the development of natural clay-based (Kaolinite, Aluminosilicate clay namely China clay) polymeric piezocatalyst for energy generation from external stimulus and simultaneous wastewater remediation. In this work, several techniques i.e., nanonization, structural modification, and foreign element incorporation have been used to enhance the physicochemical properties of the natural clays to develop polymeric piezocatalysts. Kaolinite poses very good surface properties i.e., high surface charge and surface area which enhances the piezo-response of the Polyvinylidene fluoride (PVDF, a potential fluoropolymer that is synthetic in nature), and Chitosan (a biopolymer). Polymer-based (PVDF & chitosan) clay nanocomposites successfully eradicated 96 % rhodamine B (RhB), and 88 % Congo red organic dyes under ultrasound (33 kHz) in 1 h. Piezoelectric nanogenerator device (PENG) has also been fabricated by these nanocomposite membranes which generate the highest 6.5 V, 1.5 μ A

(PVDF-based), and 34.6 V, 1.9 μ A (chitosan-based) output responses, respectively corresponding to the thrust of falling water droplets (force 4.79 N) and the impact of hand tapping (force 14.97 N) as mechanical stress. Additionally, the catalytic behavior of the membranes has also been used to eradicate pathogenic coliform *E. coli* (gram-negative) and *E. faecalis* (gram-positive) bacteria which are other available pollutants of wastewater, and found the efficiency of 100 % and 97 % under soft ultrasound (15 KHz) in less than an hour. Henceforth, these energy generation and wastewater eradication abilities of the fabricated biocompatible, cost-effective, self-poled polymer-based nanocomposite membranes can open up new avenues for the sustainable development of our nation in the field of wastewater treatment and non-invasive energy generation technologies.

Acknowledgement

On a beautiful summer morning in 2014, I stepped foot onto the Jadavpur University campus for the first time with my mama, brimming with dreams of completing my bachelor's degree in physics here. After that, I completed both my bachelor's and master's degrees from this university with the guidance of all the faculties in the Department of Physics. During my M.Sc. I first entered the lab of Prof. Sukhen Das for my M.Sc. dissertation. The environment of the lab, behaviour, and knowledge of seniors first struck my mind to engage me in research to get a Ph.D. Degree. With a mix of curiosity and anxiety, I embarked on what would become a transformative five-year journey. As the days went on, it became evident that this journey would not be very easy and I owe a debt of gratitude to the professors of the Physics Department who supported me along the way. I am deeply thankful for the guidance and mentorship of individual Professors like Sanjay Kumar, Jaydeep Chowdhury, Partha Pratim Ray, Debasish Biswas, Kaustuv Das, Argha Deb, Saikat Kumar Saith, Pabitra Kumar Paul, Nabin Baran Manik, and Professor Mitali Mondal whose invaluable assistance enriched my academic experience immeasurably.

In 2020, I decided to pursue my Ph.D. under the guidance of Professor Sukhen Das in the Biophysics Laboratory, Department of Physics, Jadavpur University. He has supported me all the time during my Ph.D. journey with his knowledge and financial support and engaged Dr. Soumyaditya Sutradhar (Soumya Da) as my Co-supervisor. I am grateful to both of my supervisors for their immense support and will remain grateful to them for the rest of my life. There I had the privilege of meeting, Prof. Papiya Nandy, Late Prof. Ashesh Nandy, Dr. Ruma Basu, Professor Tarakdas Basu, and Dr. Sarajit Manna. Their insights, advice, and extensive collaborations proved invaluable, supporting me at every turn throughout this academic journey. Their contributions have left an indelible mark, and I will forever be grateful to them.

The Physics Department of Jadavpur University played a pivotal role, extending their instrumental facilities and sharing their diverse knowledge throughout the process. Their doors were always open, helping and guidance whenever I needed. I also received invaluable support from Professor Chiranjib Bhattacharjee, Pro-Vice-Chancellor of Jadavpur University, Professor Subenoy Chakraborty, Dean of the Faculty Council of Science, and Dr. Rajat Ray, Dean of Students, who aided me in various official matters

and encouraged my participation in numerous national and international competitions. Our team achieved second place in Anveshan 2022 at the zonal level.

In the initial stages of my Ph.D., I encountered some challenges, but I was fortunate enough to receive help from Shubham Da who was beside me during all the ups and downs of my journey. The seniors like Tanumay Da, Nur Da, Biplab Da, Dheeraj Da, Souravi Di, Rituparna Di, Shilpa Di, Anupam Da, Subha Di, Debbithi Di, Satarupa Di, Minarul Da, Prosenjit da, Arpan Da, Somtirtha Di, and Somen Da helped me very much in this journey. Their warmth and assistance were constant sources of my motivation, and they generously shared their wisdom and experience. Additionally, they provided training in operating various high-end machines, which not only deepened my research interests but also fostered a warm relationship among us.

I would like to thank all my lab mates Saheli di, Tanmoy, Aliva, Subhojit, Manisha di, Debmalya da, Namrata di, Souvik da, Sanghita di, Solanky, who have also become my strong support these days for staying beside me and showing respect towards me. I feel very proud to meet the juniors like Jhilik, Anwesha Dey, Neelanjana, Suman, Indrajit, Piyali, Manisha, Anwesha Mukherjee, Anuja, Sumana, Shriparna, Leenia, Barsha, Jaba, Amartya, Parama, and Ayan.

I found various people from different departments of this university who were ready to help whenever I needed them. Panchanan, Sudip, Ishita Di, Saikat da, Swarup da, Bhaskar, Mainak da, Moishili Di, and Dhananjay da, helped me with their experimental and computational facilities in difficult times, which I will never forget. Especially, Dr. Dipak Chanda was always there for me. I would like to take the opportunity to express my feelings to him. My instrument and chemical suppliers had never let me down. I would like to thank Monoranjana Babu, Pathak, Sarada Glass and Ceramics, and Krick Enterprise for their tremendous support and timely delivery. As I take an interest in food, my Ph.D. journey would be incomplete if I did not thank Joydeb da, Abhijit Da, Mama, Hara da, and Milan da. I am thankful to the DST-SERB and UGC-DAE-CSR fellowships to continue my research work. I also want to thank Dr. Souvik Chatterjee, Dr. Rajib Mondal, and Dr. Goutam Pramanik from the UGC-DAE-CSR Kolkata centre. Additionally, I want to thank all the office staff and members of my beloved department and Ph.D. cell of this university for helping me whenever needed.

Throughout this entire journey, there is one name that stands out and resonates deeply with me: Anima (Anu), my wife. Her influence has been profound, shaping both my personal and professional life. Her unwavering support has been a pillar of strength throughout this journey. Furthermore, I want to extend my heartfelt gratitude to my family (Mama, Mami, Dida, Thakurda, Thakuma, Debu, and Manu). Amidst the demands of my busy schedule, they stood by me with understanding and encouragement. To my parents (Bapu, Maa), I owe a debt of gratitude for accepting me unconditionally and for their countless sacrifices and unwavering support. A heartfelt "Thank you" hardly seems enough to express the depth of my appreciation.

Dhananjay Mondal.

DHANANJOY MONDAL

CONTENTS

ABBREVIATION.....	i
LIST OF PUBLICATIONS.....	iii
LIST OF SEMINARS ATTENDED.....	vii
LIST OF FIGURES.....	ix
LIST OF TABLES.....	xvii

Chapter 1: Introduction

1.1 History of Wastewater remediation and energy generation at the international level.....	5
1.2 History of wastewater remediation and energy generation at the national level... 	8
1.3 Nanotechnology in wastewater remediation and non-invasive energy generation. 	10
1.4 Piezo response in nanomaterials.....	13
1.5 Mechanism of piezoelectric energy generation.....	15
1.6 Mechanism of piezocatalytic wastewater remediation.....	16
1.6.1 Screening charges effect.....	16
1.6.2 Effect of energy band edge tilting.....	18
1.7 Piezocatalytic wastewater remediation and piezoelectric energy generation.....	19
1.8 Aims and Objectives.....	27
1.8.1 Selection of nanomaterials.....	28
1.8.2 Organization of the Thesis.....	29

1.9 Methodology.....	29
1.9.1 General synthesis procedure of nano kaolinite.....	29
1.10 Characterizations and experiments of the samples.....	30
1.10.1 Structural, morphological, and elemental characterizations.....	30
1.10.2 Surface Properties Investigation of the natural kaolinite.....	33
1.10.3 Estimation of the thermal stability of the materials.....	34
1.10.4 Electrical properties investigation of the samples.....	35
1.10.5 Estimation of piezoelectric performance of the nanocomposite	
Membranes.....	38
1.10.6 Piezocatalytic wastewater remediation by optical instruments.....	40
1.10.7 Antimicrobial assessment studies of the membranes.....	43
1.10.8 Biocompatibility study of the nanocomposites.....	44
1.11 General summary.....	45
 <i>Chapter 2: Investigation of Different Physicochemical Properties of Natural Kaolinite Clay by Particle Size Modulation.</i>	
2.1 Introduction.....	59
2.2 Experimental Details.....	60
2.3 Result and Discussions.....	61

2.3.1 Purity and elemental analysis of bulk kaolinite.....	61
2.3.2 Determination of crystalline structure and microstructural properties of treated kaolinite samples.....	62
2.3.3 Spectroscopic study and bonding network analysis.....	65
2.3.4 Morphological studies and particle size analysis.....	66
2.3.5 Surface area and porosity analyses.....	66
2.3.6 Thermal characterization of the natural materials.....	68
2.3.7 Estimation of dielectric constant and loss tangent of the synthesized samples.....	69
2.3.8 AC conductivity and conduction mechanism studies.....	72
2.3.9 Impedance spectroscopy for materials.....	74
2.3.10 Estimation of specific capacitance and charge-discharge characteristics...	75
2.4 Summary.....	77
 <i>Chapter 3: Synergistic Impact on the Microstructure and Physicochemical Properties of Nano-Kaolinite Upon MWCNT Incorporation and Basal Plane Intercalation</i>	
3.1 Introduction.....	83
3.2 Experimental Details.....	84
3.2.1 Materials.....	84

3.2.2 Synthesis method.....	84
3.2.2.1 Activated nano-kaolinite synthesis (A. K).....	84
3.2.2.2 Intercalated Kaolinite Synthesis (I. K).....	85
3.2.2.3 Functionalization of multiwall carbon nanotube.....	85
3.2.2.4 Preparation of MWCNT-kaolinite nanocomposite (CK).....	85
3.3 Result and Discussions.....	86
3.3.1 Structural, morphological, and elemental properties of the nanocomposites.....	86
3.3.2 Surface properties and stability of the NPs and their modified counterparts.....	93
3.3.3 Thermal stability of the nanocomposites.....	96
3.3.4 Dielectric assays of the clay samples.....	96
3.3.5 Investigation of AC conductivity of the nanocomposites.....	99
3.4 Summary.....	101
 <i>Chapter 4: Optimizing Polarizability and Charge Storage Capacity through Varying MWCNT Concentration in Nano-Kaolinite.</i>	
4.1 Introduction.....	107
4.2 Experimental Details.....	108

4.2.1 Materials.....	108
4.2.2 Synthesis of MWCNT-kaolinite nanocomposite (CK).....	108
4.3 Result and Discussion.....	109
4.3.1 Structural, morphological, and elemental properties of the nanocomposites	109
4.3.2 Surface properties and stability of the nanocomposites.....	116
4.3.3 Dielectric assays of the clay nanocomposites.....	117
4.3.4 Investigation of AC conductivity of the nanocomposites.....	118
4.3.5 Estimation of the effect of microstructure on charge transport for percentage MWCNT doping.....	122
4.3.6 Estimation of the electrochemical performances of the clay samples by percentage-dependent MWCNT doping.....	124
4.4 Summary.....	126
 <i>Chapter 5: Exploring Piezocatalytic Wastewater Remediation and Piezoelectric Energy Generation in MWCNT-Integrated Kaolinite decorated poly (vinylidene fluoride-co- hexafluoropropylene) Membranes</i>	
5.1 Introduction.....	133
5.2 Experimental section.....	134
5.2.1 Materials.....	134

5.2.2 Synthesis of Nanocomposite Membranes.....	134
5.3 Results and Discussion.....	136
5.3.1 Structural and Morphological & Elemental Analyses of the Nanocomposites	136
5.3.2 Estimation of polarity and piezo-effectiveness of the nanocomposite Membranes.....	140
5.3.3 Piezoelectric energy generation.....	149
5.3.4 Eradication Efficiency of Rhodamine B.....	150
5.3.5 Inhibition of pathogenic bacteria.....	152
5.4 Summary.....	158
 <i>Chapter 6: Development of Chitosan Biopolymeric Membranes-based Piezocatalyst and Energy Harvester by Incorporating Structurally Modulated & 1% MWCNT-doped Kaolinite Clay Nanoparticles.</i>	
6.1 Introduction.....	165
6.2 Experimental Details.....	166
6.2.1 Materials.....	166
6.2.2 Synthesis of modified-kaolinite and chitosan nanocomposite membranes.	166
6.3 Result and Discussion.....	167
6.3.1 Determination of the physicochemical features of the bio-polymeric	

membranes.....	167
6.3.2 Electrical and piezoelectric properties of the bio-nanocomposites.....	172
6.3.3 Degradation of organic dyes.....	176
6.3.4 Pathogenic <i>E. coli</i> decomposition.....	180
6.4 Summary.....	181
<i>Chapter 7: Conclusions and outlooks</i>	<i>187</i>
Appendices	c
Publications and Seminar certificates	

ABBREVIATIONS

DTA-	Differential Thermal Analyzer
TGA-	Thermogravimetric Analyzer
KeV-	Kilo electron volt
XRD-	X-ray diffraction
FTIR-	Fourier Transform Infrared Spectroscopy
FESEM-	Field Emission Scanning Electron Microscope
TEM-	Transmission Electron Microscope
kV-	Kilovolt
1D-	1- dimensional
JCPDS-	Joint Committee on Powder Diffraction Standards
ϵ' -	Dielectric permittivity
σ_{ac} -	AC Conductivity
E_a -	Activation energy
C_v -	Specific capacitance
d_{33} -	Piezoelectric Coefficient
P-E loop	Polarization-Electric field loop
PL-	Photoluminescence
UV-	Ultra Violet
EDS-	Energy-Dispersive X-ray Spectrometer
VESTA-	Visualization for Electronic and Structural Analysis
DFT-	Density Functional Theory
ROS-	Reactive Oxygen Species
RhB-	Rhodamine B
<i>E. coli</i> -	<i>Escherichia coli</i>
<i>S. aureus</i> -	<i>Staphylococcus aureus</i>

LIST OF PUBLICATIONS

Thesis publications:

- [1] Das, S., **Mondal, D.**, Bardhan, S., Roy, S., Chanda, D.K., Maity, A., Dutta, S., Mukherjee, K. and Das, K., 2022. Particle size mediated investigation of various physicochemical properties of kaolinite clay for fabricating the separator layer of green capacitors. *Journal of Materials Science: Materials in Electronics*, 33(9), pp.7119-7133.
- [2] **Mondal, D.**, Roy, S., Bardhan, S., Das, R., Maity, A., Chanda, D.K., Das, S., Ghosh, S., Basu, R. and Das, S., 2022. Effect of microstructural evolution of natural kaolinite due to MWCNT doping: a futuristic ‘green electrode’ for energy harvesting applications. *Journal of Materials Science: Materials in Electronics*, pp.1-17.
- [3] **Mondal, D.**, Roy, S., Bardhan, S., Roy, J., Kanungo, I., Basu, R. and Das, S., 2022. Recent advances in piezocatalytic polymer nanocomposites for wastewater remediation. *Dalton Transactions*.
- [4] **Mondal, D.**, Bardhan, S., Das, N., Roy, J., Ghosh, S., Maity, A., Roy, S., Basu, R. and Das, S., Natural clay-based reusable piezo-responsive membrane for water droplet mediated energy harvesting, degradation of organic dye and pathogenic bacteria. *Nano Energy*. doi.org/10.1016/j.nanoen.2022.107893
- [5] **Mondal, D.**, Sau, A., Roy, S., Bardhan, S., Roy, J., Ghosh, S., Basu, R., Sutradhar, S. and Das, S., 2023. Functionalized MWCNT-integrated natural clay nanosystem: a promising eco-friendly capacitor for energy storage applications. *Journal of Materials Science: Materials in Electronics*, 34(21), p.1597.
- [6] **Mondal, D.**, Bag, N., Roy, J., Ghosh, S., Roy, S., Sarkar, M., Bardhan, S., Sutradhar, S. and Das, S., 2024. Natural Clay-Modified Piezocatalytic Membrane for Efficient Removal of Coliform Bacteria from Wastewater. *Langmuir*.

Co-author publications:

- [7] Bardhan, S., Roy, S., Das, S., Saha, I., **Mondal, D.**, Roy, J., Chanda, D.K., Das, S., Karmakar, P. and Das, S., 2022. Real-time sensitive detection of Cr (VI) in industrial wastewater and living cells using carbon dot decorated natural kyanite

nanoparticles. *Spectrochimica Acta Part A: Molecular and Biomolecular Spectroscopy*, 273, p.121061.

[8] Ghosh, B., Roy, S., Bardhan, S., **Mondal, D.**, Saha, I., Ghosh, S., Basu, R., Karmakar, P., Das, K. and Das, S., 2022. Biocompatible carbon dot decorated α -FeOOH nanohybrid for an effective fluorometric sensing of Cr (VI) in wastewater and living cells. *Journal of Fluorescence*, pp.1-12.

[9] Roy, J., Mukhopadhyay, L., Bardhan, S., **Mondal, D.**, Ghosh, S., Chakroborty, S, Bag, N., Roy, S., Basu, R., and Das, S., Piezo-responsive bismuth ferrite nanoparticles mediated catalytic degradation of rhodamine-B and pathogenic E. coli in aqueous medium and its extraction using external magnetic stimulation after successful treatment. *Dalton Transactions*. doi.org/10.1039/D2DT02918A

[10] Roy, S., Bardhan, S., **Mondal, D.**, Saha, I., Roy, J., Das, S., Chanda, D.K., Karmakar, P. and Das, S., 2021. Polymeric carbon dot/boehmite nanocomposite made portable sensing device (Kavach) for non-invasive and selective detection of Cr (VI) in wastewater and living cells. *Sensors and Actuators B: Chemical*, 348, p.130662.

[11] Ghosh, S., Roy, S., Bardhan, S., Khatua, N., Bhowal, B., Chanda, D.K., Das, S., **Mondal, D.**, Basu, R. and Das, S., 2021. Effect of size fractionation on purity, thermal stability and electrical properties of natural hematite. *Journal of Electronic Materials*, 50(7), pp.3836-3845.

[12] Bardhan, S., Roy, S., Chanda, D.K., **Mondal, D.**, Das, S. and Das, S., 2021. Flexible and reusable carbon dot decorated natural microcline membrane: a futuristic probe for multiple heavy metal induced carcinogen detection. *Microchimica Acta*, 188(4), pp.1-12.

[13] Roy, S., Bardhan, S., Chanda, D.K., Roy, J., **Mondal, D.** and Das, S., 2020. In situ-grown Cdot-wrapped Boehmite nanoparticles for Cr (VI) sensing in wastewater and a theoretical probe for chromium-induced carcinogen detection. *ACS Applied Materials & Interfaces*, 12(39), pp.43833-43843.

[14] Roy, S., Bardhan, S., Chanda, D.K., Maity, A., Ghosh, S., **Mondal, D.**, Singh, S. and Das, S., 2020. Cu (II) and Gd (III) doped boehmite nanostructures: a comparative study of electrical property and thermal stability. *Materials Research Express*, 7(2), p.025020.

- [15] Bardhan, S., Roy, S., Chanda, D.K., Ghosh, S., **Mondal, D.**, Das, S. and Das, S., 2020. Nitrogenous carbon dot decorated natural microcline: an ameliorative dual fluorometric probe for Fe 3+ and Cr 6+ detection. *Dalton Transactions*, 49(30), pp.10554-10566.
- [16] Roy, S., Bardhan, S., Chanda, D.K., Ghosh, S., **Mondal, D.**, Roy, J. and Das, S., 2020. Development of a Cu (II) doped boehmite based multifunctional sensor for detection and removal of Cr (VI) from wastewater and conversion of Cr (VI) into an energy harvesting source. *Dalton Transactions*, 49(20), pp.6607-6615.
- [17] Ghosh, S., **Mondal, D.**, Roy, S. and Das, S., 2023. Recent advances in the synthesis and biomedical applications of α -hematite nanoparticles. *Sayam-A Journal of Science*, 1(1), pp.01-08.
- [18] Ghosh, S., Bardhan, S., **Mondal, D.**, Sarkar, D., Roy, J., Roy, S., Basu, R. and Das, S., 2023. Natural hematite-based self-poled piezo-responsive membrane for harvesting energy from water flow and catalytic removal of organic dye. *Ceramics International*, 49(9), pp.14710-14718.
- [19] Bag, N., Bardhan, S., Roy, S., Roy, J., **Mondal, D.**, Guo, B. and Das, S., 2023. Nanoparticle-mediated stimulus-responsive antibacterial therapy. *Biomaterials Science*, 11(6), pp.1994-2019.
- [20] Ghosh, S., Choudhury, N., Dutta, D., **Mondal, D.**, Paul, M.C., Das, S., 2023. Insitu Development of AuNPs with a Nanocavity on the Surface of Optical Fibre for use in SPR Sensor Applications. *Ceramics International*.
- [21] Banerjee, A., Mukherjee, A., Bag, N., Halder, P., Mondal, I., Roy, J., **Mondal, D.**, Bardhan, S., Majumdar, A. and Das, S., 2024. Ultrasonic vibration-assisted enhanced antibacterial activity of ZnO/Chitosan bio-nanocomposite. *Journal of Molecular Structure*, 1298, p.136996.
- [22] Roy, J., Roy, S., **Mondal, D.**, Bag, N., Chowdhury, J.R., Ghosh, S., Bardhan, S., Mondal, R., Basu, R. and Das, S., 2024. Gd-doped bismuth ferrite nanocomposite: A promising candidate for piezocatalytic degradation of organic dyes and pathogenic E. coli. *Surfaces and Interfaces*, 44, p.103579.

[23] Bag, N., Roy, J., **Mondal, D.**, Ghosh, S., Bardhan, S., Roy, S., Bhandary, S. and Das, S., 2024. Utilization of experimental and theoretical piezoresponse of BTO nanocrystal for rapid decomposition of the pathogenic coliform bacteria. *Ceramics International*, 50(5), pp.7998-8009.

[24] Ghosh, S., **Mondal, D.**, Roy, S., Roy, J., Bardhan, S., Mazumder, A., Bag, N., Basu, R. and Das, S., 2023. Water flow and finger-tapping mediated piezoelectric energy generation using a natural hematite-based flexible PVDF-HFP membrane. *Journal of Materials Chemistry C*, 11(39), pp.13418-13428.

[25] Roy, J., **Mondal, D.**, Chowdhury, J.R., Bag, N., Ghosh, S., Roy, S., Mondal, R., Basu, R. and Das, S., 2024. Enhanced piezocatalytic activity of BiFeO₃ incorporated PVDF-HFP membrane for efficient degradation of carcinogenic industrial pollutant. *Ceramics International*.

[26] Chakraborty, T., Saha, S., Gupta, K., Dutta, S., Sinha M. A., **Mondal, D.**, Pradhan, A. K., Chakraborty, C., Das, S., Sutradhar, S., 2024. An Effective Microwave Absorber Using Multi-Layer Design of Carbon Allotrope based Co₂Z hexaferrite-Polymer Nanocomposite Film for EMI Shielding Applications. *Chemical Engineering Journal*.

Book Chapter:

[27] Bardhan, S., **Mondal, D.**, Roy, J., Das, S., Roy, S., Das, S., Polymeric thin film fabrication for colorimetric, ratiometric, and fluorometric detection of hazardous industrial effluents in wastewater.

LIST OF SEMINARS ATTENDED

[1] National Seminar on New Directions in Physical Sciences 2020 (NDPS 2020).

Poster on: “Multifunctional Fluorescence-based Nanosensor for Detection and Removal of Cr (VI), **Dhananjoy Mondal**, Souravi Bardhan, Shubham Roy, Sukhen Das, Jadavpur University, Department of Physics.

[2] DST-SERB Sponsored One Day Workshop on Material Synthesis and Characterization Techniques, Paper entitled “Crystallographic Analysis”, **Dhananjoy Mondal**, Jadavpur University, Department of Physics, 29th February, 2020.

[3] 7th International Conference on Nanoscience and Nanotechnology – ICONN 2023 (Virtual Conference) Poster on: “MWCNT doped natural clay: A promising separator material for energy storage application” **Dhananjoy Mondal**, Amartya Sau, Shubham Roy, Saheli Ghosh, Jhilik Roy, Ruma Basu, Sukhen Das, Department of Physics and Nanotechnology, SRM Institute of Science and Technology, 27 March, 2023-29 March, 2023.

[4] Second prize in Basic sciences category at Anveshan-2022, National research convention, Oral and Poster: “‘Vikram’: An ‘all-in-one’ module for combating water pollution and energy crisis” **Dhananjoy Mondal**, Jhilik Roy, Saheli Ghosh, Royal Global University, Assam, 1st and 2nd march 2023.

[5] Anveshan-2022, National research convention, Oral and Poster: “‘Vikram’: An ‘all-in-one’ module for combating water pollution and energy crisis” **Dhananjoy Mondal**, Jhilik Roy, Saheli Ghosh, Ganpat University, Gujrat, 17th and 18th march, 2023.

[6] A one-day seminar in commemoration of centenary birth anniversary of Prof. Shyamal Sengupta, Poster: “Natural rock-based polymeric membrane: an “all-in-one” module for combating water pollution and energy crisis” Anwesha Dey, Dhananjoy Mondal, Saheli Ghosh, Sukhen Das, Jadavpur University, WB, 7th february, 2024.

LIST OF FIGURES

Chapter 1

Figure 1.1. *a) Effect of industrial toxic dyes, b) Effect of coliform bacteria*

Figure 1.2. *Indus Valley civilization wastewater technology: (a) Drainage system and (b,c) sanitation systems.*

Figure 1.3. *Categories and profits of different nanomaterials membrane bioreactor (NMs-MBR) technology with ahistorical timeline for wastewater management*

Figure 1.4. *Induced piezo-polarization under mechanical stress*

Figure 1.5. *Schematic diagram of piezoelectric polarization and energy generation*

Figure 1.6. *Mechanism of piezocatalytic reactive oxygen species generation: (a) Screening charge effect, (b) Energy band tilting, (c) Catalysis schematic diagram, and (d) Nanocomposite membrane-based ROS production.*

Figure 1.7. *X-ray diffractogram (XRD) facility of Jadavpur University, Department of Physics.*

Figure 1.8. *Fourier transform Infrared Spectroscopy (FTIR) facility of Jadavpur University, Department of Physics.*

Figure 1.9. *Field Emission Scanning Electron Microscopy facility of Jadavpur University, Department of Physics.*

Figure 1.10. *Transmission Electron Microscopy (TEM), Jadavpur University.*

Figure 1.11. *Thermogravimetric analysis (TGA), Differential Thermal Analysis (DTA) facility of Jadavpur University, Department of Physics*

Figure 1.12. *LCR-meter facility of Jadavpur University, Department of Physics*

Figure 1.13. *a) Digital Storage Oscilloscope (DSO) (X 3012 A, Keysight), b) DAQ6510, Keithley data acquisition multimeter system, Jadavpur University, Department of Physics.*

Figure 1.14. *UV-Vis Spectroscopy facility of Jadavpur University, Department of Physics.*

Figure 1.15. *Photoluminescence (PL) Spectrophotometer of Jadavpur University, Department of Physics.*

Figure 1.16. Portrays the mechanism of ROS-mediated bacterial damage, disruption of the membrane integrity, and simultaneous leakage of cytosol.

Chapter 2

Figure 2.1. Synthesis of different kaolinite size fractions.

Figure 2.2. Elemental mapping data of the kaolinite samples showing the presence of Al, Si, and O in the samples

Figure 2.3. **a–c** Indexed XRD pattern (red line) of the sample K1, K2, and K3, and the simulated Rietveld refinement plot (continuous black line) obtained by fitting the experimental PXRD pattern using the MAUD program. The respective residue is plotted at the bottom (blue line); **d–f** bond angles and bond lengths of K1, K2, and K3, respectively, from refinement data; **g–i** Separation of alumina-silica layers in K1, K2, and K3, respectively.

Figure 2.4. Normalized FTIR spectra of the samples K1, K2 and K3

Figure 2.5. FESEM micrographs of the samples a) K1, b) K2, and c) K3, corresponding size distribution plots from the FESEM images (d–f).

Figure 2.6. N₂ adsorption/desorption isotherms of the samples a) K1, b) K2, and c) K3; Pore size distribution data for d) K1, e) K2, and f) K3.

Figure 2.7. (a) DTA and (b) TGA data of the samples

Figure 2.8. Variation of the dielectric constants with frequency (a–c); Variation of the dielectric constants with temperature (d–f); Variation of the loss tangent with frequency (g–i) of K1, K2, and K3, respectively.

Figure 2.9. AC conductivities of K1, K2, and K3 respectively.

Figure 2.10. a) Jonscher's plot for ensuring the conduction mechanism of the kaolinite samples; b–d) Arrhenius plots for estimating the activation energies of the samples.

Figure 2.11. Impedance plots are experimental and fitted of a) K1, b) K2, and c) K3, respectively, with equivalent circuits.

Figure 2.12. Cyclic voltammetry analysis of K1 and K3 showing the charge storage capacity of the natural samples

Figure 2.13. galvanostatic charge-discharge characteristics of K1 (a, b) and K3 (c, d)

Chapter 3

Figure 3.1. Schematic representation of MWCNT incorporated nanoparticle synthesis via modification and without modification of primary nanoparticles.

Figure 3.2. XRD and theoretical Rietveld refinement data of a) activated kaolinite, b) intercalated kaolinite, c) 1% functionalized MWCNT incorporated activated kaolinite, and d) 1% bare MWCNT incorporated pristine kaolinite.

Figure 3.3. Theoretical refined structures of nanoparticles by VESTA software after refinement: a) A.K, b) I.K, c) CK1, and d) CKM1.

Figure 3.4. a) FTIR spectra of the synthesized NPs, b) Magnified FTIR spectra of CK1 and K3 NPs, and c) Schematic representation of basal and prism planes of kaolinite with electronegative -NH₂ group interaction.

Figure 3.5. Schematic representation of -CONH bond formation and attachment of functionalized MWCNT with activated nano kaolinite.

Figure 3.6. a) FESEM of pristine kaolinite NPs, TEM (inset) b, c, d) FESEM of A.K, I.K, CK1, e) TEM of CK1, and f) FESEM of CKM1

Figure 3.7. a, b, g) EDAX data of K3, I.K, and CK1, c-f) mapping of I.K, and h-k) mapping of CK1.

Figure 3.8. a, b) Surface area and porosity of intercalated kaolinite and 1% functionalized MWCNT incorporated kaolinite, c) Zeta potential of CK1.

Figure 3.9. TGA-DTA of K3, A.K, I.K, and CK1.

Figure 3.10. dielectric constants, tangent loss, and A.C conductivity of A.K and I.K.

Figure 3.11. a, d, g Frequency-dependent permittivity of the nanocomposites in different temperatures show the maximum permittivity in CK1 sample, b, e, h temperature-dependent dielectric constant of the nanocomposites in different frequencies, and c, f, i tangent loss of the nanocomposites with respect to frequency represents the nominal tangent loss.

Figure 3.12. Frequency-dependent AC conductivity of the nanocomposites K3, CK1, and CKM1 shows the maximum AC conductivity in the CK1 sample, d–f Arrhenius plots of the nanocomposites to estimate the activation energies of the nanocomposites, g) Jonscher's plots of the nanocomposites show the non-zero n value of the nanocomposites which confirms the non-Debye type conduction mechanism.

Figure 3.13. Arrhenius plots of the MWCNT concentration-dependent clay samples for estimating the activation energies.

Chapter 4

Figure 4.1. Schematic representation of MWCNT incorporated nanoparticle synthesis with varying concentrations of functionalized MWCNT.

Figure 4.2. Experimental and refined XRD of 0.5 %, 1.0 %, and 1.5% functionalized-MWCNT incorporated activated-kaolinite.

Figure 4.3. Microstructural visualization and basal plane separation of all the nanoparticles by VESTA software.

Figure 4.4. FTIR spectra of all the nanoparticles

Figure 4.5. a) FESEM of nano kaolinite (K3), b, c) FESEM of CK0.5, and CK1, d) TEM image of 1% functionalized MWCNT-incorporated kaolinite (CK1), e) FESEM of CK1.5, f) EDAX of CK1, and g-j) mapping of CK1.

Figure 4.6. a) Surface area and porosity of CK1, b) Zeta potential of CK1.

Figure 4.7. Variation of dielectric constant with frequency (a–d), temperature-dependent dielectric response (e–h), and tangent loss (i–l) for the MWCNT-doped kaolinites.

Figure 4.8. a-d) Temperature-dependent ac conductivities with varying frequencies of concentration-dependent MWCNT-clay nanocomposites, e) Joncher's plot to evaluate the diffusion-limited hopping mechanism of the nanocomposite samples.

Figure 4.9. Arrhenius plots of the MWCNT concentration-dependent clay samples for estimating the activation energies.

Figure 4.10. Electrochemical impedance spectra of the MWCNT-doped samples with corresponding equivalent circuits for estimating the charge transfer process.

Figure 4.11. a) Cyclic voltammograms of various MWCNT-doped clay samples, b) voltammogram of CK1 at different scan rates.

Chapter 5

Figure 5.1. Nanocomposite sample and preparation techniques.

Figure 5.2. XRD of a) kaolinite doped PVDF b) MWCNT-kaolinite incorporated PVDF nanocomposite membranes

Figure 5.3. FESEM micrographs of a) pure PVDF, b) PVK2.5, c) PVK5, and d) PVK7.5.

Figure 5.4. EDAX (a, b) and mapping (c-i) of PVK5 membrane.

Figure 5.5. a-c) FESEM micrographs of PCK0.5, PCK1, PCK1.5 respectively, d) TEM micrograph of PCK1,

Figure 5.6. a) EDS of PCK1, b-f) mapping data of PCK1 nanocomposite membrane.

Figure 5.7. (a) Full XPS spectrum of the nanocomposite membrane (PCK1), (b), (c) deconvoluted spectrum of the C and F, (d), (e), (f) chemical states of Si, O, and Al respectively.

Figure 5.8. a) FTIR spectra of kaolinite-PVDF membranes, b) Schematic representation of polar β -phase formation, c) percentage β -phase of the nanocomposite membranes, d) Room temperature P-E loop data of the membranes, and e) Dipole orientation in α and β -phase of PVDF.

Figure 5.9. (a) FTIR spectroscopy of PVDF-based MWCNT-kaolinite nanocomposite films, (b) percentage β -phase of the PVDF-based nanocomposite films, (c) Zeta potential

of 1% MWCNT doped natural kaolinite, (d) P-E loop of PVDF-based nanocomposite films, (e) Schematic diagram of β -phase formation, (f) dielectric permittivity of the nanocomposite films, (g) variation of dielectric permittivity with percentage doping of MWCNT-kaolinite in PVDF matrix, (h) ac conductivity data of nanocomposite membranes, (i) dissipation factors ($\tan\delta$) of the nanocomposites.

Figure 5.10. a) Piezoelectric open circuit voltage, b) Impulsive time of force applied, and c) d_{33} of the nanocomposite membranes.

Figure 5.11. Piezoelectric output voltages: (a) voltages when the device is exposed to DI-water from different heights, (b) voltages from 36 cm height of different water sample, (c) PCK1 nanocomposite film-based device for piezoelectric water energy harvesting, (d) piezoelectric currents when DI-water droplets fall from a different height on the device.

Figure 5.12. (a) Organic Rhodamine-B dye degradation with time under ultrasound (PCK1), (b) Degradation of RhB by PVK5, (c) investigation of scavenger by PCK1, (d) the reaction rate constant for different scavengers by PCK1, (e) effect of different free radicals for the Rhodamine-B degradation, (f) trapping experiment to investigate the presence of OH^* radical, (g) recyclability experiment of the nanocomposite film up to five cycles h) comparison with only US data (i) pictorial representation of dye color with time.

Figure 5.13. (a) Photographs representing surviving *E. coli* colonies on the solid agar plates (after 24 of incubation); (b, c) Illustrates the amount of ROS generation and mortality percentage of *E. coli* as calculated using colony counting technique (d, e) FE-SEM images.

Figure 5.14. (a) Photographs representing surviving *E. faecalis* colonies on the solid agar plates (after 24 of incubation); (b,c) Illustrates the amount of ROS generation and mortality percentage of *E. faecalis* as calculated using colony counting technique (d, e) FE-SEM images.

Figure 5.15. Time-dependent kinetic study of bacterial degradation by PVK5 membrane and only

Figure 5.16. (a) Investigation of bacterial ROS with increasing time, (b) MWCNT-kaolinite-PVDF nanocomposite assisted mortality percentage of pathogenic bacteria under ultrasound, (c) agar plate data for investigating bacterial decomposition with time,

(e), (f), (g) FESEM images of healthy, ultrasound-assisted *E. coli*, and PCK1 and ultrasound-based degraded *E. coli*.

Figure 5.17. (a, b) Recyclability test of PVK5 membrane for *E. coli* bacteria, (c, d) Recyclability test of PCK1 membrane for *E. coli* bacteria, e, f) one-way ANOVA test for PVK5 and PCK1 respectively for *E. coli* bacteria degradation.

Figure 5.18: Biocompatibility of the nanocomposite membranes via hemolysis assay.

Chapter 6

Figure 6.1. Synthesis protocol of nanocomposite membranes

Figure 6.2. XRD of a) Functionalized-kaolinite, b) Intercalated kaolinite, and c) 1%-MWCNT loaded kaolinite doped chitosan bio-polymeric membranes.

Figure 6.3. FESEM micrographs of a) bare chitosan, b-d) functionalized kaolinite doped chitosan, e-g) Intercalated kaolinite doped chitosan, and h-j) 1%-MWCNT doped kaolinite incorporated chitosan membranes.

Figure 6.4. EDAX spectra and elemental tables of a, b) CKF5, c, d) CKI5, and e, f) CNKCI

Figure 6.5. Elemental mapping of a-f) CKI5, and g-l) CNKCI nanocomposite membranes suggest the proper stoichiometric incorporation of clay into the biopolymeric matrix.

Figure 6.6. FTIR spectra of a) functionalized, b) intercalated, and c) 1% MWCNT-doped kaolinite incorporated nanocomposite membranes

Figure 6.7. Electrical properties of the membranes: a, d, i) Dielectric constants, b, e, j) tangent losses, and c, f, k) AC conductivities

Figure 6.8. Piezoelectric open-circuit voltages a) functionalized, b) intercalated, and c) 1% MWCNT doped kaolinite incorporated membranes. Short-circuit currents d) intercalated and e) 1% MWCNT-doped clay-based membranes. f) piezoelectric coefficients

Figure 6.9. Degradation of RhB (a, d, g), Congo red (b, e, h) for CKF5, CKI5, and CNKCI. C, f, i) C/C₀ graph of degradations.

Figure 6.10. Scavenger experiments of and first-order reaction kinetics of the nanocomposite membranes: a, b) CKF5, c, d) CKI5, and e, f) CNKCI

Figure 6.11. Pathogenic *E. coli* bacteria decontamination by CKI5 membrane within 60

min of soft ultrasound (15 kHz, 50 W): a) distribution of bacterial colonies in solid agar plates and b) decontamination kinetics with time: found that the bio-polymeric membrane has a promising antibacterial efficacy which enhanced with piezocatalytic impulse

Figure 6.12. *Pathogenic E. coli bacteria decontamination by CNKC1 membrane within 60 min of soft ultrasound (15 kHz, 50 W): a) distribution of bacterial colonies in solid agar plates and b) decontamination kinetics with time: found that the bio-polymeric membrane has a promising antibacterial efficacy which enhanced with piezocatalytic impulse*

LIST OF TABLES

Chapter 1

Table 1.1. Statistical data by WHO on wastewater and its effect on the environment

Chapter 2

Table 2.1. Chemical composition (XRF-data) of bulk kaolinite.

Table 2.2. EDAX data of all samples

Table 2.3. Structural and microstructural parameters of the samples were obtained from various characterization techniques including refinement of the XRD diffractograms.

Table 2.4. Calculated activation energies from Arrhenius plots at different frequencies.

Chapter 3

Table 3.1. Synthesized nanoparticles and nanocomposites

Table 3.2. Microstructural parameters of the NPs by Rietveld refinement.

Table 3.3. Surface charge and surface area of synthesized nanoparticles

Table 3.4. Dielectric constants of nano-kaolinite and its modified counterparts

Chapter 4

Table 4.1. Synthesized nanoparticles and nanocomposites

Table 4.2. Microstructural parameters by Rietveld-refinement of all the nanoparticles.

Table 4.3. Surface charge and surface area of synthesized NPs

Table 4.4. Dielectric constants of nano-kaolinite and its modified counterparts

Table 4.5. Activation energies of % MWCNT-doped kaolinite clay samples.

Table 4.6. Equivalent circuit parameters of the samples estimated from the impedance fitting.

Chapter 5

Table 5.1. Synthesized nanocomposite membranes and respective codes

Table 5.2. Polarization, Young's modulus, and measured piezoelectric coefficients of the nanocomposite membranes (measured in two different IEEE standard methods)

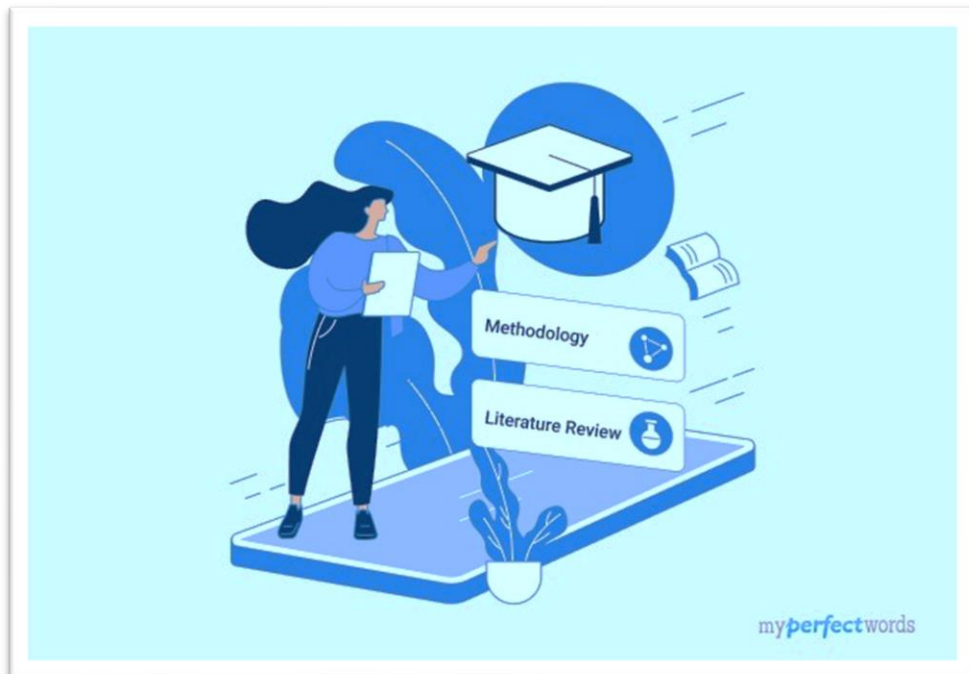
Chapter 6

Table 6.1. Synthesize bio-nanocomposites membranes and their codes

Table 6.2. Dielectric constants of the membranes

Table 6.3. Piezoelectric effectiveness i.e. piezoelectric voltages, short-circuit currents, and piezoelectric coefficients d_{33} of the nanocomposite membranes

Chapter 1



Introduction & Methodology

Chapter 1

Introduction & Methodology

The modern era is coined as the era of Globalization due to technological advancement, urbanization, and industrialization, which are the key factors of modern-day civilizations [1, 2]. But with every boon comes a bane and, in this case, it manifests as the modern devils known as water pollution and energy deficiency. Water pollution, especially from industries, agricultural farms, and residential areas releases large scale of heavy metals, organic pollutants, chemicals, etc. into the environment posing a serious threat to aquatic ecosystems and nature [3, 4]. Various diseases like cholera, diarrhoea, carcinogenicity, dysentery, arsenicosis, fluorosis, endocrine disruption, and various types of respiratory issues are increasing due to water pollution [5]. Moreover, untreated sewage waste discharged directly into the nearby water bodies can cause various life-threatening diseases to mankind due to the high load of faecal coliform bacteria [6]. A recent study by UNESCO (United Nations Educational, Scientific and Cultural Organization) reveals that various developing countries are discharging 90 % of untreated sewage directly into water bodies [7]. This sewage and other effluents are directly discharged into the world's water of about 2 million tonnes every day whereas industries are discharging about 300-400 Megatons of waste into different water sources i.e rivers, sea every year [8]. Statistical data on water pollution by the World Health Organization (WHO - 2021) has been given in Table 1 [9].

Various international organizations, NGOs, environmental groups, and governments are working on a global scale towards water pollution. Initiatives are taken to improve water quality and raise awareness about clean water. United Nations set Sustainable Development Goal 6 (SDG 6) to ensure sustainable management, sanitation, and availability of clean water and reduction of water pollution [10].

Despite these various efforts to mitigate water pollution, several challenges persist due to unorganized industrialization, inadequate infrastructure, lack of awareness, and increasing population [11]. Thus, wastewater remediation techniques are needed to mitigate this severe threat. From ancient civilizations to recent days wastewater

remediation technology has been developing and trying to minimize the water pollution level. On the other hand, widespread industrialization has elevated the demand for consuming energy which ultimately is related to the rapid extraction of fossil fuels [12]. Thus, energy generation from non-invasive sources is

Table 1.1. Statistical data by WHO on wastewater and its effect on the environment [9].

Aspect	Statistics
Global Impact	Around 80 % of global wastewater flows back untreated. Approximately 1.8 million deaths annually due to waterborne diseases.
Sources of Pollution	Agriculture runoff, untreated sewage, and industrial discharges.
Developing Nations	Water pollution challenges due to limited resources and infrastructure.
Regulatory Efforts	Establishment of regulations, and challenges in enforcement.
Impact on Biodiversity	Oxygen depletion, habitat destruction, and contamination affect aquatic life.
Economic Costs	Economic burdens from healthcare lost tourism, and damage to fisheries.

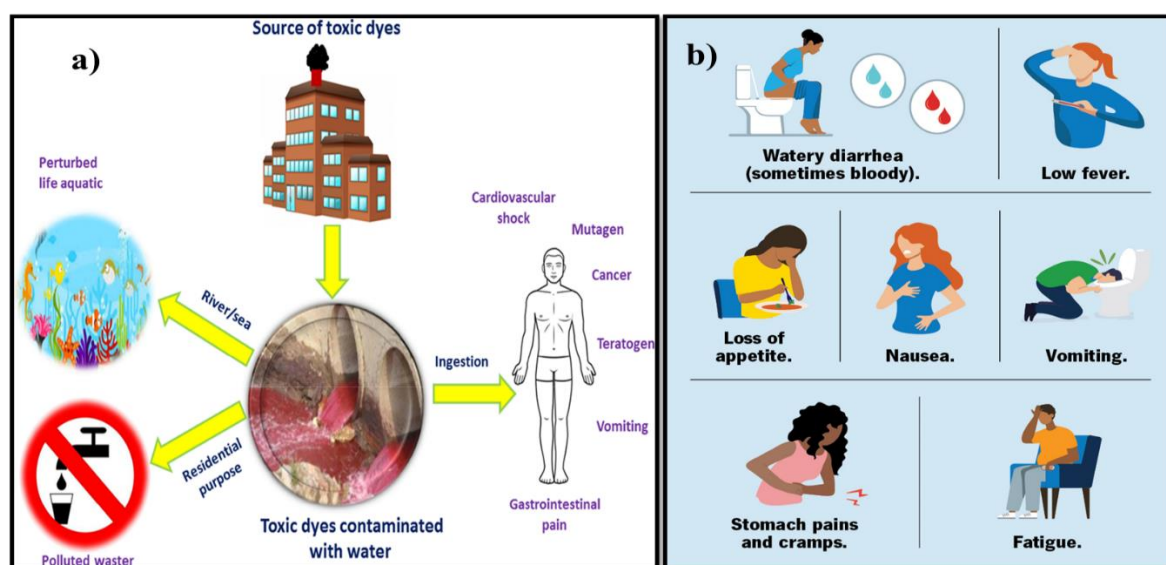


Figure 1.1. a) Effect of industrial toxic dyes, b) Effect of coliform bacteria [13]

gaining interest nowadays. A recent study reveals that energy demand is rising by 1% every year and it is expected that the share of alternative energy sources in energy consumption will grow to 63 % in 2050 from the 9.5 % share in 2015 [14]. Worldwide researchers are trying to develop new technologies to mitigate these two major issues through their research and findings.

1.1 History of Wastewater remediation and energy generation at the international level

Wastewater remediation techniques have been adopted for environmental safety even from ancient civilizations. In 2000 BCE The Indus Valley Civilization also adopted the rudimentary forms of wastewater treatment by sophisticated drainage systems with terra-cotta pipelines [15]. Whereas the Roman Empire (500 BCE - 476 CE) had developed adequate sewage and aqueduct systems. Released water from households and latrines was gone from natural filtration techniques before being released into rivers [16]. After the collapse of the Roman Empire in the Renaissance Periods (500 - 1600 CE) sanitation practices were also destroyed over time [17]. However, rudimentary treatment methods were in practice to treat the wastewater in some European cities by setting up tanks and disposing of the waste for regulation [18].



Figure 1.2. Indus Valley civilization wastewater technology: (a) Drainage system and (b,c) sanitation systems [19].

Industrial Revolution in the 18th - 19th centuries, created serious problems with water pollution due to the fast industrialization and urbanization [20]. Water sources were tainted by untreated sewage and industrial discharges, which aided in the development of diseases transmitted through the water. Chemical coagulants were used in early treatment processes, as well as sedimentation tanks [21]. The understanding of microbiology and the function of microorganisms in wastewater treatment improved in the late 19th and early 20th centuries [22]. The early 20th century saw the development of the biological treatment technique known as activated sludge, which offered a more efficient way to treat wastewater [23]. The use of primary and secondary treatment methods expanded between the 1930s and the 1950s. While biological mechanisms are employed in secondary treatment to further break down organic debris, primary treatment entails the physical removal of big solids [24]. It was at this period that trickling filters and activated sludge systems became popular. Whereas in the late 20th Century, the removal of contaminants and pathogens, advanced treatment technologies were adopted, including tertiary treatment and disinfection techniques such as ultraviolet irradiation and chlorination [25]. Additionally, efforts were made to combat the pollution of nutrients, specifically nitrogen and phosphorus. In recent times (21st Century) wastewater treatment techniques have been continuously evolving and

developed to increase treatment effectiveness, resource recovery, and overall sustainability [26]. The field of wastewater treatment technology is constantly developing, thanks to breakthroughs like the application of material science, nanotechnology, and artificial intelligence.

On the other hand, the growing population, urbanization, and industrial revolution are heavily dependent on energy. Conventionally, fossil fuels like coal and oil are the primary source of energy which are limited [27]. The increasing energy demand creates a shortage of energy and fluctuation in the energy supply as a result the price of conventional energy sources is increasing day by day [28]. The Organization of Arab Petroleum Exporting Countries (OAPEC) decreased the oil supply in several countries to support Israel in 1973 during the Yom Kippur War [29]. As a result, oil prices and supply disruptions occurred which was known as the first oil crisis. Whereas, the second global oil crisis happened and the oil price also increased during the Iranian Revolution and the Iran-Iraq War in 1979 due to production disruption [30]. Subsequently in the 1980s, there was an excess of oil on the market due to the oil crises of the 1970s and over oil production after the war. The economies of these countries that depend on oil were impacted by the sharp decline in prices which affected their economic status [31]. In the 21st century global demand for oil and gas grew as a result of the fast industrialization and urbanization of developing nations like China and India [32]. Energy prices fluctuated as a result of competition between the countries that were supplying oil all over the world. On the other hand, during the COVID-19 Pandemic in 2019-2022, the economic status of several countries was affected severely which also increased the price of conventional energy sources [33]. Whereas, when coal and oil are burned, they emit greenhouse gases like carbon dioxide into the atmosphere, which exacerbates climate change [34]. Sulfur dioxide, nitrogen oxides, and particulate matter released during the burning of coal lead to air pollution and respiratory problems [34]. Heavy metal leakage from coal mining adds to water contamination [35]. Marine ecosystems are harmed by oil exploitation and spills, with spills resulting in long-term devastation. Because they destroy habitat, both fuels contribute to land degradation [36]. Extraction techniques lead to biodiversity loss and resource depletion. Making the

switch to cleaner energy sources is essential to reducing these negative effects on the environment and promoting a more sustainable future [37].

1.2 History of wastewater remediation and energy generation at the national level

Wastewater Treatment and Wastewater Remediation in India has a long history. In the past, water purification was done using traditional methods. However, in modern times, wastewater treatment and wastewater remediation have been developed systematically. Various natural substances and water purification processes were mentioned in Ayurvedic texts of ancient India [38]. These purification methods included herbs, sand filtering, and sun exposure. Whereas Stepwells, such as those found in Gujarat and Rajasthan, are designed to collect rainwater and allow for natural filtration. During the 19th century, the British colonial administration set up basic sewage systems in major cities of our country [39]. However, these systems were often inadequate and had a limited scope. After the independence, in 1985 Ganga Action Plan had been set up because of the falling apart water nature of the Ganges Stream, the Indian government sent off the Ganga Activity Intend to control contamination and further develop the waterway's water quality [40]. This initiative concentrated on sewage treatment facilities and industrial pollution reduction. In the late 20th century rapid industrialization increased the industrial and urban waste which directly contaminate the water sources. Pollution Control Boards (PCB) were formed in every state to monitor and regulate industrial discharges to the local water bodies [41]. The National River Conservation Plan (NRCP) was also passed in 1985 to monitor the pollution level of major rivers and improve sanitation techniques and public awareness [42]. The Namami Ganges mission was launched by the government in 2014 to restore the health of the Ganges by treating sewage, encouraging sustainable sanitation practices, and controlling industrial effluents [43]. Whereas, an autonomous society National Mission for Clean Ganga (NMCG) is also working on the implementation of Namami Gange [43]. Swachh Bharat Mission was also launched in 2014 to improve wastewater management and awareness of proper sanitation all over the nation [44]. In due course, India has adopted advanced research to develop innovative wastewater technologies like membrane

filtration, biological treatment, nanotechnology, and other promising methods to address diverse sources of pollution [45]. For these purposes, government organizations (UGC, CSIR, DST) and private organizations are funding the universities and research organizations for their innovative ideas and contributions to wastewater management techniques.

On the other hand, the Indian energy demand profile has undergone a significant transformation depending upon economic, technological, and changing policies [46]. In colonial India, before 1947 conventional energy sources like animal power, human labor, and biomass were used for energy needs [47]. After independence within the period of 1951-1956 at first the focus was set on electrification and the formation of energy infrastructure all over the country [48]. Fossil fuels like coal-generated energy along with hydropower played a pivotal role in those years. The oil crisis in the 1970s created an energy deficiency while increased industrialization in the 1990s increased energy requirements, especially for oil and gas [49]. The privatizations of energy sectors in the late 1990s and 2000s tried to improve the energy infrastructures. While after the establishment of the Ministry of Non-Conventional Energy Sources in 1992 focuses were given to generate energy by non-conventional sources [50]. As India entered into the 21st century, rapid growth in industrialization, transportation, and urbanization increased the energy demand. Coal-based power generation extended, but the shortage of fossil fuel promoted renewable energy sources and nuclear power. The Jawaharlal Nehru National Solar Mission (2010) and the National Action Plan on Climate Change (2008) both are working together for the commitment to sustainability [51]. The National Solar Mission aimed to increase solar capacity, and various policies and incentives supported the integration of renewables into the energy mix [52]. The emphasis on sustainability continued, with ongoing efforts to enhance energy efficiency and reduce reliance on fossil fuels. In the current times, India faces the challenges of balancing energy security with environmental sustainability. Initiatives like the Ujwal DISCOM Assurance Yojana (UDAY) for power distribution reforms demonstrate the commitment to addressing challenges in the power sectors [53]. India's energy history reflects a dynamic evolution, with a growing emphasis on renewables, energy

efficiency, and a commitment to meeting the needs of a burgeoning economy while addressing environmental concerns on both national and global scales. Whereas the growing inventions in material science and nanotechnology are also working to develop energy by various non-invasive sources by their functionality. Government agencies like DST, UGC, CSIR, and private establishments are funding research organizations to improve their facilities and sustainable development of the energy generation profile in India.

1.3 Nanotechnology in wastewater remediation and non-invasive energy generation

In the present era, extensive global research efforts are underway to address wastewater-mediated pollution, employing diverse techniques. Traditional approaches relying on adsorption-based removal have demonstrated significant promise in mitigating these issues [54]. Nanostructures, characterized by their high aspect ratios, have proven highly effective in eliminating both organic and inorganic contaminants from wastewater [55]. However, it is crucial to recognize that adsorption alone may merely relocate specific pollutants from one phase to another, potentially leading to the generation of chemically active species and initiating secondary pollution [56]. Bioremediation methods have gained widespread adoption for wastewater treatment, encompassing processes such as hyperaccumulation, phytoremediation, mycoremediation, rhizoremediation, and more [57]. While these techniques offer cost-effectiveness and environmental friendliness, they are not without limitations, including extended reaction times, seasonal variations in microbial activities, and susceptibility to reversibility if not handled properly [57]. As a response to the shortcomings of conventional removal processes, photocatalysis has emerged as a viable alternative [58]. Various strategies, including band gap manipulation, formation of composite semiconductors, and metal ion implantation, have been proposed to enhance the photocatalytic efficacy [58]. Despite these efforts, achieving an effective charge separation process remains a challenging aspect of these systems. Additionally, photocatalysts may undergo corrosion under low pH conditions, posing a significant impediment to their degradation efficiency [59]. Piezoelectric materials have emerged

as a favorable alternative for enhancing catalytic activity, presenting a promising avenue for cleaner and more efficient processes [60]. Traditionally employed in various applications such as energy generation, charge storage, and sensor devices, these functional materials facilitate advancements in catalysis utilizing clean energies such as mechanical vibration, ultrasonic waves, and pressure [60]. Piezocatalysis harnesses these piezo-stimulations to accelerate chemical reactions [60]. In practical terms, piezoelectric materials exhibit superior charge center separation under mechanical stress, leading to the formation of reactive radicals, specifically oxygen species, which play a crucial role in initiating the catalytic process [61]. Among various inorganic nano-systems, including Pb-based materials, MoS₂, BaTiO₃, and BiFeO₃ have demonstrated noteworthy piezocatalytic activity in aqueous media, achieving catalytic efficacy levels of around 100% in many cases [62]. Piezocatalysis has even proven effective in bacterial sterilization [63]. Despite these successes, a drawback of many powdered inorganic piezocatalytic materials is their tendency to diffuse in water, necessitating separation to minimize secondary pollution. This limitation can be addressed by encapsulating these materials in different polymeric systems [64].

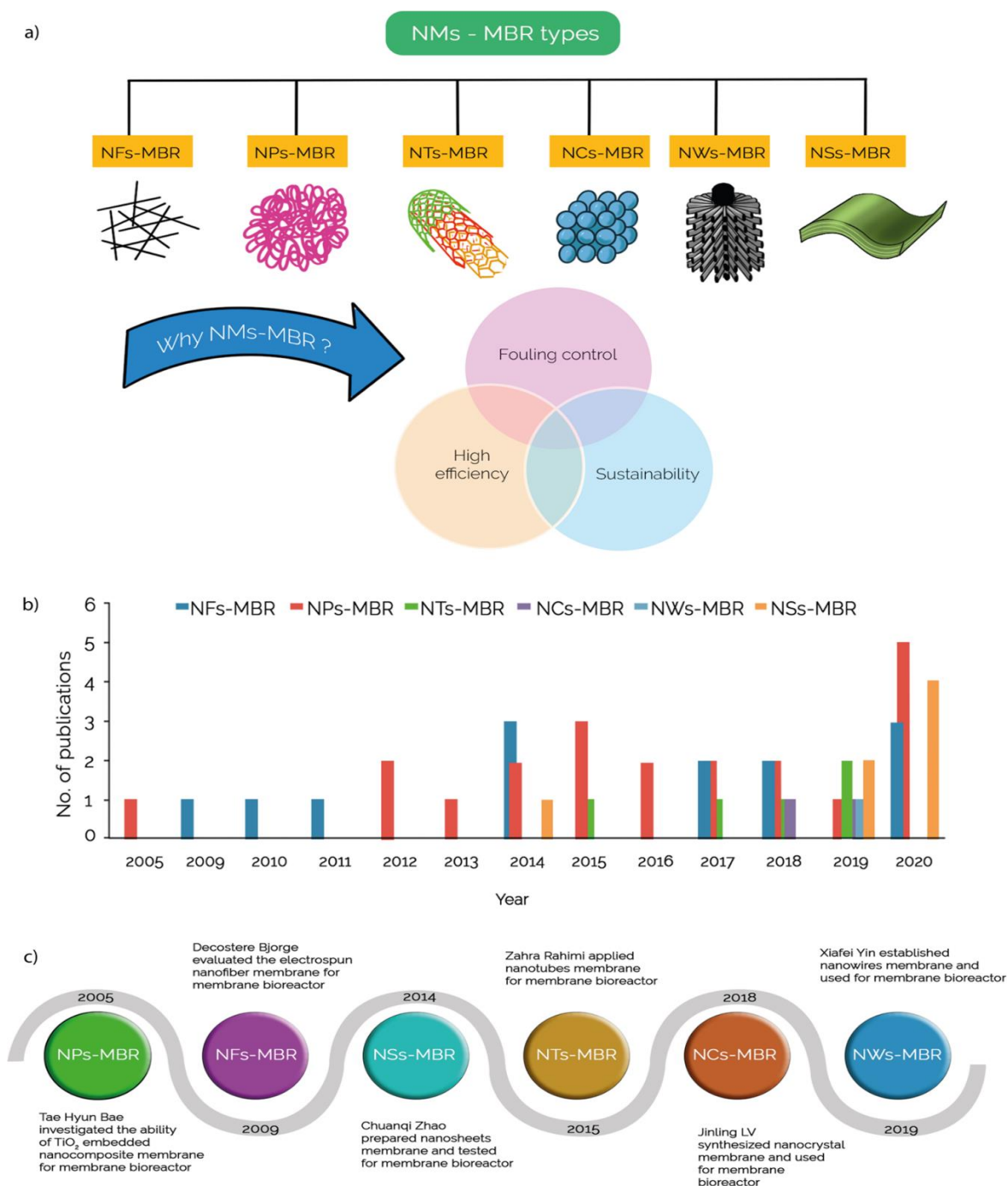


Figure 1.3. Categories and profits of different nanomaterials membrane bioreactor (NMs-MBR) technology with ahistorical timeline for wastewater management. [65]

While polymeric piezocatalysts have shown promising catalytic activity, they are still in the early stages of development [66]. This work emphasizes the natural, biocompatible

clay-tuned piezoelectric effect of polymeric piezocatalytic systems in the context of combating wastewater pollution. These hybrid polymer-nanocomposites, encapsulating piezoelectric materials, hold the potential for controlling the excessive use of hazardous pollutants, especially carcinogenic organic dyes, and pharmaceuticals. This approach aims to minimize their environmental impact, underlining the significance of polymeric encapsulation in enhancing the effectiveness of piezocatalysts. Other than pollutant degradation and bactericidal effects, energy harvesting is another crucial aspect as conventional fuels are non-renewable and most of the alternative energy sources require expensive instrumentation, and suitable locations, and are often hard to operate. Since mechanical or vibrational energies that operate the piezo-response of the nanomaterial are in abundance and easily accessible. That is why such non-invasive kinetic energy-mediated piezoelectric energy harvesting and subsequent wastewater remediation are gaining the interest of new-generation scientists. Such a technique is hassle-free and restricts the generation of harmful greenhouse gases.

1.4 Piezoresponse in nanomaterials

Piezoelectricity, a wonder where certain materials create an electric charge in reaction to mechanical stretch, includes an intriguing history. It was to begin with watched in 1880 by the brothers Pierre and Jacques Curie, who found that weight connected to quartz precious stones may create power [67]. They named this impact "piezoelectricity" from the Greek word "piezein," meaning to squeeze or press [68]. Within the taking after a long time, analysts extended this revelation, investigating different materials and applications. Amid World War I, piezoelectric gadgets were utilized in sonar innovation, checking their viable application [69]. Since that point, piezoelectric materials have found different applications in areas such as restorative imaging, sensors, actuators, and indeed vitality collecting. Nowadays, piezoelectricity proceeds to play a significant part in various mechanical progressions, from everyday devices to cutting-edge innovations [70]. It is observed that in a wide range of piezoelectric materials particle size and morphology are key parameters to enhance the piezoelectric efficiency. It is found that 1-D fiber/wire-like materials exhibit better

piezocatalytic response compared to spherical particles. On the other hand, thin sheet-like 2-D structures also exhibit better piezoelectricity. In reality, the theoretical piezoelectric output is directly proportional to the size of the catalyst as stated below [71],

$$V_p = \frac{d_{ij}\sigma_j\omega_i}{\epsilon_0\epsilon_r} i \dots\dots\dots [1.1]$$

Where V_p is the piezoelectric open circuit potential, σ_j is applied stress in j direction, d_{ij} is piezoelectric charge coefficient, ω_i is the length of piezocatalyst in i direction of polarization, and $\epsilon_{r,i}$ is the relative permittivity in i direction and ϵ_0 is permittivity in

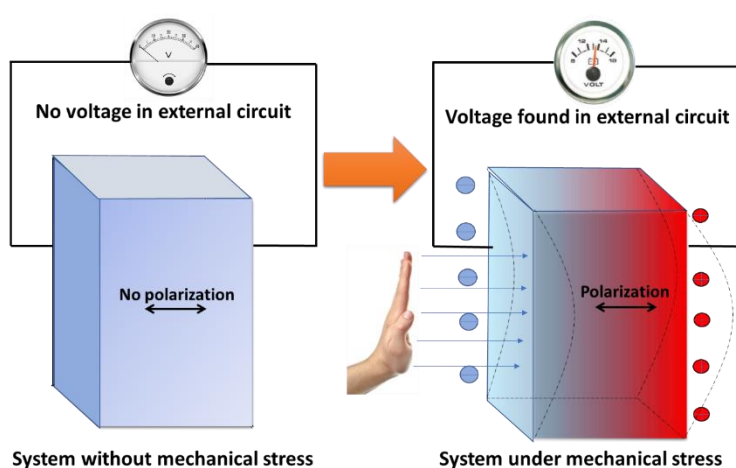


Figure 1.4. Induced piezo-polarization under mechanical stress

open space. Piezoelectricity of any material can be defined by a series of piezoelectric coefficients such as piezoelectric charge constants d_{ij} (e.g., d_{11} , d_{33}) or dielectric constants (e.g., ϵ_{11}^T , or ϵ_{22}^T) are among the best indicators of the potential performance of any given piezoelectric

material. Hence, piezoelectric polymer nanocomposites with high d_{ij} values are quite effective in generating high piezo-response to eliminate contaminants from wastewater [71]]. The piezoelectric crystals are normally electrically neutral, the atoms inside them may not be symmetrically arranged always. Despite having a non-centrosymmetric structure, a positive charge cancels out a negative charge near it, nullifying the electric dipole which makes the crystal neutral. Whenever the crystal is squeezed i.e., mechanical stress is applied across it, the structure is deformed, which in turn disrupts not only the balance of positive and negative charges but also alters their band structure. The electron and hole separation build up an electric field on its surface. However, piezocatalytic composite powders are difficult to recycle in practical applications.

Sometimes they cause secondary pollution and therefore it is necessary to prepare piezoelectric composite films with great recyclability. On the other hand, the external piezo-stimulation is an important parameter for achieving better catalytic activity. Generally, ultrasound of 20-40 kHz has been widely used to ‘excite’ piezocatalysts in bath or probe sonication systems. The acoustic pressure in these systems does not exceed 2 bar, which might not be sufficient to exert adequate stress on piezocatalysts. Additionally, continuous sonication for a prolonged duration causes internal heat generation. This could be addressed by replacing the water in the bath or adding ice cubes/water during the experiment [71]. However, such addition or alteration could greatly influence the piezocatalytic efficacy. These drawbacks have been minimized by collapsing the cavitation bubbles with pressures up to 10^8 Pa and simultaneously by using modern temperature-controlled ultrasonic bath systems.

1.5 Mechanism of piezoelectric energy generation

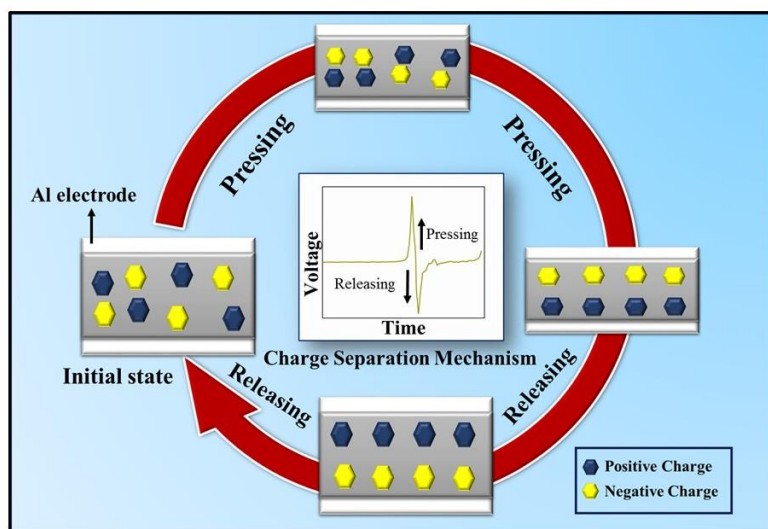


Figure 1.5. Schematic diagram of piezoelectric polarization and energy generation

The piezoelectric energy generation under external mechanical stimulus can be explained in terms of the dipolar polarization of the piezo-active samples which has been established by the researchers in last few decades. It has been

realized that external frequency can modulate the movement of the electrical dipoles. Under any mechanical stress, the piezoelectric device faces some external pressure and a dipolar polarization occurs inside the sample due to its eminent polarizability [72]. This polarization creates a charge separation and positive charges travel to one of the electrodes, whereas, negative charges move towards the other electrode. Such charge

separation introduces a potential difference between the two electrodes. After the removal of the external force, the charge carriers quickly migrated toward the opposite electrodes through the external circuit and generated an opposite potential drop [72].

1.6 Mechanism of piezocatalytic wastewater remediation

The Reactive Oxygen Species (ROS)-mediated piezocatalytic wastewater degradation is validated through the widely adopted screening charge effect and energy band tilting theory.

1.6.1 Screening charges effect

The non-centrosymmetric structure of piezoelectric nanomaterials poses obvious intrinsic polarization. This intrinsic polarization of the piezocatalyst is neutralized upon introduction to wastewater through screening charges, achieving a charge balance condition (State 1). Upon the application of ultrasonic impulses (mechanical stress), the piezocatalyst undergoes charge center separation, leading to the migration of charges to the opposite surface. This results in the quenching of polarization and additional screening charges are released from the catalyst surface [73].

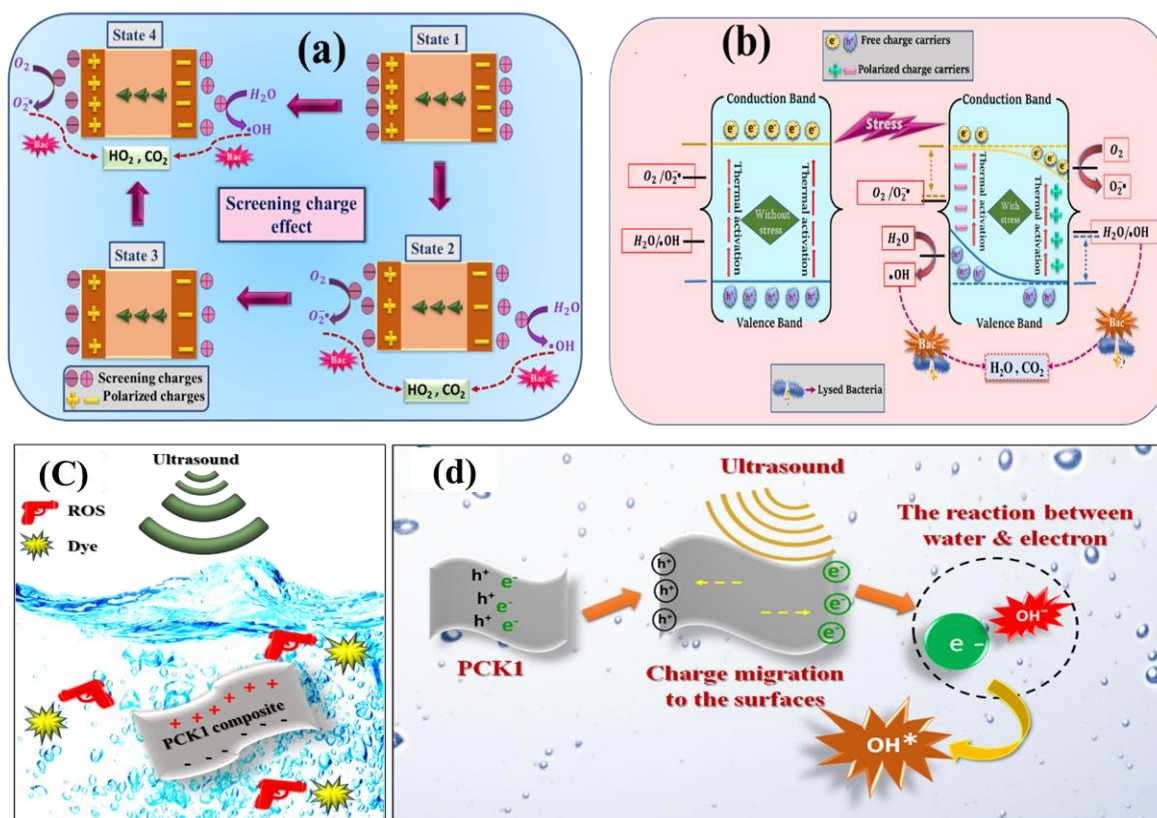
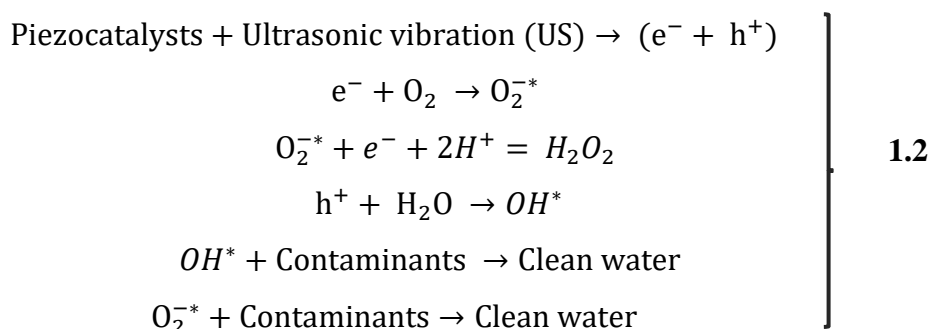


Figure 1.6. Mechanism of piezocatalytic reactive oxygen species generation: (a) Screening charge effect, (b) Energy band tilting, [74] (c) Catalysis schematic diagram, and (d) Nanocomposite membrane-based ROS production.

These supplementary screening charges actively engage in a redox reaction with hydroxyl and oxygen ions within the electrolyte, generating Reactive Oxygen Species (ROS) (State 2) until the subsequent charge balance condition is attained. The catalyst's polarization is reinstated when the applied stress is released, and charges from the electrolyte are once again adsorbed on both surfaces of the catalyst, participating in redox reactions (State 3). This cyclic catalytic redox reaction persists until the catalyst returns to its initial condition. Throughout this process, ROS is consistently generated, contributing to the decomposition of industrial pollutants and pathogenic bacteria [74].

1.6.2 Effect of energy band edge tilting

Conversely, the piezo potential induced by mechanical stress tilts the energy band, initiating a redox reaction that produces Reactive Oxygen Species (ROS) [74]. In practical terms, the polarization-induced piezo potential arises on both surfaces of the catalyst when subjected to mechanical stress. Subsequently, electrons in the conduction band are drawn and migrate toward the positive potential side, while holes in the valence band move towards the negative potential side, causing the energy band to tilt in the opposite direction and generate free charges. These electrons and holes then engage with electrolyte ions, resulting in the generation of ROS aimed at eliminating contaminants from wastewater. The steps involving in the contaminant's eradication [74],



However, the self-polled membrane-based piezocatalysis depends upon another probable mechanism which has been first time published by us in Nano Energy. The electron and hole in such self-polled membranes migrate in opposite directions under the ultrasonic stimulus, accumulate on the surfaces, and create a charge center separation. The surface accumulated electrons and holes then produce Reactive Oxygen Species (ROS) by screening the charge effect and decomposing the dye molecules [74].

While, under mechanical stress, the generated ROS can efficiently deactivate bacterial cells by disrupting transmembrane electron transfer, compromising subcellular components such as proteins and nucleic acids (DNA, RNA), inducing lipid membrane peroxidation, and halting DNA replication. As a result, elevated ROS levels lead to a progressive impairment of cellular functions, resulting in damage and eventual cell death of such pathogens [74].

1.7 Piezocatalytic wastewater remediation and piezoelectric energy generation

Initially, ZnO has emerged as a promising piezocatalyst, as demonstrated by Hong et al. in their 2010 paper showcasing the successful conversion of mechanical energy into chemical energy using piezoelectric ZnO microfibers. This conversion process, termed the piezoelectrochemical effect (PZEC), resulted in the release of H₂ and O₂ gases in a 2:1 stoichiometry, even from pure water. To address the issue of catalyst dispersion in solution, a ZnO-embedded carbon nanotube flexible network was introduced, solving the problem effectively. Additionally, the remarkable electrical conductivity of carbon nanotubes served as a high-speed channel for charge transfer, amplifying the overall piezocatalytic activity [75].

Nano-scaled perovskites have also proven themselves valuable in piezocatalytic applications. Lead-based perovskites such as Pb (Mg_{1/3}Nb_{2/3}) O₃, 32PbTiO₃ and Pb (Zr_{0.52}Ti_{0.48}) O₃ have exhibited significant potential for energy generation and dye decoloration [76]. Similarly, CH₃NH₃PbI₃ nanoparticles, synthesized through the co-precipitation method, displayed enhanced piezocatalytic activity attributed to stronger polarization resulting from a larger displacement of the Pb atom [77]. Furthermore, lead-free BaTiO₃ micro dendrites, BaTiO₃ nanofibers, and (Ba, Sr) TiO₃ nanowires, obtained through hydrothermal and sol-gel methods, showcased notable piezocatalytic activity, particularly in azo dye degradation [78-80].

In addition to various nanostructures, 2-D MoS₂ has recently emerged as a promising piezocatalyst. Single-layer MoS₂, in particular, demonstrates robust polarization and effective charge separation between the Mo₂-S layers, as indicated by piezo-electrochemical experiments highlighting promising charge mobility across these layers [81]. This inherent piezoelectric effect initiates piezocatalytic activity within the MoS₂ system. However, the double-layer MoS₂ system experiences a reduction in piezoelectric activity due to the opposite polarization direction between consecutive layers [82]. Consequently, researchers have identified that the piezoelectricity in MoS₂ is highly structure-dependent, following a periodic odd-even order [83, 84].

Wu et al. unveil a remarkable piezo-catalytic activity of MoS₂ nanoflowers (NFs) in swiftly breaking down organic dyes when exposed to ultrasonic waves sans light. Utilizing piezo force microscopy (PFM), it reveals substantial piezoelectric potential at the edges of the MoS₂ NFs, elucidating their rapid degradation mechanism. Rhodamine-B (RB) dye degradation achieves an impressive rate of 40336 ppm L mol⁻¹ s⁻¹ (about 93 % degradation in 60 seconds), surpassing commercial MoS₂ bulk sheets and TiO₂-P25 nanoparticles. The extraordinary activity of MoS₂ NFs stems from their electric field induced by spontaneous polarization, attracting polar molecules like water, thus generating highly reactive species. This study reveals the fastest degradation rate to date, highlighting piezo-catalytic enhancement of MoS₂ NFs under ultrasonic waves in darkness. [85]

Moreover, a comparative analysis by Li et al. evaluated the piezocatalytic activity of various 2-D materials, including MoS₂, WS₂, and WSe₂. The study revealed a direct correlation between piezocatalytic activity and piezoelectric coefficients obtained through calculation and Piezoresponse Force Microscopy (PFM) measurements [84].

While various nanoparticles have shown fast and efficient piezocatalytic properties, practical feasibility concerns have arisen due to issues such as direct decomposition in water, stability, efficacy, accumulation, toxicity, separation, and recyclability. To address these challenges for practical applications, researchers are increasingly focusing on polymer-based piezocatalysts. Polymers offer robust, reliable, flexible, and cost-effective substrates that resist agglomeration or degradation in ambient environmental conditions [84].

After the discovery of piezocatalysis by Hong et al. in 2010, various groups have started exploring synthetic polymers for this purpose. Piezoelectric poly (vinylidene fluoride) (PVDF) has become a favorable candidate in the field of piezocatalytic degradation of the contaminants. This semi-crystalline polymer has five crystalline polymorphs namely, α , β , γ , δ , and ϵ . Among them, the most common piezo-responsive stable polymorph of PVDF is the polar β -phase [86]. Generally, β -phase is present in very low amounts in pristine PVDF but it can be enhanced by incorporating various

nanostructures utilizing their surface charge. Under mechanical vibration, the piezocatalyst (β -PVDF) produces polarization, which can be harnessed as electrical energy. This further drives the electrons through the external circuit. After the release of the external stress, the electrons flow in the opposite direction resulting in a negative potential. Such charge center separation drives the electron-hole pair to either direction for effective piezocatalysis [86].

The first work on PVDF-based piezocatalysis was reported by Dong et al. in 2017. The authors fabricated an e-skin using PVDF/TiO₂ nanofiber for methyl blue degradation. These TiO₂ nanowires have been enforced inside the PVDF polymer for this purpose. The process involves a hybrid piezo-photocatalyst, where the TiO₂ performs the photodegradation while the PVDF moiety contributes to the piezo-response. The TiO₂ nanostructure herein promotes the electrons from the valence band to the conduction band using the piezo-response leaving the holes in the valence state. These electron-hole pairs initiate the catalytic activity tremendously [87]. According to this report, the hybrid PVDF-based e-skin completely degraded the dye solution within 40 minutes of external mechanical vibration. Besides, ZnSnO₃ (ZTO) was also recognized as an efficient piezocatalyst that modulates the band structure of the system to manipulate dye degradation efficacy [88]. In this case, the external ultrasonic stimulation bends the band edges for better electron hole separation. The dye degradation efficacy was found to be $1.5 \times 10^{-2} \text{ min}^{-1}$ under the ultrasonic stress, which is approximately four times higher than the absence of the ultrasonic vibration. The ZTO nanowire also exhibits synergistic piezophotocatalytic effect that was further enhanced by encapsulating ZTO into PVDF and polymethyl methacrylate (PMMA) matrices. It is observed that the irregular alignment of ZTO nanowires on the ITO surface experiences uneven polarization when mechanical stress is applied. Surprisingly, the polymer-coated ZTO shows better polarization due to the flexibility of the polymer, which creates better reception of the external stress resulting in a better piezoelectric effect [88]. Further, the efficacy of PVDF- ZnSnO₃ nanocomposite has been drastically improved by incorporating hydrothermally grown Co₃O₄ nanoparticles [89]. The piezo-degradation efficiency reached 100 % within 20 minutes for both methylene blue (rate constant ~ 43

$\times 10^{-3} \text{ min}^{-1}$) and rhodamine-B (rate constant $\sim 45 \times 10^{-3} \text{ min}^{-1}$) dyes. This catalytic enhancement is attributed to the hydroxyl radical ($\bullet\text{OH}$) and superoxide radical ($\bullet\text{O}_2^-$) generated during ultrasonic stress plays a pivotal role in degrading the dyes. In reality, ZnSnO_3 induces the polarizability of PVDF, whereas Co_3O_4 improves the charge transport mechanism for efficient redox reactions, which causes generation of the superoxide radicals under ultrasonic vibration [89].

Piezoelectric wurtzite ZnO nanocrystals have also emerged as promising piezocatalysts in recent times. Wu et al. (2020) have introduced the novel concept of utilization of mechanical stress generated from natural water flow accelerating piezo-response for water pollutant degradation. Wu and group fabricated two different nanocomposites namely, ZnO@PVDF and ZnO@PDMS for rhodamine-B degradation. The ZnO@PVDF film exhibited 10 times better performance than that of ZnO@PDMS which might be due to the piezoelectric effect in the case of PVDF [90]. It promotes the migration of photogenerated carriers under the stress generated by water flow. Moreover, the ZnO@PVDF film has more extensive (1 0 0) polar plane exposure that creates enhancement in active catalytic sites and causes better piezocatalytic degradation [91]. Thus, this work paved a new path for the synergistic utilization of solar energy and natural water flow for better degradation of contaminants using piezophotocatalytic effect. Besides dye degradation, certain research also dealt with the degradation of other contaminants such as pharmaceutical pollutants or microbial contaminants. A recent work by Singh et al. 2021 focuses on the piezocatalytic removal of pharmaceutical and bacterial pollutants using a flexible PVDF membrane intercalated by a well-known antibacterial silver nanoparticle embedded in LiNbO_3 nanostructure. This is probably the first time that pharmaceutical pollutants like tetracycline (69 %) and ciprofloxacin (53 %) have been decomposed within 2h using piezo response. Additionally, this work reports facile degradation of numerous pathogenic bacteria like *Escherichia coli* (99.999 %) and *Staphylococcus aureus* (96.65 %) within 180 minutes under vigorous ultrasound treatment. The Ag- LiNbO_3 nanocomposite enhances the β -phase PVDF, which in turn increases the piezoelectric nature. Under mechanical stress (from sonication) it generates free charge carriers which move opposite of the

polarization field [92]. Some of the free charge carriers ultimately interacts with the O_2 and OH^- ions resulting in production of ROS ($\bullet OH$ and $\bullet O^{2-}$) which performs the dual application of degradation of pharmaceuticals and generation of oxidative stress and lipid peroxidation that ultimately damages the nucleic acids and enzyme activity of bacteria, resulting in their death. Moreover, the occurrence of band bending due to the piezoelectric effect accelerates the migration of free charge carriers facilitating this process. This activity of ROS for contaminant degradation was explored by Bagchi et al. (2020), which illustrated a free-standing film made of PVDF-wrapped MoS_2 nanoflowers for the degradation of rhodamine-B. The composite film has been synthesized by using a simple solution casting method. This novel material gains multifunctionality when a remarkable power density (47.14 mW cm^{-3}) is achieved along with a promising piezocatalytic efficiency ($>90\%$ within 20 minutes). The primary resource of such piezo response is attributed to the polarization of the PVDF upon MoS_2 incorporation. The polar β -phase of PVDF was found to be around 80 % in this case. Increment of β -phase radically increases the charge separation process and electron-hole pair formation and thereby produces various reactive oxygen species (ROS). These ROS degrade the rhodamine-B dye in water making the material suitable for industrial effluent management [93].

Besides PVDF, MoS_2 nanoflowers, when encapsulated into the polydimethylsiloxane (PDMS) matrix show excellent piezocatalytic properties as mentioned by Lin et al. (2017). Upon external mechanical force, this polymer nanocomposite degrades rhodamine-B dye with an efficacy of 67 % under dark conditions. The degradation efficacy remains unaltered even after four test cycles. Thus, it can be believed that the catalytic efficiency of this composite is entirely dependent on the external piezo-response. This novel piezocatalyst also acts as a piezoelectric nanogenerator with an output of 23 V, 13 mA/m^2 when placed under a continuous water flow (20 mL/s). Hydrothermally grown chalcogenide (WS_2) has also been incorporated inside the PDMS polymer for piezocatalytic degradation of rhodamine-B and pathogenic *E. coli* bacteria (Masimukku et al., 2018). The degradation efficacy of rhodamine-B and *E. coli* are found to be $\sim 99\%$ and 99.99 % (in 90 minutes) respectively under ultrasonic

vibration. The recyclability of this reported polymer-nanocomposite is quite high (ten cycles) as compared to other reported samples. Initially, the piezo-response of the sample has been confirmed by tunneling atomic force microscopy and piezo-response force microscopy. The electron paramagnetic microscopy unveils the production of the reactive oxygen species (O_2^- , OH^*), which is primarily responsible for such rapid degradation of the contaminants in water [94]. Another highly stable PDMS-based nanocomposite ($BaTiO_3$ /PDMS) has been reported to be capable of reducing rhodamine-B contamination using piezocatalytic method. The degradation efficiency of this composite foam is around 94 % after twelve complete cycles [95]. A perovskite-based barium strontium titanate (BST) foam in PDMS polymer was reported, which successfully enhances the rhodamine-B degradation efficacy radically (275 %) when compared to individual photocatalysis [96]. This piezocatalytic composite has a degradation efficacy of 97.8 % even after ten cycles of repeated catalytic reaction. This hybrid piezo-photocatalyst offers a higher degree of charge center separation, which enables a promising catalytic degradation performance [97].

Roy et al. in their back-to-back two most recent articles (2022, 2024) describe the piezocatalytic efficiency of pure bismuth ferrite (BFO) and BFO-doped PVDF-HFP membrane. They have synthesized BFO by solvothermal synthesis procedure followed by high-temperature sintering and degraded RhB and pathogenic *E.coli* bacteria [98]. On the other hand, they have investigated the rare earth doping (Gd^{3+}) into BFO matrix and found the efficiency is maximum in the case of 1 % Gd^{3+} doped BFO [99]. Additionally, by preparing BFO-PVDF-HFP nanocomposite they showed that 7.5 % BFO doped PVDF poses maximum piezocatalytic efficiency against RhB under soft ultrasound [100].

Polytetrafluoroethylene (PTFE) is known to be a useful polymer with high flexural strength and high electrical resistance. Generally, PTFE is extremely inert even under harsh ambient conditions below 300°C [101]. Very recently (2021) Wang et al. reported PTFE based ROS generation method in an aqueous medium via ultrasonic vibration. This method involves a simple sonication technique to activate PTFE electrone from the

polymer. This permanent piezo-responsive polarization is fairly high (~600 pC/N) and even higher than that of conventional piezoelectric polymers (~16 times). In this work the authors have reported successful decomposition of methyl orange (~89.7 %), acid orange-7, and methylene blue (>90 %) in 60 minutes of ultrasonic exposure. The activated PTFE coating on the inner walls of a water pipeline has been proposed here for drinking water disinfection. To support this, PTFE membrane mediated degradation of *E. coli* has been studied. The results yield the promising bactericidal effect on *E. coli* within 15 min of ultrasonication (99.7 %).

Conductive polymers have been widely used over the past two decades in electrical, thermal, and thermoelectric applications. Various implantable medical devices have also been made using conductive polymers. Intercalation of numerous metallic and semiconducting nanomaterials enhances the physicochemical properties of such polymers. Polyaniline is a conductive polymer that exhibits efficient piezoelectric and thermoelectric activities under various circumstances. Das et al. (2017) successfully synthesized Fe⁰/PANI (polyaniline) nanocomposite under the reductive decomposition method, which successfully degrades Congo red dye under ultrasonic conditions. This efficient piezocatalyst decomposes ~98 % of the initial dye concentration within 30 minutes of mechanical exposure. During ultrasonic irradiation, the excited electrons of the Fe⁰/PANI composite are transferred to the conduction band and generate electron-hole pairs. As a result, dissolved oxygen and water molecules in the dye solution can react with the electron-hole pairs to produce reactive oxygen species and super-oxides. These reactive species are responsible for the degradation of the dye molecules. Such an excellent piezocatalyst could be a promising agent for wastewater treatment plants [102]. Similarly, in 2023 Lin et al. shows a unique MoS₂/polyaniline (PANI)/polyacrylonitrile (PAN)@BiFeO₃ bilayer hollow nanofiber membrane (PPBM-H) was synthesized via coaxial electrospinning. BiFeO₃ nanoparticles (NPs) and MoS₂ nanosheets (NSs) were incorporated into the PANI/PAN composites' middle and outer layers, respectively, forming a type II heterojunction with separated microtopography. This configuration notably enhances charge separation in piezocatalysis. Additionally, the hollow structure and abundant surface groups of PPBM-H enhance mass transfer

efficiency and pollutant adsorption in wastewater treatment. Its piezoelectric polarization under ultrasonic excitation boosts electron/hole separation and free radical generation. PPBM-H exhibits outstanding self-cleaning, mechanical strength (2.95 Mpa), hydrophilicity (11.6°), water flux (1248 L·m⁻²·h⁻¹), BSA rejection (98.8 %), and superior piezo-photocatalysis (99.2 % TCH within 2 h), and *E. coli* disinfection (100 % within 60 min) [103]. Biopolymers such as chitin, collagen, cellulose, starch, keratin, and fibrin can convert mechanical energy and electrical energy as well as used in various biological applications. In 2023, Bannerjee et al. introduces a novel bio-compatible polymer-based nanocomposite (ZnO/Chitosan), which accelerates catalytic processes by generating reactive oxygen species, particularly OH*, as confirmed by Photoluminescence spectroscopy. This piezo-catalytic process exhibits potent bactericidal effects, with nearly 96 % eradication of *E. faecalis* and 98 % of *E. coli* after 20 minutes, suggesting a promising antibacterial alternative [104].

Hence, the synthesis of efficient, green piezo-electric materials has captured widespread attention. The piezo-electric nature in biopolymers, especially in peptide-based biopolymers the piezo-electric nature is observed in those containing L- and D-amino acid isomers but is absent in the DL forms. It can be attributed to the C=O...CH₃ interactions in the isomers that result in piezo-response. Various reports showed that piezo-electric properties of biopolymers vary greatly with their shape, phase, growth orientation and water content [105]. In fact, collagen fibrils predominantly in axial direction are much stronger piezo-electric response than those in radial direction probably due to polarization. Among the various forms of chitosan, the α -chitin form found in crab shells and butterfly wings can exhibit piezo-response due to their non-centrosymmetric crystal structure having intrinsic molecular polarization. Although various works have been reported on biopolymer-based piezo-electric material synthesis and application in nano-generator and sensor fields, piezo-catalytic-based wastewater treatment has yet not been much invaded [106]. A recent report by Karaca et al. shows the generation of piezo-catalytic response in montmorillonite-loaded natural chitosan biopolymer by using ultrasound that can efficiently degrade various dyes like Acid Orange (AO7), Basic Red (BR4), Basic Yellow (BY2 and BY28) in aqueous solution.

According to the report, the chitosan structure has -NH_3^+ groups which are attracted to the negatively charged clay moiety. Such alteration in microstructure enhances the polarizability of the composite system and contributes toward higher piezoelectric potential. When this polarized system is stimulated through ultrasonic vibration, an electric field originates which further promotes the generation of free reactive OH^* radicals causing degradation of the dye. This method can even efficiently remove as much as 82.74 % of the dye within an hour. Although various works have been done by piezoresponsive membranes but most cases researchers have incorporated chemically derived piezoelectric materials into the polymeric matrix and made highly polarized film by an external electric field [107]. A minimal amount of interest has been paid on natural nanomaterial-based self-poled polymeric matrix. In this work, the enhanced physicochemical properties of natural clay have been used to fabricate highly efficient self-poled piezoresponsive polymer for carcinogenic organic dye degradation and non-invasive source-mediated piezoelectric energy generation.

1.8 Aims and Objectives

It has been found that in the last few decades, piezoelectric materials have gained interest in energy generation by piezoelectric nanogenerators (PENG) and wastewater remediation. But conventionally researchers incorporate chemically derived piezoelectric materials into the polymer without taking into consideration their toxic effects or directly using them in wastewater remediation. Such chemically derived nanomaterials have an intrinsic toxicity along it can generate secondary pollutants after degradation which may be harmful to the aquatic biota [108]. On the other hand, researchers generate piezoelectric energies from mechanical sources that may consume power. Keeping in mind the toxic effects of chemically derived piezomaterials and non-invasive mechanical energy sources this thesis will try to develop some piezo-responsive materials for mitigating such devil issues of society by selecting fascinating nanocomposites and mechanical energy sources. Before the selection of materials, there should follow some key factors in mind,

- ❖ Preparation of biocompatible, cost-effective, abundant nanomaterial.

- ❖ Comprehensive and meticulous characterization of the nanostructured samples using various characterizations. Particularly, emphasis will be given to Rietveld refinement-based crystallographic studies to validate the primary reason behind crystal defects and physicochemical properties.
- ❖ Fabrication of polymeric piezo-responsive materials (synthetic-polymer, bio-polymer).
- ❖ Investigation of piezoresponsive properties of the membranes by various experimental and theoretical (Density functional theory) characterization tools.
- ❖ Investigation of piezoelectric energy generation and piezocatalytic wastewater remediation efficacy of the membranes for fabricating a biocompatible, cost-effective energy harvester and water remediator.

1.8.1 Selection of Materials

Material selection and cost-effective synthesis protocols are the key factors for low production cost and mass-scale production. Aluminosilicate nanomaterials are well known for their stability, easy phase transition, biocompatibility, and enhanced physicochemical properties in nano regimes. By keeping these factors in mind non-toxic, abundant, cost-effective natural layered structured aluminosilicate (kaolinite or China clay) has been selected in this work. Kaolinite is a layered structured clay having silica tetrahedra and alumina octahedra that have been found naturally in China, raajmahal (India), a highly stable clay obtained by the weathered fraction of potassium feldspar. A top-down synthesis protocol was used to nanonize the natural bulk kaolinite by a simple ball mill grinder. The enhanced surface, and physicochemical properties of nano-clay and its modified counterparts by structural evolution and foreign element incorporation were used to fabricate polymeric piezocatalyst by poly (vinylidene fluoride-co-hexafluoropropylene) (PVDF-HFP) and chitosan. These multifunctional materials were selected for keeping mind some key factors that's are,

- ❖ High surface properties

- ❖ Non-toxic, Low-cost and biocompatible
- ❖ Impressive structure-property correlation
- ❖ Structural and thermal stability
- ❖ Possibility of mass-scale production

1.8.2 Organization of the Thesis

Chapter 1: *Introduction and Methodology.*

Chapter 2: *Investigation of Different Physicochemical Properties of Natural Kaolinite Clay by Particle Size Modulation.*

Chapter 3: *Synergistic Impact on the Microstructure and Physicochemical Properties of Nano-Kaolinite Upon MWCNT Incorporation and Basal Plane Intercalation.*

Chapter 4: *Optimizing Polarizability and Charge Storage Capacity through Varying MWCNT Concentration in Nano-Kaolinite.*

Chapter 5: *Exploring Piezocatalytic Wastewater Remediation and Piezoelectric Energy Generation in MWCNT-Integrated Kaolinite decorated poly (vinylidene fluoride-co-hexafluoropropylene) Membranes.*

Chapter 6: *Development of Chitosan Biopolymeric Membranes-based Piezocatalyst and Energy Harvester by Incorporating Structurally Modulated & 1% MWCNT-doped Kaolinite Clay Nanoparticles.*

Chapter 7: *Conclusions and Outlooks.*

1.9 Methodology

1.9.1 General synthesis procedure of nano kaolinite

Initially, the purchased bulk kaolinite sample was crushed with the help of a diamond mortar manually to reduce the agglomeration. A part of the crushed sample was sieved with the help of a 400-mesh sieve. The sample above the sieve was collected as the bulk fraction and the sample below the sieve was kept for further mechanical milling process.

5 gm of this sieved sample was then subjected to mechanical milling in a Fritsch Planetary Mono mill Pulverisette 6 ball-mill machine with the help of tungsten carbide vial and balls for 48h at 150 rpm. The milled clay sample was washed in water and then collected and dried in a hot air oven. The dried sample was further washed in acetone to reduce impurities and dried in a hot air oven for another 12 h at 60°C. Finally, the dried fine sample was collected and sent for characterizations. It has been found that the milled clay acquired particle size in 70-90 nm which is in nano regime.

1.10 Characterizations and experiments of the samples

1.10.1 Structural, morphological, and elemental characterizations

Natural materials may contain various impurities and crystallographic defects. Hence the determination of its purity is of utmost importance. XRD is an efficient characterization tool for detecting and quantifying such impurities that occur at the microstructure. It can determine the crystalline structure and other important microstructural parameters as well.

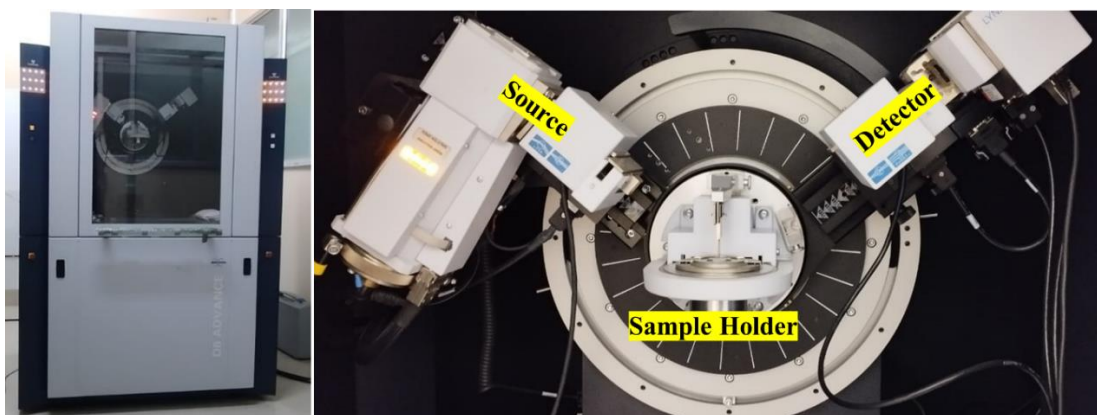


Figure 1.7. X-ray diffractogram (XRD) facility of Jadavpur University, Department of Physics.

A Bruker D-8 advanced powder X-ray diffractometer with Cu-K α target having a wavelength of 1.5418 Å was employed to find the X-ray diffractograms. The operating voltage and current during the measurement were set up at 35 kV and 35 mA [109]. The

scan speed and increment of angle were set up at 0.5 s per step and 0.0125633° respectively. The diffraction maxima of the clay samples corroborate with JCPDS card no. 80-0886, which suggests the materials to be kaolinite.

The absence of any unwanted diffraction peaks is the primary evidence of its purity. The



Figure 1.8. Fourier transform Infrared Spectroscopy (FTIR) facility of Jadavpur University, Department of Physics.

XRD diffractograms were further refined using the Rietveld software package MAUD v2.8 (Material Analysis Using Diffraction) for structural and microstructural investigations. Initially, the refinement of the diffractometer and the detector was done by imposing standard Caglioti PV functions. Instrumental broadening was also corrected during this cycle. A standard crystallographic

information file (.cif) of pure kaolinite (AMCSD file no. 1550598) was used to refine the experimental diffractograms. Various microstructural parameters, such as unit cell dimension, crystal size, and microstrain were refined to get promising fitting results. The Popa size-strain model was adopted to evaluate the crystal sizes and microstrain values. The computed .cif files were analysed using Vesta v3.4.3 to visualize layered structures of alumina and silica inside the kaolinite unit cells. The diffractograms of polymeric membranes also been collected by the XRD technique.

Phase purity at the molecular level was investigated by bonding network analysis with a

Fourier transform infrared (FTIR) spectrophotometer. An IR Affinity 900i, Shimadzu Infrared Spectrometer was used in this experiment. The thin membranes were placed

over the path of infrared light and the data in a region of $400\text{-}1000\text{ cm}^{-1}$ wavenumbers was recorded whereas the powder clay sample was analyzed by an ATR (attenuated total reflectance) directly by powder sample within the range of $400\text{-}4000\text{ cm}^{-1}$ [110].



Figure 1.9. Field Emission Scanning Electron Microscopy facility of Jadavpur University, Department of Physics.

Whereas, the surface and morphological properties of the natural clay and fabricated nanocomposite membranes were visualized by a field emission scanning electron

microscope (FESEM). An INSPECT-F50, FEI FESEM employed to collect the micrographs. Additionally, a JEM-2100 Plus, JEOL transmission electron microscope (TEM) was used to investigate the micrographs of the natural clay. Powdered nanoparticles and small pieces of membranes were cast on carbon tape and coated by gold plasma deposition to collect the micrograph under FESEM with an operating voltage of 20 kV [111]. On the other hand, well-dispersed kaolinite nano clay in acetone was cast on a 300-mesh carbon-coated copper grid to collect the TEM micrograph operated at 200 kV bias voltage [112]. Whereas, investigation of the elemental composition of the natural kaolinite and fabricated nanocomposite membranes were analyzed by Bruker, QUANTAX EDS, and mapping techniques, which were equipped with the said FESEM instrument [113].

1.10.2 Surface Properties Investigation of the natural kaolinite

Natural aluminosilicate clays pose promising surface properties in nano regimes due to the enhancement of their high surface-to-volume aspect ratio. The surface area, porosity, and surface charge play pivotal roles in any nanoparticles interacting with another. The Brunauer–Emmett–Teller (BET) and Barrer-Joy-ner-Halenda (BJH) method using N₂ gas adsorption-desorption have been employed to study the surface area and pore structures of the samples. A Twin Surface Area Analyzer, Quanta-chrome Instruments, USA was employed for this purpose. Whenever a Zetasizer, Malvern was used to determine the surface charge of the sample. To find the surface charge the natural samples were dissolved in deionized water by maintaining a 1mg/ml concentration. The high negative surface charges of the clay and its modified counterparts validate the electrostatic interaction of clay with polymeric chains [114].



Figure 1.10. Transmission Electron Microscopy (TEM), Jadavpur University.

1.10.3 Estimation of the thermal stability of the materials



Figure 1.11. Thermogravimetric analysis (TGA), Differential Thermal Analysis (DTA) facility of Jadavpur University, Department of Physics.

Thermal characterizations are very much needed for any materials as the physicochemical properties, such as dielectric constant, specific capacitance and conductivity, and optical band gap are quite vulnerable to temperature fluctuations. Differential thermal analysis and thermogravimetric analysis (DTA-TGA) measurements have been performed to check the

temperature stability of the synthesized natural samples and the polymeric membranes. A DTG-60H, Shimadzu has been employed to understand the structure–property correlation in this aspect maintaining a heating rate of 10°C/min under a nitrogen atmosphere. For this purpose, a very small amount of sample (10-20 mg) was taken into the platinum pan and placed over the instrument. Natural kaolinite shows a high-temperature stability up to 600°C whereas the polymeric membranes are also stable up to 200°C which validates that the piezocatalyst does not alter their efficiency in a wide temperature range [115].

1.10.4 Electrical properties investigation of the samples

The dielectric property reflects the charge storage ability of a sample. It depends on numerous parameters, such as grain size, temperature, humidity, frequency of the external electric field, etc. The total dielectric permittivity consists of two functions, namely, the real part of the permittivity (ϵ') and an imaginary part (ϵ''). The real part depicts the charge storage capacity, whereas, the imaginary part implies the electrical dissipation factor. These two terms are associated as [116]

$$\epsilon = \epsilon' + j\epsilon'' \dots\dots\dots 1.3$$

Where ϵ is the total dielectric permittivity of the material. Whereas, the real part of the permittivity can be calculated by using the relation [116],

$$\epsilon' = \frac{C_p d}{\epsilon_0 A} \dots\dots\dots 1.4$$

Where, C_p is the capacitance of the material, d and A are the thickness and area respectively of the solid pellets or membranes that are used to measure the permittivity and ϵ_0 is the free space permittivity (8.854E-12 F/m). Herein, 100 mg of each clay sample has been pressed by using a hydraulic press system to form solid pellets. Whereas, in the case of the membrane sample the membranes were cut having an area of 1cm². Both sides of these pellets and membranes were covered by copper strips that acted as electrical contacts. A 4294A Precision Impedance Analyzer, Agilent was used to study the electrical properties of these samples. The frequency-dependent permittivity

plots show a gradual reduction of electrical permittivity in the higher frequency domain. Such reduction is visible in all the samples. This type of frequency response could be analyzed by Maxwell-Wagner-Seller interfacial polarization. Generally, dielectric materials have conductive grains inside insulated grain boundaries. The energy of the external electric field at the lower frequency domain is insufficient to pull out these conductive grains from grain boundaries and results in an electrical polarization.



Figure 1.12. LCR-meter facility of Jadavpur University, Department of Physics.

This low-frequency polarization contributes to the total dielectric constant as stated in Koop's theory. However, the higher field frequency is capable enough to free the charges from the insulated boundaries and results in a lower permittivity value. The tangent loss has also been investigated to estimate the dissipation factor of the entire sample set. The ac conductivity of the materials has also been studied by the relation [117],

$$\sigma_{ac} = 2\pi f \epsilon_0 \epsilon' \tan \delta \dots \dots \dots 1.5$$

Where f is frequency, ϵ_0 is the permittivity in free space, and ϵ' is the permittivity of the membranes. The conduction mechanism of the clay samples has also been studied in terms of frequency and temperature variations. The frequency responses show higher conduction in the high-frequency domain. The charged grains escape the grain

boundaries after getting sufficient activation energies (E_a) at high frequencies. The activation energies have been calculated using the Arrhenius equation, as follows [118],

$$\sigma = \sigma_0 \exp\left(-\frac{E_a}{K_b T}\right) \dots\dots\dots 1.6$$

where E_a is the activation energy for conduction σ_0 is the pre-exponential factor, K_b is the Boltzmann constant and T is the temperature in the Kelvin scale. The activation energy tends to increase with increasing field frequencies making the grains more transportable at higher frequencies. The dependence of ac conductivity on frequency for the entire set of samples has also been studied through Jonscher's universal power law [119],

$$\sigma_{ac} = B\omega^n \dots\dots\dots 1.7$$

here, B and n are constant terms. B has the unit of conductivity and n is a dimensionless constant term. The non-zero values of n refer to the frequency-dependent conduction mechanism. It has been calculated for each sample by plotting $\ln\sigma$ against $\ln\omega$. The n values of the clay samples varied between 0.51 and 0.92 suggesting the non-Debye type conduction mechanisms for all the samples. Additionally, these n values validate the diffusion-limited 1-D hopping of the charge carriers through the sample.

Charge transport is an essential parameter when it comes to energy harvesting. Impedance spectroscopy can substantiate this in the microstructural proximity. Herein, the impedance spectra of the synthesized clay samples have been investigated to understand the role of microstructural modifications on carrier mobility. The R-X spectra were further fitted with an equivalent circuit model using the EIS spectrum analyzer v.1.0 program to find the charge transport phenomenon [120].

The cyclic voltammetry has been performed for further exploitation of the samples as having promising electrochemical properties. Typically, a two-electrode Netware BTS battery tester within certain voltage range was employed to conduct the electrochemical measurements. The voltammograms show typical electronic hysteresis loops. The

corresponding specific capacitances (CP) have been calculated using the following relation [121],

$$C_v = \frac{\int_{E_1}^{E_2} I(E)dE}{ms(E_1-E_2)} \dots\dots\dots 1.8$$

here, m is the mass of the material, s is the scan rate, E1 and E2 are limiting values of the potential window, and $\int_{E_1}^{E_2} I(E)dE$ is the area under the CV curve. Moreover, to assess the increment of storage capacity and discharge rate samples, galvanostatic charge–discharge has been performed.

Moreover, the polarizability of the samples has been investigated theoretically by using density functional calculations (DFT). In a typical process, the theoretical model of nanocomposite membranes has initially been designed by Avogadro v.1.2.0 software package. Orca v.4.2 software has been employed for frequency and geometry optimization of the model. The simulations have been performed using the Becke, 3-parameter, Lee-Yang-Parr (B3LYP) functional combined with 6–311 G* basis set, and RIJCOSX auxiliary basis set. The vibrational modes have been found positive in both cases, which validates the authenticity and stability of the models [122]. Whereas, experimental polarizability has been done by the polarization-electric field (P-E loop) study using precision premier-II (Radiant technologies). The room-temperature polarization-electric field (P-E) hysteresis loop at 10 Hz in the ± 200 kV/cm range was taken. The area within the loop corresponds to the heterogeneous charge density and indicates the charge storage capability of the material. The membranes show strong remnant polarization (P_r) value which suggests the intrinsic polarization and self-poled efficiency of the membranes.

1.10.5 Estimation of piezoelectric performance of the nanocomposite membranes

The piezoelectric energy harvesting devices are developed by polymeric membrane-based piezo-responsive samples having a definite dimension. Conducting electrodes are then mounted on both sides with copper wires to establish a rigid connection with the measuring device. The entire ‘sandwiched structure’ was then covered with a robust

polyethylene terephthalate (PET) jacket to arrest any kind of mechanical damage or malfunction. This PET jacket also makes this device water-repellent. The mechanical stress dependent piezoelectric open circuit voltage generation of the fabricated membranes was investigated by a digital storage oscilloscope (X 3012 A, Keysight) connected with the device by an Agilent N2862B 10:1 passive probe. Whereas, the short circuit piezo current of the same has also been measured by using a DAQ6510, Keithley data acquisition multimeter system. The piezoelectric coefficients (d_{33}) have been calculated for the membranes by using the following relation [123],

$$d_{33} = \frac{C_p \times V}{F} \dots\dots\dots \mathbf{1.9}$$

Where C_p is the specific capacitance, V is open circuit piezo voltage and F is the applied force. The force has been calculated in terms of energy conservation,

$$mgh = \frac{1}{2} mv^2 \dots\dots\dots \mathbf{1.10}$$

Where m is the mass of a striking object on the device, v is the velocity of the object, h is the height of the object from where it falls, and g is the acceleration due to gravity.

Velocity has been calculated by equation 1.10 for the height of h cm.

Now, the equation of momentum is:

$$mv = (F - mg) \Delta t \dots\dots\dots \mathbf{1.11}$$

Therefore, the applied force F is:

$$F = m (v/\Delta t + g) \dots\dots\dots \mathbf{1.12}$$

where Δt is the full width at half maxima of the output voltage vs the time graph.

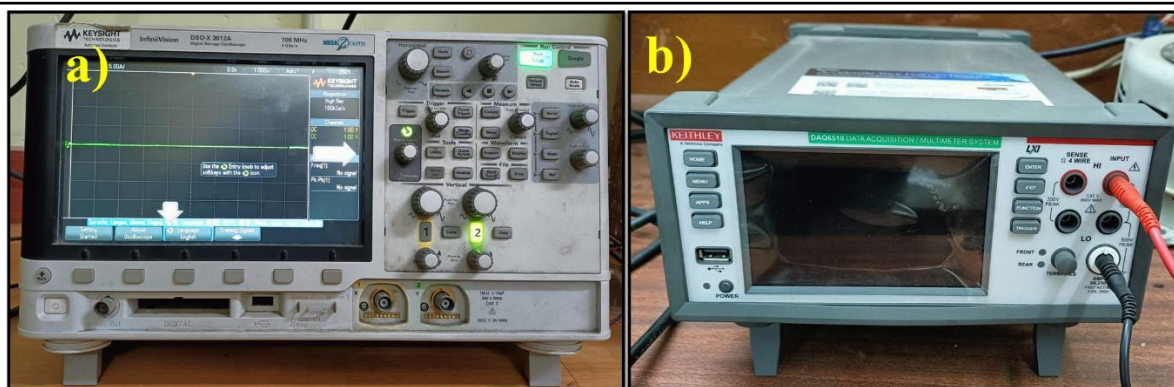


Figure 1.13. *a) Digital Storage Oscilloscope (DSO) (X 3012 A, Keysight), b) DAQ6510, Keithley data acquisition multimeter system, Jadavpur University, Department of Physics.*

1.10.6 Piezocatalytic wastewater remediation by optical instruments

The nanocomposite membranes, which have shown high isotropic polarizability, have a promising piezo coefficient along with significantly high piezoelectricity under external mechanical stimuli were selected for piezocatalytic application. An efficient charge separation under mechanical stress paved a path to exploit this material forming reactive oxygen species (ROS) such as e^- , h^+ , OH^* , $*O_2^-$ as prescribed by Hong et al. in their revolutionary work. It is observed that these reactive radicals can decompose organic pollutants such as dyes in an aqueous medium. Herein, the membranes have been used to degrade Rhodamine B (RhB) and Congo Red (CR) dye under ultrasound stimulus. In a typical catalysis experiment, 15 mL of 2.5 ppm Rhodamine B and Congo Red solution have been taken in a glass vial and 1 cm x 1 cm membranes have been placed in the solution. The vial was then submerged in a Telsonic ultrasonic bath sonicator having a frequency of 30 ± 5 kHz and an ultrasonic power of 50 W.



Figure 1.14. UV-Vis Spectroscopy facility of Jadavpur University, Department of Physics.

Prior to each experiment, the sample was immersed in the dye solution for at least 30 min to ensure full adsorption. Moreover, to eliminate any photonic contact during the experiment, the whole experiment was conducted in a dark condition. The ultrasound-mediated heating was eliminated by using a temperature-controlled water bath system. After each 10-minute interval, samples were taken out from the vessel, and the absorption spectrum was measured in a UV-1900i, Simadzu, UV-Visible spectrophotometer to ensure the catalytic activity of the membranes. It is found that the characteristic absorption maximum of RhB and CR degrades gradually under the external stimulus. The color of the dyes also faded with the duration of the ultrasound treatment and finally depicts full transparency under a certain time of treatment. The percentage piezo degradation efficiency η of the nanocomposites has been investigated by using the relation [123],

$$\eta = \frac{C - C_0}{C_0} \times 100 \% \dots\dots\dots 1.13$$

Where C_0 initial dye concentration and C is the final dye concentration. To verify the catalysis mechanism, the first-order kinetics, scavenging, and trapping experiments have been performed. In reality, piezocatalysis primarily depends on reactive radicals, especially ROS. The reactive oxygen species (ROS) generates during the catalysis experiment further decompose the hazardous dyes. Mainly four radicals, namely ($\bullet\text{OH}$),

holes (h^+), superoxide radicals ($\bullet O_2^-$), and electrons (e^-) may be produced during the catalysis to decompose the dye solution. Scavenging experiments have been carried out to find the dominating ROS radical. Initially, 15 mL of 2.5 ppm dye solution was taken into four separate glass containers, and 1 cm x 1 cm pieces of the membranes were immersed in it. Later, para benzoquinone (BQ), $AgNO_3$, ethylenediaminetetraacetic acid (EDTA), and tertiary butyl alcohol (TBA) have been added to the solution maintaining 0.5 mM of the concentration and exposed under the ultrasound. Further, the first-order kinetic constant (k) has been measured by using the following relation [123],

$$C = C_0 e^{(-kt)} \dots\dots\dots 1.14$$

The kinetic constant k has been measured by the slope of the plot $\ln(C/C_0)$ against time



Figure 1.15. Photoluminescence (PL) Spectrophotometer of Jadavpur University, Department of Physics.

to find the dominating ROS. The presence of hydroxyl radicals in the piezocatalytic reaction mixture has been investigated by the photoluminescence-probing technique of terephthalic acid (TPA). Initially, 0.01 gm TPA has been added to the 15 mL 2.5 ppm dye solution and exposed to ultrasound. 2 mL of the solution was taken every 10 min and the fluorescence intensity was measured by a Cary

Eclipse Fluorescence Spectrophotometer, Agilent Technologies. An excitation

wavelength of 315 nm was set and the fluorescence intensity was visualized at 415 nm. In reality, terephthalic acid reacts with OH* radical and generates fluorescent hydroxy terephthalate (hTPA) upon hydroxylation and increases the fluorescence intensity [123].

1.10.7 Antimicrobial assessment studies of the membranes

Using a typical Gram-negative coliform bacteria *Escherichia coli* (*E. coli*) and Gram-positive coliform bacteria *Enterococcus faecalis* (*E. faecalis*), the disinfection process of bacteria exploiting piezocatalysis was investigated. The bacterial cells were cultured in Luria-Bertani (LB) broth for a whole night at 37 °C with constant shaking (120 rpm). Six clean glass vials were filled with 10 mL of the aliquots, and two rectangular films (1cm × 1 cm) of membrane were put into two of the vials. Without any film and without being exposed to ultrasonic treatment, the vials served as the control group. The other four vials, two containing only the culture of *E. coli* or *E. faecalis* accordingly which were subjected to ultrasonic vibration, and another two comprising bacterial cultures and membranes both were subjected to ultrasonic treatment. At specific intervals of 10 minutes, 100 µl of the bacterial suspension from each vial was extracted and evenly distributed onto agar plates that had solidified at a dilution ratio of 10⁴. Each one was collected in triplicates, and the following formula was used to determine the mortality (%) based on the colony counting method [124].

$$M\% = \frac{(B-C)}{B} \times 100 \dots\dots\dots 1.15$$

Where M is the mortality rate (%), and B and C stand for the mean of bacterial colony (CFU mL⁻¹) in the control and treated samples, accordingly. Dichlorodihydrofluorescein diacetate (2', 7') was used to measure the formation of ROS in each case. Every time, 1 mL of aliquots were extracted, followed by a PBS solution wash and the addition of a 10 µM DCFDA solution. A spectrophotometer was used to detect the fluorescence intensity of the solutions after they were left in the dark for a further 30 minutes (excitation at 404 nm and emission at 525 nm). (28) Specifically, DCFH-DA reacts with ROS to create 2', 7' -dichlorofluorescein (DCF), which increases fluorescence and signals the production of ROS. The precipitates from the bottom of

each vial were collected and twice washed with filtered PBS solution at 5000 rpm for five minutes to perform bacterial FESEM. Subsequently, the pellets were mixed with paraformaldehyde solution and serially diluted with ethanol at different concentrations (5%, 20%, 50%, 75%, and 100%). Before the FESEM analysis, the solutions were dried, drop-casted onto clean coverslips, and then sputter-coated with gold [124].

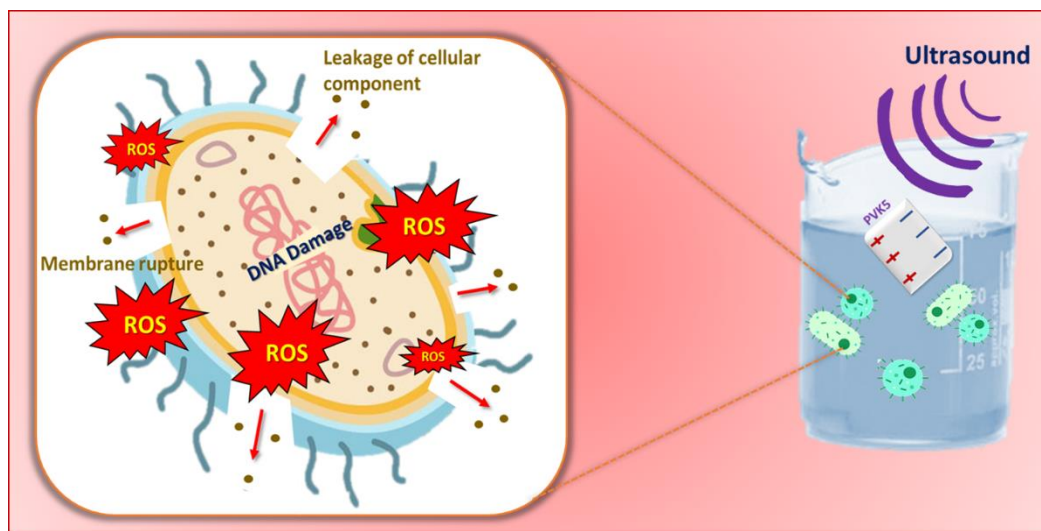


Figure 1.16. Portrays the mechanism of ROS-mediated bacterial damage, disruption of the membrane integrity, and simultaneous leakage of cytosol.

1.10.8 Biocompatibility study of the nanocomposites

Using previously published methods, the *in vitro* hemolysis test was used to evaluate the biocompatibility of nanocomposite membranes in red blood cells (RBCs). RBCs were extracted from fresh Sprague Dawley (SD) rat blood, purified in sterile PBS, and then mixed with dispersions of varying concentrations of nanocomposites. The controls were red blood cells exposed to ultrapure water (positive control) or treated with PBS (negative control). After an hour of incubation at 37°C, samples were centrifuged at 3000 rpm for 5 minutes, and the absorbance at 540 nm was determined. The hemolysis ratio was calculated using the given formula while considering the sample's absorbance values [124].

$$\text{Hemolysis rate (\%)} = \frac{(A_S - A_{NC})}{A_{PC} - A_{NC}} \times 100\% \dots \dots \dots \mathbf{1.16}$$

In contact with blood cells, the nanocomposites demonstrated a remarkable capacity to minimize hemolysis or the rupturing of red blood cells. Hemolysis may result in excessive bleeding and inflammation, impeding a lesion's healing ability. Because composites prevented hemolysis, that would instigate the nanocomposites to have no such cytotoxic effect in cells (RBCs). The red blood cells in the water completely burst, causing the solution to turn crimson in control. The samples having hemolysis rate less than 5 % are treated as biocompatible sample and it can be used in in-vitro or in-vivo biological experiments.

1.11 General summery

This thesis delves on the synthesis of natural kaolinite nanoparticles and its modified counterparts-based piezo-responsive materials. In a typical way the surface properties and other physicochemical properties of natural kaolinite clay have been modified and enhanced. Further these nanomaterials were characterized by conventional catheterization tool like XRD, FESEM, TEM. Along with the conventional characterization, surface properties, and electrical polarization of the clay and its modified counterparts have also been investigated. The enhanced surface properties (surface charge and surface area) and electrical properties of the clay further used to fabricate biocompatible, self-poled, free-standing nanocomposite membranes by incorporating them into both synthetic and bio-polymeric matrix to enhance their piezo-responsive properties. The enhanced piezo-response of the nanocomposite membranes further used to eradicate contaminants from wastewater along with non-invasive energy generation. This fascinating tool of biocompatible nanocomposite-based wastewater remediation and simultaneous energy generation may serve the society in water technology and mitigating energy deficiency in mass-scale if properly improvised.

References

- [1] Sachs, Jeffrey D. *Geography, technology, and institutions*. Columbia University Press, 2019.
- [2] Jennings, Justin. *Globalizations and the ancient world*. Cambridge University Press, 2010.

- [3] Madhav, Sughosh, Arif Ahamad, Amit K. Singh, Jyoti Kushawaha, Joginder Singh Chauhan, Sanjeev Sharma, and Pardeep Singh. *Sensors in water pollutants monitoring: Role of material* (2020): 43-62.
- [4] Singh, Jyoti, Priyanka Yadav, Ashok Kumar Pal, and Vishal Mishra. *Sensors in water pollutants monitoring: Role of material* (2020): 5-20.
- [5] Havelaar, Arie Hendrik, and J. M. Melse. "Quantifying public health risk in the WHO guidelines for drinking-water quality: a burden of disease approach." (2003).
- [6] Adegoke, Anthony A., Isaac D. Amoah, Thor A. Stenström, Matthew E. Verbyla, and James R. Mihelcic. *Frontiers in public health* 6 (2018): 376581.
- [7] Bijekar, Sangha, Hemanshi D. Padariya, Virendra Kumar Yadav, Amel Gacem, Mohd Abul Hasan, Nasser S. Awwad, Krishna Kumar Yadav, Saiful Islam, Sungmin Park, and Byong-Hun Jeon. *Water* 14, no. 16 (2022): 2537.
- [8] Kumar, Arun, and Kirti Goyal. In *Advances in chemical pollution, environmental management and protection*, vol. 6, pp. 33-63. Elsevier, 2020.
- [9] Fuller, Richard, Philip J. Landrigan, Kalpana Balakrishnan, Glynda Bathan, Stephan Bose-O'Reilly, Michael Brauer, Jack Caravanos et al. *The Lancet Planetary Health* 6, no. 6 (2022): e535-e547.
- [10] Guppy, Lisa, Praem Mehta, and Manzoor Qadir. "Sustainable development goal 6: Two gaps in the race for indicators." *Sustainability Science* 14, no. 2 (2019): 501-513.
- [11] Kurunthachalam, S. K. "Indian waters: past and present." *Hydrol Current Res S* 10, no. 2 (2013).
- [12] Erb, Karl-Heinz, Simone Gingrich, Fridolin Krausmann, and Helmut Haberl. *Journal of Industrial Ecology* 12, no. 5-6 (2008): 686-703.
- [13] El Messaoudi, Noureddine, Mohammed El Khomri, Abdelaziz El Mouden, Amal Bouich, Amane Jada, Abdellah Lacherai, Hafiz MN Iqbal, Sikandar I. Mulla, Vineet Kumar, and Juliana Heloisa Pinê Américo-Pinheiro. *Biomass Conversion and Biorefinery* (2022): 1-18.
- [14] Krakowski, Vincent, Edi Assoumou, Vincent Mazauric, and Nadia Maïzi. *Applied energy* 184 (2016): 1529-1550.

- [15] Yglesias, Caren. *The Innovative Use of Materials in Architecture and Landscape Architecture: History, Theory and Performance*. McFarland, 2014.
- [16] Angelakis, Andreas N., Andrea G. Capodaglio, Cees W. Passchier, Mohammad Valipour, Jens Krasilnikoff, Vasileios A. Tzanakakis, Gül Sürmelihiindi et al. *Water* 15, no. 8 (2023): 1614.
- [17] Smith, Cynthia, and Andrew Reeves. "Europe's Centuries of Crises and Recovery (1300-1600)." *He Huaka'i Honua: Journeys in World History I, to 1500 CE Honolulu CC HIST 151* (2023).
- [18] Jiménez, Blanca, Pay Drechsel, Doulaye Koné, Akiça Bahri, Liqa Raschid-Sally, and Manzoor Qadir. *Wastewater irrigation and health* (2009): 3-27.
- [19] Khan, Saifullah, Nese Yilmaz, Mohammad Valipour, and Andreas N. Angelakis. *Water* 13, no. 20 (2021): 2813.
- [20] Winiwarter, Verena, Gertrud Haidvogel, Severin Hohensinner, Friedrich Hauer, and Michael Bürkner. *Water history* 8 (2016): 209-233.
- [21] Wang, Lawrence K., Mu-Hao Sung Wang, Nazih K. Shammass, and Hermann H. Hahn. *Integrated natural resources research* (2021): 265-397.
- [22] Roccaro, Paolo, Antonella E. Santamaria, and F. G. Vagliasindi. *Evolution of Sanitation and Wastewater Technologies through the Centuries* (2014): 437-456.
- [23] Orhon, Derin. *Journal of Chemical Technology & Biotechnology* 90, no. 4 (2015): 608-640.
- [24] Ahmed, S. F., M. Mofijur, Samiha Nuzhat, Anika Tasnim Chowdhury, Nazifa Rafa, Md Alhaz Uddin, Abrar Inayat et al. *Journal of hazardous materials* 416 (2021): 125912.
- [25] Umar, Muhammad. *International Journal of Environmental Research and Public Health* 19, no. 3 (2022): 1636.
- [26] Daigger, Glen T. *Water environment research* 81, no. 8 (2009): 809-823.
- [27] Abas, Naeem, A. Kalair, and Nasrullah Khan. *Futures* 69 (2015): 31-49.

- [28] Asif, Muhammad, and Tariq Muneer. Renewable and sustainable energy reviews 11, no. 7 (2007): 1388-1413.
- [29] Haqem, Daniel, and Noraini Zulkifli. Asia Pacific Journal of Social Science Research 7, no. 1 (2022).
- [30] Long, David E. "Oil and the Iran-Iraq War." In The Iran-Iraq War (RLE Iran A), pp. 38-50. Routledge, 2012.
- [31] Barsky, Robert B., and Lutz Kilian. Journal of Economic Perspectives 18, no. 4 (2002): 115-134.
- [32] National Intelligence Council (US). "Global trends 2025: A transformed world." (2008).
- [33] Ślusarczyk, Bogusław, Patrycja Żegleń, Aldona Kluczek, Anna Nizioł, and Małgorzata Górka. Energies 15, no. 1 (2022): 332.
- [34] Myhrvold, Nathan P., and Ken Caldeira. Environmental Research Letters 7, no. 1 (2012): 014019.
- [35] Tiwary, R. K. Water, Air, and Soil Pollution 132 (2001): 185-199.
- [36] Onyena, Amarachi Paschaline, and Kabari Sam. Global ecology and conservation 22 (2020): e00961.
- [37] Omer, Abdeen Mustafa. Renewable and sustainable energy reviews 12, no. 9 (2008): 2265-2300.
- [38] Joshi, Vinod Kumar, Apurva Joshi, and Kartar Singh Dhiman. Journal of ethnopharmacology 197 (2017): 32-38.
- [39] Livingston, Morna. Steps to water: the ancient stepwells of India. Princeton Architectural Press, 2002.
- [40] Bhargava, Devendra Swaroop. "Nature and the Ganga." Environmental Conservation 14, no. 4 (1987): 307-318.
- [41] Bhawan, Parivesh, and East Arjun Nagar. "Central Pollution Control Board." Central Pollut. Control Board, New Delhi, India, Tech. Rep (2020): 20-21.

- [42] Dadsena, Nandkishore, and Sindhu J. Nair. "Water Pollution: A Review." In International Conference on Emerging Global Trends in Engineering and Technology, pp. 101-109. Singapore: Springer Nature Singapore, 2022.
- [43] Kumar, Ravindra. Environment, Development and Sustainability in India: Perspectives, Issues and Alternatives (2021): 115-147.
- [44] Ghosh, Sadhan Kumar. Procedia Environmental Sciences 35 (2016): 15-27.
- [45] Manikandan, Sivasubramanian, Ramasamy Subbaiya, Muthupandian Saravanan, Mohanadoss Ponraj, Masilamani Selvam, and Arivalagan Pugazhendhi. Chemosphere 289 (2022): 132867.
- [46] Gielen, Dolf, Francisco Boshell, Deger Saygin, Morgan D. Bazilian, Nicholas Wagner, and Ricardo Gorini. Energy strategy reviews 24 (2019): 38-50.
- [47] Weissenbacher, Manfred. Sources of Power [2 volumes]: How Energy Forges Human History [2 volumes]. Bloomsbury Publishing USA, 2009.
- [48] Bardhan, Ronita, Ramit Debnath, and Arnab Jana. Wiley interdisciplinary reviews: Energy and environment 8, no. 5 (2019): e340.
- [49] Asif, Muhammad, and Tariq Muneer. Renewable and sustainable energy reviews 11, no. 7 (2007): 1388-1413.
- [50] Omer, Abdeen Mustafa. Journal of Soil Science and Environmental Management 1, no. 7 (2010): 127-154.
- [51] Upadhyay, Surya Prakash, and Uttam Singh. New research directions in solar energy technologies (2021): 11-30.
- [52] Sharma, Naveen Kumar, Prashant Kumar Tiwari, and Yog Raj Sood. Renewable and sustainable energy reviews 16, no. 1 (2012): 933-941.
- [53] Veluchamy, A., Raju Ganesh Sunder, Rajesh Tripathi, and R. Mohamed Nafi. WATER And EnERGY InTERnATIOnAL 63, no. 4 (2020): 15-31.
- [54] Wibowo, Yudha Gusti, Tarmizi Taher, Khairurrijal Khairurrijal, Bimastyaji Surya Ramadan, Hana Safitri, Sudibyo Sudibyo, Ahmad Tawfiequrahman Yuliansyah, and Himawan Tri Bayu Murti Petrus. Bioresource Technology Reports (2024): 101797.

- [55] Amin, Muhammad Tahir, Abdulrehman Ali Alazba, and Umair Manzoor. *Advances in materials science and engineering 2014* (2014): 1-24.
- [56] Jain, Monika, Ackmez Mudhoo, Deepika Lakshmi Ramasamy, Mahsa Najafi, Muhammad Usman, Runliang Zhu, Gopalakrishnan Kumar, Sutha Shobana, Vinod Kumar Garg, and Mika Sillanpää. *Environmental Science and Pollution Research* 27 (2020): 34862-34905.
- [57] Negrin, Vanesa L., Lautaro Gironés, and Analía V. Serra. In *Coastal and deep ocean pollution*, pp. 184-214. CRC Press, 2020.
- [58] Hernández-Alonso, María D., Fernando Fresno, Silvia Suárez, and Juan M. Coronado. *Energy & Environmental Science* 2, no. 12 (2009): 1231-1257.
- [59] Chauhan, Husn Ara, Mohd Rafatullah, Khozema Ahmed Ali, Masoom Raza Siddiqui, Moonis Ali Khan, and Shareefa Ahmed Alshareef. *Polymers* 13, no. 14 (2021): 2374.
- [60] Li, Shun, Zhicheng Zhao, Jinzhu Zhao, Zuotai Zhang, Xu Li, and Jianming Zhang. *ACS Applied Nano Materials* 3, no. 2 (2020): 1063-1079.
- [61] Tu, Shuchen, Yuxi Guo, Yihe Zhang, Cheng Hu, Tierui Zhang, Tianyi Ma, and Hongwei Huang. *Advanced Functional Materials* 30, no. 48 (2020): 2005158.
- [62] Jin, Cheng-Chao, Dai-Ming Liu, and Ling-Xia Zhang. *Small* 19, no. 44 (2023): 2303586.
- [63] Kumar, Sandeep, Moolchand Sharma, Anuruddh Kumar, Satvasheel Powar, and Rahul Vaish. *Journal of Industrial and Engineering Chemistry* 77 (2019): 355-364.
- [64] Jennings, Brandon. *Development of piezocatalytic nanomaterials for applications in sustainable water treatment*. The University of Iowa, 2017.
- [65] Pervez, Md Nahid, Malini Balakrishnan, Shadi Wajih Hasan, Kwang-Ho Choo, Yaping Zhao, Yingjie Cai, Tiziano Zarra, Vincenzo Belgiorno, and Vincenzo Naddeo. *NPJ Clean Water* 3, no. 1 (2020): 43.
- [66] Mondal, Dhananjay, Shubham Roy, Souravi Bardhan, Jhilik Roy, Ishita Kanungo, Ruma Basu, and Sukhen Das. *Dalton Transactions* 51, no. 2 (2022): 451-462.
- [67] Anand, Gopika, and G. V. Chowdary. *Research Journal of Science and Technology* 12, no. 4 (2020): 267-276.

- [68] Mallik, Nilanjan. Piezoelectricity: Characterization. Shineeks Publishers, 2024.
- [69] Lewis, Nicholas Dale. The role of the microprocessor in the end of the Cold War. The University of Utah, 2011.
- [70] Mehrali, Mehdi, Sara Bagherifard, Mohsen Akbari, Ashish Thakur, Bahram Mirani, Mohammad Mehrali, Masoud Hasany et al. Advanced science 5, no. 10 (2018): 1700931.
- [71] Bößl, Franziska, and Ignacio Tudela. Current Opinion in Green and Sustainable Chemistry 32 (2021): 100537.
- [72] Liang, Haitong, Guangbo Hao, and Oskar Z. Olszewski. Sensors and Actuators A: Physical 331 (2021): 112743.
- [73] Wang, Kai, Chen Han, Jiaquan Li, Jieshan Qiu, Jaka Sunarso, and Shaomin Liu. Angewandte Chemie 134, no. 6 (2022): e202110429.
- [74] Bag, Neelanjana, Jhilik Roy, Dhananjay Mondal, Saheli Ghosh, Souravi Bardhan, Shubham Roy, Suman Bhandary, and Sukhen Das. Ceramics International 50, no. 5 (2024): 7998-8009.
- [75] Hong, Kuang-Sheng, Huifang Xu, Hiromi Konishi, and Xiaochun Li. The Journal of Physical Chemistry C 116, no. 24 (2012): 13045-13051.
- [76] Lin, He, Zheng Wu, Yanmin Jia, Weijian Li, Ren-Kui Zheng, and Haosu Luo. Applied Physics Letters 104, no. 16 (2014).
- [77] Wang, Mengye, Yunpeng Zuo, Jingli Wang, Yi Wang, Xinpeng Shen, Bocheng Qiu, Lejuan Cai, Feichi Zhou, Shu Ping Lau, and Yang Chai. Advanced Energy Materials 9, no. 37 (2019): 1901801.
- [78] Yuan, Baowei, Jiang Wu, Ni Qin, Enzhu Lin, and Dinghua Bao. ACS Applied Nano Materials 1, no. 9 (2018): 5119-5127.
- [79] Hong, Kuang-Sheng, Huifang Xu, Hiromi Konishi, and Xiaochun Li. The journal of physical chemistry letters 1, no. 6 (2010): 997-1002.
- [80] Hong, Kuang-Sheng, Huifang Xu, Hiromi Konishi, and Xiaochun Li. The Journal of Physical Chemistry C 116, no. 24 (2012): 13045-13051.

- [81] Tan, Dan, Morten Willatzen, and Zhong Lin Wang. *Nano Energy* 56 (2019): 512-515.
- [82] Michel, K. H., and B. Verberck. *Physical Review B* 83, no. 11 (2011): 115328.
- [83] Duerloo, Karel-Alexander N., Mitchell T. Ong, and Evan J. Reed. *The Journal of Physical Chemistry Letters* 3, no. 19 (2012): 2871-2876.
- [84] Li, Shun, Zhicheng Zhao, Dongfang Yu, Jin-Zhu Zhao, Yiping Su, Yong Liu, Yuanhua Lin, Weishu Liu, Hu Xu, and Zuotai Zhang. *Nano Energy* 66 (2019): 104083.
- [85] Wu, Jyh Ming, Wei En Chang, Yu Ting Chang, and Chih-Kai Chang. *Advanced Materials (Deerfield Beach, Fla.)* 28, no. 19 (2016): 3718-3725.
- [86] Thakur, Pradip, Arpan Kool, Biswajoy Bagchi, Nur Amin Hoque, Sukhen Das, and Papiya Nandy. *RSC advances* 5, no. 77 (2015): 62819-62827.
- [87] Dong, Chuanyi, Yongming Fu, Weili Zang, Haoxuan He, Lili Xing, and Xinyu Xue. *Applied Surface Science* 416 (2017): 424-431.
- [88] Lin, Hung-Ming, and Kao-Shuo Chang. *RSC advances* 7, no. 49 (2017): 30513-30520.
- [89] Raju, Tejas Dhanalaxmi, Sushmitha Veeralingam, and Sushmee Badhulika. *ACS Applied Nano Materials* 3, no. 5 (2020): 4777-4787.
- [90] Wu, Wen, Xin Yin, Baoying Dai, Jiahui Kou, Yaru Ni, and Chunhua Lu. *Applied Surface Science* 517 (2020): 146119.
- [91] Ma, Wei, Binghua Yao, Wen Zhang, Yangqing He, Yan Yu, Jinfen Niu, and Cheng Wang. *Environmental Science: Nano* 5, no. 12 (2018): 2876-2887.
- [92] Singh, Gurpreet, Moolchand Sharma, and Rahul Vaish. *ACS Applied Materials & Interfaces* 13, no. 19 (2021): 22914-22925.
- [93] Bagchi, Biswajoy, Nur Amin Hoque, Norbert Janowicz, Sukhen Das, and Manish K. Tiwari. *Nano Energy* 78 (2020): 105339.
- [94] Lin, Jyun-Hao, Yu-Hsiang Tsao, Mei-Hsuan Wu, Ting-Mao Chou, Zong-Hong Lin, and Jyh Ming Wu. *Nano Energy* 31 (2017): 575-581.
- [95] Masimukku, Srinivaas, Yu-Chen Hu, Zong-Hong Lin, Shuen-Wen Chan, Ting-Mao Chou, and Jyh Ming Wu. *Nano Energy* 46 (2018): 338-346.

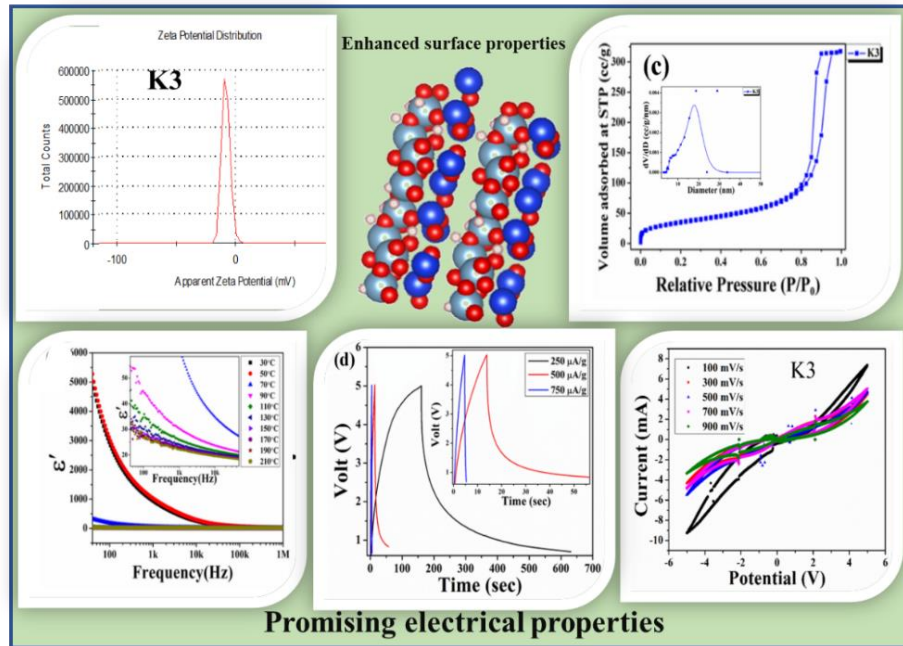
- [96] Qian, Weiqi, Kun Zhao, Ding Zhang, Chris R. Bowen, Yuanhao Wang, and Ya Yang. *ACS applied materials & interfaces* 11, no. 31 (2019): 27862-27869.
- [97] Xu, Suwen, Weiqi Qian, Ding Zhang, Xue Zhao, Xiaoming Zhang, Chuanbo Li, Chris R. Bowen, and Ya Yang. *Nano Energy* 77 (2020): 105305.
- [98] Roy, Jhilik, Leenia Mukhopadhyay, Souravi Bardhan, Dhananjoy Mondal, Saheli Ghosh, Sudip Chakraborty, Neelanjana Bag, Shubham Roy, Ruma Basu, and Sukhen Das. *Dalton Transactions* 51, no. 44 (2022): 16926-16936.
- [99] Roy, Jhilik, Shubham Roy, Dhananjoy Mondal, Neelanjana Bag, Jaba Roy Chowdhury, Saheli Ghosh, Souravi Bardhan, Rajib Mondal, Ruma Basu, and Sukhen Das. *Surfaces and Interfaces* 44 (2024): 103579.
- [100] Roy, Jhilik, Dhananjoy Mondal, Jaba Roy Chowdhury, Neelanjana Bag, Saheli Ghosh, Shubham Roy, Rajib Mondal, Ruma Basu, and Sukhen Das. *Ceramics International* (2024).
- [101] Wang, Yanfeng, Yeming Xu, Shangshang Dong, Peng Wang, Wei Chen, Zhenda Lu, Deju Ye et al. *Nature communications* 12, no. 1 (2021): 3508.
- [102] Das, Raghunath, Madhumita Bhaumik, Somnath Giri, and Arjun Maity. *Ultrasonics Sonochemistry* 37 (2017): 600-613.
- [103] Lin, Li, Qing He, Yuexing Chen, Bolin Wang, Li Zhang, Xianxiang Dai, Yuanyuan Jiang et al. *Journal of Colloid and Interface Science* 644 (2023): 29-41.
- [104] Banerjee, Arindam, Anwesha Mukherjee, Neelanjana Bag, Piyali Halder, Indrajit Mondal, Jhilik Roy, Dhananjoy Mondal, Souravi Bardhan, Abhijit Majumdar, and Sukhen Das. *Journal of Molecular Structure* 1298 (2024): 136996.
- [105] Li, Jun, Yin Long, Fan Yang, and Xudong Wang. *Current Opinion in Solid State and Materials Science* 24, no. 1 (2020): 100806.
- [106] Baniasadi, Mahmoud, and Majid Minary-Jolandan. *Materials* 8, no. 2 (2015): 799-814.
- [107] Karaca, Semra, Elif Çakmak Önal, Özkan Açışlı, and Alireza Khataee. *Materials Chemistry and Physics* 260 (2021): 124125.
- [108] Su, Chuangjian, Ruhong Li, Chaolin Li, and Wenhui Wang. *Applied Catalysis B: Environmental* 310 (2022): 121330.

- [109] Khan, Hayat, Aditya S. Yerramilli, Adrien D'Oliveira, Terry L. Alford, Daria C. Boffito, and Gregory S. Patience. *The Canadian journal of chemical engineering* 98, no. 6 (2020): 1255-1266.
- [110] Movasaghi, Zanyar, Shazza Rehman, and Dr Ihtesham ur Rehman. *Applied Spectroscopy Reviews* 43, no. 2 (2008): 134-179.
- [111] Hamdan, Halimatun, Mohd Nazlan Mohd Muhid, Salasiah Endud, Endang Listiorini, and Zainab Ramli. *Journal of Non-Crystalline Solids* 211, no. 1-2 (1997): 126-131.
- [112] Egerton, R. F., P. Li, and M. Malac. *Micron* 35, no. 6 (2004): 399-409.
- [113] Lai, C. H., S. L. Lo, and H. L. Chiang. *Chemosphere* 41, no. 8 (2000): 1249-1255.
- [114] Fagerlund, Göran. *Matériaux et Construction* 6 (1973): 239-245.
- [115] Kök, Mustafa VerşanKök, Mikhail A. Varfolomeev, and Danis K. Nurgaliev. *Journal of Petroleum Science and Engineering* 154 (2017): 537-542.
- [116] Olgun, Murat, and Mustafa Yildiz. *Arabian Journal for Science and Engineering* 37 (2012): 1833-1848.
- [117] Hill, R. M., and A. K. Jonscher. *Journal of Non-Crystalline Solids* 32, no. 1-3 (1979): 53-69.
- [118] Menzinger, M., and Re Wolfgang. *Angewandte Chemie International Edition in English* 8, no. 6 (1969): 438-444.
- [119] Schlömann, E., J. J. Green, and uU Milano. *Journal of Applied Physics* 31, no. 5 (1960): S386-S395.
- [120] Middlemiss, Laurence A., Anthony JR Rennie, Ruth Sayers, and Anthony R. West. *Energy Reports* 6 (2020): 232-241.
- [121] Chevion, Shlomit, Matthew A. Roberts, and Mordechai Chevion. *Free radical biology and medicine* 28, no. 6 (2000): 860-870.
- [122] Orio, Maylis, Dimitrios A. Pantazis, and Frank Neese. *Photosynthesis research* 102 (2009): 443-453.

[123] Mondal, Dhananjoy, Souravi Bardhan, Namrata Das, Jhilik Roy, Saheli Ghosh, Anupam Maity, Shubham Roy, Ruma Basu, and Sukhen Das. *Nano Energy* 104 (2022): 107893.

[124] Mondal, Dhananjoy, Neelanjana Bag, Jhilik Roy, Saheli Ghosh, Shubham Roy, Monisha Sarkar, Souravi Bardhan, Soumyaditya Sutradhar, and Sukhen Das. *Langmuir* (2024).

Chapter 2



Investigation of Different Physicochemical Properties of Natural Kaolinite Clay by Particle Size Modulation.

Chapter 2

Investigation of Different Physicochemical Properties of Natural Kaolinite Clay by Particle Size Modulation.

2.1 Introduction

In recent times, numerous works have been going on the synthesis and characterization of different nanocrystals. In this regard hybrid materials having high performance gaining interest due to the limited applicability of single metals, polymers, or ceramics [1]. Another big issue is biocompatibility. Researchers are trying to develop biocompatible hybrid materials after the escalated development of nanotechnology. Natural materials are gaining attention in this field for their promising physicochemical properties in nano regimes [2].

This chapter emphasises the effect of nanonization on the functionalization of naturally formed kaolinite clay; one of the most abundant clay minerals on the Earth's crust [3]. Despite the abundance of kaolinite in nature, an insufficient amount of interest is given to studying the electrical properties of this material as a function of size, temperature, and crystallinity. In general, kaolinite is reported to have a lower dielectric constant value of 11 at microwave frequency and is mostly used in the ceramic and porcelain industry. To enhance the dielectric constant and to reduce the tangent loss, various dopants like NaF, Fe, Mn, Co, Cr, Co, Ga, Mg, and Mg-Ni are used or sintered at very high temperatures [4]. In contrast, mechanical grinding is a facile, cost-effective technique that not only reduces the hassles associated with firing at higher temperatures or chances of secondary pollution from dopants but also shows a significant increment in the dielectric permittivity value. Hence in this chapter, a facile ball-milling approach has been followed herein to achieve kaolinite nanostructure to enhance dielectric properties to meet the practical application [5]. Moreover, a detailed analysis of crystallography and microstructure-mediated dielectric property variation and temperature stability study has been performed. The analyses of the dielectric constant and conduction mechanism of this green material show that the sample in the nano-

domain has the lowest degree of crystallinity along with the highest charge storage capacity compared to its other fractions [6]. This naturally available clay mineral is a low-cost material that depicts augmented electrical permittivity in nanodomain along with promising resistivity and nominal tangent loss, which is discussed in this chapter for the very first time with various experimental evidence. This high electrical permittivity value makes this nano-kaolinite sample an ameliorative agent for fabricating the separator layer of the green capacitors, which will minimize the manufacturing cost along with the environmental pollution [7]. Additionally, these enhanced physicochemical properties suggest that this nano-clay is efficient in interacting with other nanomaterials for fabricating hybrid nanocomposites for various applications for the sustainable development of nations.

2.2 Experimental Details

2.2.1 Materials

Natural kaolinite ($\text{Al}_2\text{Si}_2\text{O}_5(\text{OH})_4$) clay was obtained from Hindustan Minerals, India. The potassium bromide and acetone used in the experiment were purchased from Merck, India. All the purchased reagents are of analytical grades and were used without any further purification. Millipore water used in the following experiments has a resistivity of approximately $18 \text{ M}\Omega\text{-cm}$.

2.2.2 Synthesis method

Initially, the purchased kaolinite sample was crushed with the help of a diamond mortar manually to reduce the agglomeration. A part of the crushed sample was sieved with the help of a 400-mesh sieve.



Figure 2.1. Synthesis of different kaolinite size fractions.

The sample above the sieve was collected as the bulk fraction (K1) and the sample below the sieve (K2) was kept for further mechanical milling process. 5 gm of this sieved sample (K2) was then subjected to mechanical milling in a Fritsch Planetary Mono mill Pulverisette 6 ball-mill machine with the help of tungsten carbide vial and balls for 48 h at 150 rpm. The milled clay sample was washed in water and then collected and dried in a hot air oven. The dried sample was further washed in acetone to reduce impurities and dried in a hot air oven for another 12 h at 60°C. Finally, the dried fine sample was marked as K3 (Figure 2.1). The entire set of samples was then sent for further characterization.

2.3 Result and Discussions

2.3.1 Purity and elemental analysis of bulk kaolinite

Table 2.1. Chemical composition (XRF-data) of bulk kaolinite.

Compound	Concentration (%)
SiO ₂	66.3
Al ₂ O ₃	30.7
TiO ₂	1.4
K ₂ O	0.6
Fe ₂ O ₃	0.7

The elemental analysis of the kaolinite samples has been done by employing EDX and XRF techniques. Initially, the XRF data of the bulk kaolinite has been plotted in Table 2.1, which validates the presence of 66.3% of silicate and 30.7% of alumina in the sample. It is quite evident

from Table 2.1 that the percentage purity of this sample is around 97.1 %. In reality, the ratio of alumina and silica in pure kaolinite is 0.5, which is found to be 0.476 in our sample. This ratio corroborates the fact that the natural kaolinite is quite pure with a nominal impurity (K₂O and Fe₂O₃) as it has been directly collected from the natural source. Figures 2.2, and Table 2.2 show the EDX and elemental mapping of the entire sample set.

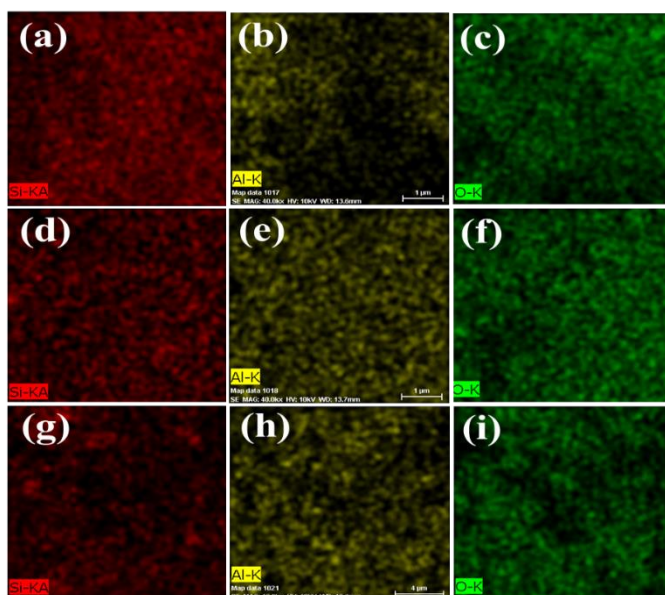


Figure 2.2. Elemental mapping data of the kaolinite samples showing the presence of Al, Si, and O in the samples

Table 2.2. EDAX data of all samples.

Sample	Element	Weight (%)
K1	Al	14.58
	Si	33.87
	O	51.55
K2	Al	10.88
	Si	24.27
	O	64.85
K3	Al	20.83
	Si	28.34
	O	50.82

The EDX spectra confirm the traces of Al, Si, and O in each case.

Elemental mapping by FESEM provides qualitative information about the distribution of elements shown by different colors that are present in the scanned area. It is observed that the marked elements (Al, Si, and O) are present in the scanned area in a uniform manner confirming the purity of the samples.

2.3.2 Determination of crystalline structure and microstructural properties of treated kaolinite samples

The diffraction maxima of the clay samples (Figure 2.3) corroborate with JCPDS card no. 80-0886, which suggests the materials to be kaolinite. The absence of any unwanted diffraction peaks is the primary evidence of its purity. A standard crystallographic information file (.cif) of pure kaolinite (AMCSD file no. 1550598) was used to refine the experimental diffractograms. Various microstructural parameters, such as unit cell dimension, crystal size, and microstrain were refined to get promising fitting results [8].

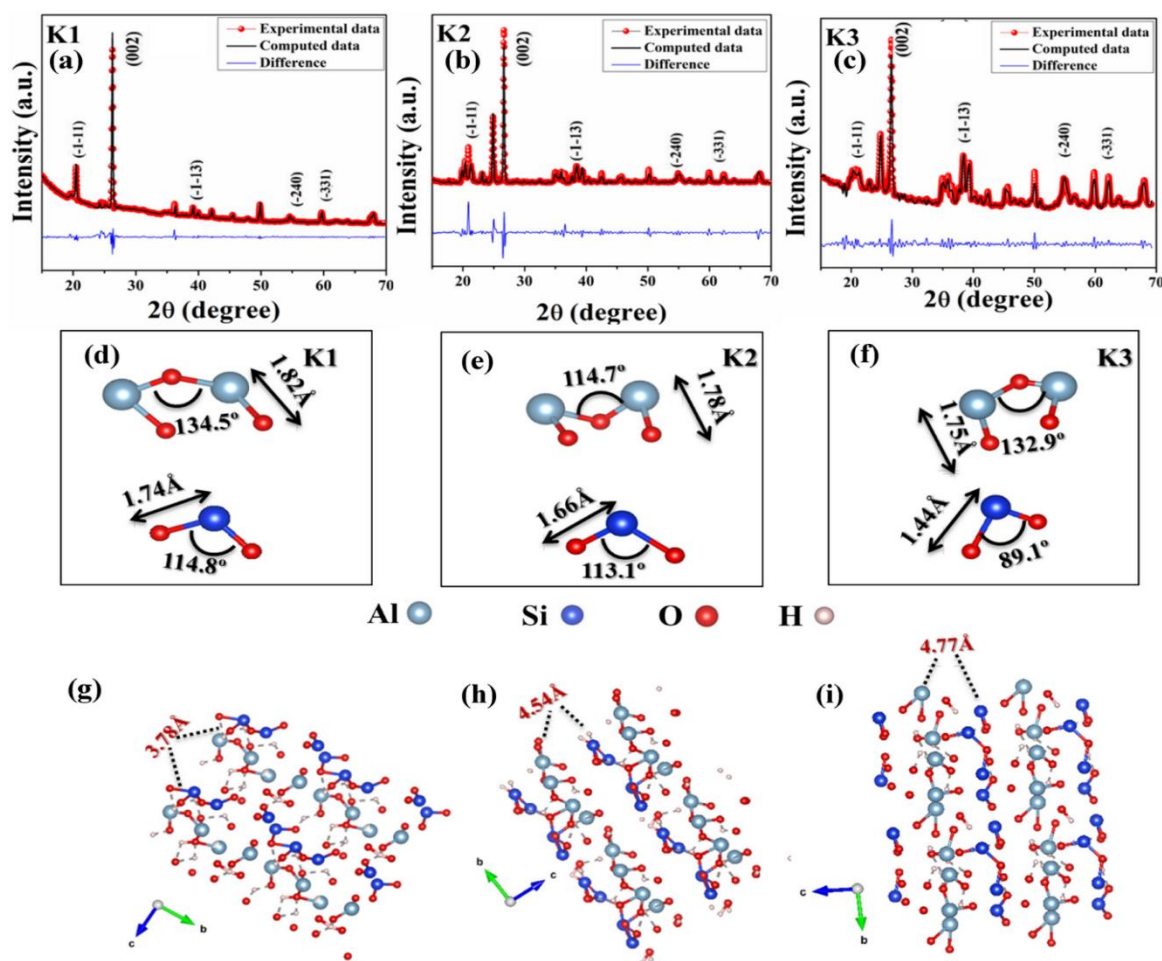


Figure 2.3. a–c Indexed XRD pattern (red line) of the sample K1, K2, and K3, and the simulated Rietveld refinement plot (continuous black line) obtained by fitting the experimental PXRD pattern using the MAUD program. The respective residue is plotted at the bottom (blue line); d–f bond angles and bond lengths of K1, K2, and K3, respectively, from refinement data; g–i Separation of alumina-silica layers in K1, K2, and K3, respectively.

The anisotropic crystal size is found to be 113 nm for K1 which has been greatly reduced to 37 nm in nano-engineered K3 sample. The enhancement of microstrain value with decreasing crystallite size is another major outcome of this study. In reality, ball milling reduces the particle dimension drastically by reducing the a and b sides of the unit cells and resulting in augmented microstrain values. Fascinatingly, the c side of the unit cell increases a bit with decreasing crystallite size. This may be due to the enhanced alumina-silica interlayer spacing (basal spacing) in this direction (Figure 2.3: g, h, i).

Table 2.3. Structural and microstructural parameters of the samples were obtained from various characterization techniques including refinement of the XRD diffractograms.

Microstructural parameters	K1	K2	K3
a (Å)	5.201 ± 0.002	5.171 ± 0.001	5.142 ± 0.001
b (Å)	9.006 ± 0.003	8.958 ± 0.002	8.956 ± 0.002
c (Å)	7.357 ± 0.002	7.409 ± 0.002	7.430 ± 0.001
α (°)	91.00	91.61	92.10
β (°)	105.11	104.87	104.89
γ (°)	91.09	89.96	90.40
Volume (Å ³)	326.568	329.610	331.491
R _{wp} (%)	4.71	6.74	6.32
R _p (%)	2.58	3.00	4.52
Crystallite size (nm)	114	104	38
Micro-strain	0.0016	0.0023	0.0028
Surface area (m ² g ⁻¹)	123.7	126.6	129.2
Pore size (nm)	5.4	15.5	18.7
Pore volume (mL/g)	0.206	0.491	0.520
Alumina-Silica basal spacing (Å)	3.78	4.54	4.77
Al-O bond length (Å)	1.819	1.776	1.746
Si-O bond length (Å)	1.745	1.664	1.444
Al-O-Al angle (°)	134.5	114.7	132.9
O-Si-O angle (°)	114.8	113.1	89.1

The texture analyses along with the atomic positions were also refined to get reasonable fitting data. The global reliability parameters (R_{wp} and R_p) are relatively low implying the consistency of the refinements [9].

All the parameters were refined for at least fifteen cycles and corresponding refinement results (Table 2.3) showed layered structures of alumina and silica inside the kaolinite unit cells. The separation of these alumina-silica layers is measured confirming a gradual increment of this basal separation with decreasing crystallite size. In the case of K1, the basal spacing is around 3.78 Å, whereas, it is found to be 4.77 Å for K3. Not only does the alumina-silica separation vary, but also the cell volume is enhanced with decreasing crystallite size. This may be due to the bond energy minimization caused by ball-milling, which slackens the bond structure in the ball-milled samples (especially K3) [10]. Henceforth, bond lengths and bond angles have been calculated (Figure 2) to justify this part. With increasing treatment time, Al–O and Si–O bond lengths have been

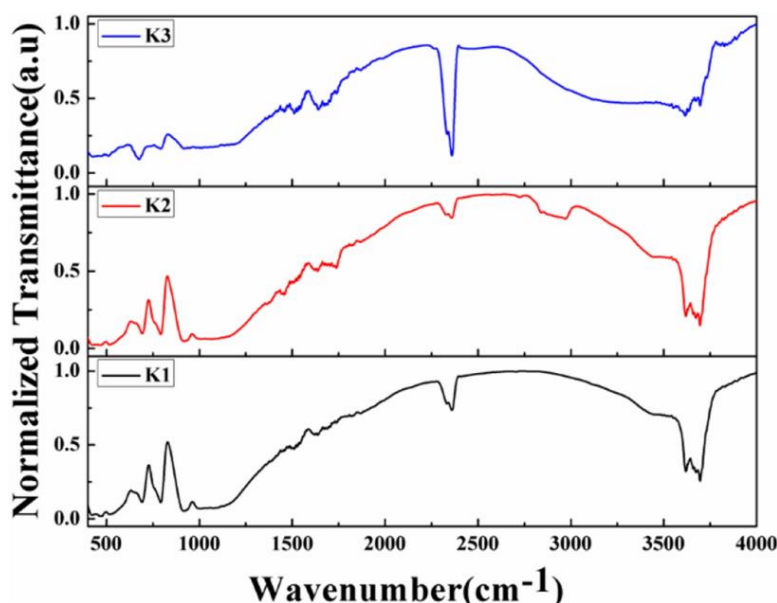


Figure 2.4. Normalized FTIR spectra of the samples K1, K2 and K3

slightly reduced which further reduces the Al–O–Al and O–Si–O angles (Table 2.3) resulting in enhanced basal separation (Table 2.3). Thus, it is observed that external stimulation, such as ball-milling significantly influences the crystal structure of natural kaolinite clay [11].

2.3.3 Spectroscopic study and bonding network analysis

Phase purity at the molecular level was investigated using FTIR spectrometry and it is depicted in Figure 2.4. The absorption bands situated at 431, 460, and 520 cm^{-1} are

attributed to Si–O, Si–O–Si, and Si–O–Al bending, respectively. Absorption bands at 695 and 798 cm^{-1} are attributed to Si–O bending. The deformation of Al–Al–OH bonds creates its signature absorption band at 919 cm^{-1} [12]. The band corresponding to Si–O stretching mode is observed between 940 and 1150 cm^{-1} . Such observations suggest that the samples are kaolinite as they have signature vibrational bands in their respective positions. The vibrational band located at 1643 cm^{-1} corresponds to the H–O–H bond vibration. The band related to the bending of H–OH can be observed at 3627 and 3695 cm^{-1} due to the presence of external and internal –OH, respectively. These bands are reduced greatly in the K3 sample depicting the fact that K3 absorbs less moisture from the local environment than the other two size fractions. Absorption bands observed at 2334 and 2367 cm^{-1} are caused due to the presence of adsorbed atmospheric CO_2 [13].

2.3.4 Morphological studies and particle size analysis

The FESEM micrographs are provided in Figure 2.5. Kaolinite generally shows basal and edge surfaces and hexagonal plate-like structures. FESEM micrographs show that particles of K1 are an admixture of distinctly large and heavily agglomerated, along with the presence of a few smaller particles [14]. These plate-like structures have diameters around 300–310 nm. This is due to the uneven grinding of natural kaolinite by mortar. K2 on the other hand shows evenly distributed sheet-like structures of kaolinite having diameters ranging from 200 to 220 nm. The width of the size distribution for K2 is smaller than that of K1 as Figure 4 suggests. This evenly distributed particle size is attributed to the sieving during size fractionation. In the case of K3, the particle size reduces significantly. K3 sample possesses an average diameter of 90–100 nm, which makes it a natural nano-system [15].

2.3.5 Surface area and porosity analyses

Estimation of average surface area and surface porosity of the prepared samples (K1, K2, and K3) were done by employing the BET-BJH method. The adsorption–desorption isotherms obtained along with pore size distributions are illustrated in Figure 2.6. The hysteresis loop obtained from these experiments suggests the type IV isotherm,

presumably due to the presence of mesopores. In the case of K2 and K3, volumes of adsorbed and desorbed N₂ gas are very similar to each other, unlike K1, which might be due to the uniformity in size distributions, as seen in FESEM micrographs. The surface area obtained for K1 is found to be 123.7 m² g⁻¹, while for K2 and K3, it is found to be 126.6 and 129.2 m² g⁻¹, respectively. Thus, there is an increase in surface area with decreasing particle size. The average pore diameter was found to be 5.4, 15.5, and 18.7 nm for K1, K2, and K3, respectively.

Similarly, the pore volume also increases with a decrease in particle size, which suggests the nanonized K3 sample to be a promising material for various industrial applications [16].

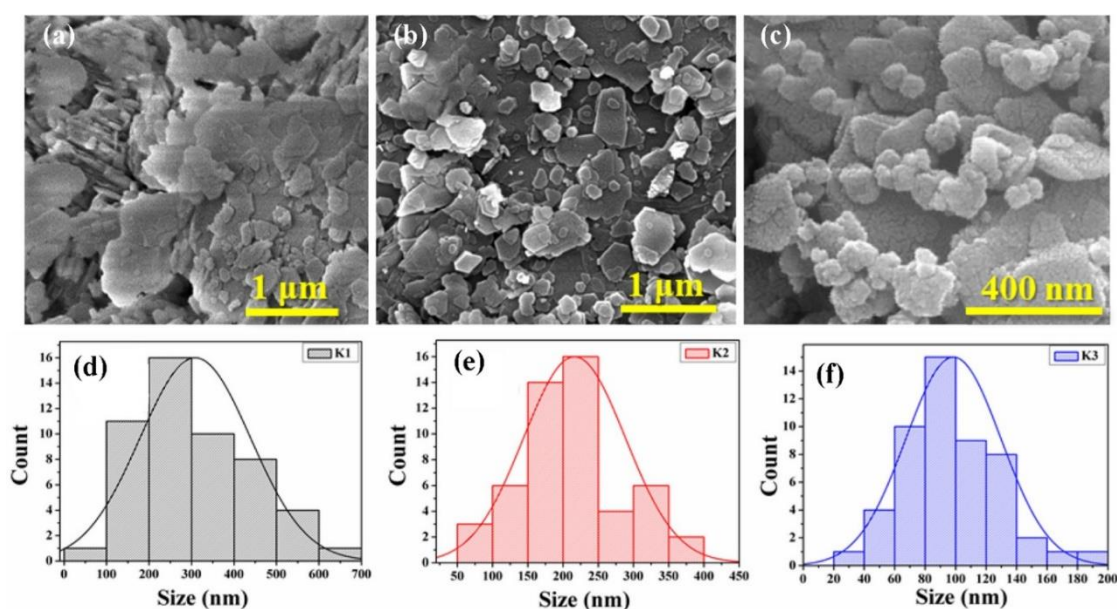


Figure 2.5. FESEM micrographs of the samples a K1, b K2, and c K3, corresponding size distribution plots from the FESEM images (d–f).

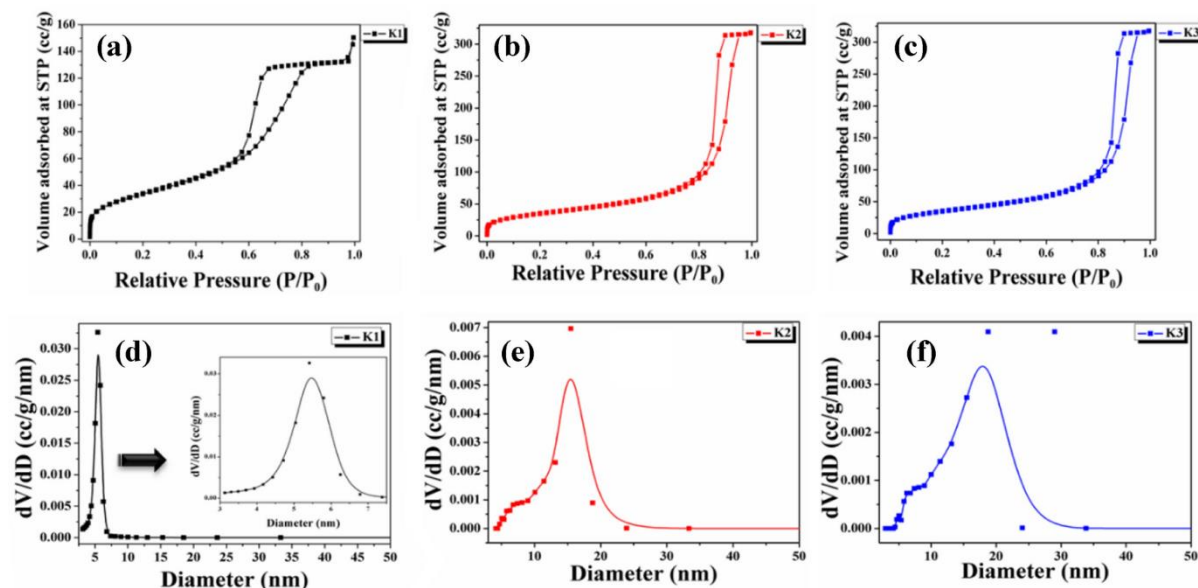


Figure 2.6. N_2 adsorption/desorption isotherms of the samples a) K1, b) K2, and c) K3; Pore size distribution data for d) K1, e) K2, and f) K3.

2.3.6 Thermal characterization of the natural materials

From DTA-TGA measurement it has been found that the overall mass loss is highest in

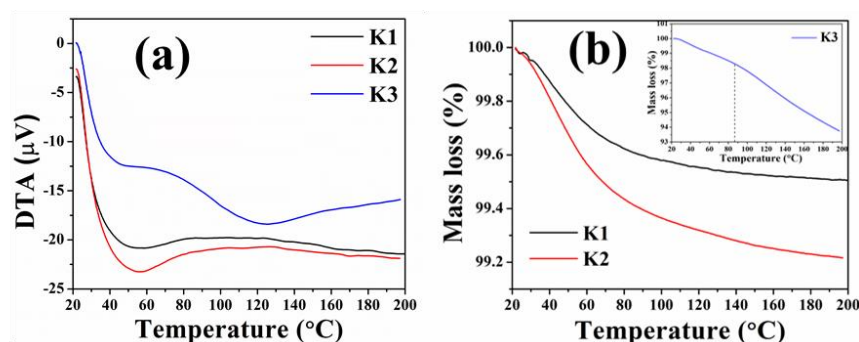


Figure 2.7. (a) DTA and (b) TGA data of the samples

the K3 sample (6 %), whereas, it is lower in K1 (0.5 %) and K2 (0.8 %) (Figure 2.7). This is probably

due to the release of surface-

adsorbed moisture and CO_2 from the K3 sample. The enhanced surface porosity of the K3 sample accommodates a higher amount of moisture and environmental CO_2 as stated in our FT-IR result [17]. At higher temperatures, these volatile substances have been eliminated from the surface of the K3 causing a broad endothermic peak located

just above 50°C. There is no sign of any alternative phase formation due to heating (up to 200°C), which makes these samples quite stable [18].

2.3.7 Estimation of dielectric constant and loss tangent of the synthesized samples

The dielectric plots by equation 1.4 were obtained over a range of varying frequencies (from 40 Hz to 10 MHz) and temperature (30–210°C), as shown in Figure 2.8. Since the imaginary part of the electrical permittivity has negligible value, hence not presented here. There is a gradual reduction of permittivity values with increasing frequency is observed in all the samples. This phenomenon is attributed to the Maxwell–Wagner interfacial polarization which is primarily formed due to various structural inhomogeneities, like imperfection in crystal alignment, vacancy, and other crystal defects created during the sample preparation [19]. This observation is in good agreement with Koop’s theory. According to this theory, the oscillating dipoles formed by the free charge carriers are trapped in the grain boundaries [20]. Those are formed due to structural defects in the low-frequency regime and can easily follow the external field causing high permittivity values, whereas, at higher frequencies, the dipoles cannot trail rapidly changing external fields resulting in reduced permittivity. The dielectric constant observed is significantly higher in the K3 sample as compared to the other size fractions [21].

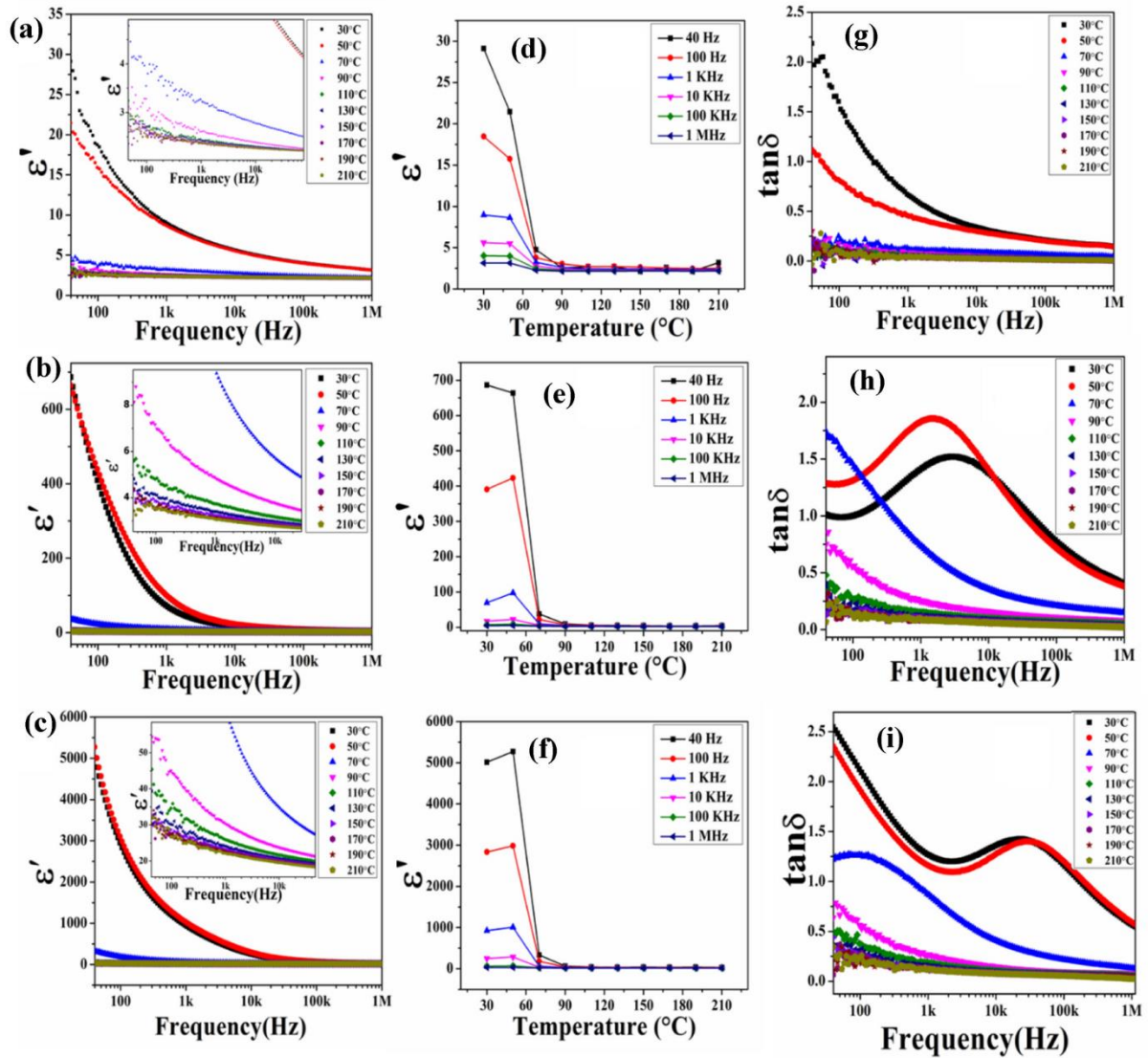


Figure 2.8. Variation of the dielectric constants with frequency (a–c); Variation of the dielectric constants with temperature (d–f); Variation of the loss tangent with frequency (g–i) of K1, K2, and K3, respectively.

Space charge polarization, which increased in the case of K3 due to lattice or crystal defects might have contributed to such a high value of dielectric constant (ϵ'). In the case of K3, the oxygen vacancies created from high-energy ball-milling lead to a higher number of oscillating dipole formations. The possibility is even enhanced when the surface area is equally enhanced in this sample due to nanonization. Thus, a higher

surface area with a greater number of interfacial oscillating dipoles augments the permittivity value radically, which is reflected in K3 (5.013×10^3 at 40 Hz) compared to K1 (29.12 at 40 Hz). The temperature-dependent studies of dielectric constant for all three samples have been carried out to ensure the real-life applicability of the synthesized natural materials as dielectric separators [22]. It can be observed from the temperature response data that the dielectric constants for the entire sample set show promising values up to 70°C beyond which, a rapid fall has been observed. This rapid fall of the dielectric constant is primarily due to the elimination of moisture and adsorbed CO₂ gas from the porous surface of natural kaolinites. The FTIR data previously ensured the presence of these volatile elements inside the porous surface of kaolinite, especially in the K3 fraction due to high porosity and enhanced surface area. It was also evident from thermal characterizations that the mass loss is quite high in K3 at the said temperature range. Thus, beyond 70°C, a sharp decrement is observed for all the samples. Although, the dielectric value of K3 at 210°C is (30.30) higher than that of the K1 sample at room temperature (29.12). This ensures that the nanoengineered kaolinite is a better option even in higher temperatures. The variation of tangent loss (Figure 7) is also following the dielectric constant values observed herein. It is observed in K2 and K3 that the tangent loss has well-defined peaks at lower temperatures (30–50°C). This type of tangent loss is generally caused due to the dominance of active elements over the reactive elements in the material. The surface-adsorbed moisture and CO₂ act as active elements in this regard, which are greatly removed at higher temperatures [23]. Additionally, this peak position shifted towards lower frequencies at higher temperatures suggesting the reduction of these polar active elements. The presence of such active elements is higher in K3 as compared to K2 and K1 (from TGA-DTA data). Thus, a greater amount of peak shifting is observed in the K3 sample. Subsequent removal of adsorbed active elements, such as moisture and surface adsorbed CO₂ from the K3 sample at higher temperatures lowers its dielectric constant [24]. But the value is still higher than its other size fractions (K1 and K2) even after the removal of active elements making K3 a potential material for charge storage applications. Another major result obtained from this study is the effect of active elements on

dielectric permittivity for natural kaolinite. Moisture affects dielectric constant and loss tangent significantly. Such knowledge will help in storing and interacting with other materials of this green and natural clay mineral for fabricating hybrid nano-systems [25].

2.3.8 AC conductivity and conduction mechanism studies

To analyze the charge transport mechanism, temperature-dependent AC conductivity studies have been carried out (equation 1.5). The ac conductivities of the samples have lower values at lower frequency domains, which increased with subsequent frequency increments due to higher electron mobility and hopping at higher frequencies [26]. The conductivity increases with decreasing particle size (Figure 2.9).

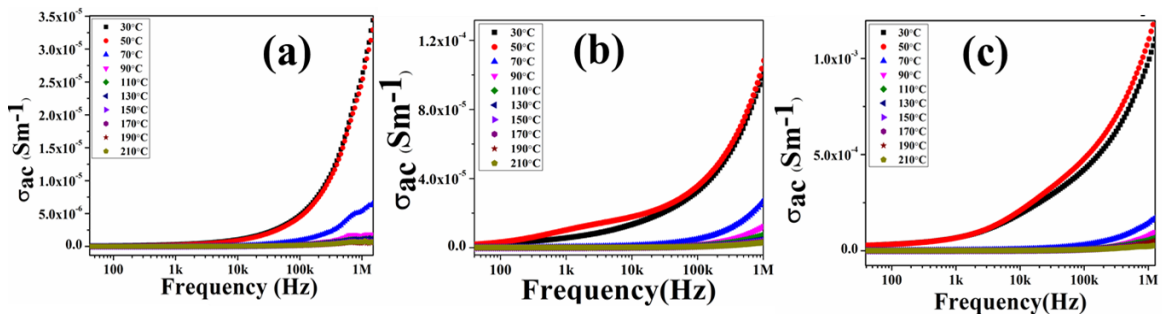


Figure 2.9. AC conductivities of K1, K2, and K3 respectively.

The enhanced surface area of K3 causes a simultaneous increase in the number of mobile charge carriers that might cause an increase in AC conductivity in this size fraction. K1 shows the lowest value as it has the lowest amount of mobile charge carriers. The frequency response of AC conductivity has also been studied through Jonscher's power law [27] (equation 1.7).

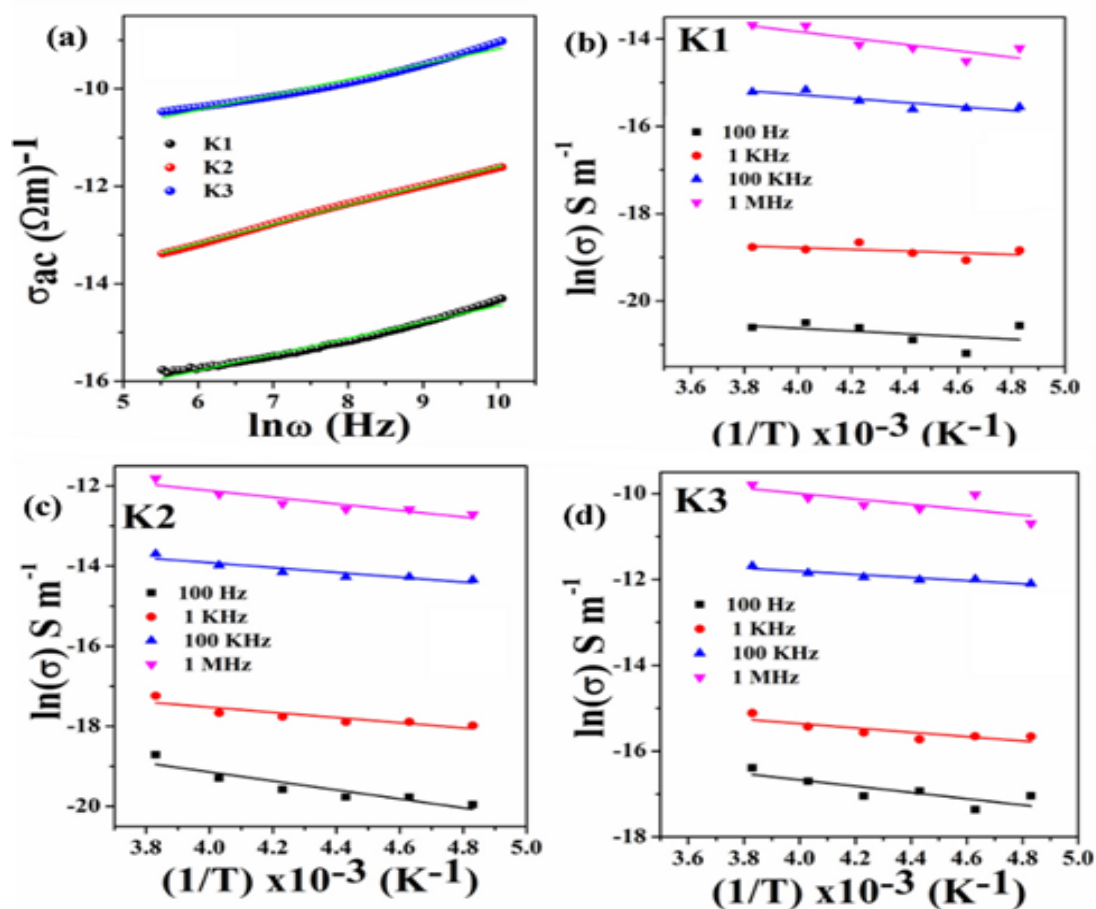


Figure 2.10. a) Jonscher's plot for ensuring the conduction mechanism of the kaolinite samples; b–d) Arrhenius plots for estimating the activation energies of the samples.

The estimated values of the “n” in this case are found to be 0.332 and 0.394 for K1 and K2, respectively, which is increased further in K3 (0.312). These non-zero n values corroborate that kaolinite samples do not follow perfectly Debye type (where $n = 0$) conduction mechanism and diffusion-limited hopping dominates in this case (Figure 2.10) [28].

Table 2.4. *Calculated activation energies from Arrhenius plots at different frequencies.*

Sample	Frequency	Activation Energy (eV)
K1	100Hz	0.026
	1 KHz	0.016
	100KHz	0.029
	1MHz	0.063
K2	100Hz	0.071
	1 KHz	0.052
	100KHz	0.056
	1MHz	0.096
K3	100Hz	0.054
	1 KHz	0.031
	100KHz	0.044
	1MHz	0.063

Initially, charge hopping starts when free charge carriers get a sufficient amount of external energy (in the form of heat) to escape from the grain boundaries, known as activation energy (E_a). Thus, it is necessary to study and estimate activation energy to establish the conduction mechanism [29]. Activation energies can be calculated using the Arrhenius equation stated in equation 1.6. Arrhenius plots were calculated from the temperature-dependent ac conductivity

data at field frequencies 100 Hz, 1 kHz, 100 kHz, and 1 MHz (Figure 2.10). A detailed description of the activation energies of the entire sample set is given in Table 2.4.

2.3.9 Impedance spectroscopy for materials

The real part of the entire set of R-X data (Figure 2.12) shows a depressed semi-circular nature at the high-frequency region followed by straight lines situated at lower-frequency domains. The radius of semi-circles implies the total charge transfer resistance (R_{ct}) values, which are highest in the case of K3. The impedance curves were further fitted using the EIS Spectrum Analyser v1.0 program with the standard Randles

circuit containing a parallel combination of a charge transfer resistance (R_{ct}) and a double-layer capacitance (C_{dl}) combined with a Warburg element [30]. A series resistance has also been provided into the circuit. The Randles circuit is widely used to fit impedance data as it approximates the behavior of any cell/interface for very small perturbations. Thus, the accuracy of this model is quite high. According to this theory, R_{ct} restricts the charge migration process through the sample. The double-layer capacitance enhances the charge-storing capacity of the system. The total experimental impedance sometimes does not match with the total contributing impedance of R_{ct} and C_{dl} alone [31]. Thus, one needs to consider the Warburg element to match this paradox. Herein, the outcome of the fitting has been depicted in Figure 2.11 showing that the K3 sample has the highest R_{ct} value (90 k Ω , 205 k Ω , and 1.9 M Ω for K1, K2, and K3 respectively) compared to other samples. Such a gradual increment of R_{ct} could be substantiated by the virtue of crystallographic data. In reality, the microstructural data shows a gradual increment of basal spacing (distance between alumina-silica bases), which restricts the charge migration through these basal spaces and results in higher R_{ct} values with reduced sample sizes.

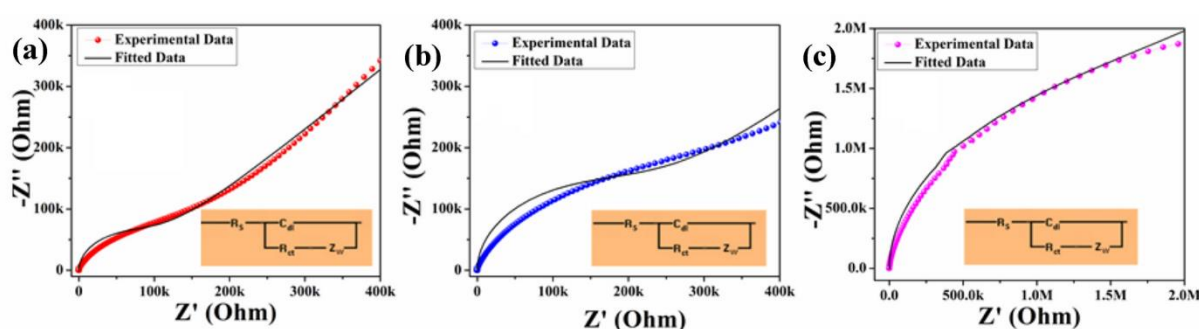


Figure 2.11. Impedance plots are experimental and fitted of a) K1, b) K2, and c) K3, respectively, with equivalent circuits.

2.3.10 Estimation of specific capacitance and charge-discharge characteristics

It is found that the specific capacity of K3 at 100 mV S⁻¹ scan rate is around 185 F g⁻¹, which is significantly higher than K1 (93 F g⁻¹) at the same scan rate (equation 1.8). This high value of specific capacitance in a natural dielectric sample is rare and quite

useful for multipurpose uses [32]. To assess the increment of storage capacity and discharge rate in K3 in comparison to K1, the galvanostatic charge–discharge carried out and the performance are illustrated in Figure 2.12. The charge–discharge curve (Figure 2.14) shows a rapid increase of voltage during charging, which gradually reduces due to discharging, thus exhibiting reversible and symmetrical charge–discharge cycles and confirming the typical capacitive properties. The discharging time is much higher (9 times) in K3 in comparison to K1.

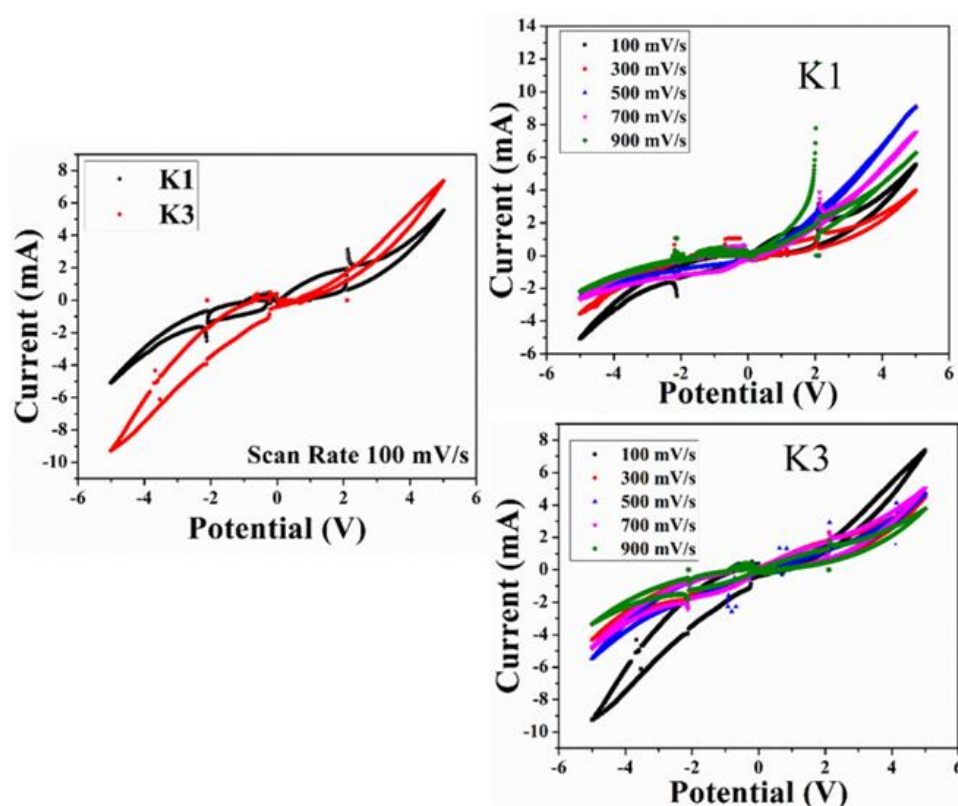


Figure 2.12. Cyclic voltammetry analysis of K1 and K3 showing the charge storage capacity of the natural samples

The specific capacitance was evaluated from the curves using the following equation:

$$C = \frac{2i\Delta t}{m\Delta v} \dots \dots \dots 2.1$$

where C denotes the specific capacitance, i represents discharge current, Δt represents discharging time, the mass of the sample is represented as m and Δv represents the change in the voltage (V) [33]. The specific capacitance calculated from the charge–discharge data are quite similar to the calculated capacitance from CV data. The specific capacitance, in this case, is found to be 247 F g^{-1} for K3, whereas it is 83 F g^{-1} for K1 showing an augment in the charge storage capacity in nano-kaolinite clay (Figure 2.13).

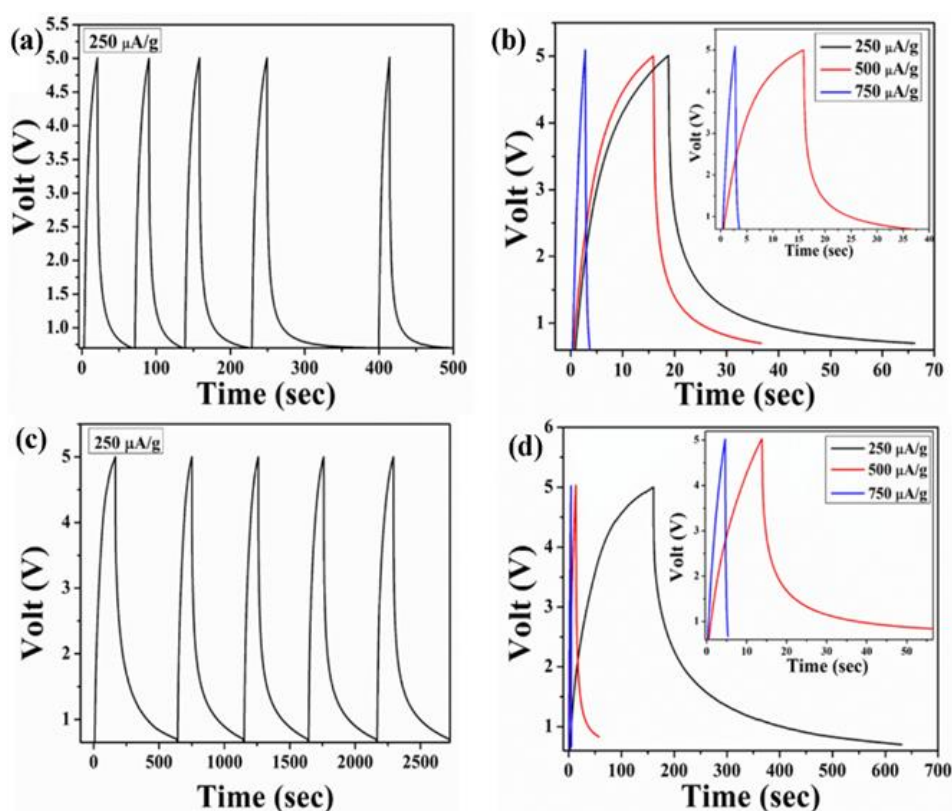


Figure 2.13. galvanostatic charge-discharge characteristics of K1 (a, b) and K3 (c, d)

2.4 Summary

Herein, the particle size reduction of the collected kaolinite clay has been performed by a one-step ball milling technique to investigate its physicochemical properties with size modulation. Initially, the purity of the sample has been assessed by employing XRF and EDX techniques. Moreover, X-ray crystallography and FT-IR spectrometry of the

samples reveal the microstructure and bonding networks, which play a pivotal role in assessing the conduction mechanism and charge storage properties of the materials. The FESEM images confirm the impact of ball-milling in reducing the particle size of this clay. These micrographs also validate the K3 sample to be in the nano regime (90–100 nm). Such nano-confinement enriches the aspect ratio in this K3 sample, which is reasonable with its high dielectric constant (5000 in 40 Hz) and higher specific capacitance (185 F g^{-1}). Further, the charge conduction mechanism of the samples has been characterized by standard Arrhenius and Jonscher's equations revealing the diffusion-limited conduction mechanism, which also corroborates the dielectric data. Such interesting dielectric relaxation with enhanced storage capacity in the nano dimension along with the enhanced surface properties suggests that the nano kaolinite can enhance the properties while conjugating with other materials for the fabrication of hybrid nanosystems by their promising physicochemical properties and high aspect ratio.

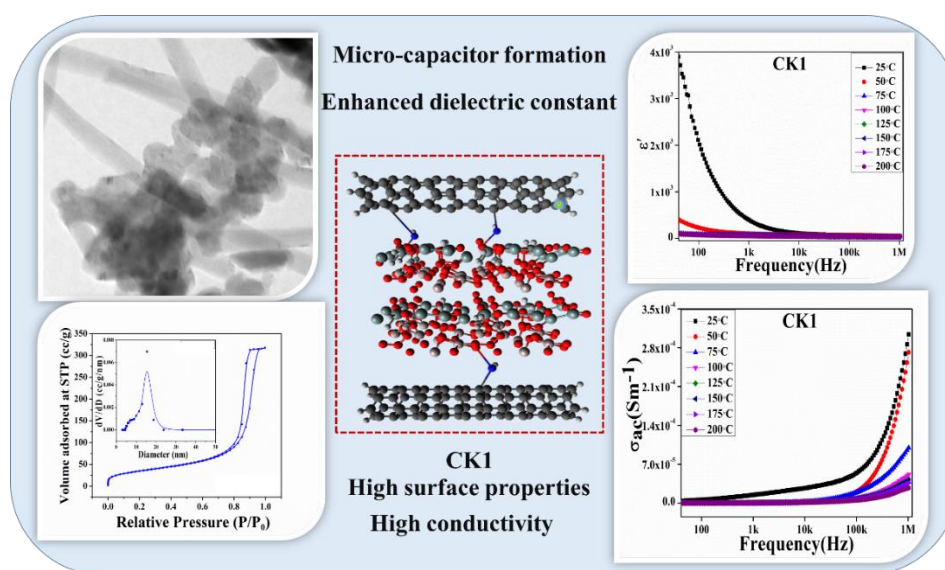
References

- [1] Sanchez, Clément, Philippe Belleville, Michael Popall, and Lionel Nicole. *Chemical Society Reviews* 40, no. 2 (2011): 696-753.
- [2] Bag, Neelanjana, Souravi Bardhan, Shubham Roy, Jhilik Roy, Dhananjay Mondal, Bing Guo, and Sukhen Das. *Biomaterials Science* 11, no. 6 (2023): 1994-2019.
- [3] Das, Solanky, Dhananjay Mondal, Souravi Bardhan, Shubham Roy, Dipak Kr Chanda, Anupam Maity, Subhojit Dutta, Kamalakanta Mukherjee, and Kaustuv Das. *Journal of Materials Science: Materials in Electronics* 33, no. 9 (2022): 7119-7133.
- [4] Saadi, H., Z. Benzarti, F. I. H. Rhouma, P. Sanguino, S. Guermazi, K. Khirouni, and M. T. Vieira. *Journal of Materials Science: Materials in Electronics* 32 (2021): 1536-1556.
- [5] Cheng, Hongfei, Yi Zhou, and Qinfu Liu. In *Nanomaterials from Clay Minerals*, pp. 285-334. Elsevier, 2019.
- [6] Md, Sayful Islam. *POLYMER* 8: 8-2014.

- [7] Mondal, Dhananjay, Amartya Sau, Shubham Roy, Souravi Bardhan, Jhilik Roy, Saheli Ghosh, Ruma Basu, Soumyaditya Sutradhar, and Sukhen Das. *Journal of Materials Science: Materials in Electronics* 34, no. 21 (2023): 1597.
- [8] Darkwah, Williams Kweku, Buanya Beryl Adormaa, Masso Kody Christelle Sandrine, and Yanhui Ao. *Catalysis Science & Technology* 9, no. 3 (2019): 546-566.
- [9] Post, Jeffrey E., and David L. Bish. *Modern powder diffraction* 20 (1989): 277-308.
- [10] Mondal, O., S. Mitra, M. Pal, A. Datta, S. Dhara, and D. Chakravorty. *Materials Chemistry and Physics* 161 (2015): 123-129.
- [11] Baki, Vahiddin Alperen, Xinyuan Ke, Andrew Heath, Juliana Calabria-Holley, Cemalettin Terzi, and Murat Sirin. *Cement and Concrete Research* 162 (2022): 106962.
- [12] Smrčok, L'ubomír, Milan Rieder, Alexander I. Kolesnikov, and Garrett E. Granroth. *American Mineralogist* 96, no. 2-3 (2011): 301-307.
- [13] Dhankhar, Sandeep Singh, and C. M. Nagaraja. *RSC advances* 6, no. 89 (2016): 86468-86476.
- [14] Liendo, Freddy, Mara Arduino, Fabio A. Deorsola, and Samir Bensaid. *Journal of Crystal Growth* 578 (2022): 126406.
- [15] Esmaeili, Mir Saeed, Zahra Varzi, Reza Taheri-Ledari, and Ali Maleki. *Research on Chemical Intermediates* 47, no. 3 (2021): 973-996.
- [16] Caputo, Paolino, Michele Porto, Ruggero Angelico, Valeria Loise, Pietro Calandra, and Cesare Oliviero Rossi. *Advances in Colloid and Interface Science* 285 (2020): 102283.
- [17] Lothenbach, Barbara, Pawel Durdzinski, and Klaartje De Weerd. *A practical guide to microstructural analysis of cementitious materials* 1 (2016): 177-211.
- [18] Dufaure, Corinne, Usman Thamrin, and Zéphirin Mouloungui. *Thermochimica acta* 338, no. 1-2 (1999): 77-83.
- [19] Quan, Bin, Xiaohui Liang, Guangbin Ji, Yan Cheng, Wei Liu, Jianna Ma, Yanan Zhang, Daoran Li, and Guoyue Xu. *Journal of Alloys and Compounds* 728 (2017): 1065-1075.

- [20] Koop, Thomas, Beiping Luo, Athanasios Tsias, and Thomas Peter. *Nature* 406, no. 6796 (2000): 611-614.
- [21] Garcia, Artur Posenato, and Zoya Heidari. In *SPWLA Annual Logging Symposium*, p. D033S003R003. SPWLA, 2018.
- [22] Roth, C. H., M. A. Malicki, and R. Plagge. *Journal of Soil Science* 43, no. 1 (1992): 1-13.
- [23] Huang, Xingyi, Bin Sun, Yingke Zhu, Shengtao Li, and Pingkai Jiang. *Progress in Materials Science* 100 (2019): 187-225.
- [24] Zha, Jun-Wei, Ming-Sheng Zheng, Ben-Hui Fan, and Zhi-Min Dang. *Nano Energy* 89 (2021): 106438.
- [25] Sharma, Maya, Vijay Srinivas, Giridhar Madras, and Suryasarathi Bose. *RSC advances* 6, no. 8 (2016): 6251-6258.
- [26] Evdokimov, Igor N., and Aleksandr P. Losev. *Energy & fuels* 24, no. 7 (2010): 3959-3969.
- [27] Greenhoe, Brian M., Mohammad K. Hassan, Jeffrey S. Wiggins, and Kenneth A. Mauritz. *Journal of Polymer Science Part B: Polymer Physics* 54, no. 19 (2016): 1918-1923.
- [28] Singh, D. P., K. Shahi, and Kamal K. Kar. *Solid State Ionics* 287 (2016): 89-96.
- [29] Hulett, J. R. *Quarterly Reviews, Chemical Society* 18, no. 3 (1964): 227-242.
- [30] Kundu, Arpan. PhD diss., Purdue University, 2018.
- [31] Pradhan, Dillip K., R. N. P. Choudhary, and B. K. Samantaray. *International Journal of Electrochemical Science* 3, no. 5 (2008): 597-608.
- [32] Gao, Mengyao, Chien-Chung Shih, Shu-Yuan Pan, Chu-Chen Chueh, and Wen-Chang Chen. *Journal of Materials Chemistry A* 6, no. 42 (2018): 20546-20563.
- [33] Li, Hanlu, Jixiao Wang, Qingxian Chu, Zhi Wang, Fengbao Zhang, and Shichang Wang. *Journal of Power Sources* 190, no. 2 (2009): 578-586.

Chapter 3



*Synergistic Impact on the
Microstructure and Physicochemical
Properties of Nano-Kaolinite Upon
MWCNT Incorporation and Basal
Plane Intercalation*

Chapter 3

Synergistic Impact on the Microstructure and Physicochemical Properties of Nano-Kaolinite Upon MWCNT Incorporation and Basal Plane Intercalation

3.1 Introduction

It is evident from the previous Chapter 2 that particle size plays a significant role in several physicochemical properties of the natural kaolinite clay. These physicochemical properties of the size-modulated clay specifically in their nano regime could be enhanced by modifying them by functional groups incorporation over its surfaces as well as structural deformation and doping by foreign elements [1]. There are several ways to incorporate the foreign elements in the NPs structures. Conventionally, researchers just mix the foreign element by different percentages with the NPs but in the case of the structurally stable natural clay minerals, this method does not give the structural stability [2]. For solving this issue functionalization of the nanoparticle surface and the foreign elements are utmost important before incorporating. Herein, the physicochemical properties of the nano kaolinite clay have been investigated by various modification techniques i.e. surface functionalization (A.K), structural modulation (I.K), and 1D multiwalled carbon nanotube incorporation in different ways (CK) [3]. It has been found from microstructural evolution in Chapter 2 that oxygen vacancies have been created in the lattice structure owing to the high-energy ball milling of the bulk kaolinite. These oxygen vacancies further result in active sites for the incorporation of functional groups over their surfaces. In this chapter electro-negative NH_2 -group was incorporated over the surface of the nonclay for better physicochemical properties. Moreover, structural deformation was also introduced to enhance the properties by the basal plane intercalation of nano-kaolinite (I.K). The enhanced surface properties by functional group incorporation were further utilized by interacting the nano-clay with 1-D multiwalled carbon nanotube (MWCNT) in different methods i.e functionalized the surface of MWCNT (CK), just mixing of MWCNT with the nano-clay (CKM) [4]. After the successful synthesis of all the nanostructures a comparative study was

performed to find the maximum physicochemical properties of the nanocomposites and further validated by X-ray crystallography and various electrical measurements to find a promising natural-clay-based conjugated nanocomposites for the improvement of the different dimensions of nanotechnology and to use them for the betterment of the society [5]. It has been found that functionalized, structure-modulated, and foreign particle-incorporated clay composites show higher physicochemical properties than pristine natural nano-clay.

3.2 Experimental Details

3.2.1 Materials

Natural kaolinite [$\text{Si}_2\text{Al}_2\text{O}_5(\text{OH})_4$] clay was purchased from Hindustan Minerals, India, and MWCNT (purity: 95 %) was purchased from Sigma Aldrich, Germany. The MWCNTs have 50–90 nm widths. Hexamine [$\text{C}_6\text{H}_{12}\text{N}_4$], hydrochloric acid [HCl , 37%], nitric acid [HNO_3 , 69 %], hydrogen peroxide [H_2O_2 , 30 %], Dimethyl sulfoxide (DMSO), and dimethylformamide [$\text{C}_3\text{H}_7\text{NO}$] were purchased from Merck, India. Acetone (HPLC grade) and ethanol (HPLC grade) were purchased from Merck, India for analytical experiments. All the reagents are of analytical grades having purity ~99 % and were used without any further purification. Millipore water was used throughout the experiment having a resistivity of approximately $\sim 18.2 \text{ M}\Omega\text{-cm}$.

3.2.2 Synthesis method

3.2.2.1 Activated nano-kaolinite synthesis (A.K)

The natural nano-clay which shows maximum physicochemical properties in chapter 2 (K3) was then activated by taking 4 gm and dissolving this in 160 ml of Millipore water by subsequent addition of 0.096 gm of hexamine under vigorous stirring. After that 40 μL of 37 %, HCL was added dropwise to the solution and kept overnight at 80°C temperature. The solution was then centrifuged and dried at 70°C overnight. The dried sample was then mortared with an agate mortar and sent for further experiments by marking it as A.K.

3.2.2.2 Intercalated Kaolinite Synthesis (I.K)

The natural kaolinite nano-clay was modified by introducing minute structure deformation by intercalating the basal planes from the previously reported article. In this experiment, 2 gm of nano clay was dissolved in 12 ml DMSO and 2 ml DI water solution. After vigorous stirring, the solution was refluxed by condensation technique at 150°C for 12h followed by another 12h at room temperature. The precipitate was then centrifuged and washed using DI water several times, dried at 70°C in a hot air oven, and collected after grinding by mortar and pestle.

3.2.2.3 Functionalization of multiwall carbon nanotube

A simple ultra-sonication technique was used to reduce the agglomeration of MWCNT. 50 mg of purchased MWCNT was dispersed in 15 ml of ethanol and sonicated by a bath sonicator for 2h. After that, the solvent was evaporated by a hot air oven at 120°C. The dried MWCNT was then dispersed in 15 ml of 3 molar HNO₃ under vigorous stirring for 15 min at 60°C. The suspension was then sonicated for another 2h. After completion of the sonication process, the sample was rinsed with water several times and further aged with H₂O₂ for 15 min at 60°C. After completing the reaction time, the black precipitate was filtered by a vacuum filtration unit. Finally, the sample was dried in a hot air oven at 70°C and sent for further treatment.

3.2.2.4 Preparation of MWCNT-kaolinite nanocomposite (CK)

The preparation of MWCNT-Kaolinite nanocomposite was performed by a simplified condensation technique. Initially, 1 gm of activated kaolinite was dissolved in 30 ml DMF and sonicated for 1 h. After that functionalized MWCNT was added to the solution maintaining the 1.0 % w/w ratio. The solution was then refluxed under vigorous stirring by a condenser unit at 90°C for 24h. The black precipitate was then collected and washed several times with deionized water until its pH achieved a neutral value. The nanocomposites were then dried in a hot air oven at 70°C for 24h and marked as CK1. Moreover, the same preparation technique was adopted with untreated kaolinite and MWCNT and marked the final nanocomposite as CKM1. A schematic

representation of MWCNT incorporation has been depicted in Figure 3.1. All the synthesized NPs by their modification techniques have been depicted in Table 3.1.

Table 3.1. *Synthesized nanoparticles and nanocomposites*

Synthesis procedures	Code of the samples
Nano-kaolinite (Chapter-2)	K3
NH ₂ - Functional group incorporated K3 (activation)	A.K
Basal planes separated K3 (intercalation)	I.K
1%- MWCNT incorporation by both the clay and MWCNT surface modification by functional group incorporation	CK1
1%- MWCNT incorporation by just mixing	CKM1

3.3 Result and Discussions

3.3.1 Structural, morphological, and elemental properties of the nanocomposites

The X-ray diffractograms of the nanoparticles in Figure 3.2 show that the diffraction planes of the activated and functionalized-MWCNT incorporated kaolinite have matched with the kaolinite JCPDS data having card no 80-0886 and found a good agreement with the theoretical data by Rietveld refinement (AMCSD file no. 1550598; triclinic lattice with P1 space group). Any undesired maxima that have not occurred in the diffractogram suggest the purity of the nanocomposite samples [6]. Moreover, in the case of intercalated kaolinite a new diffraction maximum has arisen at the 2θ value 23.8° (200) which also matched with the JCPDS card no 80-0886. This new peak generation suggested the successful structural intercalation of kaolinite in I.K nanoparticles.

In reality, the diffraction planes 111, and $1'10$ are the prism planes whereas 001, 002, and 200 are the basal planes of kaolinite. The schematic representation of the basal and

prism plane and its interaction with the functional group has been depicted in Figure 3.3 c for hexagonal kaolinite nanoparticles. The intercalation of the nano-clay increased the basal plane separation promisingly as a result x-rays are diffracted from the new basal planes and

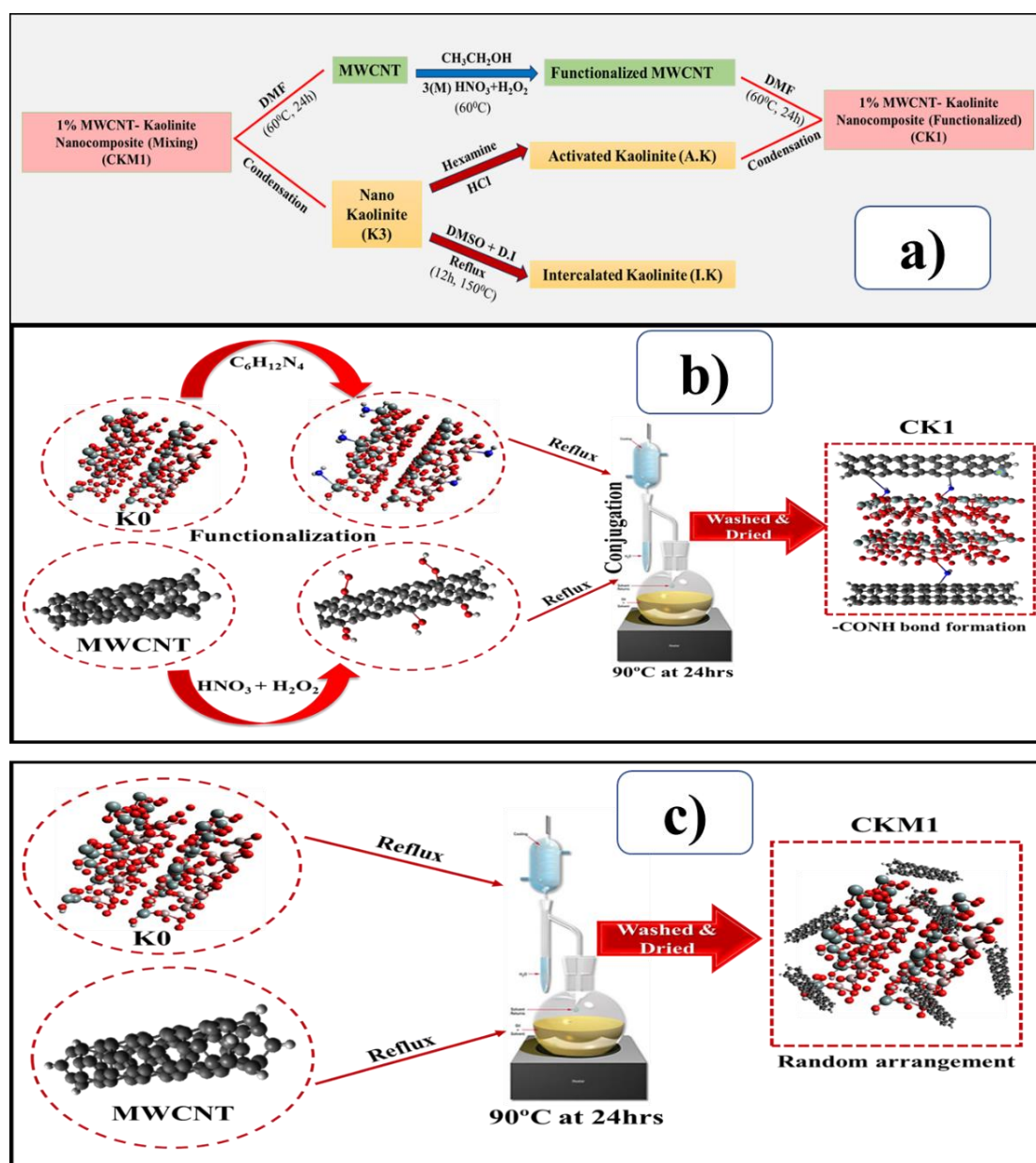


Figure 3.1. Schematic representation of MWCNT incorporated nanoparticle synthesis via modification and without modification of primary nanoparticles.

generated new diffraction maxima. The structural parameters i.e. a , b , c , α , β , γ , macrostrain, etc of the refinement have been tabulated in Table 3.2. It has been found that the basal space separation of kaolinite increases with the doping of MWCNT whereas, in the case of mixed MWCNT the separation does not alter promisingly [7]. Figure 3.3 also shows that in the case of intercalated kaolinite, the basal plane separation drastically increases which suggests the successful structural intercalation in the I.K sample. It has been found that the basal plane increases with the MWCNT doping without deforming the structural stability but in the case of intercalated kaolinite new diffraction maxima for the basal plane aroused [8].

The bonding networks of the nanocomposites have been analyzed by FTIR spectroscopy and depicted in Figure 3.4. The characteristic vibrational bands located between 430 and 700 cm^{-1} corroborate Si–O–Al bending [9]. Another major vibrational maximum found at 750 cm^{-1} refers to the AlO_6 vibration. Absorption bands at 792 and 917 cm^{-1} are attributed to Si–O and Al–OH deformation respectively [10]. The presence of Si–O stretching vibrations (940–1150 cm^{-1}) has also been confirmed. Such vibrations validate the presence of AlO_6 and SiO_4 polyhedral networks in the samples. A broad IR maximum is found between 3620 and 3700 cm^{-1} validating the presence of hydroxyl groups in the as-prepared samples. A low intense wide band has also been found in the region of 1190–1240 cm^{-1} for the N–H rocking in the activated kaolinite (Figure 3.4b) [11]. These absorption bands for N–H are absent in pristine kaolinite, I.K, and present in functionalized kaol which suggests the successful attachment of functional groups (NH_2) in the prism plane of the kaolinite (alumina facets). This electroactive NH_2 group enhanced the negative surface charge which was also validated by the zeta potential study [12]. Additionally, two very tiny vibrations have been located at 1670 and 1658 cm^{-1} that are absent in the pristine kaolinite, activated kaolinite, and intercalated kaolinite samples. The 1658 cm^{-1} band occurred due to the C=C vibration and could have originated from the MWCNT moiety, whereas, the band found at 1670 cm^{-1} is due to the –CONH vibration [13]. This –CONH vibration refers to the successful incorporation of the functionalized MWCNTs over the surface of activated kaolinite.

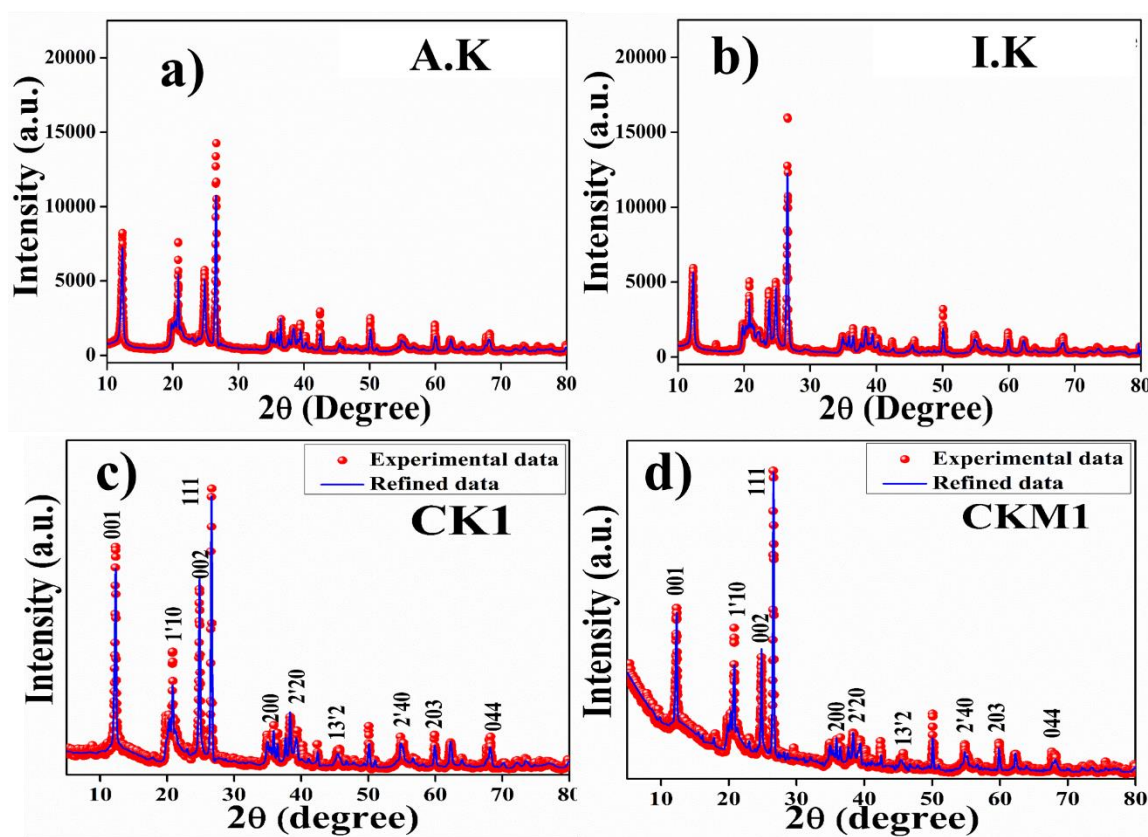


Figure 3.2. XRD and theoretical Rietveld refinement data of a) activated kaolinite, b) intercalated kaolinite, c) 1% functionalized MWCNT incorporated activated kaolinite, and d) 1% bare MWCNT incorporated pristine kaolinite.

In reality, the NH_2 group of A.K and the $-\text{COOH}$ group of functionalized MWCNT interacted with each other and formed the CONH bond by realizing a water molecule which is schematically demonstrated in Figure 3.5 and confirms the structural stability of the MWCNT-kaolinite nanocomposites. These $-\text{CONH}$ bond increases the basal plane separation in the nanocomposite (CK1) which was also validated by the XRD refinement study without any structural deformation.

The morphological investigation of the nanoparticles and their modified counterparts have been depicted in Figure 3.6 by the FESEM, TEM study. Herein, the pristine clay sample (K3) shows hexagonal sheet-like 2-D structures having 70–90 nm average length on the longer sides [14].

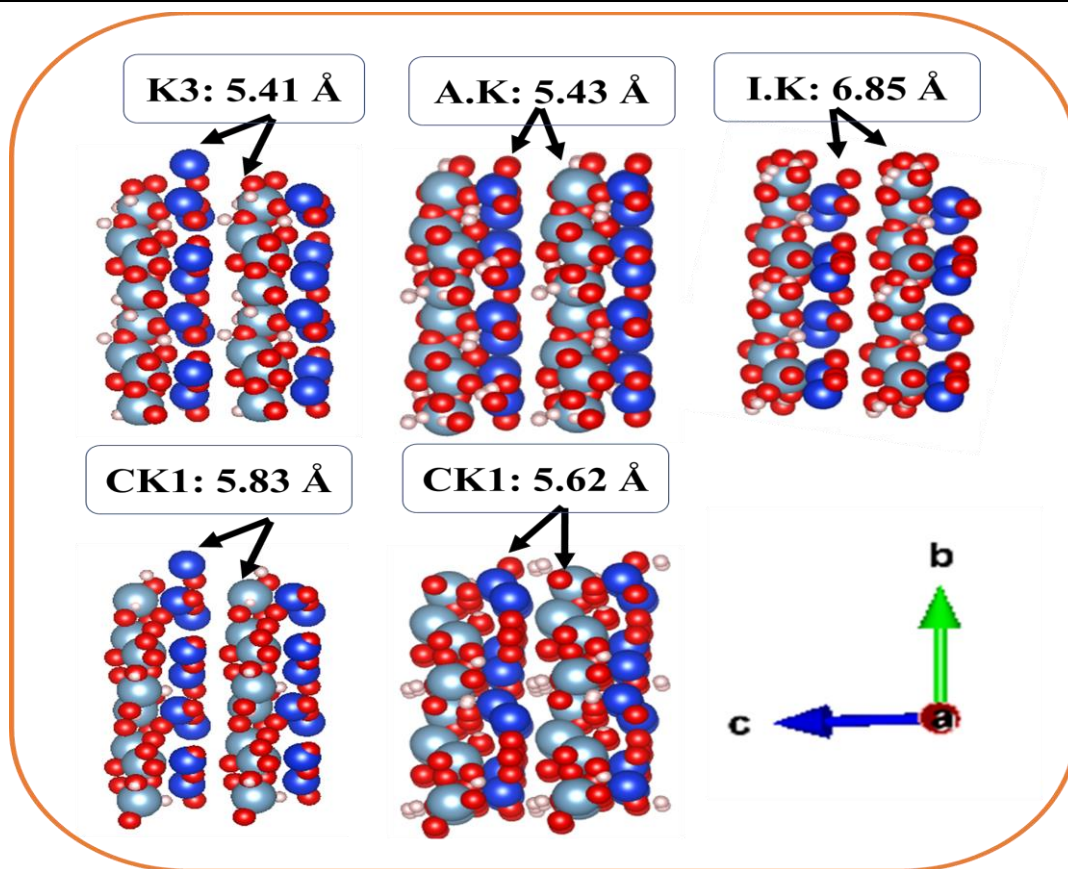


Figure 3.3. Theoretical refined structures of nanoparticles by VESTA software after refinement: a) A.K, b) I.K, c) CK1, and d) CKM1.

Table 3.2. Microstructural parameters of the NPs by Rietveld refinement.

Parameters	K3	A.K	I.K	CK1	CKM1
a (Å)	5.147	5.145	5.135	5.140	5.140
b (Å)	8.908	8.936	8.955	8.940	8.936
c (Å)	7.414	7.413	7.421	7.419	7.421
α (°)	92.034	92.293	92.030	92.207	92.098
β (°)	105.060	105.182	105.080	105.053	105.102
γ (°)	90.463	90.067	90.161	90.314	90.280

Micro strain	1.058E-4	3.244E-4	2.129E-4	6.801E-4	1.773E-4
V (Å ³)	328.013	328.639	329.263	304.068	328.861
χ^2	1.642	1.719	1.810	1.568	1.554
R _p (%)	16.849	10.707	11.527	11.636	7.998
R _{wp} (%)	27.669	18.407	20.865	18.246	12.432

The micrographs of A.K and I.K also depicted nearly about same morphology. Additionally, the FESEM and TEM micrographs of MWCNT-loaded kaolinite depict the presence of long MWCNTs attached rigidly to the kaolin surfaces, especially in activated ones. Whereas, in the case of mixing the MWCNT does not attach properly to the kaolin surface suggesting improper attachment and low stability of the mixing nanocomposite [15]. The EDX and mapping data of the natural nano clay and its nanocomposites show a uniform presence of aluminum, silicon, and oxygen in all samples (Figure 3.6). In the case of intercalated kaolinite S has been found which validated the successful intercalation of the kaolinite basal planes by DMSO precursor. In reality, DMSO entered into the two congregative basal planes of the kaolinite by forming -H bond with the oxygen moiety of the kaolinite. Additionally, the presence of carbon has been detected in the 1 % MWCNT-incorporated clay samples (Figure 3.7), which is in accordance with the loading percentages of MWCNT in a natural clay matrix.

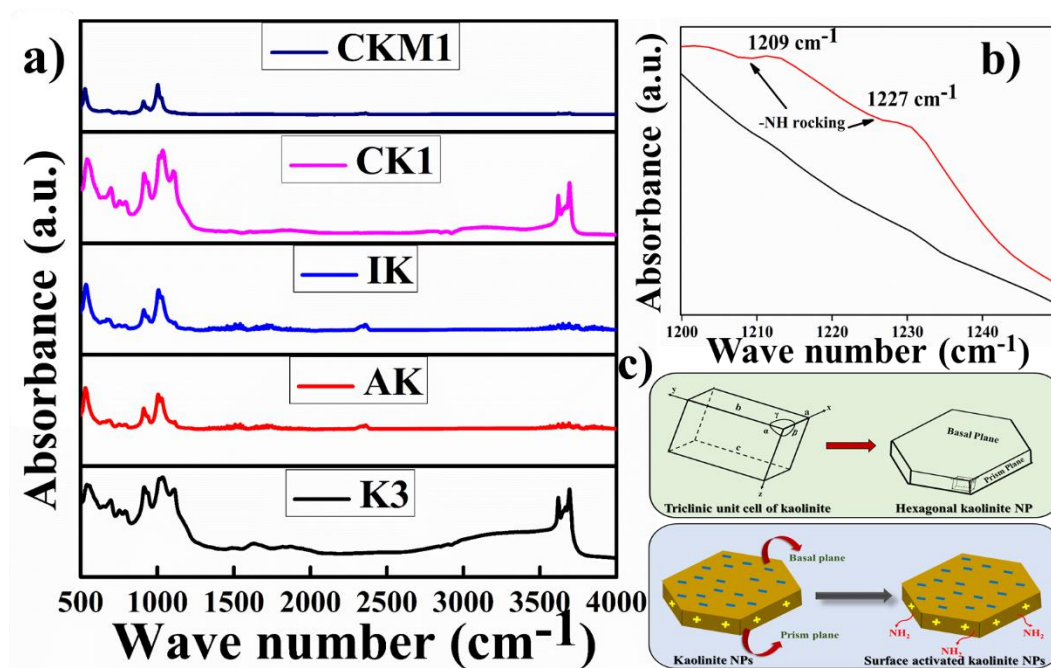


Figure 3.4. a) FTIR spectra of the synthesized NPs, b) Magnified FTIR spectra of CK1 and K3 NPs, and c) Schematic representation of basal and prism planes of kaolinite with electronegative -NH_2 group interaction.

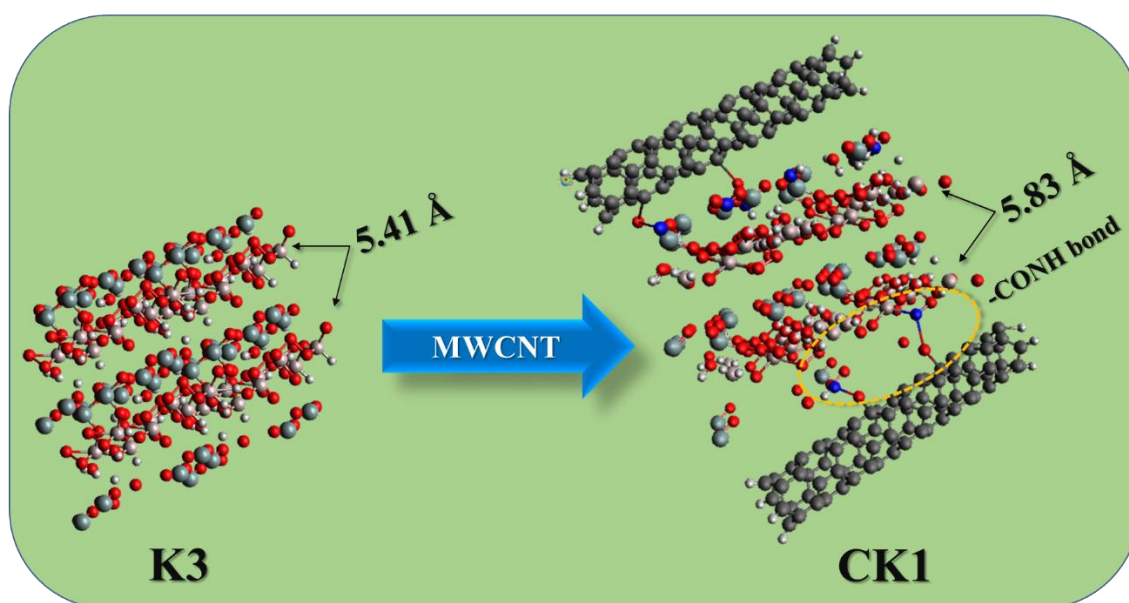


Figure 3.5. Schematic representation of -CONH bond formation and attachment of functionalized MWCNT with activated nano kaolinite.

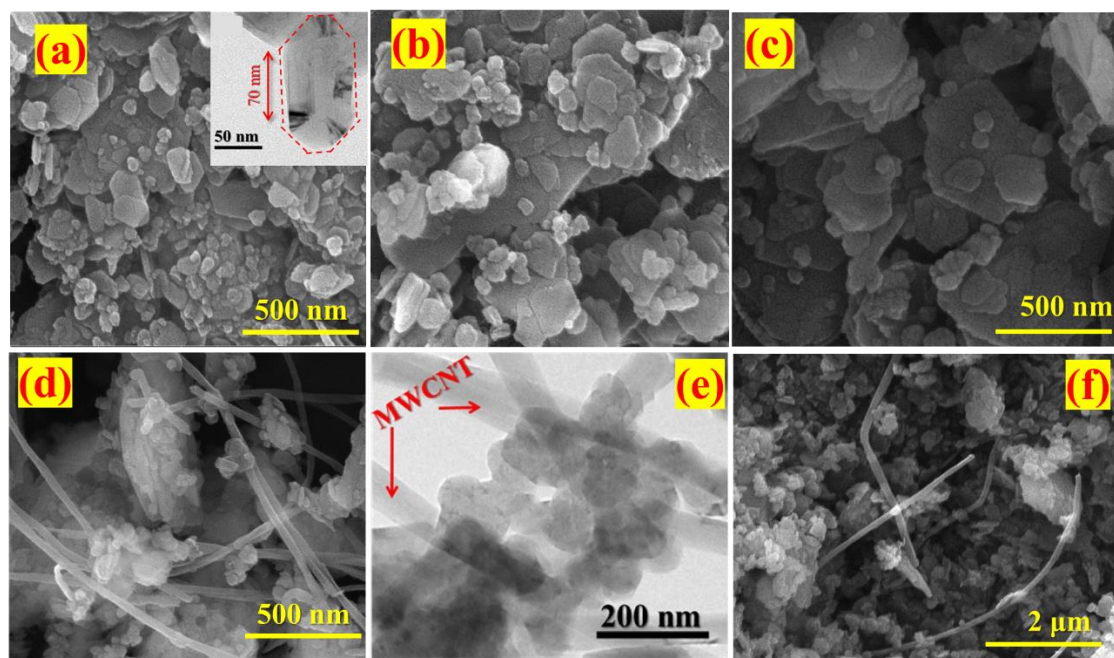


Figure 3.6. a) FESEM of pristine kaolinite NPs, TEM (inset) b, c, d) FESEM of A.K, I.K, CK1, e) TEM of CK1, and f) FESEM of CKM1.

3.3.2 Surface properties and stability of the NPs and their modified counterparts

Table 3.3. Surface charge and surface area of synthesized nanoparticles

Sample	Zeta-Potential (mV)	Surface area (m ² /g)
K3	-11.8	129
A.K	-17.1	Not-measured
I.K	-27.6	139
CK1	-37.3	139
CKM1	-15.2	Not-measured

The zeta potentials have been investigated and produced in Table 3.3, which not only substantiates the theoretical assumptions but also validates the structural stability of the natural clay nanocomposite samples [16]. It has been found that the functional group incorporation (-17.1

mV) and intercalation (-27.6 mV) of clay show higher negative zeta potential than the pristine one. On the other hand, MWCNT incorporation increases the negative zeta potential and is found -37.3 mV in the case of 1 % MWCNT doped clay (CK1) by

surface modification whereas, in mixing one the zeta potential is less [17]. These results suggest that the intercalation and 1 % MWCNT-doped natural clay nanoparticles exhibit better surface properties due to the presence of more active sites.

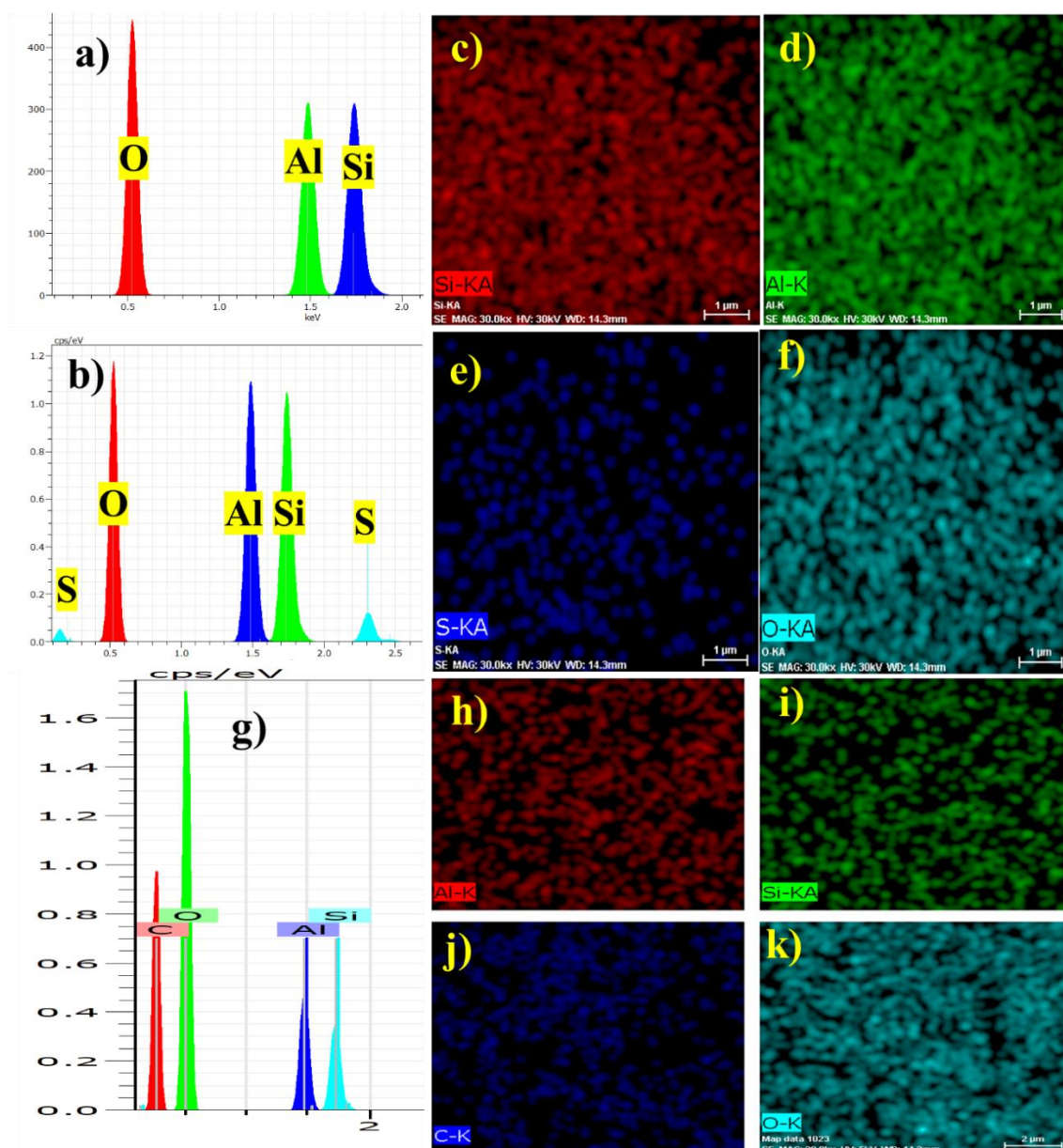


Figure 3.7. a, b, g) EDAX data of K3, I.K, and CK1, c-f) mapping of I.K, and h-k) mapping of CK1.

The BET-BJH measurement suggests that the intercalated kaolinite and 1 % MWCNT-doped (functionally) have been showing a greater surface area rather than a pristine one (Figure 3.8). These results evident that the structural modification and foreign 1D carbon incorporation show promising surface properties in the nonclay.

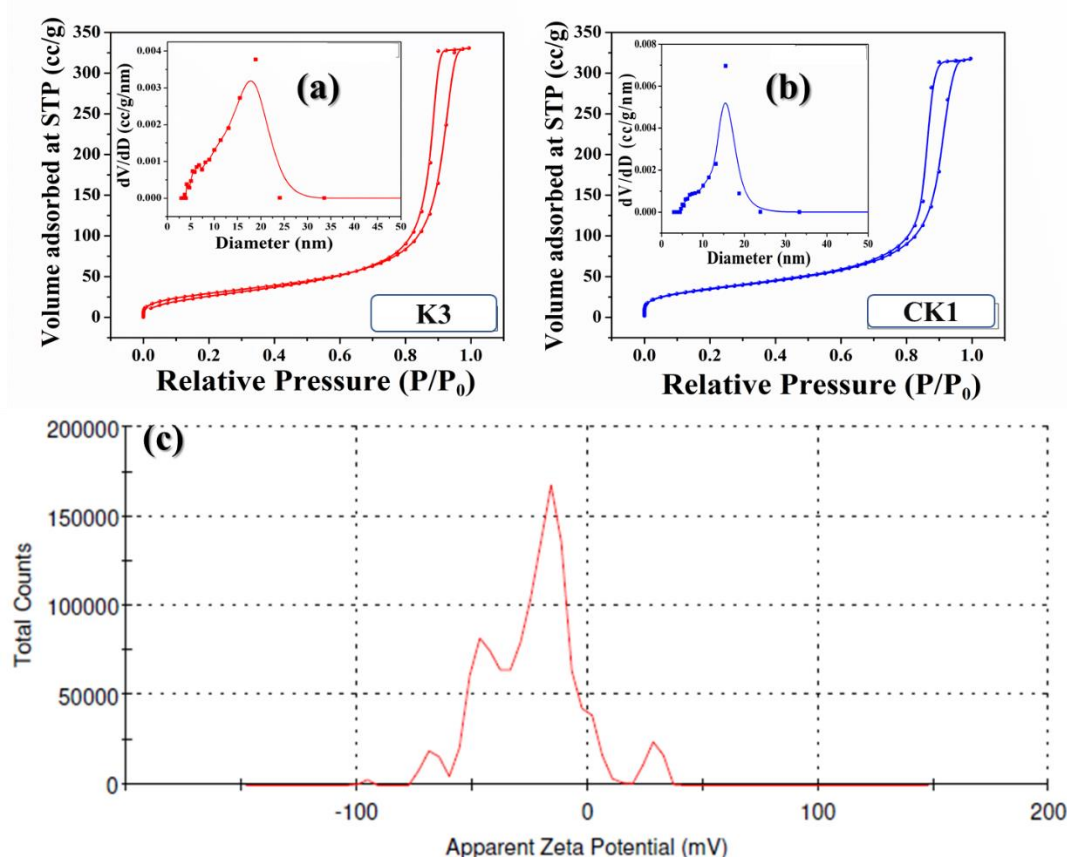


Figure 3.8. a, b) Surface area and porosity of intercalated kaolinite and 1% functionalized MWCNT incorporated kaolinite, c) Zeta potential of CK1.

3.3.3 Thermal stability of the nanocomposites

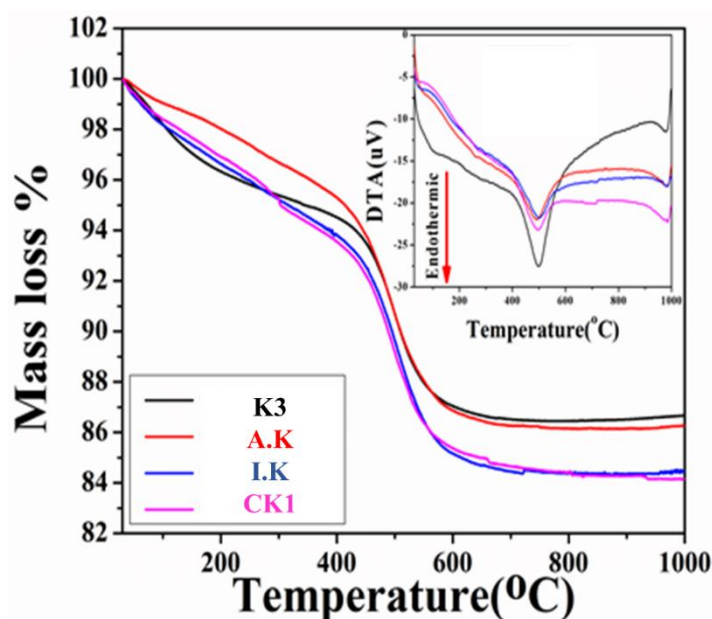


Figure 3.9. TGA-DTA of K3, A.K, I.K, and CK1.

the endothermic phase transformation of the kaolinite samples at around 500°C [18]. Generally, at this high temperature kaolinite starts its transformation into meta-kaolinite.

3.3.4 Dielectric assays of the clay samples

The dielectric constants of the nanoparticles have been investigated by relation 1.4 and

Table 3.4. Dielectric constants of nano-kaolinite and its modified counterparts

Samples	40 Hz	1 KHz	1 MHz
K3	32	26	22
A.K	388	225	30
I.K	421	237	37
CK1	3850	236	45
CKM1	510	24	19

and 510 respectively. It has been found that the intercalated kaolinite shows better D.C

DTA-TGA of the clay samples has been performed in a DTG-60H, Shimadzu to understand the structure–property correlation and thermal stability of the nano clays. It has been observed that (Figure 3.9) the samples are structurally stable (less than 6 % mass loss) up to ~425°C, beyond which a gradual drop in mass is visible. The DTA plots show

depicted in Table 3.4. It has been found that the modified nanoparticles show better dielectric constant than the pristine nano clay (K3) due to the enhanced surface properties [19]. The room temperature D.C of the K3, A.K, I.K, CK1, and CKM1 are 32, 388, 421, 3850, and 510 respectively.

without any foreign element incorporation due to higher exposed surface area for intercalation [20]. Whereas, the MWCNT incorporation in the kaolinite matrix increases the dielectric permittivity as shown in Figure 3.11. It has been observed that the dielectric permittivity value that occurs in the natural kaolinite (K3) sample is minimum (32 at 40 Hz). The dielectric permittivity attains a maximum value (3920 at 40 Hz) in the CK1 sample. Whereas, this value gets quenched for the CKM1 (510 at 40 Hz) sample.

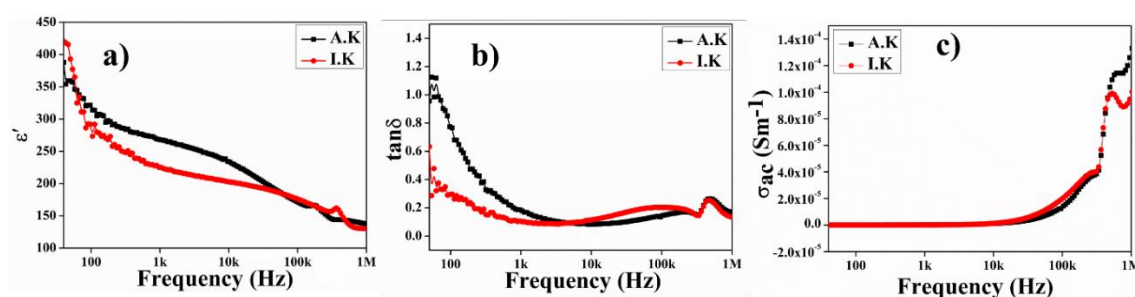


Figure 3.10. dielectric constants, tangent loss, and A.C conductivity of A.K and I.K.

In reality, this type of dielectric constant enhancement can be explained by the virtue of structural modification of the sample. In the previous sections, it has been stated that kaolinite nanoparticles have attached to two adjacent MWCNT surfaces. Periodic arrangements of parallels, attached to such capacitors make the dielectric constant high for the nanocomposites. On the other hand, just a mixed nanocomposite CKM1 sample does not show such an increment in dielectric constant. Non-functionalized clay and CNT have not formed any attachment and proficient structural deformation [21].

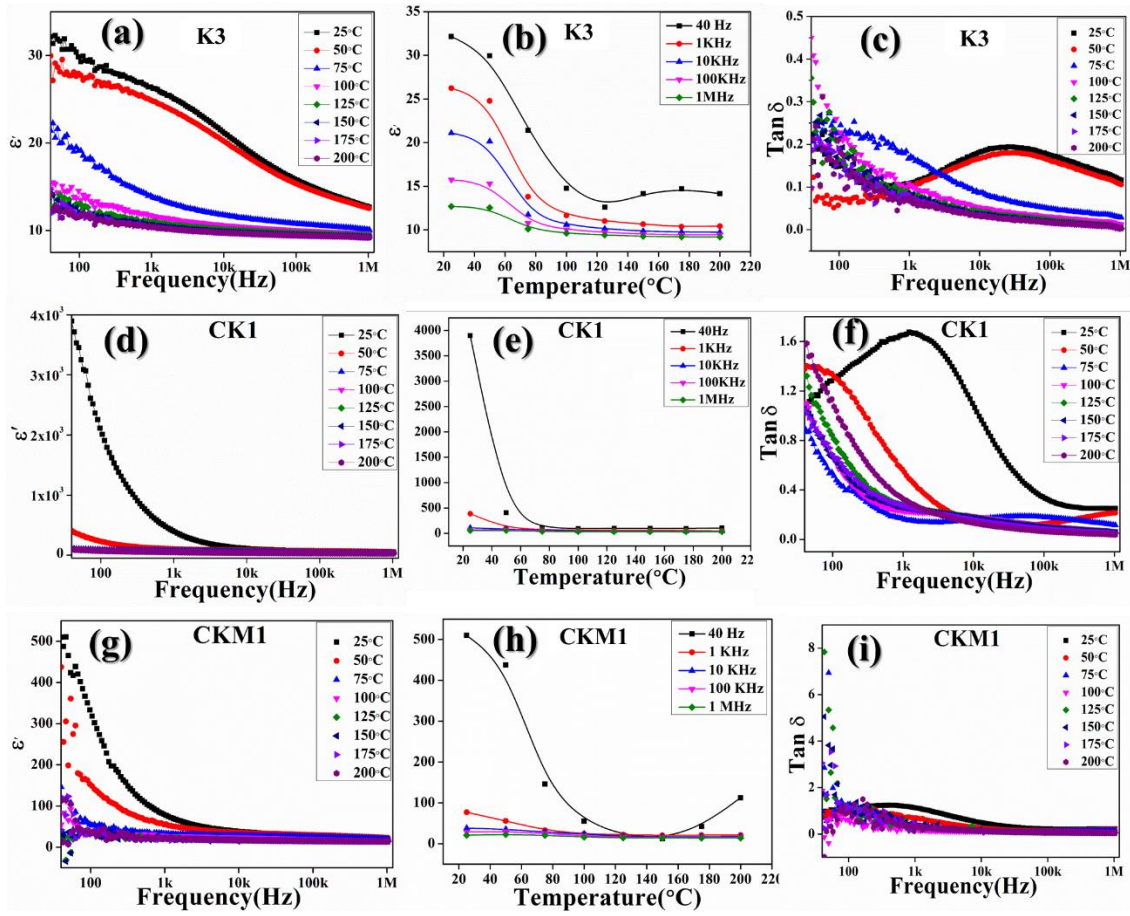


Figure 3.11. a, d, g Frequency-dependent permittivity of the nanocomposites in different temperatures show the maximum permittivity in CK1 sample, b, e, h temperature-dependent dielectric constant of the nanocomposites in different frequencies, and c, f, i tangent loss of the nanocomposites with respect to frequency represents the nominal tangent loss.

The formation of micro-capacitors has been interrupted for this reason as a result dielectric constant has not increased properly. The temperature-dependent dielectric study has also been performed in a wide range of temperatures (25–200°C) shown in Figure 3.11. The Figure shows a gradual reduction of dielectric permittivity with increasing temperature. This type of dielectric constant reduction can be explained by virtue of the charge transport phenomenon in the sample. In reality, the conductive grain and insulated grain boundary bring out quite a static nature at low temperatures [22]. The M–W polarization can take place at such a low temperature. While the temperature

increases, the conductive grain becomes free at a critical temperature value and reduces the polarization effect [23]. Such a phenomenon reduces the dielectric permittivity of the sample. Additionally, in Figure 3.9, it has been shown that the material is thermally stable up to 425°C. So, it can be easily said that the storage material formed by this sample should be thermally stable in a broad range. The dissipation factor has also been estimated by determining the tangent loss of all sample sets. It is presented in Figure 3.11, that the tangent loss is nominal for the samples. The CK1 sample showed the highest permittivity value with the nominal tangent loss that can be used as a promising storage material in the near future.

3.3.5 Investigation of AC conductivity of the nanocomposites

The frequency-dependent AC conductivity of the natural clay and its modified counterparts have been investigated and depicted in Figures 3.10 and 3.12.

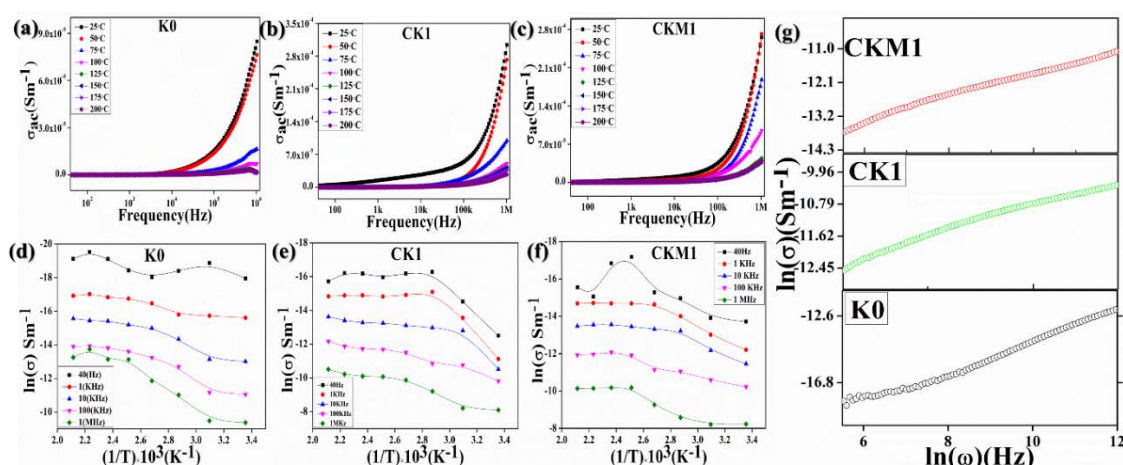


Figure 3.12. Frequency-dependent AC conductivity of the nanocomposites K3, CK1, and CKM1 shows the maximum AC conductivity in the CK1 sample, d–f Arrhenius plots of the nanocomposites to estimate the activation energies of the nanocomposites, g) Jonscher's plots of the nanocomposites show the non-zero n value of the nanocomposites which confirms the non-Debye type conduction mechanism.

It has been found that the pristine clay, A.K, I.K, CK1, and CKM1 show the room temperature AC conductivity respectively 8.5×10^{-5} , 1.0×10^{-4} , 1.2×10^{-4} , 4.4×10^{-4} ,

and 2.6×10^{-4} S/m. These data show that the activated and intercalate kaolinite show better conduction than the pure clay which also substantiates the high aspect ratio of the nanoparticles without any foreign particle incorporation [24]. It has also been shown that the conductivity also increases in the MWCNT-doped nanocomposites than in the bare clay. In reality, the conductive MWCNT increases the charge transport in the nanocomposite. The conductivity value also proved the CK1 (functionalized one) sample is more conductive than others (mixing one). The Arrhenius plot has been determined by the AC conductivity data by the relation 1.6 at the 40 Hz, 1 KHz, 10 KHz, 100 KHz, and 1 MHz external field frequencies depicted in Figure 3.12 (d-f), for the MWCNT incorporation method [25, 26].

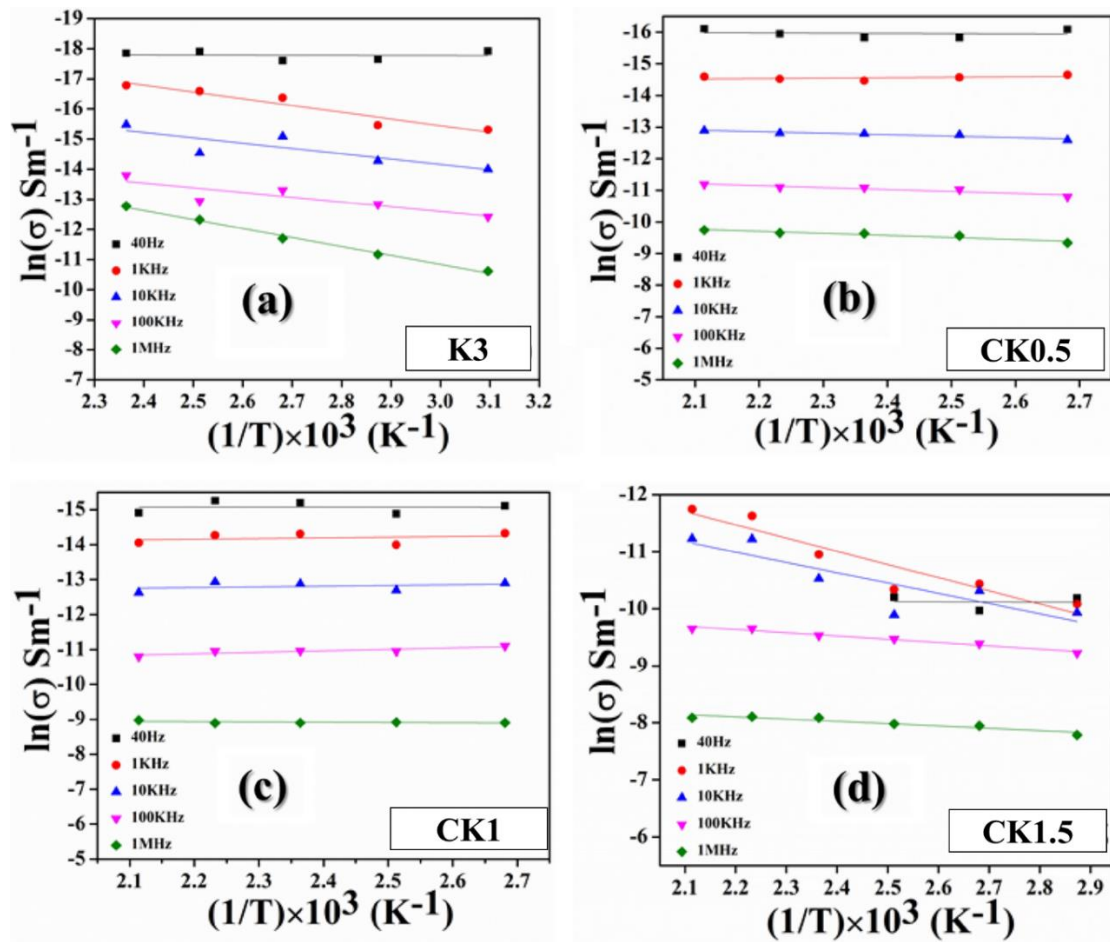


Figure 3.13. Arrhenius plots of the MWCNT concentration-dependent clay samples for estimating the activation energies.

Additionally, the frequency-dependent transport properties have been investigated by relation 1.7. It has been found that the n value lies between 0.24 to 1.01 which suggests the non-Debye type conduction mechanism of the nanoparticles (Figure 3.13). It has been shown in previous sections that the CK1 sample possesses a better attachment between clay and MWCNT. As a result, CK1 shows the most charge transport than other nanocomposites and also possesses better ac conductivity [27].

3.4 Summary

In this chapter, natural kaolinite nano clay (K3) has been modified using surface functionalization, basal plane intercalation, and foreign-particle (1D MWCNT) incorporation by modification and without modification. These simplistic synthesis processes of the abundantly available clay could be useful in industrial production on a large scale. The experimental evidence suggests that the modification enhanced the surface property correlation and physicochemical properties. In the case of intercalation and 1 % MWCNT incorporation by modification show promising properties. Detailed investigation suggests the microstructural modifications of the clay moiety, which leads to the entrapment of free charge carriers that further help in modulating the electrical parameters. The dielectric data depicts an enhanced charge storage capacity in 1 % w/w MWCNT doping by surface modification nearly 93 times compared to its pristine counterpart with very low tangent loss whereas the 1 % MWCNT mixing without modification shows a 16-fold increased permittivity value. Moreover, the clay nanostructures exhibit excellent thermal stability up to 500°C revealing potential application in high-temperature devices as well. The ac conductivities and impedance spectra suggest 1-D diffusion-limited hopping of the charge carriers and correlate microstructural modifications associated with the clay samples. Such modified natural clay could be utilized in batteries, electrochemical sensors, supercapacitors, and various other fields of nanotechnology. Minimal cost, facile synthesis process, the abundance of the kaolinite clay, and biocompatibility besides the enormous efficacy in charge transport of the CNT-modified nano-clay make it a futuristic ‘green nanocomposite’ system.

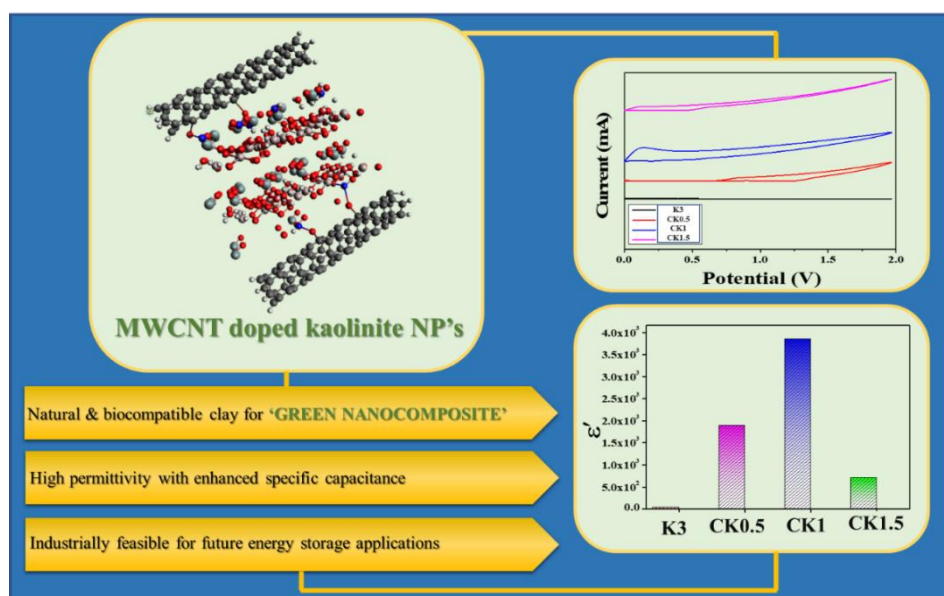
References

- [1] Malik, Parth, Rachna Gupta, Vibhuti Malik, and Rakesh Kumar Ameta. *Measurement: sensors* 16 (2021): 100050.
- [2] Deng, Hongbing, Yang Wu, Iqra Shahzadi, Rong Liu, Yang Yi, Dan Li, Shiyi Cao, Chi Wang, Jing Huang, and Huiyu Su. In *Nanomaterials from Clay Minerals*, pp. 365-413. Elsevier, 2019.
- [3] Athawale, Anjali A., and Jyoti A. Pandit. *Unsaturated Polyester Resins* (2019): 1-42.
- [4] Jimenez, Guillermo A., Byoung J. Lee, and Sadhan C. Jana. *Nanoscale Multifunctional Materials: Science and Applications* (2011): 87-124.
- [5] Gottardo, Stefania, Agnieszka Mech, Marios Gavriel, Claire Gaillard, and Birgit Sokull-Klüttgen. *Luxembourg, Publications Office of the European Union* (2016).
- [6] Mehta, B. K., Meenal Chhajlani, and B. D. Shrivastava. In *Journal of physics: conference series*, vol. 836, no. 1, p. 012050. IOP Publishing, 2017.
- [7] Harutyunyan, Lusine R., and Elena V. Lasareva. *Biointerface Res. Appl. Chem* 13 (2023): 578.
- [8] Shawky, Ahmed, Said M. El-Sheikh, Mohamed Nageeb Rashed, Sabrin M. Abdo, and Thanaa I. El-Dosoqy. *Journal of Environmental Chemical Engineering* 7, no. 3 (2019): 103174.
- [9] Partyka, Janusz, and Magdalena Leśniak. *Spectrochimica Acta Part A: Molecular and Biomolecular Spectroscopy* 152 (2016): 82-91.
- [10] Mondal, Dhananjay, Shubham Roy, Souravi Bardhan, Ratnottam Das, Anupam Maity, Dipak Kr Chanda, Solanky Das, Saheli Ghosh, Ruma Basu, and Sukhen Das. *Journal of Materials Science: Materials in Electronics* 33, no. 17 (2022): 13826-13842.
- [11] Rizwan, Komal, Zaeem Bin Babar, Shahid Munir, Ali Arshad, and Abdul Rauf. *Environmental Research* 215 (2022): 114398.
- [12] Cai, Lifang, Junjie Chen, Lu Chang, Shurui Liu, Yajuan Peng, Ning He, Qingbiao Li, and Yuanpeng Wang. *Industrial & Engineering Chemistry Research* 60, no. 11 (2021): 4321-4331.

- [13] Camus, Jean-Michel, Dolores Morales, Jacques Andrieu, Philippe Richard, Rinaldo Poli, Pierre Braunstein, and Frédéric Naud. *Journal of the Chemical Society, Dalton Transactions* 15 (2000): 2577-2585.
- [14] Majeed Khan, Mohd Abdul, Sushil Kumar, Maqusood Ahamed, Salman A. Alrokayan, and Mohammad Saleh AlSalhi. *Nanoscale research letters* 6 (2011): 1-8.
- [15] Czerniecka-Kubicka, Anna, Wiesław Frącz, Marek Jasiorski, Wojciech Błażejowski, Barbara Pilch-Pitera, Marek Pyda, and Iwona Zarzyka. *Journal of Thermal Analysis and Calorimetry* 128 (2017): 1513-1526.
- [16] Lowry, Gregory V., Reghan J. Hill, Stacey Harper, Alan F. Rawle, Christine Ogilvie Hendren, Fred Klaessig, Ulf Nobbmann, Philip Sayre, and John Rumble. *Environmental Science: Nano* 3, no. 5 (2016): 953-965.
- [17] Mondal, Dhananjay, Amartya Sau, Shubham Roy, Souravi Bardhan, Jhilik Roy, Saheli Ghosh, Ruma Basu, Soumyaditya Sutradhar, and Sukhen Das. *Journal of Materials Science: Materials in Electronics* 34, no. 21 (2023): 1597.
- [18] Pekdemir, A. D., Y. Sarıkaya, and M. Önal. *Journal of Thermal Analysis and Calorimetry* 123 (2016): 767-772.
- [19] Bakar, M., M. Lavorgna, J. Szymańska, and A. Dętkowska. *Polymer-Plastics Technology and Engineering* 51, no. 7 (2012): 675-681.
- [20] Cao, Zhou, Jingmai Li, Yunpu Zhao, Qiong Mei, Qizhao Wang, and Hongfei Cheng. *Chemical Engineering Journal* 466 (2023): 143076.
- [21] Alawi, Athar Iqbal, Ehssan Al-Bermany, Raad Shaker Alnayli, Mohammed M. Sabri, Naser Mahmoud Ahmed, and Abdul Kareem J. Albermany. *Optical and Quantum Electronics* 56, no. 3 (2024): 429.
- [22] Hota, Sudhansu Sekhar, Debasish Panda, and Ram Naresh Prasad Choudhary. *Journal of Alloys and Compounds* 976 (2024): 172900.
- [23] Yang, Haibin, Ziqing Xu, Hongzhi Cui, Xiaohua Bao, Waiching Tang, Guochen Sang, and Xiangsheng Chen. *Construction and Building Materials* 361 (2022): 129635.

- [24] Menazea, A. A., A. M. Abdelghany, N. A. Hakeem, W. H. Osman, and FH Abd El-kader. *Silicon* 12 (2020): 13-20.
- [25] Menazea, A. A., A. M. Ismail, and I. S. Elashmawi. *Journal of Materials Research and Technology* 9, no. 3 (2020): 5689-5698.
- [26] Tommalieh, M. J., Hala A. Ibrahim, Nasser S. Awwad, and A. A. Menazea. *Journal of Molecular Structure* 1221 (2020): 128814.
- [27] Wang, Guannan Roger, Lingyan Wang, Qiang Rendeng, Jianguo Wang, Jin Luo, and Chuan-Jian Zhong. *Journal of Materials Chemistry* 17, no. 5 (2007): 457-462.

Chapter 4



*Optimizing Polarizability and Charge
Storage Capacity through Varying
MWCNT Concentration in Nano-
Kaolinite*

Chapter 4

Optimizing Polarizability and Charge Storage Capacity through Varying MWCNT Concentration in Nano-Kaolinite.

4.1 Introduction

It is evident from the previous Chapter 3 that the surface functionalized MWCNT conjugated activated nano-clay with functional groups ($-NH_2$) shows maximum physicochemical properties than the other conjugation processes and structural deformation. Inspired by the results in this chapter percentages of functionalized MWCNT have been varied and conjugated with activated nano kaolinite to find the maximum effective nanocomposite system [1]. In reality, increasing the percentage of any doping in the base material generates stress in its structure without deforming the original one and creates active sites that enhance various physicochemical properties [2]. After a certain limit of incorporation of foreign elements, the structural properties will disrupt and quench their properties. In order to find the maximum efficient nanocomposite, in this work 0.5, 1.0, and 1.5 % (wt/wt) of functionalized MWCNT have been incorporated into activated kaolinite and synthesized the nanocomposites namely CK0.5, CK1, and CK1.5 [3]. The synthesized nanocomposites were then characterized by the conventional characterization tools, computed the experimental data with theoretical Rietveld refinement technique to find microstructural deformations, and measured various surface and electrical parameters to find the promising nanocomposite [4]. It has been found that the increasing doping percentage of MWCNT increases the physicochemical properties up to a certain limit (CK1) and decreases after excess doping (CK1.5). Such augmented properties in 1 % MWCNT doped kaolinite clay could be further used in the different dimensions of nanotechnology to serve society in various issues [5].

4.2 Experimental Details

4.2.1 Materials

Natural kaolinite [$\text{Si}_2\text{Al}_2\text{O}_5(\text{OH})_4$] clay was purchased from Hindustan Minerals, India, and MWCNT (purity: 95 %) was purchased from Sigma Aldrich, Germany. The MWCNTs are having 50–90 nm widths. Hexamine [$\text{C}_6\text{H}_{12}\text{N}_4$], hydrochloric acid [HCl, 37 %], nitric acid [HNO_3 , 69 %], hydrogen peroxide [H_2O_2 , 30 %], Dimethyl sulfoxide (DMSO), and dimethylformamide [$\text{C}_3\text{H}_7\text{NO}$] were purchased from Merck, India. Acetone (HPLC grade) and ethanol (HPLC grade) were purchased from Merck, India for analytical experiments. All the reagents are of analytical grades having a purity of ~ 99 % and were used without any further purification. Millipore water was used throughout the experiment having a resistivity of approximately $\sim 18.2 \text{ M}\Omega\text{-cm}$.

4.2.2 Synthesis of MWCNT-kaolinite nanocomposite (CK)

The preparation of MWCNT-Kaolinite nanocomposite was performed by a simplified condensation technique as stated in Chapter 3. Initially, 1 gm of activated kaolinite (A.K) was dissolved in 30 ml DMF and sonicated for 1 h. After that functionalized MWCNT was added to the solution maintaining the wt/wt ratio of 0.5, 1.0, and 1.5 %. The solution was then refluxed under vigorous stirring by a condenser unit at 90°C for 24 h. The black precipitate was then collected and washed several times with deionized water until its pH achieved a neutral value. The nanocomposites were then dried in a hot air oven at 70°C for 24 h and marked as CK0.5, CK1, and CK1.5 respectively (Figure 4.1 & Table 4.1).

Table 4.1. Synthesized nanoparticles and nanocomposites

Synthesis procedures	Code of the samples
Nano-kaolinite (Chapter-2)	K3
0.5, 1, 1.5% (w/w) MWCNT incorporated K3 (functionalized both the components)	CK0.5, CK1, CK1.5

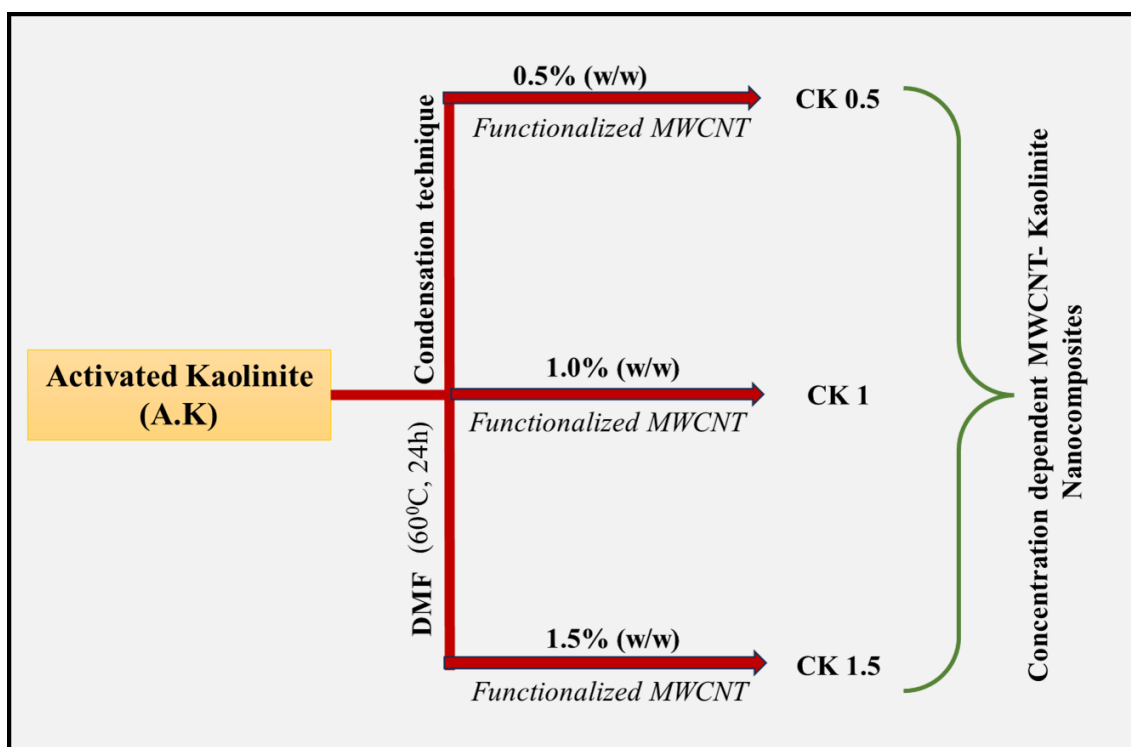


Figure 4.1. Schematic representation of MWCNT incorporated nanoparticle synthesis with varying concentrations of functionalized MWCNT.

4.3 Result and Discussions

4.3.1 Structural, morphological, and elemental properties of the nanocomposites

The X-ray diffractograms of the nanoparticles in Figure 4.2 show that the diffraction planes of the MWCNT-doped kaolinite nanocomposites have matched with the kaolinite JCPDS data having card no 80-0886 and found a good agreement with the theoretical data by Rietveld refinement (AMCSD file no. 1550598; triclinic lattice with P1 space group). Any undesired maxima that have not occurred in the diffractogram suggest the purity of the nanocomposite samples [6].

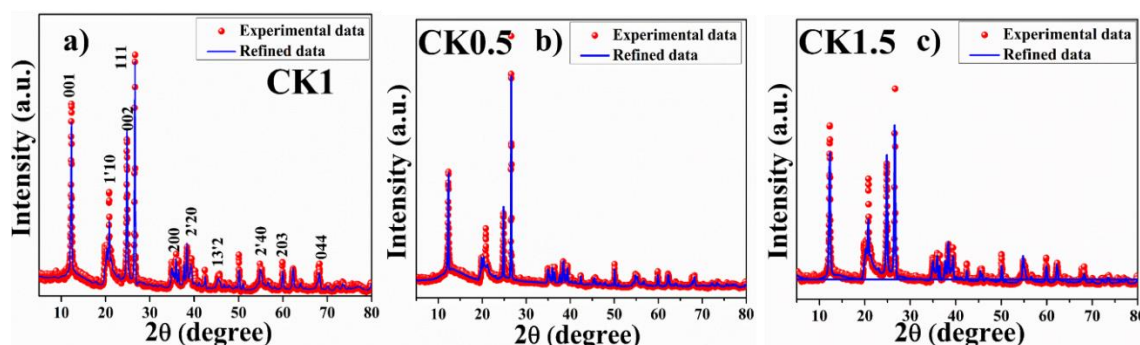


Figure 4.2. Experimental and refined XRD of 0.5 %, 1.0 %, and 1.5% functionalized-MWCNT incorporated activated-kaolinite.

The structural parameters i.e. a , b , c , α , β , γ , macrostrain, etc of the refinement have been tabulated in Table 4.2. It has been found that the basal space separation of kaolinite increases with the doping of MWCNT and again decreases after a certain amount of MWCNT incorporation (1.5% w/w) [7]. It has been found that the basal plane increases with the MWCNT doping without deforming the structural stability and attains a maximum value in the case of 1% dopant (CK1). In the previous Chapter 3, it was validated that up to a certain limit of MWCNT incorporation, conducting MWCNT and dielectric kaolinite clays creates micro-capacitors in the nanocomposite which increases the basal plane separations and disrupts after excess doping (CK1.5) (Figure 4.3).

It is evident from the XRD result that the CK1 sample poses maximum basal space separation, maximum microstrain, and lowest unit cell volume (Table 4.2) which can enhance its physicochemical properties by enhancing the active sites [8].

Table 4.2. Microstructural parameters by Rietveld-refinement of all the nanoparticles.

Parameters	K3	CK0.5	CK1	CK1.5
a (Å)	5.147	5.158	5.140	5.149
b (Å)	8.908	8.952	8.940	8.930
c (Å)	7.414	7.418	7.419	7.423
α (°)	92.034	92.122	92.207	92.185
β (°)	105.060	105.014	105.053	105.077
γ (°)	90.463	89.739	90.314	90.330
Micro strain	1.058E-4	4.970E-4	6.801E-4	9.153E-5
V (Å³)	328.013	330.571	304.068	329.568
χ^2	1.642	1.457	1.568	1.529
R_p (%)	16.849	10.040	11.636	15.089
R_{wp} (%)	27.669	14.633	18.246	23.072

The bonding networks of the nanocomposites have been analyzed by FTIR spectroscopy and depicted in Figure 4.4. The characteristic vibrational bands located between 430 and 700 cm⁻¹ corroborate Si–O–Al bending [9]. Another major vibrational maximum found at 750 cm⁻¹ refers to the AlO₆ vibration. Absorption bands at 792 and 917 cm⁻¹ are attributed to Si–O and Al–OH deformation respectively.

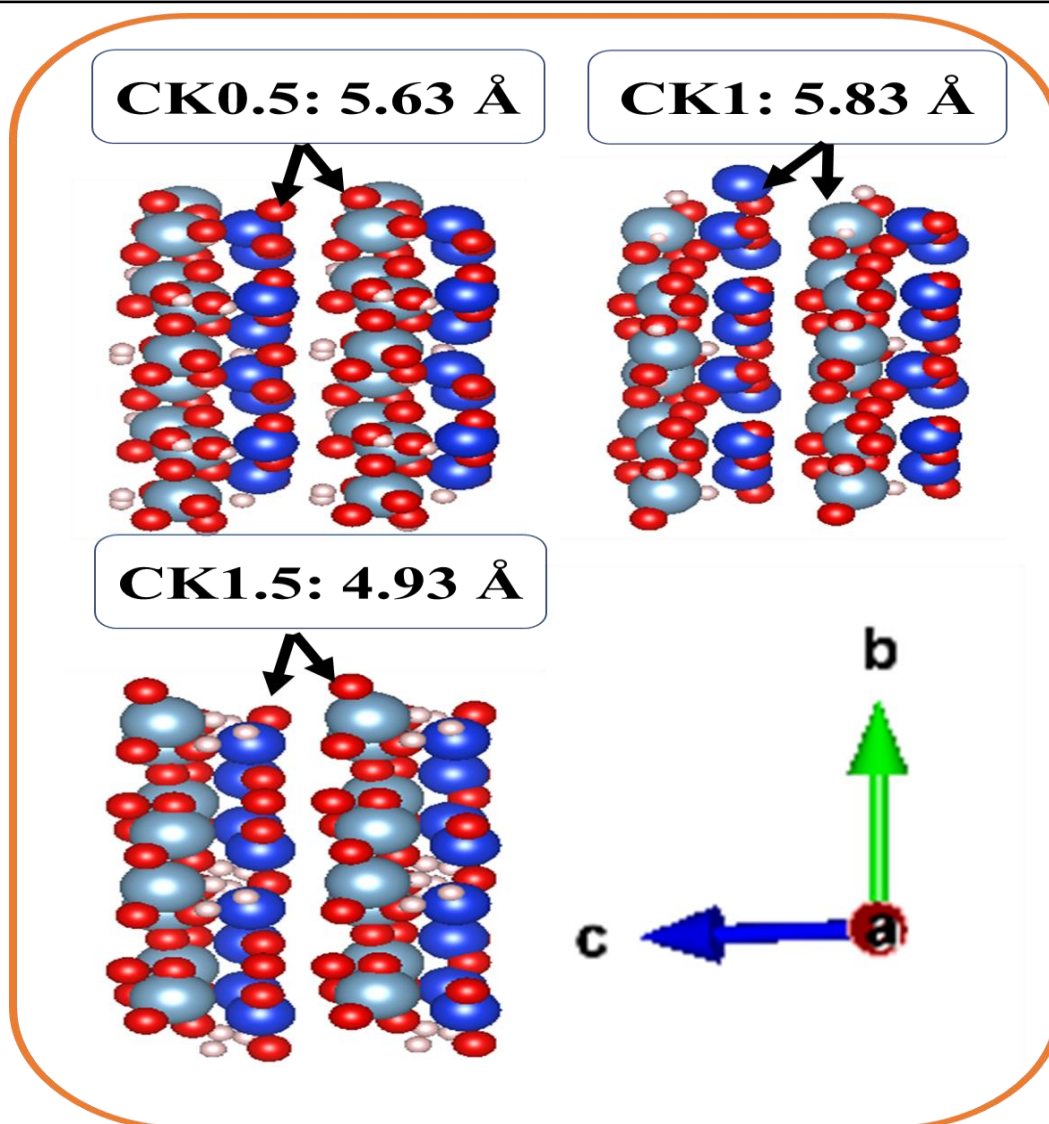


Figure 4.3. Microstructural visualization and basal plane separation of all the nanoparticles by VESTA software.

The presence of Si–O stretching vibrations ($940\text{--}1150\text{ cm}^{-1}$) has also been confirmed. Such vibrations validate the presence of AlO_6 and SiO_4 polyhedral networks in the samples. A broad IR maximum is found between 3620 and 3700 cm^{-1} validating the presence of hydroxyl groups in the as-prepared samples [10]. Additionally, two very tiny vibrations have been located at 1670 and 1658 cm^{-1} are absent in the pristine kaolinite sample. The 1658 cm^{-1} band occurred due to the C=C vibration and could have originated

from the MWCNT moiety, whereas, the band found at 1670 cm^{-1} is due to the -CONH vibration [11]. This -CONH vibration refers to the successful incorporation of the functionalized MWCNTs over the surface of activated kaolinite.

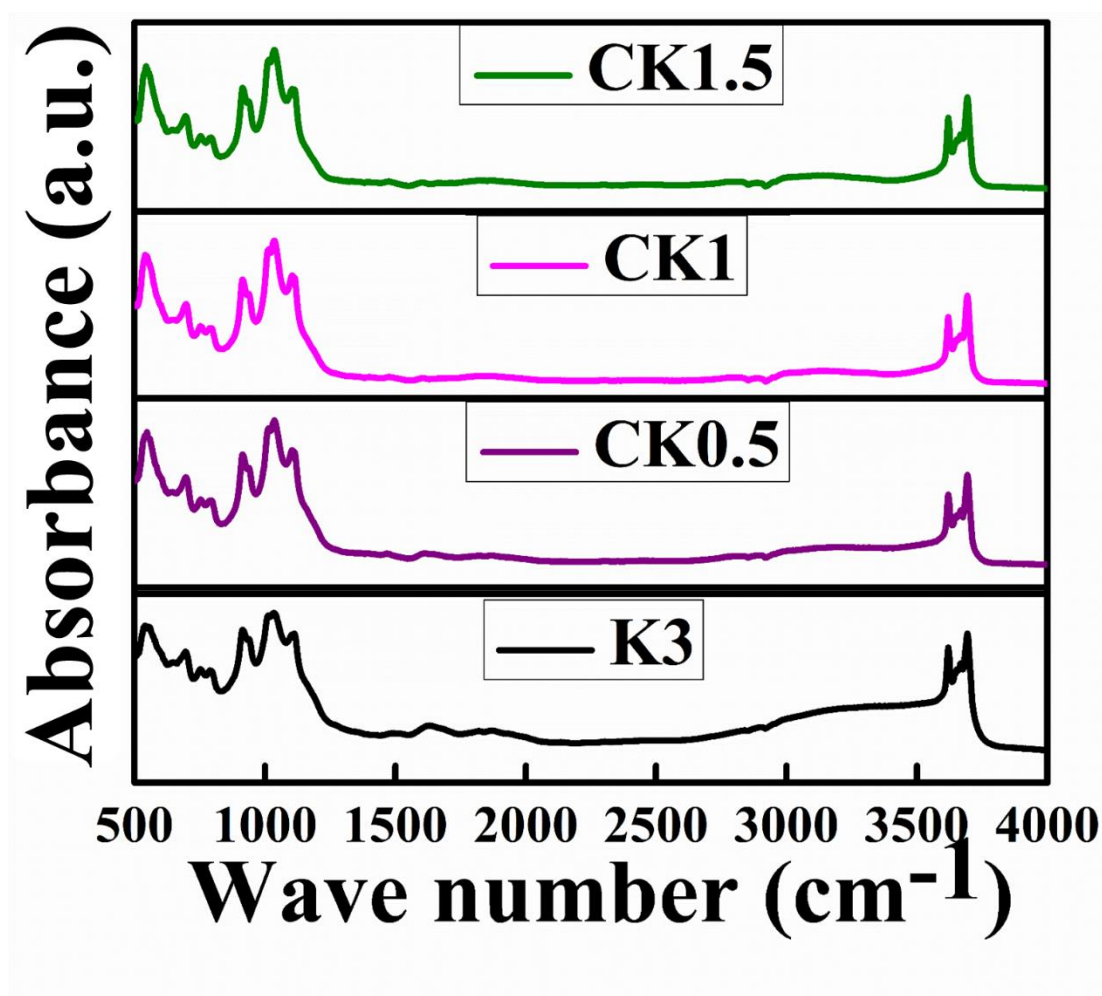


Figure 4.4. FTIR spectra of all the nanoparticles

In reality, the NH_2 group of A.K (Chapter 3, Figure 3.4) and the -COOH group of functionalized MWCNT interacted with each other and formed the CONH bond by realizing a water molecule which is schematically demonstrated in Chapter 3, Figure 3.5 and confirms the structural stability of the MWCNT-kaolinite nanocomposites [12].

These -CONH bond increases the basal plane separation in the nanocomposite (CK1) which was also validated by the XRD refinement study without any structural deformation [13].

The morphological investigation of the nanocomposites has been depicted in Figure 4.5 (a-e) by the FESEM, TEM study. Herein, the pristine clay sample (K3) shows hexagonal sheet-like 2-D structures having 70–90 nm average length on the longer sides [14]. The FESEM and TEM micrographs of MWCNT-loaded kaolinite depict the presence of long MWCNTs attached rigidly to the kaolin surfaces.

The FESEM images also show the increment of MWCNTs with increasing doping percentages, which is in accordance with the previous XRD and FTIR analyses. Interestingly, the micro-capacitor formation due to functionalized MWCNT incorporation into A.K. has been found in the TEM micrograph of CK1 depicted in Figure 4.5 d [15].

The EDX and mapping data of the natural nano clay and its nanocomposites show a uniform presence of aluminum, silicon, and oxygen in all samples (Figure 4.5, f-j). The presence of carbon has been detected in the nanocomposite clay samples, which is in accordance with the loading percentages of MWCNT in a natural clay matrix [16].

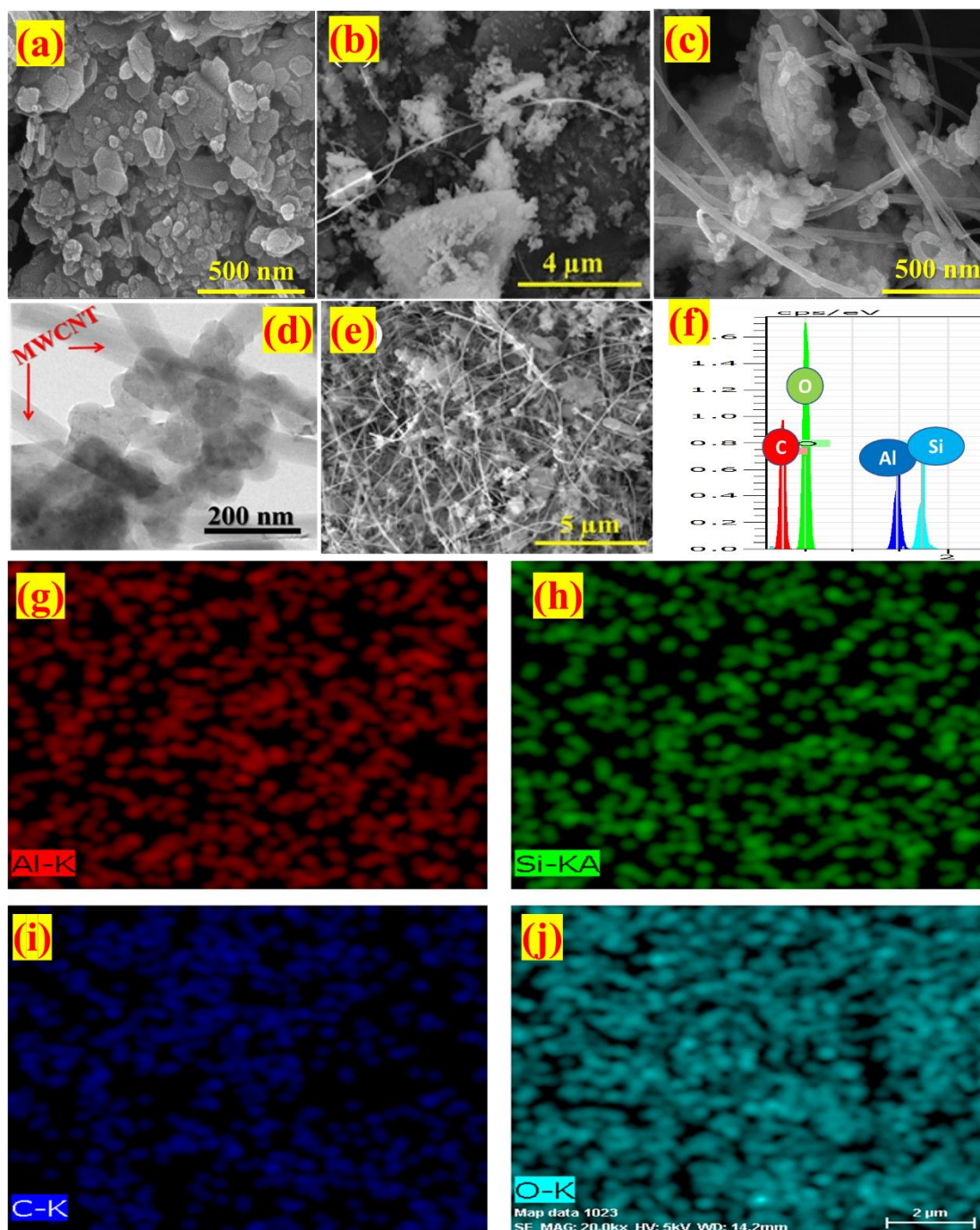


Figure 4.5. a) FESEM of nano kaolinite (K3), b, c) FESEM of CK0.5, and CK1, d) TEM image of 1% functionalized MWCNT-incorporated kaolinite (CK1), e) FESEM of CK1.5, f) EDAX of CK1, and g-j) mapping of CK1.

4.3.2 Surface properties and stability of the nanocomposites

The zeta potentials have been investigated and produced in Table 4.3, which not only

Table 4.3. Surface charge and surface area of synthesized NPs

Sample	Zeta-Potential (mV)	Surface area (m ² /g)
K3	-11.8	129
CK0.5	-25.3	Not-measured
CK1	-37.3	139
CK1.5	-16.7	Not-measured

substantiates the theoretical assumptions but also validates the structural stability of the natural clay nanocomposite samples [17]. It has been found that the MWCNT incorporation increases the negative zeta potential and is

found maximum in the case of 1% MWCNT doped clay (CK1: -37.3 mV) whereas, in the case of CK1.5 the zeta potential was found -16.7 mV [18]. These results suggest that the 1% MWCNT-doped natural clay nanoparticles exhibit better surface properties due to the presence of more active sites. The BET-BJH measurement suggests that the 1% MWCNT-doped nanocomposite poses a greater surface area rather than a pristine one (Figure 4.6). These results evident that the structural modification and foreign 1D carbon incorporation show promising surface properties in the nonclay.

Additionally, the DTA-TGA of the clay nanocomposites in Chapter 3 Figure 3.9 show that the samples are structurally stable (less than 6% mass loss) up to ~425°C, beyond which a gradual drop in mass is visible. The DTA plots show the endothermic phase transformation of the kaolinite samples at around 500°C [19]. Generally, at this high-temperature kaolinite starts its transformation into meta-kaolinite which validated the temperature stability of the nanocomposites [20].

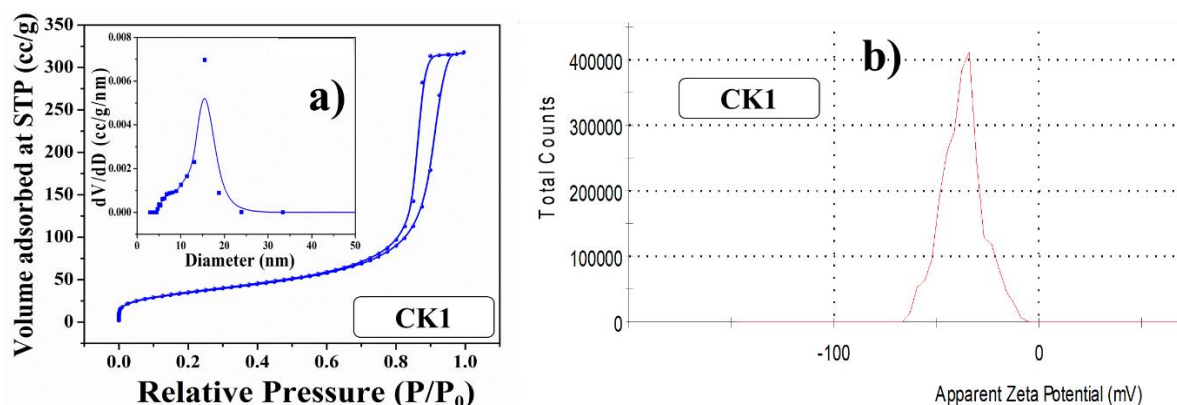


Figure 4.6. a) Surface area and porosity of CK1, b) Zeta potential of CK1.

4.3.3 Dielectric assays of the clay nanocomposites

The MWCNT concentration-dependent D.C has been investigated (Figure 4.7) by relation 1.4 and found that the MWCNT incorporation increased the D.C with increasing concentration. It can be observed that the electrical permittivity increases with increasing percentage of MWCNT and attains a maximum value in the CK1 sample (3850 at 40 Hz) after that, upon excess MWCNT loading it quenches significantly in the CK1.5 sample (710 at 40 Hz) (Table 4.4). This type of dielectric relaxation could be attributed to the structural modifications of the samples [21]. As stated earlier, the kaolinite nanoparticles are attached between two adjacent MWCNT surfaces, which creates a periodic arrangement of insulated kaolinite and conductive CNTs in a parallel manner. Such a parallel arrangement leads to the formation of micro-capacitors and enhances dielectric permittivity values with increasing MWCNT concentration. [22] However, excess CNT loading disturbs this periodic arrangement, which results in a distorted grain-grain boundary arrangement in this sample. Hence, in the low-frequency region, the distorted grain boundaries are unable to hold the charges and the electrical charges get sufficient mobility [23]. Due to the uncontrolled movement of these mobile charges, the dissipation factor is enhanced (as shown in tangent loss data) and an abrupt nature in low-frequency permittivity is observed. This phenomenon is known as electrical percolation and reported

previously by various groups [24]. The temperature response of the samples has also been studied in terms of electrical permittivity in a wide range (25–200°C) and is depicted in Figure 4.7. The tangent loss has also been investigated to estimate the dissipation factor of the entire sample set and presented in Figure 4.7. The loss tangents are in accordance with high dielectric values. It can be noted that the tangent loss increases with increasing field frequencies for all the samples. The inter-dipolar friction could be a possible reason for this, which further dissipates heat energy. The loss tangent seems to be highest in the CK1.5 sample due to the disrupted alignment of the ordered micro-capacitor structure of the MWCNT-doped nanocomposites. Henceforth, permittivity studies suggest that the CK1 sample has the highest permittivity with a nominal tangent loss and possibly could be used in energy storage applications and pose promising physicochemical properties [25].

Table 4.4. Dielectric constants of nano-kaolinite and its modified counterparts

Samples	40 Hz	1 KHz	1 MHz
K3	32	26	22
CK0.5	1888	222	40
CK1	3850	236	45
CK1.5	709	83	31

4.3.4 Investigation of AC conductivity of the nanocomposites

The room temperature AC conductivities calculated by equation 1.5 have been found 8.5×10^{-5} , 2.4×10^{-4} , 4.4×10^{-4} , and 6.2×10^{-5} S/m at 1MHz frequency for the pristine clay,

CK0.5, CK1, and CK1.5 respectively. The data show that the conductivity also increases in the MWCNT-doped nanocomposites than in the bare clay. In reality, the conductive MWCNT increases the charge transport in the nanocomposite [26]. The conductivity value also proved the CK1 sample is more conductive than others (Figure 4.8). It has already been explained that the MWCNT-loaded samples possess better attachment to the kaolinite surfaces and form prominent charge-hopping pathways [27]. Thus, increments in ac conductivities in CNT-loaded samples have been found and reduced after a certain concentration (CK1.5) for disruption of the arrangement.

The Arrhenius plot has been determined by the AC conductivity data by the relation 1.6 at the 40 Hz, 1 kHz, 10 kHz, 100 kHz, and 1 MHz external field frequencies depicted in Figure 4.9 for the MWCNT concentration-dependent nanocomposites [28]. Additionally, the frequency-dependent transport properties have been investigated by relation 1.7. It has been found that the n value lies between 0.24 to 1.01 which suggests the non-Debye type conduction mechanism of the nanoparticles.

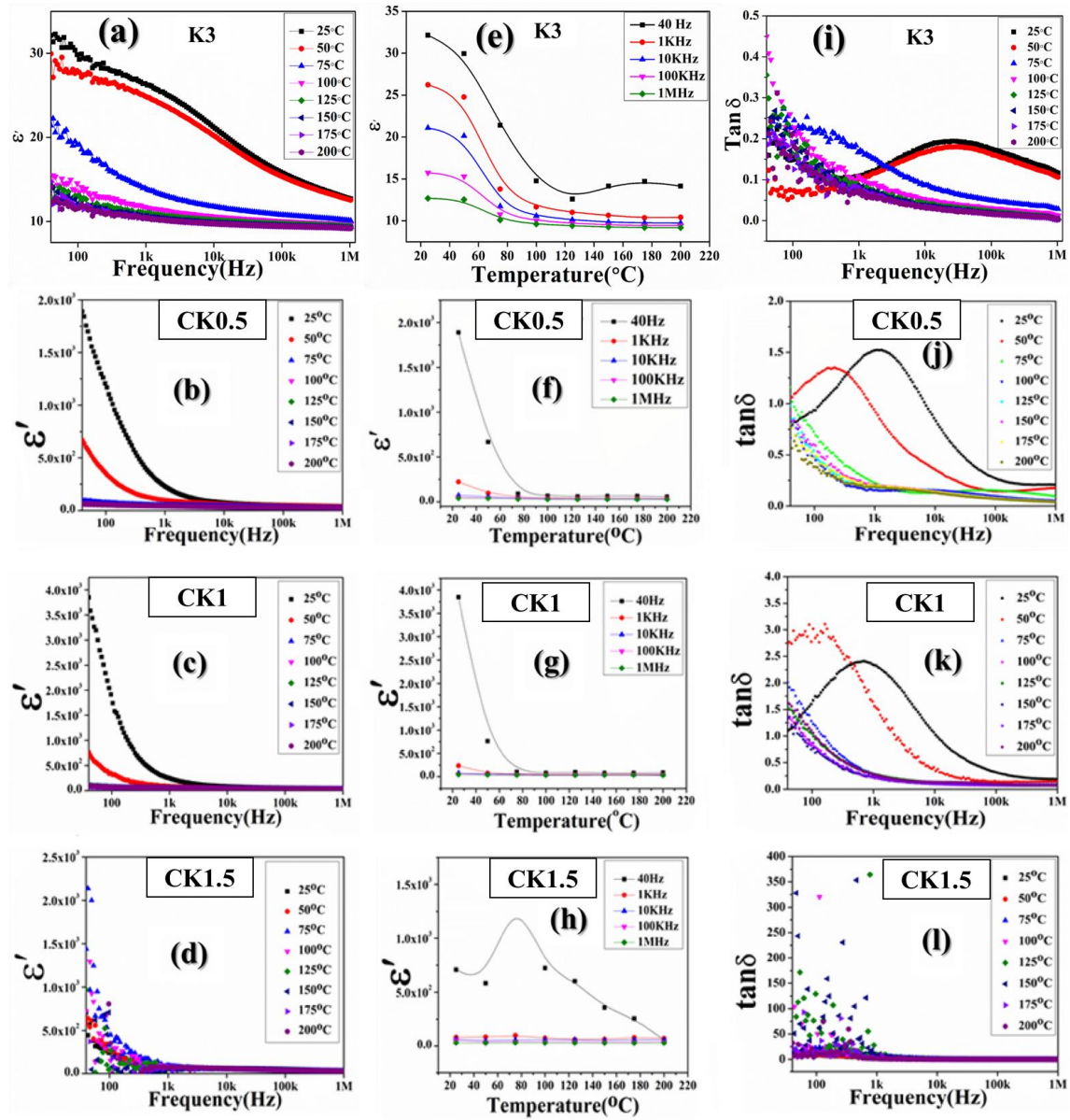


Figure 4.7. Variation of dielectric constant with frequency (a–d), temperature-dependent dielectric response (e–h), and tangent loss (i–l) for the MWCNT-doped kaolinites.

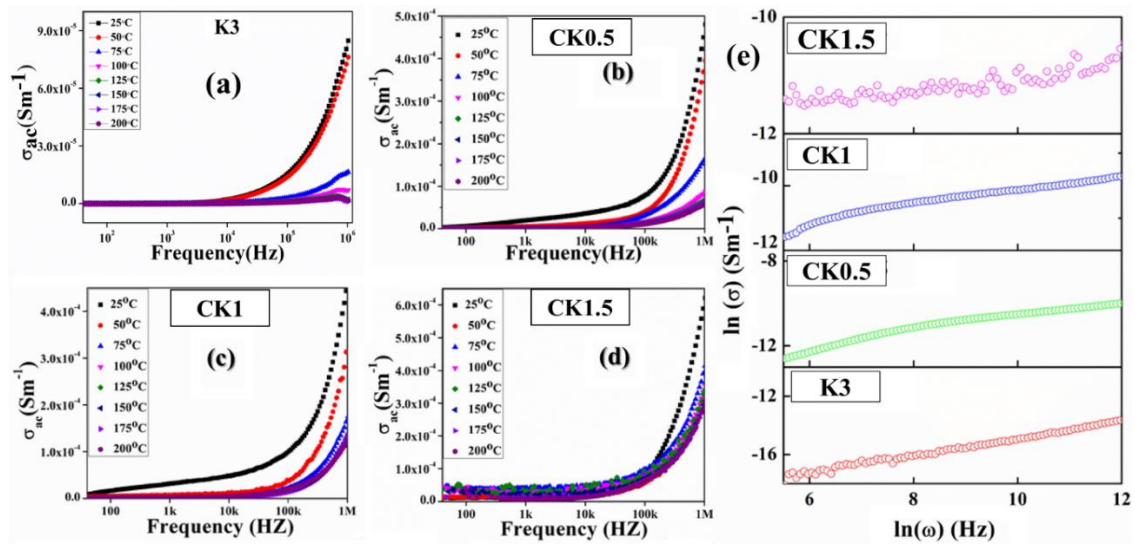


Figure 4.8. a-d) Temperature-dependent ac conductivities with varying frequencies of concentration-dependent MWCNT-clay nanocomposites, e) Joncher's plot to evaluate the diffusion-limited hopping mechanism of the nanocomposite samples.

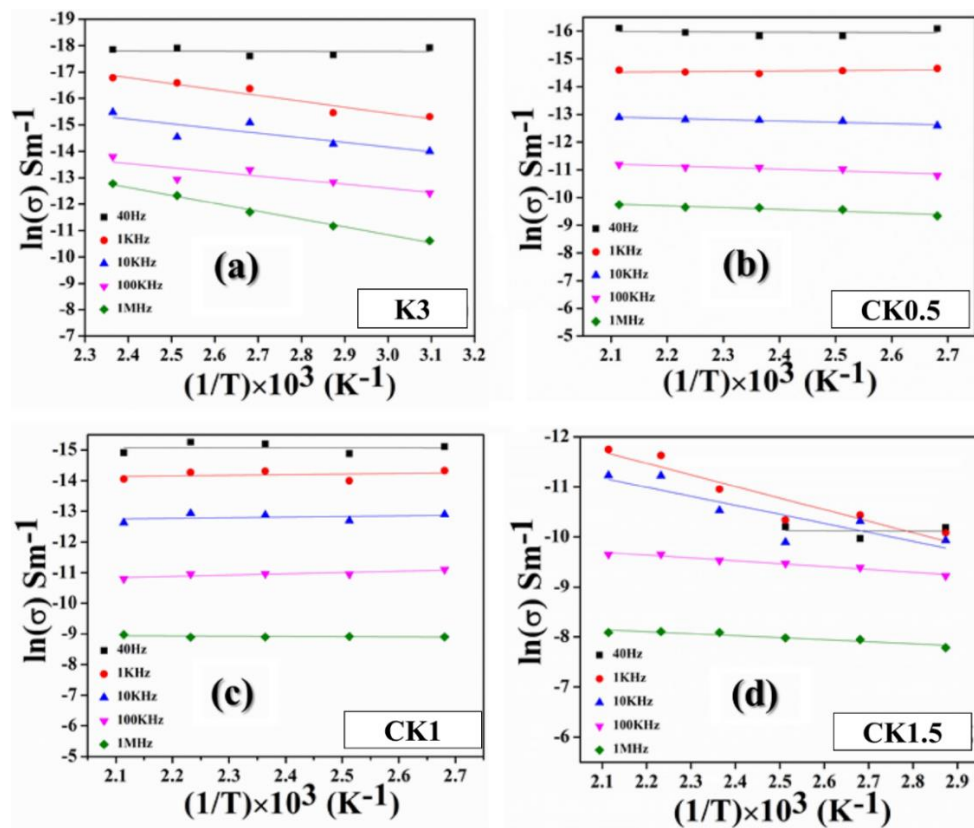


Figure 4.9. Arrhenius plots of the MWCNT concentration-dependent clay samples for estimating the activation energies.

Table 4.5. Activation energies of % MWCNT-doped kaolinite clay samples.

Sample	Frequency	Activation energy (eV)
K3	40Hz	0.00277
	1KHz	0.19237
	10KHz	0.15188
	100KHz	0.13415
	1MHz	0.25692
CK0.5	40Hz	0.00612
	1KHz	0.01198
	10KHz	0.04067
	100KHz	0.05205
	1MHz	0.05575
CK1	40Hz	0.000654
	1KHz	0.01677
	10KHz	0.01711
	100KHz	0.03561
	1MHz	0.00658
CK1.5	40Hz	0.00221
	1KHz	0.19942
	10KHz	0.15528
	100KHz	0.04903
	1MHz	0.03492

It has been shown in previous sections that the CK1 sample possesses a better attachment between clay and MWCNT. As a result, CK1 shows the most charge transport than other nanocomposites and also possesses better ac conductivity.

4.3.5 Estimation of the effect of microstructure on charge transport for percentage MWCNT doping

The charge transport phenomenon and carrier mobility of the nanoparticle were investigated by impedance data fitted by the EIS spectral analyzer [29]. The impedance spectra of the samples show depressed semicircles in the high-frequency domain along with straight lines in the low-frequency regions (Figure 4.10). The semicircle is attributed to the charge transfer process, whereas, the straight line is attributed to the diffusion

phenomenon [30]. The equivalent circuit comprises two separate loops consisting of resistance (R) with a constant phase element (CPE1).

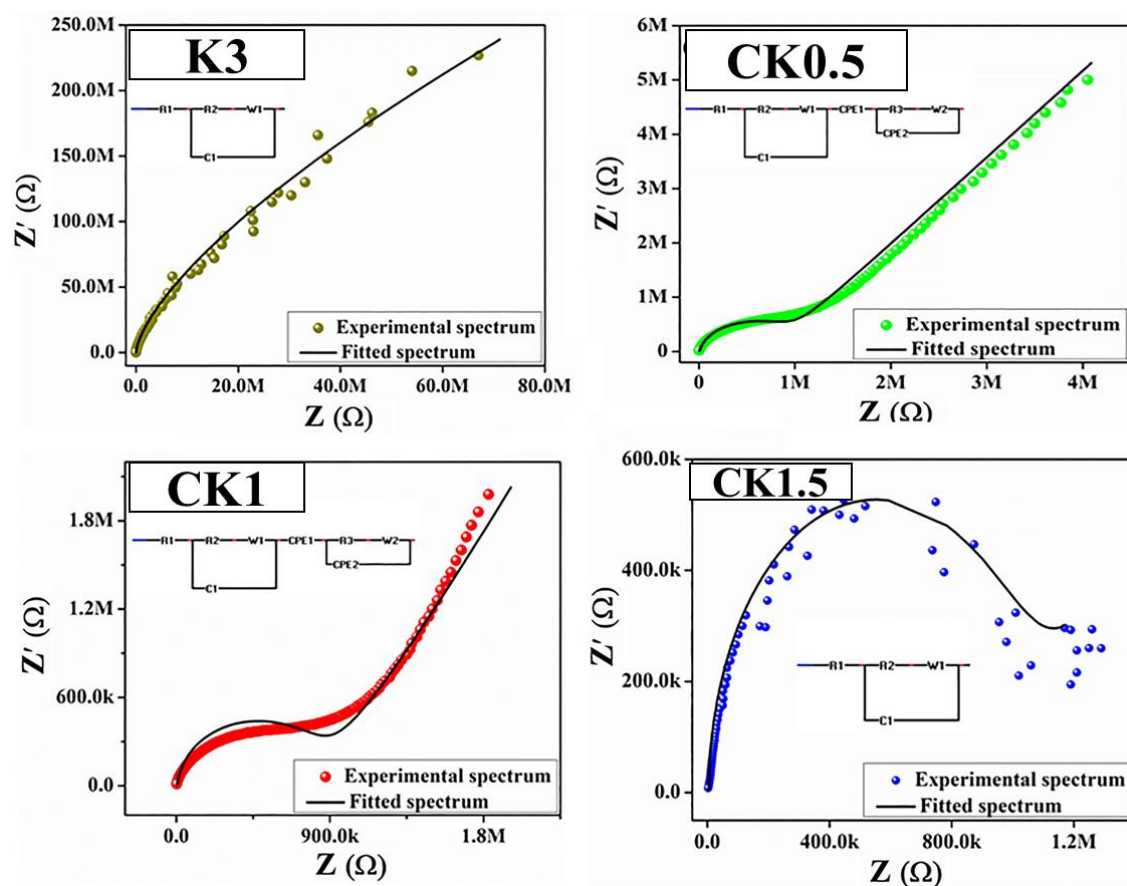


Figure 4.10. Electrochemical impedance spectra of the MWCNT-doped samples with corresponding equivalent circuits for estimating the charge transfer process.

These two loops are joined in series with another constant phase element (CPE2). The first loop represents the contribution of the sample, whereas, the second loop depicts the interfacial effects. The Warburg element represents the diffusion phenomenon [31]. The second loop in the K3 and CK1.5 are absent as there are no abrupt interfaces formed between MWCNT and kaolinite. It is evident from the data that the charge transfer resistance (R2) gradually increases with increasing doping concentration (Table 4.6). The reason behind such impedance relaxation with MWCNT doping lies in its microstructure

[32]. The pristine sample (K3) shows a low charge transfer resistance ($8.1392 \times 10^{-9} \Omega$), which alternatively validates the mobility of charge through the system. However, doping of MWCNT somewhat stretches the alignment of the kaolinite crystals from various sides and results in voids and defects, which could be a possible reason for the entrapment of free charge carriers into the defect zones. Thus, the carrier mobility decreased subsequently in CK0.5 ($R_2 = 7.6417 \times 10^5 \Omega$) and CK1 ($R_2 = 9.6442 \times 10^5 \Omega$) giving rise to the charge transfer resistances. Above a critical doping limit i.e., 1.5% in CK1.5, the permanent microstructural distortion of kaolin crystals takes place, which leads to the highest charge transfer resistance ($R_2 = 9.9381 \times 10^5 \Omega$).

Table 4.6. Equivalent circuit parameters of the samples estimated from the impedance fitting.

Parameters	CNTK0	CNTK0.5	CNTK1	CNTK1.5
C_1 (F)	9.9734×10^{-12}	2.235×10^{-11}	2.249×10^{-9}	3.173×10^{-11}
R_1 (Ω)	588.84	1.272×10^{-12}	8.891×10^{-13}	4425.9
R_2 (Ω)	8.1392×10^{-9}	7.6417×10^5	9.6442×10^5	9.9381×10^5
R_3 (Ω)	-	8.0711×10^{-13}	8.679×10^5	-
W_1 (Ω)	7.1897×10^9	6.3307×10^{-12}	9.937×10^6	9.6742×10^6
W_2 (Ω)	-	5.9256×10^{-12}	1×10^7	-
CPE1 (F)	-	4.546×10^{-9}	9.52×10^{-9}	-
CPE2 (F)	-	1.347×10^{-8}	1.2853×10^{-10}	-

4.3.6 Estimation of the electrochemical performances of the clay samples by percentage-dependent MWCNT doping

The cyclic voltammetry has been performed for further exploitation of the electrochemical performance of the nanocomposites. The voltammograms show typical electronic hysteresis loops as shown in Figure 4.11. The corresponding specific capacitances (CP) have been calculated using the relation 1.8. The calculated specific capacitance of the entire set of samples shows a gradual increment with MWCNT concentration up to a critical limit (1% loading: 22F/g), thereafter, the C_v value reduces

drastically. Such an interesting increment is related to the enriched amount of interface formation in MWCNT-kaolinite composites [33]. The successful attachment of kaolinite to the surface of MWCNT reduces the charge transport path length and thereby increases the specific capacitance. Moreover, CK1.5 depicts a reduction in C_v (7.8 F/g), which is related to the improper doping or excessive presence of MWCNT in the sample. Additionally, CNT-doped clay samples offer redox relaxation as shown in Figure 4.11. In reality, the conductive MWCNT introduces free charge carriers to the active sites of the kaolinite [34]. This charge transport results in oxidation maxima in the modified clay samples. As kaolinite has a large number of voids and defects in its crystals, these free carriers have been entrapped by such voids resulting in a relatively lower reduction peak.

The specific capacitances have also been estimated by varying the scan rate for the CK1 sample and found 22.40, 7.17, 8.87, and 6.35 F/g for the scan rates 100, 300, 500, and 1000 mV/s respectively. It is observed that, at lower scan rates, the ions have sufficient time to migrate deeper into the system contributing to higher feasible reactions and conveying improved capacitive performance. Henceforth, the electrochemical assay suggests the CK1 sample could be a promising electrode material for energy harvesting devices [35].

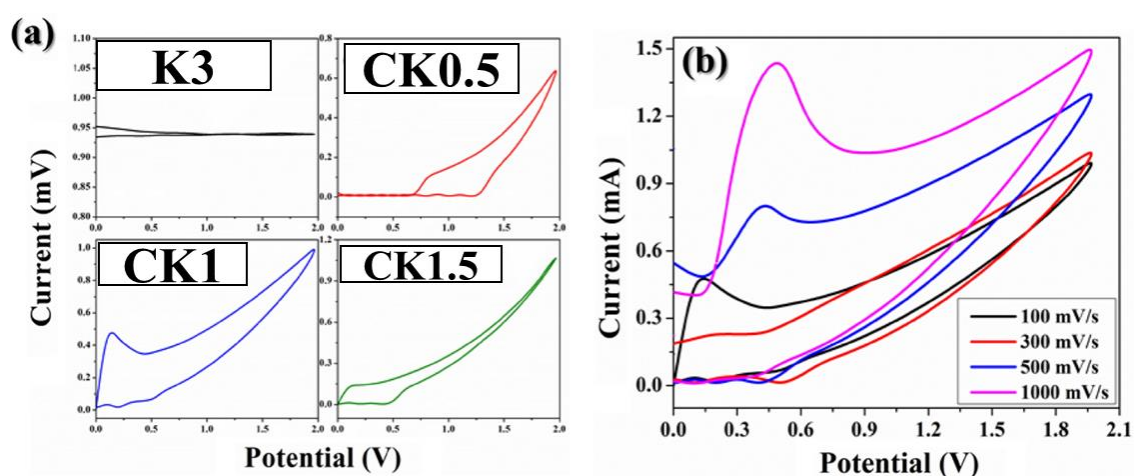


Figure 4.11. a) Cyclic voltammograms of various MWCNT-doped clay samples, b) voltammogram of CK1 at different scan rates.

4.4 Summary

In this chapter natural kaolinite, clay-based MWCNT nanocomposites have been synthesized by incorporating different concentrations of MWCNT by a typical surface modification of the clay and MWCNT followed by a condensation technique. This simplistic synthesis process of the abundantly available clay could be useful in industrial production on a large scale. Detailed investigation suggests the microstructural modifications of the clay moiety, which leads to the entrapment of free charge carriers that further help in modulating the electrical parameters. The dielectric data depicts an enhanced charge storage capacity in 1% w/w doping (nearly 93 times compared to its pristine counterpart) as the dielectric constant is found to be 3850 at a frequency of 40 Hz with very low tangent loss. Moreover, the MWCNT-modified clay nanostructures exhibit excellent thermal stability up to 500 °C revealing potential application in high-temperature devices as well. The high ac conductivity, especially in CK1 makes them potential candidates for large-scale electrode fabrication. The ac conductivities and impedance spectra suggest 1-D diffusion-limited hopping of the charge carriers and correlate microstructural modifications associated with the clay samples. This low-cost clay material shows a redox relaxation when it comes to electrochemical analysis. Such redox peaks are attributed to the carrier transport between CNT and kaolinite nanoparticles. The specific capacitance (C_v) is found to be 22.4 F/g, which is particularly important for charge storage applications. Moreover, it has also been found that the excess incorporation of MWCNT decreases the physicochemical properties due to disruption of the periodic arrangement of the micro-capacitors formed in the composites. Thus, this chapter validated the maximum polarization, storage, and surface properties of 1% MWCNT doped kaolinite clay which made it a promising alternative to use in advanced nanotechnology.

References

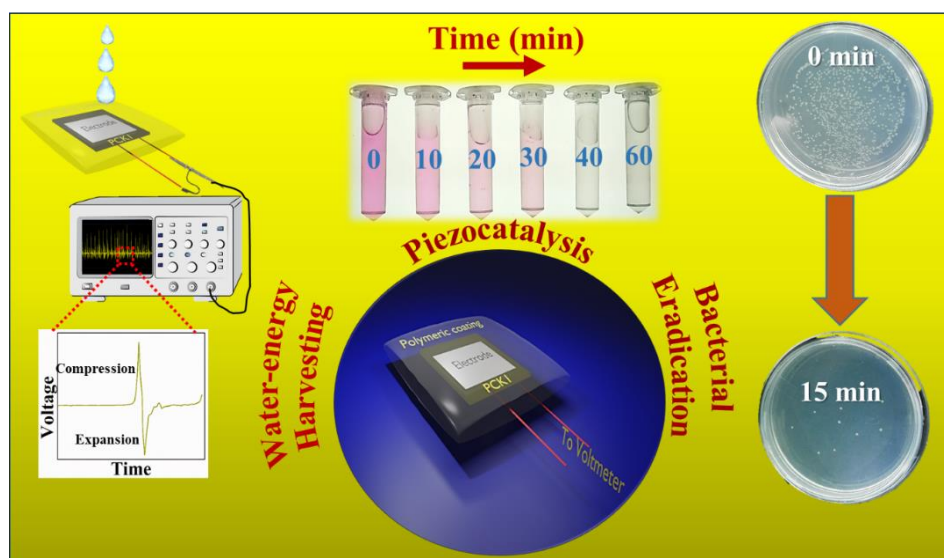
- [1] Kar, Pradip. In *Advances in Nanostructured Composites*, pp. 48-96. CRC Press, 2019.
- [2] Singh, Pardeep, Pooja Shandilya, Pankaj Raizada, Anita Sudhaik, Abolfazl Rahmani-Sani, and Ahmad Hosseini-Bandegharai. *Arabian Journal of Chemistry* 13, no. 1 (2020): 3498-3520.

- [3] Roy, Jhilik, Shubham Roy, Dhananjoy Mondal, Neelanjana Bag, Jaba Roy Chowdhury, Saheli Ghosh, Souravi Bardhan, Rajib Mondal, Ruma Basu, and Sukhen Das *Surfaces and Interfaces* 44 (2024): 103579.
- [4] Zhao, Pengxiang, Na Li, and Didier Astruc. *Coordination Chemistry Reviews* 257, no. 3-4 (2013): 638-665.
- [5] Mondal, Dhananjoy, Souravi Bardhan, Namrata Das, Jhilik Roy, Saheli Ghosh, Anupam Maity, Shubham Roy, Ruma Basu, and Sukhen Das. *Nano Energy* 104 (2022): 107893.
- [6] Desai, K. R., S. T. Alone, S. R. Wadgane, Sagar E. Shirsath, Khalid M. Batoo, A. Imran, E. H. Raslan, M. Hadi, M. F. Ijaz, and R. H. Kadam. *Physica B: Condensed Matter* 614 (2021): 413054.
- [7] Abukhadra, Mostafa R., Merna Mostafa, Ahmed M. El-Sherbeeney, Ahmed Tawhid Ahmed Soliman, and E. Abd Elatty. *Microporous and Mesoporous Materials* 306 (2020): 110465.
- [8] Wong, Li Wen, Pooria Pasbakhsh, Amir Masoud Arabi, John Keeling, and Joash Ban Lee Tan. *Journal of Environmental Chemical Engineering* 9, no. 5 (2021): 106235.
- [9] Liu, Hongshen, Seung Ho Hahn, Mengguo Ren, Mahadevan Thiruvillamalai, Timothy M. Gross, Jincheng Du, Adri CT van Duin, and Seong H. Kim. *Journal of the American Ceramic Society* 103, no. 6 (2020): 3575-3589.
- [10] Pavitha, P. A., S. Suma Mahesh, V. S. Sumi, and S. Rijith *Colloids and Surfaces A: Physicochemical and Engineering Aspects* (2024): 133646.
- [11] Han, Junxing, Juanjuan Bian, and Chunwen Sun. *Research* (2020).
- [12] Lashkari, Sima, Manila Ozhukil Valappil, Rajinder Pal, and Michael A. Pope. *Journal of Materials Chemistry A* 11, no. 21 (2023): 11222-11234.
- [13] Li, Xiaolin, Juehua Wang, Nannan Bai, Xinran Zhang, Xue Han, Ivan Da Silva, Christopher G. Morris et al. *Nature Communications* 11, no. 1 (2020): 4280.
- [14] Moradnia, Farzaneh, Saeid Taghavi Fardood, Ali Ramazani, Bong-ki Min, Sang Woo Joo, and Rajender S. Varma. *Journal of Cleaner Production* 288 (2021): 125632.

- [15] Sarker, Dali Rani, Md Nizam Uddin, Md Elias, Zidnia Rahman, Ratan Kumar Paul, Iqbal Ahmed Siddiquey, Md Abul Hasnat, Mohammad Razaul Karim, Md Azharul Arafath, and Jamal Uddin. *Cleaner Engineering and Technology* 6 (2022): 100364.
- [16] Sanusi, Olawale Monsur, Abdelkibir Benelfellah, and Nourredine Aït Hocine. *Applied Clay Science* 185 (2020): 105408.
- [17] Frank, L. A., G. R. Onzi, A. S. Morawski, A. R. Pohlmann, S. S. Guterres, and R. V. Contri. *Reactive and Functional Polymers* 147 (2020): 104459.
- [18] Mondal, Dhananjay, Amartya Sau, Shubham Roy, Souravi Bardhan, Jhilik Roy, Saheli Ghosh, Ruma Basu, Soumyaditya Sutradhar, and Sukhen Das. *Journal of Materials Science: Materials in Electronics* 34, no. 21 (2023): 1597.
- [19] Zhang, Xianghui, Junjie Wang, Ling Wang, Zhongquan Li, Ruyan Wang, Hongkui Li, Ming Luo, Huiyu Liu, Wei Hu, and Qian Feng. *Applied Clay Science* 223 (2022): 106507.
- [20] Asgar, Hassnain, Jiaqi Jin, Jan Miller, Ivan Kuzmenko, and Greeshma Gadikota. *Colloids and Surfaces A: Physicochemical and Engineering Aspects* 613 (2021): 126106.
- [21] Sharifvaghefi, Seyyedmajid, and Ying Zheng. *Resources Chemicals and Materials* 1, no. 3-4 (2022): 290-307.
- [22] Deepak, A., Pheba Cherian, and D. F. L. Jenkins. *International Journal of Nanoscience* 20, no. 02 (2021): 2150019.
- [23] Debnath, Tanumoy, Tanmoy Chakraborty, Atul Bandyopadhyay, Shivam Sharma, Abhik Sinha Mahapatra, Sukhen Das, and Soumyaditya Sutradhar. *Materials Science and Engineering: B* 280 (2022): 115688.
- [24] Forero-Sandoval, I. Y., A. P. Franco-Bacca, F. Cervantes-Álvarez, C. L. Gómez-Heredia, J. A. Ramírez-Rincón, J. Ordonez-Miranda, and J. J. Alvarado-Gil. *Journal of Applied Physics* 131, no. 23 (2022).
- [25] Das, Solanky, Dhananjay Mondal, Souravi Bardhan, Shubham Roy, Dipak Kr Chanda, Anupam Maity, Subhojit Dutta, Kamalakanta Mukherjee, and Kaustuv Das. *Journal of Materials Science: Materials in Electronics* 33, no. 9 (2022): 7119-7133.

- [26] El-Nahrawy, Amany M., Ali B. Abou Hammad, Tawfik A. Khattab, Ahmed Haroun, and Samir Kamel. *Reactive and Functional Polymers* 149 (2020): 104533.
- [27] Zaki, M. F., A. Tayel, and A. B. El Basaty. "Tuning the optical properties, AC conductivity and dielectric modulus of PVA membrane by inclusion of TiO₂ nanoparticles." *Bulletin of Materials Science* 45, no. 4 (2022): 236.
- [28] Crapse, Joseph, Nishant Pappireddi, Meera Gupta, Stanislav Y. Shvartsman, Eric Wieschaus, and Martin Wühr. *Molecular systems biology* 17, no. 8 (2021): e9895.
- [29] Grossi, Marco, and Bruno Riccò. *Journal of sensors and sensor systems* 6, no. 2 (2017): 303-325.
- [30] Yoon, Seung-Beom, Jong-Pil Jegal, Kwang Chul Roh, and Kwang-Bum Kim. *Journal of The Electrochemical Society* 161, no. 4 (2014): H207.
- [31] Aurbach, Doron, Kira Gamolsky, Boris Markovsky, Gregory Salitra, Yossi Gofer, Udo Heider, Ruediger Oesten, and Michael Schmidt. *Journal of The Electrochemical Society* 147, no. 4 (2000): 1322.
- [32] Saji, Janita, Ayush Khare, R. N. P. Choudhary, and S. P. Mahapatra. *Journal of Elastomers & Plastics* 47, no. 5 (2015): 394-415.
- [33] Mondal, Dhananjoy, Shubham Roy, Souravi Bardhan, Ratnottam Das, Anupam Maity, Dipak Kr Chanda, Solanky Das, Saheli Ghosh, Ruma Basu, and Sukhen Das. *Journal of Materials Science: Materials in Electronics* 33, no. 17 (2022): 13826-13842.
- [34] Umer, Muhammad, Muhammad Tahir, Muhammad Usman Azam, and Mohammad Musaab Jaffar. *Applied Surface Science* 463 (2019): 747-757.
- [35] Murali, Arun, Prashant K. Sarswat, and Michael L. Free. *Journal of Alloys and Compounds* 843 (2020): 155835.

Chapter 5



Exploring Piezocatalytic Wastewater Remediation and Piezoelectric Energy Generation in MWCNT-Integrated Kaolinite decorated poly (vinylidene fluoride-co-hexafluoropropylene) Membranes

Chapter 5

Exploring Piezocatalytic Wastewater Remediation and Piezoelectric Energy Generation in MWCNT-Integrated Kaolinite decorated poly (vinylidene fluoride-co-hexafluoropropylene) Membranes

5.1 Introduction

In the previous chapter 3, it was found that the physicochemical properties enhanced after the successful incorporation of functional groups (Zeta potential -17.1 mV) over the nano-clay surfaces and incorporation of 1-D MWCNT (Zeta potential -37.3). In reality, kaolinite shows a negative surface charge (-11.8 mV) for the combined effect of its negative basal planes and positive prism planes [1]. This negative surface charge is further enhanced by surface modification by incorporating an electronegative NH₂ group and MWCNT incorporation over the prism plane to minimize the effects of this positive moiety of kaolinite which has been validated by FTIR spectra. The surface charge of the clay is further enhanced due to these incorporations over its surfaces. These enhanced surface properties are further utilized to fabricate promising piezo-responsive materials [2].

This chapter deals with synthesizing a biocompatible, cost-effective, highly robust, efficient flexible, freestanding, and reusable membrane using modified kaolinite NPs and Poly (vinylidene fluoride-hexafluoropropylene) (PVDF-HFP) for effective piezodynamic destruction of carcinogenic organic dyes and coliform bacteria [3]. In this study, Rhodamine B, *Escherichia coli* (*E. coli*) and *Enterococcus faecalis* (*E. faecalis*) have been used to evaluate the mechanical stimulus-responsive piezo efficiency of the nanocomposite membranes [4][5]. To further understand the mechanism evaluation of Reactive Oxygen Species (ROS) and bacterial FESEM was performed [6]. These industrial effluent and pathogen degradation by the biocompatible membrane (96 % RhB, 100 % *E. coli*, and 97 % *E. faecalis*) paved a new path for wastewater remediation technology [7]. Further using the same nanocomposite membrane piezoelectric energy has been harvested by simple hand tapping (about 14 N force) to minimize the energy

deficiency of the society [8, 9]. Moreover, in this chapter energy has also been generated from non-invasive mechanical energy sources like water flow (flow rate $4 \times 10^{-3} \text{ L s}^{-1}$) and found a promising energy generation efficiency (50 W/m^2).

5.2 Experimental section

5.2.1 Materials

Naturally formed kaolinite clay minerals have been purchased from Hindustan Minerals, India. 2', 7'-Dichlorodihydrofluorescein diacetate (DCFDA, purity $\geq 97 \%$, $10 \mu\text{M}$), Poly (vinylidene fluoride hexafluoropropylene) (PVDF-HFP, purity: 99.99% , molecular weight: 455000) and multiwalled carbon nanotube have been purchased from Sigma Aldrich, Germany. LB broth and phosphate buffer saline (PBS) have been purchased from HiMedia Pvt. Ltd., India. The analytical-graded hydrazine hydrate (purity $\geq 99 \%$), acetone (HPLC-grade, purity $\geq 99.5 \%$), and dimethylformamide (DMF, purity $\geq 99 \%$) have been purchased from Merck, India. *Escherichia coli* DH5 α (MTCC-1652) and *Enterococcus faecalis* (MTCC-441) have been purchased from the Institute of Microbial Technology, Chandigarh, India. Millipore water having a resistance of $\sim 18.2 \text{ M}\Omega\text{-cm}$ has been used throughout the experiment.

5.2.2 Synthesis of Nanocomposite Membranes

A facile one-step solution casting method was adopted to find the kaolinite-based free-standing PVDF-HFP membrane. Initially, 0.5 g PVDF-HFP was taken in three different glass vials and dissolved into 5 ml dimethylformamide (DMF) at 60°C on a magnetic stirrer (600 rpm). The activated nano kaolinite was then added by maintaining the weight percentage of 2.5 %, 5 %, and 7.5 % with the polymer. The vials are kept in the same condition until a homogeneous gel-like transparent solution occurs. Then the homogeneous solutions were taken in different clean petri dishes and kept in a dust-free hot air oven at 60°C for 6h. The dried flexible free-standing membranes were then peeled off from the Petri dishes carefully, collected, and named PVK2.5, PVK5, and PVK7.5 respectively according to their wt%. A film of pristine PVDF-HFP was also prepared for the comparative study by the same method without adding the activated

natural clay in its matrix and labelled PVK0. All the prepared nanocomposite membranes were then sent for further experiments.

On the other hand, the same protocol was adopted to obtain the flexible, composite film of MWCNT-kaolinite-PVDF-HFP. Initially, 0.5 g of PVDF-HFP was dissolved in 10 mL of DMF under stirring conditions (600 rpm) at 60°C. The 1 % MWCNT loaded-kaolinite nanocomposite (CK1; chapter 3) was then added at different weight percentages (0.5 %, 1.0 %, and 1.5 %). The homogenous solutions were then poured into clean glass Petri plates after 12 h of vigorous stirring and the plates were kept in a dust-free hot air oven at 60°C for another 6h. The dried membranes were peeled off and marked as PCK0.5, PCK1, and PCK1.5. Pure PVDF membrane was also prepared using the same protocol, excluding the addition of MWCNT-kaolinite, and marked as PCK0 (Figure 5.1, Table 5.1).

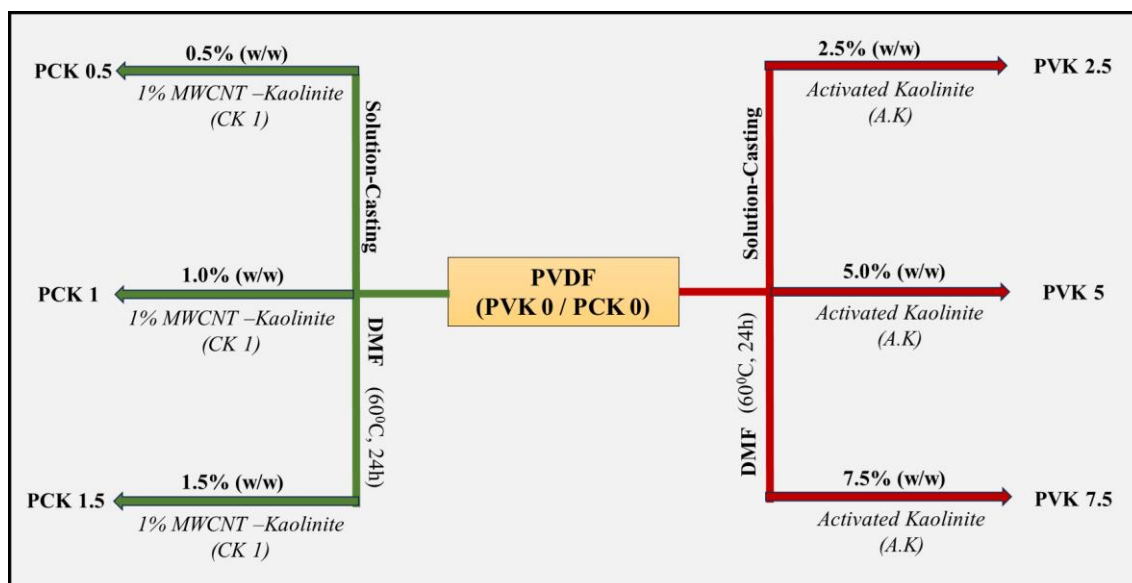


Figure 5.1. Nanocomposite sample and preparation techniques.

Table 5.1. Synthesized nanocomposite membranes and respective codes

Sample Specifications	Sample Codes
Pure PVDF-HFP	PVK0/PCK0
Functionalized kaolinite-doped PVDF-HFP (2.5, 5, 7.5%: Wt/Wt-ratio)	PVK2.5, PVK5, PVK7.5
1%-MWCNT incorporated kaolinite-doped PVDF-HFP (0.5, 1, 1.5%: Wt/Wt-ratio)	PCK0.5, PCK1, PCK1.5

5.3 Results and Discussion

5.3.1 Structural and Morphological & Elemental Analyses of the Nanocomposites

The X-ray diffractograms of the activated kaolinite, MWCNT-kaolinite doped PVDF-HFP nanocomposite membranes have been investigated and depicted in Figure 5.2 a, b.

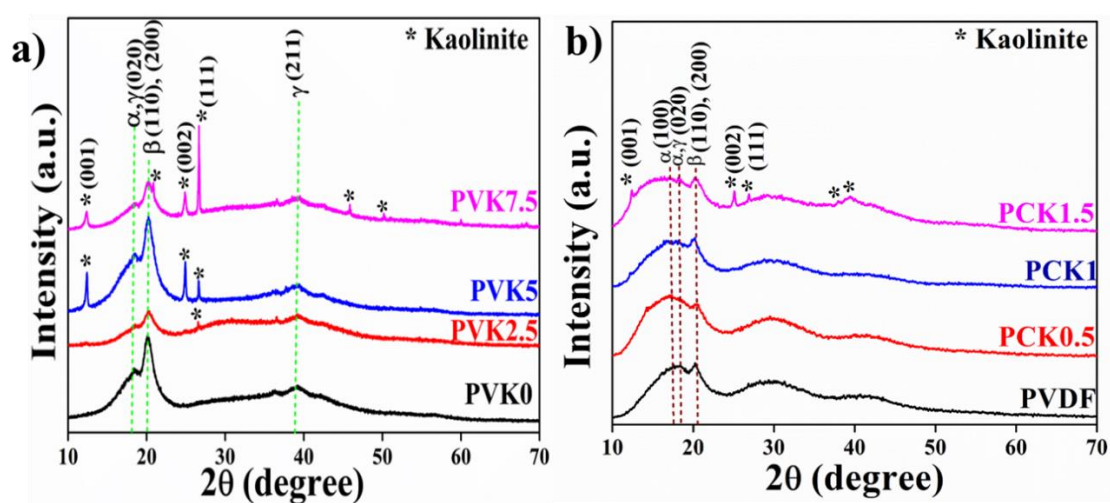


Figure 5.2. XRD of a) kaolinite doped PVDF b) MWCNT-kaolinite incorporated PVDF nanocomposite membranes

The diffractograms of the nanocomposite membranes show that the non-polar α - phase at 17.6° gets quenched whereas both polar phases of β (20.4°) and γ (39.6°) get enhanced with the natural nano-clay and MWCNT-clay incorporation in the PVDF-HFP

matrix [10]. The diffraction maxima at 12.5, 24.8, 26.6, 34.9, and 67.3° have arisen for the increased doping percentage of the kaolinite in the membranes [11, 12]. These polar phase enhancements of the PVDF-HFP membranes help to increase their piezoelectric effectiveness and get maximum for PVK5 and PCK1. It is found that, after reaching a certain doping limit, viz, 5wt% in kaolinite doped PVDF and 1 % in MWCNT-kaolinite doped PVDF, the polar phase in the polymer matrix further decreases in PVK7.5 and PCK1.5. This may be attributed to the excess presence of negative surface charge of the modified natural clay, which further disrupts the H₂ and F₂ band parity in the nanocomposite membranes [13].

The FESEM micrographs of the kaolinite doped PVDF depicted in Figure 5.3 and MWCNT-kaolinite doped PVDF depicted in Figure 5.5 show that the big bubble-like structure of PVK0 or PCK0 has been greatly reduced with the incorporation of nanoparticles in PVK2.5, PVK5, PVK7.5, PCK0.5, PCK1, and PCK1.5. This validates the formation of polar crystalline phases [14]. The clay-modified NPs-incorporated nanocomposite membranes depicted the homogeneous distribution of nanoparticles in the PVDF-HFP matrix which suggests the successful incorporation of the nanoparticles. The TEM micrograph of PCK1 has also been investigated and found clay NPs in the PVDF interior in Figure 5.5 e.

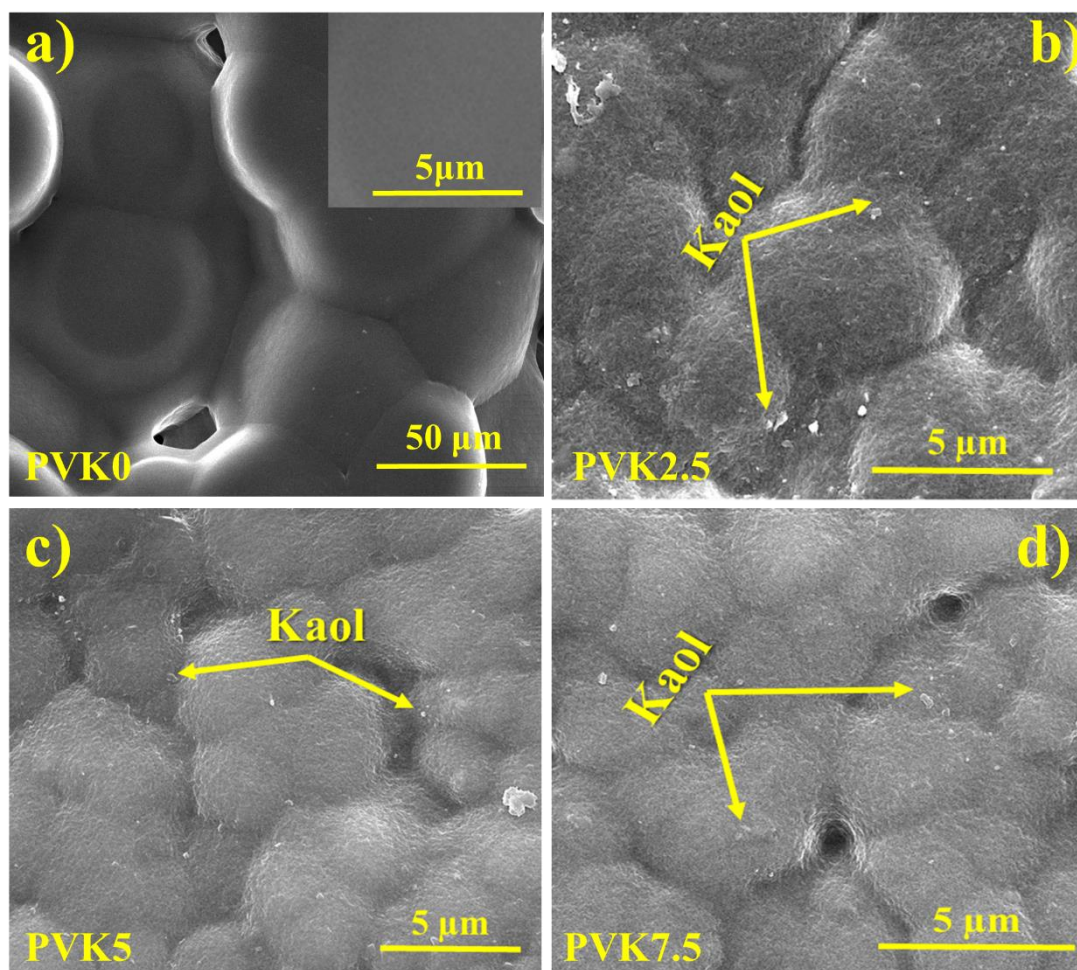


Figure 5.3. FESEM micrographs of a) pure PVDF, b) PVK2.5, c) PVK5, and d) PVK7.5.

The EDS spectra and elemental mapping data also suggest the successful incorporation of nanoparticles in the membranes (Figure 5.4, 5.6). However, for using carbon tape the carbon component has been locked in the instrument as a result carbon component is not present in the elemental table. The presence of Au in the membranes arises due to the gold sputtering while the sample has been prepared for FESEM, EDS, and mapping.

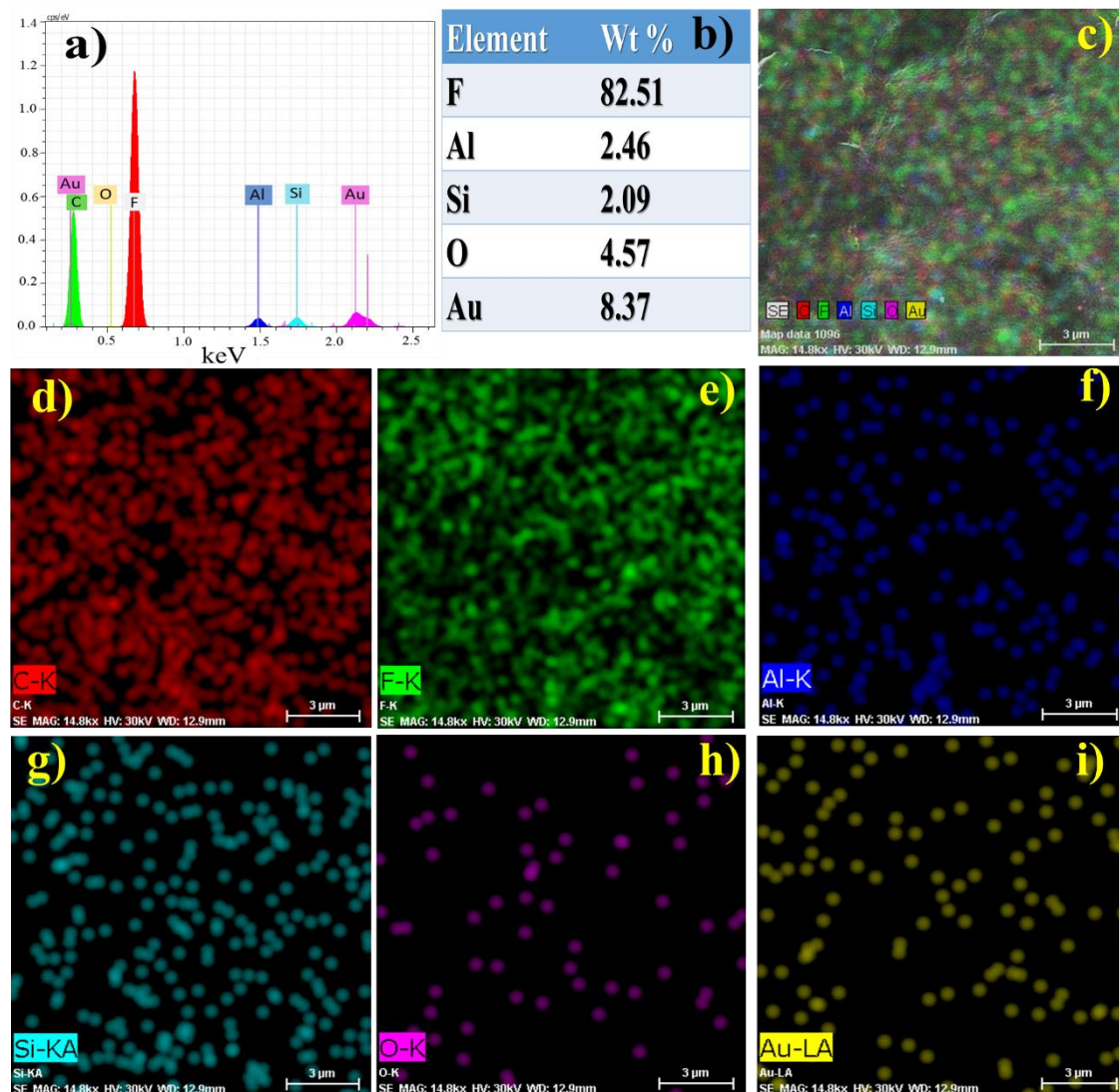


Figure 5.4. EDAX (a, b) and mapping (c-i) of PVK5 membrane.

The chemical states show the full XPS spectrum of the nanocomposite membrane (PCK1) in Figure 5.7. The C 1s XPS spectrum was deconvoluted, which exhibits the contribution of different C species [15]. The deconvoluted spectrum consists of two intense peaks suggesting major contributions of $-\text{CH}_2-$ and $-\text{CF}_2-$, while the contributions from $-\text{C}=\text{C}-$, $-\text{F}-\text{C}-\text{C}-\text{H}-$, $-\text{H}-\text{C}-\text{F}-$ are also reflected by three other less intense peaks [16]. The $-\text{CH}_2-$ and $-\text{CF}_2-$ peaks are observed at 286.3 eV and 291 eV, indicating a shift toward higher BE compared to pure PVDF-HFP. The peak shift of C

1s XPS spectra indicates a strong electrostatic interaction among the PVDF and MWCNT molecules and the formation of the β phase [17]. Figure 5.7 shows the deconvoluted XPS spectra of F1s exhibiting the shift of $-F-C-H-$ and $-F-C-F-$ species towards higher BE and is found at 688.6 eV and 687.3 eV respectively.

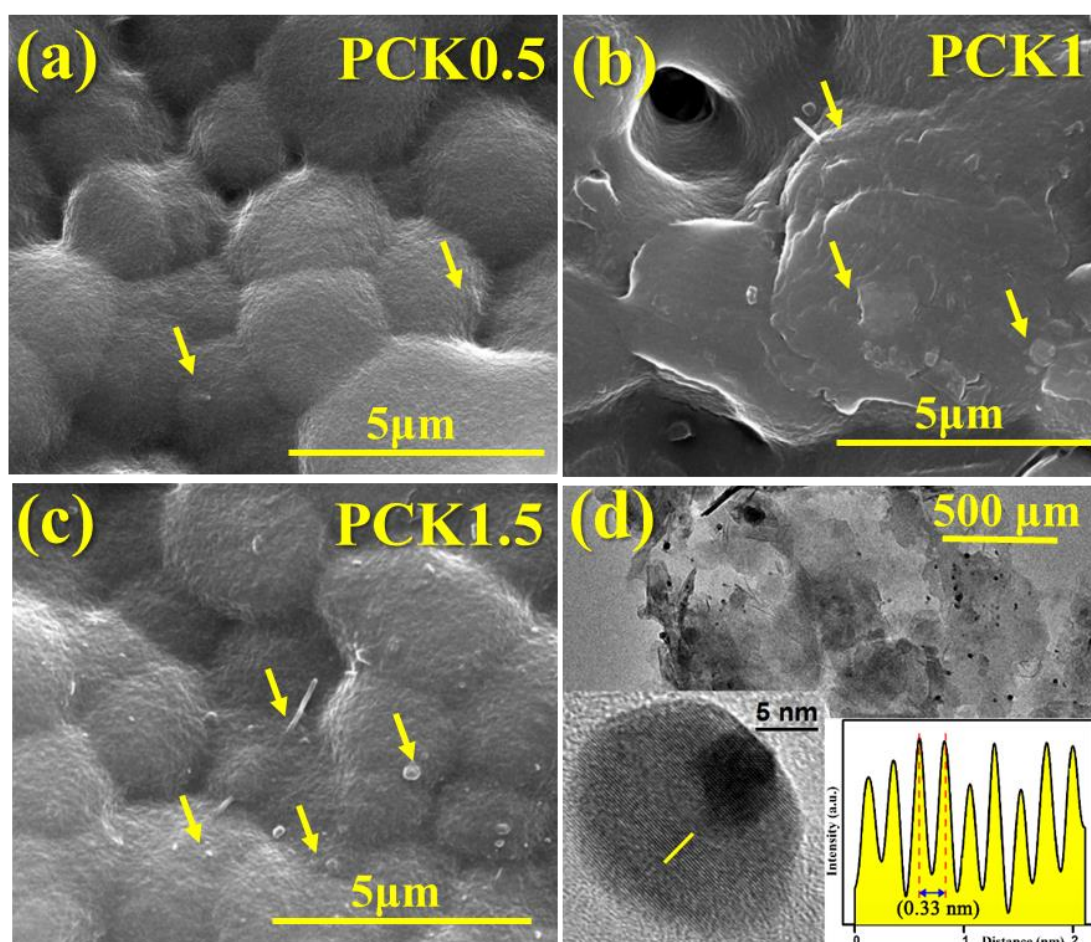


Figure 5.5. a-c) FESEM micrographs of PCK0.5, PCK1, PCK1.5 respectively, d) TEM micrograph of PCK1,

5.3.2 Estimation of polarity and piezo-effectiveness of the nanocomposite membranes

It has been found from the previous Chapter 3 that the activated kaolinite (-17.1 mV) and 1 % MWCNT doped kaolinite (-37.3 mV) pose a better negative surface charge than pristine clay (-11.8 mV) due to the incorporation of electroactive NH_2 groups and MWCNT over its surfaces.

This negative surface charge of the activated clay and MWCNT-incorporated clay enhances the polar β -phase formation probability in the nanocomposite membrane. In reality, α - phase of PVDF-HFP has electro-positive $-\text{CH}_2$ moiety and electro-negative $-\text{CF}_2$ moiety attached in carbon chains in TGTG' (trans-gauche-trans-gauche) configuration which is why the polarity of the membrane is very low. In the β -phase of the PVDF-HFP $-\text{CH}_2$ and $-\text{CF}_2$ moieties arranged in opposite directions of the carbon chain in TTTT configuration and enhanced the polar phase by forming the dipole as well as the piezo response of the membranes [18]. When the nanoparticles have a negative surface, charge entrapped into the polymer matrix the surface charge of the nanoparticles flipped the positive moiety of the PVDF-HFP on its side creating an all-trans conformation (TTTT), which resulted in the polar β -phase enhancement. The schematic diagram of dipole orientation in the different phases of PVDF-HFP has been shown in Figure 5.8 e. This enhanced polar β -phase and the bonding networks of the nanocomposite membranes have been investigated by FTIR spectroscopy. In Figure 5.8a, 5.9 a the FTIR spectra show that the nonpolar α - phases at 530 (CF_2 - bending), 614 (CF_2 - bending), 765 (skeletal bending), 796, and 976 (CH_2 -rocking) cm^{-1} get quenched and characteristic bands of polar β -phase at 489 (CF_2 -deformation), 508 CF_2 - stretching), 603 (CF_2 - wagging), and 840 (CF_2 stretching, CH_2 rocking, and skeletal C-C stretching) cm^{-1} enhanced with the increment of nanoparticle incorporation in the polymer matrix and found to be maximum in PVK5 and PCK1 [19]. The polar phase decreases after the excess incorporation of nanoparticles in the sample PVK7.5 and PCK1.5. In reality, the over-doping of nanoparticles enhances the negative charge concentration in the nanocomposite matrix and these extra negative surface charge tries to decrease the polar phase by attracting the positive moiety (CH_2 -) PVDF-HFP polymeric chain as a result the dipolar orientation is again disrupted. A schematic representation has been depicted in Figure 5.9b.

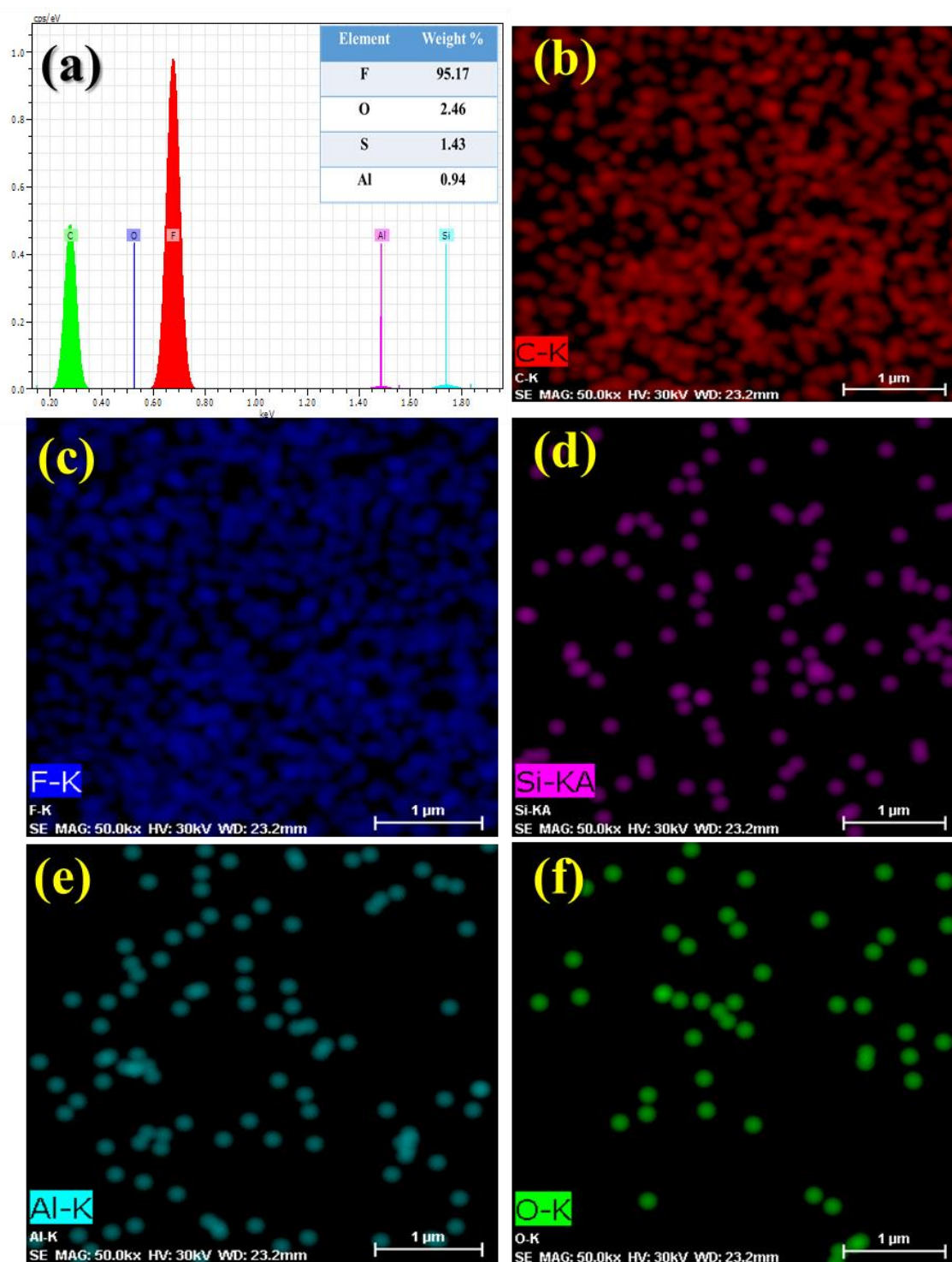


Figure 5.6. a) EDS of PCK1, b-f) mapping data of PCK1 nanocomposite membrane.

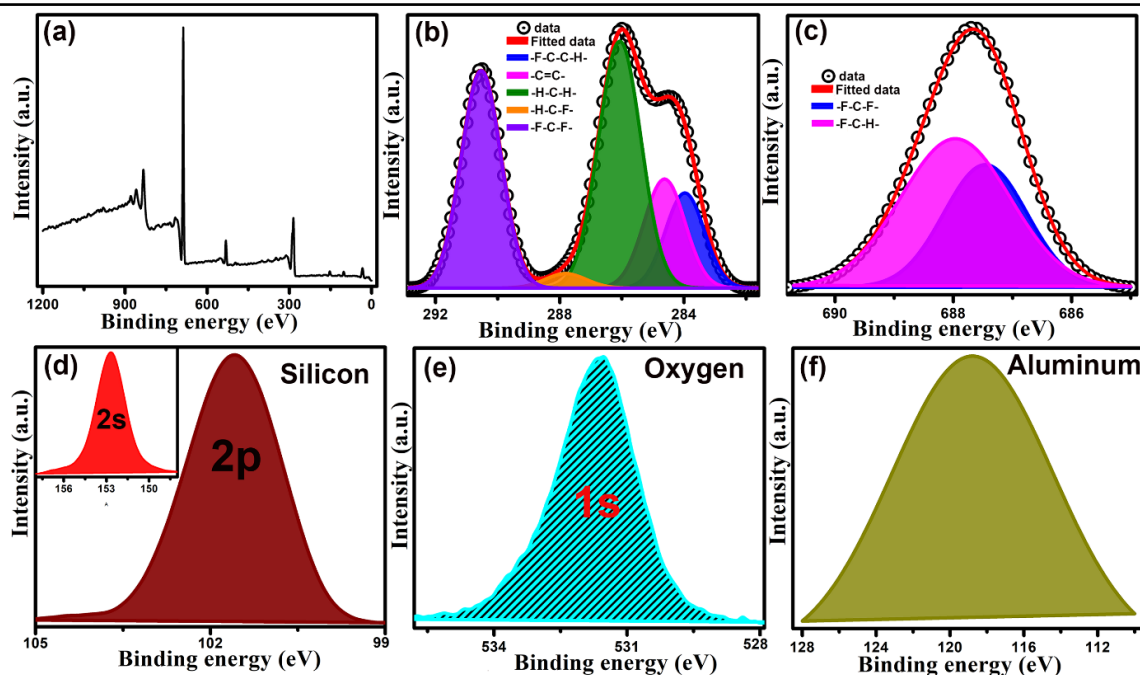


Figure 5.7. (a) Full XPS spectrum of the nanocomposite membrane (PCK1), (b), (c) deconvoluted spectrum of the C and F, (d), (e), (f) chemical states of Si, O, and Al respectively.

In terms of polar phase calculation, the polar β -phase has been calculated by the Lambert-Beer law,

$$F(\beta) = \frac{A(\beta)}{\frac{K(\beta)}{K(\alpha)} \times A(\alpha) + A(\beta)} \dots \dots \dots [4.1]$$

where $K(\alpha)$ and $K(\beta)$ are the absorption coefficients for the α and β phase at 765 and 840 cm^{-1} respectively and have the values of $6.1 \times 10^4 \text{ cm}^2 \text{ mol}^{-1}$ and $7.7 \times 10^4 \text{ cm}^2 \text{ mol}^{-1}$ whereas $A(\alpha)$ and $A(\beta)$ are the absorbance value of α and β phase respectively at the corresponding wave number [20].

From Lambert-Beer law the polar β -phase percentages have been calculated and found 61.0 %, 82.0 %, 84.2 %, and 82.7 % for the nanocomposite membrane PVK0, PVK2.5, PVK5, and PVK7.5 respectively which suggest that PVK5 membrane poses maximum polar β -phase (Figure 5.8 c) which suggest that the PVK5 poses better piezoelectric properties in kaolinite doped PVDF matrix [21]. Moreover, in the case of MWCNT-

kaolinite incorporated PVDF matrix the polar phases vary 61.0, 84.5%, 88.7%, and 85.8% for the membranes PCK0, PCK0.5, PCK1, PCK1.5 (Figure 5.9 b) respectively which validated the PCK1 having maximum polar phases can be applicable in pezo-responsive applications.

The room-temperature polarization-electric field (P-E) hysteresis loop has also been measured at 10 Hz in the ± 200 kV/cm range (Figure 5.8 d & 5.9 c). The area within the loop corresponds to the heterogeneous charge density and indicates the charge storage capability of the material [22]. It has been found that the remnant polarization (P_r) increases with the increasing doping percentage and is found to be 0.30, 0.51, 0.59, and $0.48 \mu\text{C}/\text{cm}^2$ respectively for the PVK0, PVK2.5, PVK5, and PVK7.5 nanocomposite membrane depicted in Figure 5.9 d. In the case of MWCNT-kaolinite clay-doped membranes, the remnant polarization varies 0.72, 0.92, and $0.42 \mu\text{C cm}^{-2}$ for PCK0.5, PCK1, and PCK1.5 respectively (Figure 5.10 c). The remnant polarization is found to be highest in the PVK5 membrane from the group of kaolinite-doped PVDF and PCK1 from the MWCNT-kaolinite-doped PVDF which is analogous to the FTIR, XRD, and FESEM data and indicates the maximum polar phase contained in the PVK5 and PCK1 membranes. This promising polarization in the PVK5 and PCK1 membranes made them suitable for any piezo-responsive applications [23].

Further, the dielectric properties of the nanocomposite membranes were also evidence of polarization in terms of Maxwell Wagner's interfacial polarization theory [24]. The dielectric constants of the membranes have been calculated by the equation 1.4. The dielectric constants are 9.0, 9.4, 12.9, and 9.7 respectively for the sample PVK0 or PCK0, PVK2.5, PVK5, and PVK7.5 at 40 Hz field frequency with a nominal tangent loss (Figure 5.8 f) whereas D.C of PCK based membranes varies 11.9, 18.0, 8.9 respectively for PCK0.5, PCK1, PCK1.5 (Figure 5.9 e, f). The frequency-dependent conduction mechanism (AC conductivity) of the nanocomposite membranes has also been studied by equation 1.5.

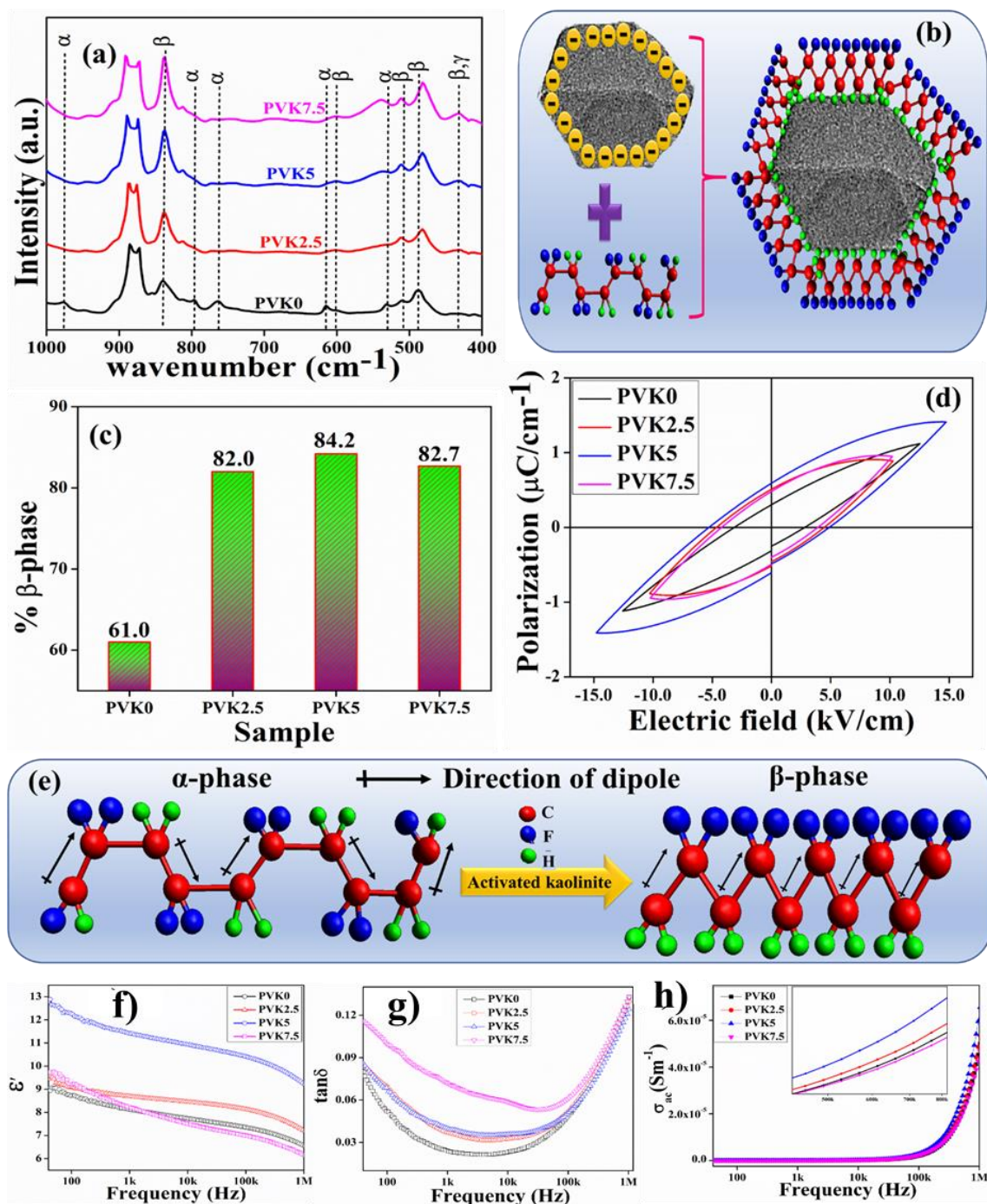


Figure 5.8. a) FTIR spectra of kaolinite-PVDF membranes, b) Schematic representation of polar β -phase formation, c) percentage β -phase of the nanocomposite membranes, d) Room temperature P-E loop data of the membranes, and e) Dipole orientation in α and β -phase of PVDF.

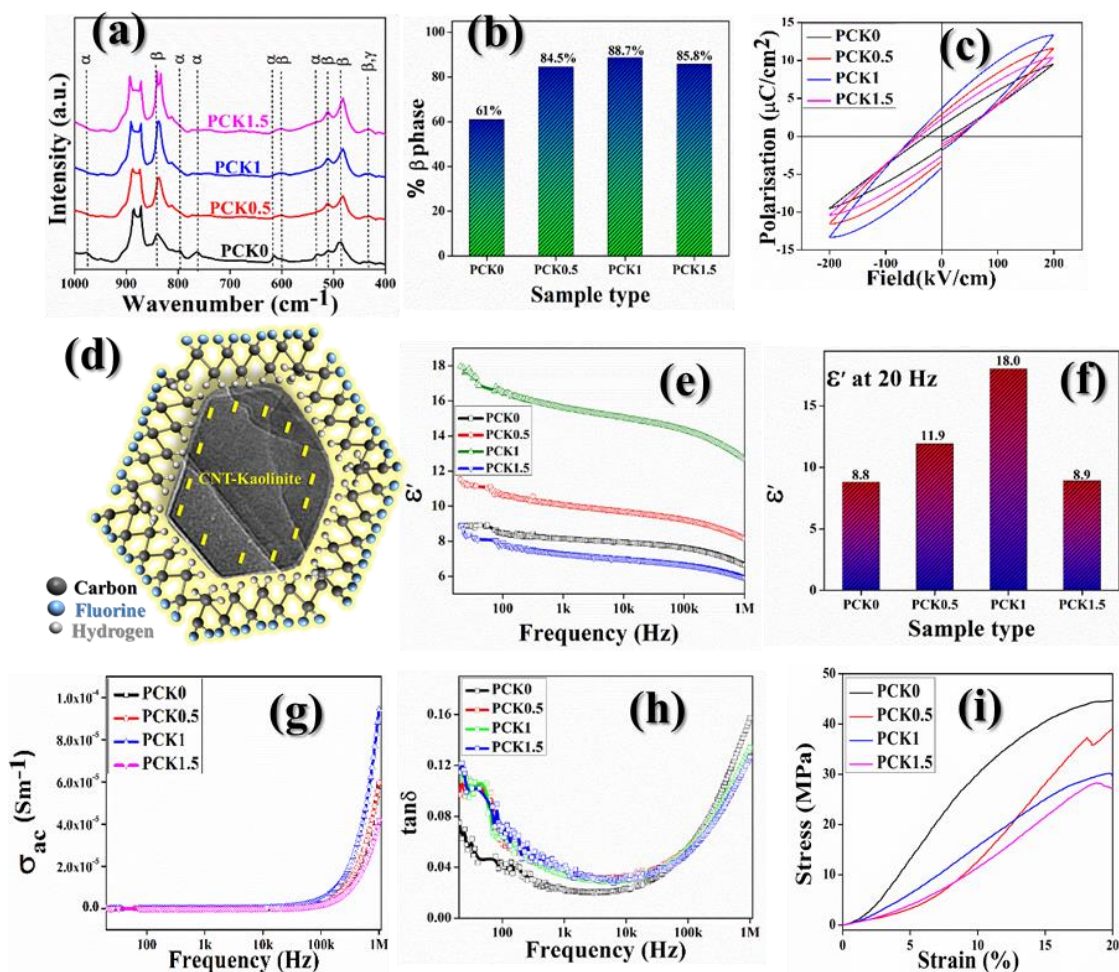


Figure 5.9. (a) FTIR spectroscopy of PVDF-based MWCNT-kaolinite nanocomposite films, (b) percentage β -phase of the PVDF-based nanocomposite films, (c) Zeta potential of 1% MWCNT doped natural kaolinite, (d) P-E loop of PVDF-based nanocomposite films, (e) Schematic diagram of β -phase formation, (f) dielectric permittivity of the nanocomposite films, (g) variation of dielectric permittivity with percentage doping of MWCNT-kaolinite in PVDF matrix, (h) ac conductivity data of nanocomposite membranes, (i) dissipation factors ($\tan\delta$) of the nanocomposites.

It has been found that the AC conductivity increases with increasing frequency and found $4.9\text{E-}5$, $5.3\text{E-}5$, $6.6\text{E-}5$, $4.7\text{E-}5$, $5.4\text{E-}5$, $9.5\text{E-}5$, and $4.6\text{E-}5\text{ Sm}^{-1}$ for PVK0/PCK0, PVK2.5, PVK5, PVK7.5, PCK0.5, PCK1, and PCK1.5 respectively (Figure 5.8 h & 5.9 g). This data is evident that the PVK5 and PCK1 possess the highest

dielectric constant which is analogous to other characterizations. Although PCK1 poses a better polarization response than PVK5 membrane in all the experiments [25].

Moreover, the polarizability of the samples has been investigated theoretically by using density functional calculations (DFT) [26]. In a typical process by the theoretical model of PCK0/PVK0 and PCK1 nanocomposite membranes have initially been designed by Avogadro v.1.2.0 software package. The DFT simulation depicts the enhanced polarizability, quadrupole moment, and dipole moment in the PCK1 sample compared to its pristine counterpart (PVK0/PCK0). The dipole moment increases from 12.09 Debye to 12.26 Debye, the quadrupole moment increases from -165.25 C m^2 to -169.02 C m^2 , and the isotropic polarizability increases from $218.54 \text{ C m}^2 \text{ V}^{-1}$ to $222.02 \text{ C m}^2 \text{ V}^{-1}$. Such augmented values validate the enhanced β -phase polarization calculated from FTIR spectra and indicate the samples, especially PCK1 to be a promising agent for piezo-responsive applications.

Further, the piezoelectric coefficients (d_{33}) of the samples by open circuit piezo voltages for the membranes under the mechanical force applied by simple finger tapping have been calculated by using the capacitance values (C_p) by the relation 1.9. The d_{33} values of the nanocomposites are found to be around 10 pC N^{-1} (PVK/PCK0), 16.5 pC N^{-1} (PVK2.5), 47.7 pC N^{-1} (PVK5), 23.7 pC N^{-1} (PVK7.5), 25.8 pC N^{-1} (PCK0.5), 50.7 pC N^{-1} (PCK1) and 12.3 pC N^{-1} (PCK1.5) for PVDF-based nanocomposite membranes. Such relaxation resembles the β -phase values and theoretical polarizabilities [27]. The piezoelectric coefficient (d_{33}) of PCK-based membranes has again been calculated using the equation $d_{33} = -P_r/Y$, where P_r , Y is the remnant polarization and Young's modulus (calculated from figure 5.9 i) respectively of the nanocomposite membrane. Young's modulus of the nanocomposite membranes has been found 328 N/mm^2 for bare PVDF and 167 N/mm^2 for PCK1 membrane. Therefore, by using the above equation, d_{33} of PCK1 comes out to be 55.1 pC/N . This value is higher than observed in PVDF (10.6 pC/N) showing that the nanocomposite membrane has superior piezoelectric properties without undergoing any poling techniques (Table 5.2).

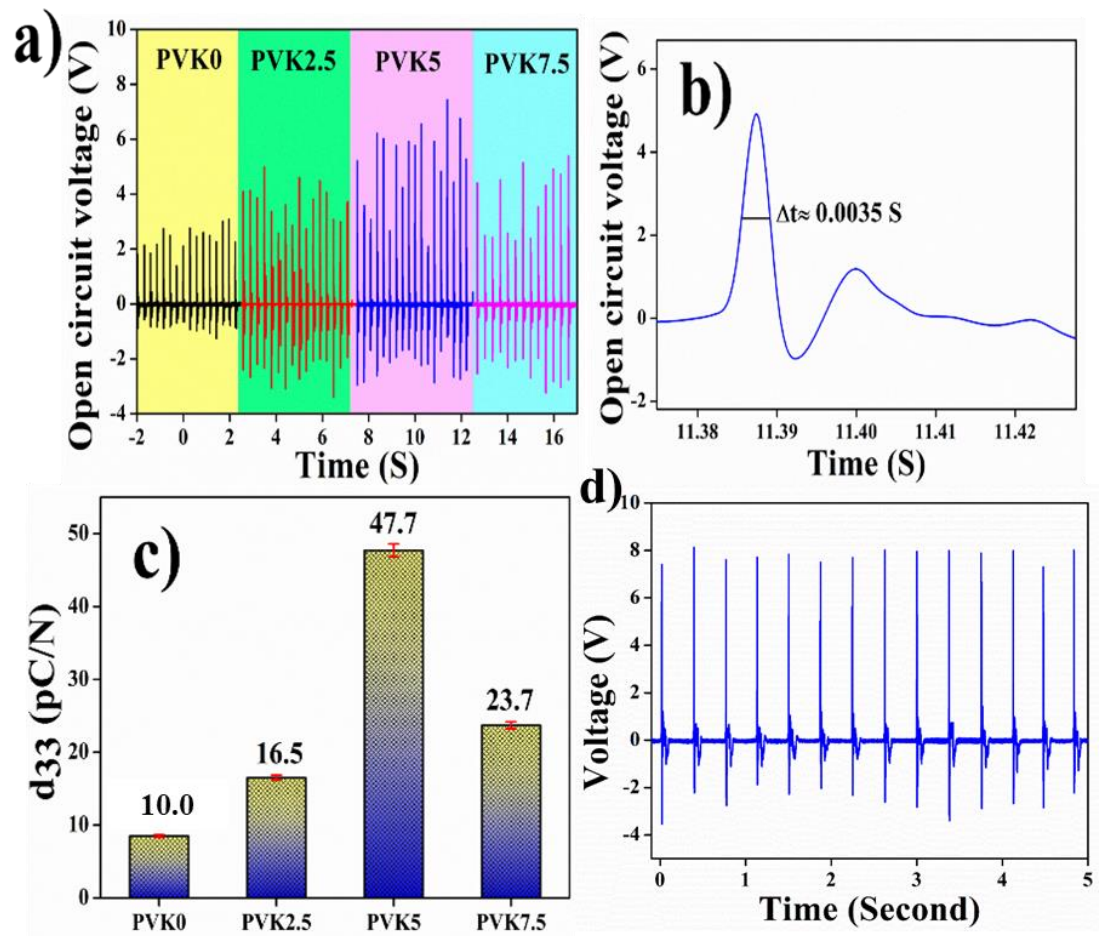


Figure 5.10. a) Piezoelectric open circuit voltage, b) Impulsive time of force applied, and c) d_{33} of the nanocomposite membranes.

Table 5.2. Polarization, Young's modulus, and measured piezoelectric coefficients of the nanocomposite membranes (measured in two different IEEE standard methods)

Samples	Polarization ($\mu\text{C}/\text{cm}^2$)	Young's modulus (MPa/mm)	$d_{33} = C_p V/F$ (pC/N)	$d_{33} = P_r/Y$ (pC/N)
PCK0/PVK0	0.349	328	11.0	10.6
PCK0.5	0.724	290	25.8	24.8
PCK1	0.924	167	50.7	55.1
PCK1.5	0.428	202	12.3	20.8

5.3.3 Piezoelectric energy generation

The devices by the membranes for piezoelectric energy generation have been fabricated in the procedure discussed in 1.10.3.2.5. It has been found that the voltages are 1.9V, 3.4V, 7.5V, 4.5V, and 8.0V, for the nanocomposite membranes PVK0/PCK0, PVK2.5, PVK5, PVK7.5, and PCK1 respectively depicted in Figure 5.10 a & 5.10 d (PCK1) by the simple finger tapping (14 N force) [28].

Moreover, the non-invasive water flow-mediated piezoelectric energy has also been generated by the PCK1 membrane for its maximum piezo efficiency. Initially, the device (Figure 5.11 c) was exposed to water droplets (Millipore or deionized water) from different heights (18 cm, 36 cm, 72 cm) under a constant flow rate ($4 \times 10^{-3} \text{ L s}^{-1}$) and output voltages were measured (Figure 5.11 a). It has been found that around 1.0 V, 2.0 V, and 4.1 V voltages have been generated when the water droplets have fallen from different heights of 18 cm, 36 cm, and 72 cm respectively [29].

The pressure exerted on the device enhances significantly, which results in an augmented voltage generation with increasing height. The exerted forces on the device have been measured and found to be 2.94 N, 4.79 N, and 7.19 N for the falling water from different heights as 18 cm, 36 cm, and 72 cm respectively. The corresponding short circuit currents have also been measured and depicted a similar relaxation. Particularly, at the highest distance (72 cm) the output current attains the highest value (1.5 μA) compared to 18 cm (0.5 μA) and 36 cm (0.8 μA) distances (Figure 5.11 d). Such high values of open circuit voltages and short circuit currents account for a relatively high power density of the device (50 W m^{-3}). Besides, water from different sources (drinking water, tap water) having distinct total dissolved solids (TDS) was collected and poured on the device from a fixed height of 36 cm. The output voltages obtained have been depicted in Figure 5.11 b showing that in the case of drinking (3.1 V) and tap water (6.5 V) the piezoelectric voltages attain higher values compared to the deionized water (2.0 V). This phenomenon can be substantiated by the virtue of the TDS of the water sample. The TDS of tap water (1876 ppm) is higher than that of drinking water (152 ppm) and deionized water (3 ppm), which exerts an augmented

force on the device and increases the output voltages. Such an interesting observation could lead to water quality monitoring in the near future along with non-invasive energy generation technology to serve society in the energy crisis [30]. The mechanism of energy generation by mechanical stress has been illustrated in Chapter 1, Section 1.5.

5.3.4 Eradication Efficiency of Rhodamine B

The PCK1 and PVK5 nanocomposite membranes have shown high isotropic polarizability, a promising piezo coefficient along with significantly high piezoelectricity under external mechanical stimuli and are therefore selected for piezocatalytic application [31]. Herein, the PCK1 and PVK5 membranes have been used to degrade Rhodamine B (RhB) dye under ultrasound stimulus by the catalysis experiment as stated in Chapter 1 Section 1.10.6. It has been found that the characteristic absorption maximum of RhB (554 nm) degrades gradually under the external stimulus [32]. The pink color of the dye also faded with the duration of the ultrasound treatment and finally depicted full transparency under 60 min of treatment (Figure 5.12 i). The absorbance spectra in Figure 5.12 a, b show the degradation kinetics of the piezocatalysts (PCK1, PVK5). The percentage piezo degradation efficiency η of the nanocomposites has been investigated by using the relation 1.13. It has been found that the degradation efficiency reaches about ~ 96 % for PCK1 and 79 % for PVK5, which is found to be 2.1 % in the absence of the catalyst under the piezo stimulation (Figure 5.12 h). Thus, it can be noted that the piezocatalyst (PCK1) offers enormous catalytic activity under mechanical stress. The mechanism of catalysis has been illustrated in Chapter 1 Section 1.6. In addition, the recyclability of the catalyst has been estimated by re-using it in a cyclic manner. Herein, the same membrane was used in five different cycles of application and found to have a consistent degradation efficacy (95.4 %) even after five cycles (Figure 5.12 g). There are several reasons for this type of alteration of the membrane efficiency i.e. accumulation of degraded contaminants or by-products over the membrane surface, distortion of the polymeric chain by ROS, and loss of active catalytic site of membrane for chemical changes [33].

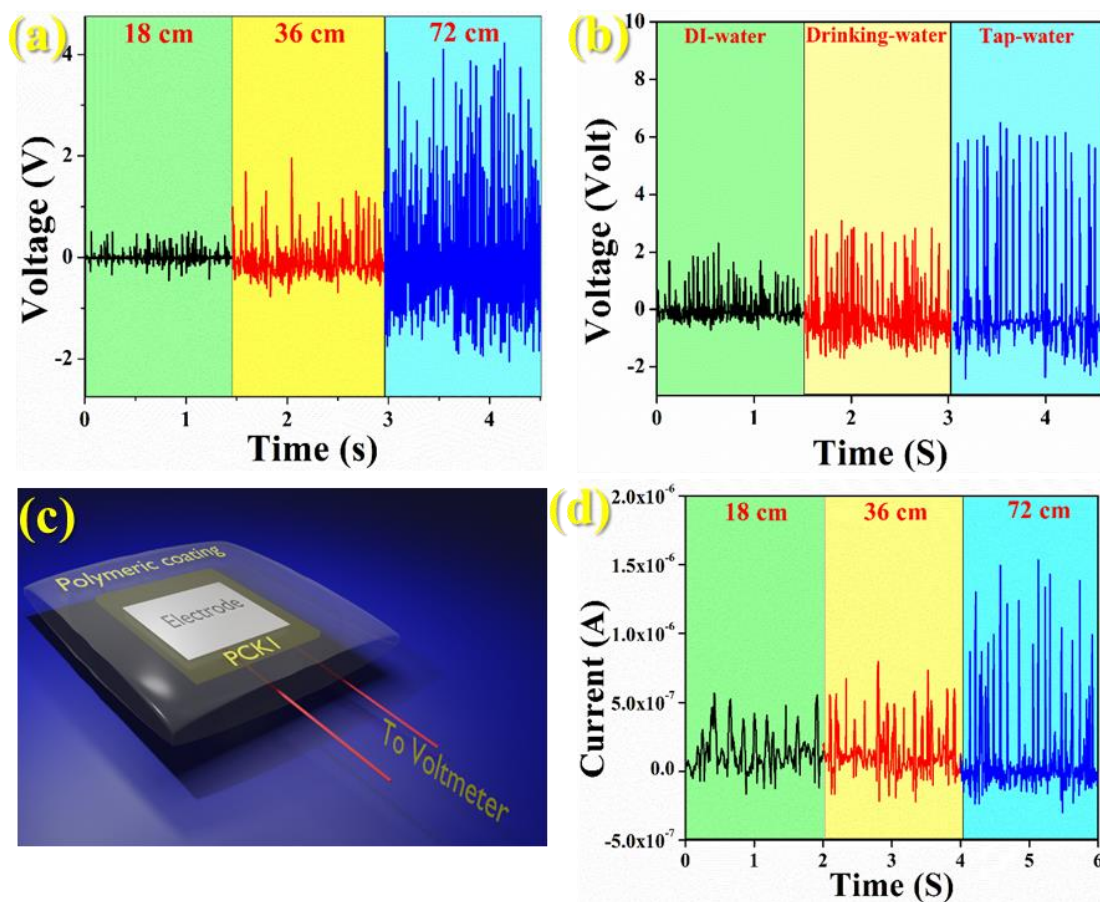


Figure 5.11. Piezoelectric output voltages: (a) voltages when the device is exposed to DI-water from different heights, (b) voltages from 36 cm height of different water sample, (c) PCK1 nanocomposite film-based device for piezoelectric water energy harvesting, (d) piezoelectric currents when DI-water droplets fall from a different height on the device.

To verify the catalysis mechanism, the first-order reaction kinetics, scavenging, and trapping experiments have been performed. The scavenging experiment was performed by adding scavenger chemicals to the organic dye-containing solution before performing the catalysis experiment [34]. It has been found that in the case of AgNO_3 , BQ, EDTA, and TBA the piezo degradation efficiency has been found 68.7 %, 52.6 %, 151 | Page

72.2 %, and 14.4 % respectively, which confirms the minimum scavenging for TBA (Figure 5.12 d, e). Further, the first-order kinetic constant (k) has been measured by using the relation 1.14.

The kinetic constants k have been measured and found to be $4.02 \times 10^{-2} \text{ min}^{-1}$ (No scavenger), $0.4 \times 10^{-2} \text{ min}^{-1}$ (TBA), $2.97 \times 10^{-2} \text{ min}^{-1}$ (EDTA), $2.90 \times 10^{-2} \text{ min}^{-1}$ (BQ), and $1.81 \times 10^{-2} \text{ min}^{-1}$ (AgNO_3). The lowest k value of TBA confirms the dominance of the OH^* radicals in our case. The presence of hydroxyl radicals in the piezocatalytic reaction mixture has been investigated by the photoluminescence-probing technique of terephthalic acid (TPA). Herein, a radical increment in fluorescence intensity over time has been found that confirms the production of OH^* radicals and validates the ROS-mediated damage to the RhB solution (Figure 5.12 f).

5.3.5 Inhibition of pathogenic bacteria

A substantial bactericidal effect has been found when the bacterial cells are exposed to ultrasound with the polymeric membranes. The mortality reaches nearly 99 % and 100 % in *E. coli* bacterium for PVK5 and PCK1 respectively and 97 % in *E. faecalis* bacterium (PVK5) after 40 min of ultrasound treatment which has been calculated from the colony counting technique, equation 1.15 (Figure 5.13, 5.14). A slight enhancement in the mortality rate in the negative controls, i.e., bacteria exposed to ultrasonic vibrations only is due to physical factors like micromechanical shocks, cavitation, and mechanical effects [35]. The movement of compression and rarefaction waves through the media during ultrasonication and the collapse of rapid oscillating bubbles have a deleterious effect on the bacterial cell membrane. In the control sample, the cellular membrane is smooth and undamaged whereas after piezodynamic therapy the bacterial cell ruptured which has been confirmed by the FESEM micrograph and depicted in Figure 5.13 d, e and 5.14 d, e. In The case of negative control by only ultrasound, the bacterial mortality was found at 74.8 % and 71.9 % suggesting the piezodynamic ROS enhances bacterial eradication efficiency.

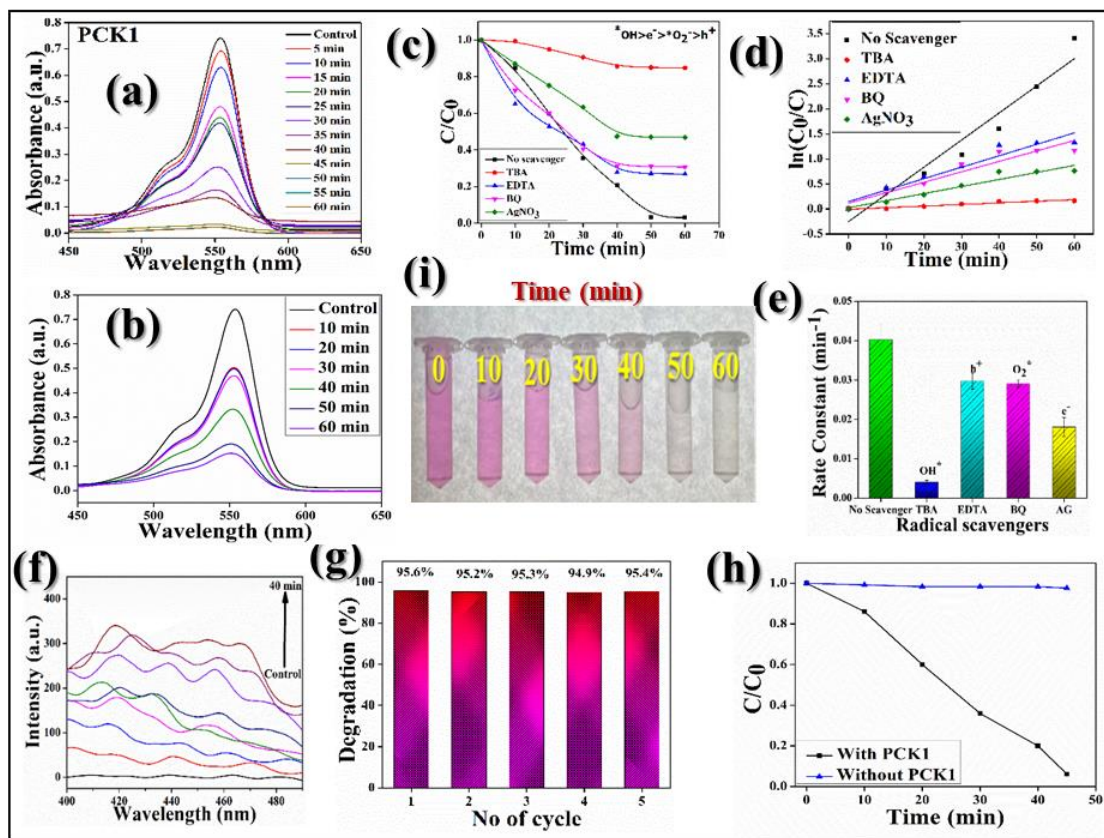


Figure 5.12. (a) Organic Rhodamine-B dye degradation with time under ultrasound (PCK1), (b) Degradation of RhB by PVK5, (c) investigation of scavenger by PCK1, (d) the reaction rate constant for different scavengers by PCK1, (e) effect of different free radicals for the Rhodamine-B degradation, (f) trapping experiment to investigate the presence of OH[•] radical, (g) recyclability experiment of the nanocomposite film up to five cycles, (h) comparison with only US data, (i) pictorial representation of dye color with time.

The fundamental cause for piezocatalysis is ROS creation, primarily OH[•] which has been confirmed by the photoluminescence study using DCFDA stated in Chapter 1 section 1.10.7. It has been found that the formation of ROS is negligible in the control group, it is gradually increased in the PVK5/PCK1-mediated treatment group (Figure 5.13, 5.14, 5.16) which validated the ROS-mediated piezocatalytic mechanism [36].

The time-dependent kinetic study has been depicted in Figure 5.15 for both the negative control and piezocatalysis. Moreover, the antibacterial test of the PVDF-HFP membrane without ultrasound and with ultrasound has been investigated.

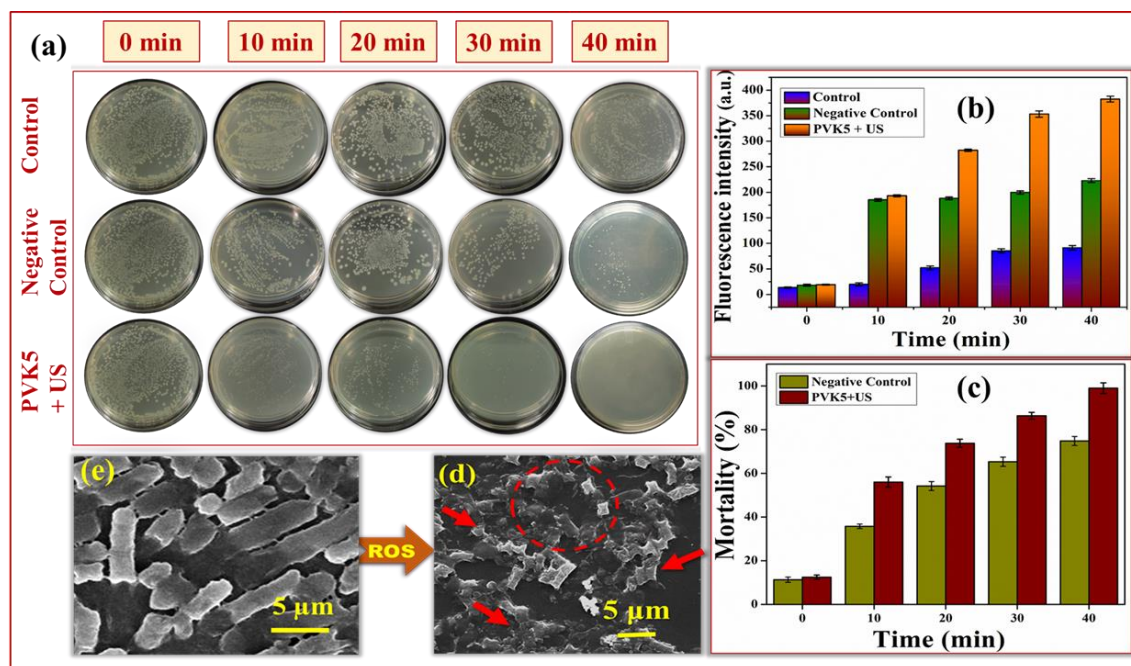


Figure 5.13. (a) Photographs representing surviving *E. coli* colonies on the solid agar plates (after 24 h of incubation); (b, c) Illustrates the amount of ROS generation and mortality percentage of *E. coli* as calculated using colony counting technique (d, e) FE-SEM images.

It has been found that the antibacterial efficiency was 8 % without US and around 35 % with ultrasound. The 35 % eradication was found due to nominal piezocatalytic efficiency in bare PVDF-HFP membrane [37]. Therefore, this work validates that the piezo-responsive PVK5/PCK1 membrane can be effectively utilized for the elimination of both Gram-positive and Gram-negative bacteria under mechanical stimulus.

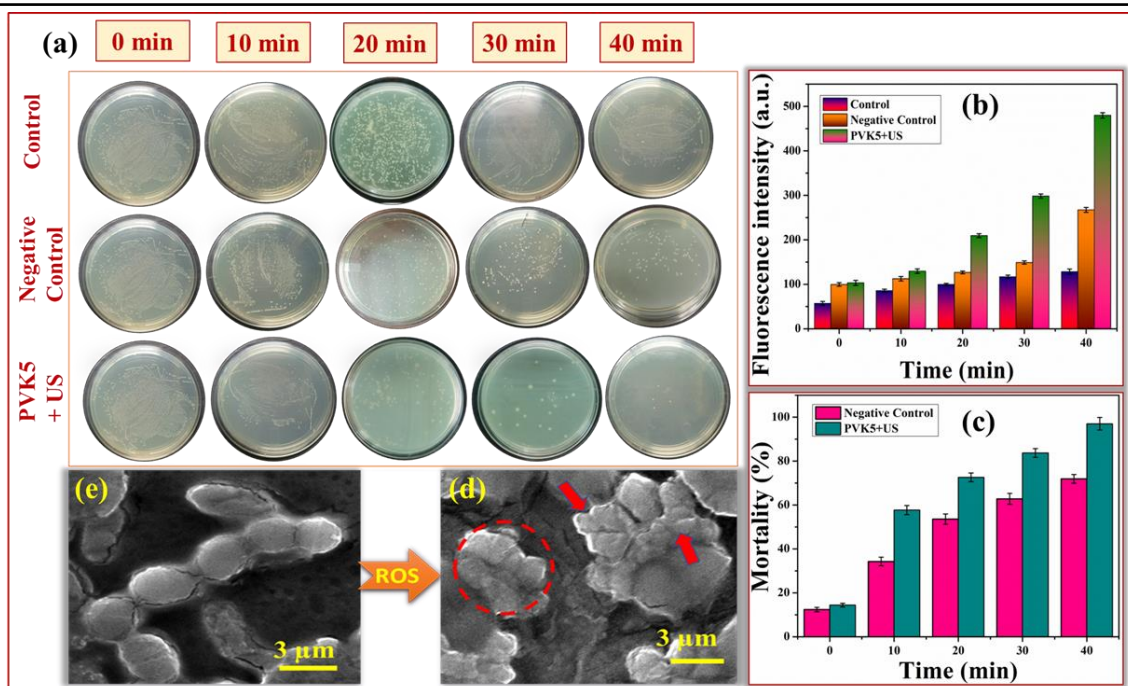


Figure 5.14. (a) Photographs representing surviving *E. faecalis* colonies on the solid agar plates (after 24 of incubation); (b,c) Illustrates the amount of ROS generation and mortality percentage of *E. faecalis* as calculated using colony counting technique (d, e) FE-SEM images.

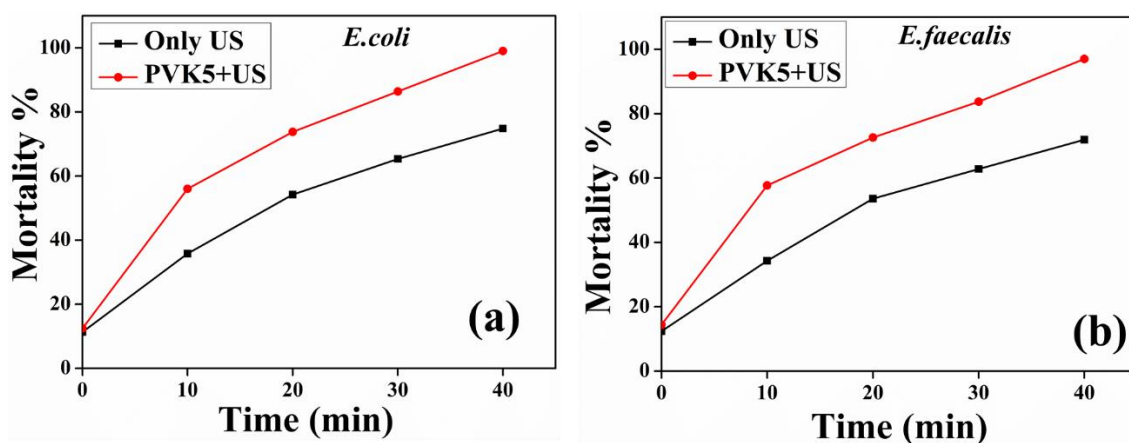


Figure 5.15. Time-dependent kinetic study of bacterial degradation by PVK5 membrane and only US

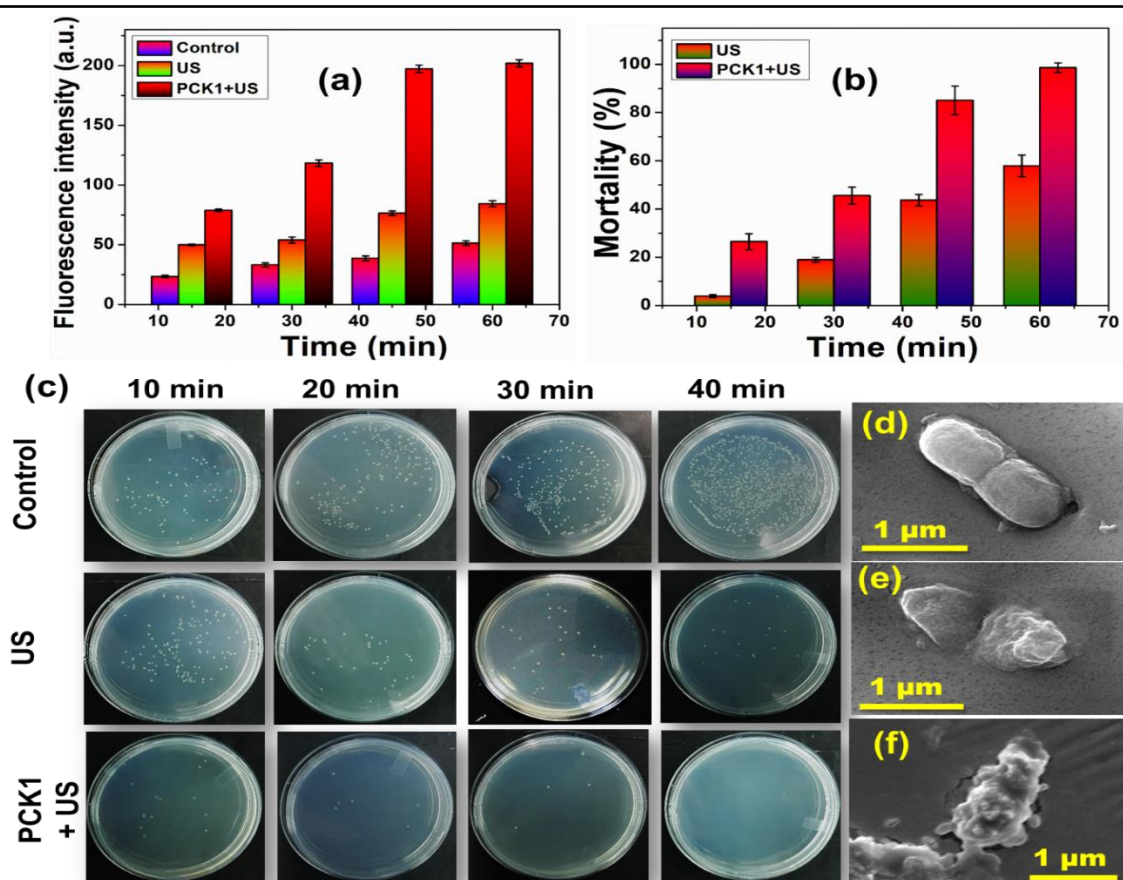


Figure 5.16. (a) Investigation of bacterial ROS with increasing time, (b) MWCNT-kaolinite-PVDF nanocomposite assisted mortality percentage of pathogenic bacteria under ultrasound, (c) agar plate data for investigating bacterial decomposition with time, (e), (f), (g) FESEM images of healthy, ultrasound-assisted *E. coli*, and PCK1 and ultrasound-based degraded *E. coli*.

Moreover, the recyclability test of the membranes has been investigated up to 4 cycles and found negligible efficiency loss suggesting the applicability of the membrane for multiple uses (Figure 5.17 a-d). The statistical validation of bacterial eradication data has been investigated with a one-way ANOVA test for membranes by the GraphPad Prism 9 software package. The statistical significance value (p-value) has been found

0.0001 for PVK5 and 0.0002 for PCK1 with a significant R^2 value of 0.9995 and 0.9989 respectively which suggests the statistical correctness of the data (Figure 5.17 e, f).

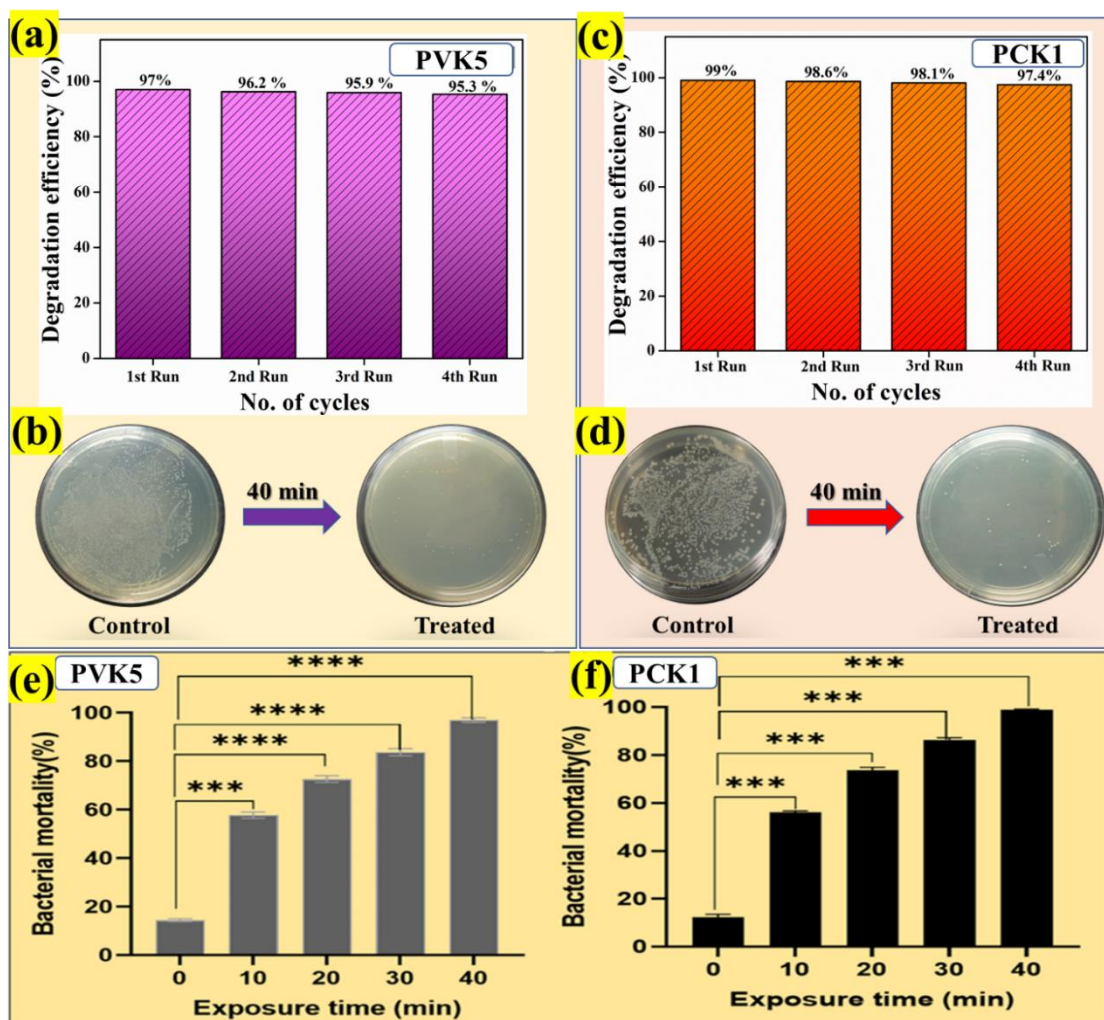


Figure 5.17. (a, b) Recyclability test of PVK5 membrane for *E. coli* bacteria, (c, d) Recyclability test of PCK1 membrane for *E. coli* bacteria, e, f) one-way ANOVA test for PVK5 and PCK1 respectively for *E. coli* bacteria degradation.

Moreover, the hemolysis rate was less than 2 % among the experimental groups of samples. The hemolysis rate was only 0.13 % at PCK1, whereas the kaolinite NPs, PVK0/PCK0, and PVK5 were respectively 1.6 %, 1.1 %, and 0.39 %, which were far less than the 5 % allowed limit (Figure 5.18). Hence, the nanocomposites membranes

(PVK5/PCK1) are considered as biocompatible membranes which can be further used for in vivo experiments as these have no such toxicity effect in cells [38].

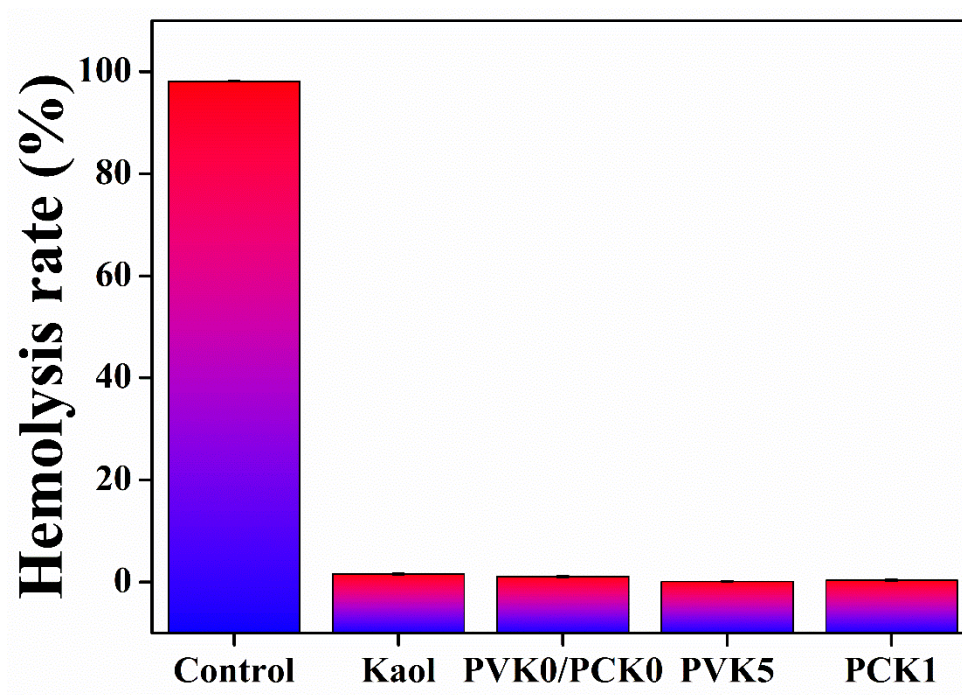


Figure 5.18: Biocompatibility of the nanocomposite membranes via hemolysis assay.

5.4 Summary

In this chapter, the surface-modified naturally formed kaolinite nano clay and 1 % MWCNT doped clay have been incorporated into the PVDF-HFP polymer matrix for the successful preparation of self-poled polymeric piezocatalyst. The fabricated natural clay-based free-standing nanocomposite membranes show promising piezo-responsive properties. This piezo-response has been confirmed by the XRD, FTIR, dielectric, P-E loop, and d_{33} measurements along with theoretical density functional calculation. It has been found that the 5 % activated clay and 1 % MWCNT doped clay incorporated PVDF polymeric membranes show maximum piezo-response. The PCK1 nanocomposite membrane shows the highest piezo-responsive efficiency and generates promising piezo voltage with a power of 50 W/m^2 by the non-invasive waste-water

flow-mediated mechanical stimuli. These highly piezoresponsive membranes have been used further to decompose carcinogenic RhB dye [79 % (PVK5) and 96 % (PCK1) in 1h], Gram-negative (*E. coli*) [99 % (PVK5) and 100 % (PCK1) in 40 min] and Gram-positive [*E. faecalis*, 97 % (PVK5)] coliform bacteria, and found promising degradation efficacy only in 40 min of soft ultrasound. The reactive oxygen species-mediated bacterial degradation mechanism has been investigated further and found OH^{*} radical generation under soft ultrasound. The FESEM study was also performed to investigate the cell death of bacteria and found the ruptured cell wall confirms the bacterial death. It has been found that the 1 % MWCNT doped clay-based polymeric membrane shows maximum piezo effectiveness both in energy generation and wastewater remediation. This highly piezoresponsive eco-friendly, low-cost, natural clay-based nanocomposite membrane can be produced on a mass scale to get rid of water-borne diseases and energy deficiency if properly improvised.

References

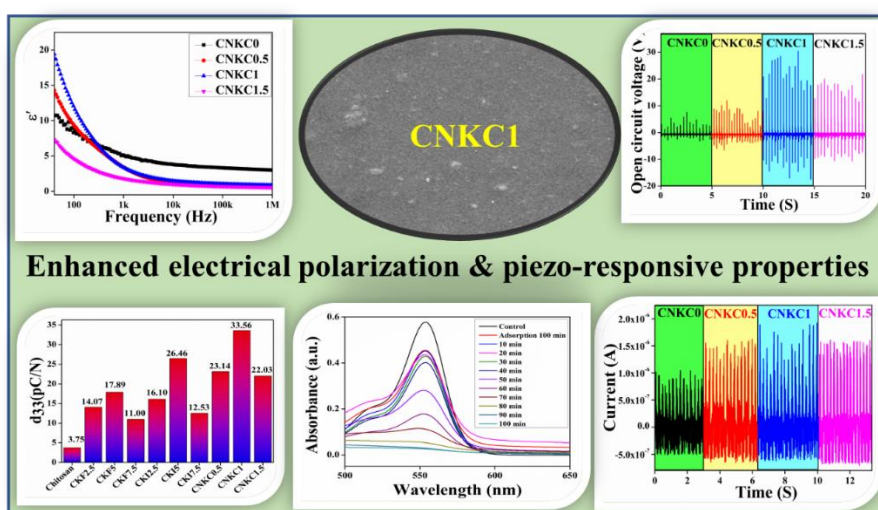
- [1] Guo, Wei, Jing Chang, Shuo Wang, Qingxia Liu, and Haijun Zhang. *Colloids and Surfaces A: Physicochemical and Engineering Aspects* 664 (2023): 131200.
- [2] Guselnikova, Olga, Roman Elashnikov, Pavel Postnikov, Vaclav Svorcik, and Oleksiy Lyutakov. *ACS applied materials & interfaces* 10, no. 43 (2018): 37461-37469.
- [3] Mondal, Dhananjay, Neelanjana Bag, Jhilik Roy, Saheli Ghosh, Shubham Roy, Monisha Sarkar, Souravi Bardhan, Soumyaditya Sutradhar, and Sukhen Das. *Langmuir* (2024).
- [4] Zhu, Zixin, Xue Gou, Laiyi Liu, Tian Xia, Jiayi Wang, Yimeng Zhang, Chenjun Huang et al. *Acta Biomaterialia* 157 (2023): 566-577.
- [5] Jariwala, Tanvi, Gerardo Ico, Youyi Tai, Honghyun Park, Nosang V. Myung, and Jin Nam. *ACS applied bio materials* 4, no. 4 (2021): 3706-3715.
- [6] Al-Shabib, Nasser A., Fohad Mabood Husain, Faheem Ahmed, Rais Ahmad Khan, Mohammad Shavez Khan, Firoz Ahmad Ansari, Mohammad Zubair Alam et al. *Frontiers in microbiology* 9 (2018): 373259.

- [7] MP, Ajith, Sonali Pardhiya, and Paulraj Rajamani. *Small* 18, no. 15 (2022): 2105579.
- [8] Yan, Jing, Min Liu, Young Gyu Jeong, Weimin Kang, Lan Li, Yixia Zhao, Nanping Deng, Bowen Cheng, and Guang Yang. *Nano energy* 56 (2019): 662-692.
- [9] Maiti, Sandip, Sumanta Kumar Karan, Jin Kon Kim, and Bhanu Bhusan Khatua. *Advanced Energy Materials* 9, no. 9 (2019): 1803027.
- [10] Amadou, Issifou, Michel-Pierre Faucon, and David Houben. *Applied Geochemistry* 143 (2022): 105378.
- [11] Maity, Anupam, Subha Samanta, Debasish Biswas, and Dipankar Chakravorty. *Journal of Alloys and Compounds* 887 (2021): 161447.
- [12] Kassa, Adamu Esubalew, Nurelegne Tefera Shibeshi, and Belachew Zegale Tizazu. *Journal of Thermal Analysis and Calorimetry* 147, no. 22 (2022): 12837-12853.
- [13] Oliot, Manon, Sylvain Galier, Hélène Roux de Balmann, and Alain Bergel. *Applied Energy* 183 (2016): 1682-1704.
- [14] Peng, Hao, Vatsal Shah, and K. Li. *Journal of Membrane Science* 641 (2022): 119857.
- [15] Yamashita, Toru, and Peter Hayes. *Applied surface science* 254, no. 8 (2008): 2441-2449.
- [16] Muzyka, Roksana, Monika Kwoka, Łukasz Smęadowski, Noel Díez, and Grażyna Gryglewicz. *New Carbon Materials* 32, no. 1 (2017): 15-20.
- [17] Li, Li, Mingqiu Zhang, Minzhi Rong, and Wenhong Ruan. *Rsc Advances* 4, no. 8 (2014): 3938-3943.
- [18] Fernandes, Margarida M., Pedro Martins, Daniela M. Correia, Estela O. Carvalho, Francisco M. Gama, Manuel Vazquez, Cristina Bran, and Senentxu Lanceros-Mendez. *ACS Applied Bio Materials* 4, no. 1 (2021): 559-570.
- [19] Fu, Yijun, Yue Cheng, Chi Chen, Dawei Li, and Wei Zhang. *Polymer Testing* 108 (2022): 107513.
- [20] Das, Namrata, Debmalya Sarkar, Md Minarul Saikh, Prosenjit Biswas, Sukhen Das, Nur Amin Hoque, and Partha Pratim Ray. *Nano Energy* 102 (2022): 107628.

- [21] Huang, Gang, Junxi He, Xia Zhang, Manman Feng, Yan Tan, Chuncheng Lv, Hao Huang, and Zhao Jin. *Construction and Building Materials* 273 (2021): 121582.
- [22] Chen, Min, Yongping Pu, Lei Zhang, Yu Shi, Fangping Zhuo, Qianwen Zhang, Run Li, and Xinyi Du. *Ceramics International* 47, no. 15 (2021): 21303-21309.
- [23] Han, Mengjiao, Cong Wang, Kangdi Niu, Qishuo Yang, Chuanshou Wang, Xi Zhang, Junfeng Dai et al. *Nature Communications* 13, no. 1 (2022): 5903.
- [24] Samet, Mariem, Ali Kallel, and Anatoli Serghei. *Journal of Composite Materials* 56, no. 20 (2022): 3197-3217.
- [25] Zaki, M. F., A. Tayel, and A. B. El Basaty. *Bulletin of Materials Science* 45, no. 4 (2022): 236.
- [26] Wang, Lu, He Qi, Shiqing Deng, Lingzhi Cao, Hui Liu, Shuxian Hu, and Jun Chen. *InfoMat* 5, no. 1 (2023): e12362.
- [27] Huang, Yanfei, Guanchun Rui, Qiong Li, Elshad Allahyarov, Ruipeng Li, Masafumi Fukuto, Gan-Ji Zhong et al. *Nature communications* 12, no. 1 (2021): 675.
- [28] Liang, Haitong, Guangbo Hao, and Oskar Z. Olszewski. *Sensors and Actuators A: Physical* 331 (2021): 112743.
- [29] Do Hong, Seong, Kyung-Bum Kim, Wonseop Hwang, Yoo Seob Song, Jae Yong Cho, Se Yeong Jeong, Jung Hwan Ahn, Gi-Hoon Kim, Haimoon Cheong, and Tae Hyun Sung. *Energy conversion and management* 215 (2020): 112900.
- [30] Hu, Xiaosong. *Automotive Innovation* 5, no. 2 (2022): 105-106.
- [31] Tu, Shuchen, Yuxi Guo, Yihe Zhang, Cheng Hu, Tierui Zhang, Tianyi Ma, and Hongwei Huang. *Advanced Functional Materials* 30, no. 48 (2020): 2005158.
- [32] Ye, Li, Jiacheng Li, Xiaolei Li, Pengcheng Zhu, Tianxing Wang, Yao Zhong, Dingyu Song, and Lin Zhuang. *ACS Applied Nano Materials* 6, no. 23 (2023): 21695-21706.
- [33] Tiwari, Neha, Deenan Santhiya, and Jai Gopal Sharma. *Environmental Pollution* 265 (2020): 115044.

- [34] Sharma, Kirti, Anita Sudhaik, Pankaj Raizada, Pankaj Thakur, Xuan Minh Pham, Quyet Van Le, Van-Huy Nguyen, Tansir Ahamad, Sourbh Thakur, and Pardeep Singh. *Environmental Science and Pollution Research* 30, no. 60 (2023): 124902-124920.
- [35] Bardhan, Souravi, Kunal Pal, Shubham Roy, Solanky Das, Abhijit Chakraborty, Parimal Karmakar, Ruma Basu, and Sukhen Das. *Journal of nanoscience and nanotechnology* 19, no. 11 (2019): 7112-7122.
- [36] Wang, Kai, Manqi Zhang, Degang Li, Lihong Liu, Zongping Shao, Xinyong Li, Hamidreza Arandiyani, and Shaomin Liu. *Nano Energy* 98 (2022): 107251.
- [37] Li, Zhifang, Chunmei Wang, Chen Dai, Ruizhi Hu, Li Ding, Wei Feng, Hui Huang, Yin Wang, Jianwen Bai, and Yu Chen. *Biomaterials* 287 (2022): 121668.
- [38] Deng, Haotian, Bo Xue, Mingyue Wang, Yuqi Tong, Chang Tan, Meizhi Wan, Yanwen Kong, Xianjun Meng, and Jinyan Zhu. *Journal of Agricultural and Food Chemistry* 70, no. 26 (2022): 8032-8042.

Chapter 6



Development of Chitosan Biopolymeric Membranes-based Piezocatalyst and Energy Harvester by Incorporating Structurally Modulated & 1% MWCNT-doped Kaolinite Clay Nanoparticles

Chapter 6

Development of Chitosan Biopolymeric Membranes-based Piezocatalyst and Energy Harvester by Incorporating Structurally Modulated & 1% MWCNT-doped Kaolinite Clay Nanoparticles.

6.1 Introduction

In Chapter 3 it has been found that the surface functionalized nano kaolinite and intercalated kaolinite show promising physicochemical properties. Inspiring from their promising surface property correlation this work demonstrated piezo-responsive biopolymeric composites which have been fabricated by incorporating functional and intercalated kaolinite in the chitosan polymer matrix [1]. In reality, Chitosan (CS) is made from the deacetylation of chitin, which is widely found in nature [2]. Owing to its excellent properties and biocompatibility over synthetic polymers, CS has been widely used in water treatment, biomedical purposes, and non-invasive energy generation by fabricating nanoparticle-modulated devices [3]. In reality, the intrinsic polarization and piezoelectric performances of pristine chitosan are very low ($d_{33} < 5$ pC/N) but the modification by incorporation of different high surface properties nanomaterials into its interior can enhance its polarization and piezoelectric performances [4]. Recently scientists have been focussing on the tunability of piezo-tribo coupling performances of CS by incorporating several nanomaterials but catalytic performances of CS-based polymeric membranes are in their infancy [5]. Keeping in mind the versatility of this bio-polymer, in this chapter a biopolymeric membrane modified by naturally found kaolinite clay and its modified counterparts by 1D MWCNT incorporation to enhance the functionality of the clay has been developed for simultaneous wastewater degradation and energy generation without harming the environment. The d_{33} value has been enhanced up to 33.56 pC/N by incorporating functional clays into the biopolymeric matrix. This multifunctional biocompatible, natural membrane can generate a new avenue for water technology and a non-invasive energy source for scientists and technologists if properly improvised.

6.2 Experimental Details

6.2.1 Materials

Naturally found bulk kaolinite clay was purchased from Hindustan Minerals, India, and activated and intercalated which is depicted in Chapter 3. Hydrochloric acid, nitric acid, acetic acid, Hexamine, dimethyl sulfoxide (DMSO), 2', 7'-Dichlorodihydrofluorescein diacetate (DCFDA), MWCNT, and hydrogen peroxide were purchased from Sigma Aldrich, Germany. Phosphate buffer saline (PBS) and LB broth were purchased from HiMedia Pvt. Ltd., India. Rhodamine B and Congo red organic dyes were purchased from Sigma Aldrich, Germany. *E.coli* bacteria having MTCC no-1652 were obtained from the Institute of Microbial Technology, Chandigarh, India. HPLC-graded ethanol and acetone were purchased from Merck, Germany. No further purification has not done with the purchased chemicals. Millipore water was used throughout the whole experiment which has a resistivity of about 18.2 MΩ cm.

6.2.2 Synthesis of modified-kaolinite and chitosan nanocomposite membranes

As synthesized functionalized, intercalated, and 1 % MWCNT doped kaolinite nanoparticles (chapter 3) were further incorporated into chitosan biopolymer to find bio-nanocomposite membranes. In this experiment at first 50 ml 1M acetic acid was taken and heated at 50°C. After that 0.5 gm of chitosan powder was added to find a homogeneous gel-like solution. When the homogeneous solution was obtained the functionalized and intercalated kaolinite powder was added to the solution maintaining the w/w mass ratio of 2.5 %, 5 %, and 7.5 %. Whereas, 1 % MWCNT doped clay has been incorporated by the mass ratio of 0.5 %, 1 %, and 1.5 %.

Table 6.1. Synthesisez bio-nanocomposites membranes and their codes

Sample Specifications	Sample Codes
Pure chitosan membrane	CKF0, CKI0, CNKC0
Activated kaolinite doped chitosan membranes (2.5%, 5%, 7.5%: Wt/Wt-ratio)	CKF2.5, CKF5, CKF7.5

Intercalated kaolinite doped chitosan membranes (2.5%, 5%, 7.5%: Wt/Wt-ratio)	CKI2.5, CKI5, CKI7.5
1% MWCNT incorporated kaolinite doped chitosan membranes (0.5%, 1%, 1.5%: Wt/Wt-ratio)	CNKC0.5, CNKC1, CNKC1.5

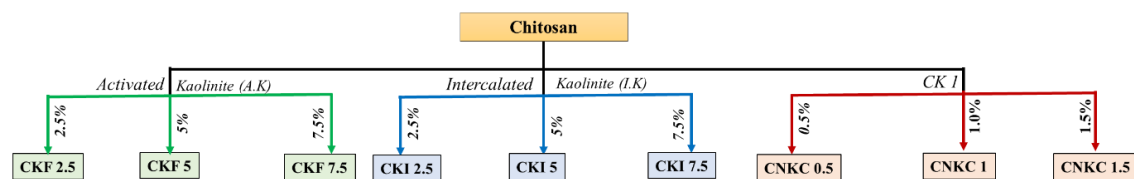


Figure 6.1. Synthesis protocol of nanocomposite membranes

The solutions were then stirred overnight to find the gel-like nanocomposites. On the next day, the homogeneous solutions were taken in separate clean plastic petri dishes and dried at 50°C in a dust-free hot air oven for 6h. The dried flexible, free-standing membranes were then marked as CKF2.5, CKF5, and CKF7.5 for the functionalized kaolinite nanoparticle-incorporated membranes whereas the intercalated nanoparticle incorporated membranes were marked as CKI2.5, CKI5, and CKI7.5. On the other hand, the 1 % MWCNT-doped kaolinite incorporated bio-nanocomposite membranes were marked as CNKC0.5, CNKC1, and CNKC1.5. A pristine chitosan film was also prepared by the same procedure without adding any nanoparticles to it and marked as CKF0/CKI0/CNKC0 for the respective sets (Table 6.1, Figure 6.1).

6.3 Result and Discussion

6.3.1 Determination of the physicochemical features of the bio-polymeric membranes

The functionalized, intercalated, and 1 % MWCNT-doped kaolinite incorporated chitosan nanocomposite membrane's XRD patterns are depicted in Figure 6.2. It has been found that the peaks of bare chitosan corresponding to the hkl planes 020 and 110

are decreasing with increasing concentration of the clay nanoparticles in its matrix. These decrements of diffraction maxima happened due to both the molecular level formation of the -H bond and the steric effect in the clay and polymeric interface by the ordered packing of the polymeric chain [6].

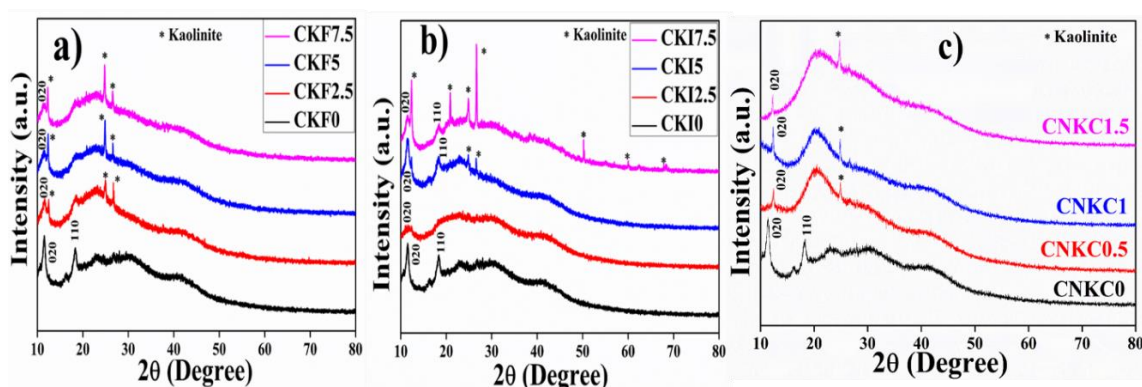


Figure 6.2. XRD of a) Functionalized-kaolinite, b) Intercalated kaolinite, and c) 1%-MWCNT loaded kaolinite doped chitosan bio-polymeric membranes.

It also has been found the diffraction maximum of kaolinite NPs is absent in pristine chitosan and increases with the incorporation percentage increase depicted by the star marks in the diffraction graph [7]. These results suggest the successful incorporation of the nano-clay into the bio-polymeric matrix and the formation of an ordered polymeric interface between NPs and chitosan.

The morphologies of fabricated biopolymeric nanocomposite membranes depicted in Figure 6.3 are observed by the FESEM. It has been found that a smooth surface morphology was observed in pristine chitosan which became rough with the incorporation of kaolinite clay and its modified counterparts and found a homogeneous surface morphology up to CKF5 and CKI5 with clay NPs in the polymeric matrix. The over-doping in the case of CKF7.5 (Figure 5.2d) and CKI7.5 (Figure 5.2g) has been observed and the NPs are exposed to the polymeric surfaces which validated the maximum incorporation limit of up to 5 % (wt/wt). Moreover, in the case of MWCNT-doped chitosan, the biopolymeric membranes (CNKC) surface is almost homogeneous due to low doping concentration (Figure 5.2h-j).

Besides structural and morphological investigations elemental compositional studies of the nanocomposite membranes have been investigated by the EDAX and mapping techniques and depicted in Figure 6.4. In Figure 6.4 the EDAX spectra of the CKF5 (a,b), CKI5 (c,d), and CNKC1 (e,f) represent the incorporation of intercalated clay NPs into the polymeric matrix in the proper stoichiometric ratio which suggests the successful incorporation of the clay and its modified NPs into the biopolymeric matrix.

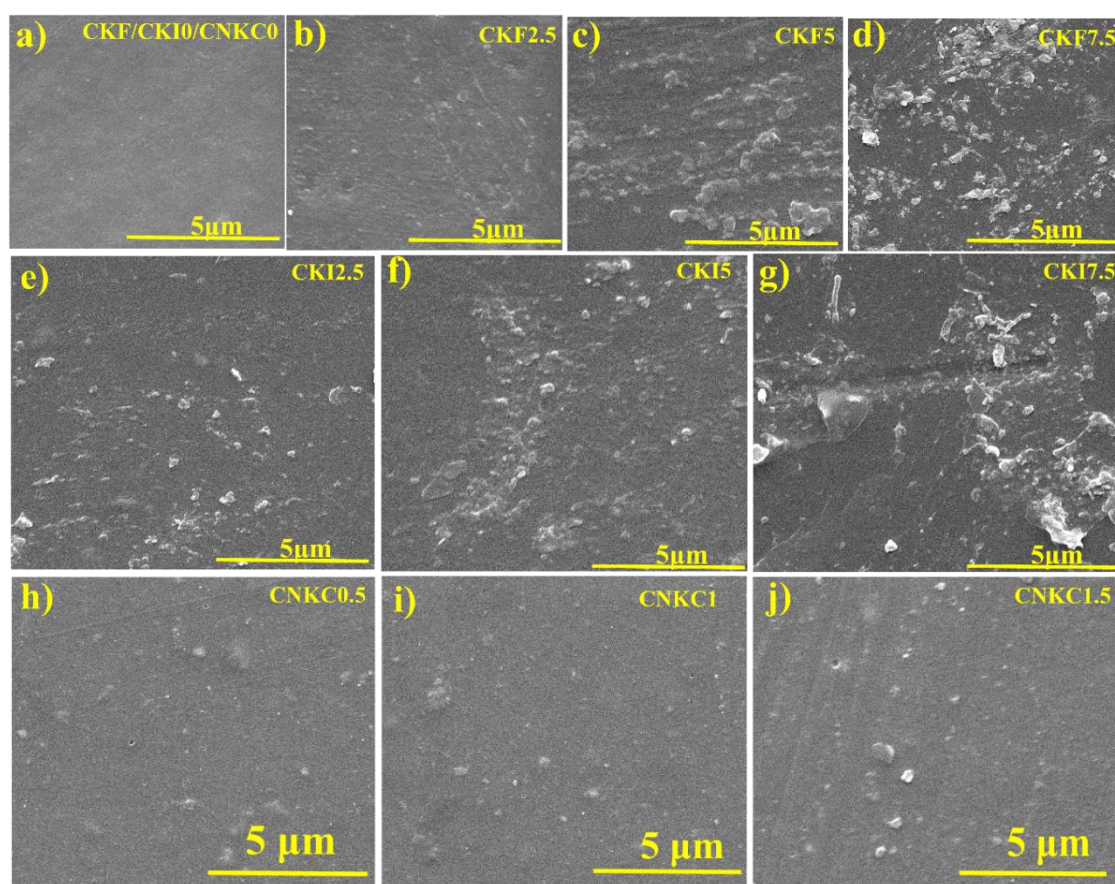


Figure 6.3. FESEM micrographs of a) bare chitosan, b-d) functionalized kaolinite doped chitosan, e-g) Intercalated kaolinite doped chitosan, and h-j) 1%-MWCNT doped kaolinite incorporated chitosan membranes.

Additionally, the homogeneous elemental spreading in mapping data of CKI5 and CNKC1 also suggests successful polymeric membrane fabrication. It has been found that the Al, Si, and O contents are lower in the case of CNKC1 than CKI5 (Figure 6.5)

which validated the lower incorporation percentage and is analogous to the EDAX data in Figure 6.4. The XRD and FESEM data suggest the successful fabrication of the NPs incorporated biopolymeric membranes.

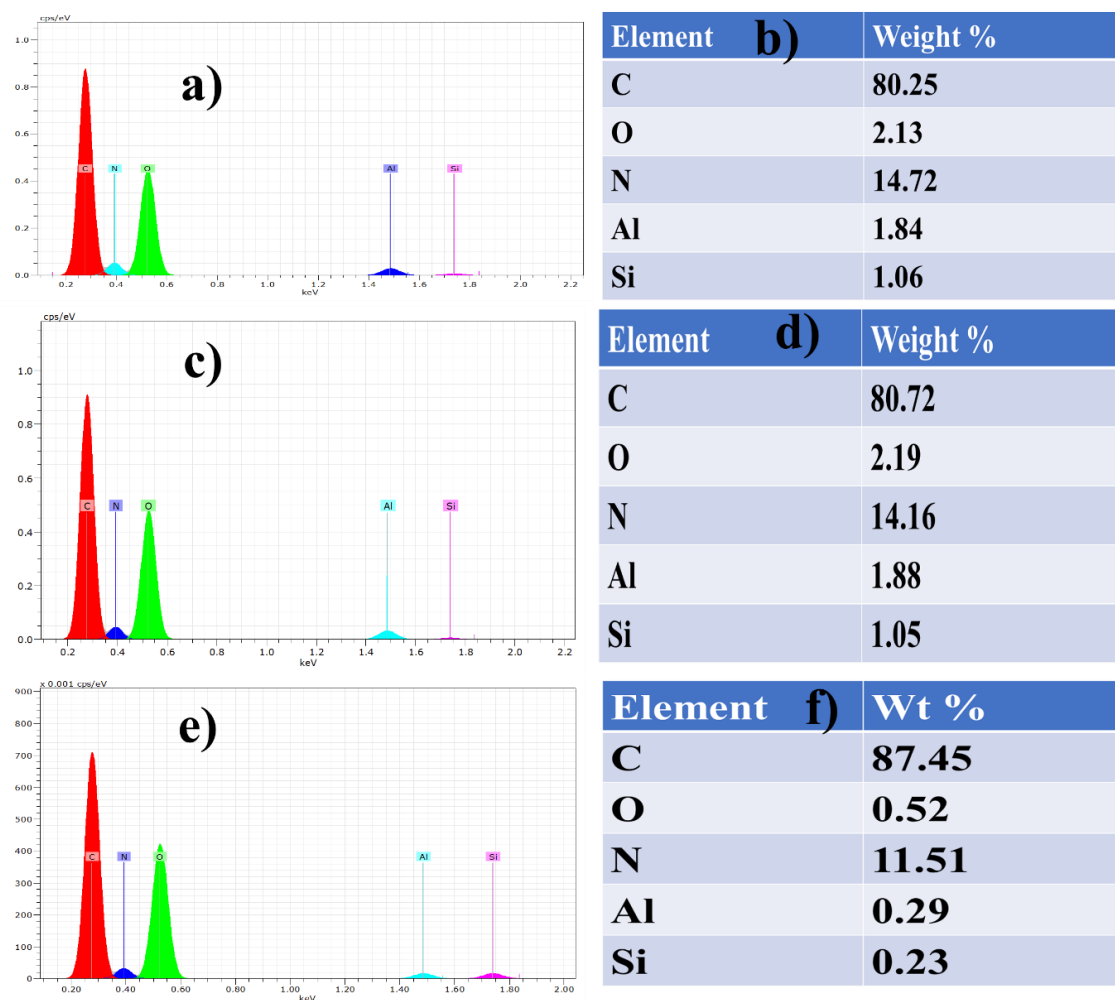


Figure 6.4. EDAX spectra and elemental tables of a, b) CKF5, c, d) CKI5, and e, f) CNKCI

The bonding networks of the fabricated membranes were investigated by FTIR in the region of 500-4000 cm^{-1} and depicted in Figure 5.6. Figure 5.6 suggests almost the same vibrational spectra for CKF (5.5 a) and CKI (5.5 b) nanocomposites. The intense vibrational bands correspond to chitosan biopolymer at 1010 and 1065 cm^{-1} due to 5'-OH and 3'-OH respectively. The vibrational bands at 1157, 1313 and 1396 cm^{-1} are

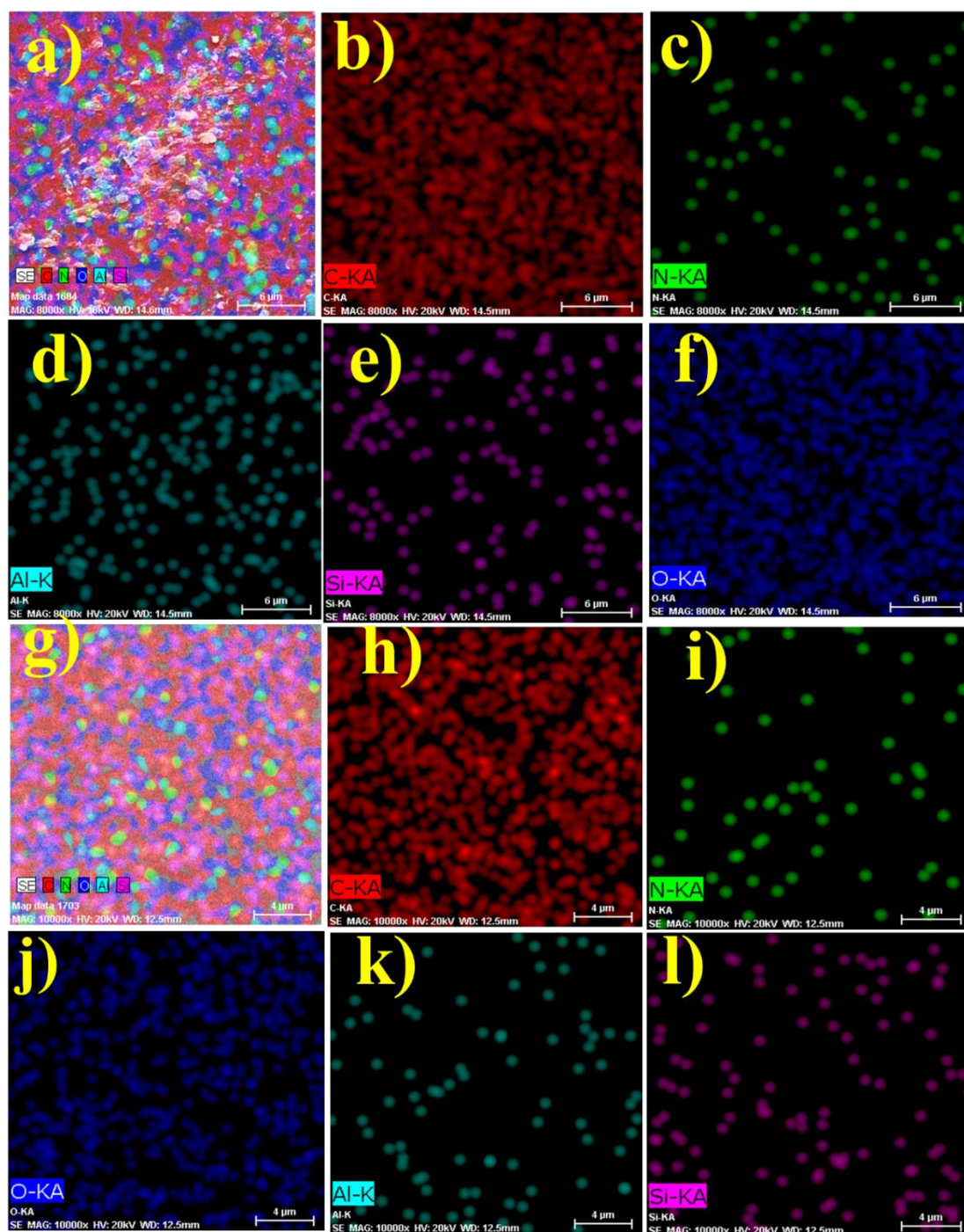


Figure 6.5. Elemental mapping of a-f) CKI5, and g-l) CNKC1 nanocomposite membranes suggest the proper stoichiometric incorporation of clay into the biopolymeric matrix.

respectively for the C-O-C, C-N, and -CH₂ asymmetric vibrations [6, 8]. Whereas the bands at 1543 and 1635 cm⁻¹ are attributed to the -NH₂ bending and NH stretching vibrations. The absorption bands at higher wave numbers at 2904 cm⁻¹ arose due to asymmetric stretching of the -CH bond whereas the band at 3694 cm⁻¹ was observed for -NH and -OH symmetric stretching [8]. Besides these vibrational bands of chitosan, intense vibrations occurred at 540, 760 and 913 cm⁻¹ in CKF5 and CKI5 which are increasing with the increasing percentage of kaolinite nanoparticles into the biopolymeric matrix. These absorption bands correspond to the Si-O-Si, AlO₆, and Si-O respectively [9]. This type of increment in vibrational bands suggests the successful incorporation of clay NPs in the biopolymeric matrix. Moreover, in the case of CNKC samples, the percentage doping of NPs in the polymeric matrix is lower, as a result, the peaks corresponding to the kaolinite which are present in CKF and CKI membranes are not intense (Figure 6.7 c). In summary, all the conventional characterization techniques suggest the successful fabrication of clay NPs incorporated bio-polymeric nanocomposite membranes.

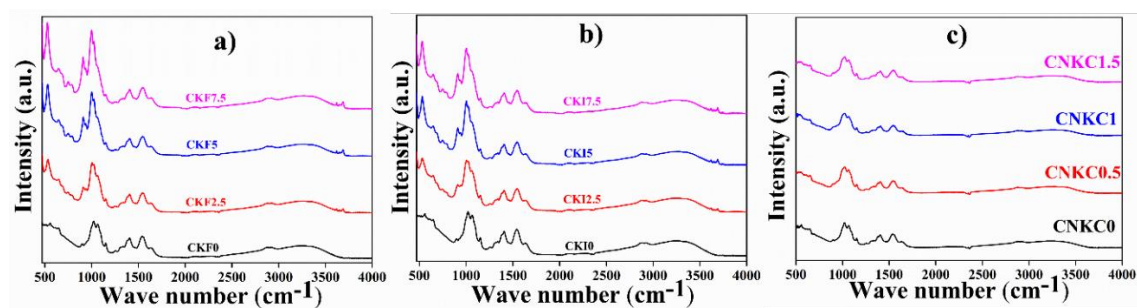


Figure 6.6. FTIR spectra of a) functionalized, b) intercalated, and c) 1% MWCNT-doped kaolinite incorporated nanocomposite membranes

6.3.2 Electrical and piezoelectric properties of the bio-nanocomposites

The polarization and storage efficiency of the nanocomposite membranes reflect on their real part of permittivity values and imaginary parts are associated with the loss factor which has been illustrated in previous chapters. The polarization is directly associated with the piezoelectric effectiveness of any nanocomposite matrix [10,11]. Thus, the permittivity values of the biopolymeric nanocomposite membranes have been

calculated by equation 1.4 and produced in Table 6.2 and Figure 6.7. It has been found that the dielectric constant increases with increasing concentration of clay and accrued a maximum value at 5 % doping in both functionalized and intercalated kaolinite although the rate of increment of D.C is higher in the case of intercalated kaolinite incorporation. This result may arise due to the maximum surface area in intercalated kaolinite by separating the layer which creates more Maxwell Wagner Interfacial polarization and enhances the polarization properties [12,13].

Table 6.2. Dielectric constants of the membranes

Sample Codes	Dielectric Constants (ϵ' at 40 Hz)
CKF0/CKI0/CNKC0	10.7
CKF2.5	12.3
CKF5	16.0
CKF7.5	11.3
CKI2.5	15.5
CKI5	18.7
CKI7.5	16.9
CNKC0.5	14.3
CNKC1	19.5
CNKC1.5	7.5

Moreover, the lower doping concentration of 1 % MWCNT incorporated kaolinite enhanced the dielectric constant more than the greater incorporation of clays and accrued maximum D.C in the sample CNKC1 (19.5) may be happened for the maximum surface properties of 1 % MWCNT doped clay (i.e. surface charge, surface area in Chapter 3). It has also been found that after a certain limit of

incorporation, D.C quenched (CKF7.5, CKI7.5, and CNKC1.5) which may result due to the dis-alignment of extra nanofillers due to increment of extra surfaces and agglomeration in the polymeric matrix.

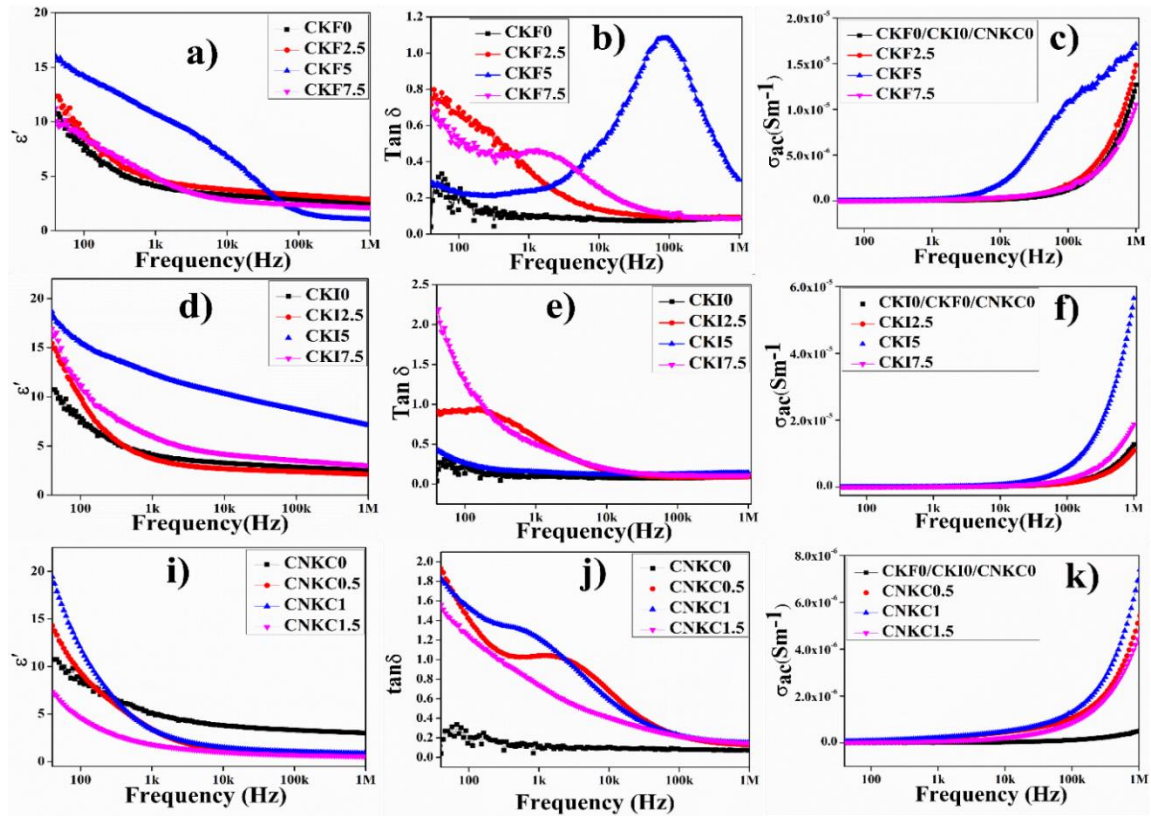


Figure 6.7. Electrical properties of the membranes: a, d, i) Dielectric constants, b, e, j) tangent losses, and c, f, k) AC conductivities

Moreover, the AC conductivity calculated by equation 1.5 also changed and found that in the case of CNKC membranes, it is lower (Figure 6.7 k) than clay-incorporated nanocomposites which validated the maximum polarization in CNKC1. The dissipation factor is low in all the cases (Figure 6.7 b, e, j). This type of electrical properties enhancement suggests that the CKF5, CKI5, and CNKC1 pose maximum polarization properties in the case of functionalized, intercalated, and MWCNT-doped clay-incorporated chitosan and makes these membranes suitable for piezo-responsive applications.

Table 6.3. Piezoelectric effectiveness i.e. piezoelectric voltages, short-circuit currents, and piezoelectric coefficients d_{33} of the nanocomposite membranes

Sample Codes	Piezoelectric Voltages (V)	Piezoelectric Currents (μ A)	Piezoelectric Coefficients (d_{33})
CKF0/CKI0/CNKC0	6.4	0.9	3.75
CKF2.5	9.9	-	14.07
CKF5	16.4	-	17.89
CKF7.5	10.9	-	11.00
CKI2.5	12.6	1.2	16.10
CKI5	25.7	1.7	26.46
CKI7.5	19.8	1.4	12.53
CNKC0.5	11.5	1.5	23.14
CNKC1	30.5	1.9	33.56
CNKC1.5	18.2	1.6	22.03

The piezoelectric open-circuit voltages and short-circuit currents have been measured for all the bio-nanocomposites and depicted in Table 6.3 and Figure 6.8. It has been found that the piezoelectric voltages and currents also vary in the same way as D.C and found maximum voltage and current for CKI5 (25.7 V, 1.7 μ A), CKF5 shows 16.4 V whereas, in CNKC1 the voltages and current are 30.51 V, 1.9 μ A. The piezoelectric coefficients for all the nanocomposite membranes have also been measured depicted in Figure 6.8 f. It has been found that the low piezoelectric constant (d_{33}) for pure chitosan (3.75 pC/N) increases with the % doping of clay NPs and is found maximum in CKF5 (17.89 pC/N), CKI5(26.46 pC/N), and CNKC1 (33.56 pC/N). This experimental evidence proves that CKF5 is most piezo-active from functionalized clay-incorporated membranes and CKI5 is most piezo-active from intercalated clay-incorporated nanocomposites whereas, CNKC1 poses maximum piezo-response from MWCNT-doped clay incorporated bio-nanocomposites and it also poses maximum than other two

groups. Thus, these three membranes have been further used for wastewater treatment by piezocatalysis technique.

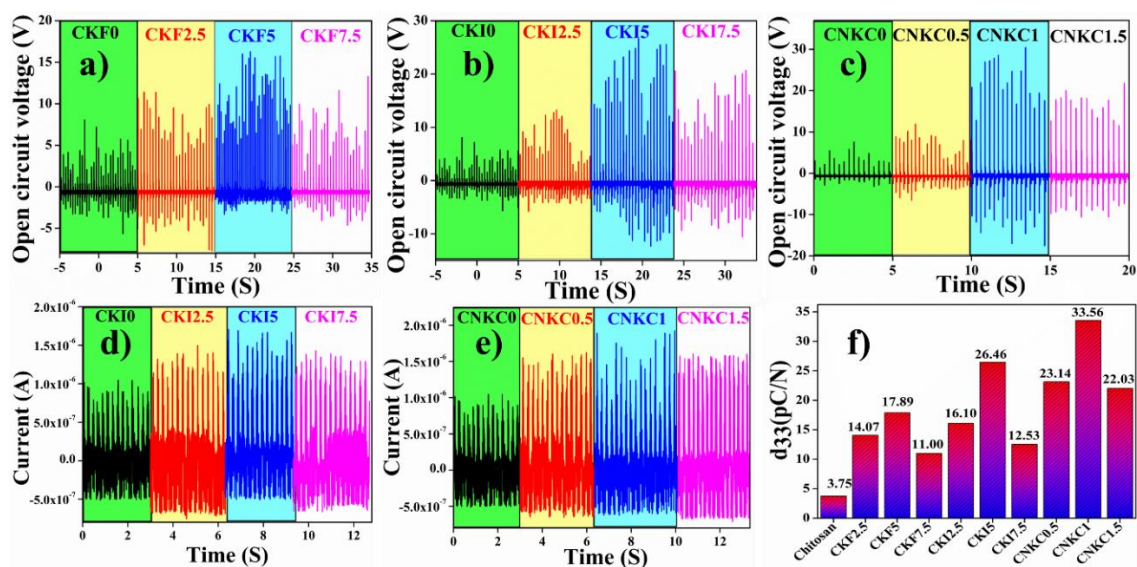


Figure 6.8. Piezoelectric open-circuit voltages a) functionalized, b) intercalated, and c) 1% MWCNT doped kaolinite incorporated membranes. Short-circuit currents d) intercalated and e) 1% MWCNT-doped clay-based membranes. f) piezoelectric coefficients

6.3.3 Degradation of organic dyes

In the previous sections, it has been found that CKF5, CKI5, and CNKC1 show the highest D.C, AC conductivity, piezoelectric voltage, piezoelectric current, and piezo-coefficient (d_{33}) from the activated, intercalated, and 1 % MWCNT-doped clay incorporated chitosan matrix respectively. Thus, these three samples have been adopted to degrade organic contaminants from wastewater. Herein, RhB and Congo-red dyes have been degraded by the typical piezocatalysis experiment described in Chapter 1 Section 1.10.6. It has been observed that the characteristic peaks of RhB (554 nm) and Congo-red (496 nm) reduce with time in UV-vis data and a visual colour change is also observed in the naked eye. The degradation kinetics of the RhB (Figure 6.9: a, d, g) and Congo-red by (Figure 6.9: b, e, h) CKF5, CKI5, and CNKC1 have been depicted in Figure 6.9. The percentage piezo degradation efficiencies η have been calculated by the

relation 1.13. It has been found that CKF5 degraded 65 % RhB and 59 % Congo-red, CKI5 degraded 96 % RhB and 88 % Congo-red whereas CNKC1 degraded 97 % RhB and 89 % CR, in 100 min of ultrasound impulse (33 KHz, 50 W). To evaluate the degradation happening due to piezocatalysis a control set of dyes was also degraded by only ultrasound and found an efficiency of only 11 % for RhB and 13 % for Congo-red. These high degradation percentages of the CKI5 and CNKC1 catalysts suggest the non-toxic, cost-effective fabricated bio-nanocomposite membranes may be used in mass-scale wastewater remediation technology.

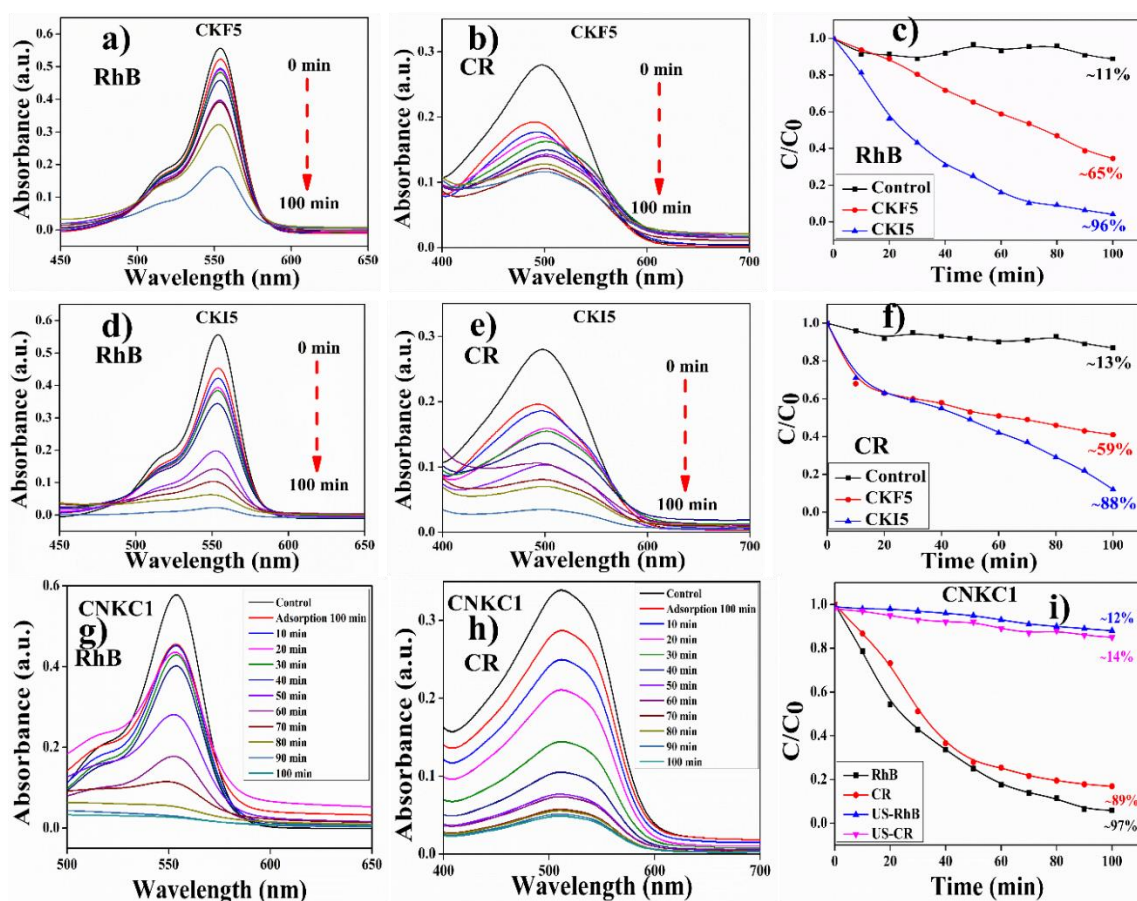


Figure 6.9. Degradation of RhB (a, d, g), Congo red (b, e, h) for CKF5, CKI5, and CNKC1. C, f, i) C/C₀ graph of degradations.

The piezocatalytic degradation mechanism of the membrane has been illustrated in Chapter 1 Section 1.6. To evaluate the piezocatalytic activity of produced ROS during

the catalysis scavenger experiment has been performed by TBA and EDTA were to trace the OH^* and $\text{O}_2^{\cdot-}$ by the RhB dye (Figure 6.10) [14]. It has been found that TBA and EDTA containing RhB solution show degradation percentages of 13 %, 25 % for CKF5, 17 %, 35 % for CKI5, and 9 % and 28 % for CNKC1. The low degradation percentage for the TBA validated the OH^* radical generation during the catalysis process [15]. It has been observed that in the case of CNKC1, the degradation by the scavenger TBA is minimal (9 %) which suggests that this catalyst produced more OH^* into the solution during catalysis than other catalysts. Moreover, the first-order reaction kinetics constant k has also been calculated by the relation 1.14. It has been found that the reaction constants of degradation by CKF5 are 10.6×10^{-3} (No scavenger), 1.0×10^{-3} (TBA), and $2.7 \times 10^{-3} \text{ min}^{-1}$ (BQ). In the case of CKI5, the constants are 28.8×10^{-3} (no scavenger), 1.5×10^{-3} (TBA), and $4.1 \times 10^{-3} \text{ min}^{-1}$ (BQ). On the other hand, in the case of CNKC1, the first-order kinetic constants are 32.0×10^{-3} (No scavenger), 0.8×10^{-3} (TBA), and $3.3 \times 10^{-3} \text{ min}^{-1}$ (BQ). The high value of the first-order reaction constant in the case of CKI5 and CNKC1 made them promising piezocatalysts.

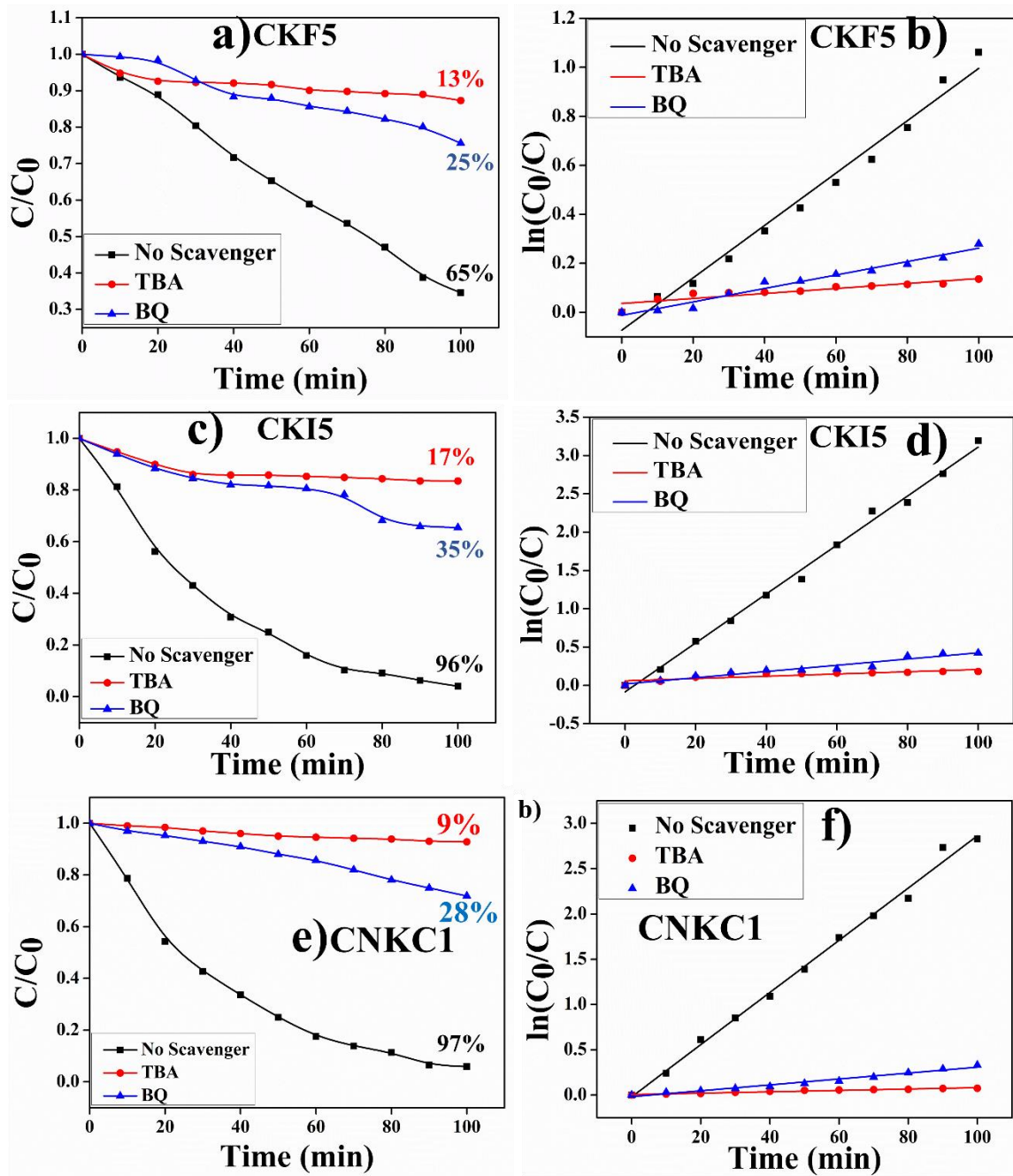


Figure 6.10. Scavenger experiments of and first-order reaction kinetics of the nanocomposite membranes: a, b) CKF5, c, d) CKI5, and e, f) CNKC1

6.3.4 Pathogenic *E. coli* decomposition

The piezocatalytic effectiveness of the CKI5 and CNKC1 nanocomposite membranes and their ROS generation ability was further used to degrade pathogenic *E. coli* bacteria by the experimental protocol depicted in section 1.10.7. It has been observed by the colony counting technique the bacterial colony almost diminished in the 1h of soft ultrasound (15 KHz, 50 W) with the CKI5 and CNKC1 membranes in Figure 6.11, 6.12.

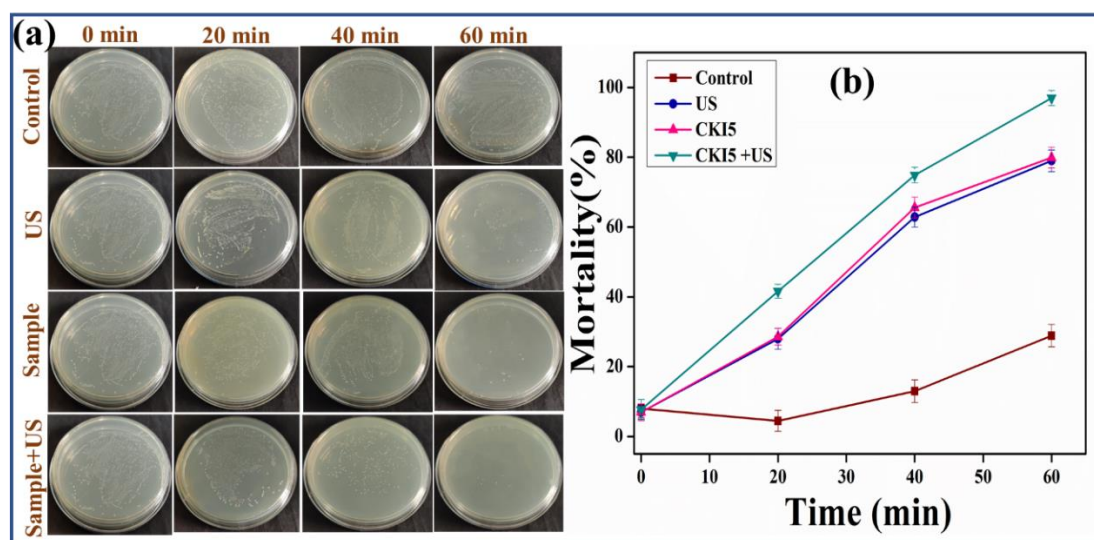


Figure 6.11. Pathogenic *E. coli* bacteria decontamination by CKI5 membrane within 60 min of soft ultrasound (15 kHz, 50 W): a) distribution of bacterial colonies in solid agar plates and b) decontamination kinetics with time: found that the bio-polymeric membrane has a promising antibacterial efficacy which enhanced with piezocatalytic impulse

The mortality percentage of the bacteria has been calculated by equation 1.15 and found 96 % (CKI5) and 97 % (CNKC1) decontamination in 60 min. Moreover, it has been found that in the case of only sample-treated bacteria, the mortality percentage was around 75 % which validated the antibacterial effectiveness of the bio-nanocomposites. The combined effect of the sample's antibacterial property and its piezo effectiveness enhanced the bacterial killing and found such a promising decontamination of harmful pathogens [16]. The mechanism of the destruction of these pathogenic bacteria has been

illustrated in Chapter 1 section 1.10.7 and Figure 1.16.

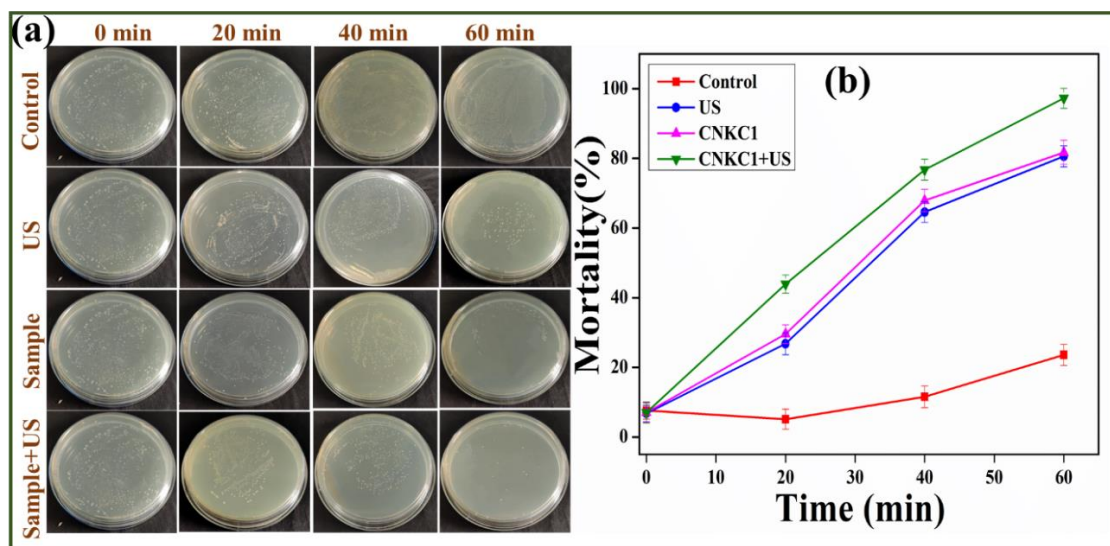


Figure 6.12. Pathogenic *E. coli* bacteria decontamination by CNKC1 membrane within 60 min of soft ultrasound (15 kHz, 50 W): a) distribution of bacterial colonies in solid agar plates and b) decontamination kinetics with time: found that the bio-polymeric membrane has a promising antibacterial efficacy which enhanced with piezocatalytic impulse

6.4 Summary

This chapter delves into the successful fabrication of the surface functionalized, structurally modified, and 1D MWCNT-doped natural kaolinite clay-based chitosan bio-nanocomposite membranes for wastewater remediation and non-invasive energy generation. The fabricated biopolymeric nanocomposites were first characterized by XRD, FERSEM, FTIR, EDAX, and mapping for verifying the successful fabrication free standing biocompatible membranes. The polarization properties were then investigated by electrical measurements like dielectric constants, AC conductivities, and piezoelectric coefficient measurements. It has been found that the nominal piezoelectric coefficient (d_{33}) of the bare chitosan (3.75 pC/N) modulated in the nanocomposite acquires a promising value (33.56 pC/N) which may be the highest findings in such

biopolymeric membrane. The 5 % functionalized (D.C: 16, d_{33} : 17.89 pC/N) and intercalated clay-doped (D.C: 18.7, d_{33} : 26.46 pC/N) bio-polymeric membranes show maximum polarization properties whereas, the 1 % doping of MWCNT-modulated kaolinite (D.C: 19.5, d_{33} : 33.56 pC/N) acquires a maximum value of polarization than the functionalized and intercalated doped clay membranes. These three maximum piezo-efficient samples pose piezoelectric voltages of 16.4 (CKF5), 25.7 (CKI5), and 30.5 V (CNKC1). CKF5 degraded 65 % RhB ($10.6 \times 10^{-3} \text{ min}^{-1}$), and 59 % Congo red dye in 100 min of US whereas, CKI5 degraded 96 % RhB ($28.8 \times 10^{-3} \text{ min}^{-1}$), and 88 % Congo red. The maximum piezo-active membrane CNKC1 degraded 97% RhB ($32.0 \times 10^{-3} \text{ min}^{-1}$), and 89 % Congo red dye in 100 min of US. Additionally, CKI5 and CNKC1 decompose pathogenic coliform *E. coli* bacteria respectively 96 %, and 97 % within 60 min of soft US. The mechanism of the catalysis was further validated by the scavenger experiment which found that OH^* ROS is most dominating to degrade the organic dye and pathogen by these bio-nanocomposite membranes. Fabrication of such biocompatible, freestanding, highly robust, low-cost, natural bio-nanocomposite for decontamination of wastewater and energy generation by non-invasive mechanical sources like water flow, sea wave, wind flow, etc. can pave a new avenue to the nanotechnology for successful treatment of wastewater and mitigating the energy shortage to developing the nations.

References

- [1] Yar, Adem, Abdulkarim Okbaz, and Şerife Parlayıcı. *Nano Energy* 110 (2023): 108354.
- [2] Dutta, Pradip Kumar, Joydeep Dutta, and V. S. Tripathi. (2004).
- [3] Ahmed, M.A. and Mohamed, A.A., 2023. p.124787.
- [4] Aziz, Shujahadeen B., Ahmad SFM Asnawi, Mohd Fakhrul Zamani Kadir, Saad M. Alshehri, Tansir Ahamad, Yuhanees M. Yusof, and Jihad M. Hadi. *Polymers* 13, no. 8 (2021): 1183.

- [5] Guzman Sierra, Dayana L., Igor Bdikin, Alexander Tkach, Paula M. Vilarinho, Claudia Nunes, and Paula Ferreira *European Journal of Inorganic Chemistry* 2021, no. 9 (2021): 792-803.
- [6] Yang, Dong, Jie Li, Zhongyi Jiang, Lianyu Lu, and Xue Chen. *Chemical Engineering Science* 64, no. 13 (2009): 3130-3137.
- [7] Mousavi, Seyyedeh Rahil, Morteza Asghari, and Niyaz Mohammad Mahmoodi. *Carbohydrate polymers* 237 (2020): 116128.
- [8] Bibi, Saira, Tariq Yasin, Safia Hassan, Muhammad Riaz, and Mohsan Nawaz. *Materials Science and Engineering: C* 46 (2015): 359-365.
- [9] Das, Solanky, Dhananjay Mondal, Souravi Bardhan, Shubham Roy, Dipak Kr Chanda, Anupam Maity, Subhojit Dutta, Kamalakanta Mukherjee, and Kaustuv Das. *Journal of Materials Science: Materials in Electronics* 33, no. 9 (2022): 7119-7133.
- [10] Sharma, Nikhil D., Ravi Maranganti, and Pradeep Sharma. *Journal of the Mechanics and Physics of Solids* 55, no. 11 (2007): 2328-2350.
- [11] Chen, Fang, Hongwei Huang, Lin Guo, Yihe Zhang, and Tianyi Ma. "The role of polarization in photocatalysis." *Angewandte Chemie International Edition* 58, no. 30 (2019): 10061-10073.
- [12] Prodromakis, T., and C. Papavassiliou *Applied Surface Science* 255, no. 15 (2009): 6989-6994.
- [13] Hall, Peter G., and Mark A. Rose. "Dielectric properties of water adsorbed by kaolinite clays." *Journal of the Chemical Society, Faraday Transactions 1: Physical Chemistry in Condensed Phases* 74 (1978): 1221-1233.
- [14] Tu, Shuchen, Yuxi Guo, Yihe Zhang, Cheng Hu, Tierui Zhang, Tianyi Ma, and Hongwei Huang. *Advanced Functional Materials* 30, no. 48 (2020): 2005158.
- [15] Nie, Gang, Ling Xiao, Jingxiu Bi, Shaobin Wang, and Xiaoguang Duan. *Applied Catalysis B: Environmental* 315 (2022): 121584.

[16] Roy, Jhilik, Shubham Roy, Dhananjoy Mondal, Neelanjana Bag, Jaba Roy Chowdhury, Saheli Ghosh, Souravi Bardhan, Rajib Mondal, Ruma Basu, and Sukhen Das. *Surfaces and Interfaces* 44 (2024): 103579.

Chapter 7



Conclusions and outlooks

Chapter 6

Conclusions and outlooks

Nowadays, our world is going through several issues due to rapid industrialization, urbanization, technological advancement, and uncontrolled population. The energy crisis is one of the major issues among them. Due to escalated technological advancement and industrialization use of fossil fuels is increasing day-by-day. Thus, the limited source of fossil fuels creates a loom of energy crisis worldwide especially in developing countries like India.

Water pollution is one of the modern devils which hinders the overall development and sustainability of nations. Especially industrial organic pollutants like carcinogenic dyes and pharmaceuticals along with various harmful pathogens directly fall into the local water sources and create harmful effects on waterbodies and mankind which affects the ecological balance. These wastewaters are creating several waterborne diseases like cholera, diarrhoea, liver and kidney problems along with various skin infections.

Numerous nanomaterials and nanocomposites have been developed by researchers over time to overcome these issues. Conventionally, researchers adopt chemically derived nanomaterials to challenge this type of problem, but the nanomaterials are suffering from low biocompatibility, high reaction time, high power consumption, complicated procedures, and secondary pollution.

This work has been designed to fabricate piezo-responsive polymeric membrane-based nanocomposite systems by enhancing the physicochemical properties of naturally found low-cost, abundant, and biocompatible kaolinite clay to face both challenges simultaneously. The physicochemical properties of bulk natural kaolinite have been enhanced by various synthesis techniques like nanonization, surface functionalization, structural modulation, and foreign element incorporation.

In Chapter 2 the natural bulk kaolinite was fractionated by top-down synthesis method by simple grinding and ball-milling to find several sized clays and categorize them as bulk

(K1), moderate size (K2), and nano-clay (K3) and investigated their physicochemical properties by various conventional characterization tools. It has been found that the purity of the clay enhanced with decreasing particle size and the K3 sample falls in the nano regime with a diameter of 70-80 nm. The microstructural evaluation by the theoretical refinement of XRD data depicted the basal plane separation and oxygen vacancies of clay increased with decreasing particle size which increases the active sites and enhances the surface properties (surface area 123.7 to 129.2 m² g⁻¹) due to its high aspect ratio in nano-dimension. The electrical properties of the different-sized clay have also been investigated and found that the nano-clay (K3) poses maximum electrical properties like dielectric permittivity, AC conductivity, specific capacitance, and charging-discharging capabilities with promising temperature stability (up to 500 °C). These results suggest that the natural clay poses the highest physicochemical properties in the nano-dimension.

In Chapter 3 the physicochemical properties of nano-kaolinite are further modulated by surface functionalization (A.K), basal plane intercalation (I.K), and 1 % 1D conducting MWCNT incorporation in different methods. Electronegative NH₂ functional groups have been attached to the positive prism plane of kaolinite NPs and enhanced its overall negative surface charge. The structural modulation by basal plane intercalation also enhanced the surface properties of the clay NPs. Additionally, MWCNT has been incorporated into the kaolinite NPs matrixes by condensation technique with (CK1) and without (CKM1) surface functionalization of both components. It has been found that all the modulated clay NPs pose better physicochemical properties than pristine nano-kaolinite and maximum in CK1 (1 % MWCNT incorporation by functionalizing both the clay and MWCNT surfaces) sample. It has been found that CK1 poses the highest surface properties (surface charge: -11.8 to -37.3 mV, surface area: 129 to 139 m²/g), basal plane separation (5.41 Å to 5.83 Å), electrical permittivity (32 to 3850), and AC conductivity (8.5×10^{-5} to 4.4×10^{-4} S/m). These results suggest that the modulated clay NPs pose better physicochemical properties than pristine clay NPs, especially the CK1 sample.

In Chapter 3 it was found that the activated clay and functionalized MWCNT conjugated NPs pose better physicochemical properties. Thus, in Chapter 4 the concentrations of

functionalized MWCNT have been varied (0.5, 1.0, 1.5 % wt/wt: CK0.5, CK1, CK1.5) into activated kaolinite nano-clay to find the maximum efficient nanocomposite sample. It has been found that the physicochemical properties increase with the percentage doping of MWCNT and attain maximum in CK1 NPs and again reduce after excess doping of MWCNT in CK1.5. Additionally, the specific capacitance of the CK1 sample has obtained a value of 22 F/g with a redox peak in electrochemical measurement which validated that CK1 NPs pose maximum surface, electrical, and polarization properties which is very crucial to fabricating piezo-responsive nanocomposite.

In Chapter 5 piezo-responsive fluoropolymer, PVDF-based nanocomposite membranes have been prepared by CK1 (high physicochemical property) and A.K for the comparative study of their piezoelectric energy generation and piezocatalytic wastewater remediation capability. It has been found that the A.K. incorporation in PVDF at 2.5, 5, and 7.5 % (PVK2.5, PVK5, and PVK7.5) increases the piezo response and attains a maximum value in PVK5. Whereas, CK1 NPs increase the piezo response with the doping percentage of 0.5, 1, and 1.5 % (PCK0.5, PCK1, PCK1.5) and found a maximum piezo response in the PCK1 nanocomposite membrane. PVK5 and PCK1 show percentage β -phases (polar phase responsible for piezo-response) of 84.2 and 88.7 % whereas, bare PVDF (PVK0) has a β -phase of 61.0 %. Additionally, these two membranes show other properties that facilitate the piezo response like remnant polarization (PVK5: $0.59 \mu\text{C}/\text{cm}^2$, PCK1: $0.92 \mu\text{C}/\text{cm}^2$, PVK0: $0.30 \mu\text{C}/\text{cm}^2$), dielectric permittivity (PVK5: 12.9, PCK1: 18.0, PVK0: 9.0), and piezoelectric coefficient (d_{33}) (PVK5: 47.7 pC N^{-1} , PCK1: 50.7 pC N^{-1} , PVK0: 10 pC N^{-1}). These results suggest that the PVK5 and PCK1 pose maximum piezo-response. These two samples were further used to fabricate piezoelectric nano generators (PENG) to generate energy from mechanical stress and piezocatalytic wastewater remediation (carcinogenic dye and pathogenic bacteria). It has been found that PVK5 and PCK1 generate 7.5 and 8.0 V energy respectively by 14.0 N force. Whereas, the PCK1 sample was further used to generate energy from water thrust and found 6.5 V energy with a power of $50 \text{ W}/\text{m}^2$ by the water flow of $4 \times 10^{-3} \text{ L s}^{-1}$. Moreover, PVK5 degraded 79 % RhB, and PCK1 degraded 96 % RhB just in 1 h of ultrasound impulse (33 KHz, 50

W). The dominating ROS has also been investigated and found that the OH* has been generated maximum during the catalysis which was also further confirmed by the trapping experiment. Additionally, the piezo-responsive membranes eradicate pathogenic bacteria (*E. coli*: 100 %, and *E. faecalis*: 97 %) in just 40 min of soft ultrasound (15 KHz, 50 W).

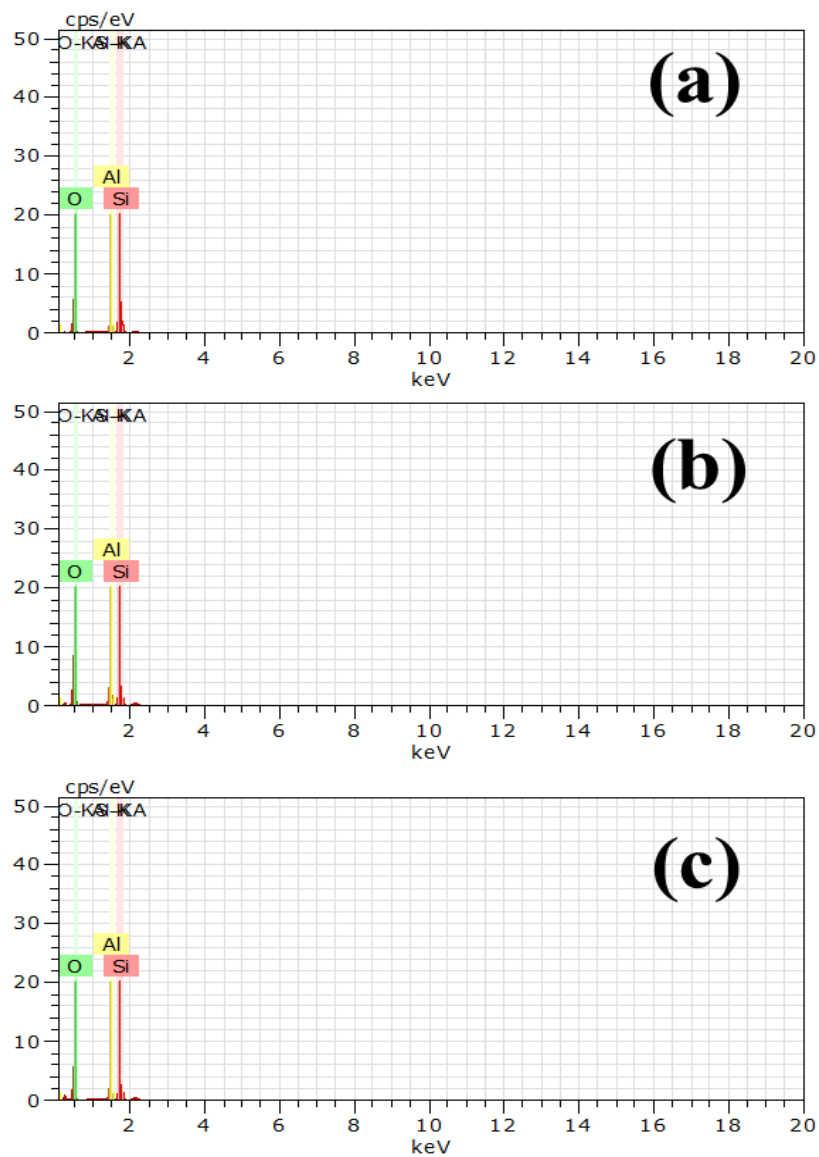
In Chapter 6 A.K, I.K, and CK1 have been incorporated in bio-polymer (chitosan) to fabricate more biocompatible piezo-responsive membranes. It has been found that 5 % A.K (CKF5), I.K (CKI5) incorporated membrane shows maximum piezo-response along with 1 % CK1 (CNKC1) incorporated chitosan matrix. It has been found that the CKF5, CKI5, and CNKC1 show dielectric constants 16.0, 18.7, and 19.5 respectively, where bare chitosan poses D.C of 10.7. The piezoelectric coefficients of bare chitosan, CKF5, CKI5, and CNKC1 have been found 3.75, 17.89, 26.46, and 33.56 pC/N respectively which validated their piezo-responsiveness. The piezoelectric voltages were found 6.4, 16.4, 25.7, and 30.5 for chitosan, CKF5, CKI5, and CNKC1 respectively at 14 N force. Whereas CKF5 (rate constant: $10.6 \times 10^{-3} \text{ m}^{-1}$) degraded 65 % RhB and 59 % Congo-red, CKI5 (rate constant: $28.8 \times 10^{-3} \text{ m}^{-1}$) degraded 96 % RhB and 88 % Congo-red and CNKC1 (rate constant: $32.0 \times 10^{-3} \text{ m}^{-1}$) degraded 97 % RhB and 89 % CR, in 100 min of ultrasound impulse (33 KHz, 50 W) for the OH* dominating ROS. It has been found that CKI5 and CNKC1 pose better piezo-response than CKF5. Thus, CKI5 and CNKC1 were further used to eradicate pathogenic *E. coli* bacteria and found 96 % and 97 % decomposition just in 60 min of ultrasound.

Thus, this thesis has validated that besides chemically derived piezoelectric NPs, natural NPs having high physicochemical properties can fabricate cost-effective, biocompatible, self-poled, free-standing piezo-responsive nanocomposite if properly improvised. These highly robust nanocomposite membranes can be produced on a mass scale in non-invasive energy generation and wastewater management technologies.

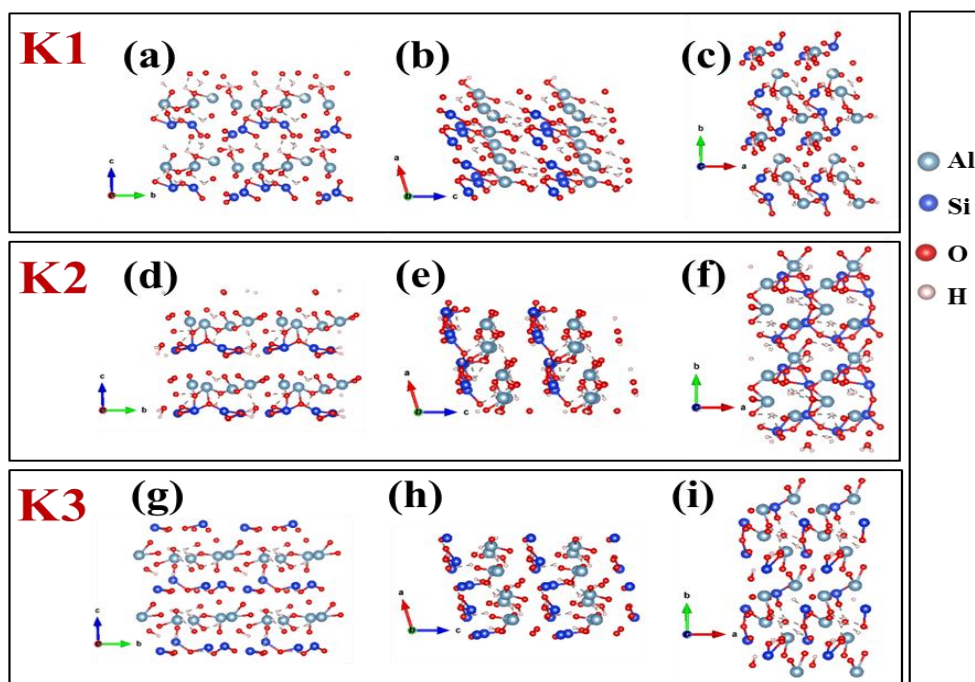
Appendices

Appendix 1

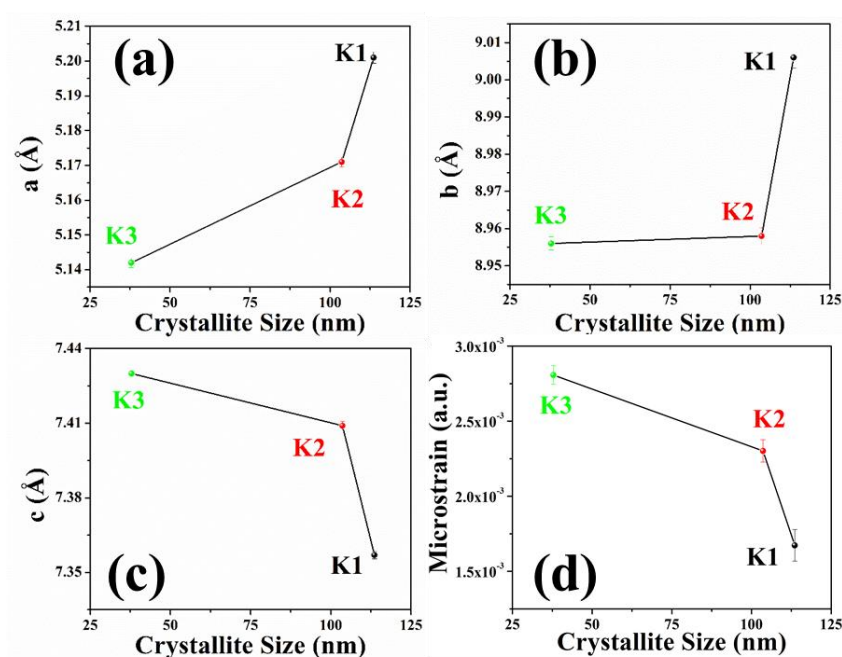
Supporting Information of Chapter 2



A1.1 EDX spectra of the samples showing the traces of Al, Si, and O in the samples (K1: a, K2: b, and K3: c).



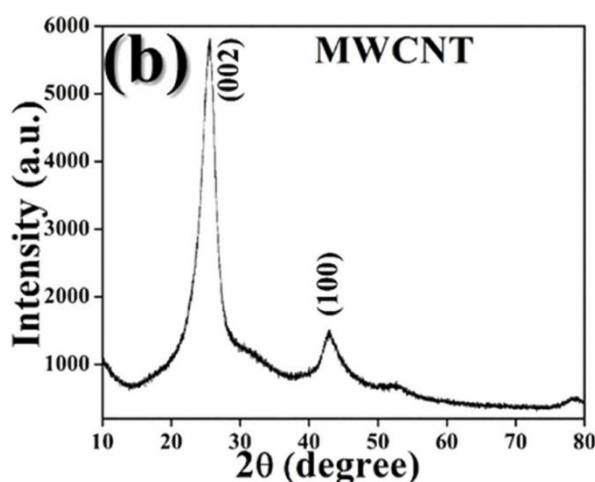
A1.2 Variation of microstructure along a , b , and c axis in (a) K1, (b) K2, and (c) K3



A1.3 Variation of the crystalline size of K1, K2, and K3 along a , b , and c axis respectively (a-c), and enhancement of microstrain value with decreasing crystallite size (d).

Appendix 2

Supporting Information of Chapter 4



A2.1 XRD of MWCNT

A2.2 Refined atomic positions of composites

K3:

Al1_Al Al 1.0 0.38317323 0.5161154 0.55914927 2.0(2) .
 Al2_Al Al 1.0 0.8886791 0.0616021 0.46674994 2.0(3) .
 Al3_Al Al 1.0 0.76844186 0.36652 0.42891902 2.0(3) .
 Al4_Al Al 1.0 0.30898088 0.7932564 0.46596026 2.0(4) .
 Si1_Si Si 1.0 0.0317228 0.34970883 0.029511383 2.0(4) .
 Si2_Si Si 1.0 0.5548957 0.82888126 0.10696704 2.0(4) .
 Si3_Si Si 1.0 0.47606033 0.15564834 0.06127408 2.0(5) .
 Si4_Si Si 1.0 0.01053329 0.70145327 0.013623475 2.0(5) .
 O1_O O 1.0 0.024969049 0.2785292 0.30620947 2.0(5) .
 O2_O O 1.0 0.5260547 0.75632936 0.31413788 2.0(8) .
 O3_O O 1.0 0.11255689 0.67371523 0.40703255 2.0(8) .
 O4_O O 1.0 0.71252525 0.20579118 0.3597132 2.0(7) .
 O5_O O 1.0 0.9985261 0.45795685 0.9913853 2.0(14) .
 O6_O O 1.0 0.3110778 0.9996806 0.99447006 2.0(6) .
 O7_O O 1.0 0.4064837 0.1635885 0.028171409 2.0(12) .
 O8_O O 1.0 0.69724405 0.67222595 0.014957482 2.0(7) .
 O9_O O 1.0 0.2593392 0.7937512 0.9894567 2.0(8) .
 O10_O O 1.0 0.88774145 0.2540447 0.99469155 2.0(9) .
 O11_O O 1.0 0.16211386 0.99311346 0.34626856 2.0(5) .
 O12_O O 1.0 0.619278 0.51880914 0.26009658 2.0(13) .
 O13_O O 1.0 0.0808656 0.21061577 0.5105567 2.0(7) .
 O14_O O 1.0 0.49671918 0.671721 0.59584475 2.0(6) .

O15_O O 1.0 0.04739986 0.45180643 0.39664876 2.0(8) .
O16_O O 1.0 0.43142655 0.9642096 0.53029835 2.0(7) .
O17_O O 1.0 0.019666325 0.8057842 0.58303124 2.0(12) .
O18_O O 1.0 0.6968128 0.28929973 0.6602452 2.0(7) .
H1_H H 1.0 0.23320617 0.15370275 0.39575428 2.0(92) .
H2_H H 1.0 0.5791665 0.5672374 0.2584563 2.0(228) .
H3_H H 1.0 0.08203103 0.06722663 0.09636757 2.0(110) .
H4_H H 1.0 0.98526996 0.8581545 0.5509887 2.0(78) .
H5_H H 1.0 0.068996824 0.66708297 0.7671907 2.0(82) .
H6_H H 1.0 0.9643237 0.002555874 0.64704597 2.0(88) .
H7_H H 1.0 0.7623855 0.6370096 0.26863536 2.0(139) .
H8_H H 1.0 0.060517807 0.7967227 0.6459735 2.0(205) .

CK0.5

Al1_Al Al 1.0 0.2424504 0.506227 0.51658636 0.001(2) .
Al2_Al Al 1.0 0.7282424 0.0207535 0.4488429 9.885973E-4 .
Al3_Al Al 1.0 0.69474757 0.37059045 0.40081728 9.885973E-4 .
Al4_Al Al 1.0 0.33807832 0.847998 0.49032414 9.885973E-4 .
Si1_Si Si 1.0 0.9612332 0.3931519 0.034755155 9.885973E-4 .
Si2_Si Si 1.0 0.45823574 0.87352645 0.11007698 9.885973E-4 .
Si3_Si Si 1.0 0.35919827 0.17320412 0.07168061 9.885973E-4 .
Si4_Si Si 1.0 0.008061439 0.71818405 0.05160182 9.885973E-4 .
O1_O O 1.0 0.036988232 0.36577597 0.3006795 9.885973E-4 .
O2_O O 1.0 0.6891704 0.8647042 0.32816744 9.885973E-4 .
O3_O O 1.0 0.055950142 0.6868748 0.39691865 9.885973E-4 .
O4_O O 1.0 0.5673766 0.21644606 0.3040821 9.885973E-4 .
O5_O O 1.0 0.9990212 0.51855636 0.9925938 9.885973E-4 .
O6_O O 1.0 0.8331225 0.9997737 0.98356855 9.885973E-4 .
O7_O O 1.0 0.14279911 0.14120722 0.013894152 9.885973E-4 .
O8_O O 1.0 0.6482531 0.7582563 0.007965953 9.885973E-4 .
O9_O O 1.0 0.21226414 0.7371807 0.997852 9.885973E-4 .
O10_O O 1.0 0.74186444 0.27581275 0.9976532 9.885973E-4 .
O11_O O 1.0 0.026122881 0.9704586 0.36151293 9.885973E-4 .
O12_O O 1.0 0.7294005 0.58716124 0.34630775 9.885973E-4 .
O13_O O 1.0 0.0131326 0.2244965 0.48675948 9.885973E-4 .
O14_O O 1.0 0.45486346 0.71594477 0.6569813 9.885973E-4 .
O15_O O 1.0 0.029601723 0.43477896 0.50847864 9.885973E-4 .
O16_O O 1.0 0.41765848 0.0705237 0.5649849 9.885973E-4 .
O17_O O 1.0 0.018358411 0.8852974 0.60523456 9.885973E-4 .
O18_O O 1.0 0.5231744 0.3582374 0.6777364 9.885973E-4 .
H1_H H 1.0 0.27538148 0.09800221 0.55664223 9.885973E-4 .
H2_H H 1.0 0.6073164 0.8133373 0.33083996 9.885973E-4 .
H3_H H 1.0 0.06962955 0.39602607 0.4552584 9.885973E-4 .

H4_H H 1.0 0.52866054 0.0050951 0.75459874 9.885973E-4 .
H5_H H 1.0 0.04269174 0.33764714 0.24013199 9.885973E-4 .
H6_H H 1.0 0.3166569 0.0017120416 0.15116543 9.885973E-4 .
H7_H H 1.0 0.59418344 0.05390921 0.74877787 9.885973E-4 .
H8_H H 1.0 0.054705326 0.57585293 0.67806363 9.885973E-4 .

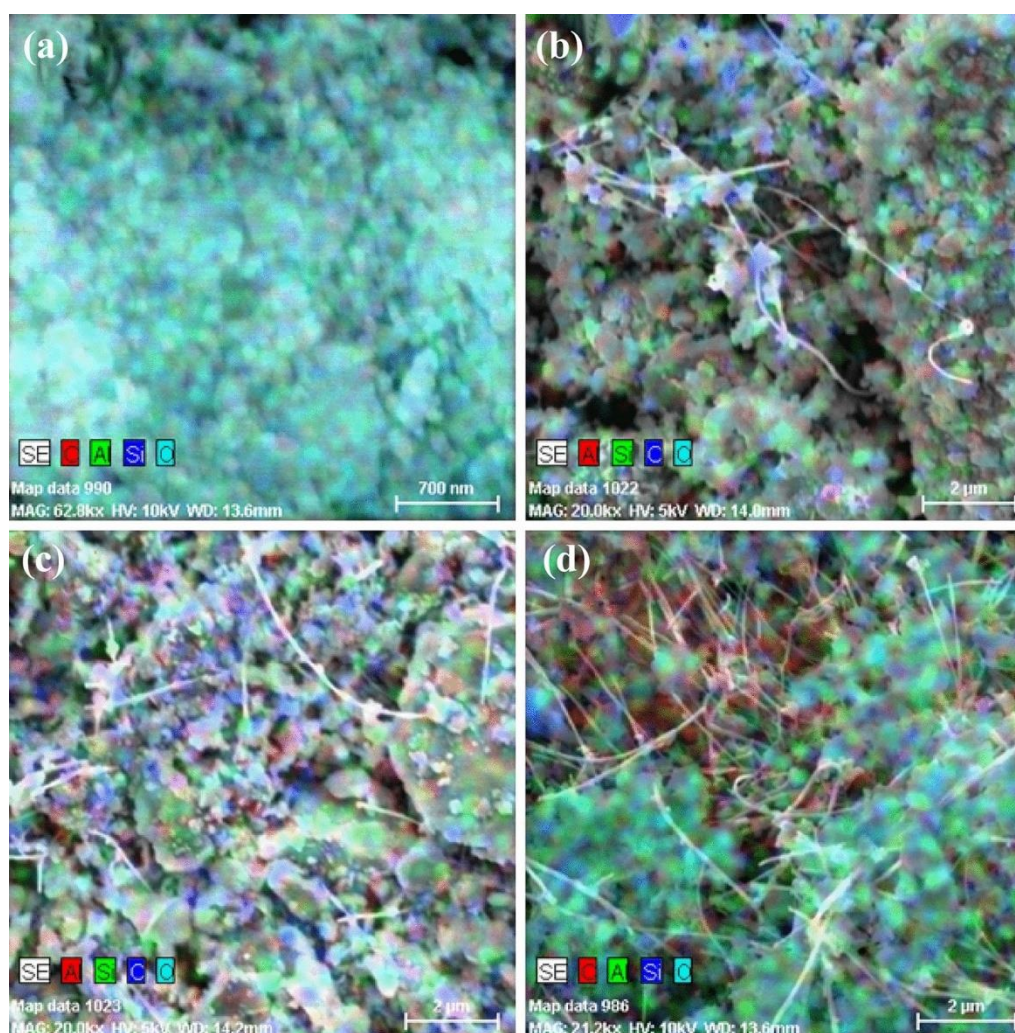
CK1:

Al1_Al Al 1.0 0.29940924 0.48710656 0.5219036 -0.3(9) .
Al2_Al Al 1.0 0.8460531 0.0160549 0.4708763 -0.3127206 .
Al3_Al Al 1.0 0.74175787 0.3424238 0.42978293 -0.3127206 .
Al4_Al Al 1.0 0.29914743 0.83610725 0.5024757 -0.3127206 .
Si1_Si Si 1.0 0.9636575 0.35764608 0.04807195 -0.3127206 .
Si2_Si Si 1.0 0.5389995 0.81933296 0.12775318 -0.3127206 .
Si3_Si Si 1.0 0.4344 0.14406449 0.05605527 -0.3127206 .
Si4_Si Si 1.0 0.006014709 0.67593193 0.009386675 -0.3127206 .
O1_O O 1.0 0.017150696 0.30785233 0.34303477 -0.3127206 .
O2_O O 1.0 0.5723813 0.6866613 0.27500832 -0.3127206 .
O3_O O 1.0 0.06425058 0.6506406 0.3771015 -0.3127206 .
O4_O O 1.0 0.7287963 0.18869391 0.37316132 -0.3127206 .
O5_O O 1.0 0.9983941 0.41571835 0.9919857 -0.3127206 .
O6_O O 1.0 0.16670106 0.99964064 0.98948604 -0.3127206 .
O7_O O 1.0 0.26094067 0.15170756 0.050951038 -0.3127206 .
O8_O O 1.0 0.64449114 0.83513314 0.011009776 -0.3127206 .
O9_O O 1.0 0.35096654 0.76700026 5.774271E-4 -0.3127206 .
O10_O O 1.0 0.831698 0.23345225 5.9239485E-4 -0.3127206 .
O11_O O 1.0 0.17797767 0.9602685 0.3441483 -0.3127206 .
O12_O O 1.0 0.7520216 0.5621161 0.3481709 -0.3127206 .
O13_O O 1.0 0.0486541 0.17058459 0.49930912 -0.3127206 .
O14_O O 1.0 0.57707745 0.6808054 0.59578246 -0.3127206 .
O15_O O 1.0 0.025224004 0.45711228 0.40967545 -0.3127206 .
O16_O O 1.0 0.5046273 0.1532208 0.63776666 -0.3127206 .
O17_O O 1.0 0.021657035 0.8333441 0.55397564 -0.3127206 .
O18_O O 1.0 0.6090752 0.32118994 0.6740456 -0.3127206 .
H1_H H 1.0 0.32034934 0.059507906 0.40616655 -0.3127206 .
H2_H H 1.0 0.5029095 0.78846043 0.50213057 -0.3127206 .
H3_H H 1.0 0.12266754 0.15083203 0.50770915 -0.3127206 .
H4_H H 1.0 0.3154314 0.18394727 0.48545745 -0.3127206 .
H5_H H 1.0 0.04106723 0.2935526 0.33909282 -0.3127206 .
H6_H H 1.0 0.4744874 0.0024170144 0.2448625 -0.3127206 .
H7_H H 1.0 0.371451 0.8863668 0.41516837 -0.3127206 .
H8_H H 1.0 0.09458593 0.7696729 0.14963444 -0.3127206 .

CK1.5:

Al1_Al Al 1.0 0.27942175 0.5013718 0.4237931 0.0(1) .

Al2_Al Al 1.0 0.81640345 0.9936886 0.4884106 -0.6190006 .
Al3_Al Al 1.0 0.7679932 0.31764904 0.44392738 -0.6190006 .
Al4_Al Al 1.0 0.38650775 0.8715398 0.4794476 -0.6190006 .
Si1_Si Si 1.0 0.0509852 0.34213907 0.077850014 -0.6190006 .
Si2_Si Si 1.0 0.63599783 0.85258144 0.062227458 -0.6190006 .
Si3_Si Si 1.0 0.48281062 0.20682566 0.014391364 -0.6190006 .
Si4_Si Si 1.0 0.014250215 0.6427231 0.07183558 -0.6190006 .
O1_O O 1.0 0.100536436 0.33691064 0.31084162 -0.6190006 .
O2_O O 1.0 0.6063237 0.83281267 0.32672963 -0.6190006 .
O3_O O 1.0 0.21369341 0.68447006 0.3513173 -0.6190006 .
O4_O O 1.0 0.5121027 0.15464032 0.3420862 -0.6190006 .
O5_O O 1.0 0.9983449 0.4976311 0.99713737 -0.6190006 .
O6_O O 1.0 0.4209668 0.99963653 0.96984076 -0.6190006 .
O7_O O 1.0 0.37616473 0.18301159 0.99785995 -0.6190006 .
O8_O O 1.0 0.6643379 0.6353402 0.99838054 -0.6190006 .
O9_O O 1.0 0.4246741 0.8308101 0.0036918905 -0.6190006 .
O10_O O 1.0 0.7158716 0.32032365 0.0041052294 -0.6190006 .
O11_O O 1.0 0.17644921 0.9864512 0.3158387 -0.6190006 .
O12_O O 1.0 0.8125776 0.48687336 0.4338475 -0.6190006 .
O13_O O 1.0 0.0464709 0.1826093 0.57063353 -0.6190006 .
O14_O O 1.0 0.44329503 0.6776364 0.46532518 -0.6190006 .
O15_O O 1.0 0.0136506725 0.4891983 0.6585577 -0.6190006 .
O16_O O 1.0 0.57151055 0.94931847 0.49296987 -0.6190006 .
O17_O O 1.0 0.026337173 0.8242018 0.6124862 -0.6190006 .
O18_O O 1.0 0.64096403 0.34558165 0.6214532 -0.6190006 .
H1_H H 1.0 0.20530826 0.07270002 0.0813619 -0.6190006 .
H2_H H 1.0 0.85951036 0.9201022 0.08360418 -0.6190006 .
H3_H H 1.0 0.08951544 0.33122995 0.32328016 -0.6190006 .
H4_H H 1.0 0.9509409 0.85257316 0.27062064 -0.6190006 .
H5_H H 1.0 0.053848967 0.9766224 0.16319267 -0.6190006 .
H6_H H 1.0 0.34958243 0.0027728525 0.24465767 -0.6190006 .
H7_H H 1.0 0.0790311 0.09945745 0.20783998 -0.6190006 .
H8_H H 1.0 0.06829589 0.9341115 0.217201 -0.6190006 .



A2.3 Mapping data of a) K3, b) CK0.5, c) CK1, and d) CK1.5.

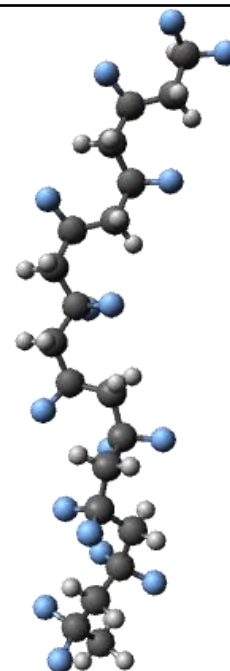
Appendix 3

Supplementary Information of Chapter 5

A3.1 Optimize structures of composite membranes from Density Functional Theory

CARTESIAN COORDINATES (Å) (α -phase)

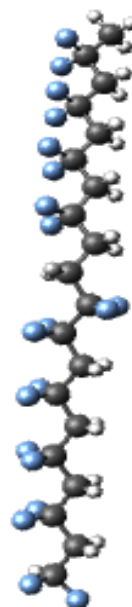
C	-9.604845	-0.334903	0.057709
C	-8.171328	0.076427	-0.239105
C	-7.872182	1.494025	0.232015
H	-7.497825	-0.610372	0.275093
H	-7.998497	-0.017070	-1.316034
C	-6.519612	2.112838	-0.124882
C	-5.277704	1.407896	0.408635
H	-6.534198	3.133248	0.262676
H	-6.450123	2.175578	-1.215549
C	-3.915004	1.961270	-0.028688
C	-3.599121	3.394009	0.387342
H	-3.838339	1.878026	-1.116843
H	-3.161962	1.300438	0.406531
C	-2.270547	3.997380	-0.086248
C	-0.995922	3.203517	0.188881
H	-2.337426	4.175354	-1.163607
H	-2.196308	4.971180	0.407958
C	0.265317	3.990055	-0.161024
C	1.620826	3.370937	0.202440
H	0.255427	4.196804	-1.235472
H	0.234422	4.950558	0.362692



C	1.930110	1.960122	-0.309164
C	3.415320	1.577374	-0.237556
H	1.579101	1.841445	-1.338646
H	1.372925	1.252935	0.309766
C	4.298524	2.091198	-1.381158
C	5.774687	2.320992	-1.040290
H	3.929309	3.054058	-1.738614
H	4.228627	1.373511	-2.203321
C	6.546680	1.172218	-0.395697
C	7.870783	1.549306	0.280131
H	5.937527	0.700436	0.377643
H	6.749018	0.426516	-1.169129
C	8.877116	2.379977	-0.508624
C	9.987848	3.010656	0.338487
H	8.370774	3.198884	-1.022114
H	9.331902	1.736339	-1.266898
C	10.735927	2.136517	1.324035
H	11.503316	2.747759	1.808107
H	11.215420	1.302941	0.803787
H	10.057623	1.741982	2.082022
F	-10.462515	0.210734	-0.853923
F	-9.691435	-1.697811	-0.054732
H	-9.944581	-0.048847	1.057228
F	-8.820152	2.344701	-0.294760
F	-8.042763	1.535045	1.597280
F	-5.285277	0.093962	-0.037117
F	-5.327329	1.349291	1.771212

Appendices

F	-4.568752	4.241444	-0.130925
F	-3.679523	3.506159	1.744968
F	-0.961350	2.795110	1.493168
F	-1.026049	2.041660	-0.572071
F	2.559722	4.256198	-0.302846
F	1.760450	3.397030	1.558936
F	3.924294	1.962297	0.972715
F	3.474599	0.195361	-0.248128
F	5.868557	3.447401	-0.267974
F	6.388377	2.632117	-2.245642
F	8.471054	0.344290	0.613553
F	7.591854	2.172318	1.469945
F	10.903899	3.528242	-0.558599
F	9.457117	4.088817	1.006222



CARTESIAN COORDINATES (Å) (β -phase)

C	-4.031887	1.377173	1.159271
C	-2.728409	2.123541	0.934379
H	-4.786040	2.096840	1.489889
H	-3.906539	0.616474	1.934743
H	-4.374770	0.898044	0.237804
C	-1.551880	1.244178	0.477664
F	-2.949808	3.109922	0.004458
F	-2.403743	2.755762	2.110150
C	-0.207068	1.968697	0.309990
H	-1.821007	0.778178	-0.475765

H	-1.417852	0.444729	1.212880
C	0.930477	1.044935	-0.168782
F	0.137288	2.524284	1.508917
F	-0.351559	2.989568	-0.585701
C	2.324025	1.698574	-0.227886
H	0.673980	0.670469	-1.164986
H	0.988151	0.186546	0.508192
F	2.660395	2.131932	1.024141
F	2.274603	2.799214	-1.038201
C	3.420463	0.738253	-0.729502
C	4.851468	1.296001	-0.731171
H	3.172982	0.417896	-1.746844
H	3.410977	-0.148792	-0.088779
C	5.927281	0.282732	-1.143613
F	5.160251	1.746025	0.531344
F	4.925863	2.389910	-1.558235
C	7.329028	0.897422	-0.990872
H	5.742354	-0.052912	-2.169811
H	5.836024	-0.587648	-0.488128
C	8.469192	-0.110348	-1.000120
H	7.374146	1.423594	-0.036296
H	7.523793	1.633830	-1.774420
F	8.764430	-0.533089	-2.272341
F	8.140746	-1.235085	-0.278373
C	9.770879	0.453422	-0.381964
C	10.933437	-0.538794	-0.355141
F	10.090197	1.568168	-1.101911

Appendices

F	9.453337	0.857888	0.884461
C	12.228310	-0.000627	0.273152
H	11.137221	-0.855838	-1.381564
H	10.604286	-1.415661	0.208627
C	13.340492	-1.061324	0.330858
C	14.728713	-0.537763	0.735705
H	13.436168	-1.541755	-0.648246
H	13.024069	-1.824158	1.048970
C	15.746303	-1.667409	0.957502
C	17.101471	-1.236556	1.534123
H	15.910927	-2.170170	-0.001420
H	15.316563	-2.401074	1.647303
C	18.151901	-2.347514	1.507022
C	19.506829	-1.911854	2.042431
H	18.296677	-2.709127	0.483479
H	17.794248	-3.182744	2.117569
F	12.657061	1.085988	-0.435798
F	11.962590	0.424810	1.547191
F	15.189027	0.288006	-0.253924
F	14.629424	0.207035	1.878015
F	17.574696	-0.140514	0.870086
F	16.931490	-0.855852	2.847901
F	20.084863	-1.029543	1.180907
F	20.315470	-3.015534	2.118438
H	19.464425	-1.448440	3.032059

Publications & Seminar

Certificates





Cite this: DOI: 10.1039/d1dt02653d

Recent advances in piezocatalytic polymer nanocomposites for wastewater remediation

Dhananjay Mondal,^a Shubham Roy,^{ib} ^a Souravi Bardhan,^a Jhilik Roy,^a Ishita Kanungo,^{a,b} Ruma Basu^b and Sukhen Das^{ib} ^{*}^a

Among several forms of water pollutants, common pesticides, herbicides, organic dyes and heavy metals present serious and persistent threats to human health due to their severe toxicity. Recently, piezocatalysis based removal of pollutants has become a promising field of research to combat such pollutions by virtue of the piezoelectric effect. In reality, piezoelectric materials can produce electron–hole separation upon external vibration, which greatly enhances the production of various reactive oxygen species (ROS) and further increases the pollutant degradation rate. Piezocatalysis does not alter the quality or composition of water, like several other conventional techniques (adsorption and photocatalysis), which makes this technique non-invasive. The simplicity and tremendously high efficacy of piezocatalysis have attracted researchers worldwide and thus various functional materials are employed for piezocatalytic wastewater remediation. In this frontier, we highlight and demonstrate recent developments on polymer based piezocatalytic nanocomposites to treat industrial wastewater in a facile manner that holds strong potential to be translated into a clean and green technology.

Received 10th August 2021,
Accepted 16th November 2021

DOI: 10.1039/d1dt02653d

rsc.li/dalton

1. Introduction

Nowadays, numerous research studies are ongoing worldwide and various techniques have been developed to combat wastewater mediated pollutions. Traditionally, adsorption-based removal techniques showed great potential against such issues. Various nanostructures, due to their high aspect ratios,

^aDepartment of Physics, Jadavpur University, Kolkata-700032, India.

E-mail: sdasphysics@gmail.com; Tel: +91 9433091337

^bDepartment of Physics, Jogamaya Devi College, Kolkata-700026, India**Dhananjay Mondal**

Dhananjay Mondal is currently pursuing his Ph.D. degree in the Department of Physics, Jadavpur University, Kolkata, India. He has received graduation and post-graduation degrees in physics from the same department. His research interest includes biocompatible material-based sensors and actuators along with piezo-responsive catalysts. He is presently working as a junior research fellow under a DST-SERB funded project at Jadavpur University, Kolkata.

**Shubham Roy**

Shubham Roy obtained his bachelor degree in physics from the University of Calcutta in 2013 and acquired his Master degree in the same discipline from Madurai Kamaraj University in the year 2015. He is presently pursuing his doctoral degree under the supervision of Prof. Sukhen Das from the Department of Physics, Jadavpur University, India. His research area includes the synthesis and characterization of nanomaterials for fabricating low cost fluorometric sensors to combat wastewater mediated heavy metal pollution. Mr. Roy has published numerous papers on multifunctional fluorometric sensors and their contamination removal efficacies.

showed remarkable efficacy in removing organic and inorganic contaminants from wastewater.¹⁻⁴ However, adsorption may simply transfer the specific pollutants from one phase to another and result in the formation of chemically active species, which can initiate secondary pollution.⁵⁻¹⁰ Bioremediation methods have also been adopted widely for wastewater treatment. These methods involve processes like hyperaccumulation, phytoremediation, mycoremediation, rhizoremediation, *etc.*^{11a} Although these techniques are cost effective and ecofriendly, they still suffer from various drawbacks such as high reaction time, seasonal alteration in microbial activities and reversibility if improperly handled.¹⁰ Therefore, photocatalysis has emerged to resolve the drawbacks of conventional removal processes.^{11b} Although numerous methods have been proposed to enhance the photocatalytic efficacy by band gap maneuvering, the formation of composite semiconductors, metal ion implantation, *etc.*, it is still challenging to achieve an effective charge separation process in these systems.¹² In fact, photocatalysts may corrode under low pH conditions and could restrict the degradation efficacy tremendously.¹⁰

This is where piezoelectric materials have become a favorable alternative to acquiring better catalytic activity. Normally, piezoelectric materials have been widely used in various applications, such as energy generation, charge storage, sensor devices, *etc.* These functional materials enable new advances in catalytic processes using clean energies, like mechanical vibration, ultrasonic waves and pressure.¹³ Piezocatalysis exploits such piezo-stimulations for accelerating chemical reactions. In reality, piezoelectric materials possess better charge center separation under mechanical stress. Such separation leads to the formation of reactive radicals (oxygen species) that are responsible for initiating the catalysis process. Besides several other inorganic nano-systems, MoS₂, BaTiO₃, and BiFeO₃ show promising piezocatalytic activity in aqueous

media.¹⁴ In some cases, the catalytic efficacy is found to be around 100%. In fact, bacterial sterilization has also been achieved through piezocatalysis. However, most of these powdered inorganic piezocatalytic materials have a tendency to diffuse in water. Thus, it is extremely necessary to separate them from the aqueous media and minimize secondary pollution. Such disadvantages of inorganic piezo-materials can be curtailed by encapsulating them into different polymeric systems.¹⁵⁻¹⁸ Though polymeric piezocatalysts are showing promising catalytic activity, these systems are still in their infancy. Henceforth, this frontier article highlights the recent advances of polymeric piezocatalytic systems for combating wastewater pollution. These hybrid and versatile polymer-nanocomposites would eventually contribute to the control of the excessive use of hazardous pollutants, minimizing their effects on the environment and definitely would reveal the importance of polymeric encapsulation of piezocatalysts.^{19,20}

2. Piezocatalysis: mechanism and discussion

2.1 Discovery and recent progress

Among various crystal point groups, researchers are focusing on mainly three types of piezo-crystals such as ZnO based composites, perovskites and 2D ultrathin materials. Initially, ZnO emerged as a promising piezocatalyst. Hong *et al.* in their 2010 paper showed the successful conversion of mechanical energy to chemical energy using piezo-electric ZnO microfibers.¹⁰ They named the conversion process the piezoelectrochemical effect (PZEC). The release of H₂ and O₂ gases in a 2 : 1 stoichiometry has also been demonstrated from pure water. Furthermore, the problem of dispersion of catalysts in solution was solved by the ZnO embedded carbon nanotube flexible



Souravi Bardhan

Ms. Souravi Bardhan is currently pursuing her Ph.D. in the Department of Physics, Jadavpur University, India. She pursued her graduation and post-graduation in environmental science from the University of Calcutta, India. Prior to joining the PhD program she worked on a project on biogeochemistry of core regions of Indian Sundarbans with the School of Environmental Science, Jawaharlal Nehru University,

India. Her present research-work involves the enhancement of the optical, electrical and biological properties of natural minerals in their nano-regime in order to design natural-multifunctional sensors for wastewater treatment.



Jhilik Roy

Jhilik Roy is presently doing her research in materials science in the Department of Physics, Jadavpur University, Kolkata, India. She has obtained both B.Sc and M.Sc degrees in physics from the University of Calcutta and Techno India University, respectively. Ms. Roy has an excellent command of theoretical molecular docking analysis and other in-silico studies. She has published several research papers recently on fluorometric sensors and their interaction with living systems.

network. Also carbon nanotubes with outstanding electrical conductivity could act as high-speed channels for charge transfer and boost the piezocatalytic activity.^{21,22}

Nanoscale perovskites can also be used in piezocatalytic applications. Lead based perovskites $\text{Pb}(\text{Mg}_{1/3}\text{Nb}_{2/3})\text{O}_3$, 32PbTiO_3 and $\text{Pb}(\text{Zr}_{0.52}\text{Ti}_{0.48})\text{O}_3$ showed great potential in generating H_2 gas and dye de-coloration.²³ Similarly, $\text{CH}_3\text{NH}_3\text{PbI}_3$ nanoparticles prepared by the co-precipitation method have stronger polarization resulting from a larger displacement of the Pb atom, demonstrating excellent piezocatalytic activity.²⁴ In fact, lead-free BaTiO_3 microdendrites, BaTiO_3 nanofibers and $(\text{Ba,Sr})\text{TiO}_3$ nanowires, obtained by hydrothermal and sol gel methods, depicted pronounced piezocatalytic activity besides azo dye degradation.^{25–27}

Besides several nanostructures, 2-D MoS_2 has been used as a potential piezocatalyst in recent years. It is observed that single layer MoS_2 exhibits strong polarization and charge separation between the bases of $\text{Mo}_2\text{-S}$ layers. Piezo-electrochemical experiments suggest promising charge mobility through these layers. Such a piezoelectric effect would definitely initiate piezocatalytic activity in a MoS_2 system.²⁸ In reality, a double layer MoS_2 system suffers from a reduction in piezoelectric activity due to the opposite polarization direction between two consecutive layers. Therefore, researchers have determined the fact that the piezoelectricity in MoS_2 is highly structure-dependent and periodically follows the odd-even order.^{29,30} Moreover, Li *et al.* performed a comparative analysis between the piezocatalytic activity of numerous 2-D materials including MoS_2 , WS_2 , and WSe_2 , which revealed that the piezocatalytic activity was directly correlated with piezoelectric coefficients obtained by calculations and PFM measurements.³¹

2.2 Mechanism of action

Piezoelectric crystals are normally electrically neutral, and the atoms inside them may not always be symmetrically arranged. Despite having a non-centrosymmetric structure, a positive charge cancels out a negative charge near it, nullifying the electric dipole which makes the crystal neutral. Whenever the crystal is squeezed *i.e.*, mechanical stress is applied across it, the structure is deformed, which in turn disrupts not only the balance of positive and negative charges, but also alters their band structures (Fig. 1). The electrons and holes thus move to opposite sides of the crystal, building up an electric field on its surface. Additionally, the piezo-potential modifies the electronic energy levels of the HOMO and LUMO within the materials.³² It lowers the conduction band (CB) to a degree below the highest occupied molecular orbital (HOMO) of the material. So the electrons will transfer from the HOMOs to the CB. On the opposite side, electrons will leave the valence band (VB) and transfer to the lowest unoccupied molecular orbital (LUMO).^{32a,b}

Piezocatalysis is an approach towards augmenting electrochemical processes using such a strain state of a piezoelectric material. Piezocatalysis is the product of an interaction between the native electronic state of the piezoelectric material, the composition of the surrounding medium and a strain induced piezoelectric potential. The action of mechanically deforming a piezoelectric material induces a steep electric field which builds up the energetics of both free and bound charges throughout the material. The thermodynamic feasibility and kinetics of electrochemical processes occurring at the surface of the piezoelectric material sensitively depend upon the electrochemical potential difference between the charges on its surface and in the surrounding medium. Additionally, the electron-hole pairs that originated from the strained catalysts migrate (in the opposite direction) and accumulate at the surface of the catalysts.³² External piezoelectric stimulation accumulates enough electron-hole pairs at the surface to initiate redox reactions (Fig. 2).



Ishita Kanungo

Ishita Kanungo is currently pursuing her doctoral degree in the Department of Physics, Jadavpur University, India. She obtained her B.Sc. and M.Sc. degrees from the University of Calcutta and Central University of Haryana, respectively. She is currently also a faculty member of the Department of Physics, Jogamaya Devi College, Kolkata, India. Her research interest includes the development of novel nano-sensors from waste

materials and studying their fluorometric and colorimetric behaviors.



Ruma Basu

Dr Ruma Basu is an Associate professor at the Department of Physics, Jogamaya Devi College. She has guided several doctoral fellows and has more than 100 research publications in reputed journals. She obtained her B.Sc. degree from Presidency College, Calcutta University, in the year 1980, M. Sc. from Calcutta University, in 1983 and Ph. D. from Jadavpur University in 1989. Dr Basu's research area includes membrane biophysics,

biophysical chemistry, fluorescence and absorption spectroscopy, photobiology, etc.

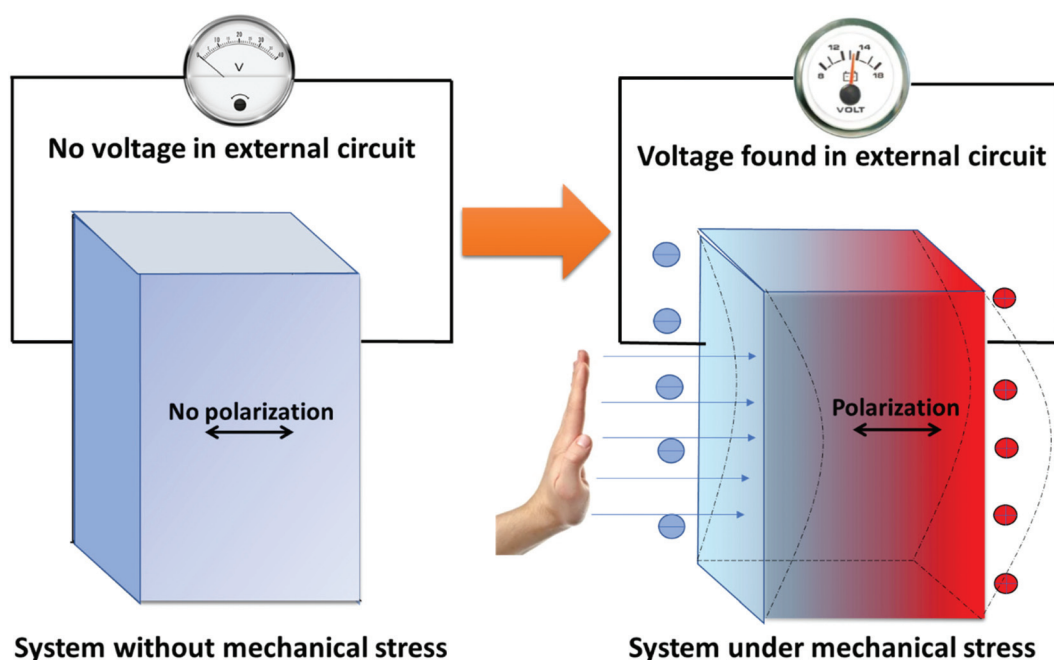
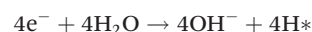


Fig. 1 The mechanical energy mediated generation of electrical energy in the external circuit showing the mechanism of piezoelectric energy generation.

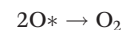
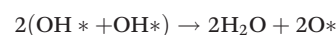
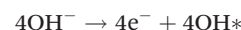
At the anode, the piezo-induced electrons on the surface of the catalyst entrap the H_2 from water to produce hydrogen radicals (H^*), thereby forming H_2 gas and OH^* . Whereas at the cathode, these hydroxyl radicals (OH^*) are released through the holes and trap electrons on the hydroxyl groups. The degradation of pollutants is primarily caused by such OH^* radicals in aqueous media.¹⁰

Piezocatalyst + mechanical energy \rightarrow Piezocatalyst ($e^- + h^+$)

Anodic reactions:



Cathodic reactions:



Pollutant degradation:

$OH^* + \text{pollutant} \rightarrow \text{degradation product of the pollutant}$

$e^- + \text{pollutant} \rightarrow \text{degradation product of the pollutant}$

$h^+ + \text{pollutant} \rightarrow \text{degradation product of the pollutant}$

2.3 Design and fabrication

It is observed that in a wide range of piezoelectric materials the particle size and morphology are key parameters enhancing the piezoelectric efficiency. It is found that 1-D fiber/wire like materials exhibit a better piezocatalytic response compared to spherical particles. On the other hand, thin sheet-like 2-D structures also exhibit better piezoelectricity. In reality, a theoretical piezoelectric output is directly proportional to the size of the catalyst as stated below,³³

$$V_p = d_{ij}\sigma_j\omega_i/\epsilon_0\epsilon_{r,i}$$

where V_p is the piezoelectric open circuit potential, σ_j is the



Sukhen Das

Prof. Sukhen Das is currently the Head of Department of Physics, Jadavpur University, India. He has guided several doctoral and post-doctoral fellows and has more than 200 research publications in reputed journals. Other than Jadavpur University, Prof. Sukhen Das has also been appointed as a visiting professor at the University of Virginia, USA; North Virginia Community college, USA; and New York University, USA. Prof. Das's

research area includes the development of ceramics, polymeric materials, antimicrobial bio-ceramics and nanomaterials for the development of piezoelectric probes and sensors. Recently, he and his group have done extensive research on fluorometric sensors to combat wastewater pollution.

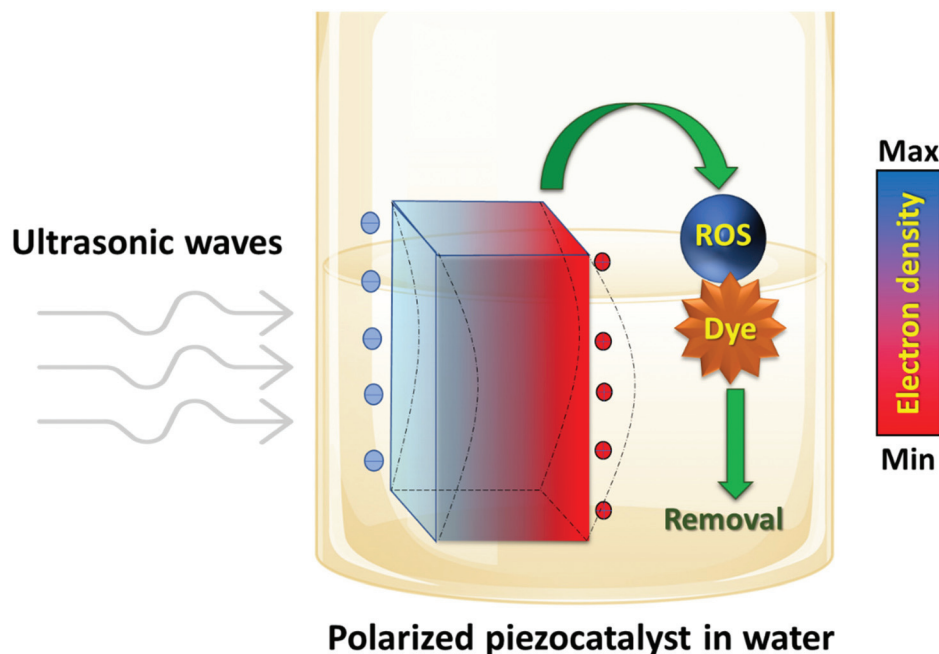


Fig. 2 The mechanism of the piezocatalytic degradation of hazardous dye molecules depicting the generation of piezo-response mediated ROS.

applied stress in the j direction, d_{ij} is the piezoelectric charge coefficient, ω_i is the length of the piezocatalyst in the i direction of polarization and $\epsilon_{r,i}$ is the relative permittivity in the i direction and ϵ_0 is the permittivity in the open space. Piezoelectricity of any material can be defined by a series of piezoelectric coefficients such as piezoelectric charge constants d_{ij} (e.g., d_{11} , d_{33}) or dielectric constants (e.g., ϵ_{11}^T , or ϵ_{22}^T), which are among the best indicators of the potential performance of any given piezoelectric material. Hence, piezoelectric polymer nanocomposites with high d_{ij} values are quite effective in generating a high piezo-response in order to eliminate contaminants from wastewater. The catalysis generally occurs in both the electrodes upon external piezo-stimulation.³³

However, piezocatalytic composite powders are difficult to recycle in practical applications. Sometimes they cause secondary pollution and therefore it is necessary to prepare piezoelectric composite films with great recyclability.³²

On the other hand, external piezo-stimulation is an important parameter for achieving better catalytic activity. Generally, ultrasound of 20–40 kHz has been widely used to 'excite' piezocatalysts in bath or probe sonication systems. The acoustic pressure in these systems does not exceed 2 bar, which might not be sufficient to exert adequate stress on piezocatalysts. Additionally, continuous sonication for a prolonged duration causes internal heat generation. This could be addressed by replacing the water in the bath or adding ice cubes/water during the experiment. However, such addition or alteration could greatly influence the piezocatalytic efficacy. These drawbacks have been minimized by collapsing the cavitation bubbles with pressures up to 10^8 Pa and simultaneously using modern temperature controlled ultrasonic bath systems.³³

3. Recent advances in polymer based piezocatalysts

Although various nanoparticles have emerged as fast and efficient piezocatalysts, most of them suffer from practical feasibility due to their direct decomposition in water, creating several problems in terms of stability, efficacy, accumulation, toxicity, separation and recyclability. Nowadays, researchers are focusing on polymer based piezocatalysts to overcome such drawbacks for practical applicability. Polymers offer robust, reliable, flexible, and cost-effective substrates that can be extensively used and do not agglomerate or degrade due to ambient environmental conditions.

3.1 Synthetic polymers

After the discovery of piezocatalysis by Hong *et al.* in 2010, various groups have started exploring synthetic polymers for this purpose. Piezoelectric poly(vinylidene fluoride) (PVDF) has become a favorable candidate in the field of piezocatalytic degradation of contaminants. This semicrystalline polymer has five crystalline polymorphs, namely, α , β , γ , δ and ϵ . Among them, the most common piezo-responsive stable polymorph of PVDF is the polar β -phase.³⁴ Generally, the β -phase is present in a very low amount in pristine PVDF but it can be enhanced by incorporating various nanostructures by means of their surface charges. Under mechanical vibration, the piezocatalyst (β -PVDF) produces polarization, which can be harnessed as electrical energy. This further drives electrons through an external circuit. After the release of the external stress, the electrons flow in the opposite direction, which

results in the generation of a negative potential. Such charge center separation drives the electron-hole pairs to either direction for effective piezocatalysis.¹³

The first work on PVDF based piezocatalysis was reported by Dong *et al.* in 2017. The authors fabricated an e-skin using PVDF/TiO₂ nanofibers for methylene blue degradation.³⁵ These electrospun TiO₂ nanowires were enforced inside the PVDF polymer for this purpose. The process involves a hybrid piezo-photocatalyst, where the TiO₂ performs the photodegradation while the PVDF moiety contributes to the piezo-response. The TiO₂ nanostructure herein promotes the electrons from the valence band to the conduction band using the piezo-response leaving the holes in the valence state. These electron-hole pairs initiate the catalytic activity tremendously. According to this report the hybrid PVDF based e-skin completely degraded the dye solution within 40 minutes of external mechanical vibration. Besides, ZnSnO₃ (ZTO) was also recognized as an efficient piezocatalyst that modulates the band structure of the system to manipulate the dye degradation efficacy.³⁶ In this case, the external ultrasonic stimulation bends the band edges for better electron-hole separation. The dye degradation efficacy was found to be $1.5 \times 10^{-2} \text{ min}^{-1}$ under the ultrasonic stress, which is approximately four times higher than that in the absence of the ultrasonic vibration. The ZTO nanowire also exhibits a synergistic piezophotocatalytic effect that was further enhanced by encapsulating ZTO into PVDF and polymethyl methacrylate (PMMA) matrices.³⁶ It is observed that an irregular alignment of ZTO nanowires on the ITO surface experiences uneven polarization when the mechanical stress is applied. Surprisingly, the polymer coated ZTO shows better polarization due to the flexibility of the polymer, which causes better reception of the external stress, resulting in a better piezoelectric effect. Furthermore, the efficacy of the PVDF-ZnSnO₃ nanocomposite has been drastically improved by incorporating hydrothermally grown Co₃O₄ nanoparticles.³⁷ The piezo-degradation efficiency reached 100% within 20 minutes for both methylene blue (rate constant $\sim 43 \times 10^{-3} \text{ min}^{-1}$) and rhodamine-B (rate constant $\sim 45 \times 10^{-3} \text{ min}^{-1}$) dyes. This catalytic enhancement is attributed to the fact that the hydroxyl radical ($\cdot\text{OH}$) and superoxide radical ($\cdot\text{O}_2^-$) generated during ultrasonic stress play a pivotal role in degrading the dyes. In reality, ZnSnO₃ induces the polarizability of PVDF, whereas Co₃O₄ improves the charge transport mechanism for efficient redox reactions, which causes the generation of the superoxide radicals under ultrasonic vibrations.

Piezoelectric wurtzite ZnO nanocrystals have also emerged as promising piezocatalysts in recent times. Wu *et al.* (2020)³⁸ have introduced the novel concept that the utilization of mechanical stress generated from natural water flow accelerates the piezo-response for water pollutant degradation. Wu and group fabricated two different nanocomposites, namely, ZnO@PVDF and ZnO@PDMS, for rhodamine-B degradation. The ZnO@PVDF film exhibited 10 times better performance than ZnO@PDMS which might be due to the piezoelectric effect in the case of PVDF. It promotes the migration of photo-

generated carriers under the stress generated from water flow. Moreover, the ZnO@PVDF film having more extensive (1 0 0) polar plane exposure shows an enhancement in active catalytic sites and causes better piezocatalytic degradation. Thus, this work paved a new path for the synergistic utilization of solar energy and natural water flow for better degradation of contaminants using the piezophotocatalytic effect. Besides dye degradation, certain research studies also dealt with the degradation of other contaminants such as pharmaceutical pollutants or microbial contaminants.³⁹ A recent work by Singh *et al.* 2021⁴⁰ focusses on the piezocatalytic removal of pharmaceutical and bacterial pollutants using a flexible PVDF membrane intercalated by the well-known antibacterial silver nanoparticles embedded in the LiNbO₃ nanostructure. This is probably the first time when pharmaceutical pollutants like tetracycline (69%) and ciprofloxacin (53%) have been decomposed within 2 h using a piezoresponse (Fig. 3). Additionally, this work reports the facile degradation of numerous pathogenic bacteria like *Escherichia coli* (99.999%) and *Staphylococcus aureus* (96.65%) within 180 minutes under vigorous ultrasound treatment (Fig. 4).⁴⁰ The Ag-LiNbO₃ nanocomposite enhances the β -phase PVDF, which in turn increases the piezoelectric nature. Under mechanical stress (from sonication) it generates free charge carriers which move opposite of the polarization field. Some of the free charge carriers ultimately interact with the O₂ and OH⁻ ions, resulting in the production of ROS ($\cdot\text{OH}$ and $\cdot\text{O}_2^-$) which performs the dual application of the degradation of pharmaceuticals and the generation of oxidative stress and lipid peroxidation that ultimately damages the nucleic acids and enzyme activity of bacteria, resulting in their death. Moreover, the occurrence of band bending due to the piezoelectric effect accelerates the migration of free charge carriers facilitating this process. This activity of ROS for contaminant degradation was explored by Bagchi *et al.* (2020), who illustrated a free-standing film made of PVDF wrapped MoS₂ nanoflowers for the degradation of rhodamine-B.¹³ The composite film was synthesized using a simple solution casting method. This novel material gains multifunctionality when a remarkable power density (47.14 mW cm^{-3}) is achieved along with a promising piezocatalytic efficiency (>90% within 20 minutes). The primary resource of such a piezoresponse is attributed to the polarization of the PVDF upon MoS₂ incorporation. The polar β -phase of PVDF was found to be around 80% in this case. The increment of the β -phase radically increases the charge separation process and electron-hole pair formation, thereby producing various reactive oxygen species (ROS). These ROS degrade the rhodamine-B dye in water, making the material suitable for industrial effluent management.

Besides PVDF, MoS₂ nanoflowers, when encapsulated into a polydimethylsiloxane (PDMS) matrix, show excellent piezocatalytic properties as mentioned by Lin *et al.* (2017).⁴¹ Upon applying external mechanical force this polymer nanocomposite degrades the rhodamine-B dye with an efficacy of 67% under dark conditions. The degradation efficacy remains unaltered even after four test cycles. Thus, it can be believed

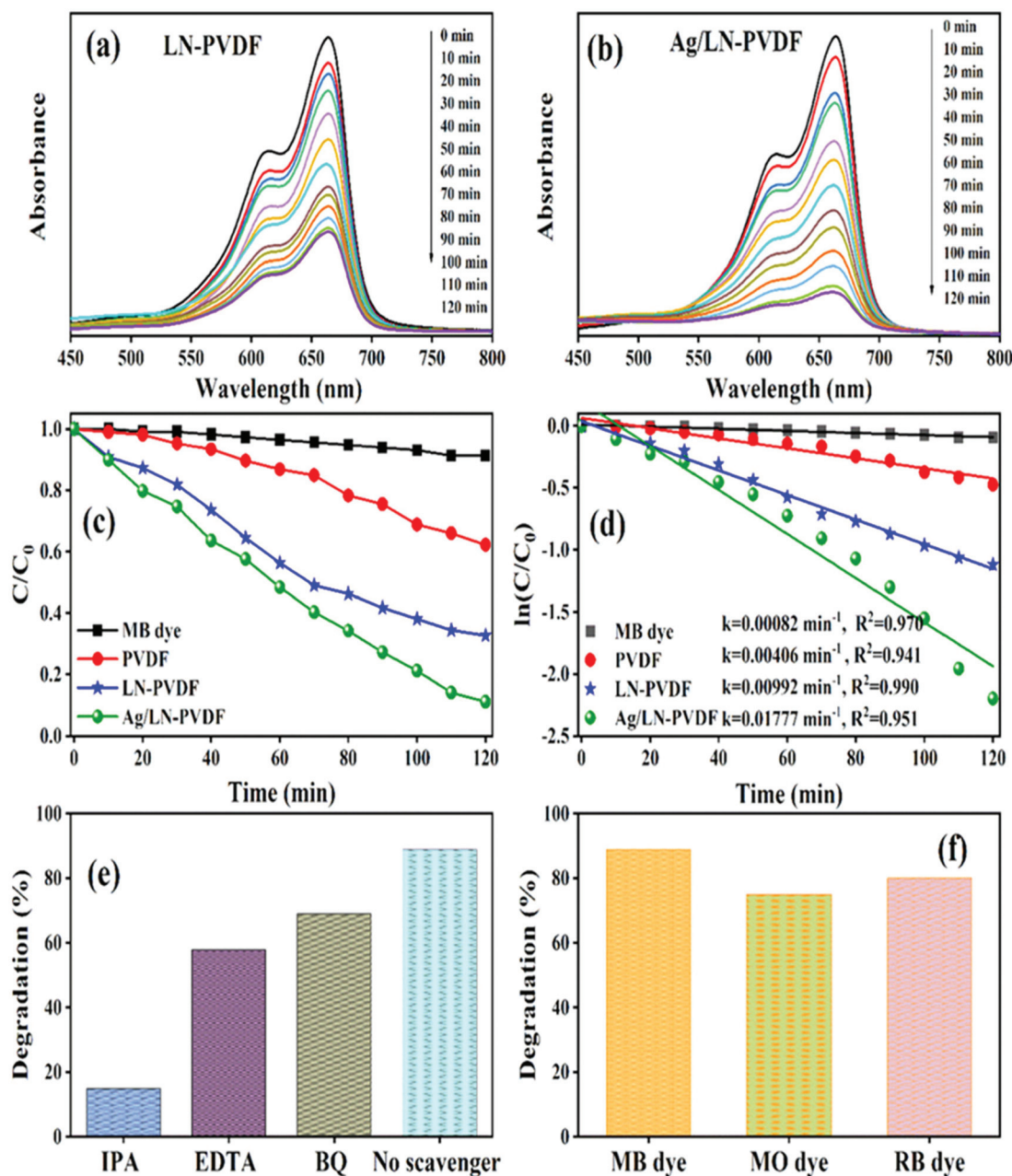


Fig. 3 UV-visible spectra illustrating the piezocatalytic degradation of the MB dye solution recorded at different vibration times using LN-PVDF (a) and Ag/LN-PVDF composite films (b); variation in (c) dye concentration in terms of C/C_0 and (d) dye degradation rate with vibration time; (e) effect of scavengers on percent dye degradation through piezocatalysis; (f) piezocatalytic dye degradation percentage in various dyes using Ag/LN-PVDF composite films. Adapted with permission from ref. 40 copyright (2021) American Chemical Society.

that the catalytic efficiency of this composite is entirely dependent on the external piezo-response. This novel piezocatalyst also acts as a piezoelectric nanogenerator with an output of 23 V, 13 mA m⁻² when placed under a continuous water flow (20 mL s⁻¹). Hydrothermally grown chalcogenide (WS₂) has also been incorporated inside the PDMS polymer for the piezocatalytic degradation of rhodamine-B and pathogenic *E. coli* bacteria (Masimukku *et al.*, 2018).⁴² The degradation efficacies of rhodamine-B and *E. coli* are found to be ~99% and 99.99%

(in 90 minutes), respectively, under ultrasonic vibration. The recyclability of this reported polymer-nanocomposite is quite high (ten cycles) as compared to those of other reported samples. Initially, the piezo-response of the sample was confirmed by tunneling atomic force microscopy and piezo-response force microscopy. Electron paramagnetic microscopy unveils the production of reactive oxygen species (O₂⁻ and OH^{*}), which are primarily responsible for such rapid degradation of the contaminants in water. Another highly stable

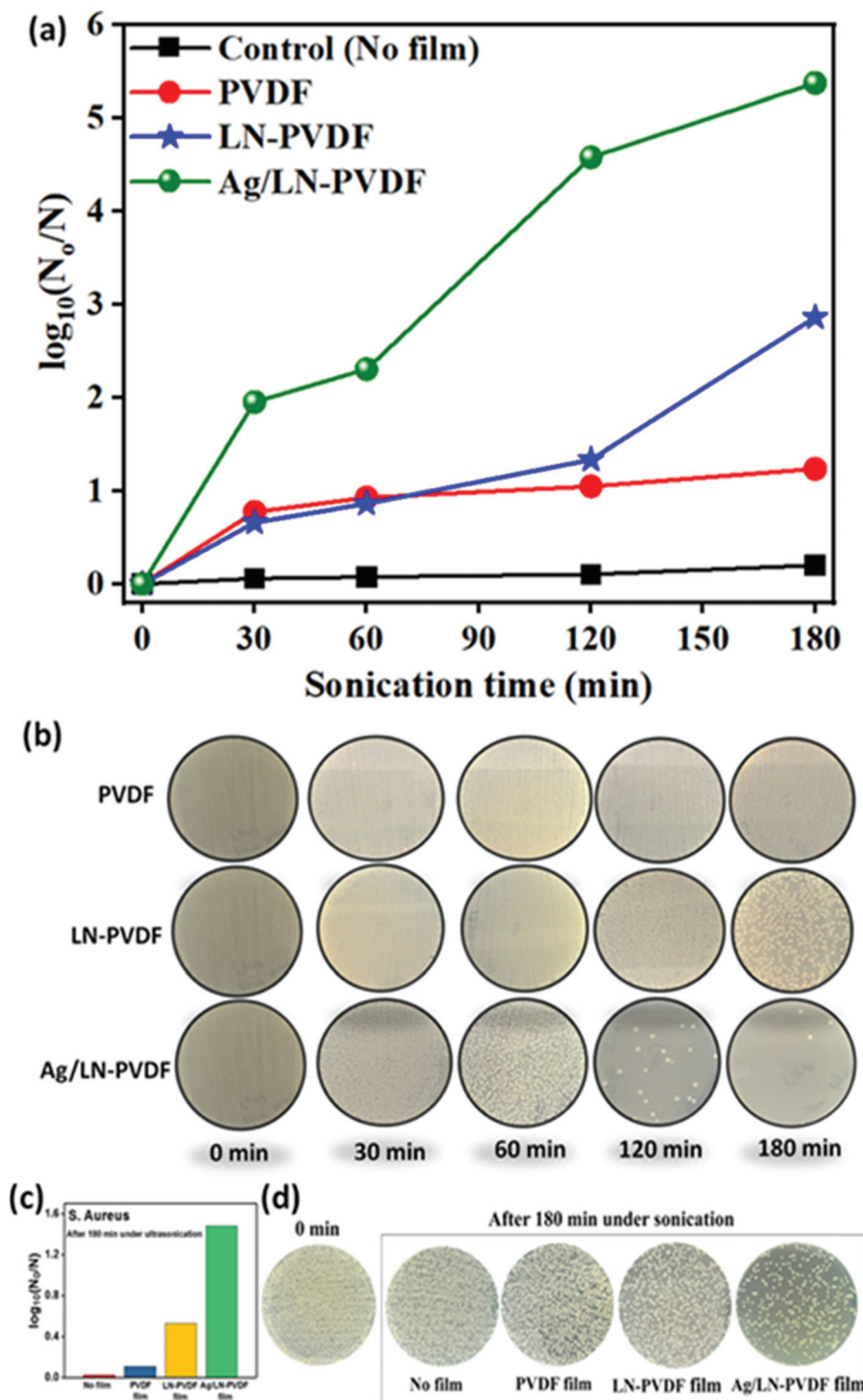


Fig. 4 (a) Time-dependent log reduction of CFUs mL⁻¹ of *E. coli* in various films; (b) illustration of CFUs of *E. coli* on agar plates (1/10 dilution) at various times demonstrating piezocatalytic bacterial disinfection; (c) log reduction of *S. aureus* for various films; (d) CFUs of *S. aureus* on agar plates (1/1000 dilution) before and after 3 h sonication demonstrating piezocatalytic bacterial disinfection. Adapted with permission from ref. 40 copyright (2021) American Chemical Society.

PDMS based nanocomposite (BaTiO₃/PDMS) has been reported to be capable of reducing rhodamine-B contamination using the piezocatalytic method.⁴³ The degradation efficiency of this composite foam is around 94% after twelve

complete cycles. Perovskite-based barium strontium titanate (BST) foam in a PDMS polymer was reported, which successfully enhances the rhodamine-B degradation efficacy radically (275%) when compared to individual photocatalysis.⁴⁴ This

piezocatalytic composite has a degradation efficacy of 97.8% even after ten cycles of repeated catalytic reactions. This hybrid piezo-photocatalyst offers a higher degree of charge center separation, which renders promising catalytic degradation performance.

Polytetrafluoroethylene (PTFE) is known to be a useful polymer with high flexural strength and high electrical resistance. Generally, PTFE is extremely inert even under harsh ambient conditions below 300 °C. Very recently (2021) Wang *et al.* reported a PTFE based ROS generation method in aqueous medium *via* ultrasonic vibration.⁴⁵ This method involves a simple sonication technique to activate the PTFE electret from the polymer. This permanent piezo-responsive polarization is fairly high (~600 pC/N) and even higher than those of conventional piezoelectric polymers (~16 times). In this work the authors have reported the successful decomposition of methyl orange (~89.7%), acid orange-7 and methylene blue (>90%) within 60 minutes of ultrasonic exposure. The activated PTFE coating on the inner walls of a water pipeline has been proposed here for drinking water disinfection. To support this, PTFE membrane mediated degradation of *E. coli* has been studied. The results show a promising bactericidal effect on *E. coli* within 15 min of ultrasonication (99.7%).

Conductive polymers have been widely used over the past two decades in electrical, thermal and thermoelectric applications.⁴⁶ In fact, various implantable medical devices have also been made using conductive polymers. Intercalation of numerous metallic and semiconducting nanomaterials enhances the physicochemical properties of such polymers. Polyaniline is a conductive polymer that exhibits efficient piezoelectric and thermoelectric activities under various cir-

cumstances. Das *et al.* (2017) successfully synthesized an Fe⁰/PANI (polyaniline) nanocomposite by the reductive decomposition method, which successfully degrades Congo red dye under ultrasonic conditions.⁴⁷ This efficient piezocatalyst decomposes ~98% of the initial dye concentration within 30 minutes of mechanical exposure. During ultrasonic irradiation, the excited electrons of the Fe⁰/PANI composite are transferred to the conduction band and generate electron-hole pairs. As a result, the dissolved oxygen and water molecules in the dye solution can react with the electron-hole pairs to produce reactive oxygen species and super-oxides. These reactive species are responsible for the degradation of the dye molecules. Such an excellent piezocatalyst could be a promising agent for wastewater treatment plants.

Though the use of conductive polymers in piezocatalytic dye degradation seems to be a newer concept, the efficacy of these conductive polymers would definitely unlock new avenues in the near future.^{48,49}

3.3 Biopolymers

Biopolymers such as chitin, collagen, cellulose, starch, keratin, and fibrin have the ability to convert mechanical energy and electrical energy.⁵⁰ Hence, the synthesis of efficient, green piezo-electric materials has captured widespread attention.⁵¹

The piezo-electric nature is observed in biopolymers, especially in peptide-based biopolymers, containing L- and D-amino acid isomers but is absent in the DL-forms. This can be attributed to the C=O...CH₃ interactions in the isomers that result in the piezo-response.⁵² Various reports showed that the piezoelectric properties of biopolymers vary greatly with their shape, phase, growth orientation and water content.

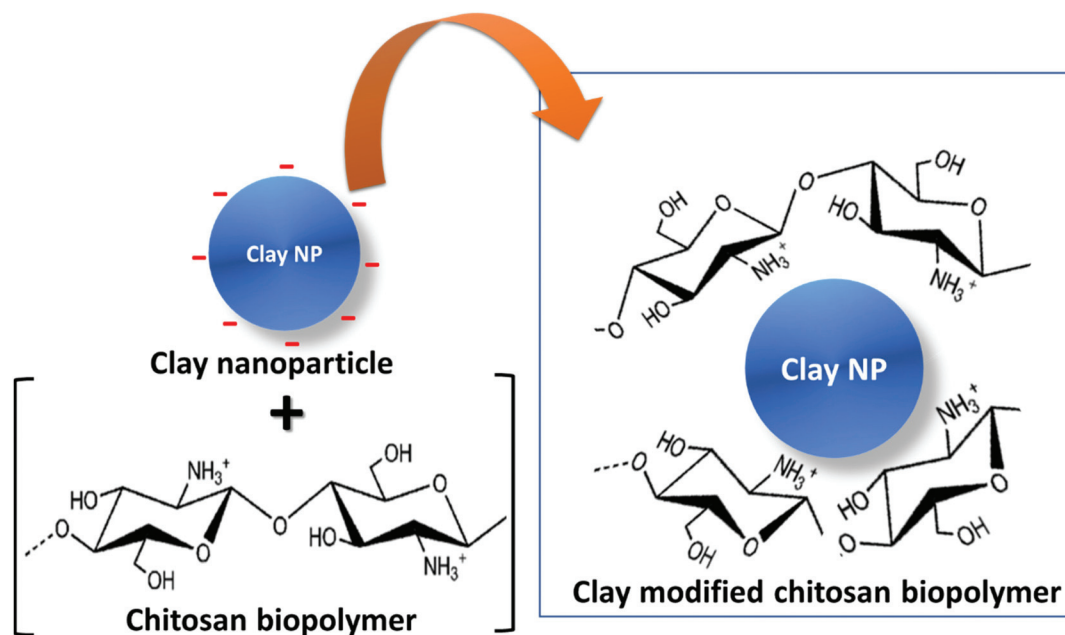


Fig. 5 Clay nanoparticle intercalation mechanism inside the bio-polymeric matrix of a chitosan biopolymer showing the contribution of the surface charge of the clay moiety.

Table 1 Comparison between various piezocatalysts and their catalytic efficacies

Type	Polymer	Targeted effluent	Efficiency (%)	Degradation time (minutes)	Reference
Synthetic	MoS ₂ nano flower/PVDF	Rhodamine-B	>90	20	Bagchi <i>et al.</i> ¹³
Synthetic	TiO ₂ /PVDF	Methylene blue	100	40	Dong <i>et al.</i> ³⁵
Synthetic	PVDF/PMMA-ZnSnO ₃	Methylene blue	71	120	Lin <i>et al.</i> ³⁶
Synthetic	Ag loaded LiNbO ₃ /PVDF	Tetracycline, ciprofloxacin, <i>E. coli</i> and <i>S. aureus</i>	69(TC) 53(CF) 99.999 (EC) 96.65(SA)	120(TC, CF) and 180 (EC, SA)	Sing <i>et al.</i> ⁴⁰
Synthetic	PVDF/ZnSnO ₃ -Co ₃ O ₄	Methylene blue, rhodamine-B	100	20	Raju <i>et al.</i> ³⁷
Synthetic	ZnO/PVDF, ZnO/PDMS	Rhodamine-B	~35(PDMS) ~90(PVDF)	100	Wu <i>et al.</i> ³⁸
Synthetic	Barium strontium titanate/PDMS	Rhodamine-B	97.8	90	Xu <i>et al.</i> ⁴⁴
Synthetic	PDMS/WS ₂ nanoflower	Rhodamine-B, <i>E. coli</i>	99 (RB) 99.99(EC)	90	Masimukku <i>et al.</i> ⁴²
Synthetic	PDMS/MoS ₂	Rhodamine-B	67	200	Lin <i>et al.</i> ⁴¹
Synthetic	BaTiO ₃ /PDMS	Rhodamine-B	94	120	Qian <i>et al.</i> ⁴³
Synthetic	PTFE	Methyl orange, acid orange-7, methylene blue, <i>E. coli</i>	89.7 (MO) >90 (MB, AO7) 99.7 (EC)	60 (MO, MB, AO7) 15 (EC)	Wang <i>et al.</i> ⁴⁵
Synthetic	Fe ⁰ /PANI	Congo red	98	30	Das <i>et al.</i> ⁴⁷
Biopolymer	Chitosan modified montmorillonite	Acid orange-7, basic red, basic yellow	82.74	60	Karaca <i>et al.</i> ⁵⁴

In fact, collagen fibrils predominantly in the axial direction exhibit a much stronger piezo-electric response than those in the radial direction probably due to polarization.⁵³ Among the various forms of chitosan, the α -chitin form found in crab shells and butterfly wings can exhibit a piezo-response due to their non-centrosymmetric crystal structure having intrinsic molecular polarization.⁵⁰ Although various works have been reported on biopolymer based piezo-electric material synthesis and application in nano-generators and sensor fields, piezo-catalyst based wastewater treatment is yet not much invaded. A recent report by Karaca *et al.* shows the generation of a piezo-catalytic response in a montmorillonite loaded natural chitosan biopolymer using ultrasound that can efficiently degrade various dyes like Acid Orange (AO7), Basic Red (BR4), and Basic Yellow (BY2 and BY28) in aqueous solutions.⁵⁴ According to the report, the chitosan structure has $-\text{NH}_3^+$ groups which are attracted towards the negatively charged clay moiety. Such alteration in the microstructure enhances the polarizability of the composite system and contributes to a higher piezoelectric potential (Fig. 5). When this polarized system is stimulated through ultrasonic vibration, an electric field originates which further promotes the generation of free reactive OH* radicals, causing the degradation of the dye. This method can even efficiently remove as much as 82.74% of the dye within an hour. This study paved the path for more such industrially feasible piezo-catalytic biopolymers that can be significant for pollutant removal.

4. Conclusion and outlook

Environmental degradation by toxic effluents from various industrial discharges is utmost essential to combat. Thus, numerous strategies have been implemented to restrict the use of such toxic chemicals and dyes in industries. But global industrialization and the need for technological advancement

enhance the use of carcinogenic precursors exponentially. These toxic effluents discharged from the industries cause enormous harm to the environment. Currently, numerous adsorbents and other chemical catalysts are being used in industries for removing such toxic dyes and pigments. But their limited efficacy and huge cost are unbearable for small scale industries (Table 1). In fact, these conventional catalysts and adsorbents are causing secondary pollution in some cases, which also needs rigorous attention. Piezocatalysis is one of the most promising and efficient ways to combat such a crisis. Polymer-based piezocatalysts have been gaining importance very recently due to their ease of use. These flexible membranes are capable of degrading toxic dyes and heavy metals completely within a few minutes. In fact, polymeric piezocatalysts have been recently used in minimizing bacterial contamination, making them more sustainable and multifunctional. Such multifunctional and effective materials are needed in real life wastewater treatment systems. In some studies, water flow mediated catalytic removal has been achieved successfully. This implies the rise of purely green piezocatalytic systems in near future. Besides various organic and synthetic polymers, biopolymers are gaining importance due to their low-cost and biocompatibility. To date, biopolymers have not been explored in a rigorous way in piezocatalytic systems, as polymer based piezocatalysis is itself a very new approach to degrade dyes and pigments. Although piezocatalysts are showing enormous potential for future applications, there are several challenges that needs to be faced before deploying such systems in real life. It is quite challenging to perform piezocatalysis on a large scale and in stable waterbodies like ponds and reservoirs due to the size of the catalyst. The piezo-response generation in these cases are difficult and will certainly need external mechanical stimuli to drive the system that may reduce the efficacy of the piezocatalytic system by increasing the cost. Therefore, further research on employing piezocatalysts in real life is much needed for better cata-

lytic activity. Moreover, the catalyst takes a long time to decompose the dyes. Thus, a wide area of research is open in this field to fabricate more versatile and multifunctional piezocatalysts that can degrade the effluents rapidly. Another major aspect of piezocatalysis is hydrogen gas generation. During the experiment, H₂ gas releases in a moderate amount and could be used for fuel cell and other energy generation applications, if suitably improvised.

Conflicts of interest

The authors declare no conflict of interest.

Acknowledgements

The authors are grateful to the Department of Physics, Jadavpur University, for extending the experimental facilities. D. M. and S. D. would like to acknowledge the DST-SERB (Grant No. EEQ/2018/000747) for funding. S. R. would like to acknowledge the Dept. of Higher Education, Govt. of West Bengal, for providing the SVMCM (Non-NET) fellowship.

References

- 1 S. Roy, S. Bardhan, D. K. Chanda, J. Roy, D. Mondal and S. Das, *ACS Appl. Mater. Interfaces*, 2020, **12**, 43833–43843.
- 2 S. Roy, S. Bardhan, D. K. Chanda, S. Ghosh, D. Mondal, J. Roy and S. Das, *Dalton Trans.*, 2020, **49**, 6607–6615.
- 3 S. Bardhan, S. Roy, D. K. Chanda, D. Mondal, S. Das and S. Das, *Microchim. Acta*, 2021, **188**(4), 1–12.
- 4 S. Roy, K. Pal, S. Bardhan, S. Maity, D. K. Chanda, S. Ghosh, P. Karmakar and S. Das, *Inorg. Chem.*, 2019, **58**, 8369–8378.
- 5 L. Wang, N. R. Stuckert and R. T. Yang, *AIChE J.*, 2011, **57**, 2902–2908.
- 6 M. Sheikhi, S. Shahab, R. Alnajjar and M. Ahmadianarog, *J. Cluster Sci.*, 2018, **30**, 83–96.
- 7 J. Björk, F. Hanke, C.-A. Palma, P. Samori, M. Cecchini and M. Persson, *J. Phys. Chem. Lett.*, 2010, **1**, 3407–3412.
- 8 F. Lin, D. Liu, S. M. Das, N. Prempeh, Y. Hua and J. Lu, *Ind. Eng. Chem. Res.*, 2014, **53**, 1866–1877.
- 9 D. T. Sun, L. Peng, W. S. Reeder, S. M. Moosavi, D. Tiana, D. K. Britt, E. Oveisi and W. L. Queen, *ACS Cent. Sci.*, 2018, **4**, 349–356.
- 10 K. S. Hong, H. Xu, H. Konishi and X. Li, *J. Phys. Chem. C*, 2012, **116**, 13045–13051.
- 11 (a) D. Mani and C. Kumar, *Int. J. Environ. Sci. Technol.*, 2014, **11**, 843–872; (b) Z. Liang, C. F. Yan, S. Rtimi and J. Bandara, *Appl. Catal., B*, 2019, **241**, 256–269.
- 12 Z. Wang, H. Yu, Y. Xiao, L. Zhang, L. Guo, L. Zhang and X. Dong, *Chem. Eng. J.*, 2020, **394**, 125014.
- 13 B. Bagchi, N. A. Hoque, N. Janowicz, S. Das and M. K. Tiwari, *Nano Energy*, 2020, **78**, 105339.
- 14 F. Bösl, T. P. Comyn, P. I. Cowin, F. R. García-García and I. Tudela, *Chem. Eng. J. Adv.*, 2021, **7**, 100133.
- 15 H. Kaczmarek, B. Królikowski, E. Klimiec, M. Chylińska and D. Bajer, *Russ. Chem. Rev.*, 2019, **88**, 749–774.
- 16 E. Lin, N. Qin, J. Wu, B. Yuan, Z. Kang and D. Bao, *ACS Appl. Mater. Interfaces*, 2020, **12**, 14005–14015.
- 17 D. Liu, C. Jin, F. Shan, J. He and F. Wang, *ACS Appl. Mater. Interfaces*, 2020, **12**, 17443–17451.
- 18 S. Ghosh, S. Remita and F. Goubard, *et al.*, *Conjugated Polymer Nanostructures for Energy Conversion and Storage*, Wiley-VCH Verlag GmbH & Co. KGaA, Germany, ISBN:978-3-572-34557-1, 2021, p. 59553.
- 19 Y. Chen, L. Wang, W. Wang and M. Cao, *Appl. Catal., B*, 2017, **209**, 110–117.
- 20 S. Wang, H. Lv, F. Tang, Y. Sun, W. Ji, W. Zhou, X. Shen and C. Zhang, *Chem. Eng. J.*, 2021, **419**, 12945.
- 21 Y. Gao, S. Li, B. Zhao, Q. Zhai, A. Lita, N. S. Dalal, H. W. Kroto and S. F. A. Acquah, *Carbon*, 2014, **77**, 705.
- 22 S. Li, M. Zhang, Y. Gao, B. Bao and S. Wang, *Nano Energy*, 2013, **2**, 1329.
- 23 H. Lin, Z. Wu, Y. Jia, W. Li, R. K. Zheng and H. Luo, *Appl. Phys. Lett.*, 2014, **104**, 162907.
- 24 M. Wang, Y. Zuo, J. Wang, Y. Wang, X. Shen, B. Qiu, L. Cai, F. Zhou, S. P. Lau and Y. Chai, *Adv. Energy Mater.*, 2019, **9**, 1901801.
- 25 B. Yuan, J. Wu, N. Qin, E. Lin and D. Bao, *ACS Appl. Nano Mater.*, 2018, **1**, 5119.
- 26 K. S. Hong, H. Xu, H. Konishi and X. Li, *J. Phys. Chem. Lett.*, 2010, **1**, 997.
- 27 K. S. Hong, H. Xu, H. Konishi and X. Li, *J. Phys. Chem. C*, 2012, **116**, 13045.
- 28 D. Tan, M. Willatzen and Z. L. Wang, *Nano Energy*, 2019, **56**, 512.
- 29 K. H. Michel and B. Verberck, *Phys. Rev. B: Condens. Matter Mater. Phys.*, 2011, **83**, 115328.
- 30 K. A. N. Duerloo, M. T. Ong and E. J. Reed, *J. Phys. Chem. Lett.*, 2012, **3**, 2871.
- 31 S. Li, Z. Zhao, D. Yu, J. Z. Zhao, Y. Su, Y. Liu, Y. Lin, W. Liu, H. Xu and Z. Zhang, *Nano Energy*, 2019, **66**, 104083.
- 32 (a) S. Tu, Y. Guo, Y. Zhang, C. Hu, T. Zhang, T. Ma and H. Huang, *Adv. Funct. Mater.*, 2020, **30**, 2005158; (b) J. M. Ji, H. Zhou, Y. K. Eom, C. H. Kim and H. K. Kim, *Adv. Energy Mater.*, 2020, **10**, 2000124.
- 33 F. Bösl and I. Tudela, *Curr. Opin. Green Sustain. Chem.*, 2021, **32**, 100537.
- 34 P. Thakur, A. Kool, B. Bagchi, N. A. Hoque, S. Das and P. Nandy, *RSC Adv.*, 2015, **5**, 62819–62827.
- 35 C. Dong, Y. Fu, W. Zang, H. He, L. Xing and X. Xue, *Appl. Surf. Sci.*, 2017, **416**, 424–431.
- 36 H. M. Lin and K. S. Chang, *RSC Adv.*, 2017, **7**, 30513–30520.
- 37 T. D. Raju, S. Veeralingam and S. Badhulika, *ACS Appl. Nano Mater.*, 2020, **3**, 4777–4787.
- 38 W. Wu, X. Yin, B. Dai, J. Kou, Y. Ni and C. Lu, *Appl. Surf. Sci.*, 2020, **517**, 146119.
- 39 W. Ma, B. Yao, W. Zhang, Y. He, Y. Yu, J. Niu and C. Wang, *Environ. Sci.: Nano*, 2018, **5**, 2876–2887.

- 40 G. Singh, M. Sharma and R. Vaish, *ACS Appl. Mater. Interfaces*, 2021, **13**, 22914–22925.
- 41 J. H. Lin, Y. H. Tsao, M. H. Wu, T. M. Chou, Z. H. Lin and J. M. Wu, *Nano Energy*, 2017, **31**, 575–581.
- 42 S. Masimukku, Y. C. Hu, Z. H. Lin, S. W. Chan, T. M. Chou and J. M. Wu, *Nano Energy*, 2018, **46**, 338–346.
- 43 W. Qian, K. Zhao, D. Zhang, C. R. Bowen, Y. Wang and Y. Yang, *ACS Appl. Mater. Interfaces*, 2019, **11**, 27862–27869.
- 44 S. Xu, W. Qian, D. Zhang, X. Zhao, X. Zhang, C. Li, C. R. Bowen and Y. Yang, *Nano Energy*, 2020, **77**, 105305.
- 45 Y. Wang, Y. Xu, S. Dong, P. Wang, W. Chen, Z. Lu, D. Ye, B. Pan, D. Wu, C. D. Vecitis and G. Gao, *Nat. Commun.*, 2021, **12**(1), 1–8.
- 46 S. Maity, N. Sepay, C. Kulsi, A. Kool, S. Das, D. Banerjee and K. Chatterjee, *ChemistrySelect*, 2018, **3**, 8992–8997.
- 47 R. Das, M. Bhaumik, S. Giri and A. Maity, *Ultrason. Sonochem.*, 2017, **37**, 600–613.
- 48 Y. Xu, L. Jin, X. He, X. Huang, M. Xie, C. Wang, C. Zhang, W. Yang, F. Meng and J. Lu, *J. Mater. Chem. A*, 2019, **7**, 1810–1823.
- 49 S. Ghosh, T. Maiyalagan and R. N. Basu, *Nanoscale*, 2016, **8**, 6921.
- 50 N. A. Hoque, P. Thakur, P. Biswas, Md. M. Saikh, S. Roy, B. Bagchi, S. Das and P. P. Ray, *J. Mater. Chem. A*, 2018, **6**, 13848–13858.
- 51 A. Hänninen, E. Sarlin, I. Lyyra, T. Salpavaara, M. Kellomäki and S. Tuukkanen, *Carbohydr. Polym.*, 2018, **202**, 418–424.
- 52 J. Li, Y. Long, F. Yang and X. Wang, *Curr. Opin. Solid State Mater. Sci.*, 2020, **24**, 100806.
- 53 M. Baniyadi and M. Minary-Jolandan, *Materials*, 2015, **8**, 799–814.
- 54 S. Karaca, E. Ç. Önal, Ö. Açıışlı and A. Khataee, *Mater. Chem. Phys.*, 2021, **260**, 124125.



Particle size mediated investigation of various physicochemical properties of kaolinite clay for fabricating the separator layer of green capacitors

Solanky Das¹, Dhananjoy Mondal², Souravi Bardhan² , Shubham Roy² , Dipak Kr. Chanda³ , Anupam Maity^{2,4}, Subhojit Dutta², Kamalakanta Mukherjee², and Kaustuv Das^{2,*}

¹Department of Geological Sciences, Jadavpur University, Kolkata 700032, India

²Department of Physics, Jadavpur University, Raja S.C. Mullick Road, Kolkata 700032, India

³Advanced Materials and Mechanical Characterization Division, CSIR-Central Glass and Ceramics Research Institute, Kolkata 700032, India

⁴School of Materials Science, Indian Association for the Cultivation of Science, Kolkata 700032, India

Received: 24 August 2021

Accepted: 1 February 2022

© The Author(s), under exclusive licence to Springer Science+Business Media, LLC, part of Springer Nature 2022

ABSTRACT

This article reports size fractionation of a natural clay namely kaolinite for fabricating cost-effective green separator material for energy storage devices. kaolinite is reportedly biocompatible and abundantly available in nature, which makes it cost-effective. Such a low-cost clay is found to be in the nano regime when treated in a ball-milling machine for a prolonged duration (12 h). The enhancement in porosity and surface area have also been observed in the treated nano-clay, which subsequently renders its dielectric constant (~ 5000 at 40 Hz frequency) remarkably. Henceforth, it can be argued that crystallinity and aspect ratio (S/V) has a prominent impact on the electrical properties of this natural clay. Cyclic voltammetry and galvanostatic charging–discharging measurements depict high specific capacitance ($\sim 185 \text{ F g}^{-1}$) in the nano-clay sample without the presence of any redox peak making it a good separator material. The slow electrical discharge rate also approves the storage property of this clay sample quite effectively. Abundance, augmented permittivity with a relatively low tangent loss, high specific capacitance and significant resistivity through the material make this nano-clay material a promising ‘green’ dielectric separator for energy storage applications.

Address correspondence to E-mail: kaustuv12@gmail.com

<https://doi.org/10.1007/s10854-022-07894-7>

Published online: 11 February 2022

1 Introduction

Traditional ways of energy harvesting involve batteries and capacitors having harmful materials like lead, mercury and various acids that can harm the local environment [1, 2]. These traditional devices are costly due to their complicated fabrication process and high-cost ingredients. Additionally, proper management of such industrial discharge from these traditional battery and capacitor industries put additional costs to the manufacturers. Thus, scientists and technologists are working on alternative energy harvesting devices, such as green capacitors and green batteries [3]. Although these green energy harvesting technologies cause less harm to the environment, the manufacturing cost of these green technologies is higher than the traditional ones in some cases.

In the present scenario, naturally formed minerals are gaining interest among material scientists and industries due to their biocompatibility, less toxicity and availability [4, 5]. These cost-effective green materials are having enormous potential in various research fields, including energy harvesting and energy generation for their remarkable physicochemical properties [6, 7]. A few recent reports established the fact that these natural materials can be exceptionally functional if properly engineered [8–12]. Controlled incorporation of foreign elements, size fractionation via different routes, composite formations is some of the techniques that have been reported recently [13, 14].

In reality, particle size and crystallinity play a pivotal role [15] when it comes to the physicochemical properties of a material. Materials having finer particles show prominent surface properties compared to their bulk counterparts [16]. Various physicochemical properties, such as optical, chemical, electrical, magnetic, and catalytic activities can be modulated by varying the surface to volume ratio [17–20]. Thus, proper modification of these naturally formed minerals could be highly beneficial to achieve greater functionality.

The emphasis of this work is given to study the effect of nanonization on the functionalization of naturally formed kaolinite clay; one of the most abundant clay minerals on the Earth's crust [21]. Despite the abundance of kaolinite in nature, an insufficient amount of interest is given to study the

electrical properties of this material as a function of size, temperature and crystallinity. In general, kaolinite is reported to have a lower dielectric constant value of ~ 11 at microwave frequency [22] and is mostly used in the ceramic and porcelain industry [23]. To enhance the dielectric constant and to reduce the tangent loss, various dopants like NaF, Fe, Mn, Co, Cr, Co, Ga, Mg and Mg-Ni are used or sintered at very high temperatures [24, 25]. In contrast, mechanical grinding is a facile, cost-effective technique that not only reduces the hassles associated with firing at higher temperatures or chances of secondary pollution from dopants but also shows a significant increment in the dielectric permittivity value. Hence in this paper, a facile ball-milling approach has been followed herein to achieve kaolinite nanostructure to enhance dielectric properties to meet the practical application. Moreover, a detailed analysis of crystallography and microstructure mediated dielectric property variation and temperature stability study has been performed. The analyses of the dielectric constant and conduction mechanism of this green material show that the sample in the nano-domain has the lowest degree of crystallinity along with the highest charge storage capacity compared to its other fractions. This naturally available clay mineral is a low-cost material that depicts augmented electrical permittivity in nano-domain along with promising resistivity and nominal tangent loss, which is reported herein for the very first time. This high electrical permittivity value makes this nano-kaolinite sample an ameliorative agent for fabricating the separator layer of the green capacitors, which will minimize the manufacturing cost along with the environmental pollution.

2 Experimental section

2.1 Materials

Natural kaolinite ($\text{Al}_2\text{Si}_2\text{O}_5(\text{OH})_4$) clay was obtained from Hindustan Minerals, India. The potassium bromide and acetone used in the experiment were purchased from Merck, India. All the purchased reagents are of analytical grades and were used without any further purification. Millipore water used in the following experiments has a resistivity of approximately $18 \text{ M}\Omega\text{-cm}$.

2.2 Top-down synthesis of natural kaolinite in different sizes

Initially, the purchased kaolinite sample was crushed with the help of a diamond mortar manually to reduce the agglomeration. A part of the crushed sample was sieved with the help of a 400 mesh sieve. The sample above the sieve was collected as the bulk fraction (K1) and the sample below the sieve (K2) was kept for further mechanical milling process. 5 gm of this sieved sample (K2) was then subjected to mechanical milling in a Fritsch Planetary Mono mill Pulverisette 6 ball-mill machine with the help of tungsten carbide vial and balls for 12 h at 300 rpm. The milled clay sample was washed in water and then collected and dried in a hot air oven. The dried sample was further washed in acetone to reduce impurities and dried in a hot air oven for another 12 h at 60 °C. Finally, the dried fine sample was marked as K3. The entire set of samples were then sent for further characterizations.

3 Results and discussion

3.1 Purity and elemental analysis of bulk kaolinite

The elemental analysis of the kaolinite samples has been done by employing EDX and XRF techniques.

Initially, the XRF data of the bulk kaolinite has been plotted in Table 1, which validates the presence of 66.3% of silicate and 30.7% of alumina in the sample. It is quite evident from Table 1 that the percentage purity of this sample is around 97.1%. In reality, the ratio of alumina and silica in pure kaolinite is 0.5, which is found to be 0.476 in our sample. This ratio corroborates the fact that the natural kaolinite is quite pure with a nominal impurity (K_2O and Fe_2O_3) as it has been directly collected from the natural source.

Table 1 Chemical composition (XRF data) of bulk kaolinite

Compound	Concentration (%)
SiO_2	66.3
Al_2O_3	30.7
TiO_2	1.4
K_2O	0.6
Fe_2O_3	0.7

Figures S1 and S2, and Table S1 show the EDX and elemental mapping of the entire sample set. The EDX spectra confirm the traces of Al, Si and O in each case. Elemental mapping by FESEM provides qualitative information about the distribution of elements shown by different colors that are present in the scanned area. It is observed that the marked elements (Al, Si and O) are present in the scanned area in a uniform manner confirming the purity of the samples.

3.2 Determination of crystalline structure and microstructural properties of treated kaolinite samples

Natural materials may contain various impurities and crystallographic defects. Hence the determination of its purity is of utmost importance. XRD is an efficient characterization tool for detecting and quantifying such impurities that occurred at the microstructure. It can determine the crystalline structure and other important microstructural parameters as well [26, 27]. Diffraction maxima of the clay samples (Fig. 1) corroborate with JCPDS card no. 80-0886, which suggests the materials to be kaolinite. The absence of any unwanted diffraction peaks is the primary evidence of its purity [28]. The XRD diffractograms were further refined using the Rietveld-based software package MAUD v2.8 (Material Analysis Using Diffraction) for structural and microstructural investigations. Initially, the refinement of the diffractometer and the detector was done by imposing standard Caglioti PV functions [29]. Instrumental broadening was also corrected during this cycle. A standard crystallographic information file (.cif) of pure kaolinite (AMCSD file no. 1550598) was used to refine the experimental diffractograms. Various microstructural parameters, such as unit cell dimension, crystal size, microstrain was refined to get promising fitting results. The Popa size-strain model was adopted to evaluate the crystal sizes and microstrain values [30]. The anisotropic crystal size is found to be 113 nm for K1 which has been greatly reduced to 37 nm in nano-engineered K3 sample. The enhancement of microstrain value with decreasing crystallite size is another major outcome of this study (Fig. S4). Unit cell dimensions (a, b, c) have been altered significantly with size (Fig. S4). In reality, ball-milling reduces the particle dimension drastically by reducing the a and b sides of the unit cells and resulting in augmented microstrain values [31].

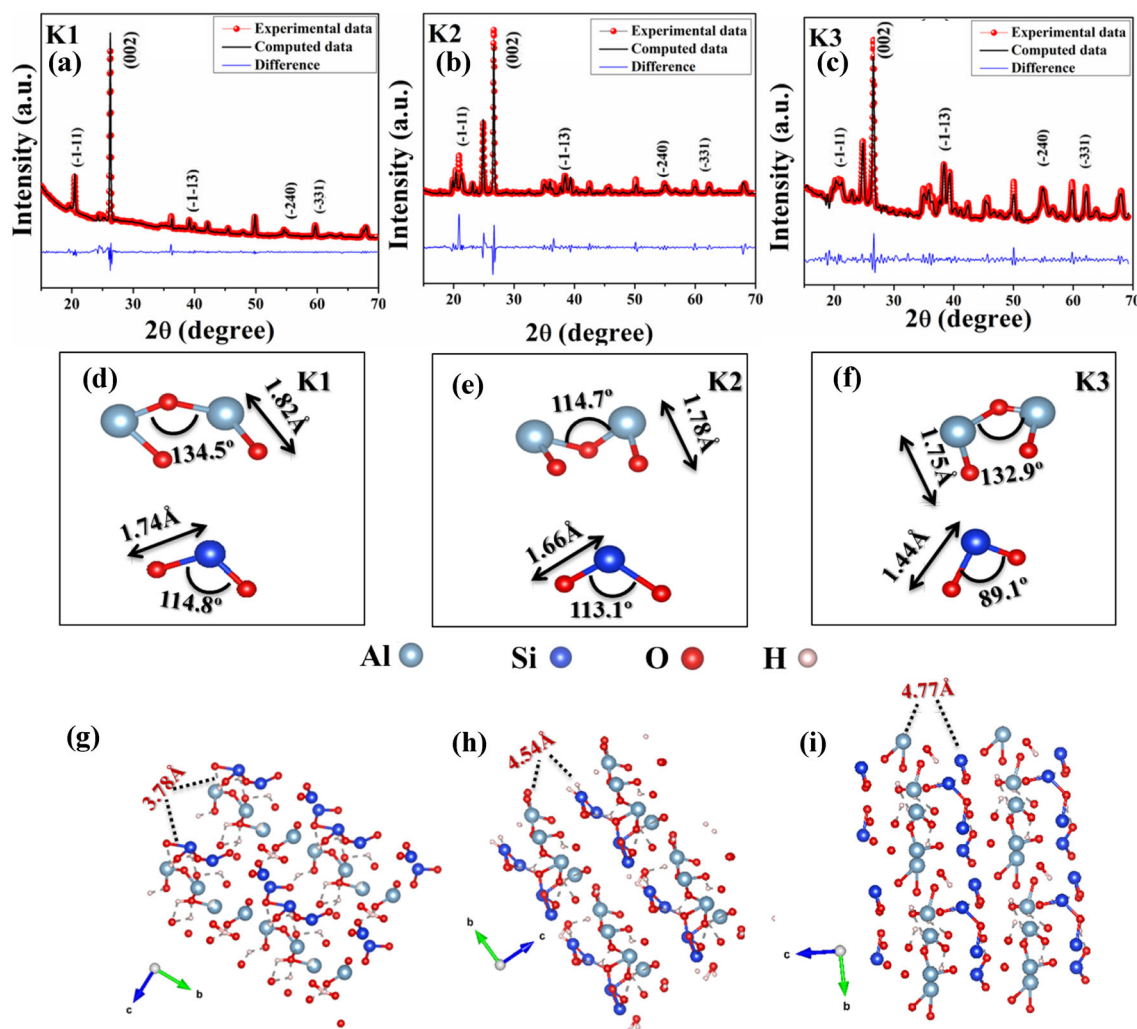


Fig. 1 a–c Indexed XRD pattern (red line) of the sample K1, K2 and K3, and the simulated Rietveld refinement plot (continuous black line) obtained by fitting the experimental PXRD pattern using MAUD program. The respective residue is plotted at the

bottom (blue line); d–f bond angles and bond lengths of K1, K2 and K3, respectively, from refinement data; g–i Separation of alumina-silica layers in K1, K2, and K3, respectively (Color figure online)

Fascinatingly, the *c* side of the unit cell increases a bit with decreasing crystallite size. This may be due to the enhanced alumina-silica interlayer spacing (basal spacing) in this direction [8]. The texture analyses along with the atomic positions were also refined to get reasonable fitting data. The global reliability parameters (R_{wp} and R_p) are relatively low implying the consistency of the refinements. All the parameters were refined for at least fifteen cycles and corresponding refinement results (Table 2) were collected as.cif files for further investigations.

The computed.cif files were analyzed using Vesta v3.4.3 (Visualization for Electronic and Structural Analysis) (Fig. S3) showing layered structures of

alumina and silica inside the kaolinite unit cells. The separation of these alumina-silica layers is measured (Fig. 1) confirming a gradual increment of this basal separation with decreasing crystallite size. In the case of K1, the basal spacing is around 3.78 Å, whereas, it is found to be 4.77 Å for K3. Not only the alumina-silica separation varies, but also the cell volume is enhanced with decreasing crystallite size. This may be due to the bond energy minimization caused by ball-milling [32], which slackens the bond structure in the ball-milled samples (especially K3). Henceforth, bond lengths and bond angles have been calculated (Fig. 1) to justify this part. With increasing treatment time, Al–O and Si–O bond lengths have been slightly

Table 2 Structural and microstructural parameters of the samples obtained from various characterization techniques including refinement of the XRD diffractograms

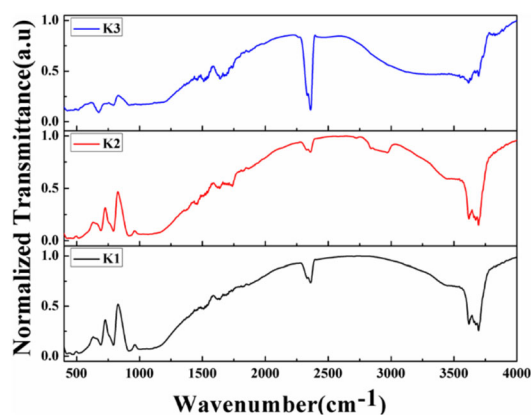
Microstructural parameters	K1	K2	K3
a (Å)	5.201 ± 0.002	5.171 ± 0.001	5.142 ± 0.001
b (Å)	9.006 ± 0.003	8.958 ± 0.002	8.956 ± 0.002
c (Å)	7.357 ± 0.002	7.409 ± 0.002	7.430 ± 0.001
α (°)	91.00	91.61	92.10
β (°)	105.11	104.87	104.89
γ (°)	91.09	89.96	90.40
Volume (Å ³)	326.568	329.610	331.491
R_{wp} (%)	4.71	6.74	6.32
R_p (%)	2.58	3.00	4.52
Crystallite size (nm)	114	104	38
microstrain	0.0016	0.0023	0.0028
Surface area (m ² g ⁻¹)	123.7	126.6	129.2
Pore size (nm)	5.4	15.5	18.7
Pore volume (ml g ⁻¹)	0.206	0.491	0.520
Alumina-silica basal spacing (Å)	3.78	4.54	4.77
Al–O bond length (Å)	1.819	1.776	1.746
Si–O bond length (Å)	1.745	1.664	1.444
Al–O–Al angle (°)	134.5	114.7	132.9
O–Si–O angle (°)	114.8	113.1	89.1

reduced which further reduces the Al–O–Al and O–Si–O angles (Table 2) resulting in enhanced basal separation (Table 2). Thus, it is observed that external stimulation, such as ball-milling significantly influences the crystal structure of natural kaolinite clay.

3.3 Spectroscopic study and bonding network analysis

Phase purity at the molecular level was investigated using FTIR spectrometry and it is depicted in Fig. 2. The absorption bands situated at 431, 460 and 520 cm⁻¹ are attributed to Si–O, Si–O–Si and Si–O–Al bending, respectively. Absorption bands at 695 and

798 cm⁻¹ are attributed to Si–O bending. Deformation of Al–Al–OH bonds creates its signature absorption band at 919 cm⁻¹ [33]. The band corresponding to Si–O stretching mode is observed between 940 and 1150 cm⁻¹. Such observations suggest that the samples are kaolinite as they have signature vibrational bands in their respective positions. The vibrational band located at 1643 cm⁻¹ corresponds to H–O–H bond vibration. The band related to bending of H–OH can be observed at 3627 and 3695 cm⁻¹ due to the presence of external and internal –OH, respectively [34]. These bands are reduced greatly in the K3 sample depicting the fact that K3 absorbs less moisture from the local environment than the other two size fractions. Absorption bands observed at 2334 and 2367 cm⁻¹ are caused due to the presence of adsorbed atmospheric CO₂ [35]. The enhanced aspect ratio (S/V) significantly advances the surface porosity and adsorption capacity of K3, which further enhances the CO₂ adsorption capacity of this sample. A similar phenomenon has been reported elsewhere [36].

**Fig. 2** Normalized FTIR spectra of the samples K1, K2 and K3

3.4 Morphological studies and particle size analysis

The alteration in morphology due to ball-milling and reduction in particle size has been ascertained using Field Emission Scanning Electron Microscopy

(FESEM). The micrographs are provided in Fig. 3. kaolinite generally shows basal and edge surfaces and hexagonal plate-like structures [37, 38]. FESEM micrographs show that particles of K1 are an admixture of distinctly large and heavily agglomerated, along with the presence of few smaller particles. These plate-like structures are having diameters around 300–310 nm. This is due to the uneven grinding of natural kaolinite. K2 on the other hand shows evenly distributed sheet-like structures of kaolinite having diameters ranging from 200 to 220 nm. The width of the size distribution for K2 is smaller than that of K1 as Fig. 3 suggests. This evenly distributed particle size is attributed to the sieving during size fractionation. Although K1 and K2 depict 2D plate-like structures, K3 shows completely different morphological aspects. Due to high-energy mechanical ball-milling, this size fraction of kaolinite depicts a mixture of spherical and rhomboidal particles. This type of morphological evolution occurred due to the continuous friction between the sample and the balls during the ball-milling process [28]. In this case, not only does the morphology change but also the particle size reduces significantly. K3 sample possesses an average diameter of 90–100 nm, which makes it a natural nano-system.

3.5 Surface area and porosity analyses

Estimation of average surface area and surface porosity of the prepared samples (K1, K2 and K3) were done by employing Brunauer–Emmett–Teller (BET) and Barrer–Joyner–Halenda (BJH) methods. The adsorption–desorption isotherms obtained along with pore size distributions are illustrated in Fig. 4. The hysteresis loop obtained from these experiments suggests the type IV isotherm, presumably due to the presence of mesopores [39, 40]. In the case of K2 and K3, volumes of adsorbed and desorbed N₂ gas are very similar to each other, unlike K1, which might be due to the uniformity in size distributions, as seen in FESEM micrographs [41]. The surface area obtained for K1 is found to be 123.7 m² g^{−1}, while for K2 and K3, it is found to be 126.6 and 129.2 m² g^{−1}, respectively. Thus, there is an increase in surface area with decreasing particle size. The average pore diameter was found to be 5.4, 15.5 and 18.7 nm for K1, K2 and K3, respectively. Similarly, the pore volume also increases with a decrease in particle size (Table 2), which suggests the nanonized K3 sample to be a promising material for various industrial applications.

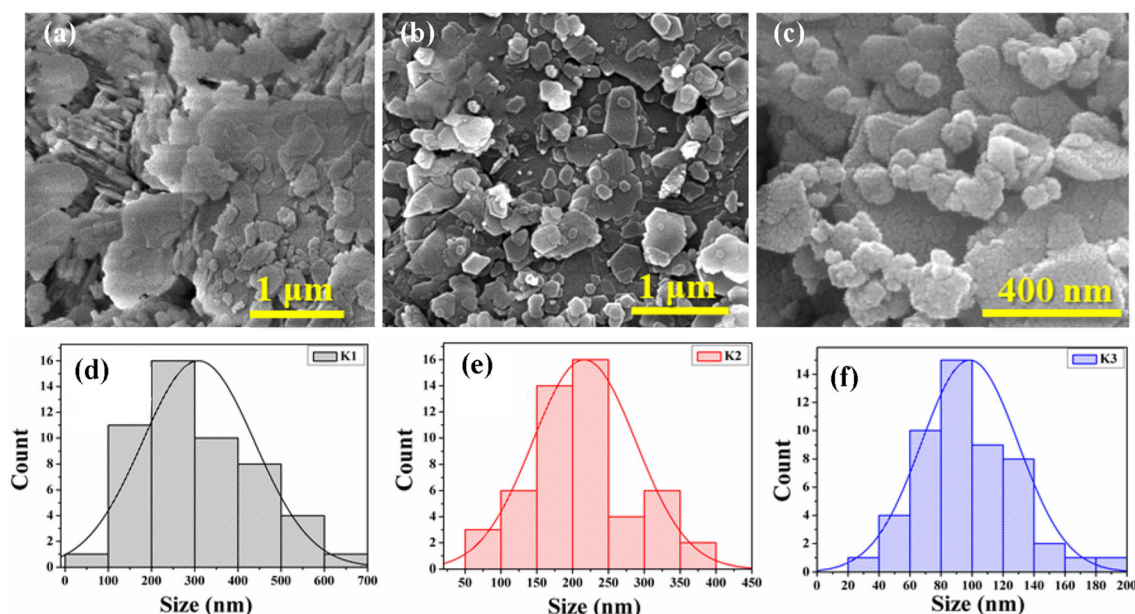


Fig. 3 FESEM micrographs of the samples **a** K1, **b** K2, and **c** K3, corresponding size distribution plots from the FESEM images (**d–f**)

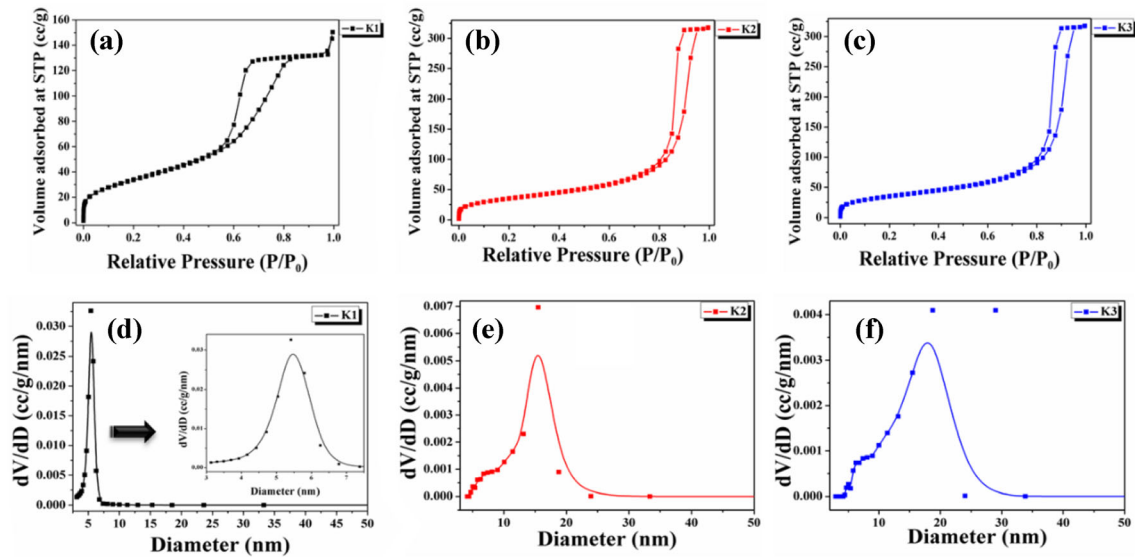


Fig. 4 N_2 adsorption/desorption isotherms of the samples **a** K1, **b** K2, and **c** K3; Pore size distribution data for **d** K1, **e** K2, and **f** K3

3.6 Thermal characterization of the natural materials

Thermal characterizations are very much needed for electronic materials as electrical properties, such as dielectric constant, specific capacitance and conductivity are quite vulnerable to temperature fluctuations [36]. DTA-TGA measurements have been performed to check the temperature stability of the synthesized natural samples (Fig. S5). It is found that the overall mass loss is highest in the K3 sample ($\sim 6\%$), whereas, it is lower in K1 (0.5%) and K2 (0.8%). This is probably due to the release of surface adsorbed moisture and CO_2 from the K3 sample. The enhanced surface porosity of the K3 sample accommodates a higher amount of moisture and environmental CO_2 as stated in our FT-IR result. At higher temperatures, these volatile substances have been eliminated from the surface of the K3 causing a broad endothermic peak located just above $50^\circ C$. There is no sign of any alternative phase formation due to heating (up to $200^\circ C$), which makes these samples quite stable.

3.7 Estimation of dielectric constant and loss tangent of the synthesized samples

Dielectric constant and dielectric loss are very important physical parameters for energy harvesting applications as they reflect the net electrical charge storage capacity of a material. The chemical

composition, thermal stability, surface properties and morphology along with the external applied electric field influences the dielectric properties of a sample. The dielectric response of a material can be described using the following relation [42],

$$\varepsilon = \varepsilon' + j\varepsilon'', \quad (1)$$

where ε' and ε'' are the real and imaginary parts of the relative dielectric constants, respectively, and ε' contributes to the quantity of energy stored in the material due to polarization and also known as dielectric constant, whereas the imaginary part (ε'') is related to the energy dissipated by the material [43]. The real part of the dielectric constant can be calculated using the following relation [44]:

$$\varepsilon' = \frac{Cd}{\varepsilon_0 A}, \quad (2)$$

where C is the capacitance of the sample, d and A are the thickness and surface area of the sample, respectively, and ε_0 is the permittivity of the free space ($8.85 \times 10^{-12} \text{ F m}^{-1}$). The dielectric plots were obtained over a range of varying frequencies (from 40 Hz to 10 MHz) and temperature (30 – $210^\circ C$), as shown in Fig. 5. Since the imaginary part of the electrical permittivity has negligible value, hence not presented here. There is a gradual reduction of permittivity values with increasing frequency is observed in all the samples. This phenomenon is attributed to the Maxwell–Wagner interfacial polarization [45, 46] which is primarily formed due to

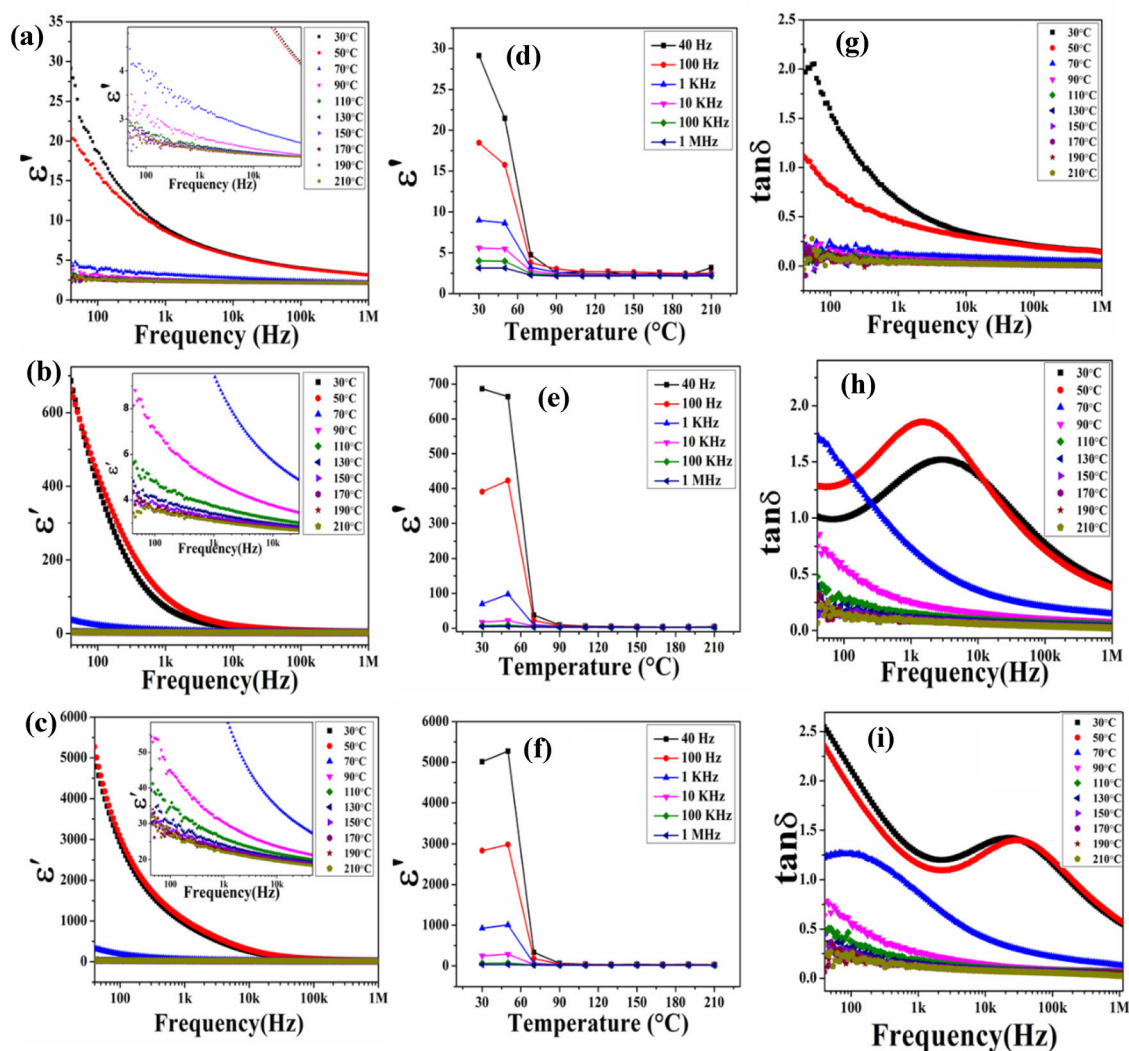


Fig. 5 Variation of the dielectric constants with frequency (a–c); Variation of the dielectric constants with temperature (d–f); Variation of the loss tangent with frequency (g–i) of K1, K2 and K3, respectively,

various structural inhomogeneities, like imperfection in crystal alignment, vacancy and other crystal defects created during the sample preparation. This observation is in good agreement with Koop's theory [47]. According to this theory, the oscillating dipoles formed by the free charge carriers are trapped into the grain boundaries. Those are formed due to structural defects in the low-frequency regime and can easily follow the external field causing high permittivity values, whereas, at higher frequencies, the dipoles cannot trail rapidly changing external fields resulting in reduced permittivity.

The dielectric constant observed is significantly higher in the K3 sample as compared to the other size fractions. Space charge polarization, which increased

in the case of K3 due to lattice or crystal defects might have contributed to such a high value of dielectric constant (ϵ'). In the case of K3, the oxygen vacancies created from high-energy ball-milling lead to a higher number of oscillating dipoles formation [13]. The possibility even enhances when the surface area is equally enhanced in this sample due to nanonization. Thus, a higher surface area with a greater number of interfacial oscillating dipoles augments the permittivity value radically, which is reflected in K3 (5.013×10^3 at 40 Hz) compared to K1 (29.12 at 40 Hz). Table S2 shows a comparison of dielectric values obtained from previous works of literature implying that K3 in our case has the highest permittivity value in both low and high-frequency

regions depicting the novelty of this natural nano-kaolinite system. The temperature-dependent studies of dielectric constant for all three samples have been carried out to ensure the real-life applicability of the synthesized natural materials as dielectric separators. It can be observed from the temperature response data that the dielectric constants for the entire sample set show promising values up to 70 °C beyond which, a rapid fall has been observed. This rapid fall of the dielectric constant is primarily due to the elimination of moisture and adsorbed CO₂ gas from the porous surface of natural kaolinites. The FTIR data previously ensured the presence of these volatile elements inside the porous surface of kaolinite, especially in the K3 fraction due to high porosity and enhanced surface area. It was also evident from thermal characterizations that the mass loss is quite high in K3 at the said temperature range. Thus, beyond 70 °C, a sharp decrement is observed for all the samples. Although, the dielectric value of K3 at 210 °C is (30.30) higher than that of the K1 sample at room temperature (29.12). This ensures that the nanoengineered kaolinite is a better option even in higher temperatures.

The variation of tangent loss (Fig. 5) is also following the dielectric constant values observed herein. It is observed in K2 and K3 that the tangent loss has well-defined peaks at lower temperatures (30–50 °C). This type of tangent loss is generally caused due to the dominance of active elements over the reactive elements in the material. The surface adsorbed moisture and CO₂ act as active elements in this regard, which are greatly removed at higher temperatures (> 70 °C). Additionally, this peak position shifted towards lower frequencies at higher temperatures suggesting the reduction of these polar active elements. The presence of such active elements is higher in K3 as compared to K2 and K1 (from TGA-DTA data). Thus, a greater amount of peak shifting is observed in the K3 sample.

Subsequent removal of adsorbed active elements, such as moisture and surface adsorbed CO₂ from K3 sample at higher temperatures lower its dielectric constant. But the value is still higher than its other size fractions (K1 and K2) even after the removal of active elements making K3 a potential material for charge storage applications. Another major result obtained from this study is the effect of active

elements on dielectric permittivity for natural kaolinite. Moisture affects dielectric constant and loss tangent significantly. Such knowledge will help in storing and fabricating capacitors using this green and natural clay mineral.

3.8 AC conductivity and conduction mechanism studies

To analyze the charge transport mechanism, temperature-dependent ac conductivity studies have been carried out. The ac conductivities of the samples have lower values at lower frequency domains, which increased with subsequent frequency increments due to higher electron mobility and hopping at higher frequencies [48, 49]. The conductivity increases with decreasing particle size (Fig. S6). The enhanced surface area of K3 causes a simultaneous increase in the number of mobile charge carriers that might cause the increase in ac conductivity in this size fraction [28]. K1 shows the lowest value as it has the lowest amount of mobile charge carriers. Frequency response of ac conductivity has also been studied through Jonscher's power law relation (Fig. 6) [45],

$$\sigma_{ac} = B\omega^n, \quad (3)$$

where “B” and “n” are constants. In this case, n is a dimensionless constant, whereas B has the unit of conductivity. The value of “n” has been estimated for each sample by plotting $\ln \sigma$ vs $\ln \omega$ graph and then taking the slope after properly fitting the experimental graphs with the mentioned equation (Eq. 4) in Fig. 6. The estimated values of the “n” in this case are found to be 0.332 and 0.394 for K1 and K2, respectively, which is increased further in K3 (0.312). These non-zero n values corroborate that kaolinite samples do not follow perfectly Debye type (where $n = 0$) conduction mechanism and diffusion-limited hopping dominates in this case [50].

Initially, charge hopping starts when free charge carriers get a sufficient amount of external energy (in the form of heat) to escape from the grain boundaries, known as activation energy (E_a). Thus, it is necessary to study estimate activation energy to establish the conduction mechanism. Activation energies can be calculated using the Arrhenius equation stated as follows [51],

Fig. 6 **a** Jonscher's plot for ensuring the conduction mechanism of the kaolinite samples; **b–d** Arrhenius plots for estimating the activation energies of the samples

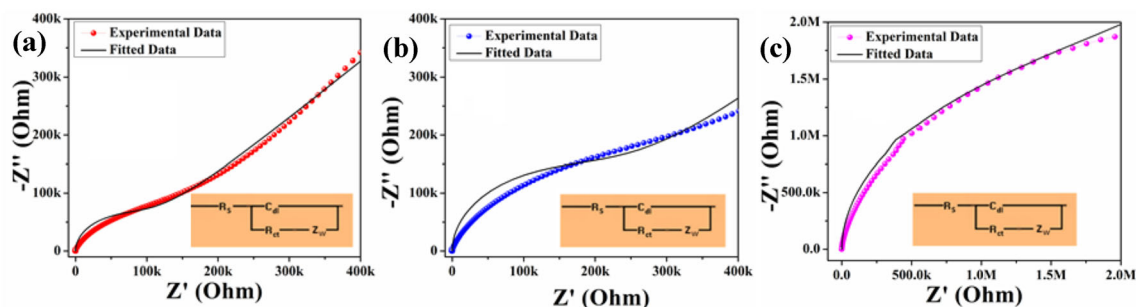
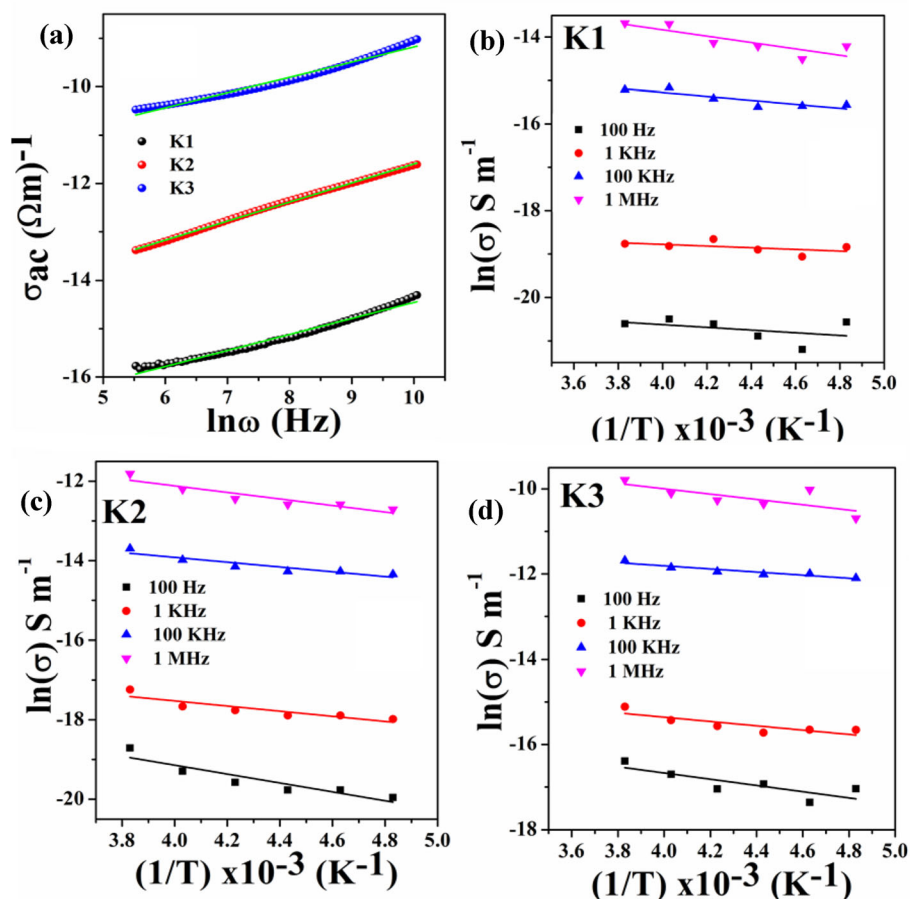


Fig. 7 Impedance plots of **a** K1, **b** K2 and **c** K3, respectively, with equivalent circuits

$$\sigma = \sigma_0 e^{\frac{-E_a}{K_B T}}, \quad (4)$$

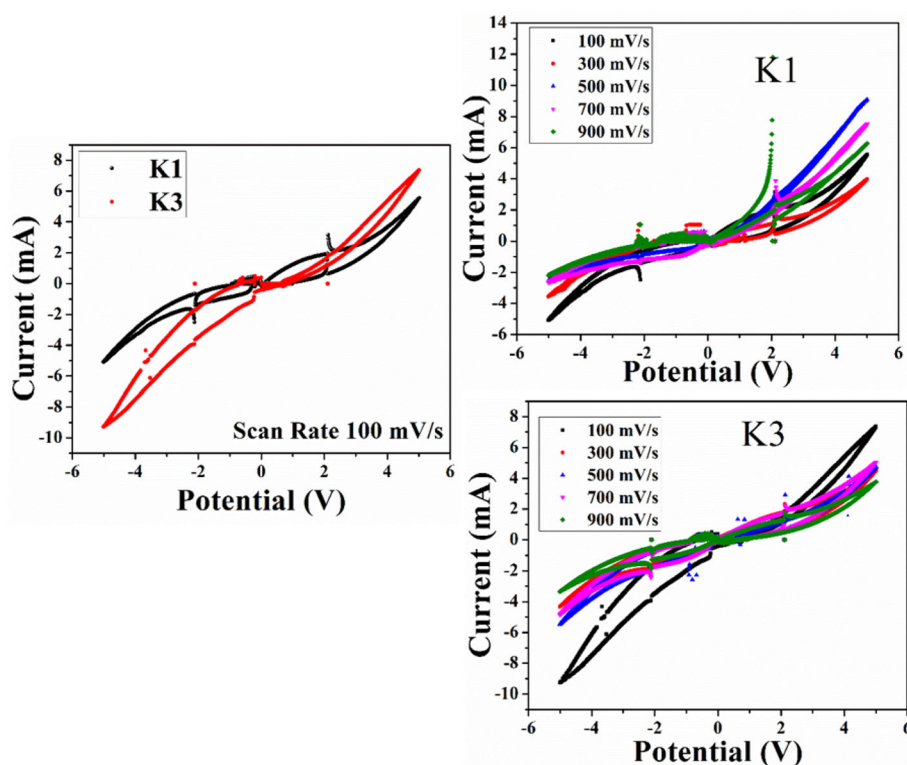
where σ_0 be the pre-exponential factor, E_a is the activation energy, K_B is the Boltzmann constant and T is the absolute temperature. Arrhenius plots were calculated from the temperature-dependent ac conductivity data at field frequencies 100 Hz, 1 kHz, 100 kHz and 1 MHz (Fig. 6). A detailed description of activation energies of the entire sample set is given in Table S3.

3.9 Impedance spectroscopy for electrode-material interface analysis

Impedance spectroscopy is a useful tool to understand the charge migration process at the electrode-electrolyte/separator interfaces. This also provides a brief idea about the overall resistivity of the sample, which is essential for electrode and dielectric separator applications. Figure 7 shows the impedance plots of different kaolinite samples. The real part of

Table 3 Internal circuit parameters of different kaolinite samples obtained by fitting the impedance spectra of the samples

Sample	Charge transfer resistance	Warburg element	Double layer capacitance (μF)
K1	90 $\text{k}\Omega$	90 $\text{k}\Omega$	0.7
K2	205 $\text{k}\Omega$	100 $\text{k}\Omega$	1.2
K3	1.9 $\text{M}\Omega$	350 $\text{k}\Omega$	2.39

Fig. 8 Cyclic voltammetry analysis of K1 and K3 showing the charge storage capacity of the natural samples**Table 4** Comparative specific capacitances at different scan rates for K1 and K3

Sample	Scan rate (mV s^{-1})	Specific capacitance (F g^{-1})
K1	100	93.4
	300	14.5
	500	9.3
	700	5.4
	900	0.7
K3	100	184.6
	300	36.9
	500	22.6
	700	16.2
	900	10.1

the impedance is plotted in the x -axis whereas, the y -axis contains the negative of the imaginary part of complex impedance [52].

The entire set of data shows depressed semi-circular nature at the high-frequency region followed by straight lines situated at lower frequency domains. The radius of semi-circles implies the total charge transfer resistance (R_{ct}) values, which are highest in the case of K3 [52, 53]. The impedance curves were further fitted using the EIS Spectrum Analyser v1.0 program with the standard Randles circuit containing a parallel combination of a charge transfer resistance (R_{ct}) and a double layer capacitance (C_{dl}) combined with a Warburg element (Z_{W}). A series resistance (R_{s}) has also been provided into the circuit. The Randles circuit is widely used to fit impedance data as it approximates the behavior of any cell/interface for very small perturbations. Thus, the accuracy of this model is quite high. According to this theory, R_{ct} restricts the charge migration process through the sample. The double layer capacitance enhances the charge storing capacity of the system. The total

experimental impedance sometimes does not match with the total contributing impedance of R_{ct} and C_{dl} alone. Thus, one needs to consider the Warburg element to match this paradox.

Herein, the outcome of the fitting has been depicted in Fig. 7 showing that the K3 sample has the highest R_{ct} value compared to other samples (Table 3). Such a gradual increment of R_{ct} could be substantiated by the virtue of crystallographic data. In reality, the microstructural data shows a gradual increment of basal spacing (distance between alumina-silica bases), which restricts the charge migration through these basal spaces and results in higher R_{ct} values with reduced sample sizes.

3.10 Estimation of specific capacitance and charge–discharge characteristics

Dielectric permittivity and impedance studies already showed the nanonized K3 is having a decent potential for energy storage applications. Herein, cyclic voltammetry (CV) measurements (Fig. 8) for K3 and K1 have been carried out to understand the alteration of charge storage capacity due to nanonization. The CV curves were obtained between voltages ranging between + 5 V and – 5 V at different

scan rates. The absence of any redox peak in the CV curves ensures the applicability of these materials as separators [54]. The specific capacitance (C_v) has been calculated for both the samples at different scan rates using Eq. (5) and depicted in Table 4 [54].

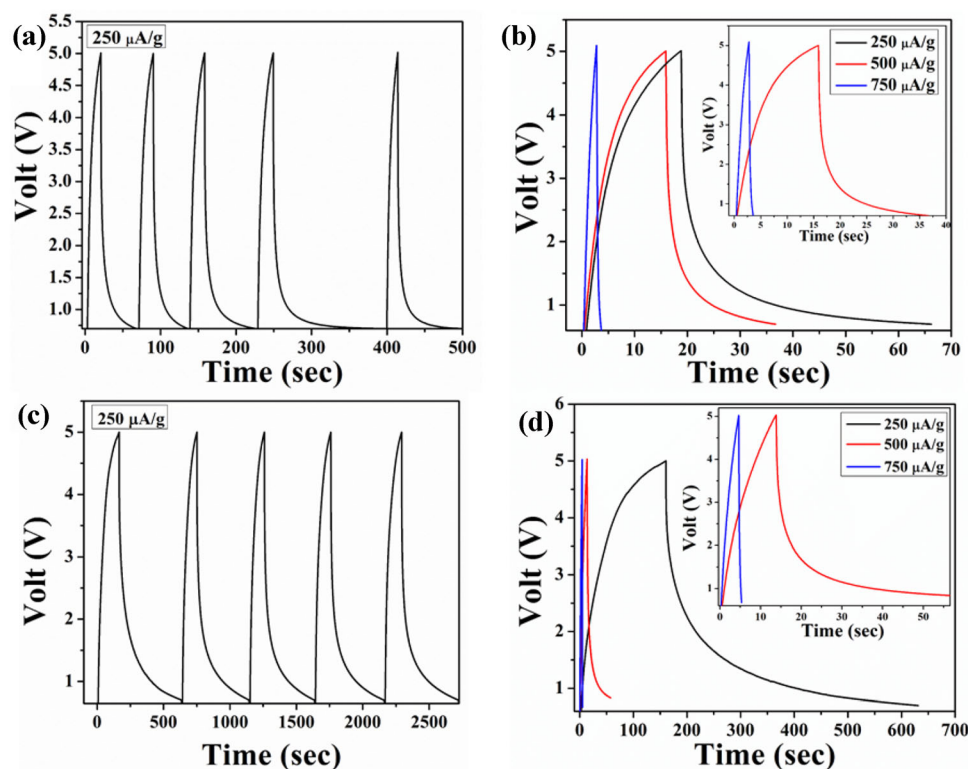
$$C_v = \frac{\int_{E1}^{E2} I(E)dE}{mk(E1 - E2)}, \quad (5)$$

where m be the mass of the material, k is the scan rate, $E1$ and $E2$ are maximum voltages at both ends of the curve and $\int_{E1}^{E2} I(E)dE$ is the area under the CV curve.

It is found that the specific capacity of K3 at 100 mV s^{-1} scan rate is around 185 F g^{-1} , which is significantly higher than K1 (93 F g^{-1}) at the same scan rate. This high value of specific capacitance in a natural dielectric sample is rare and quite useful for fabricating the separator array for a capacitor.

To assess the increment of storage capacity and discharge rate in K3 in comparison to K1, galvanostatic charge–discharge and the performance is illustrated in Fig. 9. The charge–discharge curve shows a rapid increase of voltage during charging, which gradually reduces due to discharging, thus exhibiting reversible and symmetrical charge–discharge cycles and confirming the typical capacitive properties. The

Fig. 9 galvanostatic charge–discharge characteristics of K1 (a, b) and K3 (c, d)



discharging time is much higher (~ 9 times) in K3 in comparison to K1. The specific capacitance was evaluated from the curves using the following equation [55]:

$$C = \frac{2i\Delta t}{m\Delta v}, \quad (6)$$

where C denotes the specific capacitance, i represents discharge current, Δt represents discharging time, the mass of the sample is represented as m and Δv represents the change in the voltage (V). The specific capacitance calculated from the charge–discharge data are quite similar to the calculated capacitance from CV data. The specific capacitance, in this case, is found to be 247 F g^{-1} for K3, whereas it is 83 F g^{-1} for K1 showing an augmented in the charge storage capacity in nano-kaolinite clay.

4 Conclusions

Herein, the particle size reduction of the collected kaolinite clay has been performed by a one-step ball-milling technique for fabricating a separator material for new-generation energy harvesting devices. Initially, the purity of the sample has been assessed by employing XRF and EDX techniques. Moreover, X-ray crystallography and FT-IR spectrometry of the samples reveal the microstructure and bonding networks, which play a pivotal role in assessing the conduction mechanism and charge storage properties of the materials. The FESEM images confirm the impact of ball-milling in reducing the particle size of this clay. These micrographs also validate the K3 sample to be in the nano regime (90–100 nm). Such nano-confinement enriches the aspect ratio in this K3 sample, which is reasonable with its high dielectric constant (~ 5000 in 40 Hz) and higher specific capacitance (185 F g^{-1}). Further, the charge conduction mechanism of the samples has been characterized by standard Arrhenius and Jonscher's equations revealing the diffusion-limited conduction mechanism, which also corroborates the dielectric data. Such interesting dielectric relaxation with enhanced storage capacity makes this nano-kaolinite clay a promising alternative in energy harvesting applications.

Acknowledgements

The authors would like to thank the Department of Physics, Jadavpur University, for extending the experimental facilities. S.R and S.D would like to acknowledge Dept. of Higher Education, Govt. of West Bengal for providing the SVMCM (Non-NET) fellowship.

Author contributions

SD: Data curation, Writing-Original draft preparation. DM: Data curation, Investigation. SB: Writing-Assistance, Conceptualization. SR: Conceptualization, Methodology, Computation, Writing- Original draft preparation. DKC: Writing-Assistance. AM: Data curation, Software. SD: Data curation. KM: Data curation. KD: Supervision, Funding acquisition, Writing-Assistance.

Funding

The authors have not disclosed any funding.

Data availability

The datasets generated during and/or analyzed during the current study are available from the corresponding author on reasonable request.

Declarations

Conflict of interest The authors declare that they have no conflict of interest.

Supplementary Information: The online version contains supplementary material available at <http://doi.org/10.1007/s10854-022-07894-7>.

References

1. H. Wang, A. Jasim, X. Chen, Appl. Energy **212**, 1083 (2018)
2. Y. Choi, K.J. Chen, T.L. Marsh, J. Cust. Behav. **19**, 382 (2020)
3. C. Liu, Z. Shao, J. Wang, C. Lu, Z. Wang, RSC Adv. **6**, 97912 (2016)


4. M.F. Hochella, S.K. Lower, P.A. Maurice, R.L. Penn, N. Sahai, D.L. Sparks, B.S. Twining, *Science* **319**, 1631 (2008)
5. F.W. Clarke, H.S. Washington, *U.S. Geol. Surv. Fre. Pap.* **127**, 117 (1924)
6. C. Xia, Y. Cai, B. Wang, M. Afzal, W. Zhang, A. Soltani-nazarlou, B. Zhu, *J. Power Sources* **342**, 779 (2017)
7. N. Nabbou, M. Belhachemi, M. Boumelik, T. Merzougui, D. Lahcene, Y. Harek, A.A. Zorpas, M. Jeguirim, *C. R. Chim* **22**, 105 (2019)
8. K.G. Bhattacharyya, S.S. Gupta, *Adv. Colloid Interface Sci.* **140**, 114 (2008)
9. K.G. Bhattacharyya, S.S. Gupta, *Colloids Surf. A* **277**, 191 (2006)
10. R. Polanský, P. Kadlec, Z. Kolská, V. Švorčík, *Appl. Clay Sci.* **147**, 19 (2017)
11. Y. Lan, Y. Liu, J. Li, D. Chen, G. He, I.P. Parkin, *Adv. Sci.* **8**, 2004036 (2021)
12. N.T.H. Chu, Q.L.D. Ngo, H.T.T. Le, *Mater. Sci. Fourm.* **985**, 124 (2020)
13. S. Bardhan, S. Roy, D.K. Chanda, S. Das, K. Pal, A. Chakraborty, R. Basu, S. Das, *Cryst. Growth Des.* **19**, 4588 (2019)
14. B.K. Paul, D. Roy, S. Batabyal, A. Bhattacharya, P. Nandy, S. Das, *Mater. Chem. Phys.* **187**, 119 (2017)
15. S. Roy, S. Bardhan, K. Pal, S. Ghosh, P. Mandal, S. Das, S. Das, *J. Alloys Compd.* **763**, 749 (2018)
16. P. Borm, F.C. Klaessig, T.D. Landry, B. Moudgil, J. Pauluhn, K. Thomas, R. Trottier, S. Wood, *Toxicol. Sci.* **90**, 23 (2006)
17. S. Sarkar, K.K. Chattopadhyay, *Physica E* **44**, 1742 (2012)
18. S. Biswas, H. Fukushima, L.T. Drzal, *Compos. A* **42**, 371 (2011)
19. Z. Xiang, Y. Song, D. Pan, Y. Shen, L. Qian, Z. Luo, Y. Liu, H. Yang, H. Yan, W. Lu, *J. Alloys Compd.* **744**, 432 (2018)
20. F.G. Verheijen, A. Zhuravel, F.C. Silva, A. Amaro, M. Ben-Hur, J.J. Keizer, *Geoderma* **347**, 194 (2019)
21. G. Ngnie, G.K. Dedzo, C. Detellier, *Dalton Trans.* **45**, 9065 (2016)
22. G.R. Olhoeft, US Department of the Interior, Geological Survey, (1979)
23. Y. Al-Ramadin, A.M. Zihlif, Z.M. Elimat, G. Ragosta, J. Thermoplast. Compos. Mater. **22**, 617–632 (2009)
24. B.L. Zhu, C.L. Qi, Y.H. Zhang, T. Bisson, Z. Xu, Y.J. Fan, Z.X. Sun, *Appl. Clay Sci.* **179**, 105138 (2019)
25. H. Zıpkın, L. Israel, S. Güler, Ç. Güler, *Ceram. Int.* **33**, 663–667 (2007)
26. J.T. Klopogge, Springer, Cham, **434**, pp. 97 (2019)
27. R. Ghosh, S. Kundu, R. Majumder, S. Roy, S. Das, A. Banerjee, U. Guria, M. Banerjee, M.K. Bera, K.M. Subhedar, M.P. Chowdhury, *Appl. Nanosci.* **9**, 1939 (2019)
28. S. Bardhan, K. Pal, S. Roy, S. Das, A. Chakraborty, P. Karmakar, R. Basu, S. Das, *J. Nanosci. Nanotechnol.* **19**, 7112 (2019)
29. M.T. Cooper, R. Nathans, *Acta Cryst.* **23**, 357 (1967)
30. N.C. Popa, *J. Appl. Crystallogr.* **31**, 176 (1998)
31. N. Salah, S.S. Habib, Z.H. Khan, A. Memic, A. Azam, E. Alarfaj, N. Zahed, S. Al-Hamedi, *Int. J. Nanomed.* **6**, 863 (2011)
32. L.E. Brus, *J. Chem. Phys.* **80**, 4403 (1984)
33. C. Li, Y. Huang, X. Dong, Z. Sun, X. Duan, B. Ren, S. Zheng, D.D. Dionysiou, *Appl. Catal. B* **247**, 10 (2019)
34. J. Li, X. Zuo, X. Zhao, J. Ouyang, H. Yang, *Appl. Clay Sci.* **173**, 12 (2019)
35. T. Sahraoui, H. Belhouchet, M. Heraiz, N. Brihi, A. Guermat, *Ceram. Int.* **42**, 12185 (2016)
36. N. Nagarajan, H. Humadi, I. Zhitomirsky, *Electrochim. Acta* **51**, 3039 (2006)
37. E. Pefferkorn, L. Nabzar, A. Carroy, *J. Colloid Interface Sci.* **106**, 94 (1985)
38. N. Kumar, C. Zhao, A. Klaassen, D. van den Ende, F. Mugele, I. Siretanu, *Geochim. Cosmochim. Acta* **175**, 100 (2016)
39. D.K. Chanda, D. Mukherjee, P.S. Das, C.K. Ghosh, A.K. Mukhopadhyay, *Mater. Res. Express* **5**, 075027 (2018)
40. S. Roy, K. Pal, S. Bardhan, S. Maity, D.K. Chanda, S. Ghosh, P. Karmakar, S. Das, *Inorg. Chem.* **58**, 8369 (2019)
41. S. Roy, A. Maity, P. Mandal, D.K. Chand, K. Pal, S. Bardhan, S. Das, *CrystEngComm* **20**, 6338 (2018)
42. V. Usha, S. Kalyanaraman, R. Vettumperumal, R. Thangavel, *Physica B* **504**, 63 (2017)
43. S. Roy, S. Bardhan, D.K. Chanda, S. Ghosh, D. Mondal, J. Roy, S. Das, *Dalton Trans.* **49**, 6607 (2020)
44. A.S. Lanje, S.J. Sharma, R.S. Ningthoujam, J.S. Ahn, R.B. Pote, *Adv. Powder Technol.* **24**, 331 (2013)
45. D. Chuprinko, K. Titov, *Geophys. J. Int.* **209**, 186 (2017)
46. S. Das, S. Das, A. Roychowdhury, D. Das, S. Sutradhar, *J. Alloys Compd.* **708**, 231 (2017)
47. C.G. Koops, *Phys. Rev.* **83**, 121 (1951)
48. S. Roy, S. Bardhan, D.K. Chanda, A. Maity, S. Ghosh, D. Mondal, S. Singh, S. Das, *Mater. Res. Express* **7**, 025020 (2020)
49. S. Kabashima, T. Kawakubo, *J. Phys. Soc. Jpn.* **24**, 493 (1968)
50. S.K. Saha, M.A. Rahman, M.R. Sarkar, M. Shahjahan, M.K. Khan, *J. Semiconduct.* **36**, 033004 (2015)
51. F. Jensen, *Qual. Reliab. Eng. Int.* **1**, 13 (1985)
52. S. Samanta, A. Maity, S. Roy, S. Giri, D. Chakravorty, *J. Phys. Chem. C* **124**, 21155 (2020)

53. A. Maity, S. Samanta, S. Chatterjee, R. Maiti, D. Biswas, S.K. Saha, D. Chakravorty, J. Phys. D Appl. Phys. **51**, 245301 (2018)
54. A. Maity, S. Samanta, S. Roy, D. Biswas, D. Chakravorty, ACS Omega **5**, 12421 (2020)
55. S. Chatterjee, M. Miah, S.K. Saha, D. Chakravorty, J. Phys. D Appl. Phys. **51**, 135301 (2018)

Publisher's Note Springer Nature remains neutral with regard to jurisdictional claims in published maps and institutional affiliations.



Effect of microstructural evolution of natural kaolinite due to MWCNT doping: a futuristic ‘green electrode’ for energy harvesting applications

Dhananjoy Mondal¹, Shubham Roy¹, Souravi Bardhan¹, Ratnottam Das², Anupam Maity³, Dipak Kr. Chanda⁴, Solanky Das⁵, Saheli Ghosh¹, Ruma Basu⁶, and Sukhen Das^{1,*} 

¹Department of Physics, Jadavpur University, Kolkata 700032, India

²Department of Physics, Indian Institute of Technology, Kharagpur 721302, India

³School of Materials Science, Indian Association for the Cultivation of Science, Kolkata 700032, India

⁴School of Materials Science and Nano-Technology, Jadavpur University, Kolkata 700032, India

⁵Department of Geology, Jadavpur University, Kolkata 700032, India

⁶Department of Physics, Jogamaya Devi College, Kolkata 700026, India

Received: 28 January 2022

Accepted: 21 April 2022

© The Author(s), under exclusive licence to Springer Science+Business Media, LLC, part of Springer Nature 2022

ABSTRACT

This study reports the development of natural kaolinite clay-based biocompatible electrode material, which can be a potential alternative for commercial electrodes. The nano-clay has been modified by intercalating multi-walled carbon nanotubes (MWCNT) at different concentrations (0.5%, 1.0%, and 1.5% w/w ratio). Initially, the doping-dependent microstructural alterations of the nanocomposites were determined by the Rietveld refinement technique. Some other features like purity, morphology, surface characteristics, etc. of the nanocomposites have been estimated by Fourier transform infrared spectroscopy (FTIR), electron microscopy, zeta potential, and BET (Brunauer–Emmett–Teller) techniques. Moreover, the thermal stability of this system has been assessed, which shows temperature stability up to 500 °C. This is probably the first report of making an efficient electrode material from MWCNT modified natural kaolinite having an electrical permittivity of 3850 and an ac conductivity of 10^{-4} S/m at room temperature. Additionally, the high specific capacitance of the modified clay (22.4 F/g) suggests the efficiency of the material as an electrode. The cyclic voltammogram data suggests the presence of redox relaxations, making the modified clays suitable candidates for electrode application. This type of natural clay-mediated biocompatible electrode material could be a promising alternative for low-cost energy harvesting devices.

Address correspondence to E-mail: sdasphysics@gmail.com

1 Introduction

Nowadays, due to escalated technological advancement, electrode materials have gained enormous scientific interest. Electrodes have become essential in developing sensors, batteries, capacitors, solar cells, and many other electrical devices [1–3]. The conventional metal-based electrode systems [4] are thus insufficient to reach such technological developments in terms of efficacy. Recently, various ongoing research focuses on semiconductor and nanomaterial-based electrodes due to their significant physicochemical properties [5–7]. Such systems are relatively costlier and need dedicated synthesis processes. Some of these nanomaterial-based electrodes [6, 8] are quite harmful to using toxic chemicals and could be dangerous if handled incautiously.

In the present scenario, material scientists are paying interest in natural clays and minerals [9–11] due to their excellent biocompatibility, less toxicity, chemical and mechanical stability, high cation exchange capacities, large specific surface area, and abundance in nature. These natural materials are cost-effective besides have significant potential in numerous fields of study. In fact, natural mineral-mediated sensors and separators [12–15] are opening new dimensions in materials science. Previously, various natural clays like montmorillonite, smectite, halloysite, palygorskite, and ripidolite gained importance in electrical and electrochemical applications, yet most of them suffer from various drawbacks like very low dielectric permittivity, conductivity, or charge storage capacity (Table 1). The natural clays generally exhibit a low dielectric constant due to the dominance of SiO_2 and Al_2O_3 [16], hence they are mostly used in semiconductor and microelectronic devices fabrication. As per the U.S. Geological Survey report [17], the dielectric constant of kaolinite at 1 MHz is 11.8.

It is evident from certain previous reports that particle size plays a significant role in several electrical characteristics of a material [18, 19]. Herein, MWCNT-loaded nanostructured kaolinite clay has been used to fabricate a ‘green electrode’ system for energy harvesting devices. MWCNT has a very good conductivity besides other physicochemical properties, which greatly influences the electrical properties of nanoparticles. This is probably the first report on MWCNT loading in the low dielectric kaolinite

structure. Kaolinite ($\text{Al}_2\text{Si}_2\text{O}_5(\text{OH})_4$) is primarily a weathered fraction of potassium feldspar and is abundant in our environment [20]. It consists of a periodic arrangement of alumina-silica layers [21]. Such periodicity makes it structurally stable up to a high temperature [22] threshold ($\sim 500^\circ\text{C}$). Impregnated kaolinite over the MWCNT surface makes the composite more electrically active, which has been substantiated here using x-ray crystallography and other electrical characterization techniques. The crystallographic parameters of the sample have been determined by the Rietveld refinement technique. It is an incredibly powerful tool to demonstrate the structural information of the powder diffraction than any other refinement technique. This refinement method was a step forward in line profile analysis of composite structures due to its reliability with strongly overlapping reflections. Interestingly, an electrical percolation threshold has been reached when an excessive amount of doping has been performed. Such percolation not only decays its dielectric permittivity but also reduces the microstructural periodicity of the sample. Electrochemical analyses show the augmented charge transport between the CNT-kaolinite active interfaces, which could be a possible reason for the presence of redox relaxations in the modified clay samples. These redox peaks further substantiate the applicability of the CNT-loaded samples as electrodes. It is observed that the 1% (w/w) MWCNT loaded clay sample exhibits the highest electrical permittivity along with improved redox relaxation among the entire sample set, which makes this sample a futuristic ‘green electrode’ material.

2 Materials and methods

2.1 Materials used

Natural kaolinite [$\text{Si}_2\text{Al}_2\text{O}_5(\text{OH})_4$] clay was purchased from Hindustan minerals, India, and MWCNT (purity > 95%) was purchased from Sigma-Aldrich, Germany. The MWCNTs are having 50–90 nm widths. Hexamine [$\text{C}_6\text{H}_{12}\text{N}_4$], hydrochloric acid [HCl , 37%], nitric acid [HNO_3 , 69%], hydrogen peroxide [H_2O_2 , 30%], and dimethylformamide [$\text{C}_3\text{H}_7\text{NO}$] were purchased from Merck, India. Acetone (HPLC grade) and ethanol (HPLC grade) were purchased from Merck, India for analytical

Table 1 Previous reports on clay-based dielectric performances

Sl no	Material name	Material type	Dielectric constant	AC conductivity (Sm^{-1})	Year	References
1	Epoxy-clay (montmorillonite)	Clay-resin composite	5.35	N.M	2013	[47]
2	Polyester-metakaolinite composite	Clay-polymer composite	14	N.M	2021	[48]
3	K + smectite	Natural clay	3–78	N.M	2020	[49]
4	Modified montmorillonites suspensions in polydimethylsiloxane	Polymeric organosilicate-clay composite	20	10^{-8} – 10^{-7}	2018	[50]
5	Mullite and cordierite	Ceramic	20–40	N.M	2019	[51]
6	Nontronite	Clay	1100	N.M	2021	[52]
7	Poly methyl methacrylate and acrylonitrile butadiene styrene-montmorillonite	Polymer-clay nanocomposite	10	N.M	2021	[53]
8	PVDF/6A Clay	Polymer-clay composite	230	N.M	2021	[54]
9	Ripidolite	Chloride clay	14	N.M	1986	[55]
10	Soil (Clay, Clay Loam, Loam, and Loamy Sand)	Clay	23.26	N.M	2020	[56]
11	MWCNT-kaolinite nanocomposite	CNT-clay nanocomposite	3850	10^{-4}	–	This report

*N.M = Not mentioned

experiments. All the reagents are of analytical grades having purity > 99% and were used without any further purification. Millipore water (NW ultra-pure water system) was used throughout the experiment having a resistivity of approximately $\sim 18.2 \text{ M}\Omega\text{-cm}$.

2.2 Fractionation and activation of natural kaolinite

Initially, the natural kaolinite was ground in a diamond mortar manually to reduce the agglomeration. After that, the clay was sieved by using a 400 mesh (37 μm) sieve. 0.01 kg of the sieved clay was then taken and milled in a ball-milling instrument (Fritsch Planetary Mono Mill Pulverisette-6) for 48 h with a ball to sample mass ratio of 20:1 at 150 rpm using tungsten carbide vials and balls. The milled sample was sent for further modifications.

Activation of the as-prepared nano-kaolinite was performed by dissolving 0.004 kg kaolinite in 160 ml Millipore water and subsequent addition of 9.6×10^{-5} kg hexamine under vigorous stirring conditions. 40 μl HCl solution (37%) was then added drop-wise and kept overnight at 80 $^{\circ}\text{C}$ temperature. The precipitate was collected from the bottom of the container by filtering the solution, which was dried in a hot air oven at 70 $^{\circ}\text{C}$ for another 24 h. The dried sample was then ground in an agate mortar.

2.3 Functionalization of multiwalled-CNT (MWCNT)

Agglomeration of the MWCNT (5×10^{-5} kg) was reduced by dispersing it in 15 ml ethanol followed by an ultrasonication process (Telsonic ultrasonic cleaner 20 kHz). The solvent was then evaporated at 120 $^{\circ}\text{C}$ in a hot air oven. The dried MWCNT was again dispersed in 15 ml HNO_3 (3 M) under stirring (Remi 2MLH magnetic stirrer) for 15 min at 60 $^{\circ}\text{C}$ and then re-sonicated in a bath sonicator for another 2 h. After completion of the sonication process, the sample was rinsed several times with water and further aged with H_2O_2 at 60 $^{\circ}\text{C}$ for 15 min. The black precipitate was then washed using water and collected by vacuum filtration. Finally, the dried sample was sent for further treatment.

2.4 Preparation of MWCNT-kaolinite nanocomposite (CNTK)

The MWCNT-kaolinite nanocomposites were prepared by a simple condensation technique. In a typical synthesis process, 0.001 kg of activated kaolinite was added in 30 ml DMF and sonicated for 1 h. Different weight percentages of functionalized CNTs (0.5%, 1.0%, 1.5% w/w) were added separately into the solutions. The solutions were then stirred

vigorously under reflux condensers for 24 h at 90 °C. The precipitates were collected and washed separately after the complete reaction with deionized water till the neutral pH was achieved. The nanocomposites were then oven-dried at 70 °C for 24 h and marked as CNTK0.5, CNTK1.0, and CNTK1.5 respectively for increasing percentages of MWCNT. A separate unmodified fraction of nano-kaolinite was taken for comparative analyses without any modification and marked as CNTK0. A schematic diagram of the synthesis mechanism is given in scheme 1.

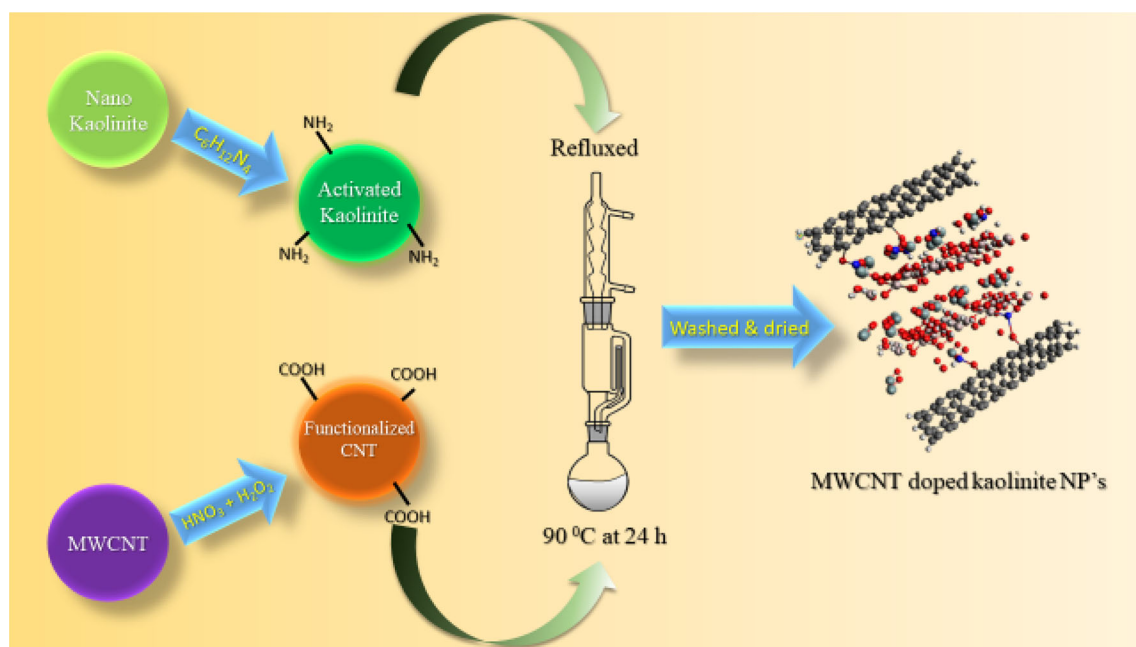
3 Results and discussion

3.1 Structure and morphological analyses of the nanocomposite

Crystallographic parameters are essential to determine the structure and purity of any natural sample. Herein, x-ray diffraction (XRD) has been employed to estimate structural and microstructural parameters of the natural kaolinite and its modified counterparts [23]. A D-8 Advanced, Bruker x-ray diffractometer equipped with Cu-K α target (1.54 Å) was operated at 35 kV, 35 mA with a scan speed of 5 s/step to collect the diffractograms (Fig. 1). It can be observed that the diffraction planes are in accordance with the JCPDS

card no 80-0886 of kaolinite. The absence of any undesired diffraction maxima in the diffractograms suggests the purity of the clay samples [24]. Although kaolinite nanoparticles have been modified by incorporating functionalized MWCNT, no shift of diffraction lines occurred. Such unaltered diffraction lines suggest successful MWCNT-kaolinite composite formation. Further, the Rietveld refinement has been carried out by superposing the standard crystallographic data of kaolinite (AMCSD file no. 1550598) over the experimental data. It shows a promising superposition having reasonable fitting coefficients (Table 2). The microstructural study shows the perturbation of the periodic polyhedral alignment of alumina-silica due to the nanonization of the pristine kaolinite. This could be ascribed to the high-energy ball-milling of the sample. Additionally, MWCNT incorporation leads to an increment in the interlayer separation between the two adjacent basal planes of nano-kaolinite (Fig. 2). Such basal separation would create entrapment zones and affect various physico-chemical properties.

In order to assess the bonding networks of the synthesized samples, FTIR spectroscopy has been performed. The samples were mixed with KBr (1:50 mass ratio) to form solid pellets. A FTIR-8400s, Shimadzu spectrophotometer was employed in a varying wavenumber range (400–4000 cm⁻¹) to collect the



Scheme 1 A flow chart on synthesis of MWCNT-kaolinite nanocomposite

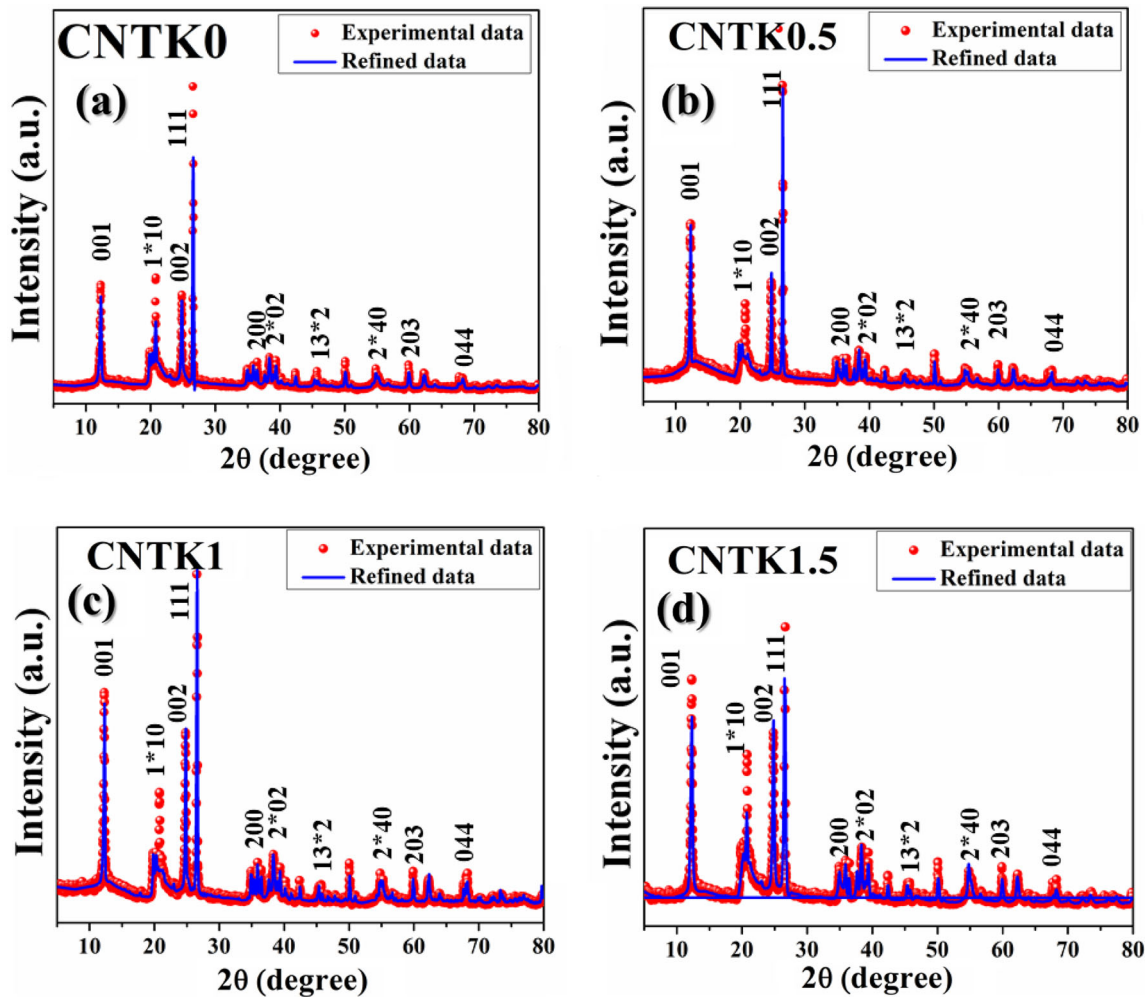


Fig. 1 Refined XRD patterns of the samples

Table 2 Refined microstructural parameters of clay samples

Parameters	CNTK0	CNTK0.5	CNTK1	CNTK1.5
a (Å)	5.142	5.158	5.140	5.149
b (Å)	8.930	8.952	8.936	8.930
c (Å)	7.421	7.418	7.424	7.423
α (°)	92.169	92.122	92.208	92.185
β (°)	105.023	105.014	105.017	105.077
γ (°)	90.323	89.739	90.265	90.330
V (Å ³)	328.933	330.571	329.157	329.568
χ^2	1.487	1.457	1.519	1.529
R_p (%)	13.274	10.040	11.323	15.089
R_{wp} (%)	19.747	14.633	17.204	23.072

IR spectra, which is depicted in Fig. 3. The characteristic vibrational bands located between 430 and 700 cm^{-1} are corroborate Si–O–Al bending [25].

Another major vibrational maximum found at 750 cm^{-1} refers to the AlO_6 vibration. Absorption bands at 792 and 917 cm^{-1} are attributed to Si–O and Al–OH deformation respectively [26]. The presence of Si–O stretching vibrations (940–1150 cm^{-1}) has also been confirmed. Such vibrations validate the presence of AlO_6 and SiO_4 polyhedral networks in the samples. A broad IR maximum is found between 3620 and 3700 cm^{-1} validating the presence of hydroxyl groups in the as-prepared samples [27, 28]. Additionally, two very tiny vibrations have been located at 1670 and 1658 cm^{-1} that are absent in the pristine kaolinite sample. The 1658 cm^{-1} band occurred due to the C=C vibration [29] and could be originated from the MWCNT moiety, whereas, the band found at 1670 cm^{-1} [30] is due to the –CONH vibration. This –CONH vibration refers to the

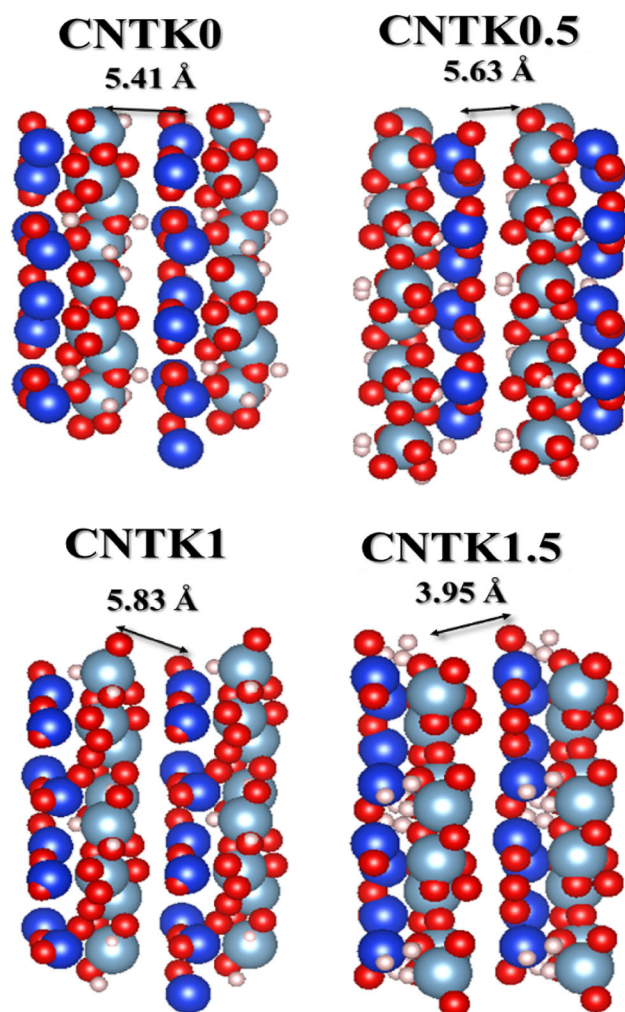


Fig. 2 Pictorial representation of the microstructures showing basal spacings, the dots in blue (silicon), red (oxygen), white (hydrogen), and grey (aluminum) colour represent specific atoms in the structure

successful incorporation of the functionalized MWCNTs over the surface of activated kaolinite.

Morphological features along with particle sizes of the entire sample set have been examined by Field Emission Scanning Electron Microscopy (FESEM) and Transmission electron microscopy (TEM) (Fig. 4). The samples were initially dispersed in acetone and sonicated in a bath sonicator to reduce the agglomeration. The sonicated sample was then cast on carbon-coated grids followed by sputter coating with gold plasma for microscopy. The accelerating voltages were set at 10–20 kV for FESEM micrography (Inspect F-50, FEI, Netherlands), whereas, it is set at 200 kV for TEM (JEOL, JEM-2000). Herein, the pristine clay sample (CNTK0) is showing hexagonal

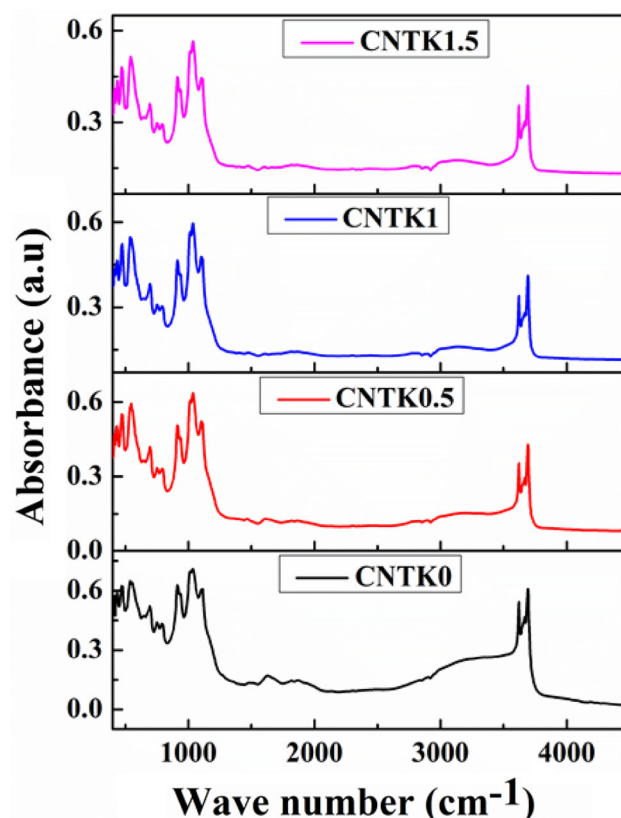


Fig. 3 FTIR spectra of clay samples

sheet-like 2-D structures having 70–90 nm average length on the longer sides. Additionally, the TEM micrographs depict the presence of long MWCNTs attached rigidly to the kaolin surfaces. This attachment implies the suitable formation of MWCNT-kaolinite nanocomposites. The FESEM images also show the increment of MWCNTs with increasing doping percentages, which is in accordance with the previous XRD and FTIR analyses.

The elemental analyses of the samples have been performed by using the EDX mapping technique. A Bruker Quantax EDS analyzer was employed for this purpose. The EDX spectra of the samples are showing a uniform presence of aluminum, silicon, and oxygen in all samples (Fig. 5). Additionally, the presence of carbon has been detected in the modified clay samples, which is in accordance with the loading percentages of MWCNT.

3.2 Investigation of surface properties of natural nanocomposite

The Brunauer–Emmett–Teller (BET) and Barrer–Joyner–Halenda (BJH) method using N₂ gas adsorption–

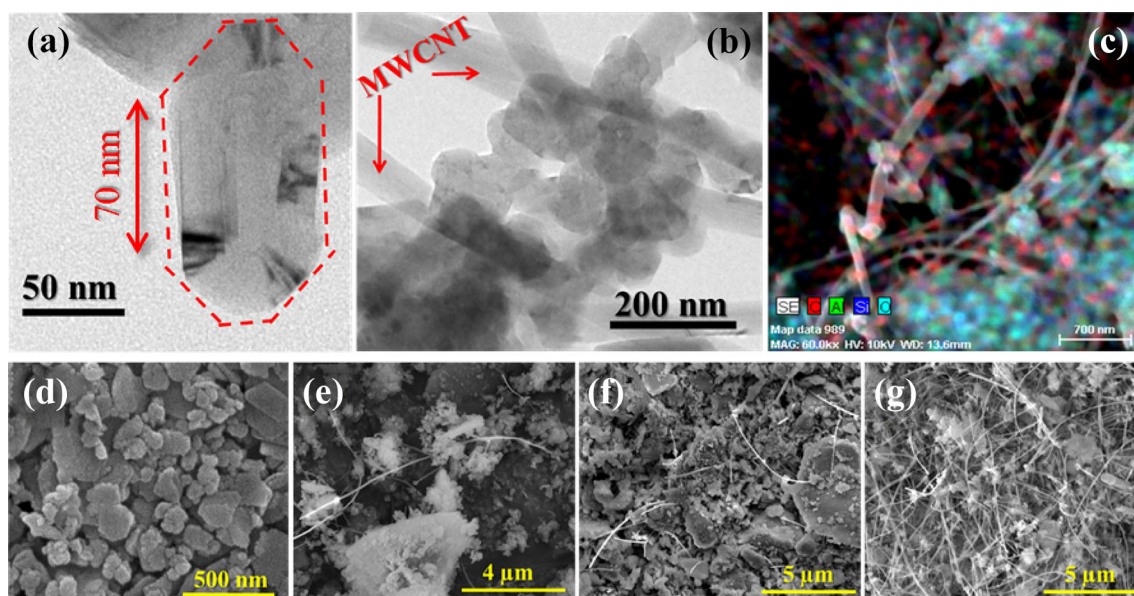


Fig. 4 **a** TEM micrograph of a single kaolinite particle; **b** TEM image of MWCNT modified CNTK1 sample; **c** EDX-mapping of the CNTK1 sample showing uniform distribution of the elements;

d–g corresponds to the FESEM images of the CNTK0 (**d**), CNTK0.5 (**e**), CNTK1 (**f**) and CNTK1.5 (**g**)

desorption have been employed to study the surface area and pore structures of the samples. A Twin Surface Area Analyzer, Quanta-chrome Instruments, USA was employed for this purpose. The BET-BJH isotherm shows (Fig. S1) nearly equal adsorption–desorption of the gas, which suggests a type-IV isotherm. These isotherms are generally associated with capillary condensation of the adsorbate making the adsorbent promising for industrial applications [31, 32]. The pore structure has been analyzed on the basis of adsorption–desorption hysteresis loops. The study shows H1 type hysteresis [33] in both samples. In reality, such hysteresis occurs when the adsorbent consists of agglomerates or compacts of approximately uniform spheres in a fairly regular array. The surface areas of both pristine and MWCNT loaded clays are found to be $139 \text{ m}^2/\text{g}$. This fairly high surface area of pristine clay is having an average pore diameter of 18.9 nm, which gets reduced in CNTK1.5 (15.5 nm) due to the incorporation of MWCNTs.

3.3 Mechanism of MWCNT-kaolinite nanocomposite formation

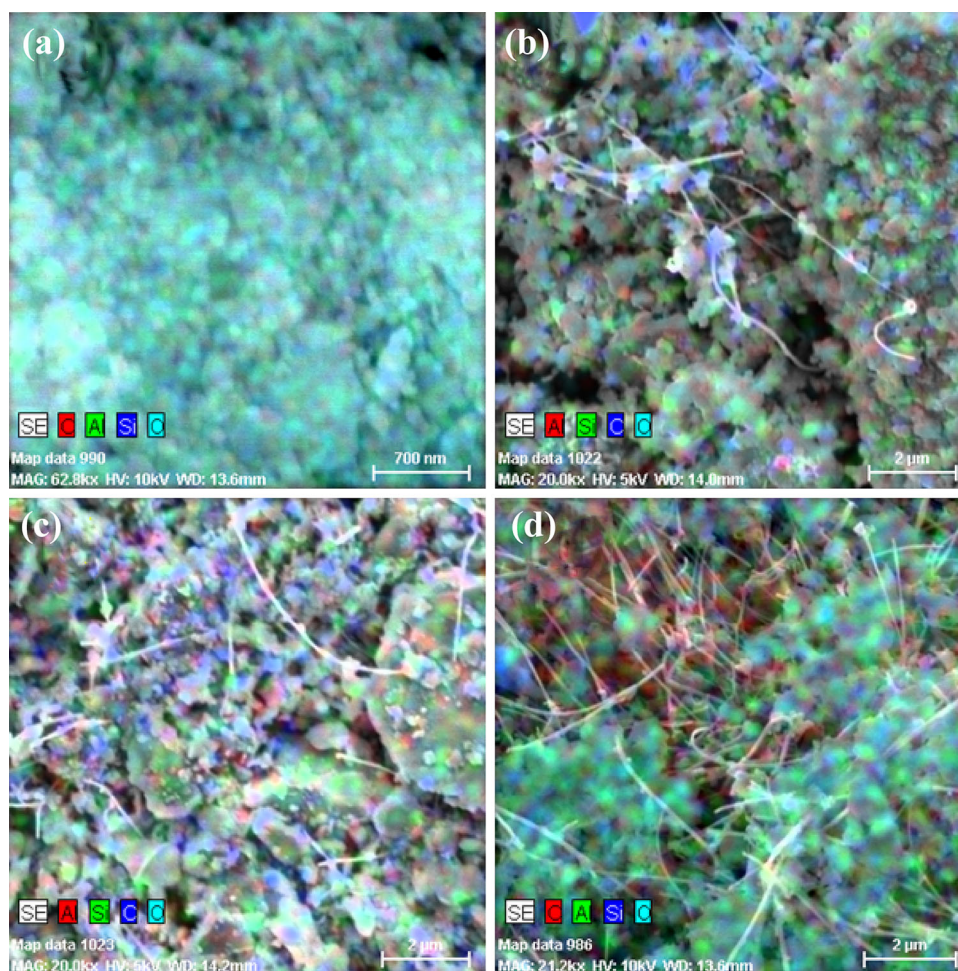
In reality, kaolinite has two negatively charged basal planes with positively charged edges. These basal planes consist of hydroxylated alumina (aluminum octahedral layer) and siloxane (silica tetrahedral

layer) facets [34]. Usually, these basal planes are assumed to carry a constant structural charge due to the isomorphous substitution of Al^{3+} for Si^{4+} in the siloxane facet and Fe^{2+} or Mg^{2+} for Al^{3+} in the alumina facet making the facets negative [35]. Herein, the surface charge of the pristine kaolinite sample has been measured by using zeta-potential (Fig. S1). The sample was suspended in water prior to the ultrasonication to reduce agglomeration. A Zetasizer, Malvern was used to study the zeta-potential of the natural clay. A highly negative (-25.3 mV) zeta-potential has been found, which not only substantiates the theoretical assumptions but also validates the structural stability of the natural clay sample.

Activation of nano-kaolinite further incorporates $-\text{NH}_2$ functional groups over the surface of the clay making the surface hydrophilic. Similarly, the functionalization of MWCNT with $-\text{COOH}$ makes its surface hydrophobic. This hydrophilic-hydrophobic interaction plays a pivotal role in making the nanocomposite. FTIR spectra of modified clay samples show a $-\text{CONH}$ vibration band, which could be ascribed to this $-\text{NH}_2\text{-COOH}$ interaction. Such an interaction rigidly binds the MWCNT with kaolinite. TEM and FESEM micrographs also validate this phenomenon.

Increasing doping percentages of MWCNT in the kaolin matrix show a gradual increment in the

Fig. 5 EDX-mapping data of **a** CNTK0, **b** CNTK0.5, **c** CNTK1 and **d** CNTK1.5



interlayer separation between two adjacent basal planes in crystallographic studies. This could be substantiated by the virtue of the attractive forces that play between functionalized MWCNT and activated kaolinite. In reality, the $-\text{CONH}$ moieties between MWCNT and kaolinite pull the kaolinite particles from different directions, which is sufficient to perturb the internal structure of the clay particle (Fig. 6) and results in an increased basal spacing as found in crystallographic data. Although, the basal spacing reduces greatly in CNTK1.5 due to excess CNT loading.

The total pore volume of the kaolinite is seemed to be quenched upon MWCNT doping in BET-BJH studies. Typically, MWCNT accommodates nano-kaolinite particles over its surface. Thus, the porosity of the attached side of the clay particles gets occupied and results in a reduction in total pore volume. This also validates proper attachment between MWCNT and nano kaolinite particles.

3.4 Dielectric assays of the clay samples

The dielectric property reflects the charge storage ability of a sample. It depends on numerous parameters, such as grain size, temperature, humidity, frequency of the external electric field, etc. The total dielectric permittivity consists of two functions,

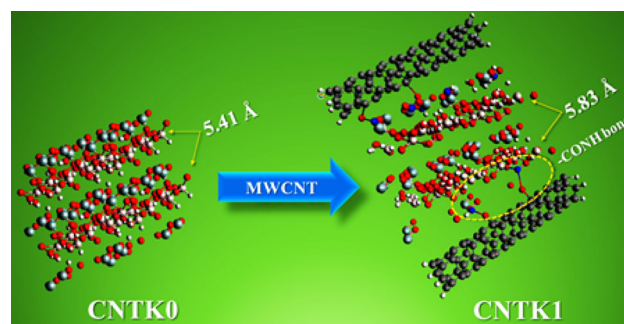


Fig. 6 Pictorial representation of the perturbed microstructure of kaolinite due to MWCNT doping that leads to increased basal spacing and formation of $-\text{CONH}$ bonds

namely, the real part of the permittivity (ϵ') and an imaginary part (ϵ''). The real part depicts the charge storage capacity, whereas, the imaginary part implies the electrical dissipation factor. These two terms are associated as $\epsilon = \epsilon' + j\epsilon''$. Where ϵ is the total dielectric permittivity of the material [36].

The real part of the permittivity can be calculated by using the relation [37], $\epsilon' = (C.d)/(\epsilon_0 A)$. Where, C is the capacitance of the material, d and A are the thickness and area respectively of the solid pellet that is used to measure the permittivity and ϵ_0 is the free space permittivity (8.85×10^{-12} F/m). Herein, 100 mg of each clay sample has been pressed by using a hydraulic press system to form solid pellets. Both sides of these pellets were covered by copper strips those are acted as electrical contacts. A 4294A Precision Impedance Analyzer, Agilent was used to study the electrical properties of these samples.

The frequency-dependent permittivity plots show a gradual reduction of electrical permittivity in the higher frequency domain (Fig. 7). In fact, such reduction is visible in all the samples. This type of frequency response could be analyzed by Maxwell–Wagner interfacial polarization [38]. Generally, dielectric materials have conductive grains inside insulated grain boundaries. The energy of the external electric field at the lower frequency domain is insufficient to pull out these conductive grains from grain boundaries and results in an electrical polarization. This low-frequency polarization contributes to the total dielectric constant as stated in Koop's theory [39]. Although, the higher field frequency is capable enough to free the charges from the insulated boundaries and results in a lower permittivity value.

The MWCNT incorporation influences the dielectric permittivity as shown in Table S1. It can be observed that the electrical permittivity attains a maximum in the CNTK1 sample (3850 at 40 Hz) upon MWCNT loading and quenches significantly when an excess amount of doping is performed in the CNTK1.5 sample (710 at 40 Hz). The pristine clay sample (CNTK0) shows a very low permittivity (41 at 40 Hz) value as stated in Table S1. This type of dielectric relaxation could be attributed to the structural modifications of the samples. As stated earlier, the kaolinite nanoparticles are attached between two adjacent MWCNT surfaces, which creates a periodic arrangement of insulated kaolinite and conductive CNTs in a parallel manner. Such a parallel arrangement leads to the formation of nano-capacitors and

enhances dielectric permittivity values with increasing MWCNT concentration. However, excess CNT loading disturbs this periodic arrangement, which results in a distorted grain-grain boundary arrangement in this sample. Hence, in the low-frequency region, the distorted grain boundaries are unable to hold the charges and the electrical charges get sufficient mobility [40]. Due to the uncontrolled movement of these mobile charges, the dissipation factor enhances (as shown in tangent loss data) and an abrupt nature in low-frequency permittivity is observed. This phenomenon is known as electrical percolation and reported previously by various groups [37, 38, 41].

The temperature response of the samples has also been studied in terms of electrical permittivity in a wide range (25–200 °C) and is depicted in Fig. 7. Figure 7 shows a gradual reduction in dielectric values with increasing temperature for the entire sample set. This type of relaxation is quite common and could be ascribed to the subsequent charge transport. In reality, temperature above a critical limit activates the bound grain and makes them free from the insulated grain boundary [42]. This activation reduces the M-W polarization and a radical quenching in permittivity can occur in the higher temperature domain. Additionally, DTA-TGA of the clay samples has been performed in a DTG-60H, Shimadzu to understand the structure–property correlation in this aspect. It has been observed that (Fig. S2) the samples are structurally stable (less than 6% mass loss) up to ~ 425 °C, beyond which a gradual drop in mass is visible. The DTA plots show the phase transformation of the kaolinite samples at around 500 °C. Generally, at this high-temperature kaolinite starts its transformation into meta-kaolinite. DTA-TGA results thus validate the fact that the electrical permittivity values do not associate with any structural or phase transformation mediated change and purely imply the grain transport phenomenon.

The tangent loss has also been investigated to estimate the dissipation factor of the entire sample set and presented in Fig. 7. The loss tangents are in accordance with high dielectric values. It can be noted that the tangent loss increases with increasing field frequencies for all the samples. The inter-dipolar friction could be a possible reason for this, which further dissipates as heat energy. The loss tangent seems to be highest in the CNTK1.5 sample due to the disrupted alignment of the ordered nano-capacitor

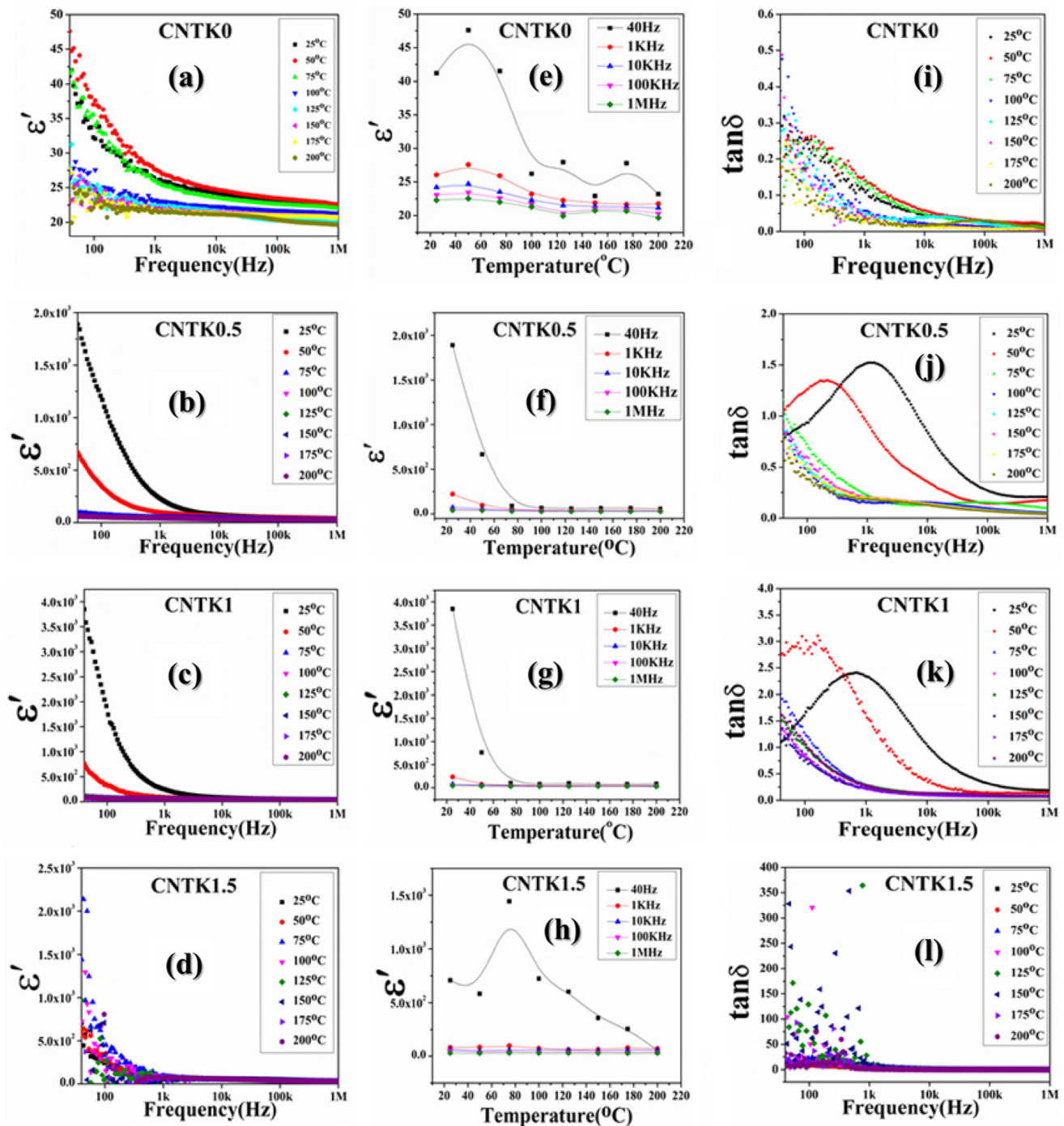


Fig. 7 Variation of dielectric constant with frequency (a–d), temperature dependent dielectric response (e–h), and tangent loss (i–l) for the samples

structure of the MWCNT doped nanocomposites. Henceforth, permittivity studies suggest that the CNTK1 sample is having the highest permittivity with a nominal tangent loss and possibly could be used in energy storage applications (Fig. 7).

3.5 Ac conductivities of the samples

The conduction mechanism of the clay samples has been studied in terms of frequency and temperature variations (Fig. 8). The frequency responses show higher conduction in the high-frequency domain. The

charged grains escape the grain boundaries after getting sufficient activation energies (E_a) at high frequencies. The activation energies have been calculated using the Arrhenius equation [43], as follows,

$$\sigma = \sigma_0 \exp(-E_a/K_B T)$$

where E_a is the activation energy for conduction and σ_0 is the pre-exponential factor. Arrhenius plots were obtained from the conductivity data calculated at frequencies 40 Hz, 1 kHz, 10 kHz, 100 kHz, and 1 MHz of the external electric field and have been shown in Fig. 9. The activation energy tends to increase with increasing field frequencies making the grains more transportable at higher frequencies (Table S2).

The dependence of ac conductivity on frequency for the entire set of samples has also been studied through Jonscher's universal power law [44],

$$\sigma_{ac} = B\omega^n$$

here, B and n are constant terms. B has the unit of conductivity and n is a dimensionless constant term.

The non-zero values then refer to the frequency-dependent conduction mechanism. It has been calculated for each sample by plotting $\ln \sigma$ against $\ln \omega$ (Fig. 10). The n values of the clay samples varied between 0.51 and 0.92 suggesting the non-Debye type conduction mechanisms for all the samples. Additionally, these n values validate the diffusion-limited 1-D hopping of the charge carriers through the sample.

It has already been explained that the MWCNT loaded samples possess better attachment to the kaolinite surfaces and form prominent charge hopping pathways. Thus, increment in ac conductivities in CNT-loaded samples have been found.

3.6 Estimation of the effect of microstructure on charge transport

The charge transport is an essential parameter when it comes to energy harvesting. Impedance spectroscopy can substantiate this in the microstructural proximity. Herein, the impedance spectra of the

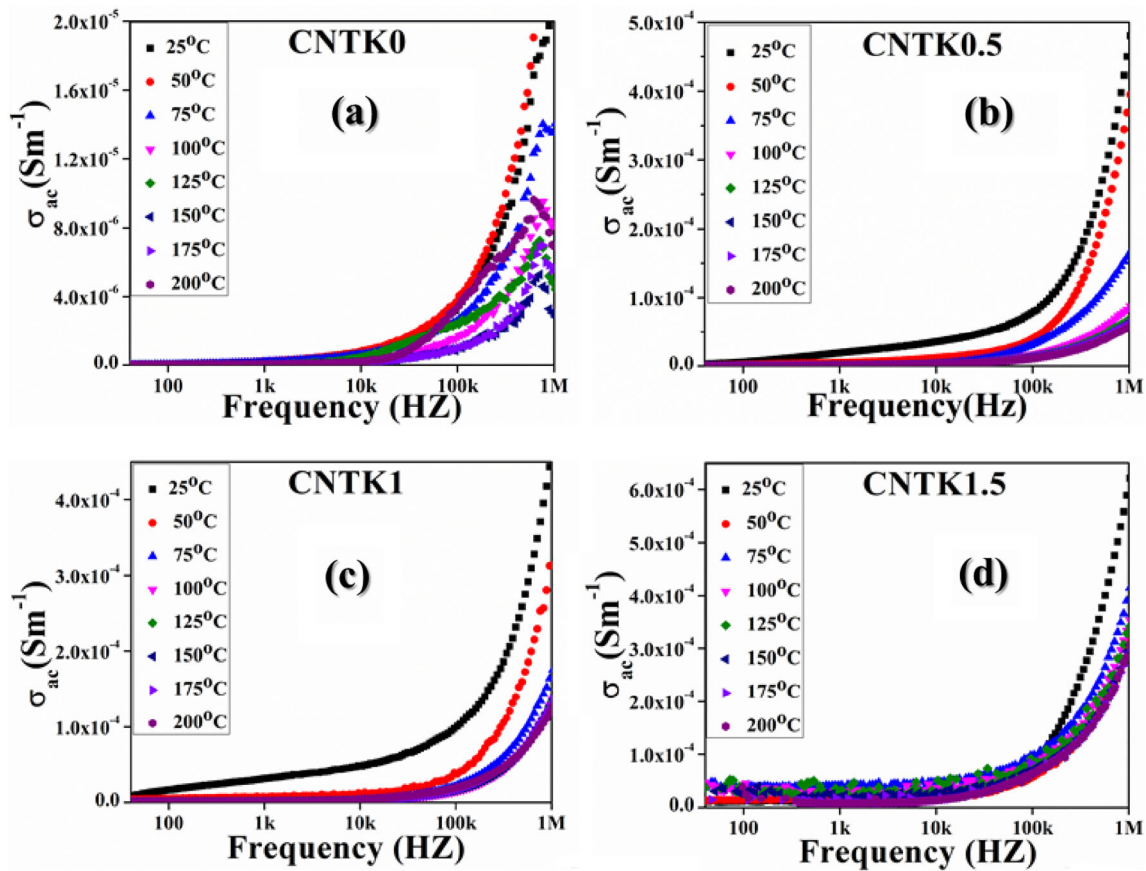


Fig. 8 Temperature-dependent ac conductivities with varying frequencies of clay samples

Fig. 9 Arrhenius plots of the samples for estimating the activation energies

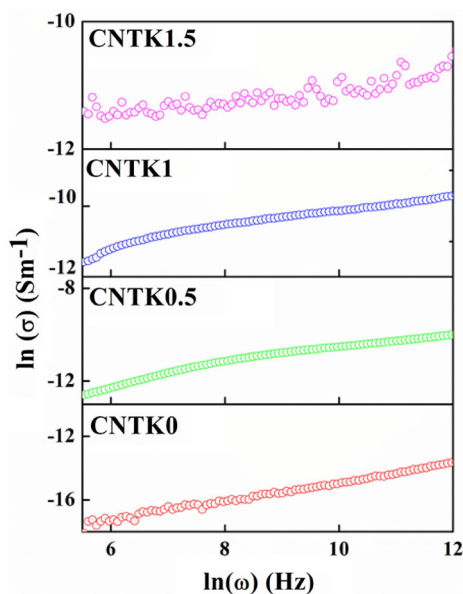
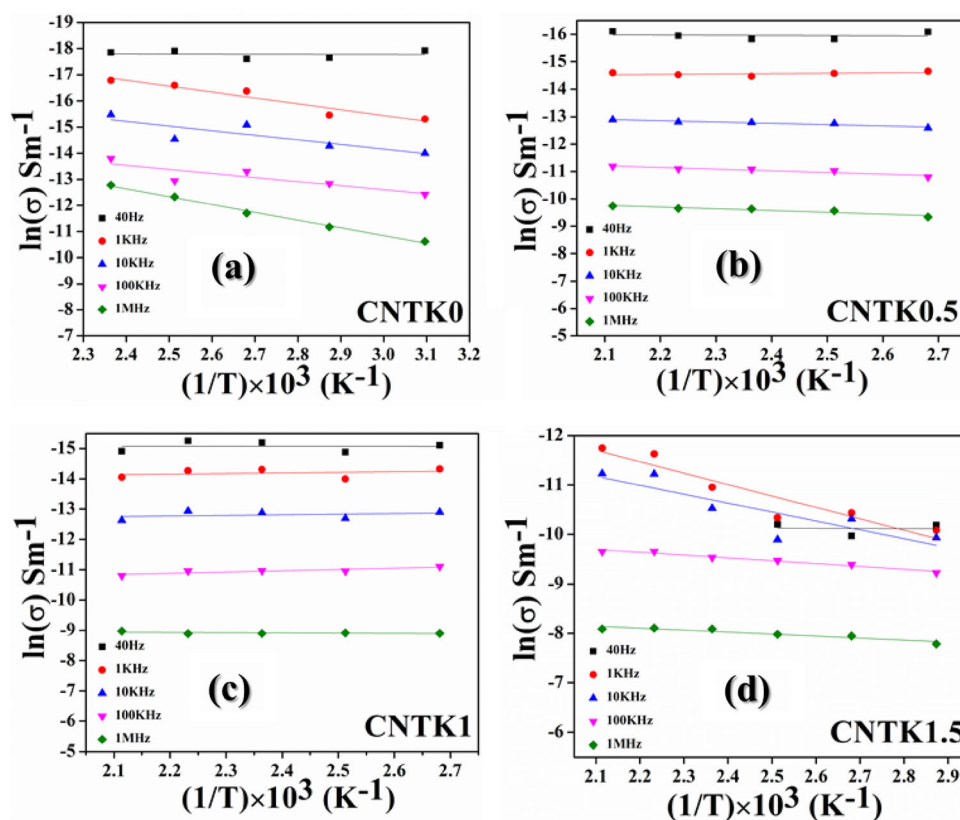


Fig. 10 Joncher's plot to evaluate the diffusion limited hopping mechanism of the samples

synthesized clay samples have been investigated to understand the role of microstructural modifications on carrier mobility. The impedance spectra of the samples show depressed semicircles in the high-frequency domain along with straight lines in the low-

frequency regions. The semicircle is attributed to the charge transfer process, whereas, the straight line is attributed to the diffusion phenomenon. The spectra were further fitted with an equivalent circuit model using the EIS spectrum analyzer v.1.0 program (Fig. 11). The equivalent circuit comprises two separate loops consisting of resistance (R) with a constant phase element (CPE1). These two loops are joined in series with another constant phase element (CPE2) [45]. The first loop represents the contribution of the sample, whereas, the second loop depicts the interfacial effects. The Warburg element represents the diffusion phenomenon. The second loop in the CNTK0 and CNTK1.5 are absent as there are no abrupt interfaces formed between MWCNT and kaolinite.

It is evident from the data that the charge transfer resistance (R_2) gradually increases with increasing doping concentration (Table S3). The reason behind such impedance relaxation with MWCNT doping lies in its microstructure. The pristine sample (CNTK0) shows a low charge transfer resistance ($8.1392 \times 10^{-9} \Omega$), which alternatively validates the mobility of charge through the system. But, doping of MWCNT somewhat stretches the alignment of the kaolinite

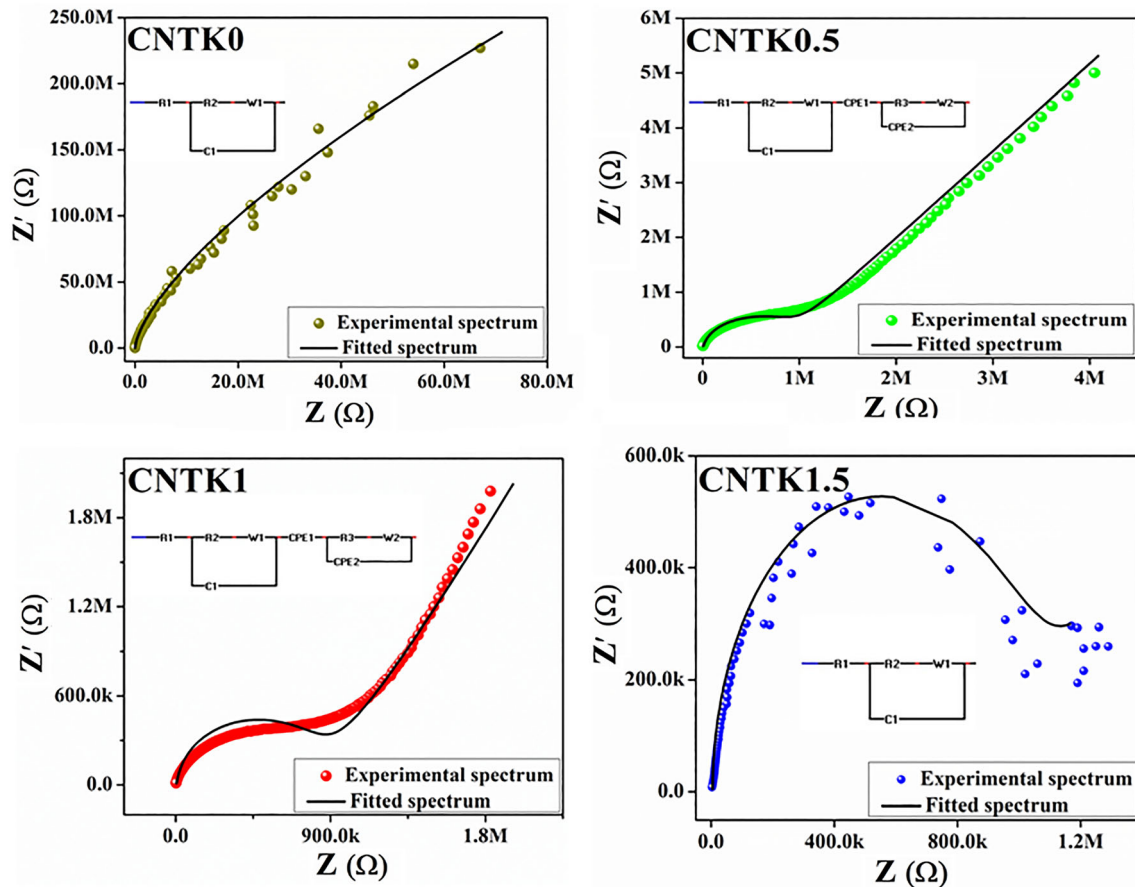


Fig. 11 Electrochemical impedance spectra of the samples with corresponding equivalent circuits for estimating the charge transfer process

crystals from various sides and results in voids and defects, which could be a possible reason for the entrapment of free charge carriers into the defect zones. Thus, the carrier mobility gets decreased subsequently in CNTK0.5 ($R_2 = 7.6417 \times 10^5 \Omega$) and CNTK1 ($R_2 = 9.6442 \times 10^5 \Omega$) giving rise to the charge transfer resistances. Above a critical doping limit i.e., 1.5% in CNTK1.5, the permanent microstructural distortion of kaolin crystals takes place, which leads to the highest charge transfer resistance ($R_2 = 9.9381 \times 10^5 \Omega$).

3.7 Estimation of the electrochemical performances of the clay samples

The cyclic voltammetry has been performed for further exploitation of the samples as promising electrode candidates in the energy harvesting systems. Typically, a two-electrode Network BTS battery tester within the range of 0 to + 2 V at the scan rates of 100, 300, 500, and 1000 mV/s was employed to conduct

the electrochemical measurements. The voltamograms show typical electronic hysteresis loops as shown in Fig. 12.

The corresponding specific capacitances (C_p) have been calculated using the following relation [46],

$$C_v = \frac{\int_{E_1}^{E_2} I(E) dE}{ms(E_1 - E_2)}$$

here, m is the mass of the material, s is the scan rate, E_1 and E_2 are limiting values of the potential window, and $\int_{E_1}^{E_2} I(E) dE$ is the area under the CV curve.

The calculated specific capacitance of the entire set of samples shows a gradual increment with MWCNT concentration up to a critical limit (1% loading), thereafter, the C_v value reduces drastically. Such an interesting increment is related to the enriched amount of interface formation in MWCNT-kaolinite composites. The successful attachment of kaolinite to the surface of MWCNT reduces the charge transport path length and thereby increases the specific

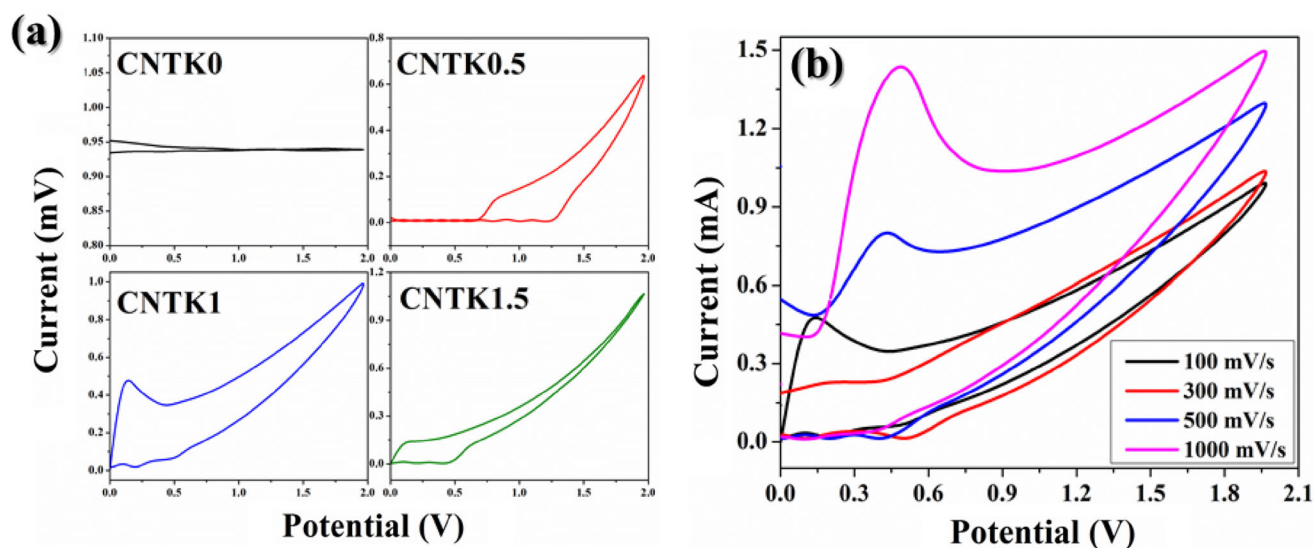


Fig. 12 **a** Cyclic voltammograms of various MWCNT-doped clay samples, **b** voltammogram of CNTK1 at different scan rates

capacitance. A detailed description of the calculated C_v values has been incorporated in Table S4. Moreover, the CNTK1.5 depicts a reduction in C_v , which is related to the improper doping or excessive presence of MWCNT in the sample.

Additionally, CNT-doped clay samples offer redox relaxation as shown in Fig. 8. In reality, the conductive MWCNT introduces free charge carriers to the active sites of the kaolinite. This charge transport results in oxidation maxima in the modified clay samples. As the kaolinite has a large number of voids and defects in its crystals, these free carriers have been entrapped by such voids and resulting in a relatively lower reduction peak.

The specific capacitances have also been estimated by varying the scan rate for the CNTK1 sample (Table S5). It is observed that, at lower scan rates, the ions have sufficient time to migrate deeper into the system contributing to higher feasible reactions and conveying improved capacitive performance. Henceforth, electrochemical assay suggests the CNTK1 sample could be a promising electrode material for energy harvesting devices.

4 Conclusion

Herein, natural kaolinite clay has been modified using multi-walled CNT. A top-down synthesis of the clay followed by a chemical modification has been executed to attach the clay nanoparticles over the CNT surface. This simplistic synthesis process of

the abundantly available clay could be useful in industrial production on a large scale. Detailed investigation suggests the microstructural modifications of the clay moiety, which leads to the entrapment of free charge carriers that further helps in modulating the electrical parameters. The dielectric data depicts an enhanced charge storage capacity in 1% w/w doping (nearly 93 times compared to its pristine counterpart) as the dielectric constant is found to be 3850 at a frequency of 40 Hz with very low tangent loss. Moreover, the MWCNT modified clay nanostructures exhibit excellent thermal stability up to 500 °C revealing potential application in high-temperature devices as well. The high ac conductivity, especially in CNTK1 makes them potential candidates for large-scale electrode fabrication. The ac conductivities and impedance spectra suggest 1-D diffusion-limited hopping of the charge carriers and correlate microstructural modifications associated with the clay samples. This low-cost clay material shows a redox relaxation when it comes to electrochemical analysis. Such redox peaks are attributed to the carrier transport between CNT and kaolinite nanoparticles. The specific capacitance (C_v) is found to be 22.4 F/g, which is particularly important for charge storage applications. Such modified natural clay could be utilized in batteries, electrochemical sensors, and supercapacitors. Minimal cost, facile synthesis process, the abundance of the kaolinite clay, and biocompatibility besides the enormous efficacy in charge transport of the CNT modified nano-clay make it a futuristic 'green electrode' system.

Acknowledgements

The authors are grateful to the Department of Physics, Jadavpur University for extending experimental facilities. D.M and S. D would like to acknowledge DST-SERB (Grant No. EEQ/2018/000747) for funding. S.R. would like to acknowledge SVMCM fellowship of Govt. of West Bengal, India for providing fellowship.

Author contribution

DM: Data curation, Investigation, Writing- Original draft preparation. SR: Conceptualization, Methodology, Computation, Writing- Original draft preparation. SB: Writing- Assistance, Conceptualization, Investigation. RD: Investigation, Software. AM: Data curation, Software. DKC: Writing- Assistance. SD: Data curation. SG: Data curation. RB: Supervision. SD: Supervision, Funding acquisition.

Funding

Funding was provided by Science and Engineering Research Board (Grant No. EEQ/2018/000747).

Data availability

The research data will be available from the corresponding author on valid request.

Declarations

Conflict of interest The authors declare that they have no conflict of interest.

Supplementary Information: The online version contains supplementary material available at <http://doi.org/10.1007/s10854-022-08314-6>.

References

1. S.M. Antony, S. Indu, R. Pandey, An efficient solar energy harvesting system for wireless sensor network nodes. *J. Inf. Optim. Sci.* **41**(1), 39–50 (2020)
2. A. Muzaffar, M.B. Ahamed, K. Deshmukh, J. Thirumalai, A review on recent advances in hybrid supercapacitors: design, fabrication and applications. *Renew. Sustain. Energy Rev.* **101**, 123–145 (2019)
3. M.N. Norizan, M.H. Moklis, S.Z.N. Demon, N.A. Halim, A. Samsuri, I.S. Mohamad, V.F. Knight, N. Abdullah, Carbon nanotubes: functionalisation and their application in chemical sensors. *RSC Adv.* **10**, 43704–43732 (2020)
4. H. Liu, X. Liu, S. Wang, H.K. Liu, L. Li, Transition metal based battery-type electrodes in hybrid supercapacitors: a review. *Energy Storage Mater.* **28**, 122–145 (2020)
5. Y.R. Kumar, K. Deshmukh, K.K. Sadasivuni, S.K. Pasha, Graphene quantum dot based materials for sensing, bio-imaging and energy storage applications: a review. *RSC Adv.* **10**(40), 23861–23898 (2020)
6. R. Kaur, A. Marwaha, V.A. Chhabra, K.H. Kim, S.K. Tripathi, Recent developments on functional nanomaterial-based electrodes for microbial fuel cells. *Renew. Sustain. Energy Rev.* **119**, 109551 (2020)
7. C.H. Kim, Y. Wang, C.D. Frisbie, Continuous and reversible tuning of electrochemical reaction kinetics on back-gated 2D semiconductor electrodes: steady-state analysis using a hydrodynamic method. *Anal. Chem.* **91**(2), 1627–1635 (2018)
8. S. Tajik, H. Beitollahi, F.G. Nejad, M. Safaei, K. Zhang, Q.V. Le, R.S. Varma, H.W. Jang, M. Shokouhimehr, Developments and applications of nanomaterial-based carbon paste electrodes. *RSC Adv.* **10**, 21561–21581 (2020)
9. Z. Esvandi, R. Foroutan, S.J. Peighambaroust, A. Akbari, B. Ramavandi, Uptake of anionic and cationic dyes from water using natural clay and clay/starch/MnFe₂O₄ magnetic nanocomposite. *Surf. Interfaces* **21**, 100754 (2020)
10. F. Liu, X. Chuan, Recent developments in natural mineral-based separators for lithium-ion batteries. *RSC Adv.* **11**(27), 16633–16644 (2021)
11. S. Bentahar, A. Dbik, M.E. Khomri, N.E. Messaoudi, A. Lacherai, Removal of a cationic dye from aqueous solution by natural clay. *Groundw. Sustain. Dev.* **6**, 255–262 (2018)
12. N. Raghavendra, H.P. Nagaswarupa, T.S. Shekhar, M. Mylarappa, B.S. Surendra, S.C. Prashantha, C.R. Ravikumar, M.A. Kumar, N. Basavaraju, Development of clay ferrite nanocomposite: electrochemical, sensors and photocatalytic studies. *Appl. Surf. Sci.* **5**, 100103 (2021)
13. W. Wang, Y. Yang, H. Luo, S. Li, J. Zhang, A separator based on natural illite/smectite clay for highly stable lithium-sulfur batteries. *J. Colloid Interface Sci.* **576**, 404–411 (2020)
14. C.A. Vieira, B.F. Ferreira, A.F. da Silva, M.A. Vicente, R. Trujillano, V. Rives, K.J. Ciuffi, E.J. Nassar, E.H. de Faria, Adsorption-based synthesis of environmentally friendly heterogeneous Chromium (III) catalysts for oxidation reactions into kaolinite, saponite, and their amine-modified derivatives. *ACS Appl. Nano Mater.* **1**(8), 3867–3877 (2018)

15. Y. Lan, Y. Liu, J. Li, D. Chen, G. He, I.P. Parkin, Natural clay-based materials for energy storage and conversion applications. *Adv. Sci.* **8**, 2004036 (2021)
16. X. Yang, W. Yang, J. Hu, Preparation of low-dielectric-constant kaolin clay ceramics by chemical cleaning method. *Front. Mater.* **8**, 198 (2021)
17. G.R. Olhoeft, Tables of room temperature electrical properties for selected rocks and minerals with dielectric permittivity statistics. US Department of the Interior, Geological Survey, 22 (1979)
18. S. Bardhan, S. Roy, D.K. Chanda, S. Das, K. Pal, A. Chakraborty, R. Basu, S. Das, Microstructure and dielectric properties of naturally formed microcline and kyanite: a size-dependent study. *Cryst. Growth Des.* **19**(8), 4588–4601 (2019)
19. S. Ghosh, S. Roy, S. Bardhan, N. Khatua, B. Bhowal, D.K. Chanda, S. Das, D. Mondal, R. Basu, S. Das, Effect of size fractionation on purity, thermal stability and electrical properties of natural hematite. *J. Electron. Mater.* **50**(7), 3836–3845 (2021)
20. J. Yuan, J. Yang, H. Ma, S. Su, Q. Chang, S. Komarneni, Hydrothermal synthesis of nano-kaolinite from K-feldspar. *Ceram. Int* **44**(13), 15611–15617 (2018)
21. J.C. Miranda-Trevino, C.A. Coles, Kaolinite properties, structure and influence of metal retention on pH. *Appl. Clay Sci.* **23**, 133–139 (2003)
22. Y. Zhang, Q. Liu, S. Zhang, Y. Zhang, Y. Zhang, P. Liang, Characterization of kaolinite/styrene butadiene rubber composite: Mechanical properties and thermal stability. *Appl. Clay Sci.* **124**, 167–174 (2016)
23. F.A. Gavru, A. Ayensu, X-Ray powder diffractometry, crystallographic phase analysis and lattice parameters of kaolinite. *J. Appl. Sci. Eng.* **6**(1), 65–71 (2001)
24. S. Bardhan, S. Roy, D.K. Chanda, S. Ghosh, D. Mondal, S. Das, S. Das, Nitrogenous carbon dot decorated natural microcline: an ameliorative dual fluorometric probe for Fe^{3+} and Cr^{6+} detection. *Dalton Trans.* **49**(30), 10554–10566 (2020)
25. T.A. Elbokl, C. Detellier, Aluminosilicate nanohybrid materials. Intercalation of polystyrene in kaolinite. *J. Phys. Chem. Solids* **67**, 950–955 (2006)
26. P.C. Lopes, F.A. Dias, L.D. da Silva, Decomposition kinetics by thermogravimetry for the intercalation of kaolin with dimethylsulphoxide. *Mater. Lett.* **57**, 3397–3401 (2003)
27. P.A. Alaba, Y.M. Sani, W.M.A.W. Daud, Kaolinite properties and advances for solid acid and basic catalyst synthesis. *RSC Adv.* **5**(122), 101127–101147 (2015)
28. L. Zhang, C.J. Wang, Z.F. Yan, X.L. Wu, Y.Q. Wang, D.W. Meng, H.X. Xie, Kaolinite nanomaterial: intercalation of 1-butyl-3-methylimidazolium bromine in a methanol-kaolinite pre-intercalate. *Appl. Clay Sci.* **86**, 106–110 (2013)
29. H.M. Zidan, E.M. Abdelrazek, A.M. Abdelghany, A.E. Tarabiah, Characterization and some physical studies of PVA/PVP filled with MWCNTs. *J. Mater. Res. Technol.* **8**(1), 904–913 (2019)
30. M.B. Moraes, L. Cividanes, G. Thim, Synthesis of graphene oxide and functionalized CNT nanocomposites based on epoxy resin. *J. Aerosp. Technol. Manag* (2018). <https://doi.org/10.5028/jatm.v10.944>
31. S. Roy, A. Maity, P. Mandal, D.K. Chanda, K. Pal, S. Bardhan, S. Das, Effects of various morphologies on the optical and electrical properties of boehmite nanostructures. *Crys-tEngComm* **20**, 6338–6350 (2018)
32. D.K. Chanda, P.S. Das, A. Samanta, A. Dey, A.K. Mandal, K.D. Gupta, T. Maitya, A.K. Mukhopadhyay, Intertwined nanopetal assembly of $\text{Mg}(\text{OH})_2$ powders. *Ceram. Int.* **40**, 11411–11417 (2014)
33. Z. Li, D. Liu, Y. Cai, Y. Wang, J. Teng, Adsorption pore structure and its fractal characteristics of coals by N_2 adsorption/desorption and FESEM image analyses. *Fuel* **257**, 116031 (2019)
34. A. Michalkova, T.L. Robinson, J. Leszczynski, Adsorption of thymine and uracil on 1:1 clay mineral surfaces: comprehensive ab initio study on influence of sodium cation and water. *Phys. Chem. Chem. Phys.* **13**(17), 7862–7881 (2011)
35. N. Kumar, M.P. Andersson, D. Van den Ende, F. Mugele, I. Sîretanu, Probing the surface charge on the basal planes of kaolinite particles with high-resolution atomic force microscopy. *Langmuir* **33**(50), 14226–14237 (2017)
36. S. Das, S. Das, A. Roychowdhury, D. Das, S. Sutradhar, Effect of Gd doping concentration and sintering temperature on structural, optical, dielectric and magnetic properties of hydrothermally synthesized ZnO nanostructure. *J. Alloys Compd.* **708**, 231–246 (2017)
37. L. Zhang, W. Wang, X. Wang, P. Bass, Z.Y. Cheng, Metal-polymer nanocomposites with high percolation threshold and high dielectric constant. *Appl. Phys. Lett.* **103**, 232903 (2013)
38. S. Roy, S. Bardhan, K. Pal, S. Ghosh, P. Mandal, S. Das, S. Das, Crystallinity mediated variation in optical and electrical properties of hydrothermally synthesized boehmite (γ - AlOOH) nanoparticles. *J. Alloys Compd.* **763**, 749–758 (2018)
39. C.G. Koops, On the dispersion of resistivity and dielectric constant of some semiconductors at audiofrequencies. *Phys. Rev.* **83**(1), 121–124 (1951)
40. G. Gregori, R. Merkle, J. Maier, Ion conduction and redistribution at grain boundaries in oxide systems. *Prog. Mater. Sci.* **89**, 252–305 (2017)

41. T. Debnath, P. Saha, N. Patra, S. Das, S. Sutradhar, Hydrothermal process assists undoped and Cr-doped semi-conducting ZnO nanorods: frontier of dielectric property. *J. Appl. Phys.* **123**, 194101 (2018)
42. T.C. Chung, A. Petchsuk, Synthesis and properties of ferroelectric fluoroterpolymers with Curie transition at ambient temperature. *Macromolecules* **35**(20), 7678–7684 (2002)
43. L.K. Sudha, S. Roy, K. Uma Rao, Evaluation of activation energy (E_a) profiles of nanostructured alumina polycarbonate composite insulation materials. *Int. J. Mater. Mech. Manuf.* **2**(1), 96–100 (2014)
44. B.M. Greenhoe, M.K. Hassan, J.S. Wiggins, K.A. Mauritz, Universal power law behavior of the AC conductivity versus frequency of agglomerate morphologies in conductive carbon nanotube-reinforced epoxy networks. *J. Polym Sci B Polym Phys.* **54**(19), 1918–1923 (2016)
45. S. Samanta, A. Maity, S. Roy, S. Giri, D. Chakravorty, Effect of microstructure on ionic transport in silica-based sodium containing nanoconfined systems and their electrochemical performance as electrodes. *J. Phys. Chem. C* **124**(38), 21155–21169 (2020)
46. A. Maity, S. Samanta, S. Roy, D. Biswas, D. Chakravorty, Giant dielectric constant of copper nanowires/amorphous SiO_2 composite thin films for supercapacitor application. *ACS Omega* **5**(21), 12421–12430 (2020)
47. A. Guevara-Morales, A.C. Taylor, Mechanical and dielectric properties of epoxy–clay nanocomposites. *J. Mater. Sci.* **49**, 1574–1584 (2014)
48. J.D. Gaiya, W.U. Eze, T. Oyegoke, A.O. Ameh, I.C. Madufor, T.K. Bello, Assessment of the dielectric properties of polyester/metakaolin composite. *Eur. J. Mater. Sci. Eng.* **6**(1), 019–029 (2021)
49. J. Zhang, M.B. Clennell, M. Josh, M. Pervukhina, Frequency and water saturation dependency of dielectric properties of clay mineral. *Appl. Clay Sci.* **198**, 105840 (2020)
50. N.M. Kuznetsov, V.G. Shevchenko, D.Y. Stolyarova, S.A. Ozerin, S.I. Belousov, S.N. Chvalun, Dielectric properties of modified montmorillonites suspensions in polydimethylsiloxane. *J. Appl. Polym. Sci.* **135**(32), 46614 (2018)
51. V.J.D. Silva, E.P.D. Almeida, W.P. Gonçalves, R.B.D. Nóbrega, G.D.A. Neves, H.D.L. Lira, R.R. Menezes, L.N.D.L. Santana, Mineralogical and dielectric properties of mullite and cordierite ceramics produced using wastes. *Ceram. Int.* **45**, 4692–4699 (2019)
52. K. Kułacz, J. Waliszewski, S. Bai, L. Ren, H. Niu, K. Orzechowski, Changes in structural and dielectric properties of nontronite caused by heating. *Appl. Clay Sci.* **202**, 105952 (2021)
53. N. Anwar, M. Ishtiaq, A. Shakoar, N.A. Niaz, T.Z. Rizvi, M. Qasim, M. Irfan, A. Mahmood, Dielectric properties of polymer/clay nanocomposites. *Polym. Polym. Compos.* **29**(6), 807–813 (2021)
54. C.V. Chanmal, S.S. Bandgar, C.D. Mungamode, S.D. Chavan, S.G. Pawar, R.N. Mulik, V.L. Mathe, J.P. Jog, Structural and dielectric properties of PVDF/6A clay nanocomposites. *Macromol. Symp.* **400**, 2100032 (2021)
55. S. Lokanatha, S. Bhattacharjee, Dielectric properties of ripidolite, a chloritic clay mineral. *Trans. Indian Ceram. Soc.* **45**(2), 41–42 (1986)
56. H. Kabir, M.J. Khan, G. Brodie, D. Gupta, A. Pang, M.V. Jacob, E. Antunes, Measurement and modelling of soil dielectric properties as a function of soil class and moisture content. *J. Microw. Power Electromag.* **54**(1), 3–18 (2020)

Publisher's Note Springer Nature remains neutral with regard to jurisdictional claims in published maps and institutional affiliations.



Functionalized MWCNT-integrated natural clay nanosystem: a promising eco-friendly capacitor for energy storage applications

Dhananjoy Mondal¹ , Amartya Sau¹, Shubham Roy² , Souravi Bardhan^{1,3} ,
Jhilik Roy^{1,4}, Saheli Ghosh¹, Ruma Basu⁴, Soumyaditya Sutradhar¹, and Sukhen Das^{1,*}

¹Department of Physics, Jadavpur University, Kolkata 700032, India

²Shenzhen Key Laboratory of Advanced Functional Carbon Materials Research and Comprehensive Application, Shenzhen Key Laboratory of Flexible Printed Electronics Technology, School of Science, Harbin Institute of Technology, Shenzhen 518055, China

³Department of Environmental Science, Netaji Nagar College for Women, Kolkata 700092, India

⁴Department of Physics, Jogamaya Devi College, Kolkata 700026, India

Received: 4 April 2023

Accepted: 18 July 2023

© The Author(s), under exclusive licence to Springer Science+Business Media, LLC, part of Springer Nature 2023

ABSTRACT

This study delves into the structural and morphological characteristics of MWCNT-doped natural kaolinite nano clays, leading to significant changes in their electrical and electrochemical properties through the doping processes. Specifically, MWCNT has been doped using two different methods, resulting in distinct physicochemical properties. In one approach, a chemical route has been employed to modify the surface of MWCNT and kaolinite, creating an alignment that forms “micro capacitors” with enhanced electrical polarizability. Conversely, the uncontrolled growth of the nanocomposite results in a random arrangement, exhibiting lower charge storage efficiency. The characterization of naturally formed kaolinite and its conjugated counterparts have been investigated via conventional characterization tools like XRD, FESEM, TEM, EDS, Zeta, etc. The XRD refinement has been adopted to investigate the microstructural evaluation of the nanocomposites by the MAUD software package. The findings indicate that natural kaolinite-MWCNT nanocomposite shows promise as a “green alternative” and has the potential to replace conventional storage materials effectively if appropriately refined.

Address correspondence to E-mail: sdasphysics@gmail.com

1 Introduction

The generation of energy and its storage is very essential for today's modern lifestyle. Conventional battery-based energy storage devices are losing interest for their complicated design procedure, high cost, and toxic nature [1, 2]. Thus scientists and technologists are paying their interest to fabricate such devices from noninvasive sources. Semiconducting materials and various nanomaterials are gaining the interest of the researcher in this purpose for their interesting physicochemical properties [3]. [4] But complicated synthesis procedures from several harmful chemicals affect the biocompatibility of this type of device [5]. [6] Thus it is important to introduce such systems which can store energy without infecting the environment.

In the present scenario, material scientists are trying to develop this type of energy storage device by using natural clay and minerals for their high mechanochemical stability, biocompatibility, non-toxic nature, low cost, and availability [7]. [8] These types of cost-effective natural materials are able to pave a new path in various applications of material science for their promising physicochemical properties. In the last few decades, natural clays such as montmorillonite, palygorskite, smectite, halloysite, and ripidolite have been used in energy storage applications, yet most of such clay materials are suffering from various drawbacks like nominal dielectric constant, conductivity, and energy storage efficacy [9]. [10] A table has been shown (Table 1) here with the data such as dielectric constant (charge storage efficacy) and AC conductivity of the previously reported natural nanosystems.

It is evident from previous research that the physicochemical properties of any material enhance its nanodomain for increasing the surface-to-volume ratio. The storage efficacy of the natural materials also increases with the deduction of size and shows a promising result in nano dimension. This enhanced storage efficacy of the nanoparticles can also be increased by incorporating foreign elements by doping or composite formation. In reality, the incorporation of any foreign element in the nanomaterials creates mechanical stress in its interior and can also create oxygen vacancy-like active sites. This type of deformation in the crystal enhances the storage efficacy as well as other physicochemical properties of

the nanoparticles. Herein, MWCNT has been incorporated into the kaolinite nano matrix and estimated the energy storage properties [11]. Basically, kaolinite is a natural clay formed by weathering of potassium feldspar having a layered structure of the periodic arrangement of octahedral alumina and tetrahedral silica. This periodic arrangement makes the clay highly stable in structural and thermal properties. MWCNT is a one-dimensional rod-like carbon nanoparticle having a high electrical conductivity [12]. The incorporation of MWCNT in the kaolinite nano matrix enhanced its physicochemical properties along with high electrical permittivity. These increments in physicochemical properties are further substantiated by X-ray crystallography and various electrical measurement. Interestingly, the electrical properties of the MWCNT-loaded nano kaolinite varied with different incorporation methods. Herein, we have incorporated MWCNT by two different methods in the nano clay. Direct incorporation of MWCNT shows lower electrical properties than functionalized nanoparticles [13]. In this method, kaolinite and MWCNT have been activated separately by incorporating functional groups over their surfaces and conjugated via a simple condensation technique. The functionalized nanosystems show a promising electrical energy storage efficacy with 1% w/w incorporation of MWCNT in natural clay [14, 15]. These increments of electrical properties can pave a new directional path for fabricating "Green Capacitors" by modifying natural materials in the near future. Technological advancement and industrialization as well as increasing demand for energy with the increasing population can get rid of the energy deficiency by modulating this type of natural nanosystems in the future.

2 Materials and methods

2.1 Material used

The china clay (kaolinite) $[\text{Si}_2\text{Al}_2\text{O}_5(\text{OH})_4]$ was purchased from Hindustan Minerals, India, and Multi-wall Carbon Nanotube was purchased from Sigma-Aldrich, Germany. Hexamine $[\text{C}_6\text{H}_{12}\text{N}_4]$, hydrochloric acid, nitric acid, hydrogen peroxide, and dimethylformamide $[\text{C}_3\text{H}_7\text{NO}]$ were purchased from Merck, India. For performing the analytical experiments, HPLC-graded acetone and ethanol have been

Table 1 Comparison of energy storage efficacy with previously reported articles (N.M- Not Mentioned)

Sl No.	Material name	Dielectric permittivity	AC conductivity (Sm^{-1})	Year	References
1	Epoxy-clay (montmorillonite)	5.35	N.M	2013	[16]
2	Ripidolite	14	N.M	2014	[17]
3	Montmorillonites suspensions in polydimethylsiloxane	20	$10^{-8} - 10^{-7}$	2018	[18]
4	Mullite and cordierite	20–40	N.A	2018	[19]
5	K+smectite	3–78	N.M	2020	[20]
6	Nontronite	1100	N.A	2020	[21]
7	Poly methyl methacrylate and acrylonitrile butadiene styrene-montmorillonite	10	N.M	2020	[22]
8	Soil (Clay, Clay Loam, Loam, and Loamy Sand)	23.26	N.M	2020	[23]
9	Polyester-meta kaolinite composite	14	N.M	2021	[24]
10	PVDF/6A Clay	230	N.M	2021	[25]
11	Finely Disperse Kaolinite Masses with Different Humidification	10.0	N.M	2022	[26]
12	mullite ceramics	16.7	N.M	2022	[27]
13	MWCNT-kaolinite	3920	3.0×10^{-4}	–	This report

purchased from Merck, Germany. Any further purifications have not been performed while using the purchased reagents. Millipore water having a resistivity of approximately $\sim 18.2 \text{ M}\Omega\text{-cm}$ has been used throughout the experiment.

2.2 Synthesis of the nanocomposite

2.2.1 Nanonization and activation of naturally formed kaolinite clay

Initially, the purchased natural clay has been pulverized with the help of a diamond mortar to minimize the agglomeration and has been sieved by a mesh having a diameter of $37 \mu\text{m}$. 10 g of that sieved clay was then taken and milled by top-down synthesis mechanism by using a ball milling instrument (Fritsch Planetary Mono Mill Pulverisette-6) for 48 h. The tungsten carbide balls and vials were used during this process by the 20:1 ball and sample mass ratio. The milled clay (namely K0) was then sent for further modifications.

The activation of the prepared natural nano clay was then performed by taking 4 gm of K0 and dissolving this in 160 ml of Millipore water by subsequent addition of 0.096 gm of hexamine under vigorous stirring. After that 40 μL of 37%, HCL was added dropwise to the solution and kept overnight at 80°C temperature. The solution was then centrifuged and dried at 70°C overnight. The dried sample was then mortared with an agate mortar and sent for further experiments.

2.2.2 Functionalization of multiwall carbon nanotube

A simple ultra-sonication technique was used to reduce the agglomeration of MWCNT. 50 mg of purchased MWCNT was dispersed in 15 ml of ethanol and sonicated by a bath sonicator for 2 h. After that, the solvent was evaporated by a hot air oven at 120°C . The dried MWCNT was then dispersed in 15 ml of 3 molar HNO_3 under vigorous stirring for 15 min at 60°C . The suspension was then sonicated for another 2 h. After completion of the sonication process, the sample was rinsed with water several times and further aged with H_2O_2 for 15 min at 60°C . After completing the reaction time, the black precipitate was filtered by a vacuum filtration unit. Finally, the sample was dried in a hot air oven at 70°C and sent for further treatment.

2.2.3 Preparation of MWCNT-kaolinite nanocomposite (CK)

The preparation of MWCNT-Kaolinite nanocomposite was performed by a simplified condensation technique. Initially, 1 gm of activated kaolinite was dissolved in 30 ml DMF and sonicated for 1 h. After that functionalized MWCNT was added to the solution maintaining the 1.0% w/w ratio. The solution was then refluxed under vigorous stirring by a condenser unit at 90°C for 24 h. The black precipitate was then collected and washed several times with deionized water until its pH achieved a neutral value.

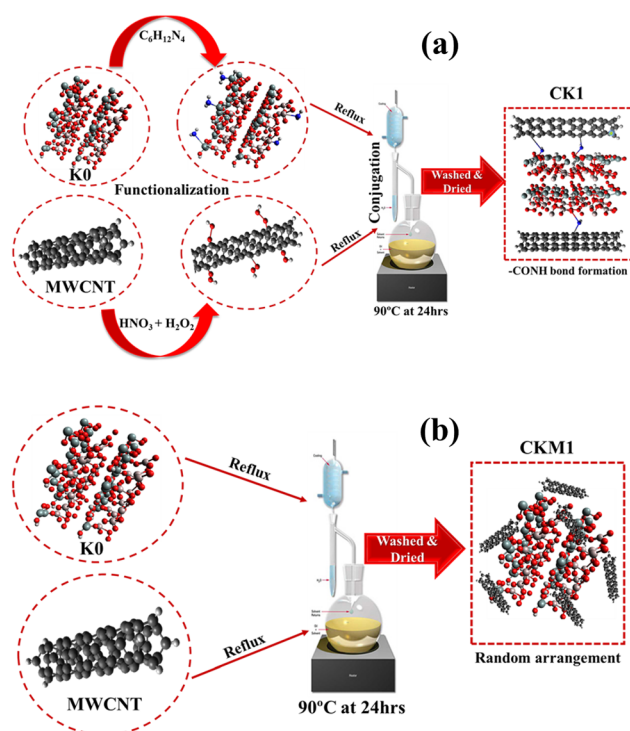


Fig. 1 Schematic representation of MWCNT-kaolinite nanocomposite formation **(a)** via surface modification represents the -CONH bond formation and proper attachment between kaolinite and MWCNT, **(b)** without any modification represents the random arrangement of the MWCNT in the nanoparticles

The nanocomposites were then dried in a hot air oven at 70°C for 24 h and marked as CK1.

Moreover, the same preparation technique was adopted with untreated kaolinite and MWCNT and marked the final nanocomposite as CKM1. After that, the samples K0, CK1, and CKM1 were sent for further experiments. The synthesis mechanism of the nanocomposites has been illustrated in Fig. 1.

2.3 Characterization techniques

Purity and structural properties are the most important issues of the natural sample that can be determined by the crystallographic information of the sample. Here X-ray diffraction (XRD) has been used to determine crystallographic information of natural kaolinite clay and its modified counterparts. A D-8 Advanced X-ray diffractometer (Cu-K_α target, 1.54 \AA), Bruker operated at 35 kV, 35 mA has been used to collect the diffractograms of the samples (scan speed 5 s/step) [28].

The interatomic bonding network is one of the best characterization tools of the sample. Here FTIR spectroscopy has been performed to distinguish the

bond vibrations. An IR-Affinity-1 S, Shimadzu spectrophotometer has been used to perform the bonding network analysis of the nanocomposite in a varying wavenumber range ($400\text{--}4000 \text{ cm}^{-1}$).

Particle size and surface morphology are the other important phenomenon. Field Emission Scanning Electron Microscopy (FESEM) (Inspect F-50, FEI, Netherlands) and Transmission Electron Microscopy (TEM) (JEOL, JEM-2000) have been used to observe the characteristics [29]. Initially, the samples were dispersed in acetone followed by sonication to reduce the agglomeration. After that, the samples were cast on the carbon-coated grids and sputtered coating on the surface of the material with gold plasma for microscopy. The accelerating voltage was set at 10–20 kV for FESEM and 200 kV for TEM micrography.

The EDX and mapping technique has been adopted to perform the elemental composition analysis of the sample by a Bruker Quantax EDS analyzer.

Thermal analysis of any material is one of the most important characterization tools to investigate the stability as well as the thermal phase information of the sample. Herein, DTA–TGA analysis of the clay and clay-MWCNT nanocomposite has been investigated by a DTG-60 H, Shimadzu thermal analyzer [30].

Zeta potential measurement has been carried out to get the surface charge of the samples [31]. Initially, the samples were sonicated in deionized water to reduce agglomeration. After that, a Zetasizer, Malvern instrument has been employed to measure the surface charge of the pristine kaolinite as well as the modified counterparts.

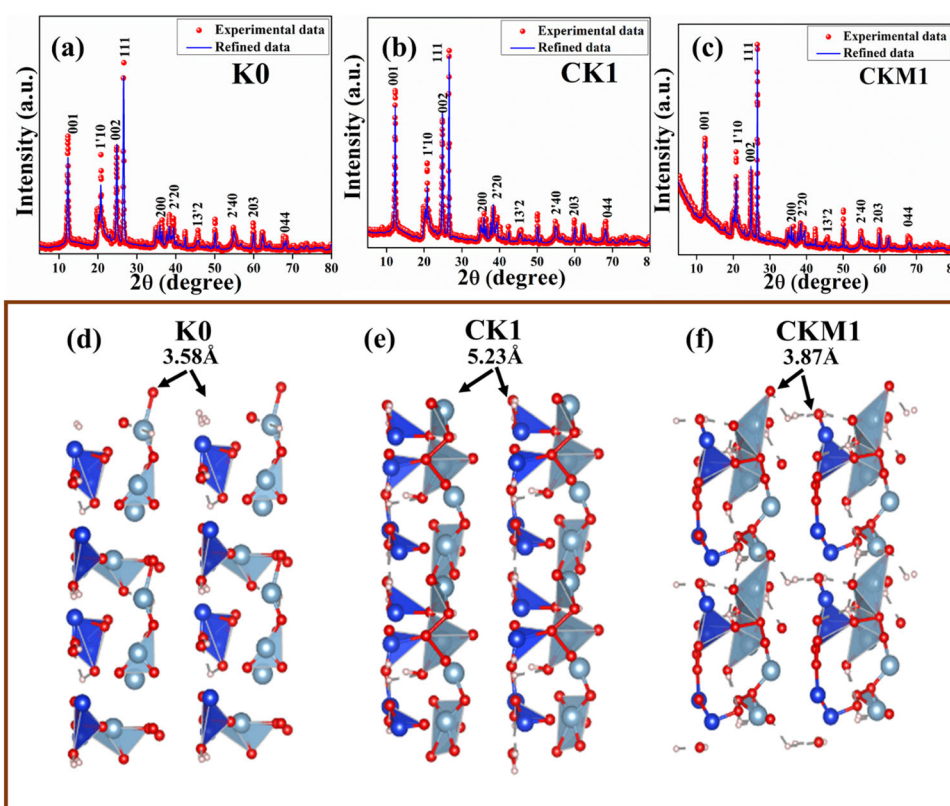
The electrical measurement at varying temperatures and frequencies has been performed by a 4294 A Precision Impedance Analyzer, Agilent.

3 Result and discussion

3.1 Structural, bonding network and morphological analysis of nanocomposite

The X-ray diffractograms of the samples in Fig. 2 show that the diffraction planes of the sample have matched with the kaolinite JCPDS data having card no 80-0886.

Fig. 2 XRD pattern and crystallographic visualization of MWCNT-kaolinite nanocomposite **a–c** XRD of nano kaolinite, surface modified nanocomposite, and unmodified nanocomposite, respectively, matched with Rietveld refinement technique conveys the purity of clay and proper doping of MWCNT, **d–f**, respectively, unit cell visualization of nano kaolinite, surface modified nanocomposite with MWCNT shows maximum basal space separation, and unmodified nanocomposite, respectively, by Vesta software



Any undesired maxima that have not occurred in the diffractogram suggest the purity of the natural kaolinite sample. The incorporation of functionalized MWCNT in the kaolinite matrix has not shown any undesired peak, as well as no shifting of the planes, which suggests the successful MWCNT-kaolinite nanocomposite formation. After that, the Rietveld refinement have been performed by the superposition of the experimental data of the nanocomposites with the standard crystallographic data of pristine kaolinite (AMCSD file no. 1550598). The refinement has shown a promising superposition with reasonable fitting coefficients [32]. The micrographs of the samples have shown perturbation of the periodic polyhedral structure of pristine kaolinite in the nano regime (Fig. 2). This phenomenon can occur through the high-energy top-down synthesis procedure of the bulk clay [33, 34]. Additionally, MWCNT incorporation creates an increment in the interlayer separation between the silica and alumina layers. In reality, natural kaolinite nanoparticles are attached to two the surface of two functionalized MWCNTs as a result the basal space separation increases (Fig. 2). Such separation can create entrapment zones and can affect various physicochemical properties. All the

microstructural parameters of the nanocomposites have been shown in Table 2.

In Fig. 3 the FTIR analysis of the nanocomposites shows bands between 430 and 700 cm^{-1} which are validating Si–O–Al bending and the vibrational maximum at 750 cm^{-1} refers to the vibration of the AlO_6 bond [35]. Another two vibrational bands at 790 and 920 cm^{-1} are related to Si–O and Al–OH deformation, respectively. The band due to Si–O stretching has also occurred in the region of 940 – 1150 cm^{-1} . These vibrational bands proved the presence of AlO_6 and SiO_4 polyhedral in the natural clay sample and its modified counterparts. Another broad IR maximum has been occurring in the region of 3620 – 3700 cm^{-1} validating the existence of –OH groups in the nanocomposites [36]. The vibrational band in the region of 2340 – 2360 cm^{-1} has been occurring by the atmospheric CO_2 . Additionally, a few tiny bands appear at 1466 , 1645 , and 1670 cm^{-1} which are missing in the pristine kaolinite sample. The bands at 1466 and 1645 appeared due to C=C vibration which may be originated from the MWCNT moiety of the nanocomposite [37]. On the other hand, the band at 1670 cm^{-1} occurs due to –CONH bond vibration which is missing in the pure kaolinite and very low in the CKM1 sample. This –CONH bond

Table 2 Crystallographic parameters of different nanocomposites

Parameters	K0	CK1	CKM1
<i>a</i> (Å)	5.1472473	5.1402044	5.14049
<i>b</i> (Å)	8.907626	8.940447	8.936471
<i>c</i> (Å)	7.4144506	7.41872	7.4211307
α (°)	92.03356	92.20726	92.09829
β (°)	105.06041	105.05344	105.10188
γ (°)	90.46312	90.31439	90.27981
Size	561.7322	997.80084	1568.4888
Micro strain	1.0578E-4	6.801E-4	1.7731E-4
<i>V</i> (Å ³)	328.013	304.068	328.861
χ^2	1.642	1.568	1.554
<i>R_p</i> (%)	16.849	11.636	7.998
<i>R_{wp}</i> (%)	27.669	18.246	12.432

refers to the successful composite formation between kaolinite and MWCNT. The –CONH bond also validates that the preparation of nanocomposites by surface modification is the right way to perform the synthesis procedure. This bond also validates the increasing basal space separation in the CK1 sample. In reality, the pulling clay particle towards MWCNT by –CONH bond increases the basal space separation which changes the physicochemical properties of the nanocomposite.

The FESEM micrograph of the pure kaolinite (K0) shows a hexagonal sheet-like 2D structure (Fig. 4) having an average dimension of 60–80 nm. Additionally, the TEM micrograph has shown the stacking of MWCNT on the surface of the kaolinite nano clay depicted in Fig. 4. This conveys the proper attachment of MWCNT to the clay surface and proved the successful nanocomposite formation which is analogous to XRD and FTIR analysis. The TEM image also shows that the natural clay formed an arrangement

between two consecutive MWCNTs which conveys the basal space separation in X-ray crystallography. This attachment also validates the proper functionalization of the kaolinite clay and MWCNT. The elemental composition analysis by EDX shows a uniform distribution of aluminum, silicon, and oxygen which depicts the purity of the natural kaolinite has been shown in Fig. 4. On the other hand, mapping spectra show the presence of all the elements of kaolinite along with it also shows the presence of carbon which has proved the successful MWXCNT-kaolinite nanocomposite formation which is analogous to the XRD and FTIR data.

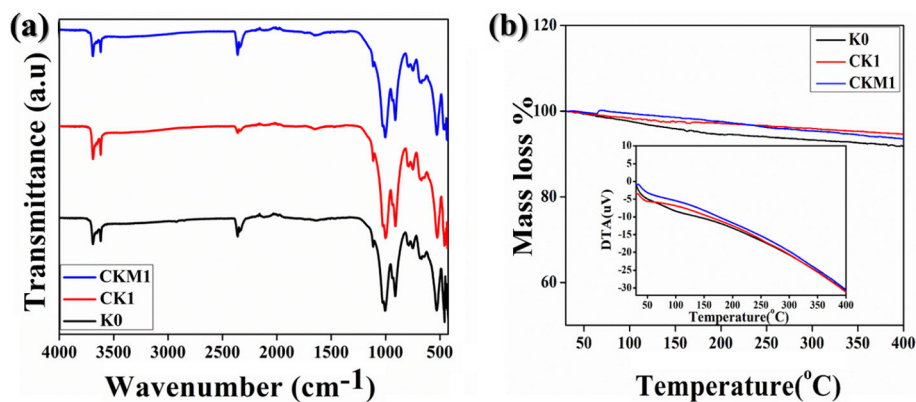
3.2 Thermal analysis of the synthesized samples

The thermogravimetric analysis of the clay and clay-modified nanocomposites show that the samples are stable up to 400 °C from room temperature which is depicted in Fig. 3. The mass loss for the samples K0, CK1, and CKM1 are taking place, respectively, 8%, 5%, and 6%. It is observed that the CK1 sample is most thermally stable than another two. From the differential thermal analysis (DTA) it has been observed that there is no phase change in the sample up to 400 °C which suggest that the nanocomposites are stable and do not change their phase into any other forms up to this temperature [38].

3.3 Surface properties of the samples

Normally, kaolinite has negatively charged basals and positively charged edges. Here basal planes consist of an alumina octahedral layer and a silica tetrahedral layer. Usually, constant structural charge due to isomorphs substitution of Al³⁺ for Si⁴⁺ in the

Fig. 3 **a** FTIR spectroscopy of the nanocomposites confirms the presence of –CONH bond in the modified nanocomposite, **b** TGA–DTA of the nanocomposites represents the percentage mass loss with the temperature of the nanocomposites



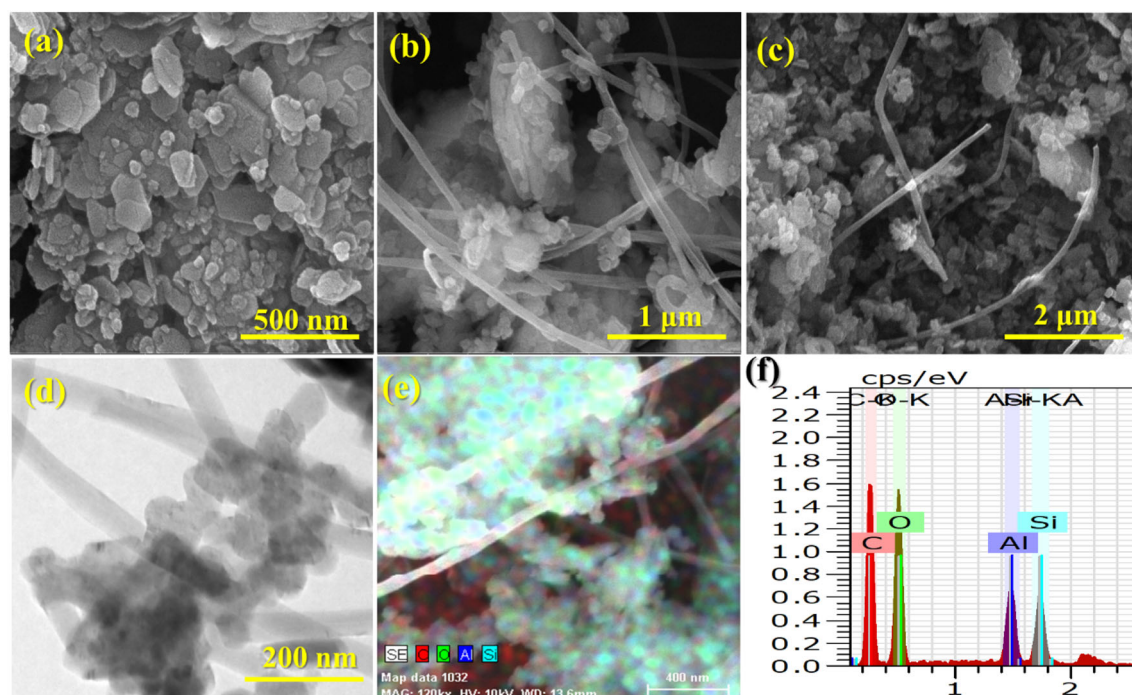


Fig. 4 FESEM micrograph of (a) nano kaolinite represents the hexagonal 2D structure of clay with the particle size in nano regime, (b) CK1 shows the presence of MWCNT and attachment of MWCNT with natural clay, (c) in CKM1 presence of MWCNT reduces because of improper attachment with nano clay, (d) TEM

image of CK1 shows proper attachment between clay and MWCNT and the formation of micro capacitors, (e, f) mapping and EDS of CK1 represents the homogeneous distribution of elements in the nanocomposites

siloxane (silica octahedral layer) facets and Fe^{2+} or Mg^{2+} for Al^{3+} in the alumina (alumina octahedral layer) facets is making the basal planes negative. Pure kaolinite shows a surface charge of around -8.11 mV, which is analogous to the theoretical explanation. The negative surface charge increases for the sample CK1 (-38.2 mV), whereas it gets quenched for the sample CKM1 (-8.72 mV). This phenomenon conveys that synthesized nanocomposite in the functionalized route has better stability than the non-functionalized one. In Fig. 5, the Zeta potential of the nanocomposites has been depicted.

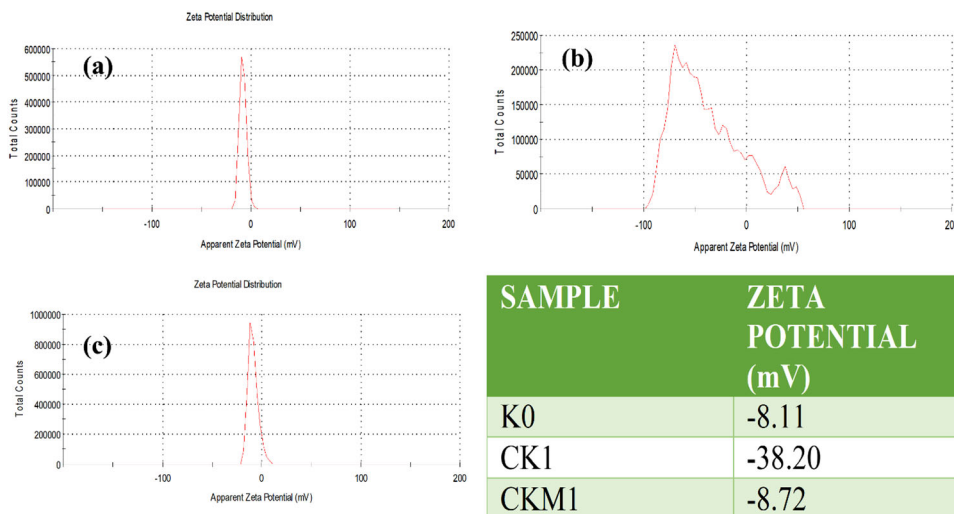
3.4 Formation mechanism of MWCNT-kaolinite nanocomposite

During the activation process of kaolinite, the $-\text{NH}_2$ functional group incorporates over its surface and makes the surface hydrophilic. Similarly, the $-\text{COOH}$ group makes the surface of MWCNT hydrophobic in nature. The probability of formation of the nanocomposite was boosted due to this hydrophilic-hydrophobic interaction. The FTIR spectra of the modified natural clay show the $-\text{CONH}$ bond

vibration which may be occurred by this $-\text{NH}_2-\text{COOH}$ interaction [39]. The formation of the bond between the nano clay and MWCNT rigidly binds the MWCNT over the surface of kaolinite and validates the nanocomposite formation. The FESEM and TEM micrographs of the sample also validate this interpretation [40].

MWCNT incorporation in the kaolinite matrix increases the basal spacing between the silica and alumina layer studied by the crystallographic studies by VESTA 4.3.0 [41]. The attraction force between activated kaolinite and functionalized CNT plays a pivotal role in this increment of interlayer separation. In reality, MWCNT pulls the kaolinite particle from a different direction through the $-\text{CONH}$ bond, which is sufficient to increase the interlayer separation. Although the basal spacing increases for the nanocomposite CK1 but remains almost unchanged for the sample CKM1. There is no modification of MWCNT or kaolinite taking place to prepare the sample CKM1. For this reason, the $-\text{CONH}$ bond formation may not occur in this case and interlayer separation remain unchanged. A schematic

Fig. 5 Zeta potential of the nanocomposites (a) K0, (b) CK1 shows the highest negative zeta potential, and (c) CKM1



representation of the formation mechanism of the nanocomposites has been depicted in Fig. 1.

3.5 Investigation of dielectric properties of the nanocomposite

The dielectric property plays a pivotal role in the energy storage application of any sample [41]. It depends on various parameters like humidity, temperature, and frequency of the external electric field. Chemical compounds, thermal stability, morphology, surface property, and the grain size of the sample also play an important role in this property. The total dielectric permittivity of any sample depends upon two functions one is the real part of the permittivity (ϵ') and another one is the imaginary part (ϵ'') [42, 43]. The real part is related to the charge storage capacity and the imaginary part is related to the electrical dissipation factor. These two important components of the sample are related to each other as $\epsilon = \epsilon' + j\epsilon''$, [44, 45]. Where ϵ is the total dielectric permittivity of the sample. The real part of the dielectric constant can be determined by the following relation, [46, 47]

$$\epsilon' = (C.d)/(\epsilon_0 A),$$

where C is the capacitance of the material, d and A is the thickness and area of the solid pellet used during the measurement and ϵ_0 denotes the free space permittivity having a constant value of 8.85×10^{-12} F/m. Here, a hydraulic press has been employed to make the solid pellet of the materials using 100 mg of each sample. A copper strip was used as the electrode material on both sides of the solid pellet [48]. Initially,

the measurement started at 25 °C and the reading was noted by increasing the temperature step by step. The dielectric permittivity has been examined in a varying frequency (40 Hz–1 MHz) and varying temperature (25 °C–200 °C) region depicted in Fig. 6.

Figure 6 shows a gradual reduction in permittivity value with increasing frequency. This phenomenon can be explained by the virtue of Maxwell–Wagner–Sillars interfacial polarization [49]. Normally, any dielectric material has conductive grains, separated by a thin layer of insulated grain boundaries. This grain boundary could be formed by various structural deformation, vacancy, and crystal defects that are created during the sample preparation. When the frequency is low the energy of the external electric field is insufficient to pull out the grains from the insulated grain boundaries as a result polarisation takes place. This phenomenon is quite analogous to Koop's phenomenological theory [50]. In the higher frequency domain, the charges are getting free from the grain boundary as a result lower permittivity value is observed.

The MWCNT incorporation in the kaolinite matrix increases the dielectric permittivity as shown in Fig. 6. It has been observed that the dielectric permittivity value that occurs in the natural kaolinite (K0) sample is minimum (32 at 40 Hz). The dielectric permittivity attains a maximum value (3920 at 40 Hz) in the CK1 sample. Whereas, this value gets quenched for the CKM1 (510 at 40 Hz) sample. In reality, this type of dielectric constant enhancement can be explained by the virtue of structural modification of the sample. In the previous sections, it has been

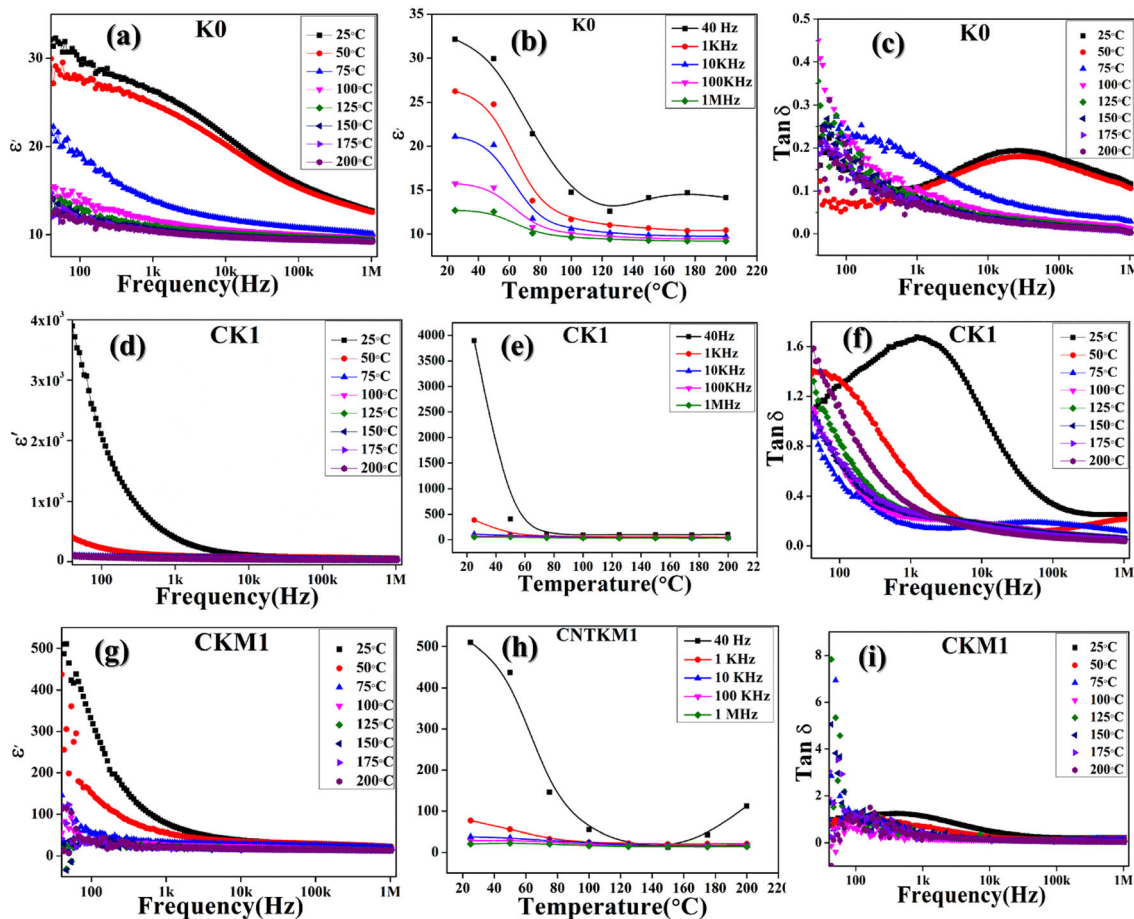


Fig. 6 a, d, g Frequency-dependent permittivity of the nanocomposites in different temperatures shows the maximum permittivity in CK1 sample, b, e, h temperature-dependent

dielectric constant of the nanocomposites in different frequencies, and c, f, i tangent loss of the nanocomposites with respect to frequency represents the nominal tangent loss

stated that kaolinite nanoparticle has attached to two adjacent MWCNT surfaces [51]. Periodic arrangements of parallels, attached to such capacitors make the dielectric constant high for the nanocomposites. On the other hand, just a mixed nanocomposite CKM1 sample does not show such an increment in dielectric constant. Non-functionalized clay and CNT have not formed any attachment and proficient structural deformation. The formation of micro-capacitors has been interrupted for this reason as a result dielectric constant has not increased properly.

The temperature-dependent dielectric study has also been performed in a wide range of temperatures (25–200 °C) shown in Fig. 6. The Figure shows a gradual reduction of dielectric permittivity with increasing temperature. This type of dielectric constant reduction can be explained by virtue of the

charge transport phenomenon in the sample [52]. In reality, the conductive grain and insulated grain boundary bring out quite static nature at low temperatures [53]. The M–W polarization can take place at such a low temperature. While the temperature increases, the conductive grain becomes free at a critical temperature value and reduces the polarization effect. Such a phenomenon reduces the dielectric permittivity of the sample. Additionally, in Fig. 3, it has been shown that the material is thermally stable up to 400 °C. So, it can be easily said that the storage material formed by this sample should be thermally stable in a broad range.

The dissipation factor has also been estimated by determining the tangent loss of all sample sets. It is presented in Fig. 6, that the tangent loss is nominal for the samples. The CK1 sample showed the highest

permittivity value with the nominal tangent loss that can be used as a promising storage material in the near future [54].

3.6 Investigation of AC conductivity of the nanocomposites

The conduction mechanism of the MWCNT-kaolinite nanocomposite has been studied in varying frequencies region at different temperatures (Fig. 7). It has been found that AC conductivity increases when the frequency of the field increases. It can be validated by virtue of the charge transport mechanism of the nanocomposite [55]. In reality, in the higher frequency region, conductive grains acquired enough activation energy to get free. This activation energy can be calculated by the following equation called the Arrhenius equation. [56, 57]

$$\sigma = \sigma_0 \exp(-E_a/K_B T),$$

here E_a is the activation energy, σ_0 is the pre-exponential factor and T is the temperature on an absolute scale. The Arrhenius plot has been determined by the AC conductivity data at the 40 Hz, 1 kHz, 10 kHz, 100 kHz, and 1 MHz external field frequencies depicted in Fig. 7.

It has been shown that the activation energy increases with increasing field frequencies. In reality, at a higher frequency region, the conductive grains get more translation energy and move freely. It has been shown that the conductivity also increases in the MWCNT-doped nanocomposites than in the bare clay. Figure 7 showed the AC conductivity for the samples K0, CK1, and CKM1 are, respectively, 8.5×10^{-5} , 3.0×10^{-4} , and 2.6×10^{-4} at 1 MHz frequency. In reality, the conductive MWCNT increases the charge transport in the nanocomposite. The conductivity value also proved the CK1 sample is more conductive than others.

Jonscher's universal power law has been adopted here to investigate the dependence of AC conductivity on the frequency which is stated below.

$$\sigma_{ac} = B\omega^n,$$

here, B is a constant having unit of conductivity and n is another constant that is dimensionless. The frequency-dependent conduction mechanism has been referred by the non-zero value of n . It has been calculated by plotting $\ln\sigma$ against $\ln\omega$ for all the samples depicted in Fig. 8. The n value of the nanocomposites varied between 0.24 and 1.01 suggesting the non-Debye type conduction mechanism. It has been

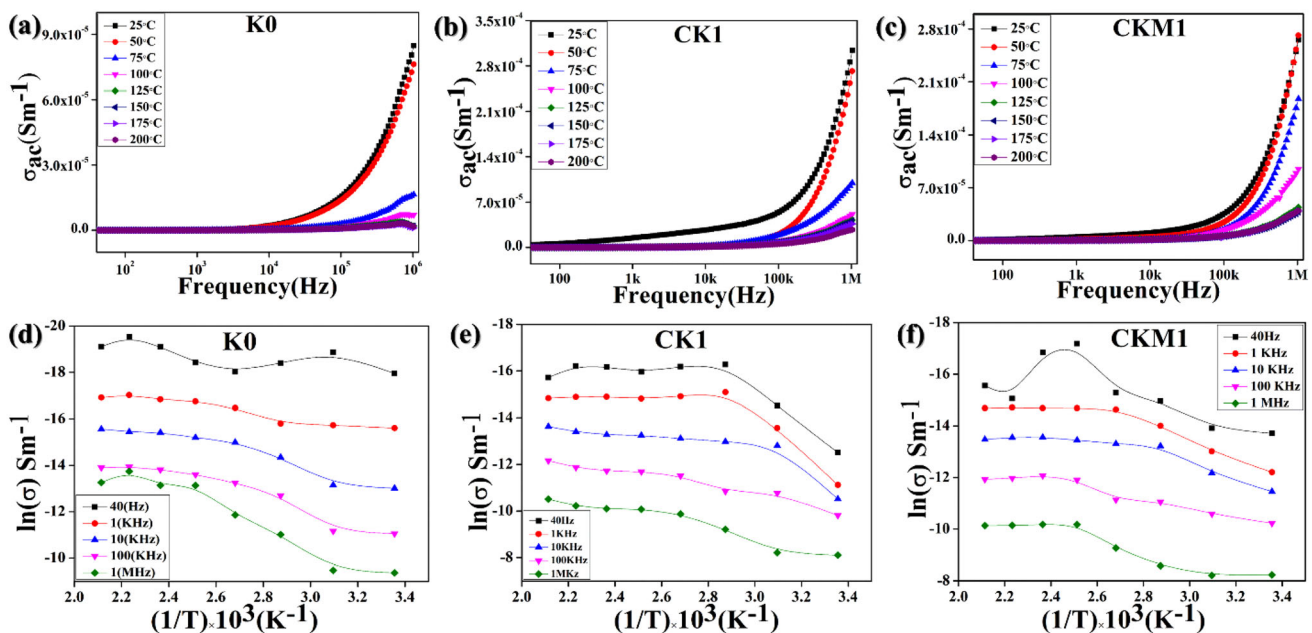


Fig. 7 a–c Frequency-dependent AC conductivity of the nanocomposites K0, CK1, and CKM1 shows the maximum AC conductivity in the CK1 sample, d–f Arrhenius plots of the nanocomposites to estimate the activation energies of the nanocomposites

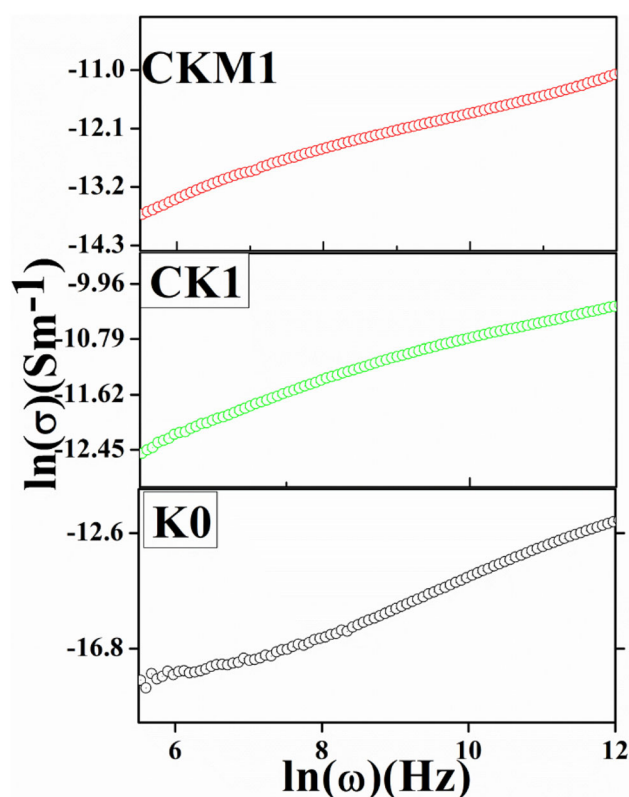


Fig. 8 Jonscher's plots of the nanocomposites show the non-zero value of the nanocomposites which confirms the non-Debye type conduction mechanism

shown in previous sections that the CK1 sample possesses a better attachment between clay and MWCNT. As a result, CK1 shows the most charge transport than other nanocomposites and also possesses better ac conductivity.

4 Conclusion

In this study, we have successfully modified naturally occurring kaolinite clay to achieve proper surface attachment with multi-walled carbon nanotubes (MWCNTs). A straightforward top-down synthesis mechanism, followed by surface modification using commonly used chemicals, has been employed to produce a functionalized nanosystem. This simple synthesis protocol allows for large-scale production, making it suitable for industrial applications.

The purity of the natural clay has been confirmed through conventional characterization techniques such as XRD (X-ray diffraction) and EDS (Energy Dispersive Spectroscopy). Microstructural evaluations using theoretical XRD refinement have revealed

an increased basal space separation, leading to enhanced oxygen vacancy and entrapment zones in the modified clay. These modifications further contribute to the modulation of electrical properties.

The incorporation of MWCNTs (1% w/w) in the kaolinite clay matrix has shown an improvement in energy storage properties and AC conductivity of the nano clay. The modified nano clay exhibits enhanced electrical properties and a negligible loss tangent, making it a promising material for energy storage applications. This nanosystem also holds potential as a separator material for the mass-scale fabrication of capacitors in industrial settings.

Experimental evidence suggests that the clay-mediated composite demonstrates superior temperature stability (up to 400 °C) and structural integrity. The combination of its easy and scalable synthesis procedure, stability, biocompatibility, abundance in nature, and promising charge storage capacity positions this nanocomposite as a strong candidate for the development of “green capacitors” in the near future.

Acknowledgements

The authors would like to thank the Department of Physics, Jadavpur University, for extending experimental facilities. S.D. and D.M would like to acknowledge UGC-DAE-CSR (Grant No. CRS/2021-22/02/498), and J.R and R.B acknowledges UGC-DAE-CSR (Grant No. CRS/2021-22/02/514) for funding.

Author contributions

DM: conceptualization, data curation, computation, writing of the original draft. AS: data curation. SR: conceptualization, investigation, computation. SB: conceptualization, investigation. JR: data curation, computation. SG: data curation. RB: investigation, funding. SS: investigation. SD: investigation, funding.

Funding

UGC-DAE Consortium for Scientific Research, India (Grant No. CRS/2021-22/02/498 and CRS/2021-22/02/514).

Data availability

Data and codes will be available on reasonable request.

Declarations

Competing interest The authors declare that they have no competing interests.

Ethical approval Not applicable.

Supplementary Information: The online version contains supplementary material available at <http://doi.org/10.1007/s10854-023-11007-3>.

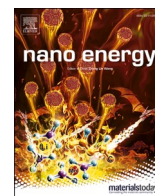
References

1. S.V. Venkatesan, A. Nandy, K. Karan, S.R. Larter, V. Thangadurai, *Electrochem. Energy Rev.* **5**, 16 (2022)
2. M.A. Mahdi, S.R. Yousefi, L.S. Jasim, M. Salavati-Niasari, *Int. J. Hydrogen Energy* **47**, 14319 (2022)
3. H. Wang, D. Tran, J. Qian, F. Ding, D. Losic, *Adv. Mater. Interfaces* **6**, 1900915 (2019)
4. P. Mehdizadeh, M. Jamdar, M.A. Mahdi, W.K. Abdulsahib, L.S. Jasim, S.R. Yousefi, M. Salavati-Niasari, *Arabian J. Chem.* **16**, 104579 (2023)
5. G. Khandelwal, T. Minocha, S.K. Yadav, A. Chandrasekhar, N.P. Maria, S.C. Joseph Raj, Gupta, S.J. Kim, *Nano Energy* **65**, 104016 (2019)
6. S.R. Yousefi, O. Amiri, M. Salavati-Niasari, *Ultrason. Sonochem.* **58**, 104619 (2019)
7. H. Pálková, M. Barlog, J. Madejová, V. Hronský, L. Petra, E. Šimon, P. Billik, M. Zimowska, *Appl. Clay Sci.* **213**, 106214 (2021)
8. S.R. Yousefi, D. Ghanbari, M. Salavati-Niasari, M. Hassanpour, *J. Mater. Sci.* **27**, 1244 (2016)
9. T.T. Zhu, C.H. Zhou, F.B. Kabwe, Q.Q. Wu, C.S. Li, J.R. Zhang, *Appl. Clay Sci.* **169**, 48 (2019)
10. S.R. Yousefi, A. Sobhani, H.A. Alshamsi, M. Salavati-Niasari, *RSC Adv.* **11**, 11500 (2021)
11. M.S. Morsy, H. Shoukry, M.M. Mokhtar, A.M. Ali, S.A. El-Khodary, *Constr. Build. Mater.* **172**, 243 (2018)
12. K. Ke, V. Solouki Bonab, D. Yuan, I. Manas-Zloczower, *Carbon* **139**, 52 (2018)
13. A.K. Choudhary, H. Pramanik, *Int. J. Hydrogen Energy* **45**, 13300 (2020)
14. D. Mondal, S. Bardhan, N. Das, J. Roy, S. Ghosh, A. Maity, S. Roy, R. Basu, S. Das, *Nano Energy* **104**, 107893 (2022)
15. S. Kouser, A. Prabhu, S. Sheik, K. Prashantha, G.K. Nagaraja, J. Neetha, K.M. D'souza, Navada, D.J. Manasa, *Appl. Surf. Sci. Adv.* **6**, 100158 (2021)
16. A. Guevara-Morales, A.C. Taylor, *J. Mater. Sci.* **49**, 1574 (2014)
17. S. Lokanatha, S. Bhattacharjee, *Trans. Indian Ceram. Soc.* **45**, 41 (1986)
18. N.M. Kuznetsov, V.G. Shevchenko, D.Y. Stolyarova, S.A. Ozerin, S.I. Belousov, S.N. Chvalun, *J. Appl. Polym. Sci.* **135**, 46614 (2018)
19. V.J. da Silva, E.P. de Almeida, W.P. Gonçalves, R.B. da Nóbrega, G. de Neves, H. de Lira, R.R. Menezes, L.N. de Lima Santana, *Ceram. Int.* **45**, 4692 (2019)
20. J. Zhang, M.B. Clennell, M. Josh, M. Pervukhina, *Appl. Clay Sci.* **198**, 105840 (2020)
21. K. Kułacz, J. Waliszewski, S. Bai, L. Ren, H. Niu, K. Orzechowski, *Appl. Clay Sci.* **202**, 105952 (2021)
22. N. Anwar, M. Ishtiaq, A. Shakoor, N.A. Niaz, T.Z. Rizvi, M. Qasim, M. Irfan, A. Mahmood, *Polym. Polym. Compos.* **29**, 807 (2021)
23. H. Kabir, M.J. Khan, G. Brodie, D. Gupta, A. Pang, M.V. Jacob, E. Antunes, *J. Microw. Power Electromagn. Energy* **54**, 3 (2020)
24. G. Jonathan, E. Wilson, O. Toyese, A. AMEH, I. MADU-FOR, T. BELLO, *Eur. J. Mater. Sci. Eng.* **6**, 19 (2021)
25. C.V. Chanmal, S.S. Bandgar, C.D. Mungamode, S.D. Chavan, S.G. Pawar, R.N. Mulik, V.L. Mathe, J.P. Jog, *Macromol. Symp.* **400**, 1547 (2021)
26. M.M. Filyak, A.G. Chetverikova, O.N. Kanygina, *Glass Ceram.* **78**, 458 (2022)
27. X. Gao, X. Feng, D. Zhang, J. Zhang, Y. Peng, Z. Pan, Z. Dai, *Int. J. Appl. Ceram. Technol.* (2022). <https://doi.org/10.1111/ijac.14486>
28. D. Wang, H. Wang, S. Larsson, M. Benzerzour, W. Maherzi, M. Amar, *Constr. Build. Mater.* **241**, 118085 (2020)
29. J.D. Raja Selvam, I. Dinaharan, S. Vibin, Philip, P.M. Mashinini, *J. Alloys Compd.* **740**, 529 (2018)
30. R.L. Frost, J. Kristof, E. Horvath, J.T. Klopogge, *Thermochim. Acta* **327**, 155 (1999)
31. S. Patil, A. Sandberg, E. Heckert, W. Self, S. Seal, *Biomaterials* **28**, 4600 (2007)
32. S. Roy, S. Bardhan, D.K. Chanda, J. Roy, D. Mondal, S. Das, *ACS Appl. Mater. Interfaces* **12**, 43833 (2020)
33. Y. Chen, Z. Hu, Y. Xu, J. Wang, P. Schützendübe, Y. Huang, Y. Liu, Z. Wang, *J. Mater. Sci. Technol.* **35**, 512 (2019)
34. P.P. Seth, N. Singh, M. Singh, O. Prakash, D. Kumar, *J. Alloys Compd.* **821**, 153205 (2020)
35. P.C. Lopes, F.A. Dias, L.R.D. Da Silva, *Mater. Lett.* **57**, 3397 (2003)

36. L. Zhang, C. Wang, Z. Fei Yan, X. Wu, Y. Qian Wang, D. Meng, H. Xie, *Appl. Clay Sci.* **86**, 106 (2013)
37. M.B. Moraes, L. Cividanes, G. Thim, J. Aerosp. Technol. Manage. (2018). <https://doi.org/10.5028/jatm.v10.944>
38. D. Kapush, S.V. Ushakov, A. Navrotsky, Q.J. Hong, H. Liu, A. van de Walle, *Acta Mater.* **124**, 204 (2017)
39. J. Schmitt, H.C. Flemming, *Int. Biodeterior. Biodegrad.* **41**, 1 (1998)
40. K. Jiao, S. Yao, C. Liu, Y. Gao, H. Wu, M. Li, Z. Tang, *Int. J. Coal Geol.* **128–129**, 1 (2014)
41. N.V. Long, Y. Yang, T. Teranishi, C.M. Thi, Y. Cao, M. Nogami, *Mater. Des.* **86**, 797 (2015)
42. R. Gerhardt, *J. Phys. Chem. Solids* **55**, 1491 (1994)
43. S. Das, D. Mondal, S. Bardhan, S. Roy, D.K. Chanda, A. Maity, S. Dutta, K. Mukherjee, K. Das, *J. Mater. Sci.* **33**, 7119 (2022)
44. A.M.M. Farea, S. Kumar, K.M. Batoo, A. Yousef, C.G. Lee, Alimuddin, *J. Alloys Compd* **464**, 361 (2008)
45. M. Humbert, B. Petit, B. Bolle, N. Gey, *Mater. Sci. Eng.* **A454–455**, 508 (2007)
46. S. Ghosh, S. Roy, S. Bardhan, N. Khatua, B. Bhowal, D.K. Chanda, S. Das, D. Mondal, R. Basu, S. Das, *J. Electron. Mater.* **50**, 3836 (2021)
47. S. Bardhan, S. Roy, D.K. Chanda, S. Das, K. Pal, A. Chakraborty, R. Basu, S. Das, *Cryst. Growth Des.* **19**, 4588 (2019)
48. T. Piasecki, K. Chabowski, K. Nitsch, *Measurement* **91**, 155 (2016)
49. Y. Zeng, C. Xiong, W. Li, S. Rao, G. Du, Z. Fan, N. Chen, *J. Alloys Compd.* **905**, 164172 (2022)
50. T.M. Meaz, S.M. Attia, A.A. EL Ata, *J. Magn. Magn. Mater.* **257**, 296 (2003)
51. M. Nofar, R. Salehiyan, S.S. Ray, *Compos. B Eng.* **215**, 108845 (2021)
52. J.W. Steeds, A. Gilmore, K.M. Bussmann, J.E. Butler, P. Koidl, *Diam. Relat. Mater.* **8**, 996 (1999)
53. M. Kumar, S. Shankar, S. Brijmohan, O.P. Kumar, Thakur, A.K. Ghosh, *Phys. Lett. A* **381**, 379 (2017)
54. C.E. Hori, H. Permana, K.Y.S. Ng, A. Brenner, K. More, K.M. Rahmoeller, D. Belton, *Appl. Catal. B* **16**, 105 (1998)
55. G. Grüner, A. Zettl, *Phys. Rep.* **119**, 117 (1985)
56. A. El Bachiri, M. El Hasnaoui, A. Louardi, A. Narjis, F. Bennani, *Phys. B Condens Matter* **571**, 181 (2019)
57. C.Y. Tan, N.K. Farhana, N.M. Saidi, S. Ramesh, K. Ramesh, *Org. Electron.* **56**, 116 (2018)

Publisher's Note Springer Nature remains neutral with regard to jurisdictional claims in published maps and institutional affiliations.

Springer Nature or its licensor (e.g. a society or other partner) holds exclusive rights to this article under a publishing agreement with the author(s) or other rightsholder(s); author self-archiving of the accepted manuscript version of this article is solely governed by the terms of such publishing agreement and applicable law.



Natural clay-based reusable piezo-responsive membrane for water droplet mediated energy harvesting, degradation of organic dye and pathogenic bacteria

Dhananjoy Mondal^a, Souravi Bardhan^{a,b,1}, Namrata Das^a, Jhili Roy^a, Saheli Ghosh^a, Anupam Maity^c, Shubham Roy^{a,d,2}, Ruma Basu^e, Sukhen Das^{a,*,3}

^a Department of Physics, Jadavpur University, Kolkata 700032, India

^b Department of Environmental Science, Netaji Nagar College for Women, Kolkata 700092, India

^c School of Materials Science, Indian Association for the Cultivation of Science, Kolkata 700032, India

^d School of Science and Shenzhen Key Laboratory of Flexible Printed Electronics Technology, Harbin Institute of Technology, Shenzhen 518055, China

^e Department of Physics, Jogamaya Devi College, Kolkata 700026, India

ARTICLE INFO

Keywords:

Piezoelectric device
Piezocatalysis
Natural clay
MWCNT
Kaolinite

ABSTRACT

Nowadays, scientists have paid attention to utilizing natural and biocompatible materials for combating global challenges such as water pollution and the energy crisis. Moreover, pathogenic bacteria have also posed a severe threat to human health and the overuse of conventional antibiotics makes this situation even worse by evolving multidrug-resistant strains (MDR). Herein, we developed a natural clay (kaolinite) and multi-walled CNT (MWCNT) based nanocomposite, which has been encapsulated in the polymeric matrix of Poly (vinylidene fluoride-hexafluoropropylene) (PVDF-HFP) to achieve a multifunctional piezo-responsive membrane. This membrane is capable to generate piezoelectric energy under the perpendicular flow of water droplets. Such stimulus generates a 4.1 V voltage and 1.5 μ A current maintaining a piezoelectric power density of 50 W m^{-3} . It is worth noting that this membrane can eliminate around 96% Rhodamine-B concentration in only 60 min in water under ultrasound. A closer look suggests that the generation of reactive oxygen species (ROS), especially OH^* accelerates the catalytic process under ultrasonic vibration. Such an interesting result motivated us to implement this piezocatalytic process to eradicate pathogenic bacteria, which shows a radical bactericidal effect (almost 99% killing) and evolves as an alternative antibacterial technique.

1. Introduction

In the current world, technological advancements and modernization are resulting in the release of various organic, inorganic, and biological contaminants in water resources at an alarming rate, thus posing a serious threat to aquatic life and the environment [1,2]. On the other hand, widespread industrialization has elevated the demand for consuming energy which ultimately is related to the rapid extraction of fossil fuels [3,4]. Hence, the present scenario seeks an immediate requirement of a biocompatible, efficient, cost-effective, and easily synthesizable system that can simultaneously be useful to combat both these issues. Traditional adsorption-based removal of pollutants has

emerged as one of the most efficient techniques to handle water-borne pollutants, but the transfer of the pollutants from one phase to another often results in secondary pollution [5–7]. Although the bioremediation methods have emerged as an eco-friendly alternative, it suffers drawbacks like high reaction time, seasonal alternation, and reversibility. Recently, piezocatalysis-based pollutant degradation has been widely reported as one of the most promising and effective techniques for water remediation [8,9]. Application of physical stimuli such as mechanical stress or ultrasound on a piezoelectric material can instantly create surface piezo potential and a built-in electric field. Various semiconductor-based nanosystems and metal ion-implanted nanocomposites have been gaining interest and researchers are

* Corresponding author.

E-mail address: sdasphysics@gmail.com (S. Das).

¹ ORCID IDs: 0000-0003-0944-2940

² ORCID IDs: 0000-0001-5245-3229

³ ORCID IDs: 0000-0001-8372-3076

focusing on band gap tuning and suppression of charge carrier recombination to enhance catalytic performance [10,11]. Nevertheless, the potential of using such a piezocatalytic effect for bacterial inhibition has been largely overlooked [12]. The piezocatalysis process generally involves the production of various reactive oxygen species (ROS) like hydroxyl radicals (OH^\bullet), singlet oxygen ($^1\text{O}_2$), and superoxide ($^\bullet\text{O}_2$) radicals in the surrounding under any mechanical stimulation, that can further decompose the water contaminants, dyes, and pathogenic bacteria present in wastewater [13]. Thus the exogenous ultrasonic waves used in this study are useful to excite piezoelectric nanocomposites for organic dye degradation and bacterial disinfection of water. Moreover, such a piezocatalytic technique along with photothermal and photodynamic therapy (PTT/ PDT) has proved to be superior in the domain of bacteriology and oncology [14,15].

Other than pollutant degradation and bactericidal effects, energy harvesting is another crucial aspect as conventional fuels are non-renewable and most of the alternative energy sources require expensive instrumentation, and suitable locations, and are often hard to operate [16]. Moreover, energy demand is rising by 1% every year and it is expected that the share of alternative energy sources in energy consumption will grow to 63% in 2050 from the 9.5% share in 2015 [17]. Since mechanical or vibrational energies are in abundance and easily accessible, harvesting such kinetic energy and converting it into subsequent electrical energy is gaining popularity [18]. Such a technique is hassle-free and restricts the generation of harmful greenhouse gases. Hence, this study intends to the development of a natural material-based nanocomposite that can be useful for solving the issues of energy generation and wastewater remediation along with bacterial disinfection [19].

In this report multi-walled carbon nanotube (MWCNT) doped natural kaolinite has been incorporated in a polyvinylidene fluoride (PVDF) polymer matrix to develop a flexible polymer film. Kaolinite is an eco-friendly, natural, economical, and highly stable alumino-silicate ($\text{Al}_2\text{Si}_2\text{O}_5(\text{OH})_4$) clay [20]. The nanonization of which enhances its aspect ratio and various physicochemical activities [21]. In reality, kaolinite has negatively charged basal planes along with positively charged edges. This negative surface charge is further enhanced due to the MWCNT doping and the final nanocomposite can create sufficient polarization in the PVDF matrix forming an efficient piezocatalyst membrane [20,22]. The incorporation of MWCNT-kaolinite composite in the PVDF matrix enhances its electrical properties as well as other physicochemical properties. The surface charge also increases which triggers the polar β -phase formation and ensures the stability of the PVDF-HFP matrix. Although the MWCNT is a costly material, the amount of MWCNT in the MWCNT-kaolinite nanocomposite is nearly 1% (w/w) and this nanocomposite is loaded in the PVDF-HFP matrices in very low amounts (0–1.5% w/w), which not only lowers the cost but also triggers the physicochemical properties of these membrane samples.

Previously, various groups have achieved efficient energy harvesting, dye removal, and bacterial eradication by using such piezo-responsive systems but their applicability has been restricted due to their bio- and cytocompatibility [23]. Herein, this natural clay-based piezo material shows enormous potential in generating clean energy from water waves. Additionally, this material is providing a new approach to be used in organic contaminant removal and bacterial eradication under piezo-response, which paved its path to be used in the multidimensional field, if properly improvised.

2. Experimental section

2.1. Materials

Natural kaolinite clay was obtained from Hindustan minerals, India. Multi-walled carbon nanotube (MWCNT), Poly (vinylidene fluoride-hexafluoropropylene) (PVDF-HFP), Para Benzoquinone (BQ), AgNO_3 ,

ethylenediaminetetraacetic acid (EDTA), terephthalic acid (TPA) and tertiary butyl alcohol (TBA) were purchased from Sigma-Aldrich, Germany. Phosphate buffer saline (PBS), LB broth was obtained from HiMedia Pvt. Ltd., India. Hexamethylenetetramine, hydrochloric acid (HCL), ethanol (HPLC-grade), nitric acid, hydrogen peroxide, dimethylformamide (DMF), acetone (HPLC-grade), and hydrazine hydrate were purchased from Merck, India and all the reagents used were of analytical grade. *Escherichia coli* DH5 α (MTCC-1652) was purchased from the Institute of Microbial Technology, Chandigarh, India. Millipore water of resistance $\sim 18.2 \text{ M}\Omega\text{-cm}$ was used for synthesis and rinsing purposes.

2.2. Synthesis of natural kaolinite-MWCNT nanocomposite

Initially, the raw clay was crushed and purified by the sedimentation method using Millipore water and dried for 24 h at 95 °C. The clay was then sieved to pass through 400 mesh (0.037 mm) and pulverized using Fritsch Planetary Mono Mill Pulverisette 6 for 48 h at 150 rpm maintaining tungsten carbide balls to sample mass ratio of 20:1. Nano-kaolinite was activated by dissolving 2 g of nano-kaolinite in 80 mL Millipore water. 0.048 g hexamine and 20 μL hydrochloric acid (37%) were subsequently added to the clay solution under stirring conditions (300 rpm) and kept overnight at 80 °C. The solution was then filtered and activated nano-kaolinite was obtained by drying at 70 °C.

MWCNT was functionalized prior to loading in nano-kaolinite. In a typical process, 50 mg MWCNT was dispersed in 15 mL of ethanol to reduce the agglomeration. The solution was then dried and the MWCNT powder was collected and dissolved in 15 mL of 3 M HNO_3 solution and stirred for 15 min at 60 °C. The sample was then rinsed with Millipore water and dissolved in 15 mL of H_2O_2 at 60 °C under vigorous stirring. The precipitate obtained was further washed with Millipore water till neutral pH was achieved and functionalized MWCNT was obtained after washing and drying.

Functionalized MWCNT was loaded in the nano-kaolinite matrix through the condensation technique. 1 g activated kaolinite was dispersed in 30 mL of DMF under ultrasound. MWCNT was added to the solution (1% w/w) and the whole solution was then refluxed at 90 °C for 24 h. Finally, it was centrifuged, and dried at 60 °C and the MWCNT-kaolinite nanocomposite was collected for further use.

2.3. Preparation of the nano kaolinite-MWCNT/PVDF composite film

A facile, one-step solution casting method was adopted to obtain the flexible, composite film of MWCNT-kaolinite-PVDF. Initially, 0.5 g of Poly (vinylidene fluoride-hexafluoropropylene) (PVDF-HFP) was dissolved in 10 mL of DMF under stirring conditions (600 rpm) at 60 °C. The MWCNT-kaolinite nanocomposite was then added at different weight percentages (0.5%, 1.0%, and 1.5%). The homogenous solutions were then poured into clean Petri plates after 12 h of vigorous stirring and the plates were kept in a dust-free hot air oven at 60 °C for another 6 h. The dried membranes were peeled off and marked as PCK0.5, PCK1, and PCK1.5. Pure PVDF membrane was also prepared using the same protocol, excluding the addition of MWCNT-kaolinite and marked as PCK0.

2.4. Experimental characterization techniques

The phase identification of all the samples was done by using X-ray powder diffractometer (D8, Bruker AXS, WI, USA) from 10° to 70° 2 θ values operating at 35 kV, and 35 mA external field. The scan speed of 0.5 s per step was set employing a Cu-K α target having a wavelength of 1.5418 Å.

The confirmation of various phases and the vibrational modes were analyzed using an IR Affinity, Shimadzu Infrared spectrometer in the region between 400 and 1000 cm^{-1} wavenumbers. The samples were cut into small pieces and placed under the attenuated total reflection (ATR) attachment for the spectroscopy.

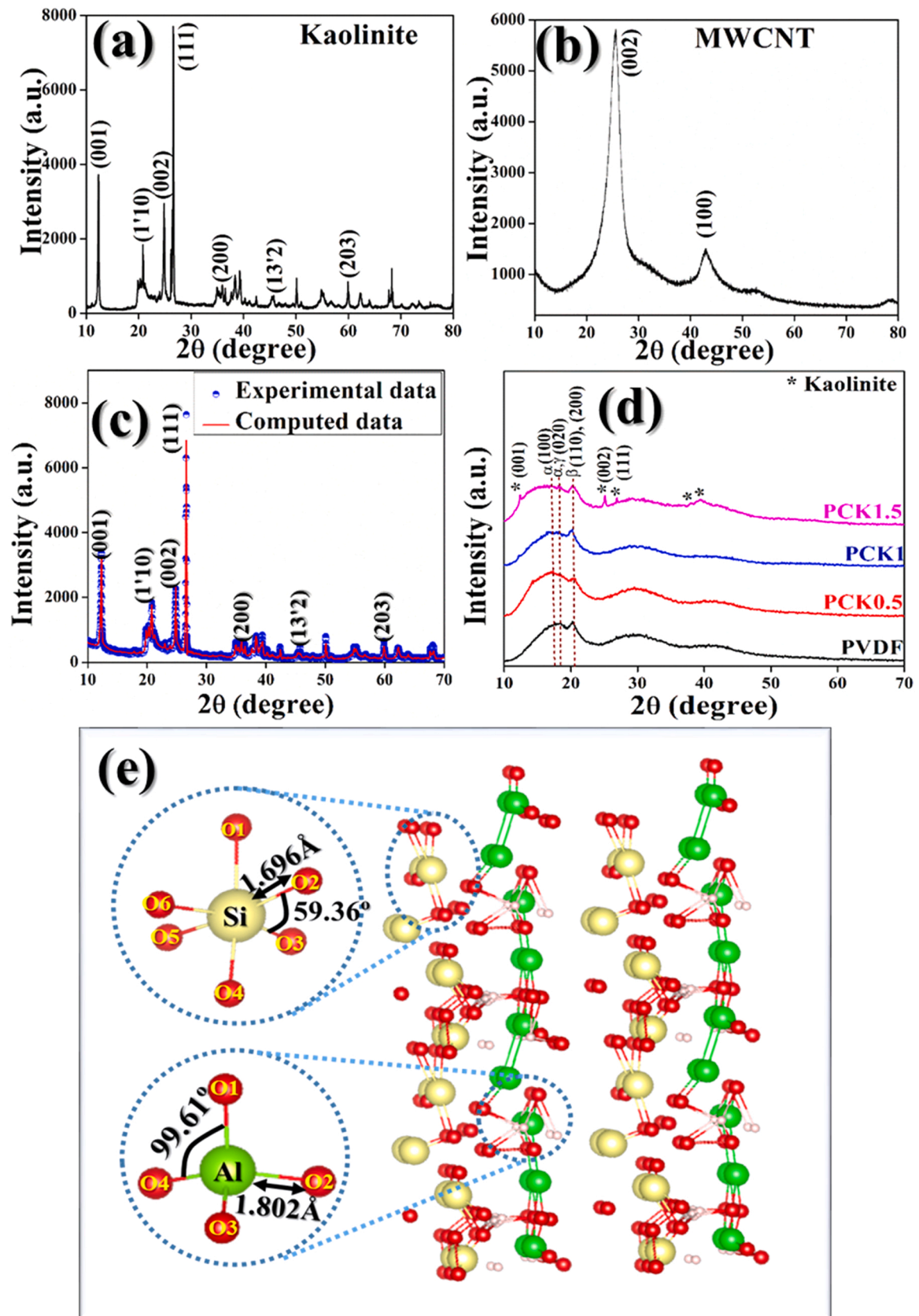


Fig. 1. X-ray diffractograms of (a) natural kaolinite, (b) MWCNT, (c) XRD crystallographic fitted data of MWCNT-kaolinite nanocomposite, (d) PVDF-based MWCNT-kaolinite nanocomposites, (e) visualization of the structure of MWCNT-kaolinite from the Rietveld refinement.

Table 1
Crystallographic parameters of MWCNT-kaolinite nanocomposite.

Parameters	MWCNT-kaolinite nanocomposite
a (Å)	5.142466 ± 5.17929E-4
b (Å)	8.940503 ± 9.6038403E-4
c (Å)	7.422964 ± 8.8799564E-4
α (°)	92.19153 ± 0.00899891
β (°)	105.081 ± 0.008500257
γ (°)	90.28371 ± 0.008146647
V (Å ³)	329.2675
χ^2	1.502
R _p	10.354423
R _{wp}	15.549485
Macrostrain	7.6238753E-6 ± 4.2253095E-9
Crystallite size	2100.1086 ± 91.06433

Determination of the morphological features of the clay mineral and its nanocomposites have been investigated by Transmission Electron Microscopy (TEM) and Field Emission Scanning Electron Microscopy (FESEM) and. A JEM-2100 Plus, JEOL transmission electron microscope operating at 200 kV has been employed to get the TEM micrographs. Nano-kaolinite clay was well-dispersed in acetone and casted on the copper grid (300 mesh) drop-wise prior to drying under vacuum. Further, the nanocomposite films were placed over carbon mesh and sputtered with gold to obtain the FESEM images in a INSPECT-F50, Netherlands equipped with Bruker Quantax EDS analyzer operating at 10–30 kV bias voltages. The elemental compositions and elemental distribution were confirmed by the EDS mapping technique.

The chemical states of each element existing in the nanocomposite membrane have been examined by X-ray photoelectron spectroscopy (XPS) study with an Omicron nanotechnology emitting Al K α X-ray source operated at 15 kV.

The electrical properties of the samples (1 cm² dimension) have been measured in the frequency ranging between 20 Hz and 1 MHz at room temperature using a HIOKI, IM 3536 LCR meter maintaining a bias voltage of 0.5 V.

In order to obtain the surface charge of the powder sample for determining the interaction between PVDF and MWCNT-kaolinite, zeta potential measurements were done in a Zetasizer, Malvern.

The polarization-electric field (P-E loop) has been measured using precision premier-II (Radiant technologies).

The transient piezo voltage of the fabricated PCK1 device has been

measured by using an X 3012 A, Keysight digital storage oscilloscope equipped with an Agilent N2862B 10:1 passive probe. Whereas, the piezo current of the same has also been measured by using a DAQ6510, Keithley data acquisition multimeter system.

3. Results and discussion

3.1. Determination of the physicochemical features of the sample

Phase purity and structural features of Kaolinite, MWCNT, and MWCNT-kaolinite composite were initially investigated by employing the X-ray diffractogram. Fig. 1 depicts a well-matched pattern of the diffraction, which corroborates the JCPDS card no. 80-0886 and the absence of any undesired maxima suggest the purity of the natural kaolinite-MWCNT nanocomposite [20,24]. Further, detailed information regarding the microstructural and crystallographic parameters was acquired by conducting the Rietveld refinement-based curve fitting technique. The refinement of the collected diffractograms was performed by using a MAUD v2.94 software package. The refined parameters obtained after the final cycle has been illustrated in Table 1. VESTA v3.5.2 software was used to visualize the refined microstructure and its bonding networks (Fig. 1) [25]. It is observed from the crystal structure that, the basal planes carry the SiO₂ and Al₂O₃ facets, which might be responsible for its negative surface charge.

Moreover, the MWCNT-kaolinite doped PVDF membranes offer semi-crystalline XRD patterns. These membranes show broad 2 θ values at 17.7° (100) corresponding to the α -phase, 18.2° (020) corresponding to both α and γ phases, and 39.3° (211) for the γ -phase of PVDF [26]. There is a significant enhancement of β -phase found at 20.3° (110) due to kaolinite-MWCNT loading, especially in PCK1. The 2 θ values at 12.1°, 25.0°, 26.1° and 49.5° peaks are arising for the kaolinite phases, which have been marked in the diffractograms [27].

The TEM micrographs (Fig. 2) depict the particle sizes lying between 60 and 80 nm of natural kaolinite. MWCNT has perfectly attached to the hexagonal sheet-like structure of nano-kaolinite. It is found that the condensation process significantly introduces the hexagonal sheets of the natural kaolinite on the surface of MWCNTs. Such attachment is much needed in achieving a higher degree of polarizability in the sample. The high-resolution TEM was obtained to confirm the presence of kaolinite in the PCK1 nanocomposite membrane which is shown in the inset of Fig. 2. The lattice spacing was obtained from the highlighted

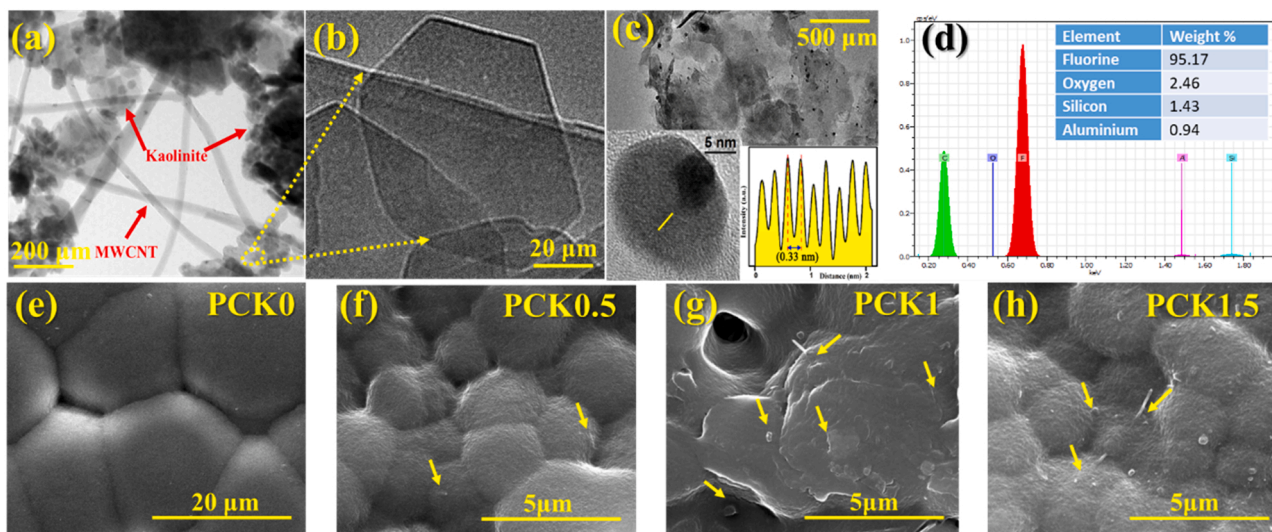


Fig. 2. Morphology investigation of the nanocomposites: (a) TEM micrograph of MWCNT-kaolinite nanocomposite, (b) TEM micrograph of natural pristine kaolinite, (c) TEM micrograph of PCK1 nanocomposite membrane with the intensity profile (d) Detail elemental composition of PCK1 membrane (e) FESEM of bare PVDF, (f) FESEM of 0.5% MWCNT-kaolinite doped PVDF, (g) FESEM of 1% MWCNT-kaolinite doped PVDF, (h) FESEM of 1.5% MWCNT-kaolinite doped PVDF, the arrowhead in the figures denote the presence of the nanocomposite in PVDF polymer matrix.

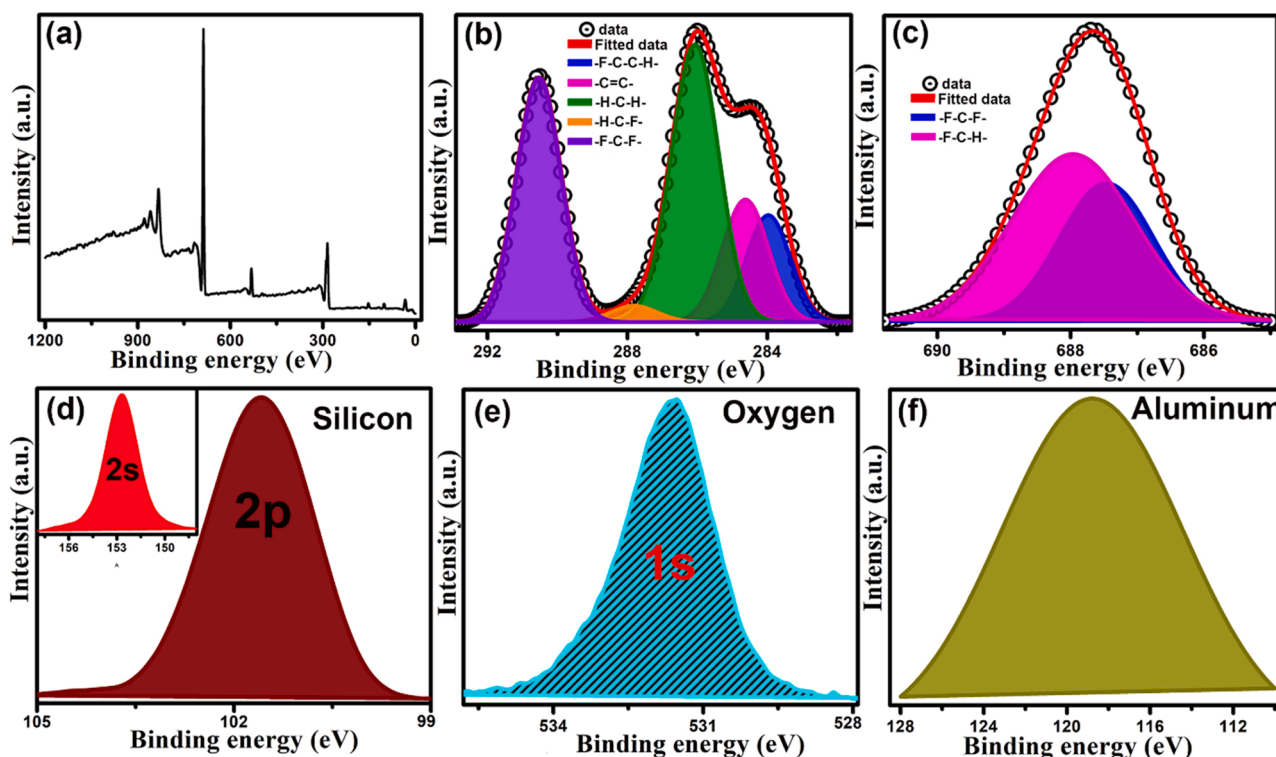


Fig. 3. (a) Full XPS spectrum of the nanocomposite membrane (PCK1), (b), (c) deconvoluted spectrum of the C and F, (d), (e), (f) chemical states of Si, O and Al respectively.

portion and the corresponding intensity profile is represented in the figure. The intensity profile (obtained using the ImageJ software (v. 1.53e)) was employed to find the d -spacing and was found to be 0.33 nm corresponding to the (111) plane of the kaolinite [27].

Besides, the FESEM micrographs of the membranes (Fig. 2) confirm the increase of roughness and spherulite morphology in kaolinite-MWCNT doped PVDF membranes, which has otherwise a homogeneous, smooth surface in pristine PVDF membrane (PCK0) [28]. This spherulite morphology assures the formation of a polar β -phase in the sample. The β -phase of the PVDF depends on its crystallinity and is called the crystallite β -phase. The partial alignment of the molecular chain is associated with the crystallinity of the polymer. This molecular chain folds together in an arranged manner and formed an ordered region which is called lamellae when it cooled from its melting condition. These lamellae compose a larger spheroidal structure which is called spherulite confirming the crystallinity and β -phase formation of the PVDF polymer matrix.

The elemental mapping using EDS (Fig. S1) shows uniform distribution of clay-MWCNT nanocomposite into the PVDF matrix, thus indicating the presence of the nanocomposite in the PVDF regime. The detailed elemental composition has also been depicted in Fig. 2.

The chemical states of the membrane have been investigated by using the XPS spectrum of the nanocomposite membrane (PCK1) (Fig. 3). The C 1s XPS spectrum was deconvoluted which exhibits the contribution of different C species. The deconvoluted spectrum consists of two intense peaks suggesting major contributions of $-\text{CH}_2-$ and $-\text{CF}_2-$ while the contributions from $-\text{C}=\text{C}-$, $-\text{F}-\text{C}-\text{C}-\text{H}-$, $-\text{H}-\text{C}-\text{F}-$ are also reflected by three other less intense peaks. The $-\text{CH}_2-$ and $-\text{CF}_2-$ peaks are observed at 286.3 eV and 291 eV, indicating a shift towards higher binding energy (BE) compared to pure PVDF [28]. The peak shift of C 1s XPS spectra indicates a strong electrostatic interaction among the PVDF and MWCNT molecules and the formation of the polar β phase. Fig. 3 shows the deconvoluted XPS spectra of F1s exhibiting the shift of $-\text{F}-\text{C}-\text{H}-$ and $-\text{F}-\text{C}-\text{F}-$ species towards higher BE and is found at 688.6 eV and 687.3 eV respectively. Additionally, the existence of Si, O, and Al in

the nanocomposite sample has been confirmed from the XPS investigation which is shown in Fig. 3(d), (e), and (f) respectively and the inset of Fig. 3(d) show the 2s spectra of Si [28].

3.2. Estimation of polarizability and piezoelectric coefficient of the samples

Piezoelectricity depends on various parameters related to the polarization and surface effect of the samples. Herein, both surface charge and piezoelectric coefficient along with the theoretical polarizability have been measured. It is observed that the MWCNT-kaolinite offers a high negative surface charge of -37.3 mV (Fig. 4). In reality, kaolinite has two negatively charged basal planes along with positively charged edges. These basal planes consist of hydroxylated aluminum octahedral (alumina) layer and a silica tetrahedral layer (siloxane). The isomorphous substitution of Al^{3+} for Si^{4+} in the siloxane facet and Fe^{2+} or Mg^{2+} for Al^{3+} in the alumina facet have been taken place in the kaolinite matrix. This isomorphous substitution creates a charge imbalance in the basal planes of the kaolinite as a result a net negative surface charge occurs. Previously, from the crystallographic assessment, it was found that the negatively charged basal planes (i.e. SiO_2 and Al_2O_3) face an outward inclination, which might cause a negative surface charge of the composite [29]. Moreover, the high value of zeta potential corroborates the stability of the system. Such negative surface charge facilitated the surface attachment of the nanocomposite to PVDF and simultaneously contributes to the proliferation of the polar β -phase of the composite film. In reality, the negative surface of the clay attracts the positive $-\text{CH}_2-$ moiety of the PVDF to form the MWCNT-kaolinite-PVDF composite (PCK1). A schematic diagram is attached herein (Scheme 1) to convey the formation mechanism and β phase enhancement of the composite.

In order to substantiate such attachment between MWCNT-kaolinite and PVDF, an FTIR study of the composite membranes has been carried out. The α -phase absorbance bands are found at 533 cm^{-1} (CF_2 bending), 615 cm^{-1} (CF_2 bending), 762 cm^{-1} (skeletal bending), and $796, 976\text{ cm}^{-1}$ (CH_2 rocking). While the β -phase absorbance bands

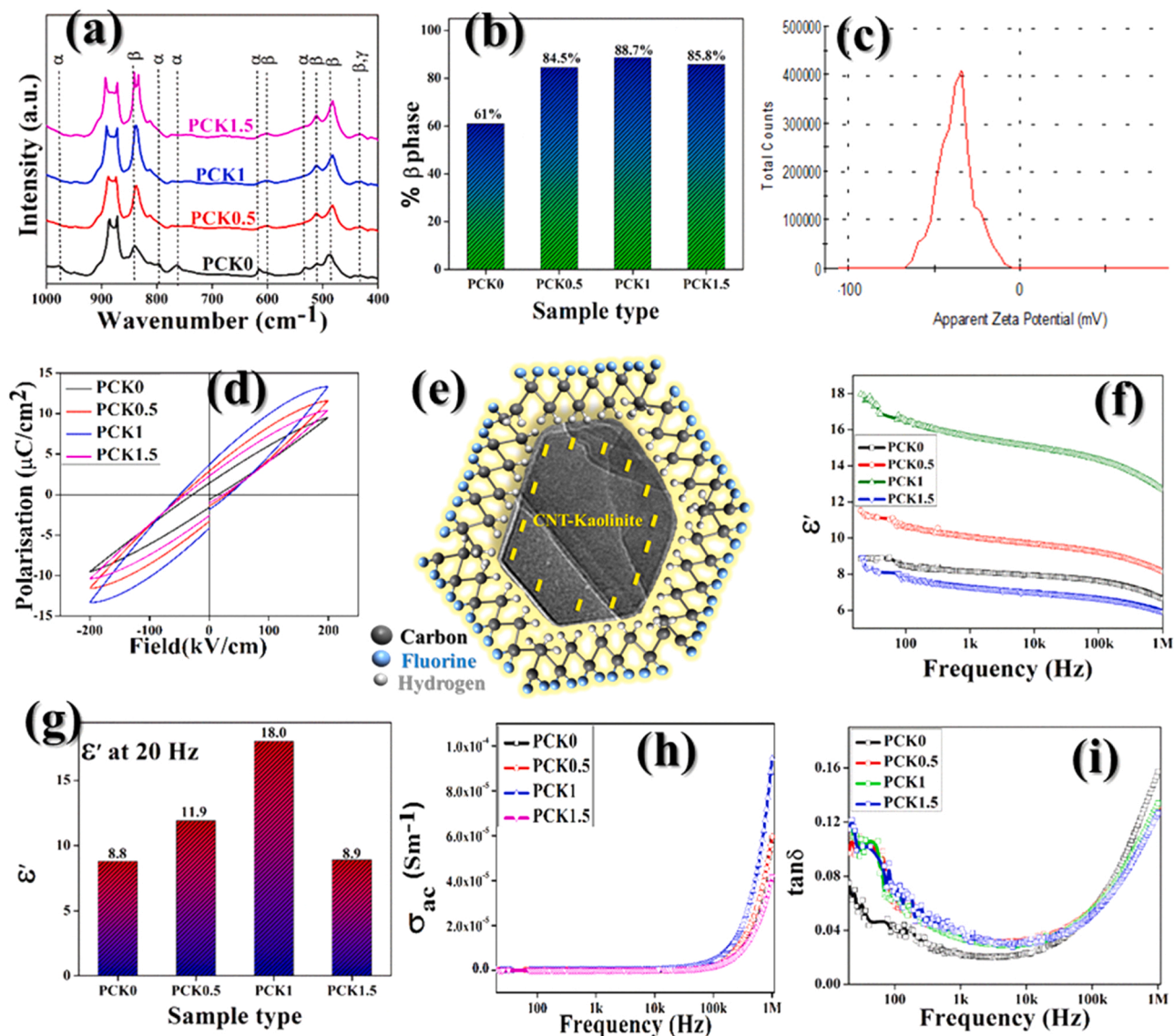


Fig. 4. (a) FTIR spectroscopy of PVDF-based MWCNT-kaolinite nanocomposite films, (b) percentage β -phase of the PVDF-based nanocomposite films, (c) Zeta potential of 1% MWCNT doped natural kaolinite, (d) P-E loop of PVDF-based nanocomposite films, (e) Schematic diagram of β -phase formation, (f) dielectric permittivity of the nanocomposite films, (g) variation of dielectric permittivity with percentage doping of MWCNT-kaolinite in PVDF matrix, (h) ac conductivity data of nanocomposite membranes, (i) dissipation factors ($\tan\delta$) of the nanocomposites.

appear at 485 cm^{-1} (CF_2 deformation) 510 cm^{-1} (CF_2 stretching), 600 cm^{-1} (CF_2 wagging) and 840 cm^{-1} (CH_2 rocking, CF_2 stretching and skeletal C-C stretching). Another absorption band due to β and γ phases appear at 434 cm^{-1} for CF_2 rocking [30]. Previously, it is suggested that the β -phase increment could reveal the polarizability of the PVDF. The fraction of β -phase $[F(\beta)]$ of the film nanocomposite has been calculated using the Lambert-Beer law [30],

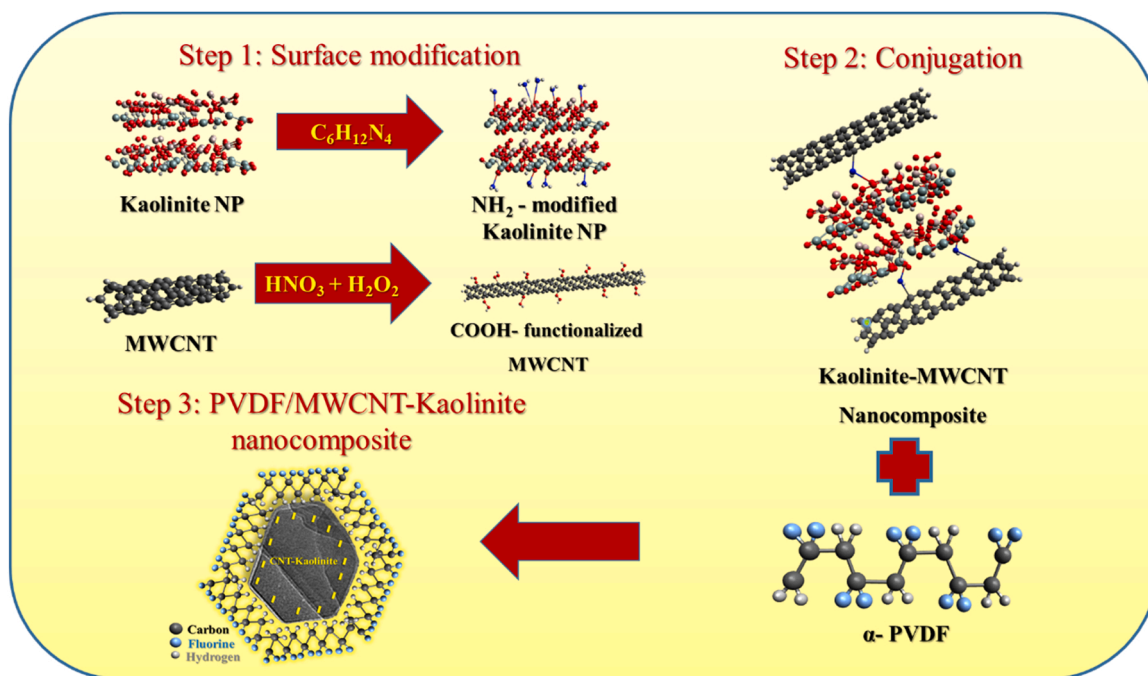
$$F(\beta) = \frac{A(\beta)}{\frac{K(\beta)}{K(\alpha)} * A(\alpha) + A(\beta)} \quad (1)$$

Where $A(\alpha)$ and $A(\beta)$ are the absorbance bands for the α phase at 764 cm^{-1} and β phase at 840 cm^{-1} , respectively. $K(\alpha)$ ($6.1 \times 10^4\text{ cm}^2\text{ mol}^{-1}$) and $K(\beta)$ ($7.7 \times 10^4\text{ cm}^2\text{ mol}^{-1}$) are the absorption coefficients at the respective wavenumber [31].

Herein, around 88.7% of polar β -phase has been achieved in the PCK1 sample suggesting a higher degree of polarizability. Surprisingly, at lower as well as higher doping concentrations the percentage β -phase lacks radically. This could be due to the minimal and excess doping of

the negatively charged MWCNT-kaolinite respectively.

Moreover, the polarizability of the samples has been investigated theoretically by using density functional calculations (DFT) [32]. In a typical process, the theoretical model of PCK0 and PCK1 nanocomposite membranes have initially been designed by Avogadro v.1.2.0 software package. Orca v.4.2 software has been employed for frequency and geometry optimization of the model. The simulations have been performed using the Becke, 3-parameter, Lee-Yang-Parr (B3LYP) functional combined with 6–311 G^* basis set, and RIJCOSX auxiliary basis set. The vibrational modes have been found positive in both cases, which validates the authenticity and stability of the models. The DFT simulation depicts the enhanced polarizability, quadrupole moment, and dipole moment in the PCK1 sample compared to its pristine counterpart (PCK0). The dipole moment increases from 12.09 Debye to 12.26 Debye, the quadrupole moment increases from -165.25 C m^2 to -169.02 C m^2 , and the isotropic polarizability increases from $218.54\text{ C m}^2\text{ V}^{-1}$ to $222.02\text{ C m}^2\text{ V}^{-1}$ [33]. Such augmented values validate the enhanced β -phase polarization calculated from FTIR spectra and indicate the samples, especially PCK1 to be a promising agent for



Scheme 1. Schematic diagram for synthesis protocol of natural kaolinite modified MWCNT nanocomposite and MWCNT-kaolinite based PVDF nanocomposite.

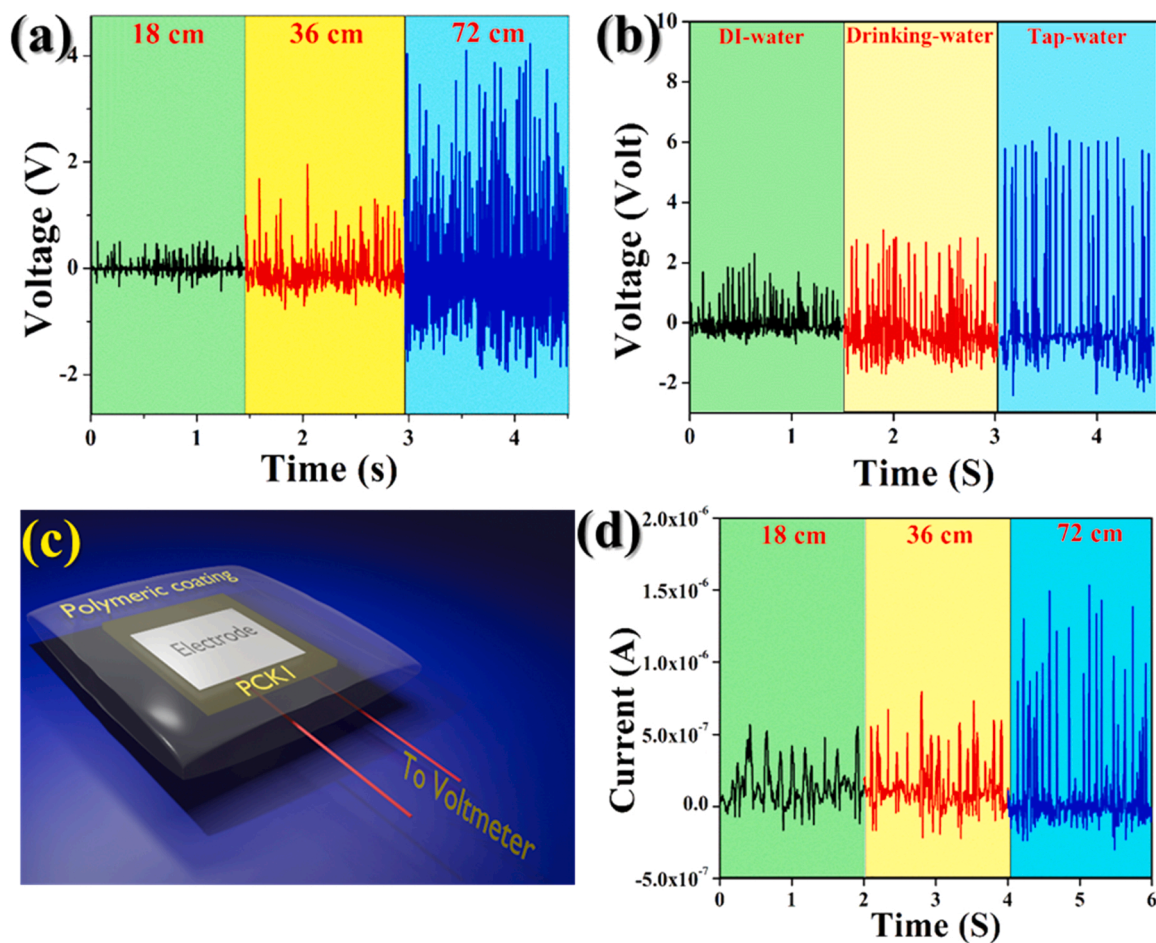


Fig. 5. Piezoelectric output voltages: (a) voltages when the device is exposed to DI-water from different heights, (b) voltages from 36 cm height of different water sample, (c) PCK1 nanocomposite film-based device for piezoelectric water energy harvesting, (d) piezoelectric currents when DI-water droplets fall from a different height on the device.

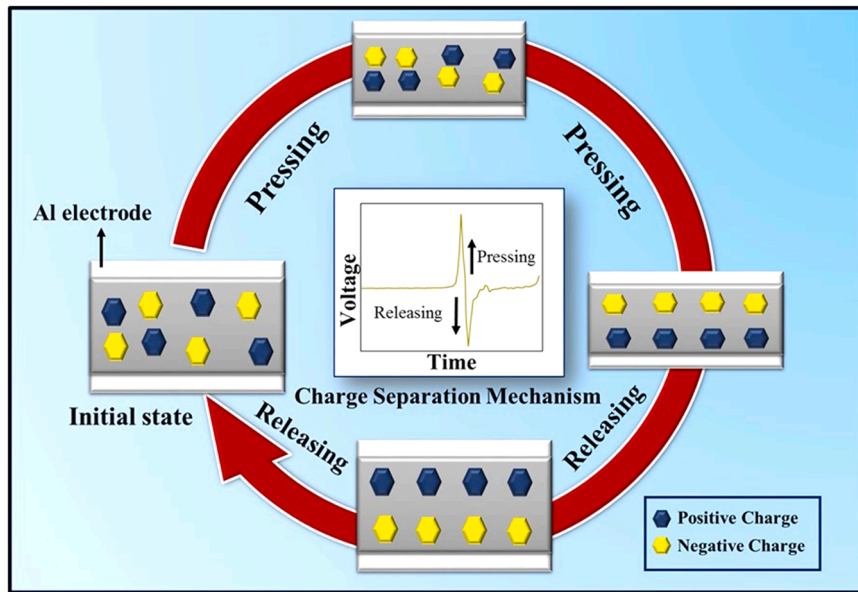


Fig. 6. Mechanism of piezoelectric energy generation of PCK1 under water droplets.

piezo-responsive applications.

Further, the piezoelectric coefficients (d_{33}) of the samples have been calculated by using the capacitance values (C_p) by the following relation [31,34],

$$d_{33} = \frac{VC_p}{F} \quad (2)$$

Here, F is the applied force during the piezoelectric experiment and V is the output piezoelectric voltage. The d_{33} values of the nanocomposites are found to be 11.0 pC N^{-1} for pristine (PCK0), 25.8 pC N^{-1} for 0.5% doped (PCK0.5), 50.7 pC N^{-1} for 1% doping (PCK1) and 12.3 pC N^{-1} for 1.5% doped (PCK1.5) PVDF membranes. Such relaxation resembles the β -phase values and theoretical polarizabilities. The room-temperature polarization-electric field (P-E) hysteresis loop has also been measured at 10 Hz in the $\pm 200 \text{ kV/cm}$ range (Fig. 4). The area within the loop corresponds to the heterogeneous charge density and indicates the charge storage capability of the material. As can be seen from Fig. 4, the PCK1 membrane shows a strong remnant polarization (P_r) value of $0.92 \text{ } \mu\text{C cm}^{-2}$ compared to pure PVDF-HFP ($0.34 \text{ } \mu\text{C cm}^{-2}$). The piezoelectric coefficient (d_{33}) has again been calculated using the equation $d_{33} = -P_r/Y$, where P_r , Y is the remnant polarization and Young's modulus respectively of the nanocomposite membrane.

Young's modulus of the nanocomposite membranes has been found to be 328 N/mm^2 for bare PVDF and 167 N/mm^2 for PCK1 membrane (Fig. S3). Therefore, by using the above equation, d_{33} of PCK1 comes out to be 55.1 pC/N . This value is higher than observed in PVDF (10.6 pC/N) showing that the nanocomposite membrane has superior piezoelectric properties without undergoing any poling techniques [34].

Herein, the capacitance of the samples has been further exploited to investigate the dielectric permittivity (ϵ') of the membranes using the following relation [35],

$$\epsilon' = (C \cdot d) / (\epsilon_0 A) \quad (3)$$

Where C , d , and A denotes the capacitance, thickness, and area of the film sample respectively. The ϵ_0 denotes the free space permittivity having a constant value of $8.85 \times 10^{-12} \text{ F m}^{-1}$ [32]. The dielectric permittivity (ϵ') and dissipation factor ($\tan\delta$) have been depicted in Fig. 4. It is worth noting that the dielectric constant increases with the doping percentage of MWCNT-kaolinite nanofillers in the PVDF matrix and attain a maximum value (18.0 at 20 Hz) for the PCK1 sample (Fig. 4), otherwise it is found to be quite low (8.8) for the pristine PVDF

(PCK0). The decrease in the permittivity values with the increasing frequency for all the samples can be attributed to the Maxwell-Wagner interfacial polarization [36]. Normally, the dielectric material consists of conductive grains separated by a thin layer of insulated grain boundaries. In the low-frequency region, the energy of the external electric field is low. This low energy is insufficient to pull out the grains from the grain boundaries as a result polarisation occurs. This phenomenon is in good agreement with Koop's phenomenological theory. In the higher frequency region, the charges are capable to be free as a result lower permittivity value occurs [37]. The conduction mechanism of the nanocomposites has been studied at varying frequencies and temperatures (Fig. 4). It has been shown that the a.c. conductivity increases with increasing field frequency. It can be examined by the virtue of the charge transport phenomenon. In reality, the conductive grains acquire activation energy and get free at a higher frequency [37]. Moreover, low dissipating factors ($\tan\delta$) as illustrated in Fig. 4 can be beneficial for long-term commercial use of the synthesized membrane. Such high polarizability along with nominal dielectric tangent loss and enhanced piezoelectric coefficient value make this PCK1 sample a promising candidate for piezo-responsive applications.

3.3. Piezoelectric energy harvesting from water droplets

3.3.1. Fabrication of the energy harvesting device

The piezoelectric energy harvesting device was developed from the PCK1 membrane as it has the highest piezo coefficient and polarizability among all the samples. A $2 \text{ cm} \times 2 \text{ cm}$ section from the PCK1 was cut to form the internal piezoelectric layer of the device. Aluminum electrodes ($1.5 \text{ cm} \times 1.5 \text{ cm}$) were then mounted on both sides with copper wires to establish a rigid connection with the measuring device. The entire 'sandwiched structure' was then covered with a robust polyethylene terephthalate (PET) jacket to arrest any kind of mechanical damage or malfunction (Fig. 5). This PET jacket also makes this device water repellent.

3.3.2. Experimental setup of water energy harvesting

Initially, the device has been exposed to water droplets (Millipore or deionized water) from different heights (18 cm, 36 cm, 72 cm) under a constant flow rate ($4 \times 10^{-3} \text{ L s}^{-1}$) and output voltages were measured (Fig. 5). It has been found that around 1.0 V, 2.0 V, and 4.1 V voltages have been generated when the water droplets have fallen from different

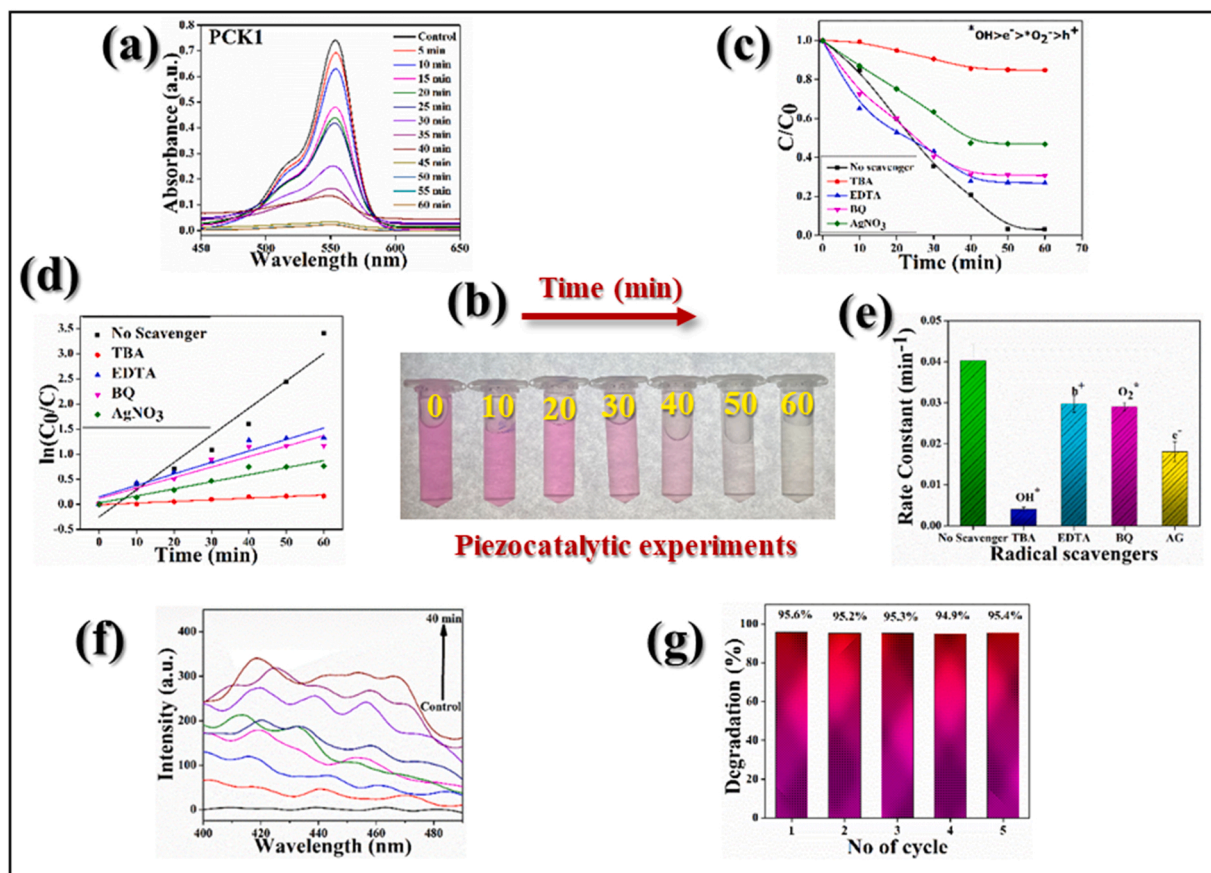


Fig. 7. (a) Organic Rhodamine-B dye degradation with time under ultrasound, (b) pictorial representation of dye color with time, (c) investigation of scavenger, (d) reaction rate constant for different scavengers, (e) effect of different free radical for the Rhodamine-B degradation, (f) trapping experiment to investigate the presence of OH^\bullet radical, (g) recyclability experiment of the nanocomposite film up to five cycles.

heights of 18 cm, 36 cm, and 72 cm respectively (Fig. 5). The pressure exerted on the device enhances significantly, which results in an augmented voltage generation with increasing height. The exerted forces on the device have been measured and found to be 2.94 N, 4.79 N, and 7.19 N for the falling water from different heights as 18 cm, 36 cm, and 72 cm respectively [37]. The corresponding short circuit currents have also been measured and depicted a similar relaxation. Particularly, at the highest distance (72 cm) the output current attains the highest value (1.5 μA) compared to 18 cm (0.5 μA) and 36 cm (0.8 μA) distances (Fig. 5) [38]. Such high values of open circuit voltages and short circuit currents account for a relatively high power density of the device (50 W m^{-3}).

Besides, water from different sources (drinking water, tap water) having distinct total dissolved solids (TDS) was collected and poured on the device from a fixed height of 36 cm. The output voltages obtained have been depicted in Fig. 5 showing that in the case of drinking (3.1 V) and tap water (6.5 V) the piezoelectric voltages attain higher values compared to the deionized water (2.0 V). This phenomenon can be substantiated by the virtue of the TDS of the water sample. The TDS of tap water (1876 ppm) is higher than that of drinking water (152 ppm) and deionized water (3 ppm), which exerts an augmented force on the device and increases the output voltages [39]. Such an interesting observation could lead to water quality monitoring in near future.

3.3.3. Mechanism of piezo-energy generation under the water droplet pressure

The piezoelectric signal generation under external mechanical stimulus can be explained in terms of dipolar polarization of the piezo-active PCK1 sample. It has been realized that external frequency can

modulate the movement of the electrical dipoles. Under the water flow, the device faces some external pressure and a dipolar polarization occurs inside the sample due to its eminent polarizability. This polarization creates a charge separation and positive charges travel to one of the electrodes, whereas, negative charges move towards the other electrode. Such charge separation introduces a potential difference between the two electrodes. After removal of the external force, the charge carriers quickly migrated toward the opposite electrodes through the external circuit and generate an opposite potential drop [31,39]. This piezo-responsive mechanism of energy generation has been illustrated in Fig. 6 for convenience.

3.4. Degradation of organic dye by the piezocatalytic efficacy of the nanocomposite

The PCK1 nanocomposite membrane has shown high isotropic polarizability, a promising piezo coefficient along with significantly high piezoelectricity under external mechanical stimuli and is therefore selected for piezocatalytic application. An efficient charge separation under mechanical stress paved a path to exploit this material in forming reactive oxygen species (ROS) such as e^- , h^+ , OH^\bullet , *O_2 as prescribed by Hong et al. in their revolutionary work [40]. It is observed that these reactive radicals can decompose organic pollutants such as dyes in an aqueous medium [41]. Herein, the PCK1 membrane has been used to degrade Rhodamine B (RhB) dye under ultrasound stimulus.

In a typical catalysis experiment, 15 mL of 2.5 ppm Rhodamine B solution has been taken in a glass vial and a 1 cm x 1 cm PCK1 membrane has been placed in the solution. The vial was then submerged in a Telsonic ultrasonic bath sonicator having a frequency of $30 \pm 5 \text{ kHz}$ and

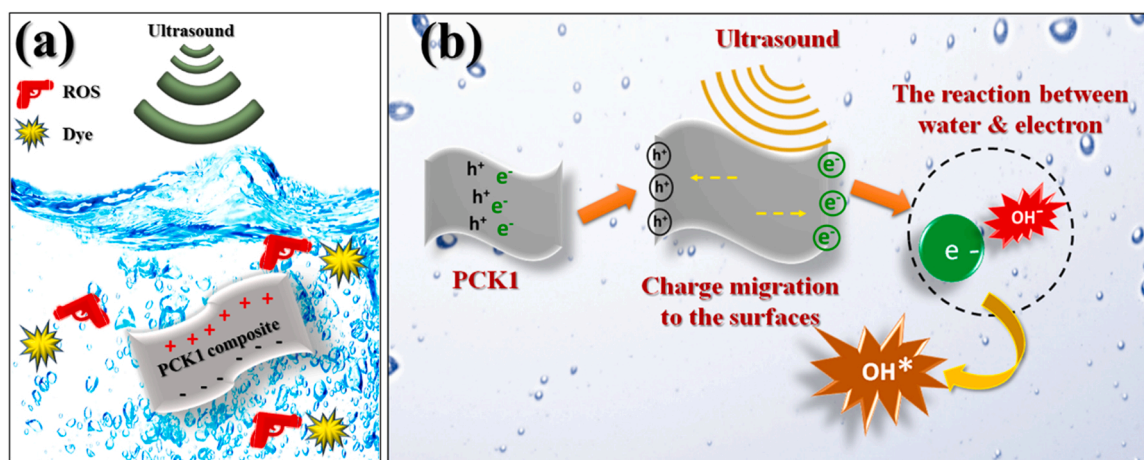


Fig. 8. (a) Mechanism of dye degradation under ultrasound, (b) mechanism of ROS production in piezocatalyst under mechanical stress.

an ultrasonic power of 50 W. Prior to each experiment, the sample was immersed in the RhB solution for at least 30 min to ensure full adsorption. Moreover, to eliminate any photonic contact during the experiment, the whole experiment was conducted in a dark condition. The ultrasound-mediated heating was eliminated by using a temperature-controlled water bath system. After each 10 min interval, samples were taken out from the vessel and the absorption spectrum was measured in a Lambda 25 UV-Visible spectrophotometer to ensure the catalytic activity of the PCK1. It is found that the characteristic absorption maximum of RhB (554 nm) degrades gradually under the external stimulus (Fig. 6). The pink color of the dye also faded with the duration of the ultrasound treatment and finally depicts full transparency under 60 min of treatment (Fig. 7).

The absorbance spectra in Fig. 6 show the degradation kinetics of the piezocatalyst (PCK1). The percentage piezo degradation efficiency η of the nanocomposite has been investigated by using the relation [42],

$$\eta = \frac{C_0 - C}{C_0} \times 100\% \quad (4)$$

Where C_0 initial dye concentration and C is the final dye concentration. It is found that the degradation efficiency reaches about $\sim 96\%$ for PCK1, which is found to be 2.1% in the absence of the catalyst under the piezo stimulation (Fig. S6). Thus, it can be noted that the piezocatalyst (PCK1) offers enormous catalytic activity under mechanical stress. In the FTIR section, it has been observed that the polar β -phase fraction increases with the doping percentage of natural kaolinite-MWCNT composite and reaches its maximum value (88.7%) for 1% doping. Such a high value of β -phase reveals that the nanocomposite membrane is self-poled. Additionally, the P-E loop measurement shows the highest remnant polarization in the piezo-active PCK1 membrane also a confirmation of the self-polling of the membrane. The electron and hole in such self-poled material migrate in opposite directions under the ultrasonic stimulus, accumulate on the surfaces, and create a charge center separation. The surface accumulated electrons then produce reactive oxygen species (ROS) by reacting with negative hydroxyl ions present in the solution and decomposing the dye molecules (Fig. 8). In addition, the recyclability of the catalyst has been estimated by re-using it in a cyclic manner. Herein, the same membrane was used in five different cycles of application and found to have a consistent degradation efficacy (95.4%) even after five cycles (Fig. 7).

In order to verify the catalysis mechanism, the first-order kinetics, scavenging, and trapping experiment have been performed. In reality, piezocatalysis primarily depends on reactive radicals, especially ROS. The reactive oxygen species (ROS) generates during the catalysis experiment further decompose the hazardous dyes (Fig. 8). Mainly four radicals, namely ($\bullet\text{OH}$), holes (h^+), superoxide radicals ($\bullet\text{O}_2^-$), and

electrons (e^-) may be produced during the catalysis to decompose the dye solution. Scavenging experiments have been carried out to find the dominating ROS radical. Initially, 15 mL of 2.5 ppm RhB dye solution was taken into four separate glass containers, and 1 cm x 1 cm pieces of the PCK1 membranes were immersed in it. Later, para benzoquinone (BQ), AgNO_3 , ethylenediaminetetraacetic acid (EDTA), and tertiary butyl alcohol (TBA) have been added to the solution maintaining 0.5 mM of the concentration and exposed under the ultrasound [43]. The dye degradation efficacy in each case is depicted in Fig. 6. The scavengers BQ, AgNO_3 , EDTA, and TBA scavenged respectively $\bullet\text{O}_2^-$, e^- , h^+ and OH^* radicals respectively. It has been found that in the case of AgNO_3 , EDTA, and TBA the piezo degradation efficiency has been found 68.7%, 52.6%, 72.2%, and 14.4% respectively, which confirms the minimum scavenging for TBA (Fig. 7). Further, the first-order kinetic constant (k) has been measured by using the following relation [43],

$$C = C_0 e^{(-kt)} \quad (5)$$

The kinetic constant k has been measured by the slope of the plot $\ln(C/C_0)$ against time and found to be $4.02 \times 10^{-2} \text{ min}^{-1}$ (Fig. 7) and thus confirming the dominance of the $\bullet\text{OH}$ radicals in our case (Fig. 7).

The presence of hydroxyl radicals in the piezocatalytic reaction mixture has been investigated by the photoluminescence-probing technique of terephthalic acid (TPA). Initially, 0.01 gm TPA has been added to the 15 mL 2.5 ppm RhB solution and exposed to ultrasound. 2 mL of the solution was taken every 10 min and the fluorescence intensity was measured by a Cary Eclipse Fluorescence Spectrophotometer, Agilent Technologies. An excitation wavelength of 315 nm was set and the fluorescence intensity was visualized at 415 nm. In reality, terephthalic acid reacts with OH^* radical and generates fluorescent hydroxy terephthalate (hTPA) upon hydroxylation and increases the fluorescence intensity [44]. Herein, a radical increment in fluorescence intensity has been found that confirms the production of OH^* radicals and validates the ROS-mediated damage to the RhB solution (Fig. 7).

3.5. Determination of pathogenic *E. coli* eradication using piezocatalysis

In order to utilize such ROS for bacterial inhibition, the piezocatalytic disinfection of bacteria has been studied using a commonly found Gram-negative, coliform bacteria *Escherichia coli* (*E. coli*). The bacterial cells were grown overnight in a Luria-Bertani (LB) broth solution in an incubator at 37°C under a continuous shaking condition (120 rpm). 5 mL of the bacterial suspensions were taken in three clean glass vials and a rectangular film (1 cm x 1 cm) of PCK1 was placed into one of the vials. The vial which was not subjected to ultrasonic treatment and contained no film has been taken as control. The other two vials, one containing only the culture and another containing culture and film,

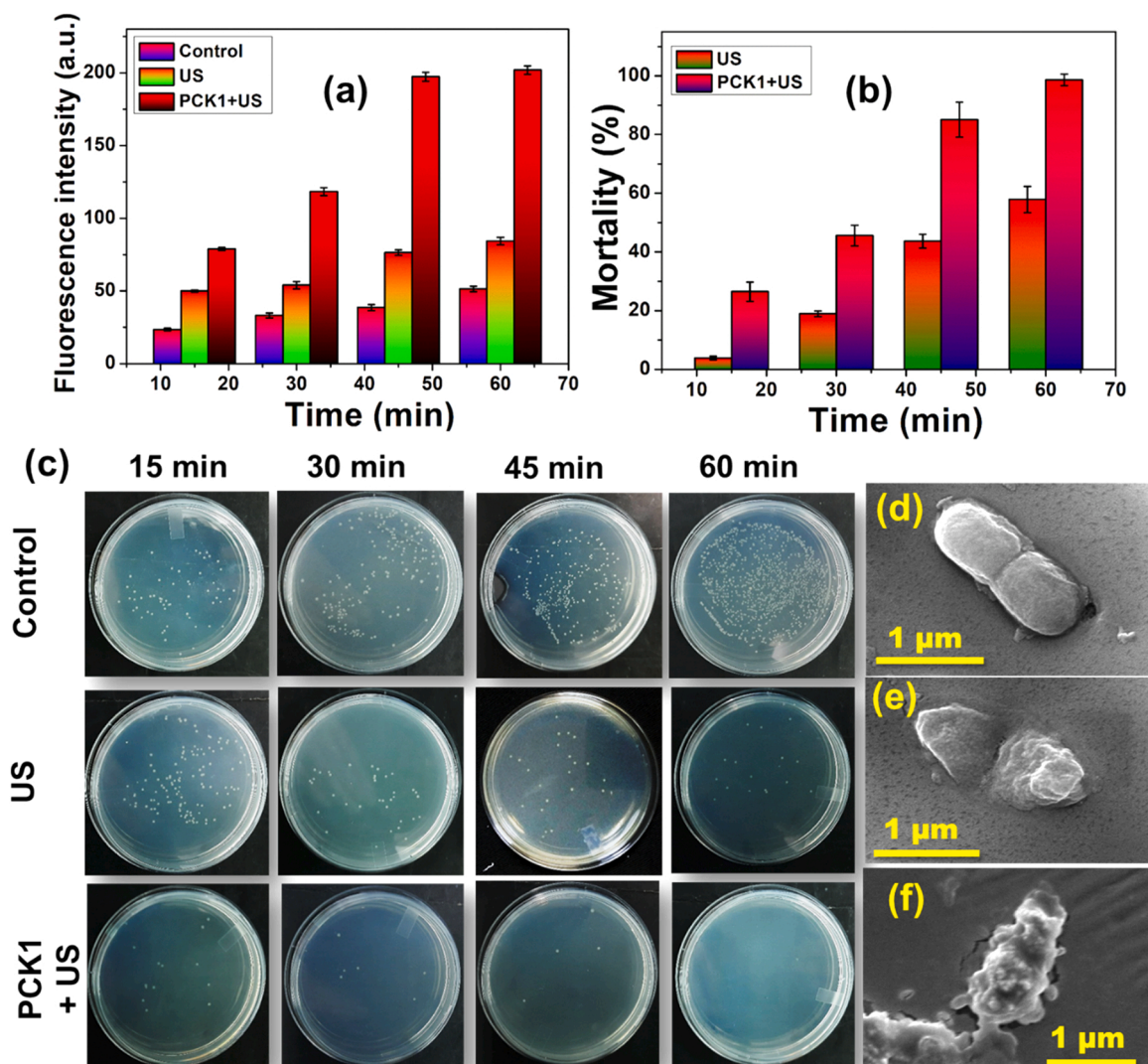


Fig. 9. (a) Investigation of bacterial ROS with increasing time, (b) MWCNT-kaolinite-PVDF nanocomposite assisted mortality percentage of pathogenic bacteria under ultrasound, (c) agar plate data for investigating bacterial decomposition with time, (e), (f), (g) FESEM images of healthy, ultrasound-assisted *E. coli*, and PCK1 and ultrasound-based degraded *E. coli*.

were subjected to ultrasound (US). The time-dependent inactivation of the cells under ultrasound treatment has been illustrated in Fig. 9. 100 μ L of the bacterial suspension from each vial was fetched at definite time intervals (15 min) and spread on solidified agar plates after the execution of suitable dilution. Triplicates were taken in each case and the mortality (%) was calculated from the colony counting technique using the following equation [45]:

$$M (\%) = \frac{B - C}{B} \times 100 \quad (6)$$

Where M represents the mortality rate (%), B and C represents the mean number of bacteria in the control and treated samples (CFU mL^{-1}) respectively.

The ROS generation in each case was measured by using 2', 7'-dichlorofluorescein diacetate (DCFH-DA) [46]. In reality, 1 mL of aliquots were extracted each time and were washed with PBS solution and a DCFDA solution of 10 μ M was added. The solutions were kept in dark for another 30 min and the fluorescence intensity was measured using a spectrophotometer (excitation at 404 nm and emission at 529 nm). Precisely, after interacting with ROS, DCFH-DA forms 2', 7'-dichlorofluorescein (DCF), which intensifies the fluorescence and indicates the

ROS generation. Bacterial FESEM was performed by collecting the precipitates from the bottom of each vial and washing them with filtered PBS solution at 2000 rpm for 2 min several times. Later 2% glutaraldehyde solution was added to the pellets, which were further subjected to dehydration using a serial dilution of ethanol. The solutions were then drop-casted on clean coverslips, dried, and sputter-coated with gold prior to the FESEM analysis.

As already mentioned above, ROS generation (mainly OH^{\bullet}) is the primary factor for piezocatalysis, such ROS production can also contribute to the disinfection of bacteria [47]. As observed from the colony counting technique, there is a significant bactericidal effect occurs when the bacterial cells are subjected to ultrasound [48]. The mortality is nearly 99% after 60 min of ultrasound treatment. Conversely, cell proliferation was observed in the control sample. Moreover, insignificant ROS production has been observed in control, while it is amplified with time in the case of PCK1-mediated treatment [49]. This signifies that the ROS generated under mechanical stress can successfully inactivate the bacterial cells as the free radicals can interrupt the trans-membrane electron transfer, deteriorate the subcellular components like protein and nucleic acids, prevent DNA replication and promote lipid membrane peroxidation [50]. Such processes ultimately result in cellular damage and cell death. The slight amount of oxidative

Table 2

Previous reports on piezocatalysts and their degradation efficacies.

Catalyst	Type of catalyst	Frequency and power of ultrasound	Degradation of hazardous material	Piezo voltage generated	Time of reaction	Degradation efficacy	year	Reference
Na _{0.5} K _{0.5} NbO ₃	synthetic	40 kHz, 300 W	RhB, MB, MO	N.A	100 min	91, 83, 77 respectively	2020	[53]
BaTiO ₃ nanocubes- Ag nanoparticles	synthetic	Not mentioned	MO	N.A	60	99.5	2021	[54]
LiNbO ₃	synthetic	40 kHz, 70 W	MB	N.A	200	99	2020	[23]
BaTiO ₃	synthetic	40 kHz, 100 W	RhB	N.A	150	97.6	2020	[55]
Bi ₂ WO ₆ nanosheets	synthetic	40 kHz, 80 W	Rhb	N.A	80	80	2020	[56]
BTO NWs	synthetic	40 kHz, 120 W	MO	N.A	160	95	2019	[57]
sodium niobate nanowires	synthetic	40 kHz	RhB	N.A	120	80	2019	[45]
BaTiO ₃ /C hybrid	synthetic	40 kHz, 150 W	RhB	N.A	40	75.5		[58]
Ag@LiNbO ₃ /PVDF	synthetic	40 kHz, 70 W	MB, Staphylococcus aureus	N.A	180	89, 99, 96.6	2021	[59]
heat-treated cellulose nanocrystal	Natural	40 kHz, 180 W	RhB	N.A	180	96.6	2022	[60]
MoS ₂ nanoflower/ PVDF	Synthetic	100 W	RhB	The voltage generated through tapping	30	90	2020	[41]
MWCNT-kaolinite-PVDF	Natural	33 kHz, 50 W	RhB,	The voltage generated from water droplets	45	96, 99	This report	This report

stress due to ultrasonic vibration is also bacteriostatic, but it is approximately 50% lesser and ineffective compared to the synergistic effect of the film in presence of ultrasound. Furthermore, the FESEM micrographs reveal that the PCK1 film under ultrasonic stress causes serious distortion and perforations in the bacterial cells, which ultimately results in membrane rupture and irreversible damage to the cellular membrane. This further facilitates the leakage of intracellular components and release of cytoplasmic materials, thus causing loss of cell membrane integrity [51,52]. The cellular membrane is otherwise intact and smooth in the control, although slight wrinkling occurs due to ultrasonic stress without the catalyst. Henceforth, this study confirms that the piezo-responsive PCK1 membrane can be used for successful bacterial eradication under the mechanical stimulus.

4. Conclusion

Herein, natural kaolinite clay has been ground by a facile top-down method to obtain its nanonized fraction. After performing certain chemical modifications, both nano-kaolinite clay and MWCNT have been surface modified and a nanocomposite has been formed by establishing a hydrophobic-hydrophilic interaction between these two. Further, this nanocomposite has been incorporated into the PVDF matrix in different weight percentages, among which a 1% doped PCK1 sample show exhibits excellent piezoelectric coefficient and polarizability. The structural and morphological characteristics of the membrane sample (PCK1) substantiate such enhanced polarizability and piezoelectric coefficient from both theoretical and experimental viewpoints. Such enhanced piezo-responsive properties influenced us to design a piezo-electric energy harvesting device to harness the energy from falling water droplets. The device is found to have pronounced sensitivity to such a minimal mechanical response and delivers an open circuit output voltage of 4.1 V with a 1.5 μ A short circuit current (A comparison table of piezocatalysts efficacy has been given in Table 2). Moreover, this piezo-responsive membrane (PCK1) has been exploited in catalytic applications. Typically, Rhodamine-B dye has been almost fully degraded (96%) under external ultrasonic vibration by generating reactive species (particularly \bullet OH). Such ROS have been further used to eradicate pathogenic bacteria making this multifunctional clay-based nanocomposite membrane a futuristic solution against numerous water-borne problems.

CRedit authorship contribution statement

Dhananjay Mondal: Data curation, Computation, Writing – original

draft. **Souravi Bardhan:** Data curation, Writing- assistance, Investigation. **Namrata Das:** Data curation, Investigation. **Jhilik Roy:** Data curation, Computation. **Saheli Ghosh:** Data curation. **Anupam Maity:** Investigation, Data curation. **Shubham Roy:** Conceptualization, Computation, Writing – review & editing. **Ruma Basu:** Supervision. **Sukhen Das:** Supervision, Funding acquisition.

Data Availability

Data will be made available on request.

Acknowledgments

The authors would like to thank the Department of Physics, Jadavpur University, for extending experimental facilities. S.D. and D.M would like to acknowledge UGC-DAE-CSR (Grant No. CRS/2021-22/02/498) and Science and Engineering Research Board (Grant No. EEQ/2018/000747), N.D would like to acknowledge University Grand Commission (UGC) (Grand ID: 191620153244), and J.R and R.B acknowledge UGC-DAE-CSR (Grant No. CRS/2021-22/02/514) for funding.

Declaration of competing interest

The authors declare that they have no competing interests.

Appendix A. Supporting information

Supplementary data associated with this article can be found in the online version at doi:10.1016/j.nanoen.2022.107893.

References

- [1] P.O. Ukaogo, U. Ewuzie, C.V. Onwuka, Environmental pollution: causes, effects, and the remedies, in: *Microorganisms for Sustainable Environment and Health*, Elsevier, 2020, pp. 419–429.
- [2] M. Nag, D. Lahiri, S. Ghosh, S. Garai, D. Mukherjee, R.R. Ray, *Emerg. Technol. Environ.* (2022) 531–560.
- [3] M. Usman, D. Balsalobre-Lorente, Environmental concern in the era of industrialization: can financial development, renewable energy and natural resources alleviate some load? *Energy Policy* 162 (2022), 112780.
- [4] S. Ali, J. Jiang, S.T. Hassan, A.A. Shah, Revolution of nuclear energy efficiency, economic complexity, air transportation and industrial improvement on environmental footprint cost: a novel dynamic simulation approach, *Nucl. Eng. Technol.* (2022).
- [5] H. Hu, W. Wen, J.Z. Ou, Construction of adsorbents with graphene and its derivatives for wastewater treatment: a review, *Environ. Sci.: Nano* (2022).
- [6] N. Morin-Crini, E. Lichtfouse, M. Fourmentin, A.R.L. Ribeiro, C. Noutsopoulos, F. Mapelli, É. Fenyvesi, M.G.A. Vieira, L.A. Picos-Corralles, J.C. Moreno-Piraján,

- Removal of emerging contaminants from wastewater using advanced treatments: a review, *Environ. Chem. Lett.* (2022) 1–43.
- [7] Y. Dehmani, D. Dridi, T. Lamhasni, S. Abouarnadasse, R. Chtourou, E.C. Lima, Review of phenol adsorption on transition metal oxides and other adsorbents, *J. Water Process Eng.* 49 (2022), 102965.
 - [8] D. Mondal, S. Roy, S. Bardhan, J. Roy, I. Kanungo, R. Basu, S. Das, Recent advances in piezocatalytic polymer nanocomposites for wastewater remediation, *Dalton Trans.* (2022).
 - [9] K. Wang, C. Han, J. Li, J. Qiu, J. Sunarso, S. Liu, The mechanism of piezocatalysis: energy band theory or screening charge effect? *Angew. Chem.* 134 (2022), e202110429.
 - [10] J. Hu, Y. Chen, Y. Zhou, L. Zeng, Y. Huang, S. Lan, M. Zhu, Piezo-enhanced charge carrier separation over plasmonic Au-BiOBr for piezo-photocatalytic carbamazepine removal, *Appl. Catal. B: Environ.* 311 (2022), 121369.
 - [11] Y. Peng, M. Du, X. Zou, G. Jia, S.P. Santos, X. Peng, W. Niu, M. Yuan, H.-Y. Hsu, Suppressing photoinduced charge recombination at the BiVO₄/NiOOH junction by sandwiching an oxygen vacancy layer for efficient photoelectrochemical water oxidation, *J. Colloid Interface Sci.* 608 (2022) 1116–1125.
 - [12] A. Ali, L. Chen, M.S. Nasir, C. Wu, B. Guo, Y. Yang, Piezocatalytic inactivation of water bacterium and heterotrophism-An overview, (2022).
 - [13] J.Q. Zhu, H. Wu, Z.L. Li, X.F. Xu, H. Xing, M.D. Wang, H.D. Jia, L. Liang, C. Li, L. Y. Sun, Responsive hydrogel based on triggered click reaction for liver cancer, *Adv. Mater.* (2022), 2201651.
 - [14] S. Sargazi, E. Simge, S.S. Gelen, A. Rahdar, M. Bilal, R. Arshad, N. Ajalli, M.F. Khan, S. Pandey, Application of titanium dioxide nanoparticles in photothermal and photodynamic therapy of cancer: an updated and comprehensive review, *J. Drug Deliv. Sci. Technol.* (2022), 103605.
 - [15] Y. Xie, M. Wang, Q. Sun, D. Wang, S. Luo, C. Li, PtBi- β -CD-Ce6 nanzyme for combined trimodal imaging-guided photodynamic therapy and NIR-II responsive photothermal therapy, *Inorg. Chem.* 61 (18) (2022) 6852–6860.
 - [16] V. Ahuja, A.K. Bhatt, S. Varjani, K.-Y. Choi, S.-H. Kim, Y.-H. Yang, S.K. Bhatia, Quantum dot synthesis from waste biomass and its applications in energy and bioremediation, *Chemosphere* 293 (2022), 133564.
 - [17] C. Yang, H. Kwon, B. Bang, S. Jeong, U. Lee, Role of biomass as low-carbon energy source in the era of net zero emissions, *Fuel* 328 (2022), 125206.
 - [18] M.P. Mahmud, S.R. Bazaz, S. Dabiri, A.A. Mehrizi, M. Asadnia, M.E. Warkiani, Z. L. Wang, Advances in MEMS and microfluidics-based energy harvesting technologies, *Adv. Mater. Technol.* (2022), 2101347.
 - [19] S.F. Ahmed, M. Mofijur, B. Ahmed, T. Mehnaz, F. Mehejabin, D. Malat, A. T. Hoang, G. Shafullah, Nanomaterials as a sustainable choice for treating wastewater, *Environ. Res.* 214 (2022), 113807.
 - [20] D. Mondal, S. Roy, S. Bardhan, R. Das, A. Maity, D.K. Chanda, S. Das, S. Ghosh, R. Basu, S. Das, Effect of microstructural evolution of natural kaolinite due to MWNT doping: a futuristic 'green electrode' for energy harvesting applications, *Mater. Sci. Mater. Electron* (2022) 1–17.
 - [21] S. Das, D. Mondal, S. Bardhan, S. Roy, D.K. Chanda, A. Maity, S. Dutta, K. Mukherjee, K. Das, Particle size mediated investigation of various physicochemical properties of kaolinite clay for fabricating the separator layer of green capacitors, *Mater. Sci. Mater. Electron* 33 (2022) 7119–7133.
 - [22] A. Gebrekrestos, T.S. Muzata, S. Ray, Nanoparticle-enhanced β -phase formation in electroactive PVDF composites: a review of systems for applications in energy harvesting, EMI shielding, and membrane technology, *ACS Appl. Nano Mater.* 5 (6) (2022) 7632–7651.
 - [23] G. Singh, M. Sharma, R. Vaish, Exploring the piezocatalytic dye degradation capability of lithium niobate, *Adv. Powder Technol.* 31 (2020) 1771–1775.
 - [24] I. Amadou, M.-P. Faucon, D. Houben, New insights into sorption and desorption of organic phosphorus on goethite, gibbsite, kaolinite and montmorillonite, *Appl. Geochem.* 143 (2022), 105378.
 - [25] M. Beekman, Teaching basic crystallography and diffraction using open access structure visualization software, *MRS Adv.* (2022) 1–6.
 - [26] R.D. Lahiru Sandaruwan, R. Kuramoto, B. Wang, S. Ma, H. Wang, White latex: appealing "green" alternative for PVDF in electrode manufacturing for sustainable Li-ion batteries, *Langmuir* 38 (29) (2022) 8934–8942.
 - [27] (a) A.E. Kassa, N.T. Shibeshi, B.Z. Tizazu, Calorimetry, Kinetic analysis of dehydroxylation of Ethiopian kaolinite during calcination, *J. Therm. Anal. Calorim.* (2022) 1–17;
(b) A. Maity, S. Samanta, D. Biswas, D. Chakravorty, Studies on nanoconfinement effect of NiO-SiO₂ spin glass within mesoporous Al₂O₃ template, *J. Alloys Compd.* 20 (887) (2021), 161447.
 - [28] (a) H. Peng, V. Shah, K. Li, Morphology and performance of polyvinylidene fluoride (PVDF) membranes prepared by the CCD method: Thermodynamic considerations, *J. Membr. Sci.* 641 (2022), 119857;
(b) P. Viswanath, M. Yoshimura, Light-induced reversible phase transition in polyvinylidene fluoride-based nanocomposites, *SN Appl. Sci.* 1 (11) (2019) 1–9;
(c) S. Samanta, A. Maity, S. Roy, S. Giri, D. Chakravorty, Effect of microstructure on ionic transport in silica-based sodium containing nanoconfined systems and their electrochemical performance as electrodes, *J. Phys. Chem. C* 124 (38) (2020) 21155–21169;
(d) A. Maity, S. Samanta, S. Roy, D. Biswas, D. Chakravorty, Magnetodielectric behaviour of composites of NiO-SiO₂ nanoglass and mesoporous silica SBA-15, *J. Non-Cryst. Solids* 1 (569) (2021), 120997.
 - [29] Y. Sun, J. Chen, W. Ge, Y. Ling, X. Chu, F. Min, Insights into the influence mechanism of Mg²⁺ doping on hydration activity of kaolinite surface: a DFT calculation, *Chem. Phys.* 560 (2022), 111576.
 - [30] Y. Fu, Y. Cheng, C. Chen, D. Li, W. Zhang, Study on preparation process and enhanced piezoelectric performance of pine-needle-like ZnO@PVDF composite nanofibers, *Polym. Test.* 108 (2022), 107513.
 - [31] N. Das, D. Sarkar, M. Saikh, P. Biswas, S. Das, N.A. Hoque, P.P. Ray, Piezoelectric activity assessment of size-dependent naturally acquired mud volcano clay nanoparticles assisted highly pressure sensitive nanogenerator for green mechanical energy harvesting and body motion sensing, *Nano Energy* (2022), 107628.
 - [32] (a) H. Liu, W. He, J. Ming, H. Xu, J. Zheng, Interaction of CO₂ with TiO₂/reduced graphene oxide as superior catalysts: Dispersion-corrected density functional theory simulation, *Diamond Relat. Mater.* (2022), 109279;
(b) Z. Liu, S. Li, J. Zhu, L. Mi, G. Zheng, Fabrication of β -phase-enriched PVDF sheets for self-powered piezoelectric sensing, *ACS Appl. Mater. Interfaces* 14 (9) (2022) 11854–11863.
 - [33] A. Patil, V.S. Hogade, S. Desai, S.S. Jadhav, S.M. Patange, Study of Elastic and Dielectric Properties of Nb₂O₅ doped Nanocrystalline NiCuZn Spinel Ferrite, (2022).
 - [34] (a) W. Dong, F. Liu, Y. Sun, B. Wang, M. Zhu, J. Li, X. Xu, J. Wang, Electro-elastic properties of a piezoelectric Te₂O(P₂O₄)₂ crystal, *CrystEngComm* 24 (2022) 5128–5134;
(b) N. Cui, X. Jia, A. Lin, J. Liu, S. Bai, L. Zhang, Y. Qin, R. Yang, F. Zhou, Y. Li, Piezoelectric nanofiber/polymer composite membrane for noise harvesting and active acoustic wave detection, *Nanoscale Adv.* 1 (2019) 4909–4914;
(c) Y. Zhao, Y. Gu, B. Liu, Y. Yan, C. Shan, J. Guo, S. Zhang, C.D. Vecitis, G. Gao, Pulsed hydraulic-pressure-responsive self-cleaning membrane, *Nature* 608 (2022) 69–73.
 - [35] S. Roy, S. Bardhan, K. Pal, S. Ghosh, P. Mandal, S. Das, S. Das, Crystallinity mediated variation in optical and electrical properties of hydrothermally synthesized boehmite (γ -AlOOH) nanoparticles, *J. Alloy. Compd.* 763 (2018) 749–758.
 - [36] M. Samet, A. Kallel, A. Serghei, Maxwell-Wagner-Sillars interfacial polarization in dielectric spectra of composite materials: Scaling laws and applications, *J. Compos. Mater.* (2022), 00219983221090629.
 - [37] (a) S. Zhao, H. Wei, P. Cieplak, Y. Duan, R. Luo, PyRESP: a program for electrostatic parameterizations of additive and induced dipole polarizable force fields, *J. Chem. Theory Comput.* 18 (6) (2022) 3654–3670;
(b) Z. Liu, G. Li, Q. Qin, L. Mi, G. Li, G. Zheng, C. Liu, Q. Li, X. Liu, Electrospun PVDF/PAN membrane for pressure sensor and sodium-ion battery separator, *Adv. Compos. Hybrid Mater.* 4 (4) (2021) 1215–1225.
 - [38] S. Landi Jr, I.R. Segundo, C. Afonso, O. Lima Jr, M.F. Costa, E. Freitas, J. Carneiro, Evaluation of band gap energy of TiO₂ precipitated from titanium sulphate, *Phys. B Condens. Matter* (2022), 414008.
 - [39] (a) K. Maity, U. Pal, H.K. Mishra, P. Maji, P. Sadhukhan, Z. Mallick, S. Das, B. Mondal, D. Mandal, Piezo-phototronic effect in highly stable CsPbI₃-PVDF composite for self-powered nanogenerator and photodetector, *Nano Energy* 92 (2022), 106743;
(b) Y. Jia, Y. Pan, C. Wang, C. Liu, C. Shen, C. Pan, Z. Guo, X. Liu, Flexible Ag microparticle/MXene-based film for energy harvesting, *Nano-Micro Lett.* 13 (1) (2021) 1–2.
 - [40] H. Pan, M.-H. Cui, C. Zhang, L.-Y. Liu, J. Li, Q. Jiang, X.-D. Zhang, Z.-Y. Zheng, Y. Zhang, H. Liu, Alkalinity regulation in a sulfur autotrophic nitrifying filter substantially reduced total dissolved solids and sulfate in effluent, *Bioresour. Technol.* 348 (2022), 126751.
 - [41] K.S. Hong, H. Xu, H. Konishi, X. Li, Direct water splitting through vibrating piezoelectric microfibers in water, *J. Phys. Chem. Lett.* 1 (6) (2010) 997–1002.
 - [42] B. Bagchi, N.A. Hoque, N. Janowicz, S. Das, M. Tiwari, Re-usable self-poled piezoelectric/piezocatalytic films with exceptional energy harvesting and water remediation capability, *Nano Energy* 78 (2020), 105339.
 - [43] J. Dolai, A. Biswas, R. Ray, N.R. Jana, Enhanced piezocatalysis by calcium phosphate nanowires via gold nanoparticle conjugation, *ACS Appl. Mater. Interfaces* 14 (23) (2022) 26443–26454.
 - [44] A. Biswas, S. Saha, S. Pal, N.R. Jana, TiO₂-Templated BaTiO₃ nanorod as a piezocatalyst for generating wireless cellular stress, *ACS Appl. Mater. Interfaces* 12 (43) (2020) 48363–48370.
 - [45] S. Wang, Z. Wu, J. Chen, J. Ma, J. Ying, S. Cui, S. Yu, Y. Hu, J. Zhao, Y. Jia, Lead-free sodium niobate nanowires with strong piezo-catalysis for dye wastewater degradation, *Ceram. Int.* 45 (2019) 11703–11708.
 - [46] S. Bardhan, K. Pal, S. Roy, S. Das, A. Chakravorty, P. Karmakar, R. Basu, S. Das, Nanoparticle size-dependent antibacterial activities in natural minerals, *J. Nanosci. Nanotechnol.* 19 (2019) 7112–7122.
 - [47] Z. Qu, H. An, M. Feng, W. Huang, D. Wang, Z. Zhang, L. Yan, Urolithin B suppresses osteoclastogenesis via inhibiting RANKL-induced signalling pathways and attenuating ROS activities, *J. Cell. Mol. Med.* (2022).
 - [48] K. Wang, M. Zhang, D. Li, L. Liu, Z. Shao, X. Li, H. Arandiyani, S. Liu, Ternary BaCaZrTi perovskite oxide piezocatalysts dancing for efficient hydrogen peroxide generation, *Nano Energy* 98 (2022), 107251.
 - [49] Z. Yuan, J.J. Aweya, J. Li, Z. Wang, S. Huang, M. Zheng, L. Shi, S. Deng, S. Yang, Synergistic antibacterial effects of low-intensity ultrasound and peptide LCMHC against *Staphylococcus aureus*, *Int. J. Food Microbiol.* 373 (2022), 109713.
 - [50] Z. Li, C. Wang, C. Dai, R. Hu, L. Ding, W. Feng, H. Huang, Y. Wang, J. Bai, Y. Chen, Engineering dual catalytic nanomedicine for autophagy-augmented and ferroptosis-involved cancer nanotherapy, *Biomaterials* 287 (2022), 121668.
 - [51] H. Deng, B. Xue, M. Wang, Y. Tong, C. Tan, M. Wan, Y. Kong, X. Meng, J. Zhu, TMT-based quantitative proteomics analyses reveal the antibacterial mechanisms of anthocyanins from aronia melanocarpa against *Escherichia coli* O157: H7, *J. Agric. Food Chem.* 70 (26) (2022) 8032–8042.

- [52] Y. Zhao, L. Shao, L. Jia, Z. Meng, Y. Liu, Y. Wang, B. Zou, R. Dai, X. Li, F. Jia, Subcellular inactivation mechanisms of *Pseudomonas aeruginosa* treated by cold atmospheric plasma and application on chicken breasts, *Food Res. Int.* (2022), 111720.
- [53] A. Zhang, Z. Liu, B. Xie, J. Lu, K. Guo, S. Ke, L. Shu, H. Fan, Vibration catalysis of eco-friendly Na_{0.5}K_{0.5}NbO₃-based piezoelectric: an efficient phase boundary catalyst, *Appl. Catal. B Environ.* 279 (119353) (2020).
- [54] E. Lin, Z. Kang, J. Wu, R. Huang, N. Qin, D. Bao, BaTiO₃ nanocubes/cuboids with selectively deposited Ag nanoparticles: Efficient piezocatalytic degradation and mechanism, *Appl. Catal. B Environ.* 285 (2021), 119823.
- [55] D. Liu, C. Jin, F. Shan, J. He, F. Wang, Synthesizing BaTiO₃ nanostructures to explore morphological influence, kinetics, and mechanism of piezocatalytic dye degradation, *ACS Appl. Mater. Interfaces* 12 (2020) 17443–17451.
- [56] Z. Kang, N. Qin, E. Lin, J. Wu, B. Yuan, D. Bao, Effect of Bi₂WO₆ nanosheets on the ultrasonic degradation of organic dyes: roles of adsorption and piezocatalysis, *J. Clean. Prod.* 261 (2020), 121125.
- [57] C. Jin, D. Liu, J. Hu, Y. Wang, Q. Zhang, L. Lv, F. Zhuge, The role of microstructure in piezocatalytic degradation of organic dye pollutants in wastewater, *Nano Energy* 59 (2019) 372–379.
- [58] L. Chen, Y. Jia, J. Zhao, J. Ma, Z. Wu, G. Yuan, X. Cui, I. Science, Strong piezocatalysis in barium titanate/carbon hybrid nanocomposites for dye wastewater decomposition, *J. Colloid Interface Sci.* 586 (2021) 758–765.
- [59] G. Singh, M. Sharma, R. Vaish, Flexible Ag@LiNbO₃/PVDF composite film for piezocatalytic dye/pharmaceutical degradation and bacterial disinfection, *ACS Appl. Mater. Interfaces* 13 (2021) 22914–22925.
- [60] J. Guan, Y. Jia, T. Chang, L. Ruan, T. Xu, Z. Zhang, G. Yuan, Z. Wu, G. Zhu, Highly efficient piezo-catalysis of the heat-treated cellulose nanocrystal for dye decomposition driven by ultrasonic vibration, *Sep. Purif. Technol.* 286 (2022), 120450.



Jhilik Roy: Jadavpur University, Kolkata, India, Jhilik Roy is presently doing her doctoral research in Materials science at the Department of Physics, Jadavpur University, India. She has obtained both B.Sc (2019) and M.Sc (2021) degrees in Physics from the University of Calcutta and Techno India University respectively. Ms. Roy has an excellent command of theoretical molecular docking analysis and other theoretical simulations. She has published several research papers recently on fluorometric sensors and their interaction with living systems. She is presently working in the field of piezoelectric and piezocatalytic nanomaterials.



Saheli Ghosh: Jadavpur University, Kolkata, India, Saheli Ghosh is currently pursuing her Ph.D. degree from Jadavpur University. She has completed B.Sc in Physics (2014) and M.Sc in Electronic Science (2016) from the University of Calcutta. Her present research work focuses on the development of dielectric, piezoelectric, and piezocatalytic performance of nanoparticles and the development of cost-effective energy harvesting devices.



Dhananjay Mondal: Jadavpur University, Kolkata, India, Dhananjay Mondal is currently pursuing his Ph.D. degree from the Department of Physics, Jadavpur University, India. He has received graduation (2017) and post-graduation (2019) degrees in Physics from the same department. His research interest involves biocompatible materials-based sensors and piezo-responsive membranes for wastewater treatment and energy harvesting applications. He has worked as a junior research fellow under a DST-SERB-funded project at Jadavpur University, Kolkata, and currently working as a Project Associate-I under a UGC-DAE-CSR-funded project in the same department.



Dr. Anupam Maity: Indian Association for the Cultivation of Science, Kolkata, India, Dr. Anupam Maity is an early career researcher who received his Ph.D. from the Department of Physics, Jadavpur University, India (2022) & M.Sc. (Applied Physics) from IIT Dhanbad (2016). Presently he is working as a Research Associate at the Indian Association for the Cultivation of Science, India. He has several peer-reviewed publications in international journals for his research on magnetic, dielectric, and electrical properties of nanowire-based thin films and transition metal ions containing glass-based nanocomposites suitable for energy storage or spintronic applications. He was awarded the *Young Researchers Award* from InSc in 2020.



Souravi Bardhan: Jadavpur University, Kolkata, India, Netaji Nagar College for Women, Kolkata, India, Ms. Souravi Bardhan is currently pursuing her Ph.D. from the Department of Physics, Jadavpur University, India. She pursued her graduation (2013) and post-graduation (2015) in Environmental Science from the University of Calcutta, India. Prior to joining the Ph.D. program, she worked on a project on the biogeochemistry of core regions of Indian Sundarbans with the School of Environmental Science, Jawaharlal Nehru University, India. Her present research work involves the enhancement of optical, electrical, and biological properties of natural minerals in their nanoregime to design natural-multifunctional sensors for wastewater treatment.



Dr. Shubham Roy: Jadavpur University, Kolkata, India, Harbin Institute of Technology, Shenzhen, China, Shubham Roy obtained his Bachelor's degree in Physics from the University of Calcutta in 2013 and his Master's degree in the same discipline from Madurai Kamaraj University in 2015. He has been awarded his Doctoral degree in science from Jadavpur University in 2022. His research involves synthesizing and characterizing nanomaterials for fabricating multifunctional fluorometric sensors to combat several environmental and biological issues.



Namrata Das: Jadavpur University, Kolkata, India, Ms. Namrata Das is currently pursuing her Ph.D. from the Department of Physics, Jadavpur University, India. She completed her Bachelor's degree and Master's degree in 2016 and 2018 respectively, in Physics from Jadavpur University. Her current research focuses on the fabrication of electroactive polymer composites, their various characterization techniques, and their application in green energy harvesting domains such as piezoelectric nanogenerators and self-powered sensors.



Dr. Ruma Basu: Jogamaya Devi College, Kolkata, India, Dr. Ruma Basu is an Associate professor at the Department of Physics, Jogamaya Devi College. She has guided several doctoral fellows and has more than 100 research publications in reputed journals. She obtained her B.Sc. degree from Presidency College, Calcutta University, in the year 1980, M. Sc. from Calcutta University, in 1983, and Ph. D. from Jadavpur University in 1989. Dr. Basu's research area includes membrane biophysics, biophysical chemistry, fluorescence and absorption spectroscopy, and photobiology.



Prof. Sukhen Das: *Jadavpur University, Kolkata, India.* Prof. Sukhen Das is a Professor in the Department of Physics, Jadavpur University. He has guided several doctoral and post-doctoral fellows and has more than 200 research publications in reputed journals. He has been working as a Scientist in CSIR-CGCRI, India in his initial years before joining Jadavpur University. He is also the recipient of the “UGC Research Award 2012–2014”. Prof. Das’s research area includes the development of ceramics, polymeric materials, antimicrobial bioceramics, and nanomaterials for the development of piezoelectric probes and sensors. Recently, he and his group have done extensive research on fluorometric sensors to combat wastewater pollution.

Natural Clay-Modified Piezocatalytic Membrane for Efficient Removal of Coliform Bacteria from Wastewater

Dhananjoy Mondal, Neelanjana Bag, Jhili Roy, Saheli Ghosh, Shubham Roy, Monisha Sarkar, Souravi Bardhan, Soumyaditya Sutradhar, and Sukhen Das*



Cite This: *Langmuir* 2024, 40, 5785–5798



Read Online

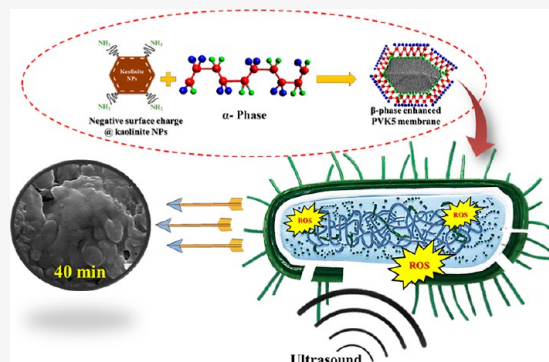
ACCESS |

Metrics & More

Article Recommendations

Supporting Information

ABSTRACT: In the modern era, water pollution, especially from industries, agricultural farms, and residential areas, is caused by the release of a large scale of heavy metals, organic pollutants, chemicals, etc., into the environment, posing a serious threat to aquatic ecosystems and nature. Moreover, untreated sewage waste discharged directly into nearby water bodies can cause various diseases to mankind due to the high load of fecal coliform bacteria. This work demonstrates the development of a biocompatible, cost-effective, highly robust, efficient, flexible, freestanding, and reusable membrane using naturally formed biocompatible kaolinite clay-doped poly(vinylidene fluoride-hexafluoropropylene) (PVDF-HFP) for effective piezodynamic destruction of coliform bacteria. In this study, *Escherichia coli* (*E. coli*) and *Enterococcus faecalis* (*E. faecalis*) have been used to evaluate the mechanical stimulus-responsive antibacterial efficacy of the nanocomposite membrane. The membrane can effectively eradicate nearly 99% viable *E. coli* and 97% *E. faecalis* within a span of 40 min under mechanical stimulation (soft ultrasound ~15 kHz). To further understand the mechanism, an evaluation of reactive oxygen species and bacterial FESEM was performed. These studies revealed that bacterial cells suffered severe visible cell damage after 40 min of piezocatalysis, elucidating the fact that the synthesized membrane is capable of producing a superior piezodynamic antibacterial effect.



1. INTRODUCTION

In the current scenario, water pollution is increasing at an alarming rate, which destroys aquatic life and the environment. Statistical data from the World Health Organization (WHO-2021) states that around 80% of global wastewater flows back untreated into the world's water. As a result, approximately 1.8 million deaths happen annually due to waterborne diseases. These wastewaters are coming from uncontrolled industrialization, agriculture runoff, and untreated sewage. Although various developing countries are trying to develop proper wastewater treatment profiles, due to limited resources and infrastructure, these technologies are in their infancy.¹ Water pollutants are not only responsible for the spread of a wide range of ailments but also have toxic impacts on aquatic habitats and human beings. Hazardous chemicals, pesticides, and herbicides from industries, farms, homes, and commercial areas can cause acute toxicity and immediate death or chronic toxicity that can lead to neurological problems or even cancers.² Solid wastes discharged into the water are comparatively easier to treat or remove, whereas it is a difficult challenge for scientists and the government to deal with liquid waste.³ Moreover, the proper treatment and removal of pathogenic contamination are currently a matter of concern. In reality, water samples collected from various sources like

wastewater effluents, sewage-mixed water from canals, sediments, and swimming pools indicated the presence of a diverse set of microbial profiles, predominantly *Enterococcus faecalis* or *E. faecalis*, *E. durans*, *E. raffinosus*, and *Escherichia coli*. Poorly treated or untreated sewage laden with bacteria and parasites are regularly discarded in nearby canals or water bodies, enhancing the chances of faecal matter-based diseases.⁴ Such pathogens also enter into drinking water supplies and cause digestive problems such as cholera and diarrhea. Indeed, disinfection is a primary concern for protecting public health and improving sanitation.⁵

Hence, to deal with such dire issues, various upcoming techniques are being popularized to tackle the situation. Currently, water treatment and disinfection techniques involve UV–C irradiation, heat or radiation treatment, anaerobic treatment, ultrafiltration, electrochemical treatment, or the use of chemical disinfectants, like chlorine, iodine, and alcohol.⁶

Received: November 20, 2023

Revised: January 22, 2024

Accepted: February 23, 2024

Published: March 6, 2024



Nevertheless, most of the approaches suffer from various drawbacks like the requirement of expert personnel, high energy consumption, the tendency for bacterial reactivation, chances for reduction of dissolved oxygen, or lack of sufficient bactericidal effect required for handling the contaminated water. Hence, there is an immediate requirement for the development of a biocompatible, efficient, cost-effective, and easily synthesizable system for combating the alarming increase in water pollution, along with efficient disinfection capability.⁷

Nowadays, piezodynamic therapy-assisted wastewater remediation is widely used.⁸ In this therapeutic approach, the piezo-responsive materials create inbuilt piezo potential in its interior by applying mechanical stress.⁸ The surface electrons and holes generated by this process react with the hydroxyl ions present in the wastewater sample and produce reactive oxygen species ($\text{ROS}—\text{OH}^*$, $^1\text{O}_2$, and $^*\text{O}_2^-$). These ROS further decompose the contaminants like organic dye, pharmaceuticals, bacteria, and viruses those are present in the wastewater sample.⁸ Some key factors made piezodynamic therapies superior for bacterial disinfection. First of all, these samples use green mechanical energies to eradicate pathogens without using any chemicals, whereas in the case of other antibacterial tools, the pathogens can evolve themselves by improving their resistance against those chemicals over time. The mechanical impales can be used long-term and do not have any harmful effects on the environment. That is why scientists and technologists are trying to develop efficient biocompatible and cost-effective piezocatalysts to degrade pathogens and organic contaminants via their versatility.

In this report, natural kaolinite-incorporated polyvinylidene (fluoride-hexafluoropropylene) (PVDF-HFP)-based flexible, free-standing polymeric nanocomposite membranes have been developed for piezodynamic antimicrobial assessment. Kaolinite is a highly stable, eco-friendly, natural, abundant, and economical aluminosilicate ($\text{Al}_2\text{Si}_2\text{O}_5(\text{OH})_4$) clay.⁹ Various physicochemical activities of this natural kaolinite are enhanced in its nano-regime due to its high surface-to-volume aspect ratio.¹⁰ Among all these physicochemical properties, surface charge is a key factor. In reality, kaolinite shows a negative surface charge for the combined effect of its negative basal planes and positive prism planes. This negative surface charge is further enhanced by surface modification by incorporating an electronegative NH_2 group over the prism plane to minimize the effects of this positive moiety of kaolinite.¹¹ The polarization of the piezoelectric PVDF-HFP polymer has been enhanced by incorporating this highly surface-charged nanocomposite to find a promising piezocatalyst.¹² Nominal (5% w/w) incorporation of this surface-activated nano-kaolinite in the polymer matrix enhanced its physicochemical properties and lowered the cost of production. Various works have been reported earlier with regard to this type of system for energy generation and wastewater remediation, but their applicability in terms of the cytotoxicity of the synthesized nanocomposite was restricted.^{13–15} Conventionally, the researchers incorporate as-synthesized chemically derived piezo-responsive nanomaterials into the polymer matrix to fabricate such piezocatalysts, which can lose their effects over time if the chemically derived nanomaterials do not have significant physicochemical stability, which can also have toxic side effects.^{16–18} But in this study, natural nano-clay (kaolinite) has been incorporated into the PVDF-HFP polymeric matrix, which has high structural and thermal stability and cannot degrade over time. Herein, this natural

clay-based piezo material shows a high piezoresponse under mechanical stimuli, which indicates an enormous potential to generate clean energy. Additionally, this cost-effective, natural, and biocompatible nanosystem has been used to eradicate harmful pathogenic bacteria from wastewater to make it potable, and it can restrict waterborne diseases. This versatile nanosystem can be produced on a mass scale to serve society if properly improvised.

2. EXPERIMENTAL SECTION

2.1. Materials. Naturally formed kaolinite clay minerals have been purchased from Hindustan Minerals, India. 2',7'-Dichlorodihydrofluorescein diacetate (DCFDA, purity $\geq 97\%$, 10 μM) and poly(vinylidene fluoride hexafluoropropylene) (PVDF-HFP, purity: 99.99%, molecular weight: 455,000) have been purchased from Sigma-Aldrich, Germany. LB broth and phosphate-buffered saline (PBS) were purchased from HiMedia Pvt. Ltd., India. The analytical-grade hydrazine hydrate (purity $\geq 99\%$), acetone (HPLC-grade, purity $\geq 99.5\%$), and dimethylformamide (DMF, purity $\geq 99\%$) have been purchased from Merck, India. *E. coli* DH5 α (MTCC-1652) and *E. faecalis* (MTCC-441) have been purchased from the Institute of Microbial Technology, Chandigarh, India. Millipore water with a resistance of $\sim 18.2 \text{ M}\Omega\text{-cm}$ was used throughout the experiment.

2.2. Nanonization of Kaolinite Clay and its Surface Activation. Initially, the bulk-purchased natural kaolinite was crushed by using a diamond mortar and pestle. After that, the sedimentation technique was adopted, using Millipore water to purify the crushed clay. Further, the top-down synthesis technique was adopted to find nanoparticles, using a ball mill grinder operating at 150 rpm for 48 h. In this experimental procedure, tungsten carbide balls were used by maintaining a ball-to-mass ratio of 20:1. After that, 1 g of nano-kaolinite was dissolved in 20 mL of deionized water and 20 mL of hydrazine hydrate and left for vigorous stirring for 6 h at room temperature so as to activate the surface of the natural clay.

2.3. Fabrication of the Activated Natural Nano-Kaolinite-Based PVDF-HFP Membrane. A facile one-step solution casting method was adopted to find the kaolinite-based free-standing PVDF-HFP membrane. Initially, 0.5 g of PVDF-HFP was taken in three different glass vials and dissolved into 5 mL of dimethylformamide (DMF) at 60 $^\circ\text{C}$ on a magnetic stirrer (600 rpm). The activated nano-kaolinite was then added by maintaining a weight percentage of 2.5, 5, and 7.5% with the polymer. The vials were kept in the same condition until a homogeneous gel-like transparent solution occurred. Then the homogeneous solutions were placed in different clean petri dishes and kept in a dust-free hot-air oven at 60 $^\circ\text{C}$ for 6 h. The dried flexible free-standing membranes were then peeled off the petri dishes carefully, collected, and named PVK2.5, PVK5, and PVK7.5, respectively, according to their wt %. A film of pristine PVDF-HFP was also prepared for the comparative study by the same method but without adding the activated natural clay in its matrix and labeled PVK0. All the prepared nanocomposite membranes were then sent for further experiments.

2.4. Characterization Techniques and Measurement Parameters. The purity, phase identification, and unit cell parameters of the nanonized natural clay minerals of nanocomposite membranes were investigated by using a Bruker D-8 advanced powder X-ray diffractometer with a Cu K α target with a wavelength of 1.5418 Å. The operating voltage and current during the measurement were set up at 35 kV and 35 mA. The scan speed and increment of angle were set up at 0.5 s per step and 0.0125633 $^\circ$, respectively.

The surface and morphological properties of the natural clay and fabricated nanocomposite membranes were visualized with a field emission scanning electron microscope. An INSPECT-F50 FEI FESEM instrument was employed to collect the micrographs. Additionally, a JEM-2100 Plus JEOL transmission electron microscope was used to investigate the micrographs of the natural clay. Powdered nanoparticles and small pieces of membranes were cast on carbon tape and coated by gold plasma deposition to collect the micrograph under the field emission scanning electron microscope

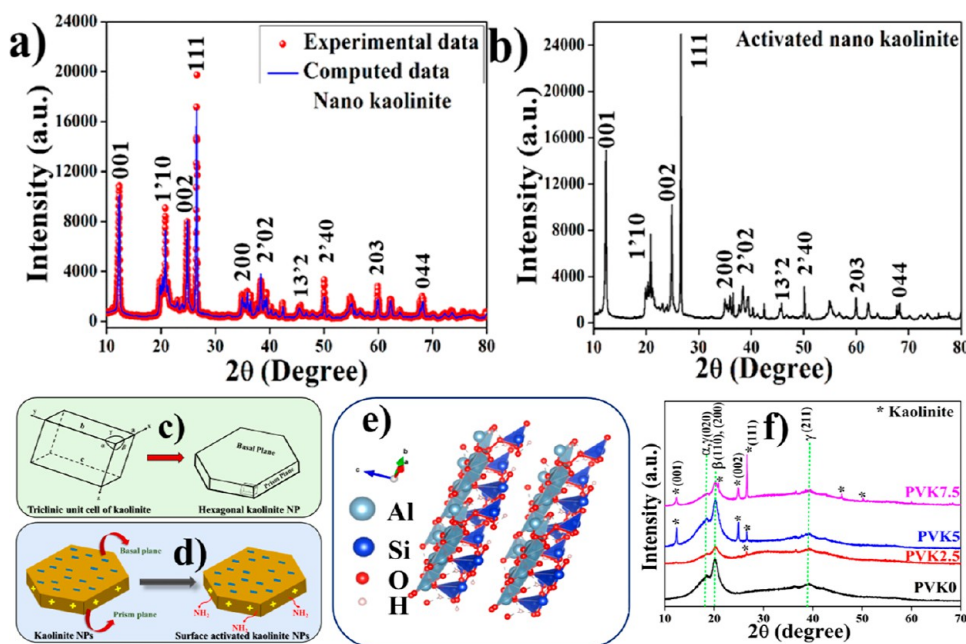


Figure 1. (a) Experimental and computed XRD data of nano-kaolinite, (b) X-ray diffractogram of activated nano-kaolinite, (c) schematic representation of the triclinic kaolinite unit cell and hexagonal kaolinite nanoparticle, (d) schematic diagram of the planes of kaolinite NPs, (e) unit cell structure of kaolinite NPs by Vesta software, and (f) XRD of kaolinite-PVDF-HFP nanocomposite membranes.

with an operating voltage of 20 kV. On the other hand, a well-dispersed kaolinite nanocandle in acetone was cast on a 300-mesh carbon-coated copper grid to collect the transmission electron microscopy (TEM) micrograph at a bias voltage of 200 kV.

Investigation of the elemental composition of the natural kaolinite and fabricated nanocomposite membranes were carried out by a Bruker instrument, QUANTAX EDS, and mapping techniques, which were equipped with the field emission scanning electron microscope.

The surface charges of the nano-kaolinite and activated nano-kaolinite were investigated by the zeta potential technique. A Malvern Zetasizer was used to collect the data by dissolving the nanoparticles in deionized water.

A Fourier transform infrared (FTIR) spectroscopy measurement tool was adopted to investigate the bonding networks and percentage β -phases of the fabricated nanocomposite membranes. An IR Affinity 900i Shimadzu Infrared Spectrometer was used in this experiment. The thin membranes were placed over the path of infrared light and the data were taken in a region of 400–1000 cm^{-1} wavenumbers, whereas the powder clay was analyzed by ATR (attenuated total reflectance) directly by powder sample within the range of 400–4000 cm^{-1} .

The electrical properties of the fabricated nanocomposite membranes were measured by using an LCR meter (4294 A Precision Impedance Analyzer, Agilent). All the membranes were cut into pieces measuring 2×2 cm and sandwiched between two aluminum electrodes and wires on both sides for measurement.

Investigation of the polarization properties of the fabricated membranes was performed by polarization-electric field (PE-loop) study. The devices were prepared by the PVK0, PVK2.5, PVK5, and PVK7.5 membranes.

Piezoelectric open-circuit voltage generation under mechanical stress of the fabricated membranes was investigated by a digital storage oscilloscope (X 3012 A, Keysight) connected to the device by an Agilent N2862B 10:1 passive probe.

The generation of ROS while the piezocatalytic bacterial eradication took place was measured by a fluorescence measurement technique using a Carry Eclipse Fluorescence Spectrophotometer (Agilent Technologies).

2.5. Antimicrobial Assessment Study. Using a typical Gram-negative coliform bacteria *E. coli* and a typical Gram-positive coliform bacteria *E. faecalis*, the disinfection process of bacteria via exploiting

piezocatalysis was investigated. The bacterial cells were cultured in Luria–Bertani (LB) broth overnight at 37 °C with constant shaking (120 rpm). Six clean glass vials were filled with 10 mL of the aliquots, and two rectangular films (1 cm \times 1 cm) of PVK5 were put into two of the vials. Without any film and without being exposed to ultrasonic treatment, the vials served as the control group, which had been marked as group 1. Of the other four vials, two containing only the culture of *E. coli* and *E. faecalis*, respectively, were subjected to ultrasonic vibration and were marked as group 2, and another two comprising both bacterial cultures and PVK5 film were subjected to ultrasonic treatment (US) and marked as group 3. At specific intervals of 10 min, 100 μL of the bacterial suspension from each vial was extracted and evenly distributed onto agar plates that had solidified at a dilution ratio of 10^4 . Each one was collected in triplicate, and the following formula was used to determine the mortality (%) based on the colony counting method.¹⁹

$$M\% = \frac{(B - C)}{B} \times 100$$

where M is the mortality rate (%) and B and C stand for the mean of the bacterial colony (CFU mL^{-1}) in the control and treated samples, respectively. Dichlorodihydrofluorescein diacetate (2',7') was used to measure the formation of ROS in each case. Every time, 1 mL aliquots were extracted, followed by a PBS solution and the addition of a 10 μM DCFDA solution. A spectrophotometer was used to detect the fluorescence intensity of the solutions after they were left in the dark for a further 30 min (excitation at 404 nm and emission at 525 nm).²⁸ Specifically, DCFH-DA reacts with ROS to create 2',7'-dichlorofluorescein (DCF), which increases fluorescence and signals the production of ROS.²⁰ The precipitates from the bottom of each vial were collected and washed twice with filtered PBS solution at 5000 rpm for five min to perform bacterial field emission scanning electron microscopy (FESEM). Subsequently, the pellets were mixed with paraformaldehyde solution and serially diluted with ethanol at different concentrations (5, 20, 50, 75, and 100%). Before the FESEM analysis, the solutions were dried, drop-cast onto clean coverslips, and then sputter-coated with gold.

Using previously published methods, the in vitro hemolysis test was used to evaluate the biocompatibility of nanocomposite membranes in red blood cells (RBCs).²¹ RBCs were extracted from fresh Sprague–

Dawley rat blood, purified in sterile PBS, and then mixed with dispersions of varying concentrations of nanocomposites (PVK0, PVK2.5, PVK5, and PVK7.5). The controls were RBCs exposed to ultrapure water (positive control) or treated with PBS (negative control). After 1 h of incubation at 37 °C, samples were centrifuged at 3000 rpm for 5 min, and the absorbance at 540 nm was determined. The hemolysis ratio was calculated using the given formula while considering the sample's absorbance values.

$$\text{Hemolysis rate (\%)} = \frac{(A_s - A_{NC})}{A_{PC} - A_{NC}} \times 100\%$$

In contact with blood cells, the nanocomposites demonstrated a remarkable capacity to minimize hemolysis or rupturing of RBCs. Hemolysis may result in excessive bleeding and inflammation, impeding a lesion's healing ability. Because composites prevented hemolysis, this would instigate the PVK nanocomposites to have no such cytotoxic effect in cells (RBCs). The RBCs in the water completely burst, causing the solution to turn crimson in the control.

3. RESULTS AND DISCUSSION

3.1. Investigation of the Physicochemical Properties of the Synthesized Materials. The structural information and phase purity of the adopted natural nano-kaolinite were initially investigated by the X-ray diffractometer depicted in Figure 1a. The diffractogram was further compared with the data from the crystallographic open database having the JCPDS card no. 80–0886 with the triclinic lattice with the P1 space group. The absence of any undesired diffraction maxima of the compared diffractogram suggests that the natural kaolinite has been found in its purest form. The (001) plane situated at 12.39° and the (002) plane at 24.99° suggest the highly ordered kaolinite structure used in the work. The X-ray diffractogram of this natural nano-kaolinite has been refined further by using the MAUD software package (version 2.996).²² A well-matched refinement with a promising goodness of fitting experimental data (Figure 1a) over theoretical data further confirms the purity of natural kaolinite. The crystallographic information such as unit cell parameters, cell volume microstrain, etc., have been found and depicted in Table 1. The visualization of refined unit cells has been acquired by VESTA software and depicted in Figure 1e.²³

It has been found from microstructural visualization (Figure 1e) that oxygen vacancies have been created in the lattice structure, which may have arisen owing to the high-energy ball milling of the bulk kaolinite.²⁴ These oxygen vacancies further result in active sites for the incorporation of functional groups over its surfaces. The X-ray diffraction (XRD) of the activated

nano-kaolinite was also performed, and it was found that there were no extra diffraction maxima, which suggests that the incorporated functional groups do not alter the structural properties of the pristine nano-kaolinite. In reality, the diffraction planes 111, 1'10 are the prism planes, whereas 001, 002 are the basal planes of kaolinite.²⁵ The schematic representation of the basal and prism planes and their interaction with the functional group has been depicted in Figure 1c,d for hexagonal kaolinite nanoparticles. The X-ray diffractograms of the activated kaolinite-based PVDF-HFP nanocomposite membranes have also been investigated and are depicted in Figure 1f. The diffractograms of the nanocomposite membranes show that the nonpolar α -phase at 17.6° gets quenched, whereas both the polar phases of β (20.4°) and γ (39.6°) get enhanced with the natural nanoclay incorporation in the PVDF-HFP matrix.²⁶ The diffraction maxima at 12.5, 24.8, 26.6, 49.5, and 67.3° have arisen due to the increased doping percentage of the kaolinite in the membranes. These polar phase enhancements of the PVDF-HFP membranes help to increase their piezoelectric effectiveness and get maxima for PVK5.

It is found that after reaching a certain doping limit, viz., 5 wt % in our case of the nanoclay, the polar phase in the polymer matrix further decreases in PVK7.5. This may be attributed to the excess presence of the negative surface charge of the activated natural clay, which further disrupts the H₂ and F₂ band parity in the nanocomposite membrane.²⁷

Investigation of the surface morphology of the natural kaolinite depicted the fact that the homogeneous distribution of particles with an average diameter between 80 and 90 nm, which lie in the nano-regime, confirms the nanoparticle formation by the facile ball milling synthesis technique (Figure 2a,b). The TEM micrograph also depicted the particles in the nano-regime as having a hexagonal particle shape. The FESEM micrographs of the polymer membranes depicted in Figure 2d–g show that the big bubble-like structure, PVK0, has been greatly reduced with the incorporation of nanoparticles in PVK2.5, PVK5, and PVK7.5. This validates the formation of polar crystalline phases. The clay-incorporated nanocomposite membranes depicted the homogeneous distribution of nanoparticles in the PVDF-HFP matrix, which suggests the successful incorporation of the nanoparticles.²⁸

The EDS spectra and elemental mapping data also suggest the successful incorporation of nanoparticles into the membranes (Figure 3). However, for using carbon tape, the carbon component has been locked in the instrument; as a result, the carbon component is not present in the elemental table. The presence of Au in the membranes arises due to the gold sputtering while the sample was prepared for FESEM, EDS, and mapping.

3.2. Estimation of Polarity and Piezo-Effectiveness of the Nanocomposite Membranes. Piezoelectric properties depend on several properties of the nanocomposite. Herein, the negative surface charge of the natural clay enhances the polar phase of the PVDF-HFP, which is a key factor that enhances the piezo-effectiveness.²⁹ In reality, kaolinite is a layered aluminosilicate clay of alumina (AlO₆) octahedrons and silica (SiO₂) tetrahedrons where the isomorphous substitution of Al³⁺ and Si⁴⁺ creates a negative charge over the basal planes and a positive charge over the prism planes (faces) of kaolinite.¹⁰ The basal plane of kaolinite is greater in length than the prism plane; therefore, a combined negative surface charge was found in kaolinite (−7.9 mV). The

Table 1. Microstructural Parameters of Natural Nano-Kaolinite Clay

parameters	kaolinite nanoparticle
<i>a</i> (Å)	5.14370 ± 0.00016
<i>b</i> (Å)	8.93381 ± 0.00076
<i>c</i> (Å)	7.42187 ± 0.00013
α (deg)	92.2375 ± 0.00446
β (deg)	105.0010 ± 0.00458
γ (deg)	90.27046 ± 0.00524
<i>V</i> (Å ³)	329.144366
χ^2	2.287
<i>R_p</i>	13.555053
<i>R_{wp}</i>	20.509154
macrostrain	9.519805 × 10 ^{−5} ± 1.0625224 × 10 ^{−5}
crystallite size	1596.4071 ± 32.8414

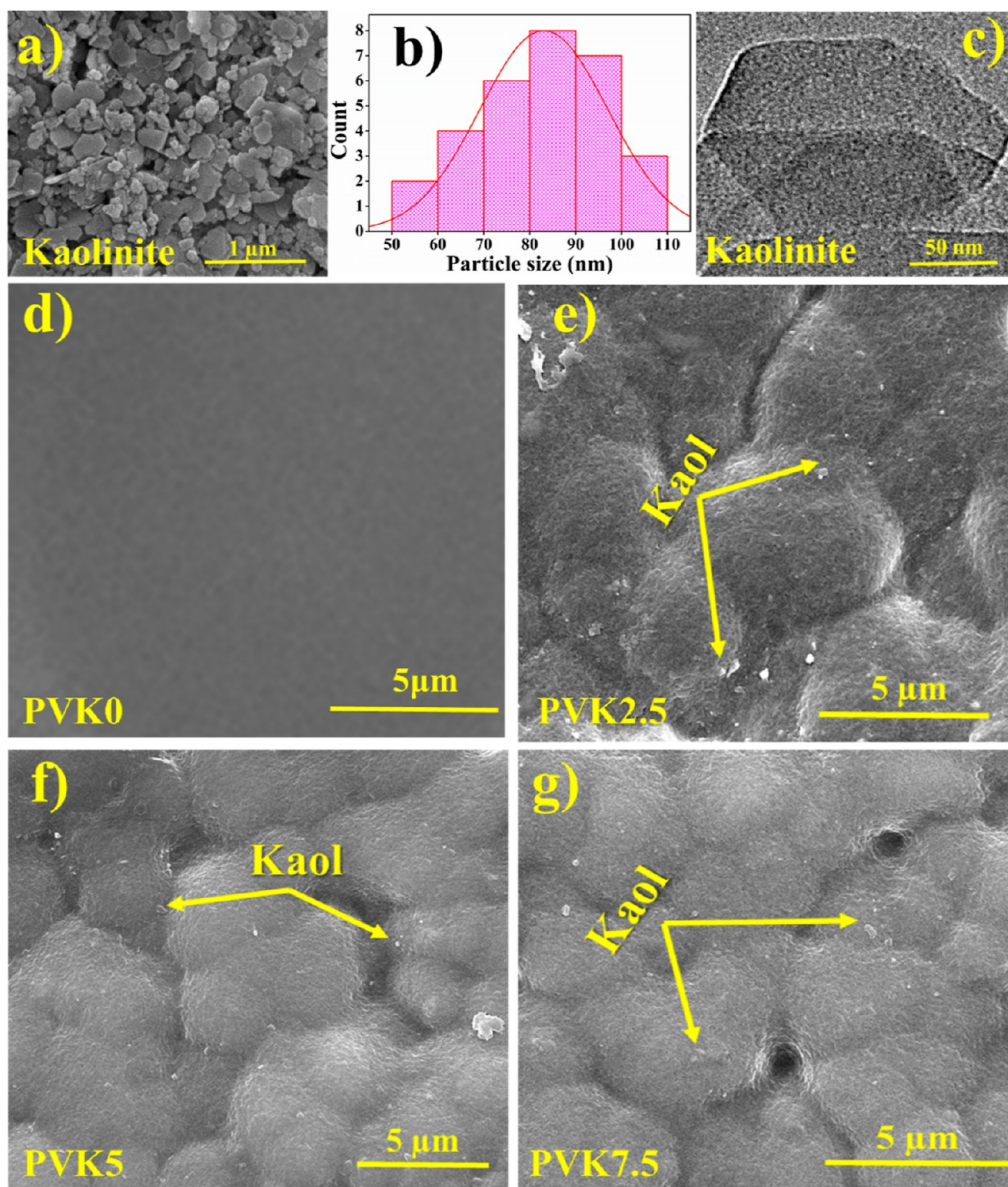


Figure 2. (a) FESEM micrograph of kaolinite NPs, (b) particle size distribution of kaolinite NPs, (c) TEM micrograph of kaolinite NPs, (d) FESEM of PVK0 actual image and EDS in S2, (e–g) FESEM micrograph of kaolinite-incorporated PVDF-HFP membranes PVK2.5, PVK5, and PVK7.5, respectively.

incorporation of electro-negative functional groups attached to the positive prism planes further influences the negative surface charge (-11.1 mV, Figure S1) of the nano-clay, as depicted in a schematic diagram in Figure 1d.

These electro-active functional groups incorporated on the kaolinite nanoparticle surface were further investigated by the FTIR measurement technique. The bonding network graphs for pristine kaolinite and surface-activated kaolinite have been depicted in Figure 4a. In Figure 4a, the characteristics of vibrational bands between 430 and 700 cm^{-1} have occurred for the bending of the Si–O–Al bond. Another vibrational maximum at 750 cm^{-1} has been observed for the AlO_6 vibration. Absorption bands at 792 and 917 cm^{-1} have been found for the Si–O and Al–OH deformations, respectively. The vibration band of Si–O stretching has also been found in the region of 940 – 1150 cm^{-1} in both pristine and functionalized nano-kaolinite. The absorption band in the region of 3620 – 3700 cm^{-1} has arisen for the present hydroxyl groups in

the as-prepared nanoparticles.³⁰ Additionally, a low-intensity wide band has also been found in the region of 1190 – 1240 cm^{-1} for the N–H rocking (inset, Figure 4a).^{31,32} These absorption bands for N–H are absent in pristine kaolinite and present in functionalized kaol, which suggests the successful attachment of functional groups (NH_2) in the prism plane of the kaolinite (alumina facets). This electro-active NH_2 group enhanced the negative surface charge, which was also validated by the zeta potential study.³³

This negative surface charge of the activated clay enhances the probability of polar β -phase formation in the nanocomposite membrane. In reality, the α -phase of PVDF-HFP has an electro-positive $-\text{CH}_2$ moiety and an electro-negative $-\text{CF}_2$ moiety attached in carbon chains in the TGTG' (trans-gauche–trans–gauche) configuration, which is why the polarity of the membrane is very low.³⁴ In the β -phase of the PVDF-HFP, the $-\text{CH}_2$ and $-\text{CF}_2$ moieties arranged themselves in opposite directions of the carbon chain in the

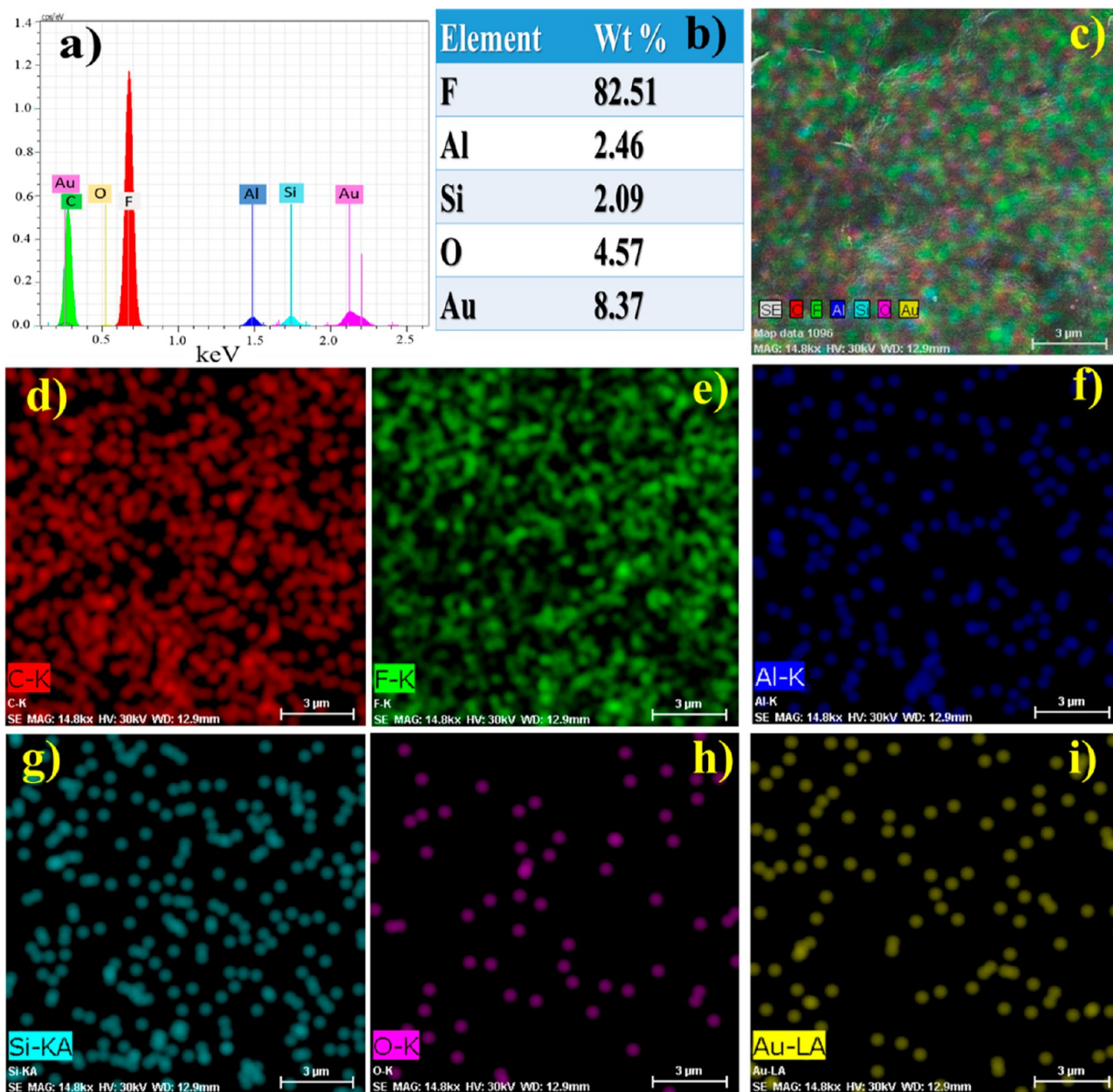


Figure 3. (a) EDS spectra PVK5 nanocomposite membrane. (b) Elemental composition of PVK5. (c–i) Elemental distribution of the PVK5 membrane by mapping.

TTTT configuration and enhanced the polar phase by forming the dipole as well as the piezoresponse of the membranes. When the nanoparticles with a negative surface charge were entrapped into the polymer matrix, the surface charge of the nanoparticles flipped the positive moiety of the PVDF-HFP on its side, creating an all-trans conformation (TTTT), which resulted in the polar β -phase enhancement. The schematic diagram of dipole orientation in the different phases of PVDF-HFP has been shown in Figure 4e.³⁴ This enhanced polar β -phase and the bonding networks of the nanocomposite membranes have been investigated by FTIR spectroscopy. In Figure 4b, the FTIR spectra show that the nonpolar α -phases at 530 (CF_2 - bending), 614 (CF_2 - bending), 765 (skeletal bending), 796, and 976 (CH_2 - rocking) cm^{-1} get quenched and the characteristic bands of the polar β -phase at 489 (CF_2 - deformation), 508 (CF_2 - stretching), 603 (CF_2 - wagging), and 840 (CF_2 stretching, CH_2 rocking, and skeletal C–C

stretching) cm^{-1} were enhanced with the increment of nanoparticle incorporation in the polymer matrix and were found to be maximum in PVK5.³⁴ The polar phase decreases after the excess incorporation of nanoparticles in sample PVK7.5. In reality, the overdoping of nanoparticles enhances the negative charge concentration in the nanocomposite matrix and this extra negative surface charge tries to decrease the polar phase by attracting the positive moiety (CH_2 -) PVDF-HFP polymeric chain; as a result, the dipolar orientation is again disrupted. A schematic representation is depicted in Figure 4c. In terms of polar phase calculation, the polar β -phase has been calculated by the Lambert–Beer law³⁴

$$F(\beta) = \frac{A(\beta)}{\frac{K(\beta)}{K(\alpha)} \times A(\alpha) + A(\beta)} \quad (1)$$

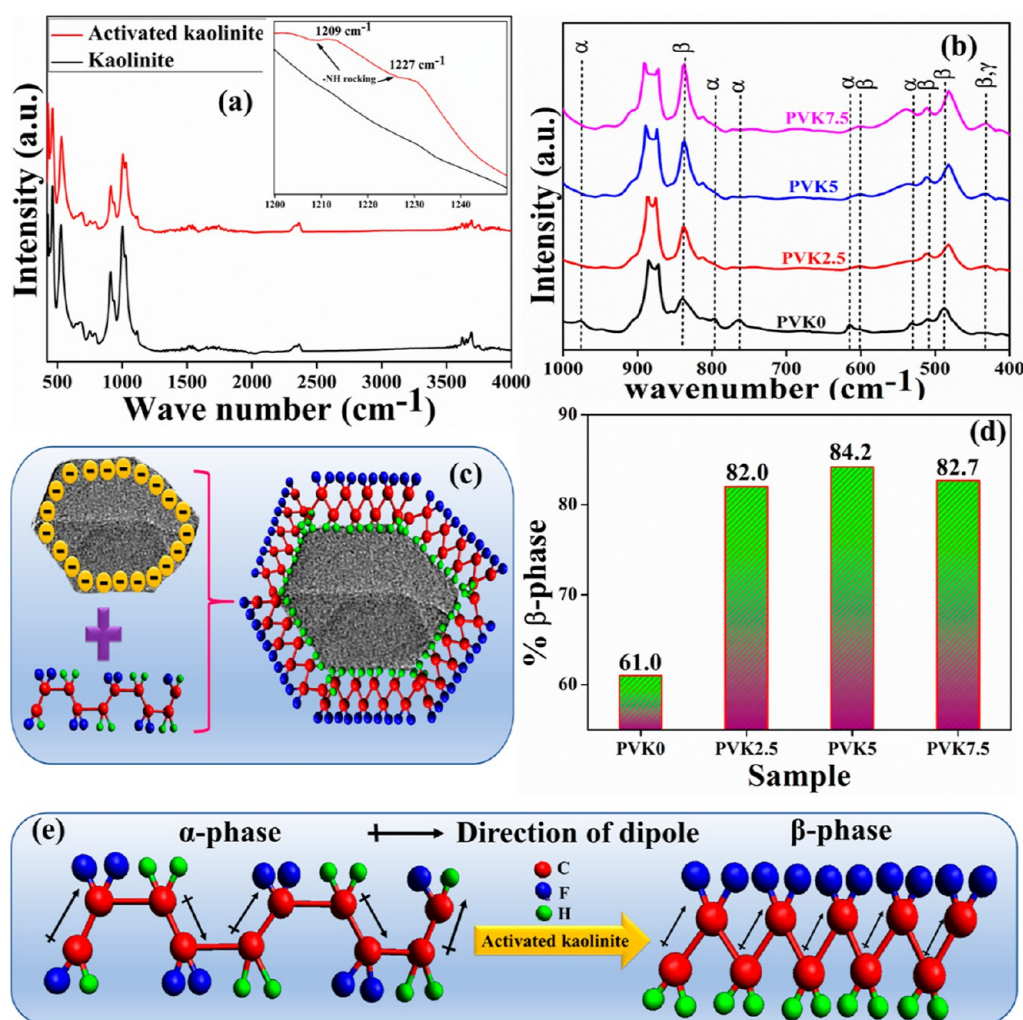


Figure 4. (a) FTIR spectra of nano-kaolinite and activated nano-kaolinite, (b) FTIR spectra of synthesized nanocomposite membranes, (c) schematic representation of β -phase formation, (d) percentage β -phase of kaolinite-doped PVDF-HFP nanocomposite membranes, and (e) schematic representation of dipole orientation of pristine PVDF-HFP and kaolinite-PVDF-HFP nanocomposite membranes.

where $K(\alpha)$ and $K(\beta)$ are the absorption coefficients for the α and β phases at 765 and 840 cm^{-1} , respectively, and have the values of 6.1×10^4 and $7.7 \times 10^4 \text{ cm}^2 \text{ mol}^{-1}$, whereas $A(\alpha)$ and $A(\beta)$ are the absorbance values of the α and β phases, respectively, at the corresponding wavenumbers. From the Lambert–Beer law, the polar β -phase percentages have been calculated and found to be 61.0, 82.0, 84.2, and 82.7% for the nanocomposite membranes PVK0, PVK2.5, PVK5, and PVK7.5, respectively, which suggests that the PVK5 membrane poses the maximum polar β -phase (Figure 4d).

The dielectric property of the nanocomposite membranes is also evidence of polarization, in terms of the Maxwell–Wagner interfacial polarization theory. The electrical storage efficiency of the nanocomposite membranes has been calculated in terms of electrical permittivity ϵ' by the relation³⁵

$$\epsilon' = \frac{C_p d}{\epsilon_0 A} \quad (2)$$

where ϵ' is the real part of the permittivity (dielectric constant: DC) that implies the storage efficiency, C_p is the specific capacitance, d and A denote the thickness and area of the membrane, and ϵ_0 is the free space permittivity with a value of $8.85 \times 10^{-12} \text{ F m}^{-1}$. It has been found that the dielectric

constant increases with the increasing doping percentage, and it is found to be maximum in the PVK5 sample. The dielectric constants are 9.0, 9.4, 12.9, and 9.7, respectively, for the samples PVK0, PVK2.5, PVK5, and PVK7.5 at a field frequency of 40 Hz (Figure 5a). It has been found that the DC is maximum at 40 Hz and decreases with increasing frequency.³⁶ In reality, any semiconductive sample has conductive grains surrounded by insulating grain boundaries. In the low-frequency domain, the applied electric field is insufficient to pull out the conductive grains from the grain boundaries, resulting in a higher degree of polarization and further contributing to the higher DC. According to the M–W theory, when the external frequency reaches a critical value, the conductive grains are capable of being free and start hopping, and thus, the DC gets lowered. The maximum DC of the PVK5 nanocomposite membrane implies that the polarization is maximum in it, and it is capable of acting as a promising piezo-responsive sample. The frequency-dependent conduction mechanism (AC conductivity) of the nanocomposite membranes has also been studied by the relation

$$\sigma_{ac} = 2\pi f \epsilon_0 \epsilon' \tan \delta$$

where f is frequency, ϵ_0 is the permittivity in free space, and ϵ is the permittivity of the membranes. It has been found that the

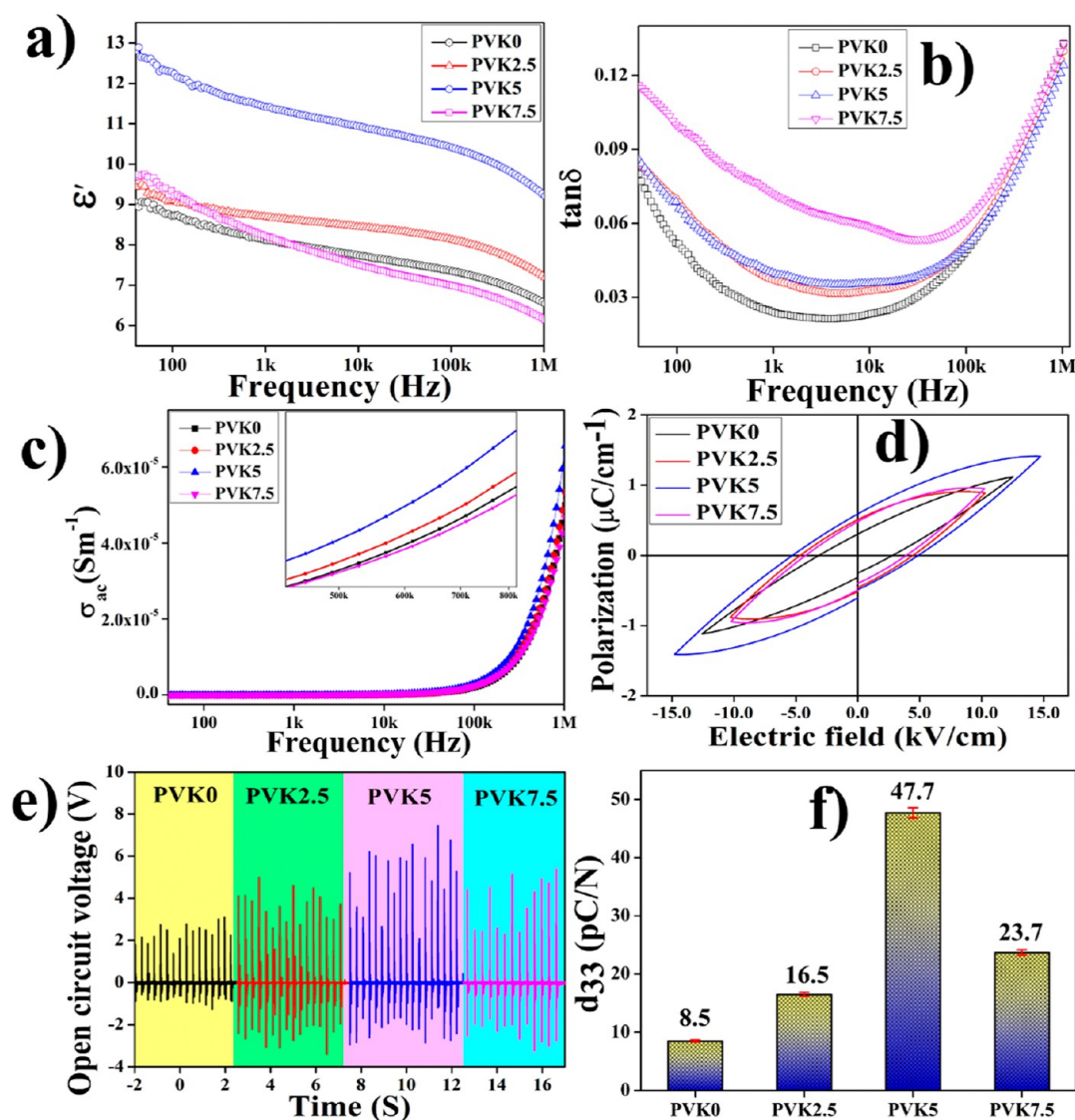


Figure 5. (a) Dielectric constant of the nanocomposite membranes, (b) tangent losses, (c) AC conductivities of the membranes, (d) polarization vs electric field hysteresis loops (P – E loop) of nanocomposite membranes, (e) piezoelectric open-circuit voltage of the membranes (under ~ 10 N force), and (f) piezoelectric coefficients (d_{33}) of the synthesized membranes.

AC conductivity increases with increasing frequency, and it is 4.9×10^{-5} , 5.3×10^{-5} , 6.6×10^{-5} , and $4.7 \times 10^{-5} \text{ Sm}^{-1}$ for PVK0, PVK2.5, PVK5, and PVK7.5, respectively (Figure 5c). In reality, with increasing frequency, the conductive grains become free from the insulating grain boundary and enhance the conductivity of the samples.³⁶

The room-temperature polarization–electric field hysteresis loop (PE -loop) was also used to investigate the polarization efficiency of the nanocomposite membranes. Devices have been fabricated by using PVK0, PVK2.5, PVK5, and PVK7.5 membranes by attaching Cu wires to both sides with aluminum electrodes.³⁷ The P – E hysteresis loop was then measured at 10 Hz in a voltage region of ± 200 V. The area within the loop indicates the heterogeneous charge density and storage efficiency of the membranes. It has been found that the remnant polarization (P_r) increases with the increasing doping percentage, and it is found to be 0.30, 0.51, 0.59, and $0.48 \mu\text{C}/\text{cm}^2$, respectively, for the PVK0, PVK2.5, PVK5, and PVK7.5 nanocomposite membranes depicted in Figure 5d. The remnant polarization is found to be highest in the PVK5

membrane, which is analogous to the dielectric data and indicates the maximum polar phase contained in the PVK5 membrane. This promising polarization in the PVK5 membrane made it suitable for any piezo-responsive applications.

In order to calculate the piezoelectric coefficient (d_{33}), the open-circuit piezo-voltages for the membranes have been calculated under the mechanical force applied by simple finger-tapping. At first, simple sandwich devices were prepared using the nanocomposite membranes by attaching single-stranded Cu wires on both sides of the membranes with aluminum electrodes. The entire device was then coated with the polymeric coating (PET jacket) for protection from any external damage. The open-circuit output voltages were then recorded by applying a force of approximately 10 N. The calculation of the applied force has been demonstrated in Supporting Information Section S4.³⁸ It has been found that the voltages are 1.9, 3.4, 7.5, and 4.5 V for the nanocomposite membranes PVK0, PVK2.5, PVK5, and PVK7.5, respectively, as depicted in Figure 5e. The open-circuit voltage without a

Table 2. Comparison of the Piezoelectric Effectiveness of Synthesized Membranes with That of Other Reported Works (N.M.: Not Mentioned)

composite name	β -phase (%)	dielectric constant	remnant polarization ($\mu\text{C}/\text{cm}^2$)	piezoelectric coefficient (d_{33} pC/N)	reference
hematite-doped PVDF-HFP	80.2	17	N.M.	46.9	39
MoS ₂ nanoflower-doped PVDF	80.0	N.M.	N.M.	36.4	40
ZnCoO-doped PVDF	63.7	N.M.	N.M.	44.7	41
ZnO/CQDs/PVDF	70.3	N.M.	N.M.	49.5	42
rGO/PVDF-HFP	67.2	N.M.	N.M.	N.M.	43
hydroxyapatite/PVDF-HFP fiber-film nanogenerator	80.0	N.M.	N.M.	30.2	44
E-MoS ₂ nanosheets	85.3	25.0	N.M.	N.M.	12
gram-scale Y-doped ZnO and PVDF	72.0	N.M.	N.M.	N.M.	45
natural kaolinite-doped PVDF-HFP	84.2	12.9	0.59	47.7	this report

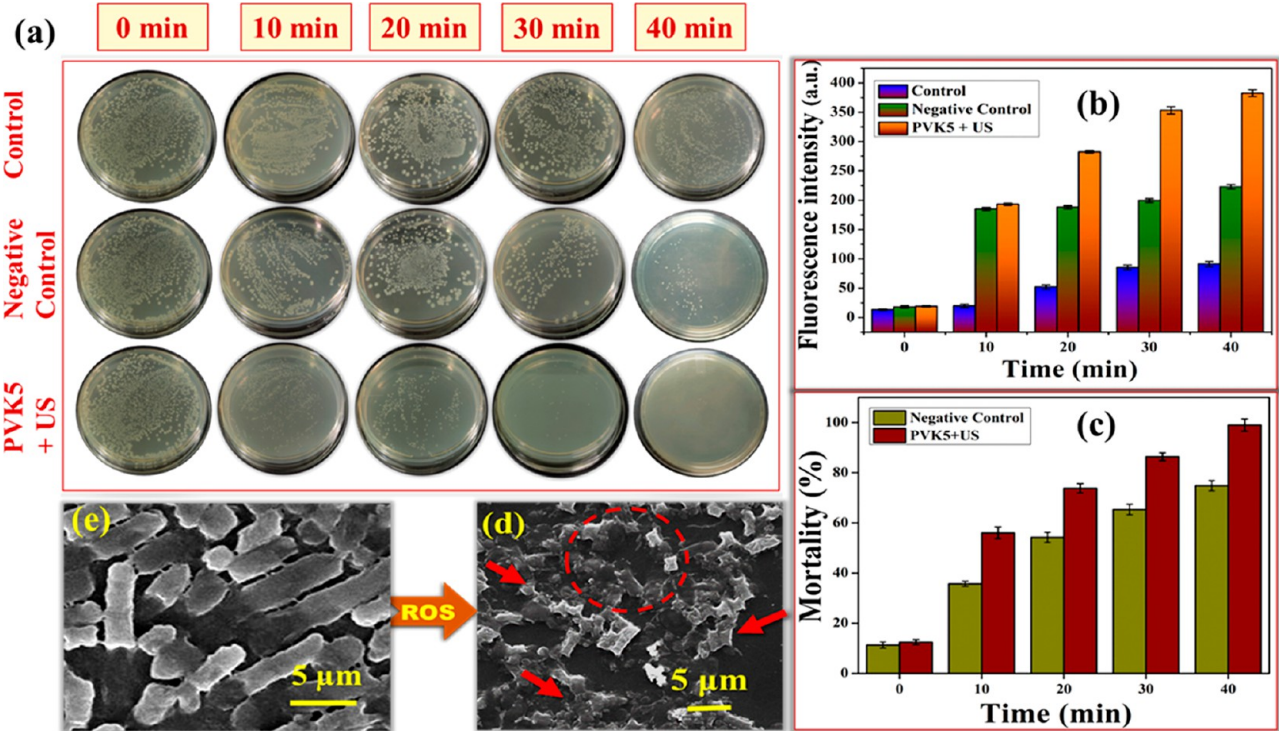


Figure 6. (a) Photographs representing surviving *E. coli* colonies on the solid agar plates (after 24 h of incubation); (b,c) illustration of the amount of ROS generation and mortality percentage of *E. coli*, as calculated using the colony counting technique; (d,e) FESEM images.

PET jacket has also been investigated for the PVK5 membrane and is depicted in Figure S5. The piezoelectric coefficients (d_{33}) have been calculated for the membranes by using the following relation³⁸

$$d_{33} = \frac{C_p \times V}{F} \quad (3)$$

where C_p is the specific capacitance, V is the open-circuit piezo-voltage, and F is the applied force. The calculated d_{33} s are 8.5, 16.5, 47.7, and 23.7 pC/N, respectively, for the nanocomposite membranes PVK0, PVK2.5, PVK5, and PVK7.5 (Figure S5f). The open-circuit piezo-voltage and piezoelectric coefficients of the nanocomposite membranes elucidate the fact that PVK5 could be exploited as a potential agent for further piezoelectric applications. A comparison table of the piezoelectric effectiveness of the nanocomposite membrane with that of other reported piezoelectric materials is given in Table 2.

3.3. Eradication Efficiency of Pathogenic *E. coli* and *E. faecalis* Using Piezocatalysis. A substantial bactericidal effect was found when the bacterial cells are exposed to ultrasound with the polymeric membrane. The mortality reaches nearly 99% in *E. coli* bacteria and 97% in *E. faecalis* bacteria after 40 min of ultrasound treatment, which has been calculated from the colony counting technique (Figures 6a and 7a). Conversely, cell proliferations were observed in the control samples. A slight enhancement in the mortality rate in the negative controls, i.e., bacteria exposed to ultrasonic vibrations, is only due to physical factors like micromechanical shocks, cavitation, and mechanical effects.⁴⁶ The movement of compression and rarefaction waves through the media during ultrasonication and the collapse of rapid oscillating bubbles have a deleterious effect on the bacterial cell membrane.

However, the piezocatalytic effect due to the presence of the membrane has an instantaneous lethal impact on the bacterial load. In reality, the induced potential difference on both sides of any piezo-responsive membrane under the mechanical

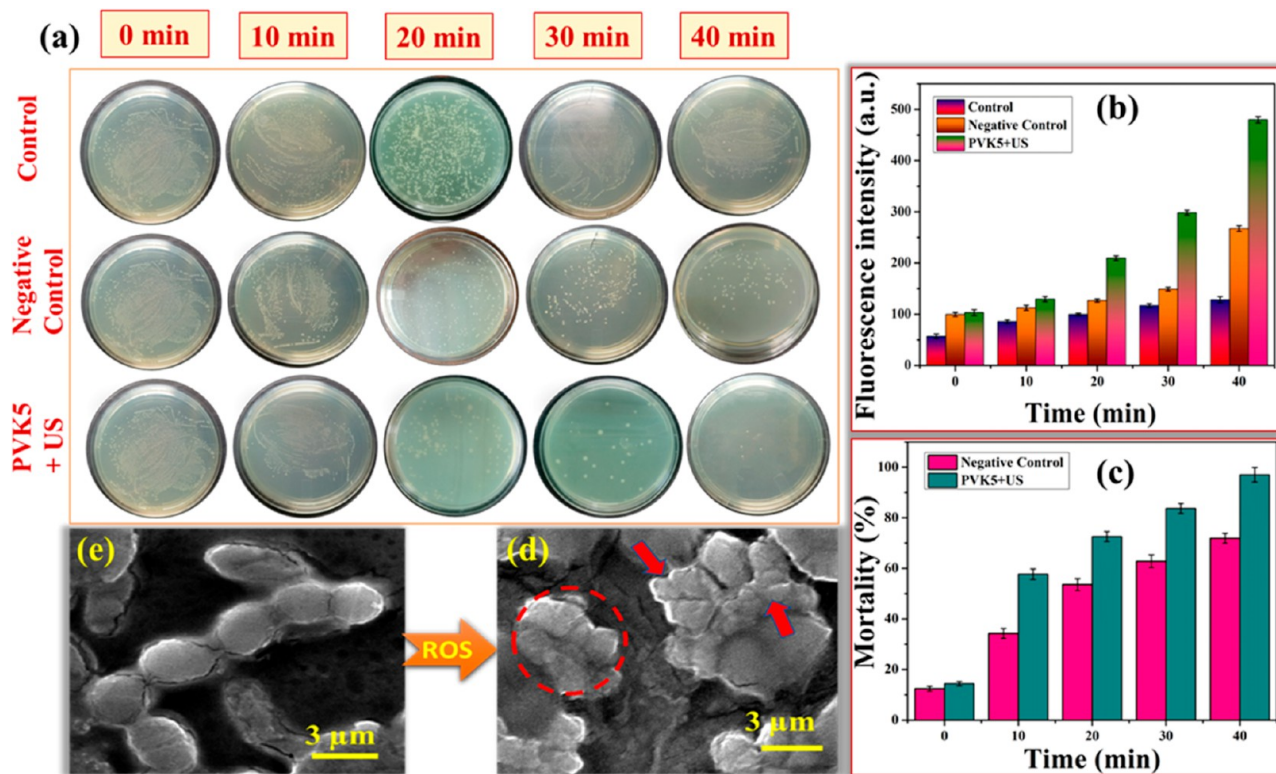
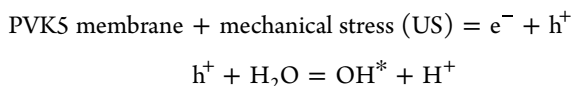


Figure 7. (a) Photographs representing surviving *E. faecalis* colonies on the solid agar plates (after 24 h of incubation); (b,c) illustration of the amount of ROS generation and mortality percentage of *E. faecalis*, as calculated using the colony counting technique; (d,e) FESEM images.

stimulus arranges the electron over the surface of the membrane.⁸ These electrons further react with the hydroxyl radicals of water and produce ROS such as hydroxyl radicals (OH^*), singlet oxygen ($^1\text{O}_2$), and superoxide ($^*\text{O}_2^-$). These generated ROS play a pivotal role in inactivating bacterial cells. The reaction of ROS generation is given below⁸



Furthermore, the PVK5 film under ultrasonic stress induces major distortion and holes in the bacterial cells, which eventually lead to membrane bursts and severe damage to the cellular membrane, as shown by the FESEM micrographs. This makes it easier for intracellular components to seep out and for cytoplasmic materials to be released, which compromises the integrity of the cell membrane. In the control sample, the cellular membrane is smooth and undamaged, whereas after piezodynamic therapy, the bacterial cell ruptured and destroyed about 99% *E. coli* and 97% *E. faecalis*. In the case of the negative control with only ultrasound, the bacterial mortality was found to be 74.8 and 71.9%, suggesting that the piezodynamic ROS enhances bacterial eradication efficiency. The time-dependent kinetic study is depicted in Figure S6 for both the negative control and piezocatalysis. Moreover, the antibacterial test of the PVDF-HFP membrane without ultrasound and with ultrasound has been investigated and is given in Figure S7. It has been found that the antibacterial efficiency was 8% without ultrasound and around 35% with ultrasound. The 35% eradication was found to be due to the nominal piezocatalytic efficiency in the bare PVDF-HFP membrane.

The fundamental cause of piezocatalysis is ROS creation, primarily OH^* , as was previously stated. This ROS production can also aid in the disinfection of bacteria. Furthermore, whereas the formation of ROS is negligible in the control group, it is gradually increased in the PVK5-mediated treatment group (Figures 6b and 7b).

The fact that free radicals can damage subcellular components like protein and nucleic acids, disrupt trans-membrane electron transfer, stop DNA replication, and encourage lipid membrane peroxidation suggests that the ROS produced under mechanical stress can effectively render bacterial cells inactive (Figure 8).⁴⁷ FESEM micrographs further demonstrated that these processes finally lead to cellular damage and cell demise (Figures 6d,e and 7d,e). As demonstrated after a 40 min treatment, the small amount of oxidative stress caused by ultrasonic vibration is likewise bacteriostatic, although it is about 50% lower and ineffectual

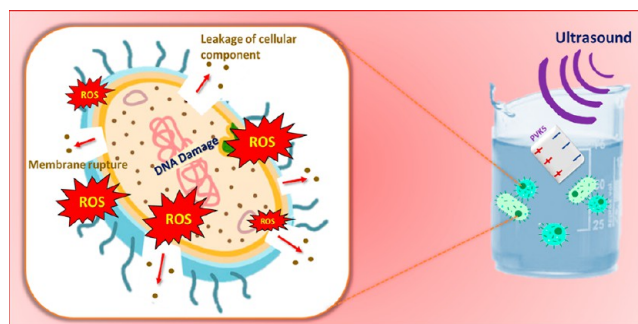
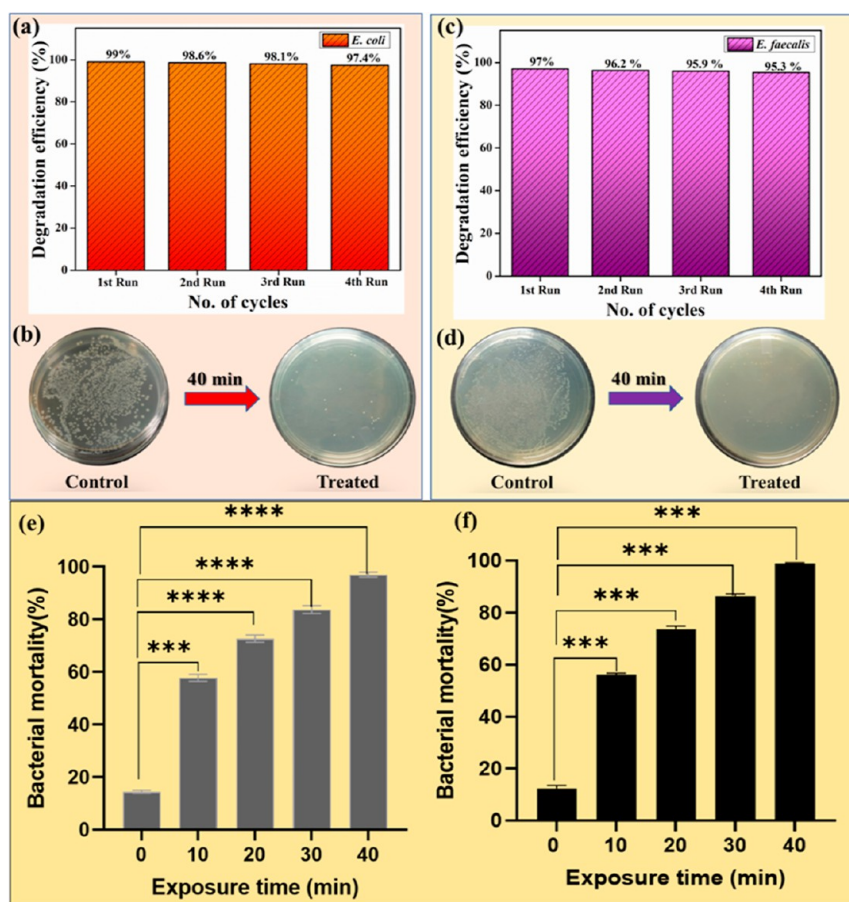


Figure 8. Mechanism of ROS-mediated bacterial damage, disruption of the membrane integrity, and simultaneous leakage of cytosol.

Table 3. Comparison of Bacterial Eradication Effectiveness of the Nanocomposite Membranes with That of Other Reported Works (N.M.: Not Mentioned)

type of the sample	stimulus used	name of the bacteria	bacterial degradation efficiency (%)	required time (min)	reference
PVDF/tea polyphenol (TPs)/Ag	N.M.	<i>E. coli</i>	85.56%	N.M.	48
PVDF composite film embedding LiNbO ₃ ceramics decorated with silver nanoparticles (Ag NPs)	ultrasonication	<i>E. coli</i> , <i>S. aureus</i>	99.99%	180 min (3 h)	49
tea polyphenols (TPs) PVDF/TPs composite thin films	N.M.	<i>E. coli</i>	96.65%	N.M.	48
Ag-NP-decorated PVDF-BaTiO ₃ composites	N.M.	<i>E. coli</i>	97.22%	N.M.	48
poly(vinylidene fluoride) (PVDF)/sphere@TiO ₂ (CST) composite	photocatalysis	<i>E. coli</i> , <i>S. aureus</i>	81%	1440 min (24 h)	50
kaolinite clay-doped poly(vinylidene fluoride-hexafluoropropylene) (PVDF-HFP)	soft ultrasound	<i>E. coli</i>	99%	40 min	51
		<i>E. faecalis</i>	97%		this report

**Figure 9.** (a,b) Recyclability test of the PVK5 membrane for *E. coli* bacteria, (c,d) recyclability test of the PVK5 membrane for *E. faecalis* bacteria, and (e,f) one-way ANOVA test for *E. coli* and *E. faecalis*, respectively.

compared to the synergistic action of the film in the event of ultrasonic vibration. A comparison table of bacterial degradation using different samples is given below (Table 3). Therefore, this work validates the fact that the piezo-responsive PVK5 membrane can be effectively utilized for the elimination of both Gram-positive and Gram-negative bacteria under mechanical stimuli. Moreover, the recyclability test of the membrane has been investigated for up to 4 cycles and negligible efficiency loss was found, suggesting the applicability of the membrane for multiple uses (Figure 9a–d). The statistical validation of bacterial eradication data has been investigated with one-way ANOVA test for both the bacteria

by GraphPad Prism 9 software. The statistical significance value (*p*-value) has been found to be 0.0001 for *E. coli* and 0.0002 for *E. faecalis*, with a significant *R*² value of 0.9995 and 0.9989, respectively, which suggests the statistical correctness of the data (Figure 9e,f). Moreover, the hemolysis rate was less than 2% among the experimental groups of samples at various doses. The hemolysis rate was only 0.13% at PVK5, whereas those at PVK0, PVK2.5, and PVK7.5 were, respectively, 1.6, 1.1, and 0.39%, which were far less than the 5% allowed limit (Figure 10). Hence, the PVK nanocomposites are considered to be biocompatible membranes, which can be further used for

in vivo experiments as these have no such toxicity effect on cells.

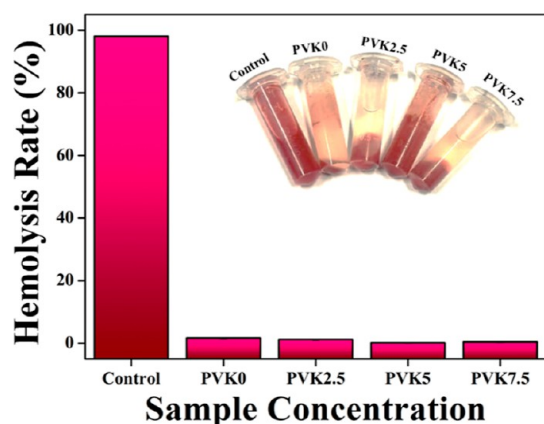


Figure 10. Biocompatibility of the nanocomposite membranes via hemolysis assay.

4. CONCLUSIONS

In this report, naturally formed kaolinite clay has been ground in a facile top-down synthesis method to find nano-clay. The surface of this nano-clay was then modified successfully to enhance its physicochemical properties, and it was incorporated into the PVDF-HFP polymer matrix. The fabricated natural clay-based free-standing nanocomposite membranes show promising piezo-responsive properties. This piezo-response has been confirmed by XRD, FTIR, dielectric, P – E loop, and d_{33} measurements. It has been found that the 5% activated clay-incorporated membrane shows maximum piezo-response. This highly piezo-responsive membrane has been used further to decompose Gram-negative (*E. coli*) and Gram-positive (*E. faecalis*) coliform bacteria, with a promising degradation efficacy of 99 and 97%, respectively, in only 40 min of soft ultrasound. The ROS-mediated bacterial degradation mechanism has been investigated further and has been found to generate OH^* radicals under soft ultrasound. FESEM study was also performed to investigate the cell death of bacteria and found that the ruptured cell wall confirms the bacterial death. This highly piezo-responsive, eco-friendly, low-cost, and natural clay-based nanocomposite membrane can be produced on a mass scale to get rid of waterborne diseases, if properly improvised.

■ ASSOCIATED CONTENT

SI Supporting Information

The Supporting Information is available free of charge at <https://pubs.acs.org/doi/10.1021/acs.langmuir.3c03560>.

Zeta potential of kaolinite and activated kaolinite, FESEM and EDS of PVK0, estimation of impulsive time (full-width half maxima), force calculation for piezoelectric coefficient determination, open-circuit output voltage of the PVK5 membrane without a PET jacket, and time-dependent kinetic study of the two bacteria by the PVK5 membrane (PDF)

■ AUTHOR INFORMATION

Corresponding Author

Sukhen Das – Department of Physics, Jadavpur University, Kolkata 700032, India; orcid.org/0000-0001-8372-3076; Phone: +91 9433091337; Email: sdasphysics@gmail.com

Authors

Dhananjoy Mondal – Department of Physics, Jadavpur University, Kolkata 700032, India

Neelanjana Bag – Department of Physics, Jadavpur University, Kolkata 700032, India

Jhilik Roy – Department of Physics, Jadavpur University, Kolkata 700032, India; Department of Physics, Jogamaya Devi College, Kolkata 700026, India

Saheli Ghosh – Department of Physics, Jadavpur University, Kolkata 700032, India

Shubham Roy – Shenzhen Key Laboratory of Advanced Functional Carbon Materials Research and Comprehensive Application, Shenzhen Key Laboratory of Flexible Printed Electronics Technology, and School of Science, Harbin Institute of Technology, Shenzhen 518055, China; orcid.org/0000-0001-5245-3229

Monisha Sarkar – Department of Physics, Jadavpur University, Kolkata 700032, India

Souravi Bardhan – Department of Environmental Science, Netaji Nagar College for Women, Kolkata 700092, India; orcid.org/0000-0003-0944-2940

Soumyaditya Sutradhar – Department of Physics, Jadavpur University, Kolkata 700032, India; orcid.org/0000-0003-3679-2583

Complete contact information is available at:

<https://pubs.acs.org/10.1021/acs.langmuir.3c03560>

Author Contributions

Dhananjoy Mondal: conceptualization, methodology, data curation, computation, and writing—original draft. **Neelanjana Bag:** data curation and writing. **Jhilik Roy:** computation, data curation, and investigation. **Saheli Ghosh:** data curation and writing—assistance. **Shubham Roy:** conceptualization, methodology, and writing—reviewing and editing. **Monisha Sarkar:** data curation. **Souravi Bardhan:** data curation and writing. **Soumyaditya Sutradhar:** supervision and funding acquisition. **Sukhen Das:** supervision and funding acquisition.

Notes

The authors declare no competing financial interest.

■ ACKNOWLEDGMENTS

The authors would like to thank the Department of Physics, Jadavpur University, and UGC-DAE-CSR, Kolkata Center, for extending experimental facilities. S.D. and D.M. would like to acknowledge UGC-DAE-CSR (grant no. CRS/2021-22/02/498), J.R. acknowledges UGC-DAE-CSR (grant no. CRS/2021-22/02/514), and S.S. acknowledges UGC-DAE-CSR (grant no. CRS/2021-22/02/529) for funding.

■ REFERENCES

(1) Summary Progress Update 2021: SDG 6—Water and Sanitation for all. https://www.unwater.org/sites/default/files/app/uploads/2021/12/SDG-6-Summary-Progress-Update-2021_Version-July-2021a.pdf (accessed Oct 06, 2023).

- (2) Roy, S.; Roy, J.; Guo, B. Nanomaterials as Multimodal Photothermal Agents (PTAs) Against 'Superbugs'. *J. Mater. Chem. B* **2023**, *11*, 2287–2306.
- (3) Parida, V. K.; Sikarwar, D.; Majumder, A.; Gupta, A. K. An Assessment of Hospital Wastewater and Biomedical Waste Generation, Existing Legislations, Risk Assessment, Treatment Processes, and Scenario during COVID-19. *J. Environ. Manage.* **2022**, *308*, 114609.
- (4) Barrass, R. Hygiene in the Home and Community. *Mastering Science*; Palgrave, London, 1991; pp 349–362.
- (5) Roy, S.; Hasan, I.; Guo, B. Recent Advances in Nanoparticle-Mediated Antibacterial Applications. *Coord. Chem. Rev.* **2023**, *482*, 215075.
- (6) Zahmatkesh, S.; Amesho, K. T. T.; Sillanpää, M. A Critical Review on Diverse Technologies for Advanced Wastewater Treatment during SARS-CoV-2 Pandemic: What Do We Know? *J. Hazard. Mater. Adv.* **2022**, *7*, 100121.
- (7) Samuel, M. S.; Ravikumar, M.; John, J. A.; Selvarajan, E.; Patel, H.; Chander, P. S.; Soundarya, J.; Vuppala, S.; Balaji, R.; Chandrasekar, N. A Review on Green Synthesis of Nanoparticles and Their Diverse Biomedical and Environmental Applications. *Catalysts* **2022**, *12* (5), 459.
- (8) Mondal, D.; Roy, S.; Bardhan, S.; Roy, J.; Kanungo, I.; Basu, R.; Das, S. Recent Advances in Piezocatalytic Polymer Nanocomposites for Wastewater Remediation. *Dalton Trans.* **2022**, *51* (2), 451–462.
- (9) Das, S.; Mondal, D.; Bardhan, S.; Roy, S.; Chanda, D. K.; Maity, A.; Dutta, S.; Mukherjee, K.; Das, K. Particle Size Mediated Investigation of Various Physicochemical Properties of Kaolinite Clay for Fabricating the Separator Layer of Green Capacitors. *J. Mater. Sci.: Mater. Electron.* **2022**, *33* (9), 7119–7133.
- (10) Mondal, D.; Sau, A.; Roy, S.; Bardhan, S.; Roy, J.; Ghosh, S.; Basu, R.; Sutradhar, S.; Das, S. Functionalized MWCNT-Integrated Natural Clay Nanosystem: A Promising Eco-Friendly Capacitor for Energy Storage Applications. *J. Mater. Sci.: Mater. Electron.* **2023**, *34* (21), 1597.
- (11) Mondal, D.; Roy, S.; Bardhan, S.; Das, R.; Maity, A.; Chanda, D. K.; Das, S.; Ghosh, S.; Basu, R.; Das, S. Effect of Microstructural Evolution of Natural Kaolinite Due to MWCNT Doping: A Futuristic 'Green Electrode' for Energy Harvesting Applications. *J. Mater. Sci.: Mater. Electron.* **2022**, *33* (17), 13826–13842.
- (12) Ma, W.; Yao, B.; Zhang, W.; He, Y.; Yu, Y.; Niu, J. Fabrication of PVDF-Based Piezocatalytic Active Membrane with Enhanced Oxytetracycline Degradation Efficiency through Embedding Few-Layer E-MoS₂ Nanosheets. *Chem. Eng. J.* **2021**, *415*, 129000.
- (13) Surmenev, R. A.; Orlova, T.; Chernozem, R. V.; Ivanova, A. A.; Bartasyte, A.; Mathur, S.; Surmeneva, M. A. Hybrid Lead-Free Polymer-Based Nanocomposites with Improved Piezoelectric Response for Biomedical Energy-Harvesting Applications: A Review. *Nano Energy* **2019**, *62*, 475–506.
- (14) Ali, A.; Zhao, J.; Yao, R.; Ahmed, S.; Wang, L.; Guo, B.; Rao, W. F.; Yang, Y. Stimulated Piezotronic Decontamination Using Cu₂MgSnS₄ Modified BaTiO₃. *Mater. Today Energy* **2021**, *21*, 100717.
- (15) Sun, J.; Guo, H.; Ribera, J.; Wu, C.; Tu, K.; Binelli, M.; Panzarasa, G.; Schwarze, F. W. M. R.; Wang, Z. L.; Burgert, I. Sustainable and Biodegradable Wood Sponge Piezoelectric Nanogenerator for Sensing and Energy Harvesting Applications. *ACS Nano* **2020**, *14* (11), 14665–14674.
- (16) Meng, N.; Liu, W.; Jiang, R.; Zhang, Y.; Dunn, S.; Wu, J.; Yan, H. Fundamentals, Advances and Perspectives of Piezocatalysis: A Marriage of Solid-State Physics and Catalytic Chemistry. *Prog. Mater. Sci.* **2023**, *138*, 101161.
- (17) Jhang, S. R.; Lin, H. Y.; Liao, Y. S.; Chou, J. P.; Wu, J. M. Local Dipole Enhancement of Space-Charge Piezophototronic Catalysts of Core-Shell Polytetrafluoroethylene@TiO₂ Nanospheres. *Nano Energy* **2022**, *102*, 107619.
- (18) Yu, S.; Tai, Y.; Milam-Guerrero, J. A.; Nam, J.; Myung, N. V. Electrospun Organic Piezoelectric Nanofibers and Their Energy and Bio Applications. *Nano Energy* **2022**, *97*, 107174.
- (19) Roy, J.; Mukhopadhyay, L.; Bardhan, S.; Mondal, D.; Ghosh, S.; Chakraborty, S.; Bag, N.; Roy, S.; Basu, R.; Das, S. Piezo-Responsive Bismuth Ferrite Nanoparticle-Mediated Catalytic Degradation of Rhodamine B and Pathogenic E. Coli in Aqueous Medium and Its Extraction Using External Magnetic Stimulation after Successful Treatment. *Dalton Trans.* **2022**, *51* (44), 16926–16936.
- (20) Bardhan, S.; Roy, S.; Chanda, D. K.; Das, S.; Pal, K.; Chakraborty, A.; Basu, R.; Das, S. Microstructure and Dielectric Properties of Naturally Formed Microcline and Kyanite: A Size-Dependent Study. *Cryst. Growth Des.* **2019**, *19* (8), 4588–4601.
- (21) Salma-Ancane, K.; Sceglows, A.; Tracuma, E.; Wychowanec, J. K.; Aunina, K.; Ramata-Stunda, A.; Nikolajeva, V.; Loca, D. Effect of Crosslinking Strategy on the Biological, Antibacterial and Physicochemical Performance of Hyaluronic Acid and ϵ -Polylysine Based Hydrogels. *Int. J. Biol. Macromol.* **2022**, *208*, 995–1008.
- (22) Ghosh, S.; Mondal, D.; Roy, S.; Roy, J.; Bardhan, S.; Mazumder, A.; Bag, N.; Basu, R.; Das, S. Water Flow and Finger-Tapping Mediated Piezoelectric Energy Generation Using a Natural Hematite-Based Flexible PVDF-HFP Membrane. *J. Mater. Chem. C* **2023**, *11*, 13418–13428.
- (23) Roy, S.; Bardhan, S.; Chanda, D. K.; Roy, J.; Mondal, D.; Das, S. In Situ-Grown CDOT-Wrapped Boehmite Nanoparticles for Cr(VI) Sensing in Wastewater and a Theoretical Probe for Chromium-Induced Carcinogen Detection. *ACS Appl. Mater. Interfaces* **2020**, *12* (39), 43833–43843.
- (24) Zou, W.; Dong, J.; Ji, M.; Wang, B.; Li, Y.; Yin, S.; Li, H.; Xia, J. Synthesis of Bi₂₅FeO₄₀ Nanoparticles with Oxygen Vacancies via Ball Milling for Fenton Oxidation of Tetracycline Hydrochloride and Reduction of Cr(VI). *ACS Appl. Nano Mater.* **2023**, *6* (6), 4309–4318.
- (25) Sachan, A.; Penumadu, D. Identification of Microfabric of Kaolinite Clay Mineral Using X-Ray Diffraction Technique. *Geotech. Geol. Eng.* **2007**, *25* (6), 603–616.
- (26) Badatya, S.; Kumar, A.; Sharma, C.; Srivastava, A. K.; Chaurasia, J. P.; Gupta, M. K. Transparent Flexible Graphene Quantum Dot-(PVDF-HFP) Piezoelectric Nanogenerator. *Mater. Lett.* **2021**, *290*, 129493.
- (27) Sasmal, A.; Senthilnathan, J.; Arockiarajan, A.; Yoshimura, M. Two-Dimensional Metal-Organic Framework Incorporated Highly Polar PVDF for Dielectric Energy Storage and Mechanical Energy Harvesting. *Nanomaterials* **2023**, *13* (6), 1098.
- (28) Pratihari, S.; Medda, S. K.; Sen, S.; Devi, P. S. Tailored Piezoelectric Performance of Self-Polarized PVDF-ZnO Composites by Optimization of Aspect Ratio of ZnO Nanorods. *Polym. Compos.* **2020**, *41* (8), 3351–3363.
- (29) Panicker, S. S.; Rajeev, S. P.; Thomas, V. Impact of PVDF and Its Copolymer-Based Nanocomposites for Flexible and Wearable Energy Harvesters. *Nano-Struct. Nano-Objects* **2023**, *34*, 100949.
- (30) Jozanikohan, G.; Abarghoeei, M. N. The Fourier Transform Infrared Spectroscopy (FTIR) Analysis for the Clay Mineralogy Studies in a Clastic Reservoir. *J. Pet. Explor. Prod. Technol.* **2022**, *12* (8), 2093–2106.
- (31) Sahu, D. K.; Rai, J.; Rai, M. K.; Banjare, M. K.; Nirmal, M.; Wani, K.; Sahu, R.; Pandey, S. G.; Mundeja, P. Detection of Flonicamid Insecticide in Vegetable Samples by UV-Visible Spectrophotometer and FTIR. *Results Chem.* **2020**, *2*, 100059.
- (32) Solonenko, D.; Lan, C.; Schmidt, C.; Stoeckel, C.; Hiller, K.; Zahn, D. R. T. Co-Sputtering of Al_{1-x}Sc_xN Thin Films on Pt(111): A Characterization by Raman and IR Spectroscopies. *J. Mater. Sci.* **2020**, *55* (36), 17061–17071.
- (33) Cai, L.; Chen, J.; Chang, L.; Liu, S.; Peng, Y.; He, N.; Li, Q.; Wang, Y. Adhesion Mechanisms and Electrochemical Applications of Microorganisms onto a GO-NH₂ Modified Carbon Felt Electrode Material. *Ind. Eng. Chem. Res.* **2021**, *60* (11), 4321–4331.
- (34) Lin, Y.; Zhang, Y.; Zhang, F.; Zhang, M.; Li, D.; Deng, G.; Guan, L.; Dong, M. Studies on the Electrostatic Effects of Stretched PVDF Films and Nanofibers. *Nanoscale Res. Lett.* **2021**, *16* (1), 79.
- (35) Ren, L.; Yang, L.; Zhang, S.; Li, H.; Zhou, Y.; Ai, D.; Xie, Z.; Zhao, X.; Peng, Z.; Liao, R.; Wang, Q. Largely Enhanced Dielectric

Properties of Polymer Composites with HfO_2 Nanoparticles for High-Temperature Film Capacitors. *Compos. Sci. Technol.* **2021**, 201, 108528.

(36) Nasrallah, D. A.; El-Metwally, E. G.; Ismail, A. M. Structural, Thermal, and Dielectric Properties of Porous PVDF/ $\text{Li}_4\text{Ti}_5\text{O}_{12}$ Nanocomposite Membranes for High-Power Lithium-Polymer Batteries. *Polym. Adv. Technol.* **2021**, 32 (3), 1214–1229.

(37) Kadir, E. S.; Gayen, R. N.; Paul, R.; Biswas, S. Interfacial Effects on Ferroelectric and Dielectric Properties of GO Reinforced Free-Standing and Flexible PVDF/ ZnO Composite Membranes: Bias Dependent Impedance Spectroscopy. *J. Alloys Compd.* **2020**, 843, 155974.

(38) Das, N.; Sarkar, D.; Saikh, M. M.; Biswas, P.; Das, S.; Hoque, N. A.; Ray, P. P. Piezoelectric Activity Assessment of Size-Dependent Naturally Acquired Mud Volcano Clay Nanoparticles Assisted Highly Pressure Sensitive Nanogenerator for Green Mechanical Energy Harvesting and Body Motion Sensing. *Nano Energy* **2022**, 102, 107628.

(39) Ghosh, S.; Bardhan, S.; Mondal, D.; Sarkar, D.; Roy, J.; Roy, S.; Basu, R.; Das, S. Natural Hematite-Based Self-Poled Piezo-Responsive Membrane for Harvesting Energy from Water Flow and Catalytic Removal of Organic Dye. *Ceram. Int.* **2023**, 49 (9), 14710–14718.

(40) Bagchi, B.; Hoque, N. A.; Janowicz, N.; Das, S.; Tiwari, M. K. Re-Useable Self-Poled Piezoelectric/Piezocatalytic Films with Exceptional Energy Harvesting and Water Remediation Capability. *Nano Energy* **2020**, 78, 105339.

(41) Meng, F.; Wang, Z.; Huo, B.; Wang, J.; Li, D.; Hao, W.; Ma, W.; Qi, J.; Cui, P.; Zhu, Z.; Wang, Y. Efficient Degradation of Chlortetracycline in Water by Ultrasound Activation of Flexible ZnCoO Doped PVDF Membranes with High β Phase. *Appl. Surf. Sci.* **2023**, 619, 156782.

(42) Wang, Z.; Xiang, M.; Huo, B.; Wang, J.; Yang, L.; Ma, W.; Qi, J.; Wang, Y.; Zhu, Z.; Meng, F. A Novel $\text{ZnO}/\text{CQDs}/\text{PVDF}$ Piezoelectric System for Efficiently Degradation of Antibiotics by Using Water Flow Energy in Pipeline: Performance and Mechanism. *Nano Energy* **2023**, 107, 108162.

(43) Wang, Z.; Tong, W.; Li, L.; Li, Y.; Yang, J.; Chai, M.; Cao, T.; Wang, X.; Wang, X.; Zhang, X.; Li, X.; Zhang, Y. Piezocatalytic Effect and Mechanism of RGO/PVDF-HFP Porous Film Driven by Water Flow. *Sep. Purif. Technol.* **2023**, 306, 122768.

(44) Wang, S.; Tong, W.; Li, Y.; Zhang, P.; Liu, Y.; Chen, Y.; Zhang, Y. Contributions of Piezoelectricity and Triboelectricity to a Hydroxyapatite/PVDF-HFP Fiber-Film Nanogenerator. *Nano Energy* **2023**, 105, 108026.

(45) Yi, J.; Song, Y.; Cao, Z.; Li, C.; Xiong, C. Gram-Scale Y-Doped ZnO and PVDF Electrospun Film for Piezoelectric Nanogenerators. *Compos. Sci. Technol.* **2021**, 215, 109011.

(46) Gavahian, M.; Manyatsi, T. S.; Morata, A.; Tiwari, B. K. Ultrasound-Assisted Production of Alcoholic Beverages: From Fermentation and Sterilization to Extraction and Aging. *Compr. Rev. Food Sci. Food Saf.* **2022**, 21 (6), 5243–5271.

(47) Li, J.; Liu, D.; Ding, T. Transcriptomic Analysis Reveal Differential Gene Expressions of Escherichia Coli O157:H7 under Ultrasonic Stress. *Ultrason. Sonochem.* **2021**, 71, 105418.

(48) Wang, A.; Shao, M.; Yang, F.; Shao, C.; Chen, C. Preparation and Properties of Antibacterial PVDF Composite Thin Films. *Eur. Polym. J.* **2021**, 160, 110803.

(49) Singh, G.; Sharma, M.; Vaish, R. Flexible $\text{Ag}@\text{LiNbO}_3/\text{PVDF}$ Composite Film for Piezocatalytic Dye/Pharmaceutical Degradation and Bacterial Disinfection. *ACS Appl. Mater. Interfaces* **2021**, 13 (19), 22914–22925.

(50) Shuai, C.; Liu, G.; Yang, Y.; Qi, F.; Peng, S.; Yang, W.; He, C.; Wang, G.; Qian, G. A Strawberry-like Ag-Decorated Barium Titanate Enhances Piezoelectric and Antibacterial Activities of Polymer Scaffold. *Nano Energy* **2020**, 74, 104825.

(51) Zhang, D.; Chen, L.; Xu, M.; Feng, G.; Zhang, B.; Zhang, H.; Yang, C.; Yu, Q.; Wang, L. G. Visible-Light Responsive PVDF/Carbon Sphere/ TiO_2 Membrane for Dye Scavenging and Bacteria Inactivation. *Appl. Surf. Sci.* **2022**, 605, 154755.

DST-SERB Sponsored
One Day Workshop on Material Synthesis & Characterization Techniques

Organized by: Department of Physics, Jadavpur University, Kolkata-700032



Certificate of Presentation

This Certificate is awarded to

*Mr./ Ms. **Dhananjay Mondal** for successfully presenting a
paper entitled **Crystallographic Analysis**. in the Workshop organized by
Department of Physics, Jadavpur University, Kolkata on 29th February 2020.*

Sd/- 29/02/2020

Head, Department of Physics, Jadavpur University



National Seminar on
New Directions in Physical Sciences 2020 (NDPS 2020)
Organised by
Department of Physics, Jadavpur University
In association with
Indian Photobiology Society



Certificate of Participation

This is to certify that Prof./Dr./Mr./Ms. Shaaniraj Mondal of

Jadavpur University has participated/presented a poster entitled Multifunctional Fluorescence Based Nanosensor for Detection and Removal of Cr(VI) at the seminar on 'New Directions in Physical Sciences 2020' at Jadavpur University, Kolkata on February 25, 2020.

Dr. Soumen Mondal
Dr. Soumen Mondal
Convener, NDPS 2020

Mitali Mondal
Prof. Mitali Mondal
Convener, NDPS 2020

Prof. Sukhen Das
25/02/2020
Prof. Sukhen Das
Head, Dept. of Physics



ASSOCIATION OF INDIAN UNIVERSITIES, DELHI
&
THE ASSAM ROYAL GLOBAL UNIVERSITY, GUWAHATI



THE ASSAM
ROYAL GLOBAL UNIVERSITY
GUWAHATI

ANVESHAN 2022

EAST ZONE STUDENT RESEARCH CONVENTION

CERTIFICATE

This is to certify that

Mr./Ms./Dr. *Dhananjay Mondal*

Son/Daughter of Shri *Thakurpada Mondal* enrolled in. *Ph.D*

Department / Faculty of *Physics* of *Jadavpur*

..... University / Institute participated in East Zone Student Research

Convention held at The Assam Royal Global University, Guwahati during March 01-02, 2023.

His/Her proposal/project entitled *"Vikram water pollution & energy crisis"*

under the category of *BASIC SCIENCES - 2nd*

Vis
Dr. Usha Rai Negi
Assistant Director (Research)
Association of Indian Universities,
New Delhi

pm
Prof. (Dr.) Rohit Singh
Pro Vice-Chancellor
Zonal Coordinator- Anveshan 22
The Assam Royal Global University, Guwahati

shsh
Prof. (Dr.) S.P. Singh
Vice Chancellor
The Assam Royal Global University
Guwahati



ANVESHAN



Ganpat University
॥ विद्यया समाजोत्कर्षः ॥

National Student Research Convention

March 16-17, 2023

Certificate of Participation

This is to Certify that Mr / Ms. Shrawanjoy Mondal
affiliated with Jodhpur University
_____ has participated in Anveshan: National

Student Research Convention organized by Association of Indian Universities, New Delhi and hosted by Ganpat University, Gujarat during

March 16-17, 2023. He/She presented a Research Project titled Vikroty : on "oil - in - oil" module
under the category of For combating water pollution and energy crisis
Basic Sciences

Kiran Amin

Dr. Kiran Amin
Anveshan Co-convenor
Deputy Pro Vice Chancellor
Ganpat University

Ajay Gupta

Dr. Ajay Gupta
Anveshan Convenor
Director - R&D
Ganpat University

Amarendra Pani

Dr. Amarendra Pani
Anveshan Convenor
Joint Director (Research)
Association of Indian Universities

Mahendra Sharma

Dr. Mahendra Sharma
Pro-Chancellor & Director General
Ganpat University



PROJECT SET



**MANIPAL UNIVERSITY
JAIPUR**

(University under Section 2(f) of the UGC Act)



Webinar on “X-ray Diffraction: Principle and Applications”
6th July, 2021

under

Academia-Industry Symbiotic Alliance (AISA), Department of Physics

&

Open Research Workshop Series (ORWS), Directorate of Research

Manipal University Jaipur

in association with Rigaku Corporation, Japan

Certificate of Participation

Presented to

Dhananjay Mondal
Jadavpur University

Dr. Ashima Bagaria
HoD, Physics, MUJ

Dr. Roheet Bhatnagar
Director, DoR, MUJ

Mr. Taisuke Yoshiki
Rigaku, Japan

Dr. S. K. Jain
Convener

Dr. Nilanjan Halder
Convener



SRM INSTITUTE OF SCIENCE AND TECHNOLOGY

Kattankulathur - 603 203, Tamil Nadu, India.

7th International Conference on Nanoscience and Nanotechnology (ICONN-2023)

(Virtual Conference) March 27 - 29, 2023

Certificate of Participation

This is to certify that Mr. / Ms. / Dr. **Dhananjay Mondal** has participated and presented a paper entitled **MWCNT doped natural clay: A promising separator material for energy storage application** in the 7th International Conference on Nanoscience and Nanotechnology (ICONN-2023) organized by Department of Physics and Nanotechnology, SRM IST, India during March 27- 29, 2023, in association with Shizuoka University, Japan; National Yang Ming Chiao Tung University, Taiwan; GNS Science, New Zealand; University of Rome Tor Vergata, Italy; Asian Consortium on Computational Materials Science (ACCMS), Japan; Indian Ceramic Society; Indian Physics Association (IPA); Solar Energy Society of India (SESI); Innovation, Science & Technology Foundation - Tirupati (ISTF-T) and co-sponsored by Defence Research and Development Organization (DRDO), India; Council of Scientific & Industrial Research (CSIR), India; The Indian Science Congress Association (ISCA) and Springer Nature.



Head
Department of Physics and Nanotechnology
SRM IST, KTR



Chairperson
School of Applied Sciences
SRM IST, KTR





**A one-day seminar in
“COMMEMORATION OF CENTENARY BIRTH
ANNIVERSARY OF PROF. SHYAMAL SENGUPTA”**



Condensed Matter Physics Research Centre
Estd. 1990

Organised by

Condensed Matter Physics Research Centre & Department of Physics, Jadavpur University

CERTIFICATE OF PARTICIPATION

This certificate has been awarded to **Dhananjoy Mondal** of Dept. Of
Physics, Jadavpur University in appreciation of his poster presentation
titled **Natural rock-based polymeric membrane: an “all-in-one”**

module for combating water pollution and energy crisis

at the one day seminar in “Commemoration Of Centenary Birth Anniversary Of Prof.
Shyamal Sengupta” held at Jadavpur University, Kolkata, India on 7th February 2024.

Atananta
07.02.2024

Baldeep Dey
7/02/2024

H.O.D. Dept. Of Physics, JU

Co-Ordinator CMPRC, JU